THE PHYSICAL UNDERSTANDING OF THE USE OF COATINGS TO MITIGATE HYPERVELOCITY GOUGING CONSIDERING REAL TEST SLED DIMENSIONS

DISSERTATION

Andrew Gerard Szmerekovsky
Major, USAF

AFIT/DS/ENY/04-06

DEPARTMENT OF THE AIR FORCE
AIR UNIVERSITY

AIR FORCE INSTITUTE OF TECHNOLOGY

Wright-Patterson Air Force Base, Ohio

The views expressed in this dissertation are those of the author and do not reflect the official policy or position of the Department of Defense or the United States Government.

AFIT/DS/ENY/04-06

THE PHYSICAL UNDERSTANDING OF THE USE OF COATINGS TO MITIGATE HYPERVELOCITY GOUGING CONSIDERING REAL TEST SLED DIMENSIONS

DISSERTATION

Presented to the Faculty

Graduate School of Engineering and Management

Air Force Institute of Technology

Air University

Air Education and Training Command

in Partial Fulfillment of the Requirements for the

Degree of Doctor of Philosophy

Andrew Gerard Szmerekovsky, B.S.E., M.S.E.

Major, USAF

September 2004

AFIT/DS/ENY/04-06

THE PHYSICAL UNDERSTANDING OF THE USE OF COATINGS TO MITIGATE HYPERVELOCITY GOUGING CONSIDERING REAL TEST SLED DIMENSIONS

DISSERTATION

Andrew Gerard Szmerekovsky, B.S.E., M.S.E.

Major, USAF

Approved:

Dr. Anthony N. Palazotto Commitee Chairman	Date
Dr. Mark E. Oxley Dean's Representative	Date
Dr. William P. Baker Committee Member	Date
Dr. Robert A. Brockman Committee Member	Date
Dr. Michael D. Hooser Committee Member	Date

Robert A. Calico, Jr
Dean

AFIT/DS/ENY/04-06

Abstract

In the investigation of high energy impact brought about at velocities exceeding the speed of sound, temperature distribution may exceed ranges in which changes in material phase occur. The research focuses on evaluating the effects of temperature and coatings on hypervelocity gouging initiation by considering friction and heat transfer. The impact velocity is evaluated over ranges much greater than the speed of sound.

A dimensional analysis with accompanying numerical investigation is conducted. A simplified model of the real test sled is created that allows test sled dimensions to be converted to a numerical model for analysis. The dimensional analysis is used as a means of directly applying the numerical results to real test sled conditions. Similarity principles are studied and tested by comparing the results from scaled numerical models. Strain rate and other time dependent parameters are not scaled, but the effect of these parameters may be quantified and studied further. The dimensional analysis also provides a comprehensive approach to the test sled system by providing parameters whose affect on the final solution may be studied and quantified. The scaling parameters may also be used to determine which quantities must be modified so that results apply. Time and length scales for studying the problem are also determined using the dimensional analysis process.

The study allows heat to flow and a thermal environment to be developed through a solution for frictional characteristics. The effect on gouging of a thermal environment brought about by friction and irreversible thermodynamics is studied. Phase changes of the coating, slipper, and rail materials is also investigated through the use of phase diagrams in comparison to the results.

The use of coatings in mitigating damage to materials under high energy impact is also studied. The research is directed toward a scientific approach in determining the potential advantage of specific coatings acting under shock loading conditions and understanding the physics behind these advantages. Friction and heat generation effects are considered for rails with and without a coating.

AFIT/DS/ENY/04-06

To my wife, for her loving patience and endurance

To my children, for the time they went without me

To my parents, their sacrifices in life gave me this opportunity

To God, from whom all blessings flow

Acknowledgements

I would be grossly negligent if I didn't acknowledge my humble advisor, Dr. Anthony Palazotto. I have been extremely blessed to have had Dr. Palazotto as my dissertation advisor. I hope when all is said and done we might be friends and not just student and teacher. I can't say enough about him. I also acknowledge and admire the time, effort, and down-to-earth mathematical sense of Dr. William Baker. His advice and input in collaboration with Dr. Palazotto helped keep me on track when we "couldn't see the forest for the trees." I also acknowledge the hard work, dedication, and genuine genial manner of Dr. Robert Brockman of the University of Dayton. He always hit the mark with his questions, covering important details I missed, and is another committee member I would be honored to work with in the future. Dr. Michael Hooser of the Holloman High Speed Test Track must also be acknowledged. He is also a dedicated committee member and deserves credit for asking the hard questions that resulted in my work to make the research applicable to the real test sled system. He is both affable and a great collaborator. His operational expertise in the HHSTT is without equal. I also acknowledge the inputs and special assistance of Dr. Paul Taylor, Dr. Stewart Silling, as well as Dr. Ron Hinrichsen, formerly of the ASC MSRC. This research has been sponsored by the Air Force Office of Scientific Research with Dr. Dean Mook and Dr. Neal Glassman as program managers.

Of course, I lovingly acknowledge the sacrifices of my wife and children. They have suffered much these past three years. They have gone countless hours without me so that I may accomplish this work. Without them, I would have simply been a PhD student, not those things that I am most proud to be called, husband and father. And finally, but most of all, I acknowledge God as the source of all wisdom, knowledge, and grace. Without Him, I can do nothing.

Andrew G. Szmerekovsky

Table of Contents

List of Figures

List of Tables

Nomenclature

Symbol — Page

Symbol Page

Symbol Page

Symbol Page

Symbol	Page
B strain displacement matrix	3-5
B strain displacement matrix	3-8
J Jacobian	3-8
$d\mathcal{V}$ calculated differential volume	3-8
$d\mathcal{V}_o$ differential reference volume	3-8

THE PHYSICAL UNDERSTANDING OF THE USE OF COATINGS TO MITIGATE HYPERVELOCITY GOUGING CONSIDERING REAL TEST SLED DIMENSIONS

I. Introduction to the Problem

High energy impact phenomena and failure is an important area of interest for the Air Force today. Specifically, the Air Force Office of Scientific Research (AFOSR), the Air Force Research Laboratory (AFRL), and AFRL's Holloman AFB High Speed Test Track (HHSTT) all have an interest in pushing the state of the art of high energy impact phenomena.

The overall system to be evaluated is depicted in Figure 1.1. The rocket sled shown in the figure is accelerated at high speed. It is attached to the rail by a slipper. The rocket sled is a vehicle used to obtain a velocity of exceptional magnitude in order to test specific payload components. The rocket depicted in Figure 1.1(a) is of a 192-pound, fully instrumented Missile Defense Agency payload tested on April 29, 2003 which validated Holloman's high-speed test track hypersonic upgrades and also set a world land speed record. The four-stage, rail-bound rocket sled reached Mach 8.5 or 6,416 mph (9410 fps). Figure 1.1(b) shows a detail of the slipper and how it is shaped around the rail.

At the HHSTT, the goal is to operate up to Mach 10 in air, or around 10,000 fps (3 km/sec). However, the damage mechanism called gouging is a limiting factor to achieving this goal. The effects of gouging vary from requiring repair to the rail to catastrophic failure. The rocket is held to the rail using a slipper. The slipper is not tight, leaving a small gap on one side or another. This results in the sled riding in free flight, subject to unsteady aerodynamic forces and rail misalignments with intermittent contact on the rail and rotations of the sled in roll, pitch, and yaw. The impact between the slipper and rail sometimes results in gouging. Gouges are characterized by the shallow removal of material from the rail and the slipper and has been observed to occur at sled speeds greater than 1.5 km/sec.

Two idealizations of the process leading to gouging have been used in the past. The slipper can be assumed to impact the rail at a pitch angle. In this case, the slipper is imparted with both horizontal and vertical velocity. This is called a vibratory or oblique impact because it simulates an impact that might occur during vibration of the test sled. The other case assumes the slipper impacts an asperity on the rail at some horizontal velocity. The asperity can vary in size, but is typically circular or spherical in shape. The asperity simulates dust, an imperfection in the rail, or ejecta from a lead slipper. Both examples of impact can result in damage to the rail and slipper known as gouging. Gouging takes the teardrop form shown in Figures 1.1(c) and 1.1(d).

(a) **Pre-test photo of high speed sled with full slipper.**

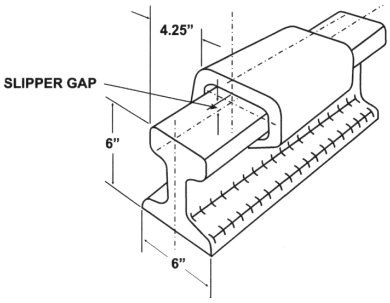

(b) **Slipper and rail configuration in the subsequent development.**

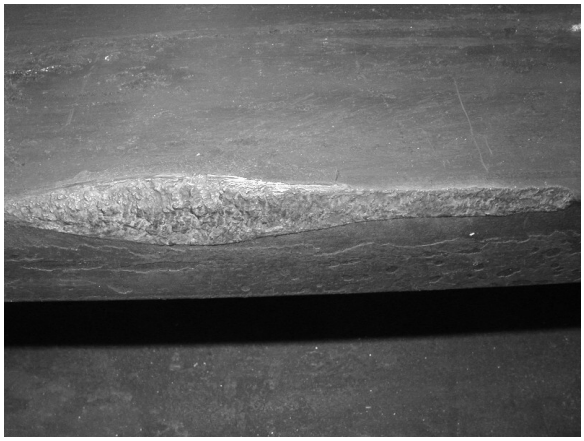

(c) **Gouge on corner of a hematite coated.**

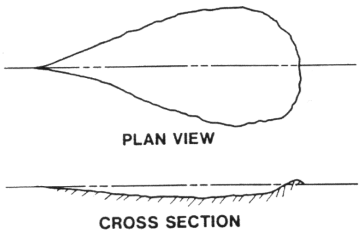

(d) **Hypervelocity gouging schematic.**

Figure 1.1 **The physical problem to be evaluated.**

1.1 The Gouging Phenomena

Laird [7], studied the phenomenon and defined gouging the following way:

> Gouging is a failure mode found in metals undergoing hypervelocity sliding contact. When inertial forces are so great that the materials exhibit fluid like behavior, shock induced pressure creates a region of plasticity under the location of impact. Tangential motion of one body with respect to the other deforms or shears material at these points and results in deformation of the parallel surfaces that impinge on each other in a continuous interaction. Once this interaction region grows large enough to shear the surface of one of the materials from the bulk material, a gouge has been formed. Continuous interaction of the materials in the region of the gouge will cause the gouge to grow further until the materials are no longer in contact.[7]

In the HHSTT gouging problem, the material sound speed (which is a function of the modulus of elasticity and the density) of the slipper made of VascoMax 300 Steel is approximately 5 km/sec. The speed of the sled is approximately 3 km/sec (i.e., 10,000 fps). At low velocity, one may consider that loads applied to a 0.2 m (i.e., 8 inch) long slipper affects the whole slipper. It takes about 40 μsecs for an applied load to be propagated throughout the length of the 0.2 m slipper. But as the sled approaches 3 km/sec, the slipper is displaced 0.12 m (about half its length) before the load is applied across the whole slipper. In this case, the application of stress must be considered as propagating with respect to time.

Current gouge reduction methodology involves altering the rail and slipper materials. Since the rail is a large infrastructure, material changes are made through the use of rail coatings. Gouging is an interaction (as shown in Figure 1.2); so one material is not necessarily the sole factor in creating gouging conditions. Gouging requires plastic flow of both materials and the subsequent formation of material "jets".

Material "jets" are defined as plastic deformations of large strain rate that are characteristically long and thin. They are material interactions that occur due to mutual penetration of rail and slipper material into one another after deformation of parallel surfaces that impinge on each other. The initial slipper penetration into the rail and the rail hump deformation at impact time step of 0.5 microseconds (see Figure 1.3(a)) leads to

sufficient horizontal impact to cause the creation of material jets later in the analysis of an oblique impact (see Figure 1.3(b)).

Another essential characteristic of the gouging phenomenon is the material that becomes separated from the bulk material of the slipper and rail during formation of gouging. These pieces of material that separate due to failure are known as "ejecta". Accurate analysis of the hypervelocity problem must trace formation, velocity, and final position of ejecta.

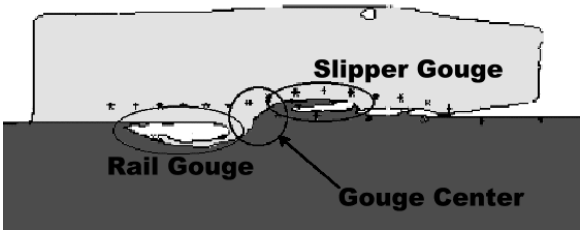

Figure 1.2 **Gouging is an interaction of slipper and rail materials.**

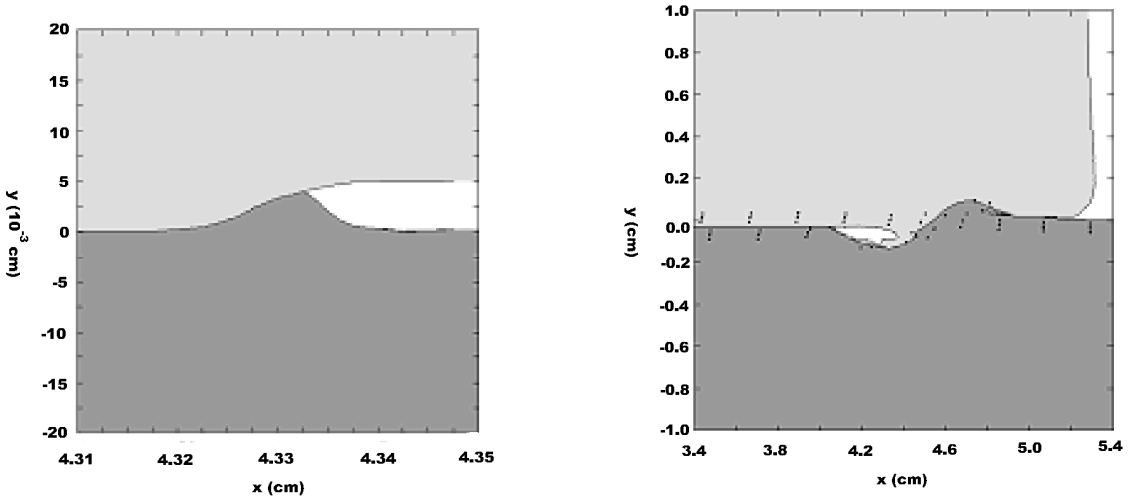

(a) **Hump development.** (b) **Creation of material jets.**

Figure 1.3 **Formation of gouging.**

If the materials are largely dissimilar, it is not expected that both materials will exhibit plasticity, flow, and jet formation at the same time. Probably, one material would fail before the other. Gouging will not form until both materials fail. Under certain

conditions, it is possible that the behavior of the first failed material may aid in preventing failure of the other material. If the first failed material responds in such a way that it prevents hump deformation, the horizontal component of impact, or the build up of pressure at the interaction region, then gouging may not occur.

There is something else to consider. Is an adiabatic assumption the best model of heat transfer to consider for the environment in which gouging occurs? Most likely, an adiabatic assumption is practical for the event of gouging. However, how does the environment brought about by a shear wave affect the onset of gouging? Might plasticity prior to the gouge event create thermal energy that must be considered? Should this be modelled as a nonequilibrium thermodynamic state? Might the flow of heat from the various plasticity cells of the travelling slipper affect the second law of thermodynamics thereby changing the equation of state? Might this last idea reflect more on the state of the material before the gouge event occurs rather than after it occurs? This idea leads to the importance of stress wave propagation. In addition, can one ever appreciate the problem without considering the appropriate dimensions? This leads to the need for a dimensional analysis using the Buckingham Pi Theorem approach to scaling the problem.

Newtonian dynamics involves rigid and deformable bodies under quasi-static conditions. Impact dynamics is very different from this. First of all, the importance of inertia effects must be considered in all of the governing equations based on the fundamental conservation laws of mechanics and physics. Also, under hypervelocity speeds, hydrodynamic pressure dominates the behavior of solids undergoing impact. At these very high pressures, metals behave as inviscid fluids [5].

Traditional computational methods in structural mechanics are based upon Newtonian mechanics in which the forcing function $F(t)$ is known in terms of application. Thus, the system of equations using traditional equations of motion can be represented by

$$F(t) = [M]\{\ddot{u}\} + [C]\{\dot{u}\} + [k_{nonlinear} + k_{linear}]\{u\} \tag{1.1}$$

where $[M]$ is the mass matrix, $[C]$ is the viscous damping matrix, $[k_{nonlinear} + k_{linear}]$ is the stiffness matrix containing both linear and nonlinear terms, $\{\ddot{u}\}$ is the acceleration vector,

$\{\dot{u}\}$ is the velocity vector, $\{u\}$ is the displacement vector, and $F(t)$ is the forcing function (a.k.a. vector of the applied forces).

Generally speaking, the $F(t)$ term in equation 1.1 is taken to be applied slowly. This is judged simply by the fact that there is a small number of oscillations once the maximum load is obtained. Loadings are considered fast when they are applied on a timescale comparable to the time it takes a wave to travel a characteristic dimension of the structure as compared to the wave speed, $c_o = \sqrt{\frac{E}{\rho}}$. In this equation c_o is the elastic wave speed, E is the elastic modulus, which is the linear elastic slope of the equivalent uniaxial stress-strain curve of the material, and ρ is the density of the material.

Thus, another important area of impact dynamics that makes it different from classical mechanics is stress wave propagation. This includes the fact that impact events are transient. For high velocity impacts, stresses may exceed the yield strength and then both plastic and elastic waves will be generated. In order to bear the stresses, the solid materials must deform. Compression will also force the material particles closer together. This process however, requires both time and movement. When subject to an instantaneous pressure, the pressure is initially supported by inertia. As the particles near the pressure disturbance begin to move, they generate stress and begin to accelerate the particles they are moving toward. This becomes the front of the stress wave. The stress wave propagates through the material, changing particle velocities and the states of stress and strain.

Once the stress between adjacent particles becomes equal to the applied pressure, relative motion ceases and the pressure is supported entirely by compression. In most solids, the wave fronts are only a few molecules thick and can be treated as discontinuities. The initial stress wave generated by the impact propagates into unstressed material at the elastic wave velocity of

$$c_o = \sqrt{\frac{E}{\rho}} \tag{1.2}$$

where E is the elastic modulus, which is the linear elastic slope of the equivalent uniaxial stress-strain (σ - ε) curve of the material, and ρ is the density of the material.

Once the material becomes plastic due to high stress gradients, plastic stress waves are allowed to travel at the plastic wave velocity of

$$c = \sqrt{\frac{d\sigma/d\varepsilon}{\rho}} \tag{1.3}$$

where, c, is the speed of sound and $d\sigma/d\varepsilon$ is the local slope of the equivalent uniaxial stress-strain curve. This slope varies within the plastic region that lies past the proportional limit. Behavior of this material dependent slope determines behavior of the stress waves and whether a shock forms through wave coalescence or the waves simply disperse throughout the material [5].

This physical description shows that wave propagation is also an important factor in ballistic and rapidly applied loads. This is a consequence of the major event of deformation occurring in a very short time span under high intensity loads. Likewise, the strain rates and deformations are extremely high. Because of the potential for a shock wave, the mass matrix $[M]$, the viscous damping matrix $[C]$, and the displacements $\{u\}$ change with time, leading to high strain rates and viscoplasticity.

In addition, the relation between deformation and the state of stress (i.e., the constitutive model) is not only time dependent, but nonlinear. Note that it is commonly assumed that events in this time scale are isothermal or adiabatic when compared to the time it takes for thermal energy to diffuse in the material. Therefore, one may consider a solution from a continuum point of view in which the conservation equations, constitutive equations, and equation of state are integrated together in an energy-fluids type approach. This approach is taken in codes that are known as "hydrocodes."

There are a number of aspects of the process that are important. At the moment of impact, how does one know whether a shock wave forms or not? How does one know whether the material plasticizes or not? What is the state of the stress, temperature, and deformation of the material during and after the impact? To characterize materials under high energy impact, various models have been developed relating particle velocity, stress wave formation and propagation, yield strength, strain rate, plastic strain, temperature, energy, density, pressure, and deviatoric stress. These models can be lumped into a cate-

gory called material models. The material models can further be broken into constitutive models and equation of state models.

In high strain, high strain-rate problems, the behavior of materials are normally modeled by decomposing the stress into spherical stress (pressure) and deviatoric stress (shear and plasticity). The two formulations can be treated independently because plastic flow has been found to be independent of pressure at low pressures in solids. The hydrostatic behavior is also assumed to be strain-rate independent. The mathematical relationship of the hydrostatic components of stress (pressure) and strain (density) is handled by the equation of state. It must also consider temperature (or energy) [8].

Because the three conservation equations have more unknown parameters than equations, the pressure, density, and temperature relations provided by the equation of state (EOS) are coupled with the solution of the conservation equations. Furthermore, when considering the presence of shock waves, the EOS may include the pressure, density, and temperature/energy relationships across a shock wave. In this case, the EOS also deals with shock velocity, U_s, and particle velocity, u_P.

The EOS is usually considered in a solid mechanics solution to be linear. But in fluid flow and impact dynamics, the materials are compressible and spherical stress, or pressure, can vary. In the hypervelocity regime, the form of the equation of state is important in predicting the dynamics, and several forms of the equation of state have been specialized for this purpose.

The material response to an applied stress is accomplished through constitutive models. These models define the stress and strain relationships in a material [5]. If stresses above the yield stress will be encountered, then the constitutive model needs to be able to account for the yield point and the onset of plasticity [3]. These models can also include the effects of temperature, large deformations, and high strain rates.

If the situation under consideration is for small thermodynamic perturbations, Newtonian dynamics can be used to represent the conservation of mass, momentum, and energy principles. In Equation 1.1, a standing wave that occurs in a time period on a couple orders of magnitude greater than stress wave propagation is considered. The first and second laws

of thermodynamics for the case of a propagating stress wave must also be addressed and an equation of state considered to relate pressure, density, temperature, and entropy. Failure in materials undergoing such changes in deformation and temperature are dependent on time and strain rate, and material nonlinearity.

In summary, classical mechanics considers the wave speed as being much faster than the material response in terms of deformation. An impact in classical mechanics can be considered to be made up of instantaneous stress waves that reflect in such a fashion that the wave comes to a standstill and thus the wave interaction ceases. In a hypervelocity impact however, the material response typically exceeds the wave velocity, so material shock physics dominate the problem.

This makes for an interesting area of research. Research has been accomplished in the past forty years or so on the hypervelocity gouging problem and hypervelocity impact failure. The past research presented here focuses on research specifically geared toward the understanding of the hypervelocity gouging phenomena.

1.2 Previous Hypervelocity Gouging Research

Having presented an overview of the hypervelocity gouging phenomenon, a review of past research is now presented. Research regarding hypervelocity gouging can be categorized into six areas:

1. Test track observations and gouge tests.
2. Laboratory gouging tests.
3. Numerical modeling of gouging.
4. Aerodynamic sled analysis.
5. Load and failure analysis.
6. Methods for gouging mitigation.

1.2.1 Test Track Observations and Gouge Tests. In this area of research, test track runs and post-gouging results are observed. The research in this area takes these observations and draws conclusions about gouging by evaluating the gouged material.

Using a monorail test sled at Sandia National Laboratory, Gerstle [9, 10, 11] conducted experiments in which he initiated hypervelocity gouging. He found that gouges frequently occurred downstream from projecting "wrinkles," or mismatches, in the rail but that three-dimensional, small radius, irregularities such as weld beads across the width of the rail did not cause gouging. This is the first indication that a state of plane strain in the sled shoe may be required to initiate gouging. A shock wave is, after all, a plastic wave of uniaxial strain [5]. Apparently, a weld bead causes uniform deformation across the width of the slipper, not allowing formation of the uniaxial strain conditions required for formation of a sharp wave front. Formation of the sharp wave front is necessary for a shock wave to form. Uniform deformation effectively relaxes the stress wave caused by the high speed impact and does not result in the high pressure differentials required for plasticity and eventual gouging to occur.

Microanalysis of damaged portions of the rail in Gerstle's work (made of AISI 1080 steel) showed gouges had a surface layer of 304 stainless steel (sled shoe material) deposited on top of martensitized 1080 steel. Subsurface examination of the gouge showed that temperatures were high enough to austenitize the steel and that the rail material was severely strained and microcracked. Gerstle believed this to be evidence of catastrophic thermoplastic shear (a.k.a., adiabatic slip). Thermoplastic shear "occurs when the local rate of temperature change is such that the resulting strength decrease exceeds the rate of increase in strength due to effects of strainhardening [11]." In other words, a large temperature change in a small localized area (typically a banded layer) softens the material in that same area quicker than strain hardening strengthens it. It then becomes an area of local weakness in the material, and thus a likely spot of shear fracture. During adiabatic slip in steel, for example, local heat generation is large enough to austenitize the material, but the large mass of metal around that thin shear zone of the austenite material will quench it quickly enough to turn it into martensite. Evidence of catastrophic thermoplastic shear such as described here, is an example of phenomena that will be investigated in the proposed research.

Surface cracks in the gouged material were found to have stainless steel in their center surrounded by layers of martensite and deformed pearlite, indicating penetration of high

temperature sled shoe material into the rail. Rail surfaces that had not been contacted by the sled shoe had no damage other than surface layer decarburization. Decarburization is a loss of carbon due to high temperatures (usually over 800 K). This indicates close proximity of a high temperature source (i.e., the sled shoe) to the rail.

Examination of the shear strain distribution below the gouge surface showed large local variations along the direction of sled travel. The shear was associated with adiabatic shear bands that turned into martensite and cracked. Gerstle also found that the local shear strain distribution suggested the shear bands formed in planes normal to the sled direction. This is an indication of combined stress waves (plastic waves of both uniaxial strain and shear). Propagation of the cracks would occur due to dynamic fracture. The behavior and distribution of shear strain and dynamic fracture will also be investigated in the proposed research.

Gerstle surmised that thermoplastic shear along the adiabatic shear bands caused the interband material to tilt in the direction of sled travel, while the normal load from the sled shoe caused the material to experience an axial compressive strain. This could be a cause of the cracks he observed below the gouge surface that angled away from the longitudinal centerline of the gouge toward the surface. He also noted the angle of the cracks are more shallow as the crack is formed further away from the longitudinal centerline.

Finally, Gerstle concluded from examination of severely strained and cracked material and the presence of austenitized steel caused by high temperatures in bands uniformly spaced along the rail, both well below the surface of the gouge, that local subsurface heating was the result of catastrophic thermoplastic shear. This is a strong indication that heating, thermal diffusion, and propagation of stress caused by local temperature differences in high energy impact are important factors in analysis of the failure mechanism initiating hypervelocity gouging. In essence, Gerstle found evidence that a high temperature projectile (e.g., a sled shoe) impacting a target (e.g., a rail) with a severe combination of heat (thermal energy) and high velocity (momentum and kinetic energy) causes layers of local temperature differentials that result in adiabatic shear bands. These shear bands act as planes of motion allowing failure of the rail material eventually resulting in the interaction of failed sled shoe and rail material known as gouging.

Krupovage and Rasmussen [12], in 1982, documented sled development. They discussed the possibility that impacts between the slipper and rail are one of the causes for rail gouging. Track tests demonstrated that control of aerodynamic downloading significantly reduces the oscillations leading to impact. To determine the thermal environment in the area of slipper and rail interaction, the authors describe slipper fire (wear products leaving the aft slipper gap) as a homogenous stream of luminous material having light emissions from white to yellow. Intense light densities surrounding the 5000 to 7000 fps sleds are attributed to aerodynamic heating and to erosive oxidation of sled and slipper material.

The authors suggest the following relationship for the work developed by friction per unit time to account for frictional heat:

$$\dot{w} = C_f N v \tag{1.4}$$

where C_f is an empirical friction coefficient, N is the normal force, and v is the sled velocity. If these values can be determined, the heat generated due to friction may be calculated if one assumes that this change of energy is entirely converted to heat.

The authors question the idea that melted metal acts as a lubricant between slipper and rail because their observations indicate that the formation of liquid metal actually acts as an abrasive. This brings up the question of how coatings might be able to help mitigate gouging. Perhaps the best coating should act as a lubricant to protect the rail against the abrasive molten metal.

Krupovage [13] again addressed rail gouging in 1984. The author describes gouging experienced in a number of rocket sled runs with different sled types and test conditions. He observed that the largest gouge measured 4" long, 3" wide, and 0.40" deep. Gouges were found at rail breaks and on the inside of slippers. In addition to those containing slipper material, some gouges were found to contain copper from an aerodynamic wedge in front of the slipper.

Krupovage also points out that at velocities exceeding 5000 fps the loss of sled material in the forward area of the sleds due to aerodynamic heating was also observed. Based on these observations, he concludes that gouging is a result of the aerodynamic heating and

oxidation of forward portions of the rocket sled and internal slipper materials, slipper wear products, debris caused by impact of the aerodynamic wedge, or other debris from external sources. Krupovage concludes that gouging occurs when debris becomes trapped between the sled slider and the rail surfaces and does not result solely from the load imparted to the rail through the slider. He also included rail breaks and rail surface irregularities as gouge initiators since they would act as asperities.

Krupovage found that greater aerodynamic heating and more gouges occurred during the sled coast phase. External material loss due to aerodynamic heating was nonexistent in the helium environment. Krupovage suggests a dynamic model composed of a sled oscillating through the slipper gap and impacting on the rail with some effective mass as a model for gouging.

In 1982, Barber and Bauer [14] compared sliding contact behavior at low, high, and hypervelocities and defined hypervelocity as velocity in which the predominant forces of interaction are inertial. They identified the existence of a hypervelocity "sliding threshold velocity" and also developed a model for hypervelocity asperity impact and gouge formation. They described the gouging phenomenon as follows:

> When two solids are brought together, actual physical contact occurs only at a small number of discrete contact points. The normal load between the two solids is supported by these discrete areas. The number and size of the contact points increases with increasing applied load. Adhesion between two bodies in contact occurs at the contact spot and "cold welds" are formed. Tangential motion of one body with respect to the other deforms or shears material in the contact spots and results in further asperity contact. Frictional forces develop because of the ability of the contact spots to resist this deformation (wear results from material fracture due to excessive straining in the contact spot region.) During contact spot shearing, energy is dissipated into the deformation zone and then removed from the deformation zone by thermal conduction into the material substrate.
>
> As sliding velocity increases, the rate of energy dissipation in the deformation zone exceeds the conduction rate out of the deformation zone, causing the deformation zone temperature to rise. As sliding velocity increases still further, the temperature of the entire surface of a slider may reach the melting point, at which point a liquid interface is formed between the sliding surfaces, greatly reducing the frictional forces observed and the coefficient of friction. The liquid interface behaves as a hydrodynamic bearing. Viscoshearing of the liquid film dissipates energy, which causes intense heating of the slider surface and results

> in surface melting. Surface recession occurs, providing an influx of melted material from the slider surface equal to the efflux from the interface due to slider motion, and a steady-state hydrodynamic interface is established. The development of this hydrodynamic fluid layer depends upon the material properties of the slider and guider, the sliding velocity, the normal load, and possibly the geometry of the slider.
>
> At hypervelocity, if a fluid interface forms, velocity gradients in the interface will increase, as will the frictional force, energy deposition, surface recession, slider wear, and interface temperature. At some velocity, it is likely that the temperature of the interface region becomes so high that the interface material is vaporized, with a resultant drop in viscosity and frictional force. If a fluid interface does not form, asperity contact continues to occur at very high velocities. The asperities, however, can no longer come into contact in a steady or quasi-steady mechanical mode. Instead, they impact generally in an oblique manner, generating shock stresses.[14]

Compare and contrast this description to Krupovage and Rasmussen's [12] assertion that a liquid metal interface acts as an abrasive rather than reducing friction. At hypervelocity however, Barber and Bauer agree with Krupovage and Rasmussen that frictional forces increase in the liquid metal interface. Also compare this description of gouging to Laird's [7]. Laird focuses on formation of plasticity due to high pressure caused by a high energy impact. This plasticity, coupled with the tangential motion of the slipper shears material from the bulk material and initiates gouging. According to Laird, gouging is a continuous interaction of materials that follows from shearing along slip planes favored in the plastic region.

The description by Barber and Bauer contains elements of thermal diffusion as well as shear and inertial loading, and an explanation for the formation of a plastic zone. It is primarily mechanistic in nature, but does not consider the formation of adiabatic shear bands and catastrophic thermoplastic shear. Therefore, it is enlightening, but not complete in describing the characteristics of gouge formation.

Barber and Bauer defined the point at which the impact-induced stress is equal to the ultimate strength of the material as the "hypervelocity sliding threshold velocity." The hypervelocity sliding threshold velocity, as well as impact stress, is related to the asperity impact velocity, the angle of impact, the density, and the shock speed of the materials involved. It is essentially a material property. They hypothesized that hypervelocity

asperity impact is a discrete, localized, violent event resembling a microscopic explosion that produces a small crater in the surface of the material. The center of mass of this explosion travels at approximately one-half of the slider velocity. Due to the relative motion of the slider, a tear-shaped crater results rather than a simple, hemispherical shape. This description provides a sense of the mechanism of gouging caused by an asperity, but does not explain gouging caused by an oblique impact or the interaction of plasticized slipper and rail materials that has been shown by metallurgic analysis of gouges such as by Gerstle [11].

Barber and Bauer did not find much quantitative data to support their hypothesis. However, they felt that the conclusion drawn by Graff, et al [15], that a minima of both sliding velocity and normal load is required to initiate gouging, confirmed the existence of a hypervelocity sliding threshold velocity. They also concluded that instances of rail gun gouging confirmed the existence of a threshold sliding velocity. They thought that the onset of gouging corresponds to the point at which asperity impact would produce stresses exceeding the ultimate strength of the material.

In 1997, Mixon [16] provided a thorough review of previous research and experimental gouging data for many runs, including where gouges occurred using a database compiled by Bob L. Kirkpatrick and Will D. Wilson. Based upon other works, he summarized factors that affect gouging. These include high stresses from dynamic loading, high velocity, asperities on the rail surface, frictional heating, ablation of the slipper and subsequent entrapment of ejecta, and externally ejected sled material due to high stagnation temperature behind normal shocks in the air.

Sled tests Mixon considered for analysis included tests for the Low Mass Interceptor (LMI), Medium Mass Interceptor (MMI), and Patriot PAC3. Each of these test series used an independent forebody sled that carried the payload pushed by the final stage. Gouges could be initiated by either the front or rear slippers of the forebody, or the final stage pusher rocket (Roadrunner) front or rear slippers. The forebody slippers were all web bearing slippers (monorail) for additional roll stability.

The two LMI tests Mixon evaluated included the use of a helium environment. Gouging started to occur at about 5800 fps, and the tests reached a peak velocity of 6863 fps. Seventy-five to eighty-three percent of major gouges occurred after peak velocity. All of the gouges occurred within the helium environment, where aerodynamic heating is low with minimal external burning and oxidation but slipper surfaces have already been deteriorated.

The MMI testing consisted of seven runs with a peak velocity of 6660 fps. In four of these tests, the documentation included the location of the gouge on the railhead. Gouging started at 5400 fps, and in total 408 gouges were found, including twenty-four major gouges that required welding. A comparison of the velocity profile and the number and location of gouges is shown in Figure 1.4. In this figure, the line represents the sled velocity vs. track station, and the bars indicate the number of gouges present per 500 feet of track. This shows the velocities at which gouging occurs is above 5400 ft/s, and that the highest concentration of gouges occurred in the region of peak velocity. Most gouges were found at the corners of the railhead, and relatively few occurred on the flat surfaces. In other words, most gouges occurred in areas in a state of plane strain in which transverse deformation is restricted.

Diagrams of the rail and location of the gouges are given in the report. There were instances of simultaneous gouging, where multiple gouges were found at the same track station. One run in particular accounted for 114 (27.9%) gouges, nine (37.5%) major gouges, and a large six inch gouge that broke the rail and led to catastrophic failure. The number of gouges per 100 feet was found to be significantly higher after peak velocity than before, which is attributed to slipper deterioration.

However, the velocity of impact which imparts a certain amount of kinetic energy and inertia could be the deciding factor for gouging. Ten major gouges occurred before the peak velocity and eight formed after. All of the gouges found were in the helium environment where peak velocity was reached, but aerodynamic heating was lowered.

The PAC3 tests consisted of fourteen runs reaching a peak velocity of 6000-6100 fps. It included a rigorous repainting program. The entire rail was sandblasted and repainted

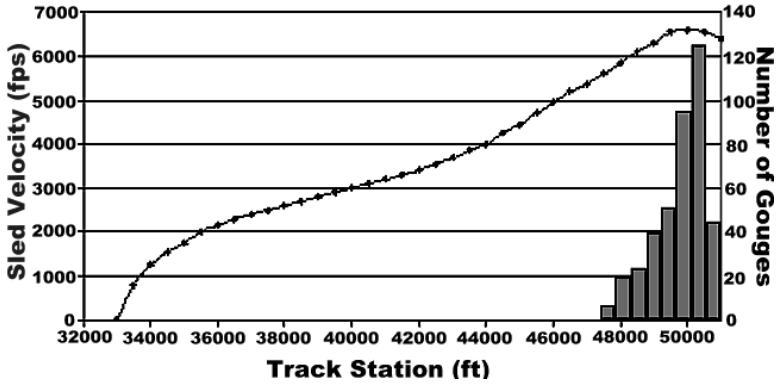

Figure 1.4 **Sled Velocity and Number of Gouges for MMI Tests.**

with a controlled thickness of paint (6 mils, ± 1 mil) every four runs, with spot repainting where needed between every run. Gouging started at 5750 fps. In this case, it was found whether the sled was before or after peak velocity did not affect the tendency to gouge. Again, all gouges occurred in helium. Only two major gouges occurred in these tests, both of which were on the same run. This run had more gouging than any other PAC3 run, ending in a major structural failure of the final stage pusher.

Mixon concludes that there is a relationship between gouging and the tendency for roll forces. Sleds are described as having a tendency to roll or lift based on the gouge location, and it is likely that gouging leads to excessive roll, which often leads to failure. And conversely, roll and lift significantly influence gouge position on the railhead. In high wear/gouge conditions, a tendency exists for gouging to occur at a higher rate after burnout, likely due to the successive deterioration of the slipper surfaces. However, this is inconclusive because gouging also occurred after peak velocities, so the high horizontal velocities could be a factor rather than the deterioration of the slipper. In addition, the heating between slipper and rail is largest at the peak velocities so this could be a cause of the larger number of gouges.

Mixon found that the highest gouging rates occurred within a small range of velocities (less then 50 fps) immediately before and after peak velocity was reached. Structural failures also resulted in a considerable number of gouges. High stress, high velocity, rail

imperfections, deteriorated slipper surfaces, and frictional heating were considered to be prime contributors to the onset of gouging.

Since well-maintained rail coatings significantly reduce the number of gouges, gouging may be mitigated by the establishment of the best coating and thickness, and improved coating application methods. In addition, improved track alignment and machining methods, and new slipper materials and design concepts are likely to be valuable based on Mixon's research.

Mixon suggests an accurate model of gouging could prove beneficial in studying rail coatings. However, this is conditional on the model being capable of determining the various coating material properties and their direct effect on hypervelocity gouging.

Analysis of gouged materials from hypervelocity test track runs has produced some theories on the causes and mechanisms of hypervelocity gouging. Primarily, the concepts that have been surmised to contribute to gouging are the formation of adiabatic shear bands and thermoplastic shear, high temperature effects, inertial effects of hypervelocity impact, and shock wave formation. In addition, formation of a plastic zone, high strain rates, viscoshearing, and hydrodynamic bearing may also be mechanisms causing hypervelocity gouging based on analysis of gouged test track materials.

1.2.2 Laboratory Gouging Tests. Another important source of experimental data for hypervelocity gouging are laboratory gouging tests. These tests usually use the controlled hypervelocity impact of a known projectile at a glancing or oblique angle to form gouges in a known target material. The gouges that are formed are then analyzed.

In 1968, Graff, et al [15] designed experiments to create high velocity sliding contact using a special gun facility that enabled them to shoot projectiles on a grazing angle of impact at a flat or curved target at up to 9000 fps.

They thought the basic nature of gouging was one of high velocity sliding contact or grazing impact between metallic surfaces. Beginning with a review of sled tests, the researchers catalogued data from gouge damage at the Holloman AFB rocket sled test track and noticed that gouging seemed dependent on many parameters including rail and slipper materials, slipper geometry, rail straightness, airflow in the slipper gap, velocity,

and contact stresses. They studied previous sled runs showing that gouging began between 5200 and 5500 fps. Gouges were defined as a tear drop shape with a typical gouge being two to four inches long, one inch wide, and 1/16 inch deep.

The authors also discussed coloring and metal deposits in the gouge. The maximum observed amount of gouges occurred after peak velocity. This had been attributed to increased gap size and wear effects, not necessarily higher velocity. However, Graff, et al's review showed that the sled velocity was the primary factor affecting the frequency of gouge occurrence. They also learned that about 80% of the gouges were on the side or top edges of the rail, 15% were on the undersides, and only 5% were on the top surface of the rail. This is another indication that a state of plane strain would be an appropriate model for gouging. Downward biasing by canards and high strength maraging steel slippers appeared to produce less gouging.

In the laboratory, the study focused on impact velocity, slipper and rail materials, and interfacial stresses. Using projectiles of brass, copper, steel, and aluminum, Graff, et al successfully created gouges on steel target surfaces that had the essential characteristics of rocket sled gouges. While initial attempts at firing at a twenty foot radius curved steel target did not produce gouging, reducing to a three foot radius to increase stress resulted in gouges similar to those at seen at Holloman AFB.

After impact, projectiles left marks on the target plate indicating the width or wear of the projectile. A layered structure of target base materials, oxide coating, molten projectile material, and projectile base material was created, suggesting the existence of a molten interface during gouging.

It was suggested that aerodynamic flow conditions in the gap would be capable of producing melting of the slipper without metal-to-metal contact. Graff, et al cited evidence that the coating material acts as a lubricant, or fluid interface, under hydrodynamic loading and only transmits the normal stresses and not the shear stresses that would initiate gouging. Melt lubrication eases high-speed friction by forming a liquid layer between the sliding surfaces. In essence, the liquid interface acts as an incompressible fluid. It transmits spherical (i.e., volume changing) stresses and not deviatoric (i.e., shape changing) stresses.

The effects of tangential motion in the liquid interface are limited to a small viscous boundary layer near the surface of the moving body (i.e, the slipper).

Calculations were made to support the conclusion that due to the velocity and size of projectiles, transient stresses are small in comparison with the steady pressure and may be effectively ignored. Sample calculations of the normal stresses encountered in the experiments were 78,000 psi for a steel projectile weighing 0.27 oz.

They also found that sudden jumps in stress caused by discontinuities in the curved target resulted in gouge initiation. Gouges were more likely to occur at slight kinks in the curved projectile track, where normal forces were maximum, and that gouges were predictably initiated at transverse scratches and grains of sand deliberately placed on the track surface. Furthermore, orienting the ground surface-finish of the target plate transverse to projectile motion resulted in more gouging than when the surface-finish was parallel to the motion, and sanded finishing produced fewer gouges than other finishes. They concluded that for the same velocity and stress, fewer surface imperfections produced fewer gouges.

Based on their observations, the authors described gouge initiation as the point when, at critical conditions of normal stress and velocity, the oxide film on the target and the molten film at the projectile/target interface is penetrated and direct metal to metal contact occurs, resulting in a welded junction.

This penetration of the surface layer can occur from a sudden stress jump resulting from a high spot, or from a local surface imperfection. Projectile material deforms and slightly penetrates into the target, while simultaneously, target material penetrates into the projectile. Initially, the amount of deformation is small, but continuing interaction at the metal-to-metal interface causes pressure and shearing action that causes the size of the interaction to increase. The growth and propagation of the gouge requires the continued shear of material at the base of the junction. Gouge termination happens due to the passage of the projectile trailing edge beyond the effected region.

Further studies by Graff, et al [17] in 1970 examined various projectile materials and target coatings subjected to normal stresses up to 200,000 psi. It was found that all metallic

projectiles caused gouging while Teflon did not. It was also found that soft metals gouged more frequently, while harder metals had higher threshold gouging velocities. Harder maraging steels gouged less, but excessively hard steels resulted in a machining action. It was recommended that a slipper with hardness just slightly greater than the hardness of the rail would give the best results. General results for coating materials was that successful coatings were low in density, low in strength, and non-metallic. Use of low strength coatings caused all of the material shear behavior to occur in the coating and not on the projectile. Plastics and ceramics were found to have insufficient strength to withstand imposed stresses, except cemented tungsten carbide that was tough enough to withstand contact shock without fracturing, welding, or gouging. Tests showed that high normal stresses were not sufficient to cause gouging if direct metal-to-metal contact was prevented.

Tarcza [18], in 1995, used a special gun assembly to conduct gouging studies at relatively low velocities. The primary purpose of Tarcza's work was to demonstrate that gouging is possible at velocities lower than those at which it had been previously reported, and to show that there existed a correlation between gouging and material properties, which may be used to accurately predict the onset of gouging. The experiment was designed to confirm a correlation in gouging between velocity and slider strength and hardness. Tarcza also set out to confirm an extrapolation of the velocity-slider strength relation to lower relative velocities. He also sought to determine the velocity of gouging initiation for a chosen material and a given set of conditions. Lastly, Tarcza sought to create gouges in a manner that would be relatively inexpensive and readily duplicated.

Tarcza started with a literature review of selected papers on gouging in rocket sleds and rail guns and concluded that all the proposed theories held the following points in common with regard to hypervelocity gouging initiation. Each held that gouging initiation was dependent on slipper velocity, stress at the contact surfaces, and material properties.

Examining past data, a linear relationship was recognized between gouge onset velocity and yield strength divided by density (Figure 1.5). Using this relationship, Tarcza theorized that a lead slider impacting against a lead guider would start gouging at 715 fps. Though each study in Tarcza's review had its differences, the velocity at which gouging

initiated was determined by observing the pressure core from the point of impact. The velocity of gouging initiation was the velocity at which the high pressure core was observed to grow. If the core was observed to decrease in size from impact or remain stable, then gouging was not determined to have occurred.

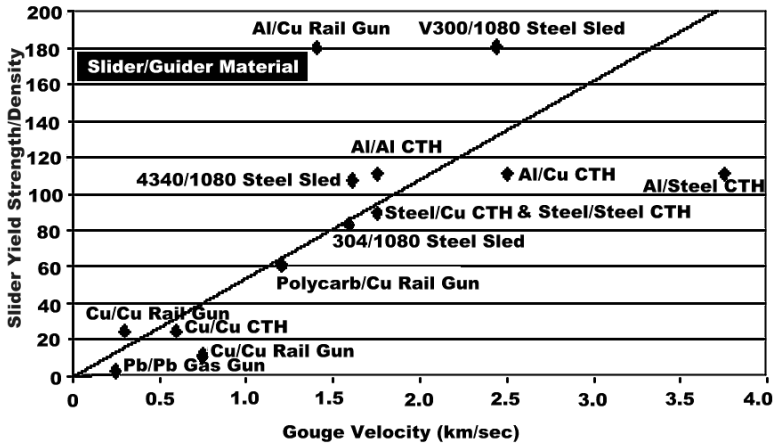

Figure 1.5 **Comparison of Slider Yield Strength and Density to Gouge Initiation Velocity.**

Tarcza believed that given the proper conditions and materials with appropriate properties, gouging would be possible at velocities other than those at which it has previously been observed. Tarcza used the definition of hypervelocity as velocities in which inertial forces dominate. Tarcza searched for a material combination that would exhibit hypervelocity gouging at relatively low speeds.

His experiments were conducted using a .22-caliber light gas gun, a curved surface target in a catch fixture, and instrumentation similar to Graff, et al. Using a lead pellet projectile against a lead target, Tarcza found that gouging occurred consistently at sliding velocities above 272 m/s ($\approx$ 892 fps). He examined the resulting wear and impact damage, and found that gouges occurred in the shape of teardrops, ovals, or peanuts. The highest velocities produced the largest gouges. All of the gouges had the dull finish, rough appearance, and raised lip normally associated with gouging. Though most gouges seemed to develop from incidental slider-guider contact, a few of the gouges appeared to result directly from scratches or other pre-existing nonuniformities in the surface of the lead sheet guider. Further, a raised manufacturing seam across the entire width of the sheet had the

opposite effect. Not only did the seam prevent gouging, in every case it seemed to cause an extended period where the slider and guider were not in contact. This period increased with increased velocity. His observations agreed with experimental findings of Gerstle at the Sandia Test Track. Numerous instances of overlapping gouges were observed. In addition, a number of instances were observed where gouges were initiated within the width of a wear track but continued outside of the track. Tarcza found that there is a regime between gouging and no gouging.

He sometimes observed what he termed to be "incipient" gouging. In this case, gouges were not fully developed. Tarcza felt that in testing, gouging must have occurred after a period of sustained contact between the slider and guider as opposed to a sudden material interaction. Neither plate thickness nor the presence of an oxide layer seemed to affect the wear, impact fan, or gouging.

Because the gouging impact speed was significantly below the material wave speed, Tarcza concluded that gouging is not limited to being a hypervelocity phenomenon in which the velocity of impact must be near or greater than the elastic wave speed of the material. This, however does not preclude that gouging is a result of shock wave physics and plasticity.

After use, the pellets were elongated to the rear and their leading edges displayed a protruding, curled lip, which grew more pronounced with increasing velocity. While rearward elongation is the logical result of relative motion forcing slider material to the rear, the surprising lip on the leading edge indicates that material was also being pushed forward ahead of the slider. Tarcza found that the higher the velocity, the more mass that was lost from the slider. This could be from impact, wear (including against the catch tank after the lead sheet), or gouging. No evidence was found of gouging on the slider surface, but significant wear after the last gouge (especially in the catch tank) would have removed any gouging evidence. Because of slider surface marring, it can only be speculated that if slider gouging does occur, it must be less severe than that which occurs on the guider. Otherwise, the cumulative effects of all guider gouges from any given wear track, particularly those with large gouges, should have resulted in far more slider damage than was observed in any recoverable pellet.

Tarcza surmised that the magnitude of normal force generated during slider-guider contact is also critical to the onset of gouging. The normal force could be generated by a surface asperity impact, gouge initiating particles, or normal slider velocity components. The fact that an appropriate curvature was needed in lab tests further confirms the requirement for a sufficient amount of normal force for gouging to occur. The velocity of gouging initiation is assumed to be a function of the normal force as well as slider material properties. At present there is no data that can quantify the normal force or inconclusively relate slider normal forces to gouging.

In 2003, Ramjaun, et al [19] investigated hypervelocity impacts on thin metallic and composite space debris bumper shields. In their research, they investigated hypervelocity impact crater formation for both normal and oblique impacts at 5.0 ± 0.2 km/sec. Using a two-stage light gas gun, a cylindrical projectile was used to create craters in space debris bumper shield material. Their research is important because of the failure mechanisms and similarities to slipper and rail impacts at similar velocities. They performed a microscopic study and found adiabatic shear bands formed near the crater zone of impact. The angles of impact they used were 90^o, 51^o, and 64^o. What makes this research especially interesting is the fact that they estimated the debris cloud temperature and temperature near the crater at impact using a time-integrated spectrum of the light emission during crater formation. They estimated the debris cloud temperature using this method to be between 7300 ± 300 K and 7600 ± 300 K for the impacts.

The authors described the mechanism of fracture due to hypervelocity impact by stating that at impact strong shock waves propagate within the target and projectile (slipper and rail for the gouging problem). As these shock waves propagate, the materials are heated adiabatically but not isentropically. Once the shock waves reflect off the free surface of the projectile, rarefaction waves are formed. This release of the shock wave compression is considered to be an isentropic process. However, the materials are not returned to their original state after the process of release is complete and the materials are left in a high energy state. This high energy state can cause the material to fragment, melt, or vaporize.

Macroscopic examination of the craters after impact showed elongated contours of deformation for the oblique impacts. The elongated contours showed craters at entry and lip formation at exit. This lip formation indicated plastic deformation according to the authors.

Microstructural examination of the oblique impact craters showed secondary cracks radiating from adiabatic shear bands. These adiabatic shear bands are indications of localized melting and thermoplastic shear. According to the authors, cracking is due to the work done during intense plastic deformation. This causes a sharp increase in local temperature. The intersection of shock waves caused by the initial impact results in high tensile stress from rarefaction waves. Coupled with local melting in thin layers, this could easily result in the cracking that is observed. Hardness measurements were inconclusive. The hardness did not change substantially between undeformed and impacted materials.

Ramjaun, et al concluded that shear instabilities occur at various sites along the projectile and target interface under the high shear stresses and high strain rates that arise as penetration occurs. The local plastic work is converted into heat and bands of concentrated shear displacements grow from these shear instabilities and into thermally softened material. When the rarefaction waves cause tensile stresses that result in cracking along these sites of shear weakness. This was observed mainly at shear band intersections in the shock-heated material immediately beneath the crater. As shear band cracks linked up, they isolated pieces of material allowing them to fracture from the bulk material.

Spall pressure was found to increase within shear bands due to void nucleation and growth during shear band formation and thermal softening which lowers the resistance to void growth, increasing spall pressure. Spalling was determined to be caused by the intersection of shock wave and rarefaction waves at the adiabatic shear bands.

Ramjaun, et al also noted that normal impact tests gave lower temperatures for the debris cloud than the oblique impacts. They surmised that a higher energy state of the debris cloud (i.e., “ejecta”) occurred in the oblique impacts.

The primary cause of damage during high velocity impact in this investigation was determined to be the formation of adiabatic shear bands. In order to mitigate failure due

to hypervelocity impact, the authors concluded that materials which have no tendency to form adiabatic shear bands would have the best resistance to hypervelocity impact. For them, the best material would:

- have uniform and homogenous flow properties during viscoplastic deformation to prevent formation of adiabatic shear bands caused by uneven formation of viscoplastic zones,
- have a high melting point to prevent adiabatic shear band formation and subsequent cracking,
- and not transform into a brittle phase during shock loading which increases the likelihood of fracture under loading.

With these criteria in mind, the authors recommended pure aluminum, pure titanium, and Ni-Ti shape memory alloys as potential space debris bumper materials.

This section completes the review of experimental tests conducted to initiate and study gouging. This means of research is very valuable, but limited because of the high cost of performing such tests. To gain better insight into the phenomenon and because of the high cost of creating and running such tests, numerical investigation of gouging has taken place in parallel with experimental procedures such as test track observations and laboratory testing with special gun facilities.

1.2.3 Numerical Modeling of Gouging. Numerical modeling of gouging has benefitted from results of testing from high speed rails and laboratory special gun setups. Numerical investigators are able to qualitatively compare the results of their investigation to gouging tests and verify their results. Numerical investigation has been successful because it offers a means of gaining improved understanding of the gouging phenomenon without the drawbacks of physical experimentation. Theories may be tested at a relatively low cost and the physics observed according to the model as the event happens. This section describes the major numerical models for hypervelocity gouging and their results.

In 1977, the earliest attempt at modeling hypervelocity gouging was published by Boehman, et al [20]. They developed a computer model to study hypervelocity friction,

wear, and gouging at the slipper/rail interface. They were able to identify the velocity regimes for stability, but were unsuccessful in implementing gouging criteria.

Numerical work was continued by Barker, et al [21] at Sandia National Laboratory in 1987. Using the hydrocodes CSQ and its successor CTH, the Parallel Impact Thermodynamics (PIT) model was developed to model parallel slider impact on the guider/rail. The model was named for the parallel impact of the slider with the guider and the fact that the CTH computational algorithm also modeled the thermodynamics of the gouging event. The PIT model involves a slider with a small gap and a forty-five degree angle at the front for impacting an asperity to initiate gouging (see Figure 1.6).

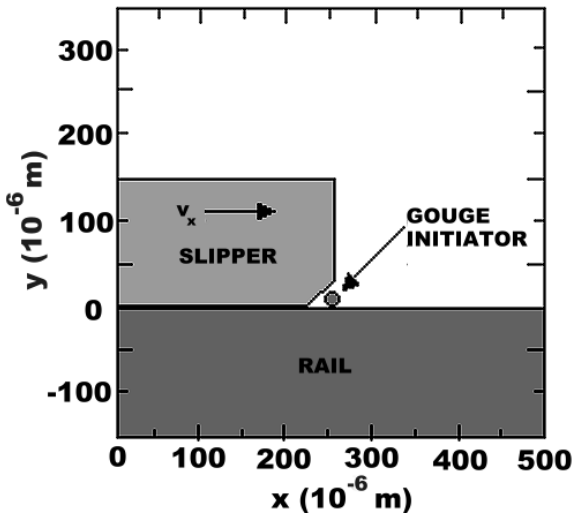

Figure 1.6 **Barker's PIT Model.**

To obtain an understanding of the heat generated from friction, it was found that frictional surface heating of a 30 mm diameter steel projectile sliding at 3 km/s in a barrel with a nominal curvature of 1 mil per 10 inches would be expected to result in surface melting of the projectile after 2000 microseconds (60 cm) of travel and to a depth of 6.7 cm.

Barker, et al understood gouging to be an impact phenomenon and developed a theory and computer model accordingly. The CTH program uses high shock physics solution methods to solve the high energy ballistic impact problem.

They were able to show that a numerical model of high velocity tangential impact, where the slider impacts something in front of it horizontally, models gouging under certain conditions. To function properly, two-dimensional models required a gap between the slider and guider, an asperity, and a normal load generated by giving the leading edge of the slider a forty-five degree angle to impart downward motion to the asperity during impact. Three-dimensional models were used in an attempt to verify results, and they found that gouging would not occur with a slipper gap. But gouging did occur if no gap was present. They determined that both models confirmed the validity of the PIT model.

Their study found that the conditions under which gouging exists due to an asperity impact are extreme local deformation, heating, melting, and vaporization. Results from the model show the progressive development of a gouge, and also indicate the similarities between gouging modeling and hypervelocity impact problems. The impact of a steel asperity travelling at 2 km/s against a stationary steel asperity generates a shock pressure of about 5800 ksi, which is about forty times higher than the 150 ksi yield strength of typical heat treated steel. They theorized that an asperity impact would result in the development of a growing high-pressure interaction region.

Their theory of gouge initiation states that the high pressure acts to deform the parallel surfaces that impinge on each other in a continuous interaction that produces gouges. Barker, et al suggested that this type of interaction would be self-sustaining, and would continue until the slider passes beyond the point of interaction. They also noted that stress wave propagation, reflection, and release waves likely affect gouge development.

Barker, et al conducted a parametric study to quantify the physical conditions that must exist when gouging takes place and to verify the validity of the assumptions they made for the computer model. By varying the model parameters, Barker, et al concluded that gouge mitigation may be accomplished by increasing the size of the gap between the slipper and rail, increasing the slider yield strength with respect to the guider, using plastic as a slipper material, pitching the slider into a small angle with respect to the guider, or decreasing the normal load between slider and guider.

Another experiment was run without friction to test Graff, et al's [15] theory of gouge initiation in which they described gouge initiation as the point when, at critical conditions of normal stress and velocity, the oxide film on the target and the frictionless molten film at the projectile/target interface is penetrated and direct metal to metal contact occurs, resulting in a welded junction. In Barker, et al's results, gouging occurred with and without friction. This apparently showed that inertial forces are more dominant than the formation of a frictionless surface that may be penetrated to form a welding junction as theorized by Graff, et al.

Based on these results, Barker, et al designed a laminated slider that allowed release waves to arrive faster in order to relieve pressure in the gouge nucleus, provided shock absorption to decrease peak normal pressure, and provided melt lubrication at high velocity. A slider using this design was tested on a small monorail sled that reached 1.9 km/s and produced no gouges.

However, a number of difficulties remain with the Barker model. In real world testing, gouges did not develop across a uniform asperity such as a weld bead. Also, the 45 degree angle leading edge of the slipper is inaccurate. No such wedge exists on the slipper. Finally, it assumed that there has to be some asperity that causes gouging. This assumption remains unproven although commonly accepted in the literature at the time.

In high velocity guns such as rail guns and two stage gas guns, hypervelocity gouging was found at the gun barrel/projectile interface. In 1989, Barker et al [22] reviewed the data collected in Susoeff and Hawke's 1988 report [23] on rail gun gouging and then acknowledged that the source of gouging damage was still uncertain; the experiments that had produced gouging were designed to improve rail gun performance rather than to study gouging. Barker, et al suggested that molten droplets of the aluminum slider "impinging" at low angles into the rails and "digging in" might have caused the gouging damage. They reasoned that the higher energy levels used on the last five shots likely resulted in complete vaporization of the aluminum slider and thus no gouging, whereas earlier shots that produced gouging did so because of incomplete vaporization of the foil.

Barker, et al used the PIT model in 1989 to conduct a CTH hydrodynamic code parameter study to predict the conditions under which gouging can occur. In the study, they evaluated all possible slider-guider combinations of copper, steel, aluminum, and plastic at velocities from 0.5 to 12 km/s. The results were examined to determine whether the initial microasperity impact at a slider-guider interface would result in a growing, stable, or decaying interaction region; a growing interaction region would indicate the formation of a gouge. Barker, et al determined that materials that gouge each other do so only within a certain range of velocities. They also determined that there are both upper and lower gouging threshold velocities, although the upper threshold has never been experimentally observed.

When sliding exceeds twice the wave velocities of the interacting materials, gouging does not occur. This is apparently because there is insufficient time for material to be continually pushed up in front of the interaction zone and the reaction dies out. They saw that higher yield strengths raise the lower gouging threshold (and may lower the higher threshold as well).

Numerical analysis also showed that a nearly steady "stream of gas" emanates from the leading shoulder of plastic sabot projectiles. Plastic sabot projectiles have plastic sleeves behind the projectile that conform to the barrel of the gas gun and capture the high pressure to propel the flat plate projectile down the barrel of the gun. This emanating stream of gas is caused by shock vaporization caused by micro impacts of gun barrel particles on the leading shoulder of the projectile (commonly known as blow-by). Finally, they found that a ten-degree oblique impact angle of the projectile on the gun barrel reduces this stream of gas and the tendency for gouging to occur.

CTH was again used by Tachau [24, 25] to perform numerical analysis of gouge development in 1991. Beginning with a review of the available literature, Tachau noted that Barker's theory required a gap, an asperity, and an angled leading edge to impart downward motion on the asperity and subsequent normal loading of the rail during impact. He also found that Barker's model did not include the effects of sliding friction.

Tachau's hypothesis was that an oblique impact could generate the environment necessary to form a gouge. Tachau improved upon the PIT model presented by Barker, et al by eliminating the gap between the slider and guider as well as the gouge initiating asperity from the CTH computer model. Instead, an initial slider velocity component normal to the sliding surface was applied to the model (see Figure 1.7). This model produced highly oblique impacts. Tachau hypothesized this would result in the development of antisymmetric humps as described by Abrahamson and Goodier in 1961 [26].

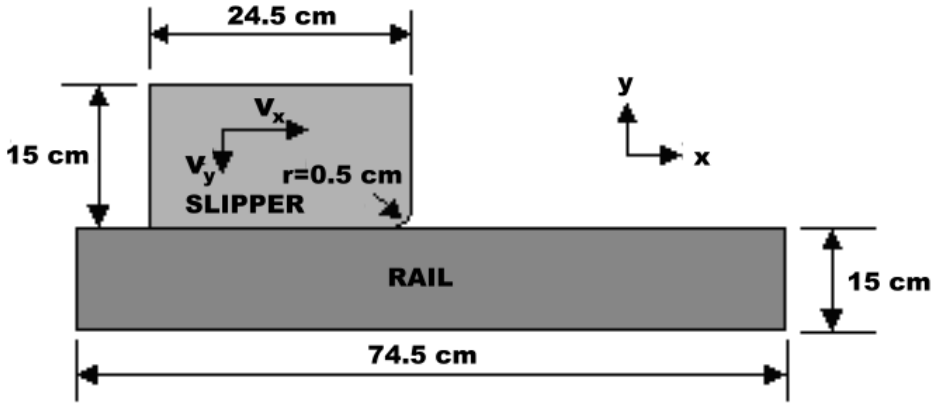

Figure 1.7 **Tachau's Model.**

The initial velocities Tachau used were 2.0 km/s horizontally and 100 m/s vertically. Tachau observed that the crater from his results was deeper than observed in rocket sled gouges, but this was attributed to the selected vertical velocity component, which is larger than what is expected in actual testing. Temperature contours showed high temperatures up to 1800 K resulted from plastic deformation at impact and were sustained only at the contact surface. The impacts readily heated the surfaces to near melting conditions. The core pressures were high, on the order of 5 GPa. Tachau also performed a matrix study of steel and aluminum sliders at different velocities.

He concluded that a strong pressure core developed by the impact accompanied gouging, and that tangential (horizontal) and normal (vertical) velocities were contributing factors. In simulations for a slider and guider both made of steel, he found that a slider at 2.0 km/s with a 100 m/s downward velocity component caused gouging, but one at 1.0 km/s and 100 m/s downward did not.

These results led Tachau to conclude that the temperature at the contact surface must be sufficiently high to cause the materials at and near the contact surface to become viscoplastic, and that the impact condition must be severe enough to ensure the creation of a growing, high-pressure core at the contact surface. He also concluded the heat necessary to produce this high temperature is generated primarily by contact friction and impact, conditions that occur at high speed and large normal loads. When the heated surfaces are obliquely impacted, the shallow heated zone of softened material allows the formation of antisymmetric deformations described above. Since both the slider and the guider become very hot, antisymmetric deformations would be expected to form on both contact surfaces. If conditions permit a continuous interaction of the heated, viscous layers, a gouge would be initiated in a manner similar to the PIT model. Addressing the asperity model, Tachau found that impact of the slider with a sloped impact surface on the asperity provides the vertical momentum or impulse component necessary for gouge formation. This study suggests that the magnitude of the vertical momentum does not need to be large. If the temperature produced by the oblique impact is sufficient to cause melting, and the contact and loading conditions are sustained, a gouge will be formed. To mitigate gouging, Tachau recommended carefully aligning the entire slider-guider system, designing sliders for aerodynamic stability, and eliminating slider-guider contact while minimizing slider-guider clearance. He also proposed a design for a non-gouging slipper.

In 1998, Schmitz [1] followed up on Tachau's work by developing a new software tool based on CTH results to investigate gouging and wear. The tool predicted slipper wear and gouging phenomena based on empirical data and initial conditions. Schmitz expected that experimental testing would be performed to validate the output of the tool. To develop this tool, Schmitz used CTH with an asperity impact simulation (see Figure 1.8) based on Barker's model as described in [21]. Schmitz observed that growth of the high pressure core in the first four microseconds of impact predicted the formation of a gouge, while if the pressure core did not grow, no gouge formed. Schmitz was also able to correlate the gouge velocities for different slipper and rail materials in CTH with experimental and test track data as presented in Figure 1.9.

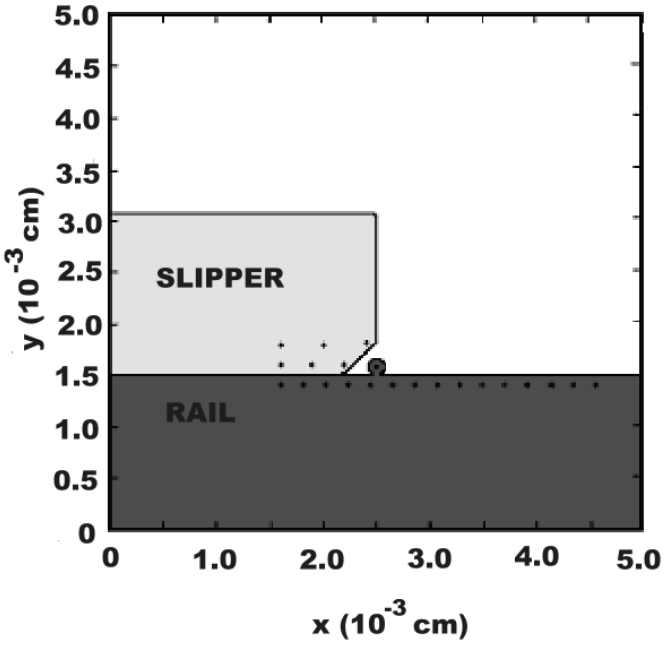

Figure 1.8 **Schmitz's Model.**

In 2002, Laird [7] performed an investigation of hypervelocity gouging with an emphasis on understanding the phenomenon. His major contribution to the literature was the understanding of material jet formation that leads to gouging and showing that temperature effects prior to gouging affect its formation. As part of that effort, he performed a numerical investigation of gouging using CTH [27] and investigated the effect of high temperature on gouging [28]. He modeled gouging after scaling the dimensions of Tachau's oblique impact model down by 1/10. His work is a comprehensive analysis of gouging and the factors involved in gouging formation, including temperature. He made a number of conclusions that are important for further investigation into the subject area.

He found that plastic deformation, vertical force, and low material strength are contributing factors of gouge initiation. He also stated that none of these alone are sufficient to initiate gouging. He indicated the key feature of gouging is the initiation of the material jets. Jet formation characterizes gouging as interaction and mixing between two materials. The jet formation requires viscoplasticity of both materials. If one material has conditions or properties that inhibit gouging, it will not occur.

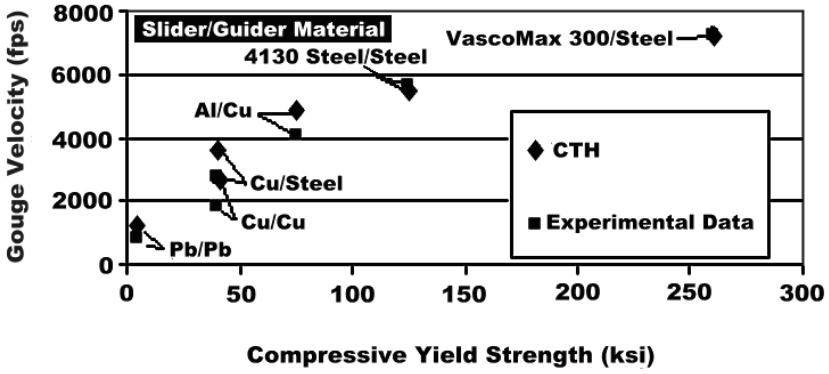

Figure 1.9 **Validation of CTH to Experimental Data.**

He also found that when jet formation initiates, the stress wave in the rail caused by the oblique impact is still propagating away from the impact and the stress wave in the slipper is just reaching the top free surface of the slipper. Since the release waves have not occurred at the time the gouge is developed, spallation is not influential in gouge initiation. However, high pressure compression caused by the initial impact is likely a factor that sets up the environment conducive to gouging.

Another aspect of Laird's work was basic numerical modeling of the high temperature environment typical in high velocity test track runs. Laird determined that high temperatures lower the yield stress of the materials, leading to less resistance to gouging. While he found that room temperature gouging resulted in high temperatures contributing to weakening of the material, the slider model at high temperatures before impact provided a "jump-start" to these higher temperatures, making it easier for gouging to develop and leading to similar behavior and deformation as the unheated case. The difference between numerical model gouging in the heated slipper and the unheated slipper was timing. In the heated slipper model gouging occurred earlier. "Clearly," states Laird, "elevated slipper temperatures affect the onset and subsequent development of gouging."

In addition, Laird found that a shallow leading edge angle of less than 1.790^o did not gouge under the same velocity conditions that caused gouging to occur in a slipper with a rounded leading edge. The maximum penetration depth was similar in both cases, but

the shallow leading edge resulted in a shallow slope at the material interface, inhibiting the development of material jets.

Finally, Laird determined that increasing the rail yield stress would inhibit gouging. To him, this was a direct result of the fact that changing a property of either the slipper or the rail material above or below a certain threshold would affect hypervelocity gouging initiation since gouging initiation must occur in both materials simultaneously. He also found that an increase in rail yield stress did not inhibit the penetration of the slipper into the rail, only the interaction between viscoplastic slipper and rail materials that lead to formation of material jets that cause gouging.

The most obvious limitation of the previous computational works is that an accurate time-varying thermal environment (due to aerodynamics and friction) was not included in the simulations. Furthermore, size and shape of the slippers simulated were not representative of real slippers, making it difficult to conclusively compare numerical results to test track data. Besides experimental testing and numerical investigations of the slipper and rail gouging interaction, some research has been accomplished to model the aerodynamic heating effects and the load and damage induced failure caused by slipper impact on the rail.

1.2.4 Aerodynamic Sled Analysis. The thermal environment of gouging is affected not only by the mechanics of the sled and rail, but also by the aerodynamics of the sled riding through the air and producing strong shocks that raise the stagnation temperature behind the shock. The aspects of the thermal environment that aerodynamic solutions provide is important. Aerodynamic solutions provide an important input to a numerical investigation. For instance, aerodynamic heating can be modeled using an analytical or numerical flow model which provides a thermal input to the CTH model for further investigation of the gouging phenomenon.

In 1968, Korkegi and Briggs [29, 30] developed a model to perform a two-dimensional analytical study of the steady state flow through the slipper/rail gap. They calculated the flow conditions and heat flux by dividing the gap flow into four regions: a laminar flow near the stagnation point at the front of the slipper, a turbulent boundary layer region

before the upper and lower boundary layers merge, a merged region, and a Couette flow asymptote (flow between a moving plate and parallel stationary plate).

They found that air flowing through the gap is shock compressed to high pressure and temperatures resulting in high lift loads and high heat rates on the inner surface of the slippers. At speeds between Mach numbers five and ten, the aerodynamic heating caused by compression and confinement of the shock waves to the inner slipper surface are as high as those at the leading edge stagnation points, and that at higher velocities these heat rates are comparable to those of sliding friction. At 10,000 fps, heating rates were about 104 Btu/ft^2-sec. This indicates that aerodynamic heating of the slipper with a gap between the rail is equally as important as the frictional heating produced when no gap is present. Thus, extreme heating will always be a factor in the environment leading up to gouging, whether it is caused by friction or shock waves in air.

Korkegi and Briggs developed an expression for gap pressure p as a function of the distance from the slipper leading edge x (see Figure 1.10) from one-dimensional isentropic flow relations relating effective area to local Mach number and pressure as follows:

$$\frac{p(x)}{p_\infty} = \left(\frac{(\gamma+1)M_\infty^2}{2+(\gamma-1)M^2(x)}\right)^{\frac{\gamma}{\gamma-1}} \left(\frac{\gamma+1}{2\gamma M_\infty^2-(\gamma-1)}\right)^{\frac{\gamma}{\gamma-1}} \tag{1.5}$$

where p_∞, is the pressure at the free stream, $M(x)$ is the Mach number as a function of the downstream distance from the slipper leading edge x, M_∞ is the Mach number at the free stream, and γ is the ratio of the specific heats. The model is valid from the leading edge of the slipper to location where the upper and lower boundary layers meet. The model was developed for $M >> 1$, and should therefore be valid in the velocity regime being studied. This equation should also be valid for the helium environment using the proper Mach number and value of γ.

Among Korkegi and Briggs' conclusions were that the flow conditions in the gap are almost independent of M_∞ for $M_\infty \geq 4$, and that while the slipper wall is cold, the pressure in the gap decreases from the leading edge to the trailing edge. However, as the slipper heats up, the gradient diminishes until a condition of constant pressure results in the limit of adiabatic wall temperature. In addition, a decrease in gap height results in a drop in the

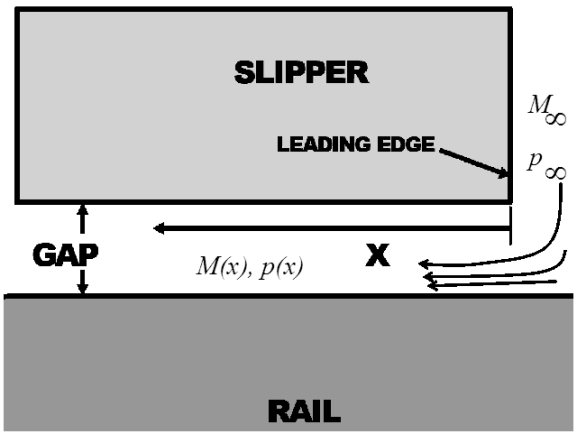

Figure 1.10 **Dimensional model for Korkegi and Briggs equation.**

gap pressure and an increase in gap size results in an increase in gap pressure. Therefore, the configuration is statically unstable. This results in the intermittent bouncing of the slipper against the rail.

Lofthouse, et al [31] in 2002, performed an external flow field investigation for a hypersonic test sled using computational fluid dynamics. He presented inviscid aerodynamic pressure results for a nominal rocket sled with increasing Mach numbers of 2.0, 3.0, 4.0, and 5.0. He found that shock front reflections on the slipper caused the highest pressure gradients to occur on the outer slipper surface. He sought to obtain solutions for flow in the gap between the slipper and rail. Extrapolating the pressure data to the area between the slipper and rail, Lofthouse found that shock interactions created sharp rises in pressure (jumps up to 75 psi) within the slipper/rail gap. These pressure differentials would become a source of temperature change on the slipper, especially as one considers viscous flow solutions.

Both analytical and numerical research in aerodynamic flow of a sled with a slipper on a rail shows that at high speed flows, an additional source of heating between the slipper and rail would be aerodynamic effects. These effects are basically caused by compressibility effects within the small gap between slipper and rail and are of a magnitude that must be considered in a nonequilibrium thermodynamic environment.

1.2.5 Load and Failure Analysis. Another aspect of the hypervelocity gouging phenomena is loading and failure of the materials of the slipper and rail. Research has been accomplished on the load and failure mechanisms of high energy impact. The previous sections have already mentioned the importance of normal loading due to impact on the formation of gouging, but determination of failure and damage is also important in understanding how materials fail and ejecta form during hypervelocity gouging. Failure and damage research is focused primarily on developing the theory used for setting criteria for material failure, including thermodynamics of deformation and damage.

In 1961, Abrahamson and Goodier [26] observed that humps precede moving loads on layers of soft or viscous material, similar to a hump deformation being driven in front of a rolling pin when a slab of bread dough is being rolled out. They concluded that this behavior is the result of inelastic behavior of the layer. If the material were elastic, the deformation would be symmetrical with equal bumps upstream and downstream of the load. For a stationary viscous material, the surface profile changes due to penetration of the load. If the penetration is stopped and the material is given a horizontal velocity, the leading hump is drawn under the penetrating load. The actual profile then, is determined by the combination of penetration and plastic flow. For a symmetric loading of an incompressible material, the surface displacement, which is significant only near the load, creates the characteristic hump.

Voyiadjis, et al [32] in 2003, presented a framework for analysis of heterogenous media that assessed a strong coupling between viscoplasticity and anisotropic viscodamage evolution for impact problems using thermodynamic laws and nonlinear continuum mechanics. Their proposed development included thermo-elastic-viscoplasticity with anisotropic thermo-elastic-viscodamage, a dynamic yield criterion of a von Mises type and a dynamic viscodamage criterion, the associated flow rules, nonlinear strain hardening, strain rate hardening, and thermal softening. The model presented in the research should be considered as a framework to derive various nonlocal and gradient viscoplasticity and viscodamage theories by introducing simplifying assumptions. This theoretical development of a framework for a damage model is an example of development of a nonequilibrium thermodynamic damage and failure model that could be used to improve the definition of failure

for high velocity problems such as hypervelocity gouging. Subsequent use of this model could aid in the understanding of the failure mechanisms involved in gouging.

Dr. Sathyanaraya Hanagud [33] is currently investigating a set of constitutive equations for high energy impact under a state of nonequilibrium thermodynamics. The objectives of this research are:

- To formulate constitutive models and equations of conservation, for metallic projectile materials, in appropriate continuum mechanics and nonequilibrium thermodynamics framework. The formulated models should be able to explain shock induced phase changes (including melting).
- To simplify the constitutive model, as found necessary, and use the model, with other equations of conservation and interface conditions, to understand the penetration mechanism of metallic projectiles into isotropic and granular media at high initial impact velocities (e.g., 850 to 2000 m/sec). The term understanding the penetration mechanism includes the projectile phase changes, melting, any failure of the projectile and deviation of the trajectory from the intended trajectory.
- To determine the parameters of the constitutive model and the penetration mechanism through testing.
- To design new materials, their microstructure and the spatial variation of the thermomechanical characteristics and structural design of the projectile to avoid trajectory deviation and any failure of the projectile.

The Hanagud constitutive models may be used to better describe the thermoplastic failure mechanisms of gouging. To accurately describe phase transition and nonequilibrium thermodynamics in which the first and second laws of thermodynamics are of uttermost importance, the Hanagud constitutive model is required. Most constitutive model assume adiabatic or isothermal states of thermodynamics.

Having presented research pertaining to loading under high energy impact and theoretical development of failure and damage in a thermodynamic framework, it is time to consider research specifically designed to mitigate gouging. The previous discussions have been leading up to this specific area. How does understanding the mechanisms that control

hypervelocity gouging allow us to interrupt that process and mitigate gouging? That is the question for which the following research seeks an answer.

1.2.6 Methods for Gouging Mitigation. Slipper and rail materials have been shown to dissipate energy through the formation of damage. A coating or change in material hardness might be used to improve the material's resistance to impact. In addition, thermal cycling of the coating likely affects its properties. As such, thermal effects on the capability of coatings to resist impact are of special interest.

Since gouging results from the antisymmetric deformation of the heated zone of softened material, the process may be mitigated by the use of special coatings to protect the surface from the high heating environment. Coatings have been used in the past, and have resulted in fewer occurrences of gouging.

Two types of coatings are available, refractory and ablative. While these coatings are typically intended to protect various parts of the sled from thermal effects, they may also be useful for protecting the rail surface. Refractory coatings such as tantalum, nickel-aluminum, zirconium oxide, tungsten, and cobaltech have been used on rocket sleds in the past [12]. Tantalum sheets have been used to protect slipper leading edges but the mounting hardware had failed in the severe thermal environment. The other refractory coatings are applied in layers using a plasma sprayer. These plasma sprayed coatings offer very good protection, however, great care needs to be taken in their application. A reliable interlock between layers must be established to avoid the formation of cracks, which may be initiated by the difference in the thermal expansion coefficients of the metal surface and the coating.

Ablative coatings include Teflon, carbon-carbon, and carbon-phenolic coatings. These have been used to protect sled components at velocities greater than Mach 6. Teflon has been used, but its effectiveness is surpassed by the carbon-carbon. Both of these, however, are of limited usefulness under high shock loading conditions. Carbon-phenolic layers are applied in sheets, using epoxy to bond and stack the layers. The use of ablative materials can result in configuration changes, which are undesirable and could be detrimental to operation [12].

A proposed slipper design by Barker, et al uses a laminated slider design composed of alternating layers of plastic and high strength, high toughness steel at a 10-degree angle of attack [21]. This design combines several gouge mitigating factors, and was first tested in 1987 at 1.9 km/s without gouging the rail. Tachau [24] also proposed a slipper design that uses a corrugated contact surface, intended to disrupt the growth of the high-pressure core.

Of course, Schmitz's work focused on mitigating gouging using coatings [1]. Schmitz performed a study of various coatings and thicknesses using CTH and compared the velocity at which gouging occurred to the coating thickness and properties. His results show that for greater than four mils thickness, coatings made of aluminum, epoxy, polyethylene, polyurethane, and teflon raised the velocity for the onset of gouging substantially more than the other coatings including hematite, molybdenum, and zinc. These results from Schmitz's work can be viewed in Figure 1.11.

Various methods of mitigating gouging have been presented. Innovative slipper designs and coatings have been suggested as a means to mitigate hypervelocity gouging. In order to provide a true physical understanding of various means for mitigating gouging, one must first understand the mechanisms that occur up to and during gouging. Once these mechanisms are understood and an accurate cause and effect storyboard is developed, gouging mitigation will be in reach.

1.2.7 Summary of Previous Research. In the work on gouging done to date, the cause to which gouging has been directly attributed is impact initiated by debris on the guider due to environment, sled deterioration, or alignment defects, and bouncing motion or vibration of the slider against the guider. After impact, proposed mechanisms that cause the gouge to develop have included thermoplastic shear, hypervelocity microasperity impact between the slider and guider contact surfaces, shock induced pressure accumulation at the slider-guider interface, and the existence of viscoplastic materials at the contact surfaces.

Sled impacts involving large slippers are subject to high normal loads due to aerodynamics and structural dynamics coupled with a large mass. Rail gun projectiles are much

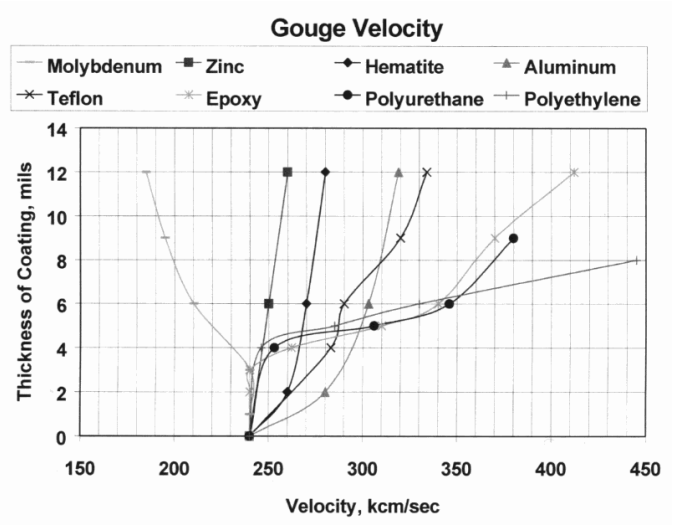

(a) **Various coatings and the effect of their thickness on gouging velocity.**

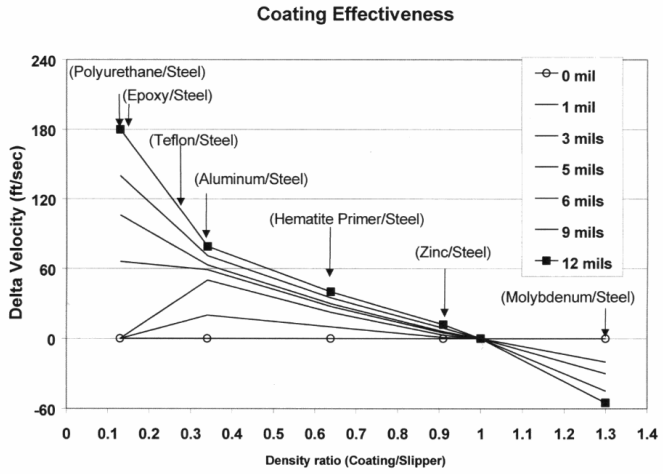

(b) **Coating effectiveness.**

Figure 1.11 **CTH analysis of coatings on the rail and their effectiveness in mitigating the onset of hypervelocity gouging according to Schmitz [1].**

smaller, lighter, and more precisely balanced, resulting in relatively small normal loads. Laboratory gas guns have high impact angles but small mass compared to sleds. Despite the differences and variety of causes and mechanisms suggested and the three different systems (sled runs, rail guns, and laboratory tests) involved, there are common threads in

these findings. Slider velocity, stresses at the contact surface as a function of slider normal force, and material properties of the slider and guider are repeatedly identified as important factors that determine if gouging will occur. Whether imposed by asperity impacts or the contact between deformed slider and guider surface layers, it is generally agreed that some minimum amount of normal force at a slider-guider interface, relative to the properties of the materials involved, is likely required for gouging to occur. It seems that if the normal forces at a slider-guider interface lead to an accumulation of shock induced pressure at the point of contact, phase transformations, softening, melting, and possibly vaporization and gouging of both slider and guider surfaces may occur.

There is strong evidence that the phenomena of gouging is really a shear mechanism. Metallurgical evidence indicates that gouging occurs due to catastrophic thermoplastic shear. Adiabatic shear bands are evident in high velocity gouging in test tracks, rail guns, and projectile gouging in curved surfaces. Large local temperature gradients create planes of thermal softening that generate shear bands and spalling pressure in turn generates cracks that are evident in post-gouged material. Shear waves move in directions perpendicular to the interface of projectile and target and have particle velocities that are parallel to the interface. Combined with a large compressive spherical stress (or pressure) these planes of motion of the particle velocities would provide planes of "slippage" that would allow portions of the bulk material of the rail or slipper to deviate into each other.

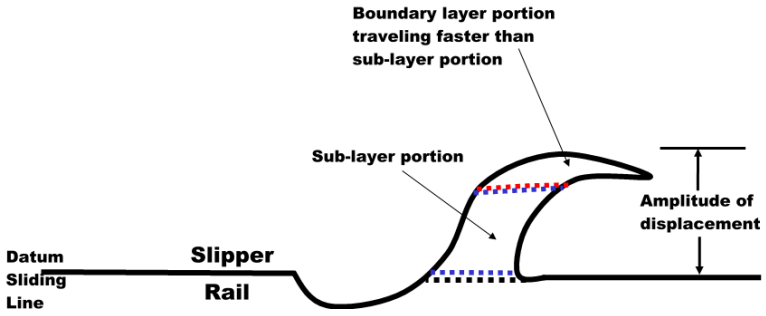

Figure 1.12 **Jetting initiates when a layer of the furthest penetrating material is imparted with a velocity relatively faster than the sub-layer.**

It is proposed that jetting with gouging initiation be defined in the following way (see Figure 1.12).

- Plastic displacement must create a steep amplitude above or below the datum sliding line.
- For a gouge to develop, a relative velocity with respect to the bulk of the displacement must form at the portion of furthest penetration.
- The portion of furthest penetration with a relative velocity is called the boundary layer portion of the plastic displacement.
- The bulk of the displacement closest to the slide line is called the sub layer portion of the penetrating plastic displacement.

1.3 Further Considerations for Hypervelocity Gouging Research

Hypervelocity gouging has been approached from experimentation, observation, numerical investigation, and analytical viewpoints. The previous section describes the conclusions drawn from this body of research on how gouges form and what are the factors which affect the formation and development of gouging. It can be difficult separating the root causes of gouging from its effects because the phenomenon is almost instantaneous and many features of hypervelocity gouging are coupled.

For instance, whether the high pressure core that is seen during gouging is the underlying *cause* of gouging, or whether it is a *result* of normal forces and inertial effects due to the initial impact and gouging formation is a big question. Another question is whether the root cause of gouging is the deformation due to impact and tangential velocity or whether the deformation is due to gouging stresses? In addition, what are the conditions conducive to gouge formation? These questions lead to certain aspects of the gouging environment and event that have not been considered or explained in the literature.

Recently, the gouging problem has been studied from several viewpoints. The onset of gouging has been studied using temperature [28] and a protective coating on the rail as parameters [1]. These studies have shown that determination of the onset of gouging may be affected by both the consideration of temperature and a protective coating on the rail.

These studies lead to consideration of what environment is conducive to gouging, or conversely, what environment may be created to mitigate gouging. To do this properly, an

accurate model for the initiation of gouging must be created and then those parameters that affect gouging must be investigated and the effects they have on gouging phenomenon determined.

The slipper is exposed to time varying heat sources (e.g., friction, aerodynamic heating, and plasticity). This begs the question of whether isothermal and adiabatic assumptions are valid for this case. To analyze these situations, one must consider appropriate constitutive models that account for heat transfer, nonadiabatic heating, and plasticity. Equations of state that are coupled with heat transfer models as well as heat transfer models themselves must also be considered.

The conditions that affect the thermal environment of hypervelocity gouging include large stagnation temperatures behind oblique shocks in air and within the gap between slipper and rail. Contact friction between the slipper and rail is another source of heat. The slipper is subject to these conditions for a period of time much longer than any one section of the rail. This allows time for the thermal environment to develop through the diffusion of heat within the slipper. Thus, the slipper is the structure most affected by heat fluxes. Clearly, if one compares the expected thermal state and state of stress in the slipper and rail, the slipper represents the most extreme case.

Friction between the rail and slipper creates a thermal environment along a thin layer on top of the rail, but this thermal layer has been treated adiabatically because of the extremely short period of time it is subject to this condition. The period of time upon which the slipper is in contact with a section of the rail is extremely short, on the order of microseconds at speeds of 1.5 to 3 km/sec. However, this thin layer of frictional heating directly affects analysis of any coatings that may be considered for the mitigation of gouging.

A state of stress caused by intermittent impacting of the slipper on the rail through flight creates a stressed environment in both the slipper and rail that must also be considered. Furthermore, the slipper amounts to a high speed heat source which sets up a thermal stress wave in the rail. This compounds the stressed condition experienced by the slipper-

rail system just prior to gouging. Thus, a means to model this extreme thermodynamic situation is of great interest.

How do phase changes of the slipper and rail materials affect material failure and the initiation of gouging? To capture such a complex area in a gouging model, the constitutive models must be derived to account for this factor. Terms must be included that account for a mixture of phases of a material and the effect of their material properties on the mechanics of the entire mixture. This is what the Hanagud equations [33] provide for analysis of the hypervelocity gouging problem. The Hanagud equations are a constitutive model developed from a nonequilibrium thermodynamics point of view and accounting for both phase transitions and dislocation dynamics. In addition, the constitutive model is derived with nonequilibrium thermodynamic assumptions and could also be written using damage parameters to develop a more accurate failure criteria.

Failure criteria are an important aspect of any numerical investigation of the hypervelocity gouging problem. Failure criteria affect the development of gouging in the numerical model and should take into account heat transfer effects. Most numerical tools used for high energy impact use simple maximum stress or maximum strain failure criteria. A more sophisticated failure model would enable exploration of varying modes of failure affecting the onset of gouging [34, 32].

Another consideration is whether the scaled down dimensionality of the Laird model is accurate. To initiate an oblique impact event in Laird's model, the slider is given a horizontal velocity of 2.0 km/s and a vertical velocity of 50 m/s as initial conditions. Load and vibration simulations of the sled assembly by Hooser using the Dynamic Analysis and Design System (DADS) [35, 36] have shown that a more realistic vertical impact velocity is approximately 1 to 2 m/s. The slipper mass used in the simulations is much less than the mass of an actual sled. The kinetic energy of a 227 kg sled impacting at 1 m/s is equivalent to the Laird's 89.77 g slipper impacting at 50.26 m/s. The two materials are already in contact along the slider length, representing the instant that any gap between the two materials is closed and the impact begins. Basically, Dr. Laird emulated the *in situ* kinetic energy seen by the slipper as it travels on the rail. However, this approximation underestimates the momentum of the impact. The question also remains whether this

energy oriented approach is still valid for a heat transfer analysis. The actual slipper and rail geometry have not been investigated to this point. A dimensional analysis is performed to provide answers to these questions and determine a method for applying numerical results to a real test sled.

Finally, further investigation of the hypervelocity gouging problem should also consider the slipper and development of the thermal and stress environments it is subjected to. In addition, the stress waves generated by the "shock" of a high speed heat source acting on the rail and a potential protective coating on the rail or slipper must be considered along with rarefaction waves and spallation due to shock wave interaction. Viscoplasticity is a factor and temperature differentials that cause adiabatic shear bands with their associated failure modes is not adequately modeled at this time. Further investigation of the gouging problem and mitigation of the gouging phenomena should approach any model with as many of these factors as possible, in mind.

II. Theoretical Background

This chapter provides a theoretical basis for the approach taken in the research. Computational algorithms designed to provide solutions for the theoretical conditions are also presented. The understanding of these algorithms is essential to judging the realism inherent in the solutions. The objectives of this research include studying development of a nonequilibrium thermodynamic environment prior to gouging, characterizing friction, and studying potential failure mechanisms leading to gouging so that gouging can be mitigated. The primary CTH algorithms required to perform this study include the explicit heat conduction algorithm for calculating heat transfer, the boundary layer algorithm for characterizing friction forces and deviatoric stress along sliding interfaces, and fracture models to characterize material failure. Detailed analysis and the theoretical background for the dimensional analysis and scaling of the test sled is provided in appendix IV.

2.1 CTH Method

CTH solves for the conservation equations of mass, momentum, and energy. It does this by integrating explicitly in time using a two-step Eulerian scheme consisting of a Lagrangian step and a remap step. The Lagrangian step [37] solves finite volume approximations of the conservation equations. Finite difference approximations are used to determine velocity gradients. Velocity components are centered on cell boundaries. All other parameters (e.g., stress, pressure, and temperature) are centered in each cell and are assumed to be uniform within the entire cell.

Eulerian meshes are fixed in space. There are two sources of change in the Eulerian mesh that must be accounted for. There are changes due to source (Lagrangian) terms, and changes due to convection (Eulerian) terms. There are two approaches to solving this. The first updates the solution variables in one step. The second approach is used by CTH. In this approach, the Lagrangian terms and Eulerian terms are separated and solved in two steps. First the Lagrangian terms and then the Eulerian terms. This approach is called the operator split technique. This technique is relatively simple. yet allows for second-order accuracy [38].

To explain the operator split technique used in CTH, we will use the linear advection equation.

$$\frac{\partial \phi}{\partial t} + c\frac{\partial \phi}{\partial x} = f,\ \phi(x,0) = \phi_0(x)$$

Where ϕ is the field variable, c is the constant flow velocity, and f is the source. This equation is "split" into two equations that are solved in sequential steps: the Lagrangian and the remap steps. The Lagrangian step contains the source term and solves the equation

$$\frac{\partial \phi}{\partial t} = f$$

and the remap step contains the convective term and solves the equation

$$\frac{\partial \phi}{\partial t} + c\frac{\partial \phi}{\partial x} = 0$$

The same algorithms are used to solve both "split" equations.

In the Lagrangian step, Eulerian cells are allowed to distort according to the magnitude and direction of the velocity components which are centered on and perpendicular to the cell faces. This means the mesh deforms by following material movement. Thus, there is no mass flux across the cell boundaries and conservation of mass is met trivially. Explicit finite volume representations of the integral form of the conservation equations of momentum and energy use current values of mass, volume, and stress to determine new cell velocities. The conservation of energy equation is a balance of internal energy, kinetic energy and mechanical work. Velocities used in the energy equation are determined from the momentum equation and mechanical work. Mechanical work is generated from pressure, deviatoric stress, and artificial viscosity [39] and is treated as an internal energy source. Energy and work is divided among the materials in a cell using the Cell Thermodynamics algorithm [40, 41].

The equation of state [42] is used to convert the internal energy of the cell into temperature. If it is desired that heat be allowed to flow, this is also calculated during the Lagrangian step. The Explicit Heat Conduction algorithm [2] is used in CTH to calculate the flow of heat between cells. A heat flux term is used to transport energy so that material

specific energies may be updated in this step. The equation of state is then used to update the material temperatures through the thermodynamic energy balance routines [40, 41].

The constitutive model is also applied in the Lagrangian step. Models available to the user are the Johnson-Cook, Zerilli-Armstrong [3] and Steinberg-Guinan-Lund [43] viscoplastic models, and the Transverse-Isotropic model [44], as well as others [45]. Stress deviators are updated after the conservation equations are solved by using the updated cell velocities. The deviatoric stress in this update is limited by the constitutive model.

If a friction solution is desired, one may use the Boundary Layer Algorithm for Sliding Interfaces in Two Dimensions [46] to calculate the effect of frictional forces between sliding interfaces. Otherwise, CTH assumes a fluid-like interface between materials in which there is no deviatoric stress at the interface [47]. In the Lagrangian step, the interface between materials can be treated either way. For frictional effects, the layer of zero deviatoric stress is moved from the sliding material interface into what is defined as the "softer" material. This allows the penetrator to maintain deviatoric strength at the material interface during sliding. The frictional force is calculated using the Cauchy stress and the coefficient of kinetic friction and treated as a body density force which is then applied in the momentum balance equation [46].

The energy balance routine is used to calculate cell thermodynamic data (i.e., pressure, density, and temperature) at the end of the Lagrangian step and prior to the remap step. In the remap step, parameters of the distorted Lagrangian step are recalculated and advected back to the original Eulerian computational grid. In other words, the mass, momentum, and energy of the deformed mesh of the Lagrangian step are related back to the original Eulerian mesh [39].

Using cell-face motion based on velocities, the volume flux between the distorted and Eulerian mesh cells is determined. The volume of the materials to be moved is then determined using an interface tracking algorithm that estimates the location of material interfaces within mixed cells [**?**]. Each material's mass and internal energy are moved using this information. The final step is to apply the thermodynamic energy balance routines

[40, 41] one last time. The equation of state package is also used again to calculate the new cell pressures, temperatures, and sound speeds.

Cauchy stress is used in development of the constitutive models in CTH, as well as for the various other algorithms. It is used in the Lagrangian step because the Eulerian Cauchy stress is related to the deformed mesh using the rate of deformation tensor. The viscoplastic constitutive equations are also developed using the spin tensor, which is an important consideration in the development of the stress and strain relations for large movement of rigid bodies. See section 2.7.2 for a description of the rate of deformation and spin tensors and how they relate to Cauchy stress and strain.

2.2 Nonequilibrium Thermodynamics

Kreith and Bohn [48] define thermodynamics as the "branch of science which deals with the relation between heat and other forms of energy". This science typically deals with systems of heat, work, and other properties of systems in equilibrium.

Thermodynamics is based on two basic laws. The first law of thermodynamics states the principle of energy conservation. It says that energy cannot be created or destroyed. It relates the work done on a system with the heat flux into the system and the change of energy of the system.

$$\rho \frac{du}{dt} = \mathbf{T} : \mathbf{D} + \rho r - \nabla \cdot \mathbf{q} \tag{2.1}$$

where u is the internal energy per unit mass, t is time, $\mathbf{T}$ is the Cauchy stress tensor, $\mathbf{D}$ is the rate of deformation tensor, **:** is the scalar tensor product operator, ρ is the density, r is the distributed heat source strength per unit mass (such as a radiation field), and $\mathbf{q}$ is the outward heat flux vector.

The second law of thermodynamics governs the direction of energy transformation. This law states that heat can only flow from areas of high heat to low heat. It is also stated in terms of entropy, a measure of the disorder within a system. The state of entropy of a system can only increase. This law describes irreversible processes. Written in the form of the Clausius-Duhem inequality, it places a limitation on internal entropy production and thus, the direction of transformation of energy. Expressed mathematically, it states that

internal entropy production is always positive for an irreversible process. In others words, the rate of entropy increase is always greater than or equal to the rate of entropy input [4] for irreversible processes.

$$\frac{ds}{dt} \geq \frac{r}{T} - \frac{1}{\rho}\mathbf{div}\frac{\mathbf{q}}{T} \tag{2.2}$$

where s is the entropy per unit mass.

Frictional dissipation and the flow of heat from high temperature to low temperature regions are examples of irreversible processes. Using a friction brake, kinetic energy of a wheel can be converted into internal energy which could cause the temperature of the wheel to increase. This process cannot be reversed by changing the internal energy of the wheel into kinetic energy to set the wheel in motion again. Likewise, heat only flows from regions of high temperature to regions of lower temperature. Both of these processes are irreversible and are governed by both the first and second laws of thermodynamics.

The heat flux $\mathbf{q}$, is the process by which energy transport takes place. This process changes the internal energy of a system. When temperature gradients exist in solid continuums, heat flows from the regions of high temperature to the regions of lower temperature. The rate that this transfer occurs at is proportional to the product of the temperature gradient and the area of the transfer region. This can be expressed mathematically as [48]

$$q_x = -kA\frac{dT}{dx}$$

where q_x is the heat flux (rate of heat transfer) in the x direction, k is the thermal conductivity (which is a material property), A is the area through which heat is transferred, and T is temperature as a function of x. The negative sign is there to ensure heat flows from high to low temperature regions and that flow in the positive x direction is positive. This relation is called Fourier's Law.

2.3 Heat Conduction Algorithm

This investigation studies development of a nonequilibrium thermodynamic environment in which gouging occurs. To develop the conditions for nonequilibrium thermody-

namics, heat energy is allowed to flow between areas of varying temperature and heat energy. The system is not in a state of thermodynamic equilibrium in which the second law of thermodynamics is satisfied. CTH develops a solution to these conditions by solving the heat conduction equation as part of its algorithm for heat flux [2]. With this algorithm, heat is allowed to flow and temperature changes occur. These thermal changes are then allowed to affect material properties, energy balance, or stress. The explicit heat conduction algorithm occurs in the Lagrangian step of the CTH numerical scheme.

Typically, a diffusion representation of heat conduction is used.

$$\frac{\partial T}{\partial t} = \frac{1}{\rho C_v} \nabla \cdot (k \nabla T) \tag{2.3}$$

where T is temperature, k is thermal conductivity, ρ is density and C_v is specific heat at constant volume. If the thermal conductivity can be approximated by a constant, then the equation becomes:

$$\frac{\partial T}{\partial t} = \alpha \nabla^2 T \tag{2.4}$$

where $\alpha = \frac{k}{\rho C_v}$, is called thermal diffusivity.

By comparison, CTH uses the heat flux to transport energy and update material specific energies. The equation of state is then used to update material temperatures through the energy balance routines.

$$\overrightarrow{Q} = -k \nabla T \tag{2.5}$$

where Q is the heat flux.

The heat conduction model is an explicit method and thus has a Courant condition that must be satisfied for numerical stability.

$$dt_{HC} < \frac{\rho C_v dx^2}{2k} \tag{2.6}$$

In most cases, the heat conduction time step will not dominate the calculation.

Currently, heat flux is not allowed across boundaries, making the system adiabatic in this respect. This models insulating physical boundary conditions at the edge of the mesh and gives correct behavior across reflecting boundaries.

In a two-dimensional rectangular geometry, CTH represents the heat flux by:

$$\overrightarrow{Q} = -k\left(\hat{i}\frac{\partial T}{\partial x} + \hat{j}\frac{\partial T}{\partial y}\right) \tag{2.7}$$

The heat flux in the x-direction is calculated first. The resulting heat flux is then multiplied by the area of the distorted interfacial cell boundary to get the total heat transport between cells. The process is repeated for the y-direction.

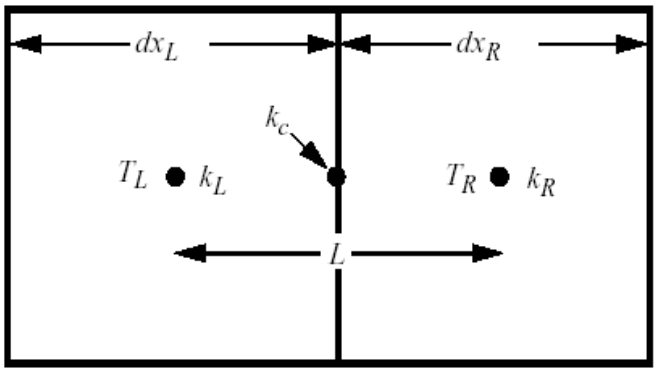

Figure 2.1 **Heat conduction between cells in CTH. Figure from CTH reference manual [2].**

Figure 2.1 shows an example of one-dimensional heat conduction between cells. Q_x^*, the heat flux between left and right cells in the positive x-direction (left to right) is

$$Q_x^* = -k_c(T_R - T_L)A_c dt/dx_c \tag{2.8}$$

where dt is the time-step centered at $t^{n+1/2}$, $dx_c = (dx_L + dx_R)/2$, $A_c = dy$ for a two-dimensional rectangular geometry, and $k_c = (dx_L + dx_R) \,/\, \left(\frac{dx_L}{k_L} + \frac{dx_R}{k_R}\right)$

A similar method is used to calculate the conducted heat in the y-direction, Q_y^*. The conducted heat must then be distributed among the material specific energies, ε_m of each

cell through thermal conductivity fraction.

$$\varepsilon_m^{n+1} = \varepsilon_m^n + \frac{k_m \phi_m Q^*}{kM} \tag{2.9}$$

where k_m is the material conductivity of material m, ϕ_m is the volume fraction of material m, $k \equiv \sum_m k_m \phi_m$, M is the total cell mass, and $Q^* = Q_x^* + Q_y^*$ is the total heat conducted into the cell. The heat conduction cycle is completed in CTH's energy balance routines where energy is exchanged between materials within mixed computational cells. The equation of state is used to transform the updated material specific energies into temperatures.

The exchange of energy (after transfer of heat) between materials within a mixed cell is performed in the energy balance routines of CTH. Here a thermodynamically consistent cell-centered average temperature for mixed cells, based on specific heats obtained from the equations of state, is calculated.

A cell may consist of a number of different materials. Individual material temperatures within the cell are adjusted towards the average temperature in the cell, but there is a limit to this adjustment. Only ten per cent of a materials internal energy is allowed to move during a single computational cycle. This limits the adjustment of the individual material temperatures within a cell.

Temperature changes then affect the constitutive equation depending on the model. In some cases (such as the Johnson-Cook model), this will affect the flow stress, in others (such as the Steinberg-Guinan-Lund model), it will affect the shear modulus or other properties.

2.4 Friction

In general, when a difference in velocity between two surfaces in contact occur, if the surfaces are not completely smooth, there occurs a component of the resultant force that is tangent to the surfaces (see Figure 2.2). While the surfaces are in motion relative to each other, this frictional force is more specifically known as a kinetic frictional force. The kinetic frictional force opposes motion of the surfaces as they slide against each other. The amount of frictional force developed as a response to sliding motion can be characterized

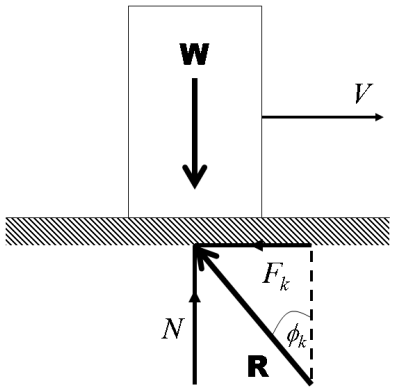

Figure 2.2 **Kinetic frictional force, normal force, and resultant.**

by the equation (known as Coulomb's Law):

$$f_k = \tan \phi_k = \frac{F_k}{N}$$

where f_k is the coefficient of kinetic friction, ϕ_k is the angle of kinetic friction force vector, F_k is the frictional force, and N is the component of the resultant force between the two materials normal to the surface.

The coefficient of friction varies for different materials and for different relative velocities between the materials. For dry surfaces, the amount of friction between the two surfaces is directly proportional to the pressure exerted at the surface interface between the materials. The coefficient of kinetic friction is generally independent of the pressure and the area of contact. At relatively low velocities, the kinetic coefficient of friction is constant.

In the theory of lubrication, friction for lubricated surfaces is determined by either *hydrodynamic* or *boundary* friction [49]. Each of these cases of lubrication may occur in high speed impacts if a layer of molten metal is formed upon impact between the materials such as would occur for high contact pressures. If this layer of molten metal is thick compared to surface irregularities, then hydrodynamic forces dominate and the liquid layer carries the load.

If however, this layer is thin, then boundary frictional forces dominate. In boundary friction, the surfaces are extremely close to each other and the load is carried by thin

layers of lubricant (i.e., molten metal) attached to each surface. In this case, the material properties of both the liquified metals and the solid metals are of importance. In the hydrodynamic case, the properties of the liquid form of the metals are of greater significance in the mechanics of sliding.

If the load is increased until the boundary layers can no longer carry the load, the materials will come into contact with one another at high points of the rough sliding surfaces. Experimental evidence indicates the surfaces may weld at the points of contact due to highly localized pressures and that these welds are subsequently broken due to sliding motion of the materials. These welds likely account for the resistance to the sliding motion. In general, the coefficient of kinetic friction for this case lies between the kinetic coefficient of friction for dry surfaces and hydrodynamic surfaces.

At the HHSTT, the portion of the rail at which critical speeds of the slipper occur (greater than 1.5 km/s) is coated to mitigate hypervelocity gouging. As the sled reaches this velocity, it rides on an uncoated portion of the rail. Along the clean rail surface, the slipper may ride on a layer of molten metal where either hydrodynamic or boundary friction may dominate. For the section of the rail at which the highest velocities are attained, the rail is coated with either a tough polymer such as epoxy or with an iron oxide such as hematite.

The above characterizations for high speed friction may be applicable to coatings on a rail. For instance, thick and smooth (relative to the substrate) coatings can be said to act as a hydrodynamic layer between slipper and rail. Thinner coatings may act under boundary friction conditions between slipper and rail materials.

Bowden and Freitag [50] found from experiments on friction at low velocities that friction is due in large part to local adhesion and shearing of regions in contact. At velocities around 3 m/s, the temperature in these regions can exceed the melting temperature of metals and thermal softening can occur. At this velocity, heat diffusion may have and effect on the state of the material. They did not find the coefficient of friction to change at low velocities. However, for high velocities (in the order of 800 m/s), they found the

coefficient of kinetic friction decreased to 0.2 or lower for a variety of metals on metal (e.g., steel on copper and steel on duraluminum).

For the metals under consideration, they found the surface temperature between the metals to be near the melting temperature. Metals under consideration included steel on copper, steel on aluminum, steel on duraluminum, steel on bismuth, steel on antimony, steel on molybdenum, copper on molybdenum, steel on diamond, copper on diamond, and chromium on diamond. They concluded that friction and wear of metals at high velocity are dependent on the relative material properties of the materials at elevated temperatures.

They further modified the theory of adhesion by stating that shearing of the welded contacts is facilitated by steep temperature gradients that soften or melt leaving a thin film along the surfaces. This implies that boundary friction may be dominant under these conditions. The area of contact would then depend on the velocity of plastic deformation propagation for the materials. They also found evidence that at a critical velocity (above the plastic wave velocity) brittle failure may dominate. This description of the effect of friction at high speeds is similar to the description of hypervelocity gouging by Barber and Bauer [14].

Barber and Bauer's description of the gouging phenomenon is worth repeating here:

> When two solids are brought together, actual physical contact occurs only at a small number of discrete contact points. The normal load between the two solids is supported by these discrete areas. The number and size of the contact points increases with increasing applied load. Adhesion between two bodies in contact occurs at the contact spot and "cold welds" are formed. Tangential motion of one body with respect to the other deforms or shears material in the contact spots and results in further asperity contact. Frictional forces develop because of the ability of the contact spots to resist this deformation (wear results from material fracture due to excessive straining in the contact spot region.) During contact spot shearing, energy is dissipated into the deformation zone and then removed from the deformation zone by thermal conduction into the material substrate.
>
> As sliding velocity increases, the rate of energy dissipation in the deformation zone exceeds the conduction rate out of the deformation zone, causing the deformation zone temperature to rise. As sliding velocity increases still further, the temperature of the entire surface of a slider may reach the melting point, at which point a liquid interface is formed between the sliding surfaces, greatly reducing the frictional forces observed and the coefficient of friction. The liquid

> interface behaves as a hydrodynamic bearing. Viscoshearing of the liquid film dissipates energy, which causes intense heating of the slider surface and results in surface melting. Surface recession occurs, providing an influx of melted material from the slider surface equal to the efflux from the interface due to slider motion, and a steady-state hydrodynamic interface is established. The development of this hydrodynamic fluid layer depends upon the material properties of the slider and guider, the sliding velocity, the normal load, and possibly the geometry of the slider.
>
> At hypervelocity, if a fluid interface forms, velocity gradients in the interface will increase, as will the frictional force, energy deposition, surface recession, slider wear, and interface temperature. At some velocity, it is likely that the temperature of the interface region becomes so high that the interface material is vaporized, with a resultant drop in viscosity and frictional force. If a fluid interface does not form, asperity contact continues to occur at very high velocities. The asperities, however, can no longer come into contact in a steady or quasi-steady mechanical mode. Instead, they impact generally in an oblique manner, generating shock stresses.[14]

Contrast this description to Krupovage and Rasmussen's [12] assertion that a liquid metal interface acts as an abrasive rather than reducing friction. At hypervelocity speeds however, Barber and Bauer agree with Krupovage and Rasmussen that frictional forces increase in the liquid metal interface.

CTH is used in this investigation to evaluate the effect of frictional sliding at high speeds. There are two treatments of material sliding available to the user in CTH. The first approach treats the interface as a frictionless surface. The deviatoric stress is set to zero at the interface. The second treatment allows deviatoric stress at the interface, but does this by moving the frictionless slip layer into the material defined as "soft."

The two sliding interface algorithms in CTH are known as the Slide Line and Boundary Layer Interface algorithms. These models allow for the simulation of sliding interfaces by allowing the materials at an interface to retain their strength properties, yet move independently. The Slide Line algorithm allows materials along designated interfaces to keep their strength in compression and tension, but sets the shear strength to zero to allow the materials to slide. The behavior can be computed at material interfaces using a Lagrangian calculation by providing spatial slidelines, which are used when large transverse deflections of the material interface are expected [47]. When this Lagrangian method is used in an Arbitrary Lagrangian Eulerian algorithm, it must then be remapped to an Eulerian mesh

and the functions convected. The Boundary Layer Interface model couples the deformation of materials where they share an interface. One surface is deformed using the forces on both materials, and the adjoining surface is transversely constrained to move with it, although the materials may maintain distinct tangential velocities.

2.5 Boundary Layer Algorithm

Deformations due to sliding between various materials in contact are characterized in CTH by the Boundary Layer Interface algorithm for sliding interfaces in two dimensions [46]. In this algorithm, the sliding process is moved away from the mixed cells in the material interface and into the target (or "soft") material. This allows the development of a deviatoric stress component at the sliding material interface and avoids problems that occur when the material strength of the projectile is decreased in mixed cells. Mixed cells contain a yield strength that is an average of the strengths of the materials in the cell. Thus, the mixed cell has a strength that is less than the stronger material and greater than the weaker material, which can cause numerical rather physical effects within the results.

CTH was originally developed as a tool for modeling continuum mechanics under extremely high pressures and shock waves. In these cases, shear stress is small compared to normal stress. Hydrodynamic treatments are applicable and relatively crude treatment of material interfaces are appropriate.

However, as the ability of materials to carry shear loads and respond to shear stress and in tension becomes significant, other treatments for material behavior and for sliding interfaces is required. The Boundary Layer Interface algorithm was developed as a response to modelling penetration of a projectile into deep targets. In this case, sliding between the projectile and target becomes a significant problem in the analysis. If removal of material at the interface occurs as the primary response to the sliding interface between projectile and target, then the Boundary Layer Interface algorithm may not be required. However, if the projectile retains enough of its strength, then it may travel as a rigid body into the target and it would then be necessary to accurately model this sliding interaction. In this case, friction effects would also become more important.

The alternative to the Boundary Layer Interface algorithm is treating the sliding interface as a frictionless surface by setting deviatoric stress along the material interfaces (i.e., mixed cells) to zero. This alternative is known as the Sliding Line algorithm. This treatment, however, dilutes material strength of the penetrator within the mixed cells. The penetrator surface is then essentially a fluid and is treated as such in the analysis. This surface erodes and the penetrator shape changes. One of the questions that is important to consider in the investigation, and for which there is yet no definitive answer, is which treatment is most close to reality: projectile erosion or projectile friction.

Typical markings on rails due to impacts that are not gouges indicate deformations similar to wear. This is true also for impacts on coated sections of the rail. This implies the slipper maintains its strength during impact during these common events. Observation of gouged materials however, indicate a hydrostatic and eroding surface may be more apropos. It is important to note however, that hypervelocity gouging is a result of mutual interactions of rail and slipper materials and not necessarily just erosion of a penetrator (i.e., slipper). Thus, whether the event is an impact that results in gouging or not, the Boundary Layer Interface treatment may still be most appropriate for a realistic analysis. This section (based on the CTH reference manual for the Boundary Layer algorithm [46]) discusses how CTH treats friction in the analysis, and this is accomplished through the Boundary Layer Interface algorithm. To understand how the algorithm works, let us first assume that solids are in contact across a surface, S. For the two materials, one is defined as *soft* and the other *hard*. For purposes of this discussion, let us assume the soft material is the target and the hard material is the penetrator, or projectile. In hypervelocity gouging, this would be the rail and slipper, respectively. The soft material in where the slip layer (defined later) will be contained. Let us first define some important terms that are used in this discussion:

Interface Layer The layer of cells about two cell widths thick that contains the material interface.

Hard Boundary Layer In this layer of cells, processes take place that model all physical interactions across the material interface. Cells are considered to be in this layer if

its center is within a specified distance, ω_{bl} of the center of a cell within the interface layer. Usually, cells in the interface layer are considered as part of the hard boundary layer. Mixed cells usually end up in the hard boundary layer.

Soft Boundary Layer In this layer of cells, processes take place that model all physical interactions across the material interface. Cells are considered to be in this layer if its center is within a specified distance, ω_{bl} of the center of a cell within the interface layer. Cells are in this layer if they are filled with at least 99% of soft material. Mixed cells are almost never in the soft boundary layer. The slip layer lies within the soft boundary layer.

Slip Layer This layer of cells models a frictionless sliding interface. In this layer, flow stress is zero. Deviatoric stress tensors are set to zero here. This layer lies within the soft boundary layer. If a cell is in the soft boundary layer, and its center is within ω_{sl} cell diagnols of the center of a cell in the interface layer, then it is in the slip layer.

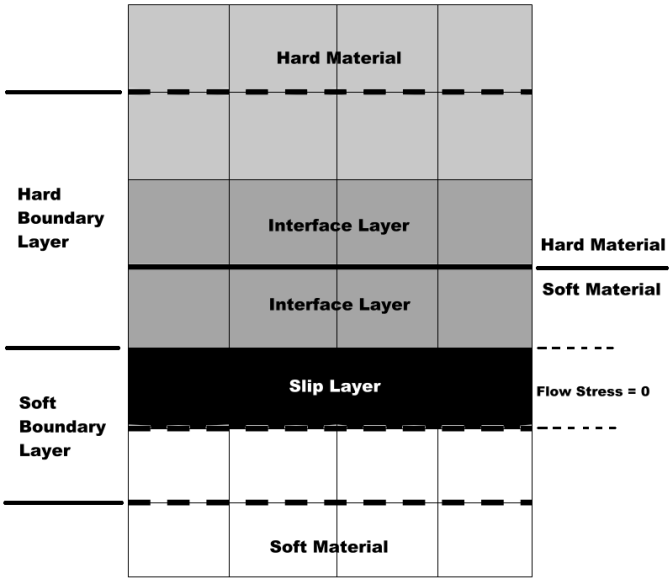

Figure 2.3 **Various layers as defined for the Boundary Layer Interface algorithm.**

Figure 2.3 depicts these various definitions graphically. In many cases, the slip layer will coincide with the soft boundary layer.

Let $\nabla\phi_{h_x}$ be the hard material volume fraction in the x direction and $\nabla\phi_{s_x}$ be the hard material volume fraction in the x direction. Also let Δx be the cell width in x direction. The central differencing relation used to evaluate the vector gradients of the hard and soft material volume fractions within the cells are:

$$(\nabla\phi_{h_x})_{i,j} = \frac{(\phi_h)_{i+1,j} - (\phi_h)_{i-1,j}}{2\Delta x}$$

$$(\nabla\phi_{s_x})_{i,j} = \frac{(\phi_s)_{i+1,j} - (\phi_s)_{i-1,j}}{2\Delta x}$$

Similar relations exist for gradients of the hard and soft material volume fractions in the y direction where Δy be the cell width in y direction.

$$(\nabla\phi_{h_y})_{i,j} = \frac{(\phi_h)_{i,j+1} - (\phi_h)_{i,j-1}}{2\Delta y}$$

$$(\nabla\phi_{s_y})_{i,j} = \frac{(\phi_s)_{i,j+1} - (\phi_s)_{i,j-1}}{2\Delta y}$$

The interface layer contains all cells in which both $|(\nabla\phi_h)_{i,j}| \geq 0.1$ and $|(\nabla\phi_s)_{i,j}| \geq 0.1$. Each cell has a unit normal in the interface layer that points in to the hard material.

$$\mathbf{n}_{i,j} = \frac{(\phi_h)_{i,j} - (\phi_s)_{i,j}}{|(\phi_h)_{i,j} - (\phi_s)_{i,j}|} \tag{2.10}$$

At this point, it is important to note that **frictional forces are not included through deviatoric stress components.** Instead, they are included as body forces within the cells in the boundary layers, including the slip layer. The reason for this is that if the friction force was applied to the cells within the interface, there would be forces aligned in opposite directions with in the interface and within a cell. CTH is unable to do this because one set of kinematic variables is used for all materials within a cell [51]. The subsequent portion of this discussion describes how the frictional force is calculated in the boundary layer algorithm.

First, let us consider the average velocity of the hard layer, V_{hard}. This velocity is determined using all cells with $\phi_h \geq 0.9$. There is also an average velocity of the soft layer, V_{soft}. This velocity is determined using all cells with $\phi_s \geq 0.9$. In the calculation of V_{soft}, cells in the the slip layer are excluded. These values are used to determine an average relative velocity between the hard and soft layers, $\bar{V}$.

$$\bar{V} = \mathrm{V}_{hard} - \mathrm{V}_{soft}$$

In addition, the normal, **n** for each cell is used to calculate the average normal, $\bar{n}$. These values are then used to determine the unit vector tangential to the surfaces, **u**.

$$\mathbf{u} = \frac{\bar{n} \times \bar{V}}{|(\bar{n} \times \bar{V}) \times \bar{n}|}$$

The shear traction vector due to the frictional force is then calculated by

$$\vec{t_f} = \pm f \min\{0, \bar{n} \cdot (\bar{T}\bar{n})\}\mathbf{u} \tag{2.11}$$

where $\vec{t_f}$ is the shear traction vector due to frictional force, f is the coefficient of friction, $\bar{T}$ is the average Cauchy stress, and $\bar{n} \cdot (\bar{T}\bar{n})$ is the normal traction which is a scalar value. The normal traction must be negative (i.e., in compression) in order for the traction due to friction to be a nonzero value. $\bar{T}$ is obtained by averaging the values of the Cauchy stress tensor, **T** among all the cells within and around the boundary layer. Shear traction is negative if the cell lies within the soft layer and positive if it lies within the hard layer.

Frictional forces are only applied to cells in one of the boundary layers, but **not in the interface layer**. This is due to the inability of CTH to apply body forces separately to materials within mixed cells. The frictional shear traction per cell is first converted to a body force density, $\vec{b_f}$

$$(\vec{b_f})_{i,j} = \frac{(\vec{t_f})_{i,j}}{\omega_{bl}}$$

The body force density appears in the momentum balance equation as

$$\rho\vec{a} = \nabla \cdot \mathbf{T} + \vec{b_f}$$

where $\vec{a}$ is the acceleration.

Using this algorithm, it is possible to find an effective coefficient of friction during high speed sliding. An estimated kinetic frictional coefficient is used as an input to the boundary layer algorithm. The frictional force would be calculated and used as a body force density within the solution method. The deviatoric stress and pressure would develop through the boundary layer algorithm and the usual CTH routines. The effective coefficient of friction could then be found by comparing the deviatoric stress at the interface with the pressure. It is estimated that this coefficient would be extremely low based on the similarity of results for frictional coefficients of 0.3 and 0.0.

There is some error in this algorithm due to mesh coarseness that always occurs when determining the boundary layers. Over many time steps however, the fluctuations due to this error in the applied frictional force will average out and the net force added to the system will be close to the correct value.

One final note, the flow stress in the mixed material cells is set to the maximum material flow stress among the various materials within the cell. This is done to prevent erosion of the hard material surface that may not be physical. Otherwise, the hard surface layer strength may become diluted within mixed cells.

2.6 Materials Science

Materials science principles underlie the understanding of the behavior of materials in a high speed impact such as in hypervelocity gouging situations. The fundamentals described in this section include thermal behavior, hardness, impact energy, phase changes, wear, and coatings materials (specifically, polymers) [52].

2.6.1 Thermal Behavior. Material behavior under nonequilibrium thermodynamic conditions is dependent on the thermal behavior of that material. There are a

variety of properties that reflect this thermal behavior. Those that are discussed briefly in this section are: heat capacity, thermal expansion, thermal conductivity, and thermal shock.

The heat capacity of a material, C is defined as the amount of heat required to raise the material's temperature by 1 degree Kelvin.

$$C = \frac{Q}{\Delta T}$$

where Q is the amount of heat producing a rise in temperature of ΔT. This version of heat capacity is dependent on the amount of material. More material requires greater amount of heat to raise it one degree. An alternative form is the specific heat, c.

$$c = \frac{q}{m\Delta T}$$

which puts the specific heat in terms of a unit mass.

Specific heat is measured at either constant volume, or constant pressure. These specific heats are represented by c_p and c_p, respectively. In general, specific heats are constant, but for high temperatures, they change depending on the material. Specific heats are typically double or more in value for polymers than they are for most engineering metals.

In general, when a material absorbs heat and its temperature rises, it leads to an increase in thermal vibration of the atoms making up that material. An increase in vibration leads to an increase in average separation distance of adjacent atoms and an increase in the dimensions of the material. This is characterized by the linear coefficient of thermal expansion, α.

$$\alpha = \frac{dL}{LdT}$$

where L is the length of the material in one direction and T is temperature. The linear coefficients of thermal expansion for metals are typically much lower than most engineering polymers. The linear coefficient of thermal expansion is a function of temperature and tends to increase for high temperatures.

Thermal conductivity is a form of diffusivity. It can be described mathematically by Fourier's Law

$$k = -\frac{dq/dt}{A(dT/dx)}$$

where dq/dt is the rate of heat transfer across an area, A due to a temperature gradient, dT/dx. Thermal conductivity in materials is due to atomic vibrations and the conduction of free electrons. In materials such as polymers, which do not conduct electricity well, the primary mechanism of thermal conductivity is atomic vibration. In metals, which do conduct electricity well, the primary mechanism is free electrons due to the additional kinetic energy of these conducting electrons. Thermal conductivity is a function of temperature. In general, the thermal conductivity of polymers decreases with temperature, while that of metals increases. In addition, the thermal conductivity of polymers is typically an order of magnitude or more less than that of metals.

Thermal shock is the last property of thermal behavior of materials discussed here. It is the fracture of a material due to temperature change (usually a rapid temperature change). Fracture follows from the thermal behavior properties of thermal expansion and thermal conductivity. Thermal expansion under constrained conditions will cause stress within a material. The rapid temperature change then results in temperature gradients in the material that cause internal residual stresses. Another example would be uniform expansion of a material due to a rise in temperature. With a rapid cooling of the surface, the finite thermal conductivity leaves a surface that contracts around a hot interior. This results in a surface that is in tension and a hot core that is in compression, which could lead to fracture caused by the thermal shock loading of the surface.

Other material properties such as the elastic modulus, shear modulus, and yield strength will be affected by changes in temperature. The effect of these changes will be dependent on the constitutive model and what parameters in the model are dependent on temperature. In addition, the temperature, depending on the equation of state, will also affect the state of the material with regards to pressure and density.

2.6.2 Hardness and Impact Energy. Hardness provides an indication of a material's strength by measuring its resistance to indentation. Hardness tends to increase as

ultimate strength of materials increase. In hardness tests, there is a significant amount of plastic deformation.

Impact energy of a material is the energy necessary to cause fracture of a standard test piece under an impact load. It is similar to fracture toughness in the area of fracture mechanics. In general, materials with large values of yield strength and ductility have large impact energies. The impact energy of polymers is generally much smaller than the impact energy of most engineering metals. Impact energy is measured by a test that takes the tensile test to a very rapid completion. This energy is essentially related to the area under the stress-strain curve.

2.6.3 Phase Changes. Phase is defined a s a chemically and structurally homogeneous part of the microstructure of a material. There are also components of a material which are distinct chemical substances that make up a phase. For instance, a solid solution of copper and nickel consists of the solid phase with two components: copper and nickel. The degree of freedom is then the number of independent variables in the system. At its melting point, a solid has no degrees of freedom and is in both solid and liquid phases at the same time. There are also conditions known as state variables which are pressure, temperature, and composition. These state variables help determine the microstructure of a material. The number of degrees of freedom can be found using the Gibbs phase rule [52]:

$$\text{DOF} = \text{C} - \text{P} + 2$$

where DOF is the degrees of freedom in the material system, C is the number of components in the material system, and P is the number of phases in the material system. The number 2 limits the state variables to pressure and temperature, which is a typical application of this relationship. This relationship tells us that changing the temperature of a material changes the compositions of the phases of the material. For example, a pure material (i.e, consisting of one component) that is in a state of two phases simultaneously (such as at melting point) leaves one degree of freedom. This means that temperature may vary while maintaining the two phase microstructure. Degrees of freedom thus tells us how many independent variables we have control over while maintaining the state of the material

we choose. In the example, temperature is the sole independent variable we may vary without changing the number of components or the state of the material at the melting point (solid-liquid phases). This rule is depicted graphically in phase diagrams.

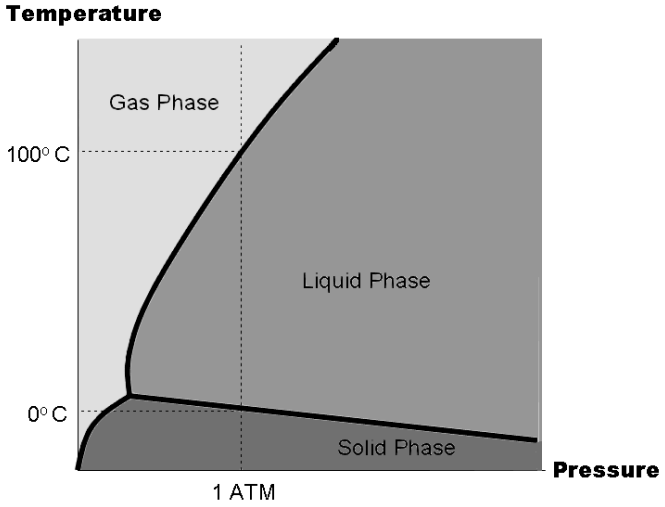

Figure 2.4 **One component phase diagram of water as an example to depict Gibbs phase rule.**

In Figure 2.4 is the one component phase diagram of water (C=1). In this diagram the thick lines separating the gas, liquid, and solid phases indicate two phase states (P=2) that exist for water. For example, the line separating liquid and solid phases is the melting point line. If the pressure is fixed at 1 atmosphere, the pressure is removed as a state variable and the Gibbs phase rule becomes DOF=C-P+1. To analyze the degrees of freedom available at the melting point for 1 ATM (a two phase solid-liquid state of water) which occurs at 100^o C, we have DOF=1-2+1=0. There are zero degrees of freedom available to the system. Any change in temperature will change the phase of the water. In the liquid phase, the degrees of freedom are DOF=1-1+1=1. This means that there is one independent variable available to the liquid phase of water. The temperature can change without changing phase from a liquid, at least until the melting point or boiling point boundaries (the thick lines that indicate two phase states) are reached.

Phase diagrams in most engineering applications show two and three component material systems. If the effect of pressure is assumed to be small, phase diagrams can show the relationship of equilibrium phases for different combinations of temperature and

composition. The phase diagram's usefulness is apparent for showing changes in phase and microstructure caused by changes in state variables such as temperature and composition. A more comprehensive treatment of phase diagrams for materials can be found in Shackelford's book on materials science [52].

The phase diagrams discussed here are similar to phase diagrams such those used in equation of state applications for relating pressure, temperature, and specific volume of a material in thermodynamic equilibrium. The difference between these treatments is the composition of the material as a state variable described in this discussion rather than specific volume*.

2.6.4 Wear. Wear may be defined as "the removal of surface material as a result of mechanical action [52]." There are four forms of wear:

Adhesive wear Two smooth surfaces slide over each other. Fragments are pulled off one surface and adhere to the other. Erosion is a related mechanism. However, erosion occurs due to a stream of sharp particles.

Abrasive wear A rough, hard surface slides on a softer surface and leaves grooves in the softer material.

Surface fatigue wear Repeated sliding or rolling over a track causes subsurface and surface cracking.

Corrosive wear Sliding in a corrosive environment compounds wear by the addition of chemical effects.

Adhesive wear can be defined by the equation

$$V = \frac{k_w P x}{3H}$$

where V is the volume of material worn away under a load P over a distance x, H is the hardness of the surface being worn, and k_w is the wear coefficient. The wear coefficient represents the probability that an adhesive fragment will be formed.

*see pages 46-51 of Laird's dissertation [7] for a discussion of these other types of phase diagrams.

Nonmetallic materials such as polymers and ceramics are highly resistant to wear mechanisms. This is evident in the wear coefficient of stainless steel on stainless steel (which is 21) as compared to phenol-formaldehyde on phenol-formaldehyde (which is 0.02).

2.6.5 Coatings - Polymers. This section is limited to discussion of thermosetting polymers. Epoxy, a thermosetting polymer, is the coating of choice at the HHSTT. It has been found to obtain the best results for mitigating gouging when used to coat critical sections of the rail.

Polymers are organic materials composed of long chains organic molecules formed from small molecules by polymerization. Thermosetting polymers become hard and rigid upon heating and remains so even after cooling. Polymerization takes place upon cooling after the polymerization reactions occur at higher temperatures. Polymers typically have lower strength than metals [52].

Typical thicknesses of the epoxy coating used at the HHSTT range from 6 to 70 mil (0.01524 to 0.1778 cm) thickness. In summary, this polymer coating has the following properties in comparison to metals:

- Specific heat greater than metals. Polymers can usually absorb more heat before increasing in temperature.
- Linear coefficient of thermal expansion greater than most metals. Polymers will expand more for the same temperature increase than the same length of metal.
- Thermal conductivity less than most metals. The rate of heat flux in polymers is slower than that for metals with the same area and temperature gradient.
- Wear coefficient less than metals. Polymers are typically more resistant to wear than metals.
- Strength less than metals. Polymers have a lower yield and ultimate strength than most metals and thus will usually fracture sooner than metals for the same load.

Thus, in polymers we have a material that takes longer to transfer heat energy, requires a greater amount of heat to increase in temperature, is resistant to wear, yet is weaker than most metals under the same conditions. These properties make polymers a

good candidate for a tough sacrificial coating that will be resistant to heat effects and wear. The low strength and impact resistance of polymers means it is more likely to fail than resist impact and transfer impact energy to the substrate (i.e., rail material).

A functionally graded material for instance, may be used to reduce the effects of shock waves, or delay the onset of shock waves that form during impact. The top layer that would be subjected to impact could be designed with high wear resistance, low thermal conductivity, or even to fail before transferring energy and momentum to lower, harder layers underneath. This would protect the rail substrate and prevent conditions such as plastic deformation and high temperature that lead to gouging formation.

2.7 Viscoplasticity

This next section will concentrate on the development of viscoplasticity as incorporated in CTH. The major relations will be presented. Deformation at a point in a body can be classified as being either **elastic** or **plastic**. Elastic deformations are recoverable after loading is released. Plastic deformations are permanent. Some deformation remains after loading is removed. For small displacements, metals are typically elastic, whereas for larger displacements, after the yield point is reached, metals are plastic [3].

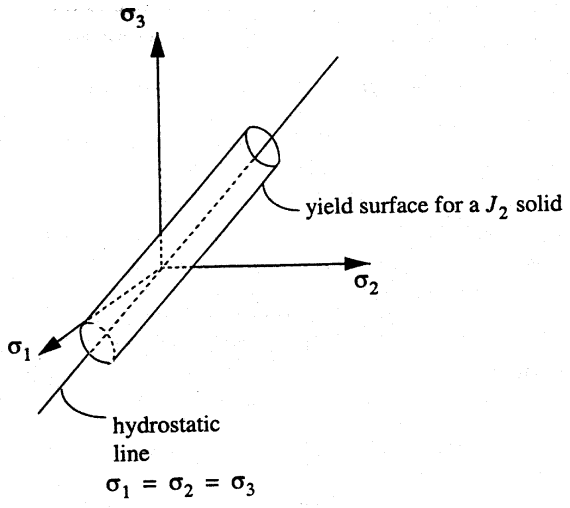

Figure 2.5 **Yield surface for a J_2 solid [3].**

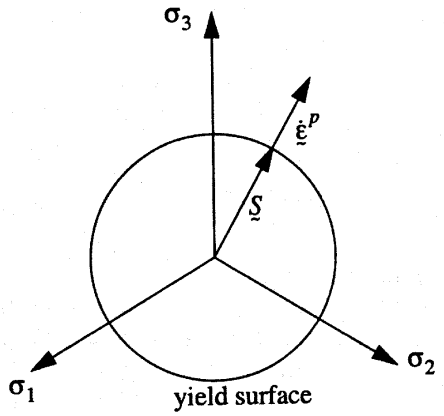

Figure 2.6 **Yield surface for a J_2 solid as viewed from a point on the hydrostatic line [3].**

We use **stress space**, which is a mathematical space in which the coordinates are the components of the stress tensor at a given point in the body. If the material is isotropic we can simplify the space by working in **principal stress space**. Yielding is modeled using the **yield surface** (as shown in Figures 2.5 and 2.6). The yield surface is typically defined using the second invariant of the deviatoric stress, J_2. This surface is a closed mathematical surface in stress space at which the transition from elastic to plastic deformation occurs [3].

2.7.1 Assumptions. We assume that a state of stress cannot exist outside the yield surface (as shown in Figure 2.6). However, a state of stress is permitted to exist *on* the yield surface. The yield surface is also allowed to contract, expand, or change shape depending on the material's constitutive response. The yield surface can be described by various yield criteria such as Tresca or Von Mises. We can also use various hardening rules (e.g., isotropic or kinematic) to describe the response due to permanent deformation in the plastic regime. Figure 2.7 shows how the yield point would vary according to temperature, plastic strain, and plastic strain rate. These variations thus change the shape of the yield surface shown in Figure 2.6.

2.7.2 Deformation Tensor, Spin Tensor, and Eulerian Strain Rate [4]. When the displacement gradient components are not small compared to unity, the problem of

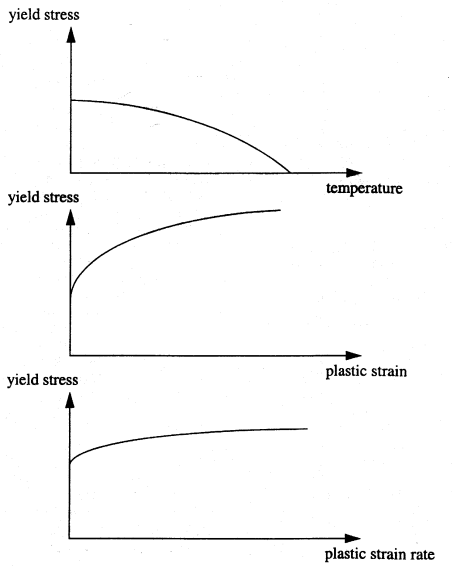

Figure 2.7 **Dependence of yield stress on temperature, plastic strain, and plastic strain rate for a typical metal [3].**

characterizing strain from the initial state is more difficult. Such is the case for viscoplasticity. Strain rates are large and displacements and rotations are large as compared to small strain theory and elasticity. Rigid body rotation affects analysis of the strain. Another consideration is to avoid use of second order nonlinear terms that can arise in the development of stress-strain relations using the full order Almansi or Green strain. Thus, we must make the transition from small strain to finite strain theory. By considering the rate of deformation tensor in the rate of deformation tensor, $\mathbf{D}$ we consider both the rotation and displacement of a particle and are able to avoid making development of stress and strain for finite displacements too cumbersome. In this section we use Malvern's [4] notation and follow his formulation.

Let us begin by considering large displacements and rotations with the displacement of an initial line segment $d\mathbf{X}$ in Eulerian space to a final line segment $d\mathbf{x}$. We can define this motion in terms of a relative velocity and a rate of deformation.

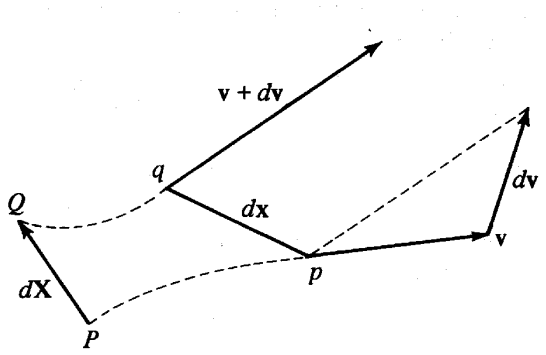

Figure 2.8 **Relative velocity $d\mathbf{v}$ of particle Q at point q relative to particle P at point p [4].**

The tensor equations for relative velocity of the particle at q relative to the particle at p (see Figure 2.8) are given by:

$$d\mathbf{v} = \mathbf{L} \cdot d\mathbf{x} = d\mathbf{x} \cdot \mathbf{L}^T \tag{2.12}$$

where $\mathbf{v}$ is the velocity vector of the particles and the spatial gradients of the velocity are

$$\mathbf{L} = \mathbf{v}\overleftarrow{\nabla}_x = \frac{\partial v_1}{\partial x_1} + \frac{\partial v_1}{\partial x_2} + \frac{\partial v_1}{\partial x_3} + \frac{\partial v_2}{\partial x_1} + \frac{\partial v_2}{\partial x_2} + \frac{\partial v_2}{\partial x_3} + \dots \tag{2.13}$$

where $\overleftarrow{\nabla}_x = \frac{\partial}{\partial x_1} + \frac{\partial}{\partial x_2} + \frac{\partial}{\partial x_3} + \frac{\partial}{\partial x_1} + \frac{\partial}{\partial x_2} + \frac{\partial}{\partial x_3} + \dots$ and

$$\mathbf{L}^T = \overrightarrow{\nabla}_x\mathbf{v} = \frac{\partial v_1}{\partial x_1} + \frac{\partial v_2}{\partial x_1} + \frac{\partial v_3}{\partial x_1} + \frac{\partial v_1}{\partial x_2} + \frac{\partial v_2}{\partial x_2} + \frac{\partial v_3}{\partial x_2} + \dots \tag{2.14}$$

where $\overleftarrow{\nabla}_x$ and $\overrightarrow{\nabla}_x$ is the del operator $\mathbf{i}\frac{\partial}{\partial x_1} + \mathbf{j}\frac{\partial}{\partial x_2} + \mathbf{k}\frac{\partial}{\partial x_3}$

In Cartesian spatial components, these are

$$L_{km} = v_{k,m} \tag{2.15}$$

$$(L^T)_{km} = \partial_k v_m = v_{m,k} \tag{2.16}$$

These various forms of $\mathbf{L}$ are known as the **spatial gradients of the velocity**. $\mathbf{L}$ can be written as the sum of the symmetric **rate of deformation/stretching tensor**,

D and the skew symmetric **spin/vorticity tensor**, **W** as follows:

$$\mathbf{L} = \mathbf{D} + \mathbf{W} \tag{2.17}$$

$$\mathbf{D} = \frac{1}{2}(\mathbf{L} + \mathbf{L}^T) = \frac{1}{2}(\mathbf{v}\overleftarrow{\nabla}_x + \overrightarrow{\nabla}_x\mathbf{v}) \tag{2.18}$$

$$\mathbf{W} = \frac{1}{2}(\mathbf{L} - \mathbf{L}^T) = \frac{1}{2}(\mathbf{v}\overleftarrow{\nabla}_x - \overrightarrow{\nabla}_x\mathbf{v}) \tag{2.19}$$

In Cartesian spatial components these are

$$D_{km} = \frac{1}{2}(v_{k,m} + v_{m,k}) \tag{2.20}$$

$$W_{km} = \frac{1}{2}(v_{k,m} + v_{m,k}) \tag{2.21}$$

Note that the time rate of change of the segment $d\mathbf{x}$ is

$$\frac{d}{dt}(d\mathbf{x}) = \mathbf{L} \cdot d\mathbf{x} \tag{2.22}$$

In Cartesian spatial components, this is written as

$$\frac{d}{dt}(dx_k) = v_{k,m}dx_m \tag{2.23}$$

In terms of the rate of deformation, the rate of change of the squared length $(ds)^2$ of the material instantaneously occupying any infinitesimal relative position $d\mathbf{x}$ at p is determined by the tensor **D** at p. This is shown mathematically as:

$$\frac{d}{dt}\left[(ds)^2\right] = 2dx_k D_{km} dx_m = 2d\mathbf{x}\cdot\mathbf{D}\cdot d\mathbf{x} \tag{2.24}$$

We now begin formulation of the Eulerian strain tensor which allows us to use the Eulerian and Cauchy stress tensors. The **Eulerian strain** components, as defined by Cauchy for infinitesimal strains and by Almansi for finite strain are:

$$E^*_{ij} = \frac{1}{2}\left[\frac{\partial u_i}{\partial x_j} + \frac{\partial u_j}{\partial x_i} - \frac{\partial u_k}{\partial x_i}\frac{\partial u_k}{\partial x_j}\right] \tag{2.25}$$

In terms of the Eulerian (a.k.a. Cauchy or Almansi) strains, the change in squared length of the material vector $d\mathbf{X}$ is:

$$(ds)^2 = (ds)^2 - (dS)^2 = 2dx_k E^*_{km} dx_m \tag{2.26}$$

In order to determine the Eulerian strain rate in terms of the squared length of the material vector in material coordinates, we take the *material time derivative* of both sides of Equation 2.26

$$\frac{d}{dt}\left[(ds)^2\right] = 2\frac{d}{dt}\left[dx_k E^*_{km} dx_m\right] \tag{2.27}$$

Using the chain rule we have

$$\frac{d}{dt}\left[(ds)^2\right] = 2\frac{d}{dt}(dx_k)E^*_{km}dx_m + 2dx_k\frac{d}{dt}\left[E^*_{km}dx_m\right] \tag{2.28}$$

We apply the chain rule to the product of the last term

$$\frac{d}{dt}\left[(ds)^2\right] = 2\frac{d}{dt}(dx_k)E^*_{km}dx_m + 2dx_k\frac{d}{dt}(E^*_{km})dx_m + 2dx_k E^*_{km}\frac{d}{dt}(dx_m) \tag{2.29}$$

Differentiating the last two terms and using Equation 2.23 on the first term we have

$$\frac{d}{dt}\left[(ds)^2\right] = 2v_{k,r}dx_r E^*_{km}dx_m + 2dx_k\dot{E}^*_{km}dx_m + 2dx_k E^*_{km}v_{m,p}dx_p \tag{2.30}$$

By interchanging summation indices and using Equation 2.16 we can write this as

$$\begin{aligned}
\frac{d}{dt}\left[(ds)^2\right] &= 2v_{r,k}dx_k E^*_{rm}dx_m + 2dx_k\dot{E}^*_{km}dx_m \\
&\quad +2dx_k E^*_{kp}v_{p,m}dx_m \qquad (2.31)\\
&= 2v_{1,1}dx_1E^*_{11}dx_1 + 2dx_1\dot{E}^*_{11}dx_1 \\
&\quad +2dx_1E^*_{11}v_{1,1}dx_1 \qquad (2.32)\\
&\quad +2v_{2,1}dx_1E^*_{21}dx_1 + 2dx_1\dot{E}^*_{11}dx_1 \\
&\quad +2dx_1E^*_{11}v_{1,1}dx_1 \qquad (2.33)\\
&\quad +2v_{3,1}dx_1E^*_{31}dx_1 + 2dx_1\dot{E}^*_{11}dx_1 \\
&\quad +2dx_1E^*_{11}v_{1,1}dx_1\ldots \qquad (2.34)\\
&= 2dx_k\left[(\partial_k v_r)E^*_{rm} + \dot{E}^*_{km} + E^*_{kp}v_{p,m}\right]dx_m \qquad (2.35)\\
&= 2d\mathbf{x}\left[\mathbf{L}^T\cdot\mathbf{E}^* + \dot{\mathbf{E}}^* + \mathbf{E}^*\cdot\mathbf{L}\right]\cdot d\mathbf{x} \qquad (2.36)
\end{aligned}$$

for arbitrary $d\mathbf{x}$.

Equating this to Equation 2.24, we can then show that:

$$\dot{\mathbf{E}}^* = \mathbf{D} - \left(\mathbf{E}^*\cdot\mathbf{L} + \mathbf{L}^T\cdot\mathbf{E}^*\right) \qquad (2.37)$$

This then, is the **Eulerian strain rate $\dot{\mathbf{E}}^*$** which includes both **spherical** and **deviatoric** components of the strain rate.

2.7.3 Deviatoric Strain Rate [3]. Further development of the plastic relations does not require use of the full Eulerian strain rate, $\mathbf{E}^*$ as long as we make use of the rate of deformation tensor, $\mathbf{D}$. This approach allows us to consider only the **deviatoric** component of strain for plasticity.

The total *deviatoric* component of the strain rate can be written as [3]:

$$\dot{\mathbf{e}} = \mathbf{D} - \frac{1}{3}\mathbf{I}(Tr\ \mathbf{D}) \qquad (2.38)$$

where $\dot{\mathbf{e}}$ is the total *deviatoric* strain rate.

We assume the total deviatoric strain rate can be decomposed into elastic and plastic components as follows:

$$\dot{\mathbf{e}} = \dot{\mathbf{e}}^e + \dot{\mathbf{e}}^p \tag{2.39}$$

Physically, this means that part of an incremental strain $d\mathbf{e} = \dot{\mathbf{e}}dt$ is recoverable and the remainder is permanent. For metals, the elastic part is described by Hooke's Law.

Subsequently, we will use the strain rate that characterizes the strain rate for plasticity and we will need to consider objectivity. In order to make use of the strain rate, it is important the stress and strain are objective. Therefore, we need to include the Jaumann corotational stress rate in order to make the stress rate axis independent. The Jaumann corotational stress rate is required because under large deformations, the deviatoric stress rate is changed by local rigid rotation and is not frame indifferent. The Jaumann corotational stress rate is frame indifferent, and "cancels out" this rigid body rotation so we can observe the effects of strain.

For elastic deviatoric strain rate, Hooke's Law takes the following form:

$$\dot{\mathbf{e}}^e = \frac{1}{2\mu}(\dot{\mathbf{S}} - \mathbf{WS} + \mathbf{SW}) \tag{2.40}$$

where $\dot{\mathbf{S}} - \mathbf{WS} + \mathbf{SW}$ is the Jaumann corotational stress rate. $\mathbf{S}$ is the deviatoric stress tensor, $\mathbf{W}$ is the spin tensor, and μ is the shear modulus, also known as G. In sections 2.7.7.1 and 2.7.7.3 we see the corotational stress is not important for the solution. However, it is essential to finding the solution for the deviatoric stress tensor.

The stress tensor can be written as the sum of two tensors, one representing a spherical, dilatational, or hydrostatic state of stress in which each normal stress is equal to $-p$, the **mean normal stress** and all shear stresses are zero, and the second called the **stress deviator** or **deviatoric stress tensor** representing shear stress in which all normal stresses are zero.

$$\sigma = \mathbf{S} - p\mathbf{I} \tag{2.41}$$

where $p = \frac{-Tr\ \sigma}{3} = \frac{-\sigma_{kk}}{3}$, p is the hydrostatic pressure, $\mathbf{I}$ is the identity tensor, σ is the Cauchy stress tensor, and $\mathbf{S}$ is the deviatoric stress tensor. So the **deviatoric** stress

tensor, $\mathbf{S}$ is simply

$$\mathbf{S} = \sigma + p\mathbf{I} \tag{2.42}$$

Thus, the **spherical** component of stress has been removed from the Cauchy stress tensor to obtain the **deviatoric** stress component. It is usually supposed that the deviatoric stress component brings about the change in shape while the hydrostatic stress produces volume change without shape change in an isotropic continuum.

In specifying dependence on rate and history of deformation, it is cumbersome to use a formulation where **yield stress** depends explicitly on all components of the tensor quantities. Instead these dependencies have been reduced to functions of scalar variables. Thus, we are interested in **equivalent stress** and **equivalent strain** quantities.

In Von Mises theory, yielding occurs when the magnitude of $\mathbf{S}$ is

$$S = |\mathbf{S}| = \sqrt{S_{ij}S_{ij}} = \sqrt{\frac{2}{3}}Y \tag{2.43}$$

where Y is the yield stress of the material and

$$\mathbf{S} = \begin{pmatrix} \frac{2Y}{3} & 0 & 0 \\ 0 & \frac{-Y}{3} & 0 \\ 0 & 0 & \frac{-Y}{3} \end{pmatrix} \tag{2.44}$$

This is the deviatoric stress tensor that occurs for a uniaxial test specimen at yield.

This tensor is derived as follows for a uniaxial test specimen at yield

$$\begin{aligned} \mathbf{S} &= \sigma + p\mathbf{I} \\ \mathbf{S} &= \begin{pmatrix} Y & 0 & 0 \\ 0 & 0 & 0 \\ 0 & 0 & 0 \end{pmatrix} - \frac{1}{3}\begin{pmatrix} Y & 0 & 0 \\ 0 & Y & 0 \\ 0 & 0 & Y \end{pmatrix} \\ \mathbf{S} &= \begin{pmatrix} \frac{2Y}{3} & 0 & 0 \\ 0 & \frac{-Y}{3} & 0 \\ 0 & 0 & \frac{-Y}{3} \end{pmatrix} \end{aligned} \tag{2.45}$$

It is also convenient to express the Von Mises yield criteria in terms of the second deviatoric stress invariant, J_2.

$$J_2 = \frac{S^2}{2} \tag{2.46}$$

Equivalent plastic strain rate is defined through its time derivative.

$$\dot{\varepsilon}^p = \sqrt{\frac{2}{3}\dot{\mathbf{e}}^p \cdot \dot{\mathbf{e}}^p} \tag{2.47}$$

where $\dot{\mathbf{e}}^p$ is the plastic deviatoric strain rate tensor.

The plastic deviatoric strain rate tensor is

$$\dot{\mathbf{e}}^p = \begin{pmatrix} \dot{\varepsilon}^p & 0 & 0 \\ 0 & \frac{-\dot{\varepsilon}^p}{2} & 0 \\ 0 & 0 & \frac{-\dot{\varepsilon}^p}{2} \end{pmatrix} \tag{2.48}$$

This tensor is derived as follows for a uniaxial test specimen at yield

$$\begin{aligned}
\dot{\mathbf{e}}^p &= \begin{pmatrix} \dot{\varepsilon}^p & 0 & 0 \\ 0 & 0 & 0 \\ 0 & 0 & 0 \end{pmatrix} - \nu \begin{pmatrix} 0 & 0 & 0 \\ 0 & \dot{\varepsilon}^p & 0 \\ 0 & 0 & \dot{\varepsilon}^p \end{pmatrix} \\
\dot{\mathbf{e}}^p &= \begin{pmatrix} \dot{\varepsilon}^p & 0 & 0 \\ 0 & \frac{-\dot{\varepsilon}^p}{2} & 0 \\ 0 & 0 & \frac{-\dot{\varepsilon}^p}{2} \end{pmatrix} \\
\dot{\mathbf{e}}^p &= \sqrt{(\dot{\varepsilon}^p)^2 + \left(\frac{-\dot{\varepsilon}^p}{2}\right)^2 + \left(\frac{-\dot{\varepsilon}^p}{2}\right)^2} \\
\dot{\mathbf{e}}^p &= \sqrt{\frac{3}{2}}\dot{\varepsilon}^p \\
\dot{\varepsilon}^p &= \sqrt{\frac{2}{3}\dot{\mathbf{e}}^p \cdot \dot{\mathbf{e}}^p}
\end{aligned} \tag{2.49}$$

where $\nu = \frac{1}{2}$ for plastic deformations.

The most common flow rule in use assumes the plastic flow occurs in the direction normal to the yield surface. This means the flow occurs in the same direction as the

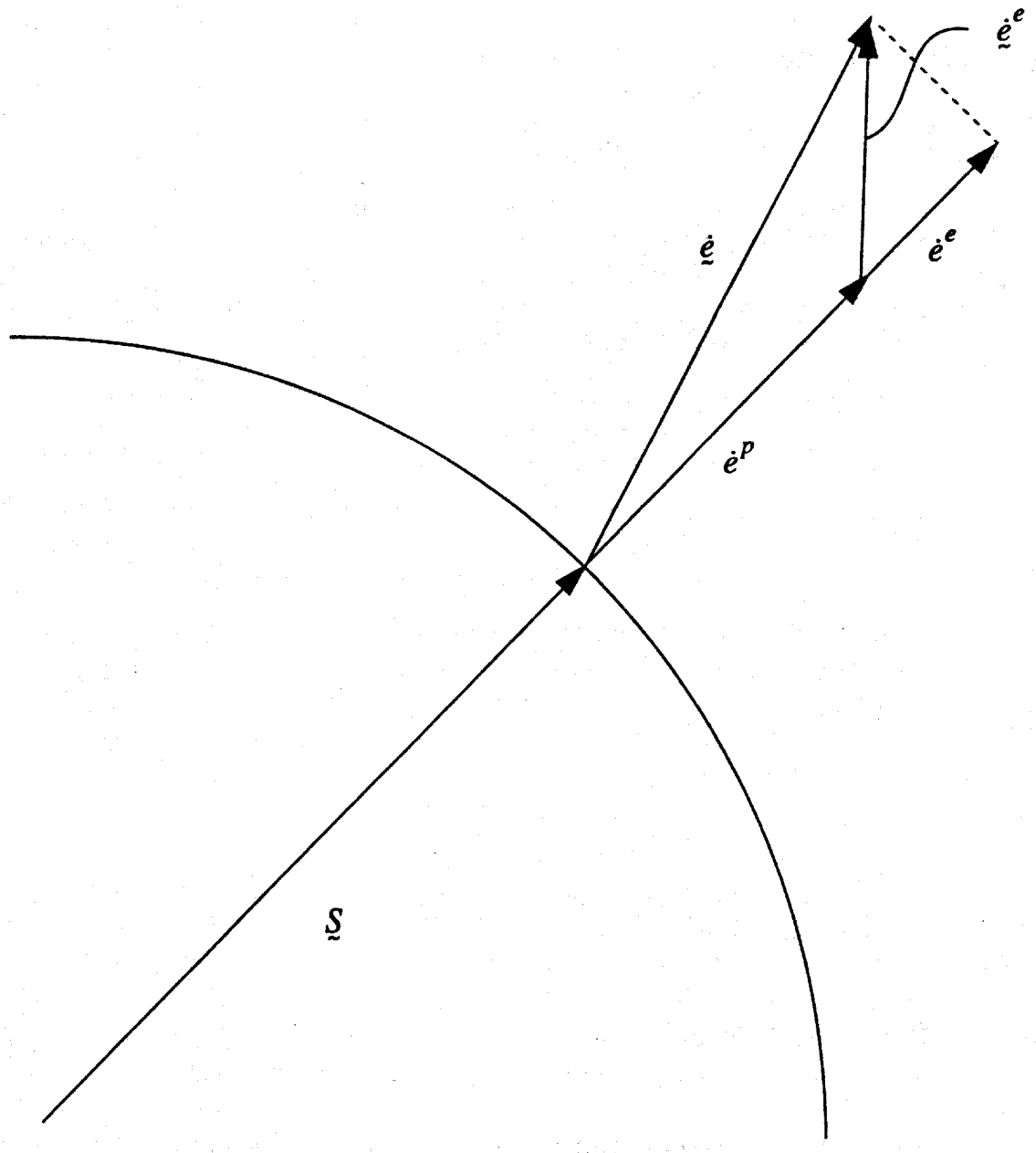

Figure 2.9 **Decomposition of the deviatoric strain rate tensor for the associated flow rule [3].**

deviatoric stress (see Figure 2.9). For a J_2 solid, this means the flow occurs in order to most rapidly accommodate the stress tensor components of stress that cause flow. This results in the Prandtl-Reuss relations.

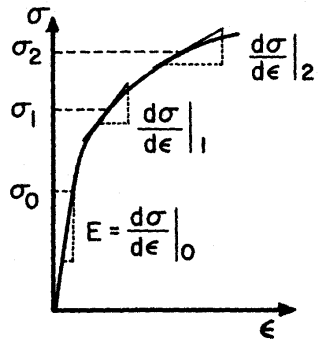

Figure 2.10 **Stress-strain curve for a uniaxial test specimen [5].**

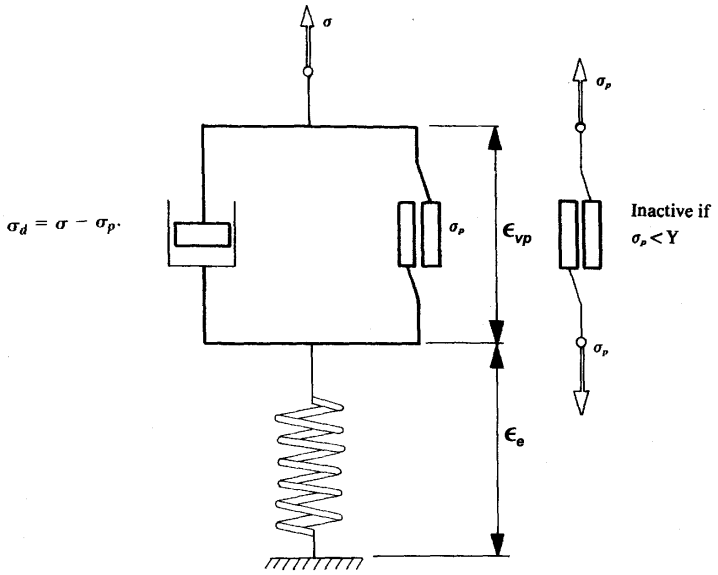

Figure 2.11 **Viscoelastic-plastic conceptual model [6].**

It may be helpful to use the elastic-viscoplastic model in pure shear used by Owen and Hinton [6] to help understand the Prandtl-Reuss relation used here (see Figure 2.11). In their conceptual description, the material is modeled as a dynamic system with stiffness and damping (consisting of a dashpot and friction slider). The total applied stress is $\sigma = \sigma_d + \sigma_p$. The "spring stiffness" can be likened to the elastic modulus, E (see Figure

2.10). The "friction slider" develops a stress, σ_p and is active only when the total applied stress, σ exceeds yield stress. The stress from this "friction slider" will just be equal to the yield stress in the viscoplastic regime. The dashpot allows the system to take higher stress than plasticity theory allows for equilibrium. When the stress exceeds the yield stress, the "dashpot" stress, σ_d is the difference. The presence of the dashpot stress allows the stress level to instantaneously exceed the stress allowed by plasticity theory. The total strain in this model is $\epsilon = \epsilon_e + \epsilon_{vp}$. The stress in the linear spring is equal to the total applied stress and is related to the elastic strain by $\sigma_e = \sigma = E\epsilon_e$. The stress in the dashpot is related to viscoplastic strain by $\sigma_d = \mu \frac{d\epsilon_{vp}}{dt}$. The dashpot stress is related to the viscoplastic strain rate through a viscosity coefficient, μ and use of the viscoplastic strain rate.

$$\dot{\epsilon_{vp}} = \dot{\mathbf{e}}^p = \lambda \mathbf{S};\ \dot{\varepsilon}^p_{kk} = 0;\ \lambda \geq 0 \tag{2.50}$$

where λ is some scalar that relates to the conceptual "viscosity coefficient" mentioned above $\left(\lambda = \frac{1}{\mu}\right)$, $\mathbf{S}$ is the deviatoric stress tensor (σ_d in the model), and $\dot{\mathbf{e}}^p$ is the plastic strain rate tensor.

This proposed expression is based on the isotropic form of the Prandtl-Reuss flow law which is taken to be a physical law by itself independent of a yield criterion [53]. This states that plastic deformation is incompressible.

In terms of the plasticity strain rate this is

$$\dot{\mathbf{e}}^p = \dot{e}^p \frac{\mathbf{S}}{S} \tag{2.51}$$

where $\dot{e}^p = |\dot{\mathbf{e}}^p|$ and $S = |\mathbf{S}|$.

Using this associated flow rule, we have equivalent plastic strain rate equal to

$$\dot{\varepsilon}^p = \sqrt{\frac{2}{3}} \dot{e}^p \tag{2.52}$$

The primary difference between viscoplastic models and yield criteria such as Tresca and Von Mises is that the yield stress changes with time. It is dependent on temperature, rate of deformation, and history of deformation (through strain hardening). Thus, we

require *viscoplastic* models beyond simple plasticity relations in order to solve for the stresses and strains at a point in the material.

The next section discusses constitutive equations that have been used in this dissertation. CTH has several others internal to the program that are not discussed.

2.7.4 Johnson-Cook Model. The Johnson-Cook model is used to determine the yield stress as a function of temperature, equivalent plastic strain, and equivalent plastic strain rate. It is a curve fitting model.

$$Y = f(T, \varepsilon^p, \dot{\varepsilon}^p) \tag{2.53}$$

At low and constant strain rates, metals are known to work along the well-known relationship called parabolic hardening [5].

$$\sigma = Y + \kappa \varepsilon^n \tag{2.54}$$

where σ is the effective stress, Y is the yield stress, ε is the effective strain, n is the work hardening coefficient, and κ is the pre-exponential factor. The effects of temperature and strain rate are separately given.

One must take note that because the Johnson-Cook model makes use of the ***effective*** stress and strain rather than the ***tensorial*** stress and strain, it's usefulness is best suited to determining the yield surface for later use in determining the stress and strain tensors.

The effect of temperature on effective stress can be represented as

$$\sigma = \sigma_r \left[1 - \left(\frac{T - T_r}{T_M - T_r} \right)^m \right] \tag{2.55}$$

where T_M is the melting point, T_r is a reference temperature at which σ_r, a reference stress is measured, and T is the temperature for which σ is calculated. This is basically curve fitting.

The effect of strain rate on effective stress can be expressed as

$$\sigma \propto ln\ \dot{\varepsilon}$$

This relationship is observed for strain rates that are not too high. Johnson and Cook used these basics to formulate their model.

$$Y = [A + B(\varepsilon^p)^N][1 + C\ ln(max(0.002, \dot{\varepsilon}^p))][1 - \theta_h^m] \tag{2.56}$$

where

$$\theta_h = \frac{T - T_r}{T_M - T_r} \tag{2.57}$$

and $ln(max(0.002, \dot{\varepsilon}^p))$ indicates the natural logarithmic function of either 0.002 or $\dot{\varepsilon}^p$, whichever is largest. The reference temperature T_r is taken to be room temperature. A, B, C, N, and m are constants that depend on the material. This model is applicable up to strain rates of $\approx 10^5 sec^{-1}$, but this model has found widespread use in solid dynamics.

2.7.5 Zerilli-Armstrong Model. The Zerilli-Armstrong model is based upon a physical model and is dependent on whether the crystals of the material are body (*bcc*) or face-centered cubic (fcc). Like the Johnson-Cook model it gives unreasonable results for zero or very small strain rates.

$$Y = \begin{cases} \Delta\sigma'_G + k\sqrt{l} + c_2\sqrt{\varepsilon^p}\ exp(-c_3T + c_4T\ ln(\dot{\varepsilon}^p)), & for\ fcc\ crystals \\ \Delta\sigma'_G + k\sqrt{l} + c_1\ exp(-c_3T + c_4T\ ln(\dot{\varepsilon}^p)) + c_5(\varepsilon^p)^N, & for\ bcc\ crystals \end{cases} \tag{2.58}$$

$$Y = \Delta\sigma'_G + k\sqrt{l} + (c_1 + c_2\sqrt{\varepsilon^p})\ exp(-c_3T + c_4T\ ln(\dot{\varepsilon}^p)) + c_5(\varepsilon^p)^N \tag{2.59}$$

where $\Delta\sigma'_G, k, l, c_1, \ldots, c_5$, and N are constants.

This model is not as popular as the Johnson-Cook model, but actually better models the coupling of strain hardening, rate dependence, and temperature change. The main problem is that there are few metals characterized for this model.

2.7.6 Steinberg-Guinan-Lund Model. The Steinberg-Guinan-Lund is a strain-rate dependent constitutive model that defines the dynamic yield stress.

$$Y = [Y_T(\dot{\varepsilon}^p, T) + Y_A f(\varepsilon^p)]\frac{G(P,T)}{G_o} \tag{2.60}$$

where Y_T is the thermally activated component, Y_A is the yield stress at the Hugoniot elastic limit, ε^p is the plastic strain, $\dot{\varepsilon}^p$ is the plastic strain rate, P is the pressure, T is the temperature, G is the shear modulus, and G_o is the initial shear modulus.

The work hardening function, $f(\varepsilon^p)$ is defined as

$$f(\varepsilon^p) = \{1 + \beta(\varepsilon^p + \varepsilon_i)\} \tag{2.61}$$

where β and ε_i are fitting parameters.

The thermally activated component of yield is defined in the plastic strain rate equation

$$\dot{\varepsilon}^p = \left(\frac{1}{C_1} exp\left[\frac{2U_K}{T}\left(1 - \frac{Y_T}{Y_P}\right)^2\right] + \frac{C_2}{Y_T}\right)^{-1} \tag{2.62}$$

where Y_P is the Peierl's stress, $2U_K$ is the energy necessary to form a pair of kinks in a dislocation segment, and C_1 and C_2 are defined in terms of various dislocation mechanics parameters and are specific to the material being modeled.

The shear modulus, G is defined as a function of pressure and temperature

$$G(P,T) = G_o\left[1 + \frac{AP}{\eta^{1/3}} - B(T - 0.02585eV)\right] \tag{2.63}$$

where A and B are material constants, η is the density ratio $(\frac{\rho}{\rho_o})$ and the unit of eV is equivalent to 11605 K.

Melting is also modeled in the Steinberg-Guinan-Lund constitutive model through use of a modified Lindemann Law. The melting temperature, T_m is modeled as

$$T_m = T_{mo} exp\left[2a\left(1 - \frac{1}{\eta}\right)\right]\eta^{2(\gamma_o - a - 1/3)} \tag{2.64}$$

where T_{mo} is the melting temperature at constant volume, γ_o is the initial Grüneisen coefficient, and a is a material constant. When the temperature exceeds T_m, melting has occurred, which results in the loss of yield and shear strength. Y and G are then set to minimum values in this case.

There are also two additional limits imposed on the model:

$$\begin{aligned} Y_A f(\varepsilon^p) &\leq Y^o_{max} \\ Y_T &\leq Y_P \end{aligned}$$

where Y^o_{max} is the work-hardening maximum in the rate-dependent version of the model.

The rate-independent form of the model assumes $Y_T = 0$ and applies the limit $Y_A f(\varepsilon^p) \leq Y_{max}$.

2.7.7 Solution Method Using Strength Models. This section describes a solution method used in the CTH [3] hydrocode for calculating viscoplastic parameters. It consists of three main parts: evaluation of yield strength, evaluation of deviatoric stress, and evaluation of equivalent plastic strain. A yield strength model must first be chosen in order to determine the yield stress and then use that evaluation to find the deviatoric stress and finally the equivalent plastic strain for the time step. Either of the yield strength models described previously (i.e., Johnson-Cook, Zerilli-Armstrong, or Steinberg-Guinan-Lund) would suffice. This method occurs within the Lagrangian step of the CTH algorithm. Stresses and strains within this step are all in Eulerian coordinates because the Eulerian equations are solved in two steps using the operator splitting technique (see section 2.1.

2.7.7.1 Evaluation of the Yield Stress. In each time step, for each Eulerian cell that contains any amount of elastic-plastic material, the code must compute a current value of yield stress. Let n be the current time step and $n - \frac{1}{2}$ is one half time step back. At the point in the calculation at which Y_n is to be computed, the full rate of deformation tensor $\mathbf{D}_{n-\frac{1}{2}}$ is known.

$$\mathbf{D}_{n-\frac{1}{2}} = \frac{1}{2}\left(\nabla \mathbf{v}_{n-\frac{1}{2}} + (\nabla \mathbf{v}_{n-\frac{1}{2}})^T\right) = \frac{\mathbf{D}_n - \mathbf{D}_{n-1}}{2} \tag{2.65}$$

$$\begin{aligned}\mathbf{D}_{n-\frac{1}{2}} &= \frac{1}{2}\left(v_{k,m}^{n-\frac{1}{2}} + v_{m,k}^{n-\frac{1}{2}}\right) \\ &= \frac{1}{2}\left(v_{1,1}^{n-\frac{1}{2}} + v_{1,1}^{n-\frac{1}{2}}\right) + \frac{1}{2}\left(v_{1,2}^{n-\frac{1}{2}} + v_{2,1}^{n-\frac{1}{2}}\right) + \frac{1}{2}\left(v_{1,3}^{n-\frac{1}{2}} + v_{3,1}^{n-\frac{1}{2}}\right) + \\ &\quad + \frac{1}{2}\left(v_{2,1}^{n-\frac{1}{2}} + v_{1,2}^{n-\frac{1}{2}}\right) + \frac{1}{2}\left(v_{2,2}^{n-\frac{1}{2}} + v_{2,2}^{n-\frac{1}{2}}\right) + \cdots \end{aligned} \tag{2.66}$$

where $\nabla \mathbf{v}_{n-\frac{1}{2}} = \dfrac{\nabla \mathbf{v}_n - \nabla \mathbf{v}_{n-1}}{2}$ and ε_{n-1}^p and T_{n-1} are known.

A time step of Δt is used and the function Y_n becomes a function of

$$Y_n = f\left(T_{n-1}, \varepsilon_{n-1}^p, \frac{\dot{\varepsilon}_{n-1}^p - \dot{\varepsilon}_{n-2}^p}{\Delta t_{n-\frac{3}{2}}}\right) \tag{2.67}$$

where $\Delta t_{n-\frac{3}{2}} = t_{n-1} - t_{n-2}$.

However, since this method results in unacceptable numerical noise, the following expression is used instead

$$Y_n = f\left(T_{n-1}, \varepsilon_{n-1}^p, \frac{\dot{\varepsilon}_{n}^p - \dot{\varepsilon}_{n-1}^p}{\Delta t_{n-\frac{1}{2}}}\right) \tag{2.68}$$

where $\Delta t_{n-\frac{1}{2}} = t_n - t_{n-1}$. But ε_n^p depends on Y_n so this function gives the value of Y_n implicitly.

A von Neumann stability analysis was performed for a one-dimensional model problem by the developers of the CTH [3] code to determine that the function in Equation 2.67 was unstable numerically and had unacceptable numerical noise. The stability analysis showed that the method is always unstable except for trivial cases. The analysis also showed that certain other differencing schemes for the plastic strain rate term do not involve any additional restriction beyond the usual Courant-Friedrichs-Lewy condition. The approach was to replace the function in Equation 2.67 with Equation 2.68 in which the *current* value of equivalent plastic strain appears in the strain rate term. This approach does not result in numerical noise when the numerical stability analysis is applied.

All quantities are known in the time step n.

Now we define the scalar $\dot{e}$ in order to simplify calculations by dealing with a scalar term rather than tensorial terms.

$$\dot{\mathbf{e}} \cdot \mathbf{S} = |\dot{\mathbf{e}}||\mathbf{S}| = \dot{e}S \tag{2.69}$$

$$\dot{e} = \frac{\dot{\mathbf{e}} \cdot \mathbf{S}}{S} \tag{2.70}$$

Using Equation 2.7.7.3 with the decomposition of the equation 2.39, the total scalar deviatoric strain rate can be decomposed into elastic and plastic scalar components

$$\begin{aligned}
\dot{\mathbf{e}} &= \dot{\mathbf{e}}^e + \dot{\mathbf{e}}^p \\
\dot{e}^e &= \dot{\mathbf{e}}^e \cdot \frac{\mathbf{S}}{S} \\
\dot{e}^p &= \dot{\mathbf{e}}^p \cdot \frac{\mathbf{S}}{S} \\
\dot{e} &= \dot{\mathbf{e}} \cdot \frac{\mathbf{S}}{S} \\
\dot{\mathbf{e}} \cdot \frac{\mathbf{S}}{S} &= \dot{\mathbf{e}}^e \cdot \frac{\mathbf{S}}{S} + \dot{\mathbf{e}}^p \cdot \frac{\mathbf{S}}{S}
\end{aligned}$$

$$\dot{e} = \dot{e}^e + \dot{e}^p \tag{2.71}$$

where

$$\dot{e}^e = \frac{\dot{\mathbf{e}}^{\mathbf{e}} \cdot \mathbf{S}}{S} \tag{2.72}$$

from $\dot{\mathbf{e}}^{\mathbf{e}} \cdot \mathbf{S} = |\dot{\mathbf{e}}^{\mathbf{e}}||\mathbf{S}| = \dot{e}^e S$.

We will solve for the incremental form of the equation

$$\dot{e} - \dot{e}^p - \dot{e}^e = 0 \tag{2.73}$$

Differentiating the deviatoric stress in Equation 2.43 with respect to time,

$$\dot{S} = \frac{\dot{\mathbf{S}} \cdot \mathbf{S}}{S} \tag{2.74}$$

Now making use of the generalized Hooke's Law in Equation 2.40 with Equations 2.72 and 2.74 we obtain

$$\begin{aligned}
\dot{\mathbf{e}}^e &= \frac{1}{2\mu}(\dot{\mathbf{S}} - \mathbf{WS} + \mathbf{SW}) \\
2\mu\dot{\mathbf{e}}^e &= (\dot{\mathbf{S}} - \mathbf{WS} + \mathbf{SW}) \\
2\mu\dot{\mathbf{e}}^e \cdot \frac{\mathbf{S}}{S} &= \frac{\mathbf{S}}{S} \cdot (\dot{\mathbf{S}} - \mathbf{WS} + \mathbf{SW}) \\
2\mu\dot{\mathbf{e}}^e \cdot \frac{\mathbf{S}}{S} &= \frac{\mathbf{S}}{S} \cdot \dot{\mathbf{S}} \\
2\mu\dot{\mathbf{e}}^e \cdot \frac{\mathbf{S}}{S} &= \dot{S}
\end{aligned}$$

Thus,

$$2\mu\dot{e}^e = \dot{S} \tag{2.75}$$

where μ is the shear modulus and the spin tensors cancel out because for any symmetric tensor $\mathbf{S}$ and any skew-symmetric tensor $\mathbf{W}$, $(\mathbf{WS} - \mathbf{SW}) \cdot \mathbf{S} = 0$.

If at the end of the time step n the material has yielded, Equation 2.43 can be used with Equation 2.75 to find the incremental elastic deviatoric strain.

$$\begin{aligned}
S &= \sqrt{\frac{2}{3}}Y \\
\dot{S} &= 2\mu\dot{e}^e \\
\dot{S} \cdot \Delta t &= S \\
2\mu\dot{e}^e \cdot \Delta t &= S \\
2\mu\dot{e}^e \cdot \Delta t &= \sqrt{\frac{2}{3}}Y \\
\dot{e}^e \cdot \Delta t &= \frac{\sqrt{\frac{2}{3}}Y}{2\mu} \\
e^e &= \frac{\sqrt{\frac{2}{3}}Y}{2\mu\Delta t}
\end{aligned} \tag{2.76}$$

Because the total deviatoric incremental strain can be found in time step n by Equation 2.70, the plastic strain increment can be found. With this, the incremental plastic

strain rate and equivalent plastic strain are determined. Along with the temperature, we now can determine the yield stress from an appropriate model (e.g., Johnson-Cook or Zerilli-Armstrong).

$\mathbf{S}_{n-1}, S_{n-1}$, and $\dot{\mathbf{e}}_n$ are used to obtain $\dot{e}_n$ where

$$\dot{e}_n = \dot{\mathbf{e}}_n \cdot \frac{\mathbf{S}_{n-1}}{S_{n-1}} \tag{2.77}$$

Then $\dot{e}_n, \dot{e}_{n-1}, t_n$, and t_{n-1} are used to obtain e_n where

$$e_n = \frac{\dot{e}_n - \dot{e}_{n-1}}{t_n - t_{n-1}} = \frac{\dot{e}_n - \dot{e}_{n-1}}{\Delta t_n} \tag{2.78}$$

e_n and e_{n-1} are then used to determine $\Delta e_{n-\frac{1}{2}}$ where

$$\Delta e_{n-\frac{1}{2}} = \frac{e_n - e_{n-1}}{2} \tag{2.79}$$

We then have the incremental from the of the equation $\dot{e} - \dot{e}^p - \dot{e}^e = 0$ which can be solved.

$$\Delta e_{n-\frac{1}{2}} - \Delta e^p_{n-\frac{1}{2}} - \frac{1}{2\mu}\left[\sqrt{\frac{2}{3}} f\left(T_{n-1}, \varepsilon^p_{n-1}, \sqrt{\frac{2}{3}}\frac{\Delta e^p_{n-\frac{1}{2}}}{\Delta t_{n-\frac{1}{2}}}\right) - S_{n-1}\right] = 0 \tag{2.80}$$

This equation can be characterized as a function $q(\Delta e^p_{n-\frac{1}{2}}) = 0$. This can be used to obtain the root $\Delta e^p_{n-\frac{1}{2}}$ of the function using the Newton-Raphson Method (called a modified Newton method in the CTH manual [3]). The Newton-Raphson Method is an iteration scheme that finds the positive root of the function $q(\Delta e^p_{n-\frac{1}{2}}) = 0$.

Once this root is found, then one of the constitutive models may be used to find $Y_n = f\left(T_{n-1}, \varepsilon^p_{n-1}, \sqrt{\frac{2}{3}}\frac{\Delta e^p_{n-\frac{1}{2}}}{\Delta t_{n-\frac{1}{2}}}\right)$.

2.7.7.2 Evaluation of the Deviatoric Stress. Once the yield stress Y_n is known, the deviatoric stress tensor in the cell can be evaluated. The yield stress is treated as a constant in the cell. The spherical stress tensor components are found from solving the conservation equations. The spherical stress tensor (hydrostatic pressure) with the

deviatoric stress tensor provides a complete state of stress for the point in space and at the time under consideration.

In order to determine the deviatoric stress, an elastic estimate, $\mathbf{S}_n^e$ of the deviatoric stress tensor is found based on the assumption that the material is elastic during incremental displacements that occur during the time step.

$$\mathbf{S}_n^e = \mathbf{S}_{n-1} + 2\mu\Delta\mathbf{e}_{n-\frac{1}{2}} + \Delta t_{n-\frac{1}{2}}\left(\mathbf{W}_{n-\frac{1}{2}}\mathbf{S}_{n-\frac{1}{2}}^e - \mathbf{S}_{n-\frac{1}{2}}^e\mathbf{W}_{n-\frac{1}{2}}\right) \tag{2.81}$$

where

$$\mathbf{S}_{n-\frac{1}{2}}^e = \frac{1}{2}(\mathbf{S}_{n-1} + \mathbf{S}_n^e) \tag{2.82}$$

and $\mathbf{W}$ is the spin tensor. This represents a nonhomogeneous linear algebraic system of equations that can be solved for $\mathbf{S}_n^e$.

This system of equations was derived as follows

$$\begin{aligned} 2\mu\dot{\mathbf{e}}^e &= (\dot{\mathbf{S}} - \mathbf{WS} + \mathbf{SW}) \\ \dot{\mathbf{S}} &= 2\mu\dot{\mathbf{e}}^e + \mathbf{WS} - \mathbf{SW} \\ \frac{\mathbf{S}_n^e - \mathbf{S}_{n-1}}{\Delta t_{n-\frac{1}{2}}} &= \frac{2\mu\Delta\mathbf{e}_{n-\frac{1}{2}}}{\Delta t_{n-\frac{1}{2}}} + \mathbf{W}_{n-\frac{1}{2}}\mathbf{S}_{n-\frac{1}{2}}^e - \mathbf{S}_{n-\frac{1}{2}}^e\mathbf{W}_{n-\frac{1}{2}} \end{aligned}$$

The next step is to find $\mathbf{S}_n$ which is the new deviatoric stress tensor. The cases of non-yielded and yielded $\mathbf{S}_n^e$ are treated as

$$\mathbf{S}_n = \begin{cases} \mathbf{S}_n^e, & |\mathbf{S}_n^e| < \sqrt{\frac{2}{3}}Y_n \\ \dfrac{\sqrt{\frac{2}{3}}Y_n\mathbf{S}_n^e}{|\mathbf{S}_n^e|}, & |\mathbf{S}_n^e| \geq \sqrt{\frac{2}{3}}Y_n \end{cases} \tag{2.83}$$

Because the second part of this equation represents radial return to the yield surface, this ensures that any stress state lies within or on the yield surface. It also accounts for elastic straining and rigid rotation through the spin tensor.

2.7.7.3 Evaluation of the Equivalent Plastic Strain Rate. The final step in this solution method is to determine the equivalent plastic strain rate at time step n. The

equivalent plastic strain rate is found by beginning with

$$\dot{\mathbf{e}} \cdot \mathbf{S} = |\dot{\mathbf{e}}||\mathbf{S}| = \dot{e}S$$

except, we substitute plastic strain for total strain

$$\begin{aligned}
\dot{e}^p &= \dot{\mathbf{e}}^p \cdot \frac{\mathbf{S}}{S} \\
&= (\dot{\mathbf{e}} - \dot{\mathbf{e}}^e) \cdot \frac{\mathbf{S}}{S} \\
&= \left[\dot{\mathbf{e}} - \frac{1}{2\mu}(\dot{\mathbf{S}} - \mathbf{WS} + \mathbf{SW})\right] \cdot \frac{\mathbf{S}}{S} \\
&= \left[\dot{\mathbf{e}} \cdot \mathbf{S} - \frac{1}{2\mu}(\dot{\mathbf{S}} - \mathbf{WS} + \mathbf{SW}) \cdot \mathbf{S}\right] \frac{1}{S} \\
&= \left[\dot{\mathbf{e}} \cdot \mathbf{S} - \frac{\mathbf{S}}{2\mu} \cdot \mathbf{S}\right] \frac{1}{S} \\
&= \left[\dot{\mathbf{e}} - \frac{\dot{\mathbf{S}}}{2\mu}\right] \cdot \frac{\mathbf{S}}{S}
\end{aligned} \tag{2.84}$$

Recall that for any symmetric tensor $\mathbf{S}$ and skew-symmetric tensor $\mathbf{W}$, $(\mathbf{WS}-\mathbf{SW})\cdot\mathbf{S} = 0$.

The differenced form of this equation is used so that CTH can make time incremented calculations and solve for the plastic strain rate.

$$\begin{aligned}
\dot{e}^p &= \left[\dot{\mathbf{e}} - \frac{\dot{\mathbf{S}}}{2\mu}\right] \cdot \frac{\mathbf{S}}{S} \\
\frac{\Delta e^p}{\Delta t} &= \left[\frac{\Delta \mathbf{e}}{\Delta t} - \frac{\Delta \mathbf{S}}{\Delta t}\frac{1}{2\mu}\right] \cdot \frac{\mathbf{S}}{S} \\
\frac{\Delta e^p}{\Delta t} \cdot \Delta t &= \left[\frac{\Delta \mathbf{e}}{\Delta t} \cdot \Delta t - \frac{\Delta \mathbf{S}}{\Delta t}\frac{1}{2\mu} \cdot \Delta t\right] \cdot \frac{\mathbf{S}}{S} \\
\Delta e^p_{n-\frac{1}{2}} &= \left[\Delta \mathbf{e}_{n-\frac{1}{2}} - \frac{\Delta \mathbf{S}_{n-\frac{1}{2}}}{2\mu}\right] \cdot \frac{\mathbf{S}_{n-\frac{1}{2}}}{S_{n-\frac{1}{2}}}
\end{aligned} \tag{2.85}$$

where $\Delta \mathbf{S}_{n-\frac{1}{2}} = \mathbf{S}_n - \mathbf{S}_{n-1}$ and $\mathbf{S}_{n-\frac{1}{2}} = \dfrac{\mathbf{S}_n + \mathbf{S}_{n-1}}{2}$.

The equivalent plastic strain can then be found from numerical integration of the equivalent plastic strain rate (see Equation 2.47)

$$\begin{aligned}
\dot{\varepsilon^p} &= \sqrt{\frac{2}{3}\dot{\mathbf{e}}^p \cdot \dot{\mathbf{e}}^p} \\
\dot{\varepsilon^p} &= \sqrt{\frac{2}{3}}\dot{e}^p \\
\frac{\Delta\varepsilon^p}{\Delta t} &= \sqrt{\frac{2}{3}}\frac{\Delta e^p}{\Delta t} \\
\frac{\varepsilon^p_n - \varepsilon^p_{n-1}}{\Delta t} &= \sqrt{\frac{2}{3}}\frac{\Delta e^p_{n-\frac{1}{2}}}{\Delta t} \\
\varepsilon^p_n &= \varepsilon^p_{n-1} + \sqrt{\frac{2}{3}}\Delta e^p_{n-\frac{1}{2}}
\end{aligned} \tag{2.86}$$

2.7.8 Solution Synopsis.

Knowns: $\mathbf{v}_n, \mathbf{v}_{n-1}, \mathbf{D}_n, \mathbf{D}_{n-1}, \mathbf{W}_n, \mathbf{W}_{n-1}, \mathbf{S}_{n-1}, S_{n-1}, T_{n-1}, e_{n-1}, \dot{\mathbf{e}}_n, \dot{\mathbf{e}}_{n-1}, \varepsilon^p_{n-1}, \dot{\varepsilon}^p_{n-1}, e^p_{n-1}, \mathbf{e}_{n-1}, t_n, t_{n-1}, \mu$

Yield Strength Solution Method (See section 2.7.7.1 for details)

Use $\mathbf{S}_{n-1}, S_{n-1}$, and $\dot{\mathbf{e}}_n$ to get $\dot{e}_n$ using $\dot{e}_n = \dot{\mathbf{e}}_n \cdot \dfrac{\mathbf{S}_{n-1}}{S_{n-1}}$.

Use $\dot{e}_n, \dot{e}_{n-1}, t_n$, and t_{n-1} to get e_n using $e_n = \dfrac{\dot{e}_n - \dot{e}_{n-1}}{t_n - t_{n-1}} = \dfrac{\dot{e}_n - \dot{e}_{n-1}}{\Delta t_n}$.

Use e_n and e_{n-1} to get $\Delta e_{n-\frac{1}{2}}$ using $\Delta e_{n-\frac{1}{2}} = \dfrac{e_n - e_{n-1}}{2}$.

Use $q(\Delta e^p_{n-\frac{1}{2}}) = \Delta e_{n-\frac{1}{2}} - \Delta e^p_{n-\frac{1}{2}} - \dfrac{1}{2\mu}\left[\sqrt{\dfrac{2}{3}} f\left(T_{n-1}, \varepsilon^p_{n-1}, \sqrt{\dfrac{2}{3}}\dfrac{\Delta e^p_{n-\frac{1}{2}}}{\Delta t_{n-\frac{1}{2}}}\right) - S_{n-1}\right] = 0$ to get the root $\Delta e^p_{n-\frac{1}{2}}$ using Newton's Method.

Use the Johnson-Cook or Zerilli-Armstrong model to get $Y_n = f\left(T_{n-1}, \varepsilon^p_{n-1}, \sqrt{\dfrac{2}{3}}\dfrac{\Delta e^p_{n-\frac{1}{2}}}{\Delta t_{n-\frac{1}{2}}}\right)$

Deviatoric Stress Solution Method (See section 2.7.7.2 for details)

Use $\mathbf{S}_{n-1}, \mathbf{W}_n, \mathbf{W}_{n-1}, t_n, t_{n-1}$, and $\Delta\mathbf{e}_{n-\frac{1}{2}}$ to get the elastic estimate for the deviatoric stress, $\mathbf{S}^e_n$ using $\mathbf{S}^e_n = \mathbf{S}_{n-1} + 2\mu\Delta\mathbf{e}_{n-\frac{1}{2}} + \Delta t_{n-\frac{1}{2}}\left(\mathbf{W}_{n-\frac{1}{2}}\mathbf{S}^e_{n-\frac{1}{2}} - \mathbf{S}^e_{n-\frac{1}{2}}\mathbf{W}_{n-\frac{1}{2}}\right)$.

Then use $\mathbf{S}_n = \begin{cases} \mathbf{S}^e_n, & |\mathbf{S}^e_n| < \sqrt{\dfrac{2}{3}} Y_n \\ \dfrac{\sqrt{\frac{2}{3}} Y_n \mathbf{S}^e_n}{|\mathbf{S}^e_n|}, & |\mathbf{S}^e_n| \geq \sqrt{\dfrac{2}{3}} Y_n \end{cases}$ to get the current deviatoric stress tensor.

Equivalent Plastic Strain Solution Method (See section 2.7.7.3 for details)

Use $\Delta e^p_{n-\frac{1}{2}}$ to get the equivalent plastic strain, ε^p_n using $\varepsilon^p_n = \varepsilon^p_{n-1} + \sqrt{\dfrac{2}{3}}\Delta e^p_{n-\frac{1}{2}}$.

n becomes $n-1$

Note that $\mathbf{v}_n$ is known from the previous time step information and the solution to the dynamic equations. With $\mathbf{v}_n$, the rest of the time step n values for the "Knowns:" quantities can be found.

In this strength solution method, calculation of the effective plastic strain and effective stress are integral to the method. Also, this solution method, steps forward in time and uses information from the previous time step to calculate current time step values. The Johnson-Cook and other models used in this method utilize a scalar, equivalent plastic strain, in its solution method.

2.7.9 Heat Generation. Heat is generated due to viscoplastic deformation. This occurs in three primary situations: during sliding motion between the slipper and rail (or coating), during plastic deformation caused by shock waves or large impact stresses, and during gouging as large deformations occur during the material interaction. During these situations, high strain rates lead to large deformations in a small time period. This results in shock waves with large pressure and temperature differentials and a sharp increase in deviatoric stress. This high area of deviatoric stress results in development of viscoplastic zones through the viscoplastic stress-strain relations in the constitutive equation for the material. The constitutive equations model development of plasticity. This plastic straining performs work on the system and the total energy of the system increases. This energy increase causes a rise in temperature through the equation of state because the increase in internal energy is not allowed to dissipate in the short time period that deformations occur. This increase in energy causes a rise in temperature within the areas of plasticity. Allowing this heat to flow between areas of high and low temperature results in a nonequilibrium thermodynamic condition.

2.8 Shock Waves

Shock waves are very important in the consideration of high energy impact dynamics. When the amplitude of an elastic stress wave exceeds the dynamic flow strength (a.k.a., dynamic yield stress) of a material, shear stresses may be neglected in comparison to the compressive hydrostatic stress components. This "hydrodynamic" approach, though

simple, contains inaccuracies. Thus, care must be taken when applying such a concept to the analysis of normal shock waves.

Shock waves are surfaces across which the velocity, pressure, and density are discontinuous and upon which the differential equations of continuity do not hold. Physically these surfaces are actually thin layers through which the parameters vary so rapidly that continuum analysis is invalid. They are represented in continuum analysis as surfaces separating regions of continuous flow. This usually occurs at impact velocities far exceeding the speed of disturbance propagation in solids (around 2 km/sec) and 10 GPa of hydrodynamic stress.

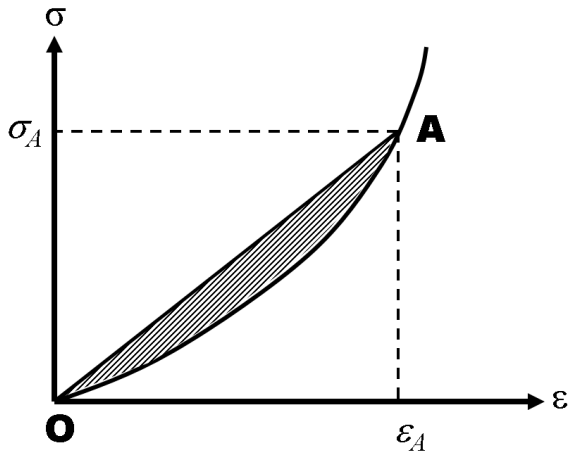

Figure 2.12 **Uniaxial stress-strain curve for a material at high pressure.**

Consider Figure 2.12. Materials that form shock waves follow behavior at uniaxial strain conditions shown by the concave upward curve. If an impact on the material causes a stress of σ_A, a shock wave will form with a velocity of propagation at c

$$c = \sqrt{\frac{\sigma_A/\varepsilon_A}{\rho}} \tag{2.87}$$

in solids, where σ_A is the one dimensional Cauchy stress, ε_A is the true strain, and ρ is the density.

The difference between the behavior of the shock wave at these conditions and an elastic wave at the same conditions is that a shock wave's strength changes with time and

position. It becomes stronger or weaker as it travels though the material. An elastic wave by contrast, can also have a sharp wave front but it does not change in strength as it propagates. As the shock wave dissipates, the unloading of the material follows the actual stress-strain curve denoted by the straight line OA. The shaded portion of the curve is equivalent to the energy dissipated during the loading and unloading of the material that is subjected to the shock wave [54]. shock waves may form at low stresses in which deviatoric stress is important, or high stresses (above 10GPa) in which pressure is important and hydrodynamic treatment of the shock wave is appropriate. The key definition of shock waves in either case is variation of the shock front in time and space and development of the front due to coalescence of wavelets.

Note that as the stress at impact, σ_A increases, the velocity at which the disturbance propagates also increases. As the higher amplitude disturbances catch up to the lower pressure disturbances, they coalesce and increase the gradient of pressure across the lower amplitude disturbances. The pressure jump gradually increases until a sharp discontinuity is formed in pressure, volume, density, and temperature.

When unloading occurs, it will initially happen at the shock wave front stress, σ_A. Each unloading wave mechanism follows the mechanism dictated by straight line OA. In Figure 2.12, one can see that as the stress decreases along the high pressure curve, the slope of the unloading line decreases and the speed of propagation of the unloading wave decreases. The unloading wave ends up being dispersed due to this continual decrease in wave speed.

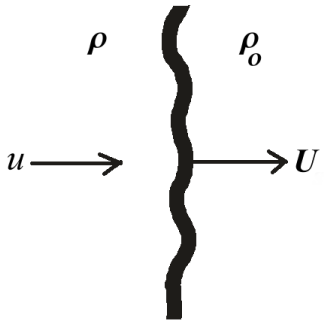

Figure 2.13 **Propagating wave front, conservation of mass.**

In order to analyze shock wave phenomena, we require use of the conservation equations of mass, momentum, and energy. These fundamental physical laws are used extensively in engineering and physics applications to model the behavior of materials under varying loading mechanisms. In this section, we do this in the context of shock wave loading of a material.

Let us consider a one-dimensional wave front propagating into a stationary continuum (see Figures 2.13 through 2.15). In the figures, u is the particle velocity behind the wave front and U is the velocity of the travelling wave front. First consider the conservation of mass for the propagating wave (see Figure 2.13). The wave front is moving to the right so the mass moving through the front is $A\rho_o(U-u)dt$ where ρ_o is the density in front of the shock and A is the cross-sectional area of the continuum and t is time. The mass travelling through the wave front has a relative velocity with respect to the moving continuum of $U-u$.

Mass of compressed material behind the shock	=	Mass of "virgin" uncompressed material in front of shock

OUTPUT	=	INPUT

$$\int_V \rho dV = \text{constant} \tag{2.88}$$

$$\rho \cdot A \cdot (U-u) \cdot t = \rho_o \cdot A \cdot U \cdot t \tag{2.89}$$

for a stationary continuum that undergoes a shock. This equation reduces to $\rho_o U = \rho(U-u)$ [54].

Next consider the conservation of momentum (see Figure 2.14). The change in momentum is equivalent to the impulse of force across the wave front.

Conservation of momentum can be described by Newton's Law

$$F = ma = m\frac{dv}{dt} \tag{2.90}$$

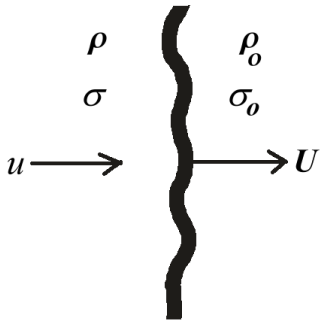

Figure 2.14 **Propagating wave front, conservation of momentum.**

The impulse-momentum law is then

$$I = \int F dt = \int m dv = m v_f - m v_i \tag{2.91}$$

That is, the impulse, I is equivalent to the change in momentum, mv of a body.

Impulse applied = Change in momentum

stress · area · dt = mass · velocity - initial momentum

$$\sigma A \Delta t = mu - 0 = (\rho A U \Delta t) u$$

for a stationary continuum that undergoes a shock where σ is the state of stress caused by impact and Δt is the incremental time under consideration.

This leads to the momentum relation for shock waves, $\sigma = \rho U u$ [54].

Finally, we consider the conservation of energy (see Figure 2.15). The work done by the external forces applied plus the change in internal energy must be equal the final energy state.

Final energy = Internal energy plus work done

The mass that enters the shock over a period of time, Δt is $\rho_o U \Delta t$. This mass adds kinetic energy to the final system configuration. The final energy for the system is the sum of the stored energy plus the final kinetic energy. The work done on the system is equal to

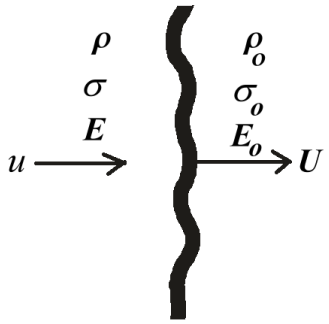

Figure 2.15 **Propagating wave front, conservation of energy.**

the stress moving through the distance $u\Delta t$. If the internal energy per unit mass behind the shock is E and the internal energy per unit mass in front of the shock is E_o, then the conservation of energy is

$$\rho(U-u)E\Delta t + \frac{1}{2}\rho_o U\Delta t u^2 = \rho_o U E_o \Delta t + \sigma u \Delta t$$

for a stationary continuum that undergoes a shock.

$$(E\rho(U-u) - E_o\rho_o U)\Delta t = \sigma u\Delta t - \frac{1}{2}\rho_o U\Delta t u^2$$

Using conservation of mass, $\rho_o U = \rho(U-u)$ and conservation of momentum, $\sigma = \rho U u$:

$$(E\rho_o - E_o\rho_o)U\Delta t = \sigma\frac{(\rho-\rho_o)U}{\rho}\Delta t - \frac{1}{2}\rho_o U\Delta t\frac{\sigma}{\rho U}\frac{(\rho-\rho_o)U}{\rho}$$

It can be shown that the energy conservation equation reduces to

$$E - E_o = \frac{1}{2}\sigma\left(\frac{1}{\rho_o} - \frac{1}{\rho}\right)$$

Each of these conservation equations make up what is known as the Rankine-Hugoniot relations for a material in which a pressure discontinuity propagates. They determine the various states of a shock based on pressure and volume.

Shock waves have a steep front and require a state of uniaxial strain (i.e., no lateral propagation). This allows buildup of hydrodynamic components of stress to high levels. When this hydrodynamic component (i.e., spherical stress, or pressure) exceeds the dynamic flow stress by several factors, one can assume the solid exhibits no resistance to shear. That is, the yield stress at the strain rate established at the front of the shock wave is exceeded by several factors. Note that **dynamic flow stress** is defined as the *yield stress of the material at a particular strain rate.* In this case, the dynamic flow stress is defined at the same strain rate as the shock front.

2.8.1 Rankine-Hugoniot Curves. We have shown three conservation equations that are in terms of five variables: stress, particle velocity, shock velocity, density, and internal energy. Therefore, we need an additional equation in order to determine all parameters as a function of one of them. This fourth equation can be expressed as the relationship between shock and particle velocities and must be determined experimentally. This fourth equation is called the equation of state and it relates the hydrodynamic stress, internal energy, and density (or specific volume).

This relation can be thought of as the hydrodynamic version of the constitutive model. The constitutive model relates stress and strain at various temperatures, while the equation of state models the relationship between hydrodynamic stress (pressure) and hydrodynamic strain (specific volume) at various internal energies [54].

A polynomial equation consisting of parameters $C_o, S_1, S_2, S_3, \ldots$ can be used to empirically describe the relationship between shock velocity and particle velocity.

$$U = C_o + S_1 u + S_2 u^2 + S_3 u^3 + \ldots$$

This is often called an equation of state of a material because it describes the state of a material by relating pressure, internal energy, and density (or volume) of the material. These parameters can be related to each other using this polynomial relationship between the shock and particle velocities as a beginning. The parameters $S_1, S_2, S_3, \ldots$ are empirical parameters that can be found from experimentation. C_o is the speed of sound of the material at zero pressure.

For moderate pressures, $S_2, S_3, \ldots$ are equal to zero and the equation of state becomes a linear relationship.

$$U = C_o + S_1 u$$

This relationship describes fairly well the shock response of materials not undergoing phase transitions. If the material is porous, or undergoes phase transformation, this equation of state is no longer valid and must be modified.

From this point forward, we will refer to the stress as pressure, also called hydrodynamic stress, for our discussion of the Rankine-Hugoniot curve. This curve is shown in terms of the pressure and the specific volume. The specific volume is the inverse of the density, $\frac{1}{\rho}$.

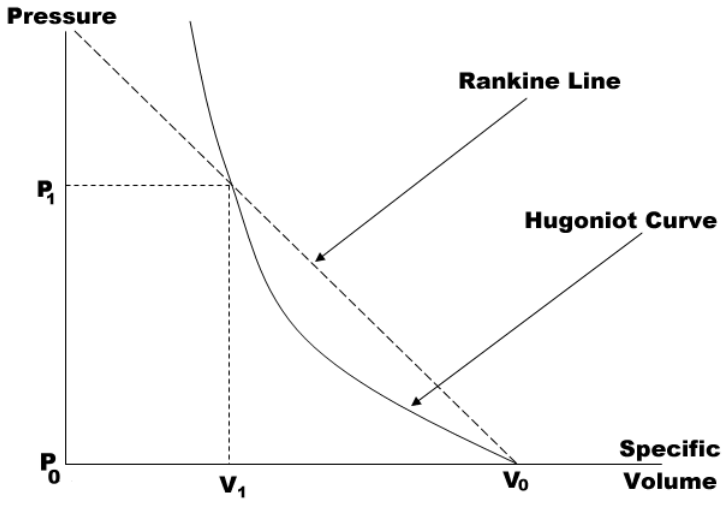

Figure 2.16 **The Rankine-Hugoniot curve.**

In Figure 2.16 we see the Hugoniot curve. This curve is the locus of all points of every shocked state of a material. The Rankine line joins the points P_o, V_o and P_1, V_1. The slope of this line is $\frac{P_1 - P_o}{V_1 - V_o}$ which is equal to $-\rho_o^2 U^2$ through the momentum and mass conservation equations.

This Hugoniot curve refers to the state of the shock at P_1 and V_1. When pressure is increased in a shock front, it does not follow the Hugoniot curve. Instead, the pressure changes discontinuously from P_o to P_1. It "jumps" from P_0 to P_1. In other words, a

shock with initial conditions of pressure, P_o and specific volume, V_o and shocked state of pressure, P_1 and specific volume, V_1 exists on the Hugoniot curve.

Each hydrodynamic state of the shock (i.e., each match of P and V behind a shock wave) also has a value of $-\rho_o^2 U^2$ that can be used to help evaluate other parameters of the shock. Thus, in the Hugoniot curve we have the relationship between the pressure, specific volume, density, and speed of the shock. For example, if the original density is known, the original pressure and velocity of the material is known, and the speed of the shock wave is known, then the values of pressure and volume behind the shock are also known based on what material we have. The Hugoniot curve consists of all potential values of the pressure and volume behind a shock wave for a specific material. It contains all the points P, V that exist for a shock wave.

The shock wave velocity is also related to the particle velocity through the equation of state. With pressure and specific volume (i.e., density) changes behind a shock, the energy can be found through the conservation of energy equation. These concepts are contained in the CTH algorithms to solve for high pressure shocks in the CTH solution. In the frictional development of the slipper-rail interaction, one would expect low shock waves in which deviatoric stresses dominate. In vibratory impact models such as rail roughness impacts, one would expect to see high pressure shock waves with stronger wave fronts.

2.8.2 Impact. In this section we present a simple case of high speed impact to better illustrate the concepts already discussed. Planar, normal impact is the simplest case for showing the method of shock wave analysis. Let us consider two parallel surfaces that contact each other simultaneously with all points at the same time between impact surfaces (see Figure 2.17). The direction of impact velocity is normal to the surfaces.

There are two conditions that must be met at the impact surfaces:

- The material must be continuous across the impact interface. That is, $Velocity - u_1 = u_2$

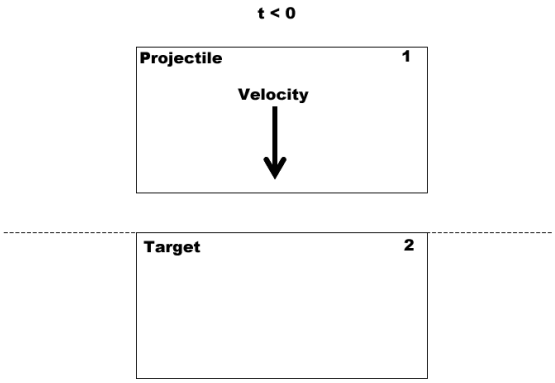

(a) **Planar impact prior to impact.**

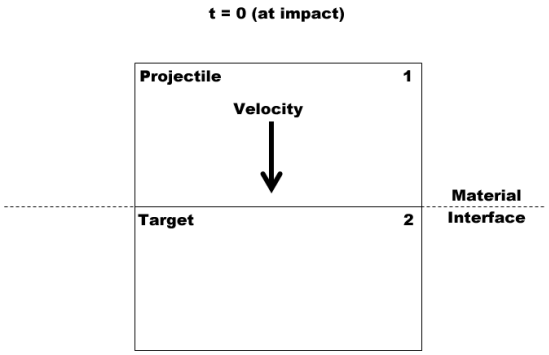

(b) **Planar impact at impact.**

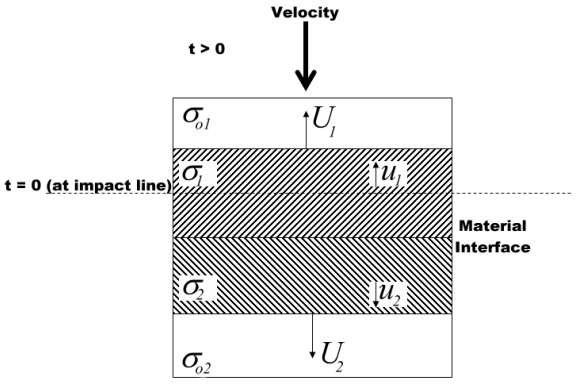

(c) **Planar impact immediately after impact.**

Figure 2.17 **The planar impact case.**

- The pressure must also be the same across the impact interface. Otherwise, another pulse would be generated by the discontinuous hydrodynamic stresses. That is, $\sigma_1 = \sigma_2$.

The particle velocity in the projectile is measured with respect to a moving reference (the impact interface). Let V be the velocity of the projectile. By conservation of mass behind the shock in the target,

$$\rho_2 A_o(U_2 - u_2) = \rho_{o2} A_o(U_2) \tag{2.92}$$

$$\rho_2(U_2 - u_2) = \rho_{o2}(U_2) \tag{2.93}$$

Using the conservation of momentum equation with the conservation of mass, we get

$$\rho_2(U_2 - u_2)tU_2 - 0 = (\sigma_2 - \sigma_{o2})t \tag{2.94}$$

$$\rho_{o2}(U_2)tu_2 - 0 = (\sigma_2 - \sigma_{o2})t \tag{2.95}$$

$$\rho_{o2}(U_2)u_2 - 0 = \sigma_2 - \sigma_{o2} \tag{2.96}$$

If there is no residual stress in the target material ($\sigma_{o2} = 0$) then $\sigma_2 = \rho_{o2}U_2u_2$. Likewise, $\sigma_1 = \rho_{o1}U_1u_1$.

If we consider a simple equation of state where $U_1 = C_{o1} + S_1u_1$ and $U_2 = C_{o2} + S_2u_2$. The momentum equations then become

$$\begin{aligned}
\sigma_1 &= \rho_{o1}u_1(C_{o1} + S_1u_1) \\
\sigma_1 &= \rho_{o1}C_{o1}u_1 + S_1u_1^2 \\
\sigma_2 &= \rho_{o2}u_2(C_{o2} + S_2u_2) \\
\sigma_2 &= \rho_{o2}C_{o2}u_2 + S_2u_2^2
\end{aligned}$$

By the first condition, $\mathrm{V} - u_1 = u_2$ so $u_1 = \mathrm{V} - u_2$. Therefore,

$$\sigma_1 = \rho_{o1}C_{o1}(\mathrm{V} - u_2) + \rho_{o1}S_1(\mathrm{V} - u_2)^2$$

Since the other condition states that $\sigma_1 = \sigma_2$. We then have

$$\rho_{o1} C_{o1} (\mathrm{V} - u_2) + \rho_{o1} S_1 (\mathrm{V} - u_2)^2 = \rho_{o2} C_o u_2 + \rho_{o2} S_2 u_2^2$$

Solving for u_2 and assuming the target and projectile are the same material, we get

$$u_2 = \frac{\rho_{o1}(C_{o1}\mathrm{V} + S_1\mathrm{V}^2)}{\rho_{o2}C_{o2} + \rho_{o1}C_{o1} + 2\rho_{o1}S_1\mathrm{V}}$$
$$u_2 = \frac{\rho_o(C_o\mathrm{V} + S\mathrm{V}^2)}{2\rho_o C_o + \rho_o S\mathrm{V}}$$
$$u_2 = \frac{\mathrm{V}}{2}$$

That is, the projectile particles for a planar impact with a projectile and target of the same material, transfers half their momentum to the target.

The initial impact produces a shock wave which travels back in to the plate from the impact surface at wave speed, U. The particle velocity of the plate material behind the shock wave is u. as the wave travels into the plate, the stress of the wave changes from σ_o to σ for each plate. Both plates are compressed as the shock wave travels through it. If the impact results in a high stress shock wave, the stress is considered to be uniaxial and a hydrodynamic treatment is appropriate.

Therefore, the stress behind each compressive shock wave is equivalent to pressure. In this treatment, the Rankine-Hugoniot relations may be used as an equation of state to evaluate the state of the shock and provide an additional relation to solve all unknowns of the governing equations.

When the compression wave in each plate reaches the free surface at the opposite end, it will result in an expansion wave that reflects off the free surface. If no plastic work is done, the impact is elastic and the particle velocity will be equal to the initial velocity of the plate [54]. Otherwise, the final velocity will be different depending on how much plastic work was performed.

If the plates are made of different materials, then the speed of the wave in each plate will be different and the expansion waves that reflect off the back of the plates will not

meet at the impact surface. One of the waves will propagate into the other plate and further complicate the process. A similar analysis to what has been described here may be used to analyze these more complicated situations as the shock waves propagate into each other.

2.8.3 Low Pressure Shock Wave Profiles. There are problems with the simple hydrostatic treatment for solids. It does not account for plasticity and it does not predict low pressure shock wave profiles, only extremely high pressure ones as shown in Figure 2.18. A high pressure shock wave is predicted by a hydrodynamic treatment and contains a sharp discontinuity at the shock front, a pressure pulse duration at the top, and a gradual return to zero stress via a release mechanism. In the frictional sliding cases to be studied in this research, low pressure shocks will be the dominant mechanism until impact with the rail roughness or when gouging occurs.

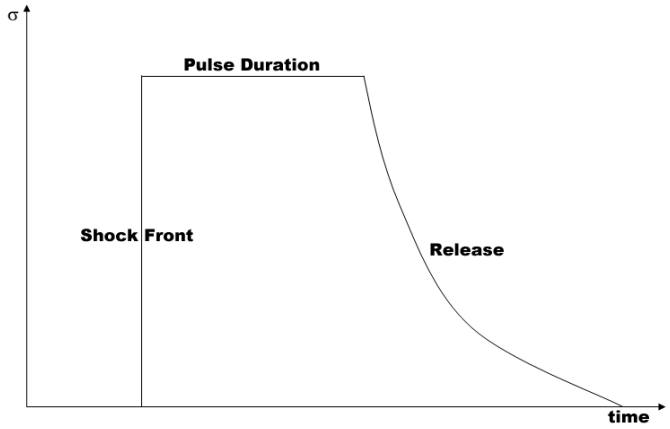

Figure 2.18 **High pressure shock wave profile of Eulerian stress vs. time for a particle through which a normal shock passes.**

Low pressure shock waves are quite different from this hydrodynamic model (see Figure 2.19). The deviatoric stress component plays a large role in the treatment of the shock and so does the material's strength. Also, the pressure-volume curve for a real material is very different than that predicted by the Hugoniot curve. This is primarily due to the deviatoric component of stress.

In low pressure shocks, the rate at which the stress increases with volume is much higher in the elastic range of a low pressure shock wave. When the Hugoniot elastic limit

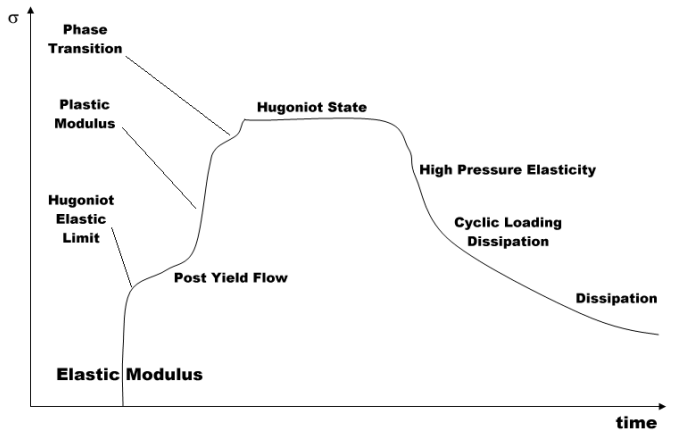

Figure 2.19 **Low pressure shock wave profile of Eulerian stress vs. time for a particle through which a normal shock passes.**

is reached, the pressure-volume curve shows a change in slope. After an initial rise in pressure at the shock front, the Hugoniot elastic limit is reached. Beyond the Hugoniot elastic limit, the pressure rises continuously to the Hugoniot state at the top of the curve. The rate at which this rise occurs is dictated by the constitutive behavior of the material. At the top of the curve lies the relatively flat run of the Hugoniot state. When unloading occurs, it is initially elastic, but soon becomes plastic. The elastic portion of the wave front is separated from the plastic portion of the shock wave. The elastic portion (the portion below the Hugoniot elastic limit) travels at a velocity higher than the plastic wave (see the slope of the uniaxial stress-strain curve in Figure 2.12). The dissipation region is that portion of the curve in which the pressure degenerates toward the original state of the material. However, in a low pressure shock wave, this original state is never reached. This is a result of shock hardening which occurs after plastic straining.

In the vibratory impact of a high strength slipper upon a rail, shock waves that form will not usually be uniaxial and will resemble the low pressure shock profile more than it will the high pressure shock. The CTH models account for deviatoric stress and two-dimensional effects. The frictional sliding case is an example in which deviatoric stress dominate and any shock waves that form in this case will be affected by factors that are depicted in the low pressure shock wave profile such as plasticity, deviatoric stress, lateral strain, and shock hardening. The hydrodynamic treatment is only valid for high

pressure shocks above 10 GPa. The region between low and high pressure shocks will contain characteristics of both. There is no simple analytic treatment of shocks, that is why numerical algorithms are invaluable.

III. Investigation of Numerical Tools

It is impractical to study high energy impact phenomena and gouging by conducting numerous gouging experiments. In order to effectively study high energy impact phenomena, numerical tools are required. Some of these numerical tools and the hardware necessary to use them are discussed in this chapter. There are a number of numerical tools available for the study of hypervelocity impact. This study investigates those that are available at the Air Force Institute of Technology; specifically, CTH, ABAQUS, and LS-DYNA3D.

Previous models for the study of hypervelocity gouging are two-dimensional plane strain models. The test sled undergoes three-dimensional effects that have been simulated by David Laird [7]. His three-dimensional model simulated an impact of a slipper at the corner of a rail in a pitching motion. He found the two-dimensional plane strain model to be conservative. That is, gouging initiated sooner in the two-dimensional model. What was not simulated was the flat distributed loading of a three-dimensional slipper on the flat of a rail.

Also, the velocity of impact in the three-dimensional Laird simulation was much higher than dynamic analysis of test sleds show it to be. Laird approximated an actual impact by changing impact velocity so that the impact of the slipper matched the kinetic energy of an impact of a slipper with a test sled mass attached to it. By doing this, momentum is not matched. Velocity is squared in the kinetic energy term. Momentum contains a linear relationship with velocity. Approximating an actual impact via kinetic energy means the momentum term is underestimated. For example, a slipper of mass, m that is one hundred times smaller than the mass of the test sled, M requires an impact velocity that is ten times greater than a real test sled. That is, $\frac{1}{2}MV^2 = \frac{1}{2}\frac{M}{100}(10V)^2 = \frac{1}{2}mv^2$. In this case, the momentum of the test sled will be $MV = \frac{M}{100}(10V) = \frac{MV}{10}$ which is ten times smaller than it needs to be in order to approximate the momentum effects of the impact.

The only way to match momentum and kinetic energy without creating an unrealistic material of super-high density is to add mass to the slipper to approximate the mass of the test sled. In this way, the actual estimated velocity of impact may be used. Finite

element codes offer this possibility because nodal masses may be added to a mesh without changing the material properties of the slipper. To investigate this possibility as well as investigate the capabilities of LS-DYNA3D for use in the proposed research, a three-dimensional slipper-rail distributed loading impact was studied using the LS-DYNA3D code. This study provided information on the capabilities of LS-DYNA3D and the finite element method to simulate actual conditions in the field. It was found that:

- Nodal masses were an effective means of adding mass to the system so that kinetic energy and momentum of an impact could both be approximated.
- Lagrangian meshes of finite element codes have difficulties when the mesh becomes highly distorted.
- Distributed loading at impact does not result in a gouging situation, but simulates a condition reminiscent of wear.

Following this study, three nonlinear explicit codes available for solving the nonlinear equations of conservation were studied and compared. Requirements for this research, such as the ability to model heat flow and high strain rate characteristics of the material meant that further study of available numerical tools was warranted. The three most likely candidates available for use at AFIT are CTH, ABAQUS, and LS-DYNA3D. The capabilities of these codes were studied in their own right, and then compared with each other using a high speed asperity impact model. The results are presented after discussion of the three-dimensional LS-DYNA3D distributed impact loading investigation.

3.1 LS-DYNA3D 3D Oblique Impact Run

Most of the results in Laird's dissertation [7] were accomplished with a two-dimensional plane strain model. To verify the validity of that model a three-dimensional model with an impact at the corner of the rail was also run. Laird found that the gouge initiated at a later time than it did in the two-dimensional model. He concluded that the two-dimensional plane strain case is a conservative estimate of the actual conditions that initiate gouging.

The actual test sled undergoes roll, pitch, and yaw components of motion as the test sled accelerates along the rail. Laird's three-dimensional numerical study was the

first to study this aspect of the problem. The sole similitude parameter used by Laird in this study was to match the kinetic energy of a realistic test sled. This parameter was determined heuristically. Because of hardware limitations, the actual mass of a realistic test sled could not be simulated. This meant that even though kinetic energy could be matched, momentum could not.

To study realistic momentum as well as kinetic energy effects the mass of an actual test sled should be simulated in some manner. Finite element codes offer a way to do this, since nodal masses may be added to the slipper model without complicating the model. In addition, a common mode of impact during a test sled run includes a vibratory impact that strikes on the top of the rail. To gain a better understanding of the conditions that occur during this type of impact with a realistic mass, a three-dimensional Lagrangian finite element slipper and rail model was developed.

The results of this study leads to a better analysis of a three-dimensional test sled. It confirmed the use of a two-dimensional plane strain model for studying hypervelocity gouging. It also provided insight into the three-dimensional effects of a flat impact on the top of the rail in which there is not a restricted plane strain condition.

A highly nonlinear finite element code called LS-DYNA3D was used to analyze the hypervelocity gouging problem and explore the use three-dimensional effects of a vibratory impact on a prismatic rail. Parallel processing capabilities of the code are used to obtain solutions in the shortest amount of time for this complex problem. The LS-DYNA3D code is used so that momentum effects that are not captured by finite volume hydrocodes such as CTH [39] may be characterized in the solution.

Based on previous research [55], it is not expected that the three-dimensional model will result in gouging except in a plane strain condition. This plane strain condition only occurs in the three-dimensional model within the midplane in which the out-of-plane response is restricted. Therefore, visualization of the state of stress and plastic strain within the midplane of the model will be analyzed. The value of the three-dimensional model is to aid in a study of LS-DYNA's capability to model:

- three-dimensional effects at impact

- possible gouging in the midplane of the model (plane strain condition)
- a common state of the slipper impacting the rail

By varying the yield strength of the slipper and rail materials the case of a stronger target is contrasted with a stronger projectile at impact. In addition, this will provide greater insight into the potential effect of the yield strength on the initiation of gouging. For example, some research has indicated that a rail material with a higher yield strength than the slipper would mitigate gouging [7].

3.1.1 Finite Element Approach. Finite element techniques treat the computational space as many small, interconnected elements rather than a pointwise discretization of the continuum as in finite difference methods. In this way, piecewise approximations of the differential equations is made. Finite element methods provide an approximation of the real problem. However, this means that only an exact solution for an approximated problem can be determined.

LS-DYNA3D [56] uses the balanced force approach for the conservation of momentum in the form

$$\sigma_{ij.j} + \rho b_f = \rho \ddot{x}_i$$

that satisfies the traction boundary conditions

$$\sigma_{ij} n_i = \mathrm{t_i}(t)$$

where σ_{ij} is the Cauchy stress, ρ is the current density, b_f is the body force density, $\ddot{x}$ is the acceleration, t is the traction, and n_i is the outward normal to a boundary element with boundary ∂b.

Mass conservation is trivial for the Lagrangian mesh:

$$\rho V = \rho_o$$

The energy equation is

$$\dot{E} = V s_{ij} \dot{\varepsilon}_{ij} - (p + q)\dot{V}$$

where E is the total energy, V is the volume, s_{ij} is the deviatoric stress tensor, ε is the strain tensor, p is the pressure, q is the bulk viscosity, and V is the volume. The $\dot{}$ terms are time derivatives. This equation is integrated in time and used for global energy balance and equation of state calculations.

After applying the weak form of the equilibrium equations and using the finite element method with interpolation functions, the matrix form of the equilibrium equation that is solved becomes

$$\sum_{m=1}^{n} \left\{ \int_{v_m} \rho \mathrm{N}^t \mathrm{N} a dv + \int_{v_m} B^t \sigma dv - \int_{v_m} \rho \mathrm{N} b dv - \int_{\partial b_1} \mathrm{N}^t \mathrm{t} ds \right\}^m = 0$$

where N is the interpolation matrix, a is acceleration, b is the body force load vector, t is the applied traction loads, and B is the strain displacement matrix.

This particular model consists of two bounded continuous domains, the slipper and rail. These two domains are first extruded to the third dimension and then discretized into three-dimensional solid brick elements. Thus the continuous model is transformed into a discrete model. The resulting meshes are Lagrangian in the sense that they are based on material coordinates. In other words, the meshes are attached to each object and deform and travel as each object deforms or travels. In this way, LS-DYNA3D can accurately track material boundaries and interfaces. The elements of the discrete model are transformed into a computational model based on an interpolation function. This function is used to approximate the value of stress and deformation within the elements. The interpolation function used to describe deformation and stress in the solid brick elements of this model is quadratic in nature.

To more efficiently conduct computations, the discretized model is transformed into a normalized coordinate system. The same interpolation function is used to normalize the nodal coordinates as is used to approximate properties within the elements. Refer-

ence coordinates are used to map the discretized physical model into a reference element that is square or cube, by using the same basis function as that used to interpolate the displacement.

The problem domain is discretized into three-dimensional Lagrangian finite element meshes. In this case, the slipper material and rail material are discretized and meshed. This may be compared to an Eulerian mesh in which the slipper and rail materials pass through the mesh. The Eulerian mesh is fixed in space. The Lagrangian mesh travels with the deformed material.

The meshes used in this test consisted of eight-noded solid elements as shown in Figure 3.1. In the figure, the darkest portions are finer areas of the mesh. The meshes are finest in the areas of expected contact interaction. To capture the entire event, based on the dimensions of the model and the velocity of the slipper, a total time of 20 microseconds is simulated.

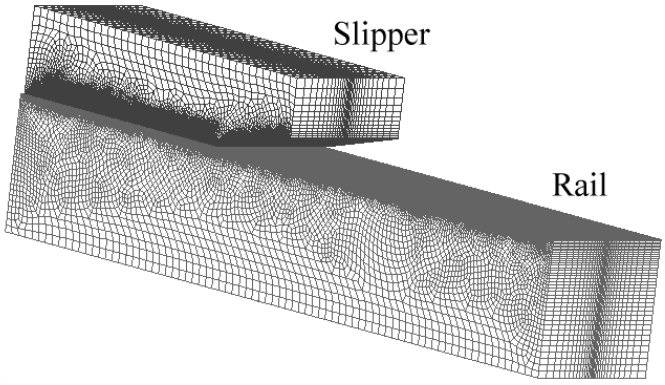

Figure 3.1 **Three-dimensional finite element Lagrangian mesh of the slipper and rail**

This three-dimensional Lagrangian mesh uses an elastic-plastic isotropic hardening constitutive model and a penalty method contact model for the gouging problem. In the elastic-plastic isotropic hardening constitutive model, the center of the yield surface is fixed, but the radius is a function of the plastic strain [57]. The contact model used in this simulation is an automatic single surface type of model that uses a penalty formulation to define contact. The penalty formulation searches the problem domain for regions where penetration of contact surfaces take place. Springs are then inserted into the penetrations.

These springs have a default stiffness that is a function of a penalty factor. The springs then push back the surfaces so that penetration does not occur [58]. This process would restrict the jetting we would expect to occur during gouging. Thus, the mesh is only allowed to simulate the final shape of gouging in the bulk material.

Rankine-Hugoniot relations are used in LS-DYNA3D to model states of the shock-waves that are generated upon impact. The energy equation relates density, pressure, and energy. This equation must be satisfied for all shocks. The equation of state defines all equilibrium states that can exist in a material and also relates density, pressure, and energy. It must also be satisfied. By eliminating energy from the equations, a relationship between pressure and density (i.e., volume) is obtained. This relation is called the Rankine-Hugoniot and it describes all pressure-compression states possible behind the shock. A bulk viscosity is also required to treat the shock waves and is commonly used in wave propagation codes [5].

Shockwaves are sharp discontinuities of pressure. They also generate large temperature variations that are typical of high energy impact situations. These characteristics present a special problem for the finite element solution method in LS-DYNA3D because discontinuities occur between element boundaries rather than as smooth distributions across elements. In LS-DYNA3D, artificial viscosity is introduced into the momentum equation to dissipate or smear the solution across a finite number of elements and allow calculation of shock wave fronts. This artificial viscosity is used to model irreversible effects associated with shocks and to prevent oscillations behind a shock [59].

Low pressure shocks are also handled in LS-DYNA3D through the normal solution algorithms. Since deviatoric stresses become important, the constitutive model and conservation equations become important in the solution of this condition. The volumetric response does not dominate the mechanical response of the material and a hydrodynamic treatment of low pressure shocks would be inaccurate.

3.1.2 Potential Difficulties. When the cells in the Lagrangian mesh undergo large distortions, they can end up twisting on themselves which results in negative volume. When this happens, elements become so distorted the contact simulation is erroneous and

the calculations fail. This happens when the cell boundaries cross one another, resulting in a computed negative volume. If cells are made extremely small to avoid this problem, the time step becomes extremely small to satisfy the stability condition.

The finite element method solves for the conservation of momentum in the form

$$\sigma_{ij.j} + \rho b_f = \rho \ddot{x}_i$$

that satisfies the traction boundary conditions

$$\sigma_{ij} n_i = \mathrm{t_i}(t)$$

where σ_{ij} is the Cauchy stress, ρ is the current density, b_f is the body force density, $\ddot{x}$ is the acceleration, t is the traction, and n_i is the outward normal to a boundary element with boundary ∂b.

To solve this, the finite element solution method performs an integration of the strain displacement matrix, B over the volume:

$$\int_{\mathcal{V}} B^t \sigma_{ij} d\mathcal{V}$$

The Lagrangian solution method to this integration uses the Jacobian, which is the ratio of the volume to the known original volume, $J = d\mathcal{V} \ / \ d\mathcal{V}_o$. This is done so the integration may be carried out using a known configuration, the reference volume $\mathcal{V}_o$.

$$\int_{\mathcal{V}} B^t \sigma_{ij} d\mathcal{V} = \int_{\mathcal{V}_o} B^t J \sigma_{ij} d\mathcal{V}_o$$

When elements become highly distorted, the $d\mathcal{V}$ part of the Jacobian becomes negative. This causes difficulties in the integration and the solution cannot continue. In the Lagrangian method, this will always be present as a potential difficulty. Therefore, the Lagrangian method is limited to problems with small deformations of the elements. One way to reduce large distortion of the elements, is to use smaller elements that would respond to the same loading with individually smaller deformations.

However, this dramatically increases the resources and time required to accomplish such a solution. Eventually there is a point at which making the elements smaller does not benefit the solution. Another option is to reduce the amount of deformation that occurs by making the material stiffer so the deformations under similar loads are smaller. This however, results in the obvious ramifications of changing the material properties. For example, a less accurate solution might result if a strain rate independent constitutive model is used to stiffen the material and reduce distortion of the elements.

3.1.3 Expected Advantages. The primary advantage of Lagrangian codes is their ability to accurately track material boundaries and interfaces. Since the grid is attached to the material, it deforms with the material. Another advantage of the Lagrangian mesh is that Lagrangian meshes have historically been used in finite elements more often than Eulerian meshes. Therefore, sophisticated material models have been developed in the Lagrangian coordinate system in addition to the equation of state models. Also, it is relatively easy to add mass to the model without adversely affecting the resources required to solve the problem. Nodal masses may be added to the slipper's finite element mesh to add mass and momentum to the impact without changing the dimensions or velocity of the slipper. In CTH, in order to match kinetic energy without adding mass to the model, the velocity must be changed. This change does not conserve momentum, however. By adding mass to the nodes on the top surface of the slipper to simulate the actual mass of the sled, the expected velocities of a real test sled may be used to match both kinetic energy and the momentum in the field.

3.1.4 Previously Used Models. The gouging problem has been investigated using the CTH hydrocode [27]. The finite volume hydrocode approach in CTH provides a physics based solution that allows the flow of material while maintaining load carrying properties. Hydrocodes vary from computational fluid dynamics (CFD) codes in that the fluids evaluated in CFD are not load carrying and thus there are no constitutive properties of fluid that are required for analysis.

Solids that undergo high energy impact and high strain rates usually plasticize and act like fluids, but still maintain both hydrostatic and deviatoric stress properties that

affect the solution. Thus, hydrocodes are useful in treating these types of problems. CTH uses a finite volume approach to solve high energy impact problems and it has become somewhat of a standard in this area of research [39].

To scale the problem so a solution can be obtained in a reasonable amount of time, the actual dimensions of the slipper and rail are reduced. Since there are extreme changes in material properties for high energy impact, a small time scale is considered ($\approx$ 10 to 20 μsecs). In order to properly scale the impact velocity so that the physical problem is accurately simulated, the mass should be scaled to create the same forces that the material would see in the actual physical problem domain.

However, any attempt to increase the density to compensate for the smaller dimensions of the problem inordinately slows down the finite volume Eulerian CTH solver. The maximum time step is a function of the wave speed which is inversely proportional to the density.

Thus, higher densities equate to extremely small time steps which slow down the solver dramatically. Artificially high densities also cause erroneous results because the equations of state are not well defined for these high densities. Instead, the velocity is changed to maintain the same kinetic energy as the actual sled and rail might see. This approach however, changes the actual momentum that would be found in the real sled and rail. In order to maintain the momentum, a different approach is required.

By using a finite element Lagrangian code, the effects of momentum change on the gouging problem can be captured. In the finite element approach, nodal masses may be added to the Lagrangian mesh in a finite element code with relative ease, and these masses do not cause the computational slow down seen in a finite volume approach because the density can remain the same. Nodal masses would not affect the wave speed as a change in density would, but still impart the momentum that is required for the problem.

3.1.5 Results and Visualization of the 3-D Impact Phenomenon. Since the finite element solution is dependent upon the size, shape, and type of elements used, we first look closely at the deformed elements. Elements that are distorted greatly, lose their accuracy.

The area of largest distortion for the mesh of elements is at the interaction between slipper and rail. In this investigation, we used solid elements with 8 nodes each.

The first case that is analyzed for the three-dimensional slipper on rail impact has a rail material with a yield strength (1.79 GPa) greater than the slipper (1 GPa). Figure 3.2 shows a closeup of the front left corner where the slipper and rail meet. We see a three-dimensional effect where the slipper mesh protrudes out along the edge of the rail side. We also see the distortion of the slipper mesh at the line of impact. Recall that the slipper has an initial velocity of 2 km/sec tangential velocity and 50 m/sec normal velocity with respect to the rail. The slipper impacts the rail evenly and penetrates into the rail a finite distance. Tangential velocity causes a strong interaction at the front of the slipper and rail contact. The slipper mesh in this view is distorted, but not so much that results should not be reasonable.

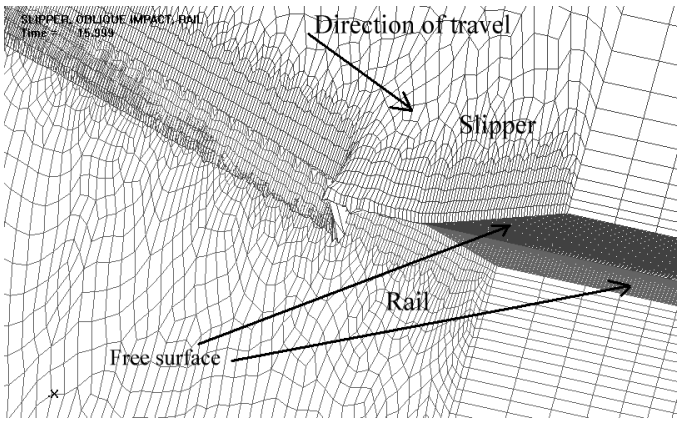

Figure 3.2 **Post solution mesh, slipper and rail interaction details**

We observe the slipper from the bottom in Figure 3.3, where the largest deformations occur. We note that the Lagrangian mesh has deformed greatly along the line of greatest energy transfer. The shape is just beginning to take on the characteristic front of a gouge, but gouging *interaction* has not yet begun to occur. This is due to the fact that the rail has not deformed to the extent that the slipper has. Gouging only occurs when there is a high pressure concentrated in a small area (i.e., a high pressure differential). In a three-dimensional mesh, this will only occur if there is an impact at a surface discontinuity or some type of plane strain scenario such as a discrete collision with respect to the shoe

and rail. Also, this interaction is prevented by the penalty contact algorithm used in LS-DYNA3D that does not allow penetration of one material into another.

The entire bottom of the slipper impacts at the same time. The load is distributed. A total mass of 227 kg has been distributed along the top surface of the slipper and is evenly distributed among the nodes of the finite element mesh. This results in a concentration of mass along the centerline of the slipper. When the slipper impacts at an angle, the momentum is imparted from the top of the slipper through the slipper structure to the rail in a flat plate type of impact. As the slipper moves tangentially, the front of the slipper deforms the greatest amount.

We also note that the three-dimensional deformations along the front line of impact (annotated as "Line of impact" in Figure 3.3) grow larger as one moves from the center line of the slipper to either of the edges. In essence, there is a plane strain condition along the center line of the slipper and rail, but this gradually changes to a plane stress condition at the edges. This results in little to no three-dimensional deformations in the center plane of the structure and maximum out of plane deformations at the edges.

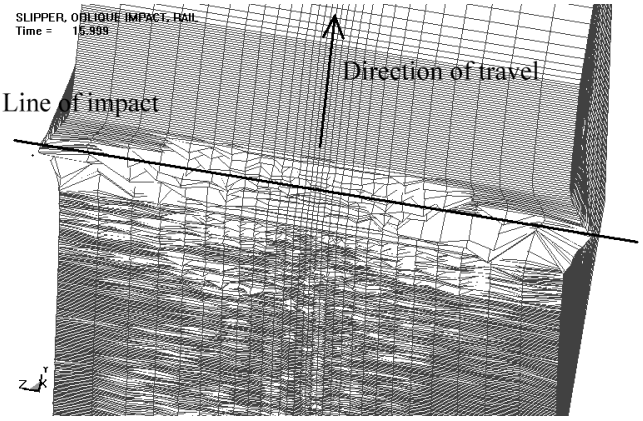

Figure 3.3 **Post solution mesh, slipper bottom details**

We have already noted the out-of-plane deformations that take place in the mesh, and particularly in the slipper along the front line of slipper-rail impact. We now look at the plastic strains (i.e., strains exceeding the proportional limit) that occur at 16 μsecs within the contact between slipper and rail. We know the gouging phenomena is driven

by the formation of plastic strain which allows the material to act like an inviscid fluid. Without this plasticity, gouging does not occur.

In Figure 3.4, plastic strain contours are plotted for rail and slipper. An isotropic plasticity model is used for both materials. For gouging to occur, we would expect regions of plasticity in both slipper and rail. This would allow for the interactions that are required for gouging to occur. However, the slipper appears to contain plastic areas, while the rail contains very little regions of plasticity. The effects on the slipper in reaction to the high energy oblique impact are more dramatic than the rail. To better understand why this is happening, we must investigate the volumetric response of the slipper and rail to the oblique impact. We now look at the pressure to do this.

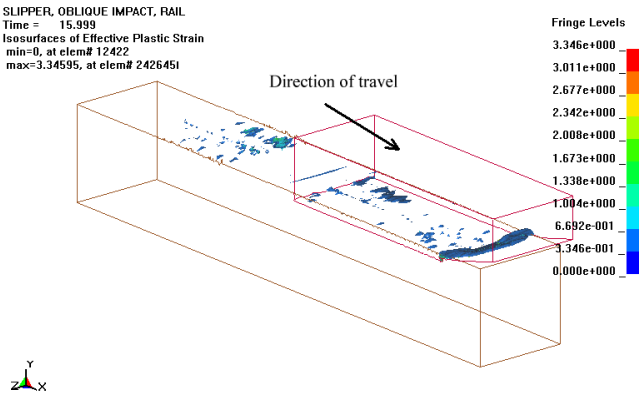

Figure 3.4 **Plastic strain contours**

We observe in Figure 3.5 the volumetric stress, a.k.a. pressure, contours in the slipper and rail structure for 16 μsecs. Units of stress in the figures are in 10^6 bars, which equates to 10^{11} GPa.

We do not see the pressure differentials we would expect in the rail which would lead to gouging. The higher pressure differentials in the slipper as compared to the rail are driven by the velocity of the slipper that are not transferred to the rail in the form of a volumetric response. This results in a layer of plasticity along the bottom of the slipper which allows for the deformations we see in the slipper. The impact does not create the same large area of plasticity in the rail that it does on the bottom of the slipper. The reason for this is the yield strength of the slipper is lower than the yield strength of the

rail, resulting in a higher limit for the onset of plasticity in the rail. This layer of plasticity on the slipper allows release of the momentum so that it never transfers to the rail in the form of high pressure differentials. The distributed impact of the slipper on the rail imparts a momentum that is allowed to propagate without the creation of a high pressure differential in the rail. Therefore, gouging interactions do not develop.

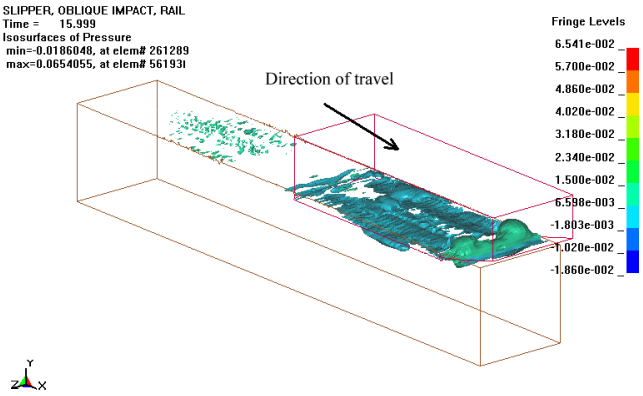

Figure 3.5 **Pressure contours**

More insight into the mechanics of the impact can be gained by evaluating the effective stress contours at 16 μsecs of Figures 3.6 through 3.8. The effective stress is a scalar quantity that includes both shear and normal stresses. Figure 3.6 shows the effective stress contours in both slipper and rail. Figure 3.7 shows the effective stress in the slipper and Figure 3.8 shows the effective stress in the rail only.

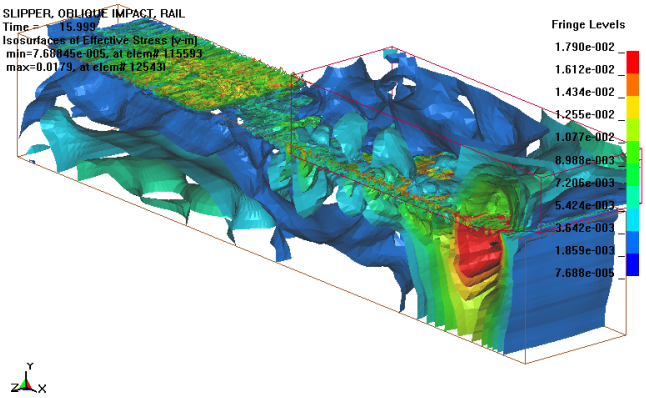

Figure 3.6 **Effective stress**

Effective stress contours extend beyond the pressure contours observed in Figure 3.5. Accounting for shear stress, the stresses that occur in the rail are greater than those in the slipper. However, a large pressure differential is never developed in the rail and a plastic region does not develop. As a result, the rail is deformed superficially, more in accordance with the definition of wear. Material is never sheared from the bulk material of the rail. Therefore, no gouge develops.

The Lagrangian mesh theoretically has the capability of modelling a shallow gouge-like shape even if it cannot model the interaction of materials expected in gouging. This gouge-like deformation never develops because a state of high pressure gradients never develop in the rail. The slipper effectively impacts and then skips intermittently along the rail forming shear and surface waves, but little else. This simulation models a common state of the slipper and rail structure during HHSTT runs, but not gouging.

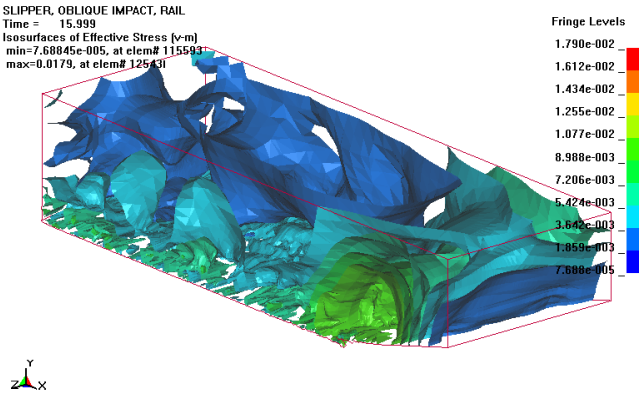

Figure 3.7 **Effective stress, slipper**

The situation shown here possibly models a common dynamic state of the slipper and rail structure during HHSTT runs when the energy of impact is not sufficient to cause transfer of inertia and momentum in the form of high pressure waves from the slipper to the rail. Without these large pressure differentials, a region of plasticity will not form in the rail that would eventually lead to mutual hydrostatic fluid-like deformations and velocity and geometric instabilities. These instabilities are needed to develop the rotational velocities at the rail and slipper interface that form the interaction of materials known as jetting. Jetting is the primary cause of hypervelocity gouging.

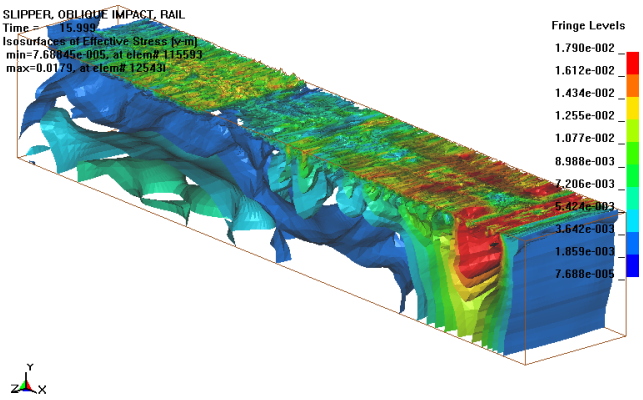

Figure 3.8 **Effective stress, rail**

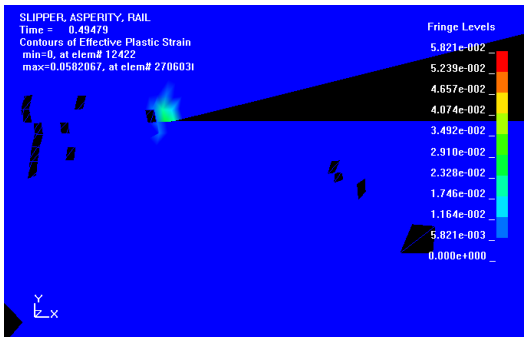

(a) **Plastic strain at impact, enlarged view of leading edge of slipper impacting rail.**

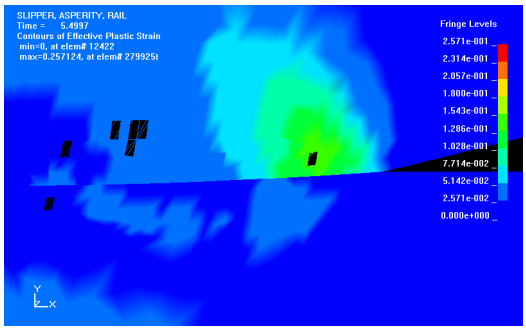

(b) **Plastic strain at 5.5 μsecs, enlarged view of leading edge of slipper impacting rail.**

Figure 3.9 **Plastic strain at midplane, plane strain condition.**

The only area where a plane strain condition occurs is in the centerline cross sectional plane. This area is investigated to determine the potential for gouging to occur in the three-dimensional model. Figures 3.9 through 3.11 show the midplane (plane strain condition) of the three-dimensional model at impact and at 5.5 μsecs after impact. The figures show contours of plastic strain, pressure, and shear stress in the midplane for the case in which the slipper has a lower yield strength than the slipper.

Here is one interpretation of what the plots at midplane show. At the leading edge of oblique impact, a plastic zone develops and is concentrated in the leading edge area in the "softer" slipper. This zone of plasticity continues to grow in the slipper primarily due to the increasing pressure gradients that occur in that region of the slipper. There is high

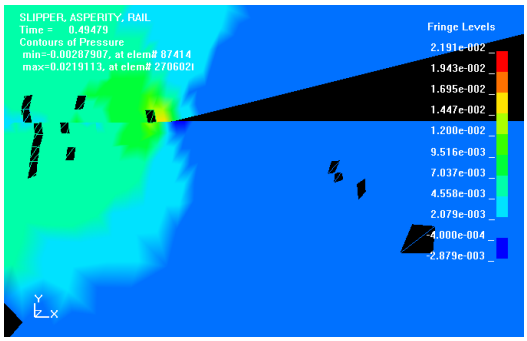

(a) **Pressure at impact, enlarged view of leading edge of slipper impacting rail.**

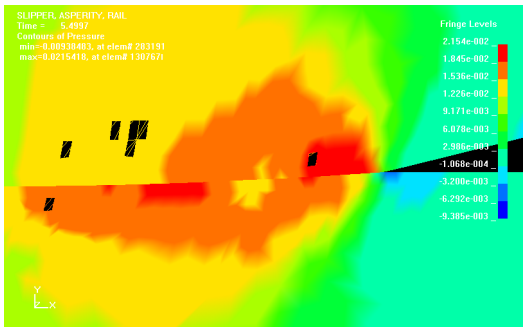

(b) **Pressure at 5.5 μsecs, enlarged view of leading edge of slipper impacting rail.**

Figure 3.10 **Pressure at midplane, plane strain condition.**

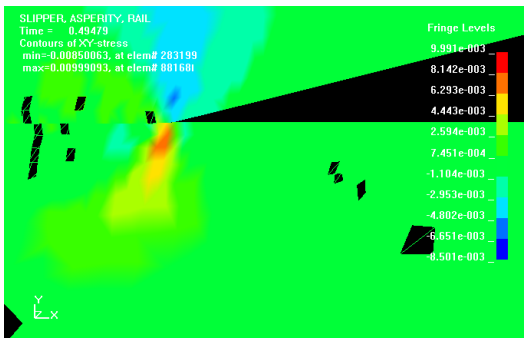

(a) **Shear stress at impact, enlarged view of leading edge of slipper impacting rail.**

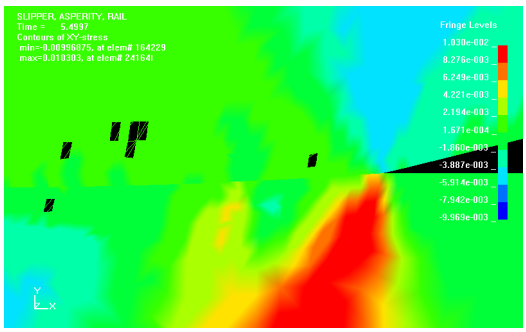

(b) **Shear stress at 5.5 μsecs, enlarged view of leading edge of slipper impacting rail.**

Figure 3.11 **Shear stress at midplane, plane strain condition.**

pressure in the rail, but it is not matched in location with the slipper high pressure core and the plastic zone is not growing in the rail. This prevents formation of gouging because there can be no interaction of hydrodynamic flow materials.

The deformations are only minimally plastic and the rail material responds elastically and recovers, for the most part, the deformations it experienced at impact. the shear plots are promising, but without the plasticized material that is allowed to flow hydrodynamically, the conditions conducive top gouging will not occur. In this case, we do not expect the material jetting interaction, but enough of an interaction between slipper and

rail materials to create plastic deformations that resemble a gouge. In this case, the plastic deformations remain small and gouging does not form.

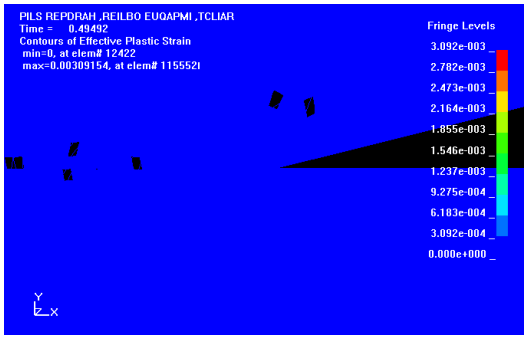

(a) **Plastic strain at impact, enlarged view of leading edge of slipper impacting rail.**

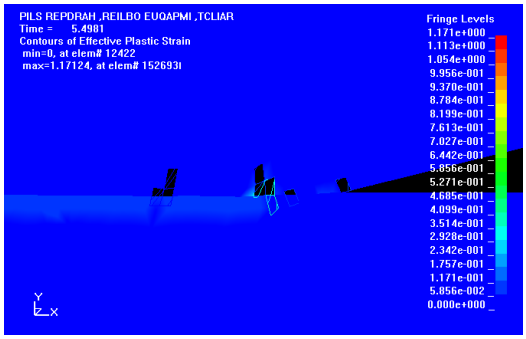

(b) **Plastic strain at 5.5 μsecs, enlarged view of leading edge of slipper impacting rail.**

Figure 3.12 **Plastic strain at midplane, plane strain condition for slipper with higher yield strength.**

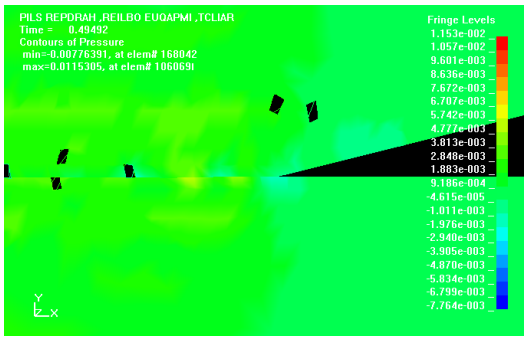

(a) **Pressure at impact, enlarged view of leading edge of slipper impacting rail.**

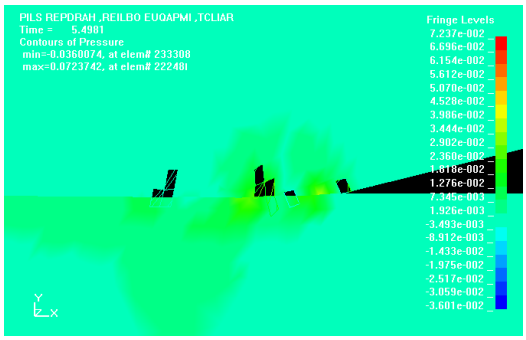

(b) **Pressure at 5.5 μsecs, enlarged view of leading edge of slipper impacting rail.**

Figure 3.13 **Pressure at midplane, plane strain condition for slipper with higher yield strength.**

The next case considered varies the yield strength of the materials so that the slipper is now made of the higher strength material. The rail material now has a lower yield strength (1 GPa) than the slipper (1.79 GPa). Figures 3.12 through 3.14 show the midplane (plane strain condition) of the three-dimensional model at impact and at 5.5 μsecs after impact for the higher strength slipper model. The figures show contours of plastic strain,

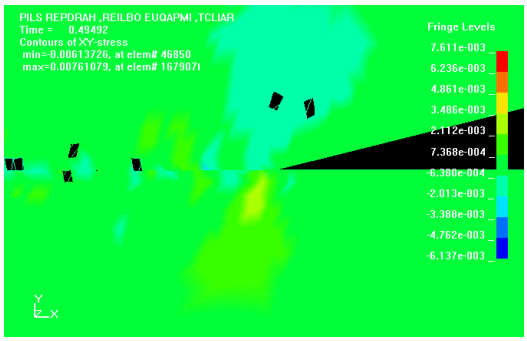

(a) **Shear stress at impact, enlarged view of leading edge of slipper impacting rail.**

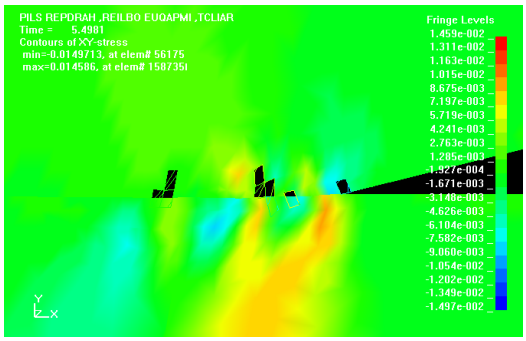

(b) **Shear stress at 5.5 μsecs, enlarged view of leading edge of slipper impacting rail.**

Figure 3.14 **Shear stress at midplane, plane strain condition for slipper with higher yield strength.**

pressure, and shear stress in the midplane. Overall, similar results were obtained as for the higher strength slipper, but the results at midplane were a little different.

For this case, plasticity never develops in the slipper upon impact with the rail. Some plasticity zones form in the rail and eventually in the slipper also (within an extremely localized area), but regions similar to what is seen for the lower strength slipper never materialize. The pressure response remains relatively low and the shear response is not as dramatic. The overall responses are less localized.

In the real case, the slipper would undergo extremely high temperatures that put it under a state of thermal softening, which increases the likelihood of plastic formation and gives the slipper an effective yield strength that is lower than the room temperature strength. Thus, this last case in unrealistic in terms of the test track runs. However, it may provide a state that is desirable for mitigating gouging. If the thermal effects of the high speed test run can be minimized, then perhaps gouging can be prevented all together. For instance, a high strength ceramic or low conductivity composite slipper might be appropriate.

3.1.6 Analysis. It has not been proven that the Lagrangian mesh in LS-DYNA3D can accurately model gouging phenomena. The mesh deforms, but not enough to show true gouging. Another problem in accurately portraying gouging phenomena is the nature of the

impact that is modelled. The three-dimensional impact distributes the impact loading and does not allow for the localized area of high pressure differentials that leads to plasticity in both the slipper and rail. Plasticity is required for gouging to occur.

Instead of gouging, what occurs in the three-dimensional Lagrangian slipper-rail model is "scoring" or "raking" of the rail by the slipper. In the LS-DYNA3D run, the slipper impacts the rail at an oblique angle, simulating a flat vibratory impact with no pitch or yaw components. This distributes the impact along the entire surfaces of the bottom of the slipper and the top of the rail. Momentum and energy is transferred from the slipper to the rail, but it is also allowed to dissipate without creating any regions of high pressure gradients. Without a localized area of high pressure gradients, plasticity does not form in the rail and no interaction is allowed to occur along the shear planes between the slipper and rail. Instead, the slipper continues to drive into the rail and slide as it rides on portions of plasticity developed from the initial impact. The phenomenon becomes a scenario of wear.

Tangential motion of the slipper and plasticity force the greatest deformation to occur at the front end of the slipper in contact with the "stiffer" rail material. In addition, nodal masses concentrated along the center line of the slipper result in a plane strain condition at the center line which ends up absorbing the majority of the impact energy. The slipper reacts with lateral motion that finds its way to the free edges of the slipper where a state of plane stress exists. This three-dimensional effect leads to the maximum deformations of the slipper along the outside edges of the rail.

In order to accurately model gouging, an oblique and asymmetric impact must be imparted to the slipper. This would create an localized region of high pressure gradients in the slipper *and* rail so that plasticity forms in both structures and allows the interaction required for gouging.

Also, the contact model between sliding surfaces is important. In this investigation, the penalty contact algorithm did not allow gouging because it does not allow materials to mix. This contributes to the modeling conditions in which the slipper "skips" along the rail rather than gouges.

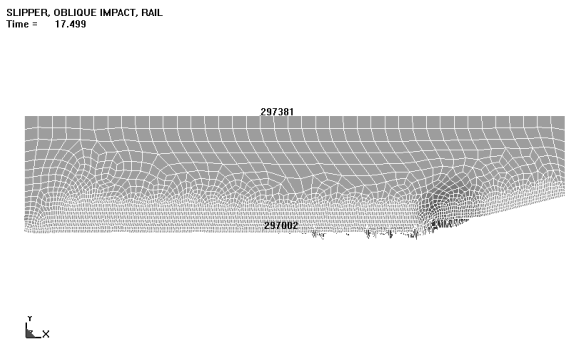

Figure 3.15 **Side view of slipper, selected nodes**

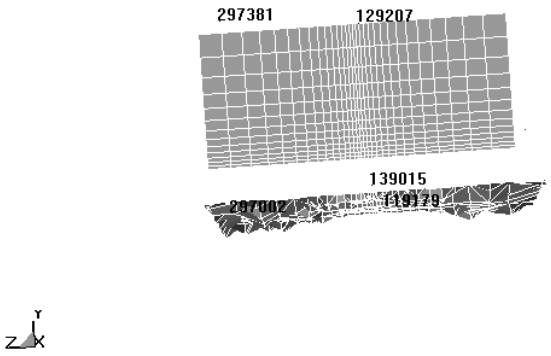

Figure 3.16 **Front view of slipper, selected nodes**

To better observe this, refer to Figures 3.15 to 3.18. As shown in Figures 3.15 and 3.16, five different nodes are chosen on the slipper for their position with respect to the rail and with respect to the centerline. The vertical displacement of the nodes with respect to time is plotted in Figure 3.17 and the vertical velocity of the nodes with respect to time is plotted in Figure 3.18. As the slipper drives down into the rail due to the initial vertical velocity, the combined response of the plasticized material of the slipper against the still elastic material of the rail results in the vertical velocity increasing and decreasing. This effect is more pronounced in nodes nearest the contact between rail and slipper. The nodes furthest away from this interaction maintain a constant vertical velocity. This is likely the result of the contact model being used. The spring constants preventing penetration of the slipper into the rail react in the method depicted. Thus, careful consideration of the contact model is required.

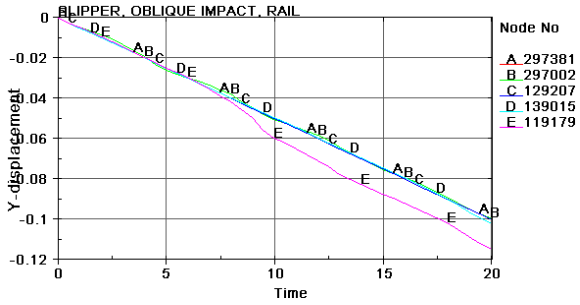

Figure 3.17 **History of displacement of selected nodes**

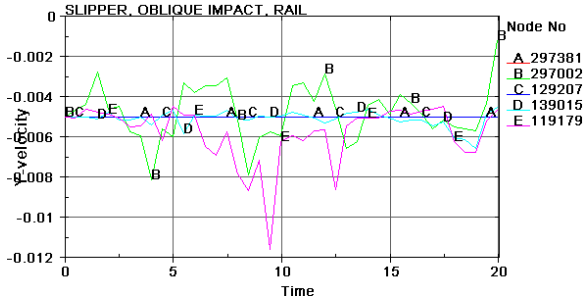

Figure 3.18 **History of velocity of selected nodes**

3.1.7 Conclusions. This investigation shows that an Eulerian mesh may be the best type of mesh for accurately modelling gouging phenomena. Although a gouge-like deformation occurred in this model along the edges of the rail, an interaction of slipper and rail materials was not modelled because the contact algorithm does not allow this. This study also confirmed that use of a two-dimensional plane strain model for studying hypervelocity gouging is a valid conservative estimate of the real world scenario. Finally, it provided insight into three-dimensional effects of a flat slipper-rail impact in which there is no restricted plane strain condition.

3.2 Comparison of the Finite Volume Eulerian Method to Finite Element Lagrangian Methods

To support the decision making process used to determine what tools will be used in the research, a direct comparison of the capabilities of available computational tools to model hypervelocity gouging is performed. The following capabilities and considerations are explored for each computational tool:

1. Mesh capabilities and their ability to capture the large deformations and high strain rates of the gouging phenomenon without excessive distortion.
2. Availability of equation of state and constitutive model capabilities.
3. Representation of failure and availability of failure models.
4. Ability of the solution methods and material models to accurately model high energy impact phenomena such as normal shock waves.
5. Availability of models for heat flux and heat flow due to deformation.
6. Availability of contact and material mixing algorithms.
7. Capability to model conditions (e.g., plastic zone, shear bands, and high pressure core) that lead to gouging.
8. Capability to model interacting material "jets" and ejecta associated with gouging.
9. Availability of the code on readily accessible high performance computational platforms.
10. Availability of technical support.
11. Previous work done on similar problems.

The computational tools explored and analyzed in this study are the Lagrangian finite element codes ABAQUS and LS-DYNA3D, and the Eulerian finite volume hydrocode CTH. The capabilities in the numbered list above are used as criteria for determining which portions of each code are useful for subsequent research. An asperity impact model is used to explore and compare the capabilities of the codes and judge them against the listed criteria.

The study begins with CTH as a baseline since it has been used extensively in the literature for studying hypervelocity gouging. The study then compares ABAQUS and LS-DYNA3D in relation to CTH and each other. Conclusions based on the listed criteria are made regarding the capabilities of each code and their utility for subsequent research.

3.2.1 CTH, An Eulerian Finite Volume Study. When Dr. David Laird used CTH for his numerical investigation of gouging, heat transfer capabilities were not available. One

primary purpose of this study is to investigate the heat transfer analysis capability of CTH. CTH is available on the Hydra and Aspen Beowulf-type systems at AFIT and the ES-45 Compaq systems at the ASC MSRC. In addition, a 64-bit version of CTH is available on the Tahoe Beowulf-type system at AFIT.

The gouging problem has been investigated using the CTH hydrocode [27]. The finite volume hydrocode approach in CTH provides a physics based solution that allows the flow of material while maintaining load carrying properties [39]. Hydrocodes vary from computational fluid dynamics (CFD) codes in that the fluids evaluated in CFD are not load carrying and thus there are no constitutive properties of the fluid that are required for analysis.

Solids that undergo high energy impact and high strain rates can become plastic in some areas and act as hydrostatic fluids, yet still maintain deviatoric stress properties. Hydrocodes are useful in treating these types of problems. CTH uses a finite volume algorithm to solve shock physics governing equations for high energy impact problems [39].

CTH uses a two-step, second-order accurate Eulerian solution algorithm to solve the equations of mass, momentum, and energy conservation. CTH contains constitutive models that include strain and strain-rate effects, and is well suited for problems pertaining to large distortions such as those considering high energy impact. Models are included for strength, fracture, porous materials, high explosives, and a variety of boundary conditions. Rate-dependent models for material strength formulations of Johnson-Cook, Zerilli-Armstrong, and Steinberg-Guinan-Lund are standard options.

CTH contains two major equation of state packages that can be used to investigate problems pertaining to shock propagation, melting, and vaporization, such as those that occur in hypervelocity impact. These are the Analytic Equation of State (ANEOS), and SNL-SESAME, a tabular EOS. The analytic package ANEOS includes Mie-Grneisen, Jones-Wilkins-Lee, and ideal gas law equations of state. The SNL-SESAME tabular data is based on experimental data and may include multiple liquid-vapor, liquid-solid, and solid-solid transitions.

3.2.1.1 Sample Problems. CTH has been used extensively in the published literature to model hypervelocity gouging. Thus, it is expected that CTH would contain all the capabilities needed to accurately describe hypervelocity gouging and its characteristics. The main question that needs to be answered in this investigation is whether CTH has the heat conduction analysis capabilities necessary to model heat flow in the hypervelocity gouging problem. Previous numerical analyses have not considered this. Therefore, the sample problems chosen in this case are gouging analysis models with the addition of running a simple heat conduction problem to verify that CTH has the capability to calculate heat flow in the model.

The primary means to verify that the CTH model accurately describes hypervelocity gouging is comparison of the results to test track observations. Gouging has been shown to occur at speeds greater than 1.5 km/sec horizontal slipper velocity at the HHSTT. In the CTH analysis, a horizontal slipper velocity of 2 km/sec is used. The vertical slipper velocity is estimated to occur at 1-2 m/sec on the HHSTT, but a vertical velocity of 50 m/sec is used to maintain the same kinetic energy between the CTH model and the real world sled of 227 kg mass. The assumption of kinetic energy similitude will be reconsidered in the model improvement and dimensional analysis section.

The problem is scaled by reducing the actual dimensions of the slipper and rail so that a higher resolution may be used to study the gouging phenomenon. Since there are extreme changes in material properties for high energy impact, a small time scale is considered ($\approx$ 10 - 20 μsecs). In order to properly scale the impact velocity so that the physical problem is accurately simulated, the mass should be scaled to create the same forces that the material would see in the actual test sled.

However, any attempt to increase the density causes inordinate reductions in speed of the calculation and increases in memory requirements for the problem and may cause erroneous results. These are due to the stability requirement that a wave not traverse more than one computational cell in a single time step. The maximum time step is a function of the wave speed, which is inversely proportional to the density. In addition, material models are not available for such inordinately large densities and these artificially large densities may adversely effect the solution.

Thus, higher densities equate to extremely small time steps which slow down the solver dramatically. Additionally, artificially high densities may cause erroneous results because the equations of state and constitutive models are not well defined in CTH for these high densities. Instead, the velocity is changed to maintain the same kinetic energy that the actual sled and rail might see.

Three cases are considered. The first is a "standard" vibratory impact case in which the kinetic energy is matched to a real test sled. The second is a simple heat conduction problem to explore the heat conduction modeling capabilities of CTH, and the third case is an asperity impact. The asperity impact gouge initiator is also run for comparison to the finite element codes under consideration.

3.2.1.2 Results and Analysis. Figure 3.19 shows hypervelocity gouging caused by a sample vibratory impact of 2 km/sec horizontal and 50 m/s vertical velocity. The Eulerian mesh and finite volume method of CTH readily capture gouging phenomenon such as "jetting" and large plastic strains.

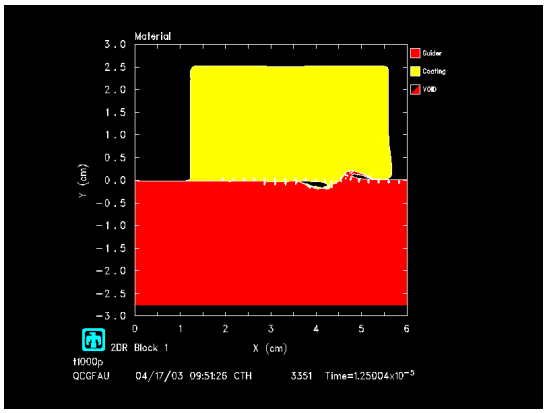

(a) **Slipper and rail materials undergoing hypervelocity gouging at 12.5 μsec.**

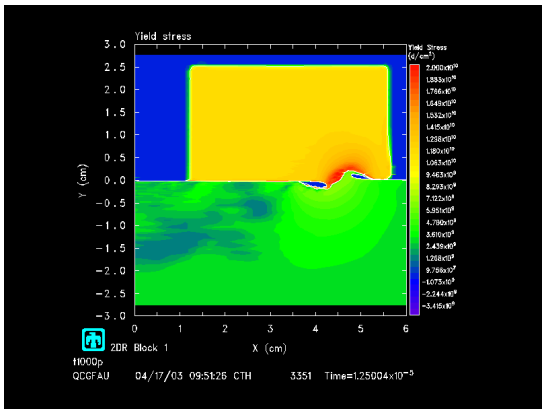

(b) **Contour plot of yield strength for slipper and rail undergoing hypervelocity gouging at 12.5 μsec.**

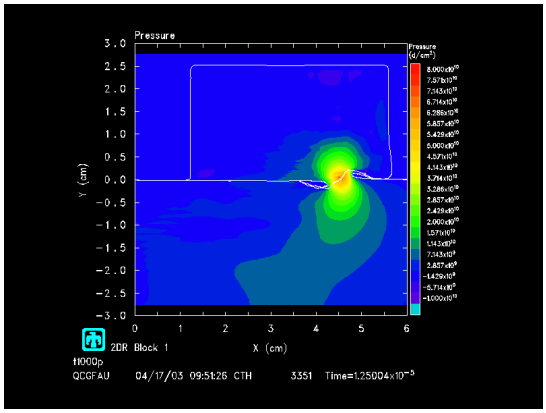

(c) **Contour plot of pressure for slipper and rail undergoing hypervelocity gouging at 12.5 μsec.**

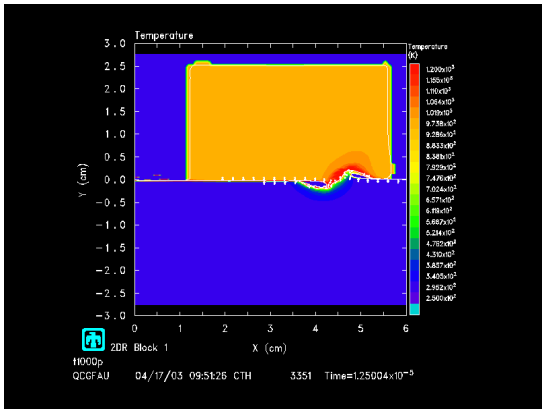

(d) **Contour plot of temperature for slipper and rail undergoing hypervelocity gouging at 12.5 μsec.**

Figure 3.19 **Plots of gouging phenomena at 12.5 μsec.**

The following characteristics of hypervelocity gouging appear in both the HHSTT runs and CTH simulation shown in Figure 3.19.

- The characteristic tear-drop shaped permanent deformation of gouging under plane strain conditions.
- An interaction of slipper and rail materials characterized by large deformations and material "jetting" which leaves a thin layer of the slipper material on the rail gouge and vice versa
- A thin region of plastic material between the slipper and rail materials forms after impact.
- Large temperature changes in the area of large plastic deformation commensurate with equation of state calculations for changes in pressure and volume.
- Propagation of combined stress waves in the slipper and rail corresponding to regions of high pressure and large shear stress.
- Formation of a "hump" in the plasticized region of rail material immediately after impact that eventually leads to gouging.
- Shock hardening of the rail and slipper materials.

Materials were modeled using the tabular equation of state package in CTH for slipper and rail materials of VascoMax 300 and 1080 steel, respectively. The Johnson-Cook constitutive model for the rail used the model for Iron with a modified yield strength to simulate 1080 steel. The Steinberg-Guinan-Lund constitutive model was used to describe the plastic behavior of the slipper materials under high strain rate deformation.

In Figure 3.20 an instantaneous thermal distribution is applied to the rail material and CTH calculates propagation of the resulting stress wave. This was accomplished by David Laird [60] as part of his work. These results illustrate the capability of the CTH equation of state models to track propagation of pressure and volume changes due to large thermal gradients. This capability will be extremely important if thermal gradient profiles are applied to simulate high stagnation temperatures behind oblique shocks in air and the heating interaction of friction at the slipper and rail interface.

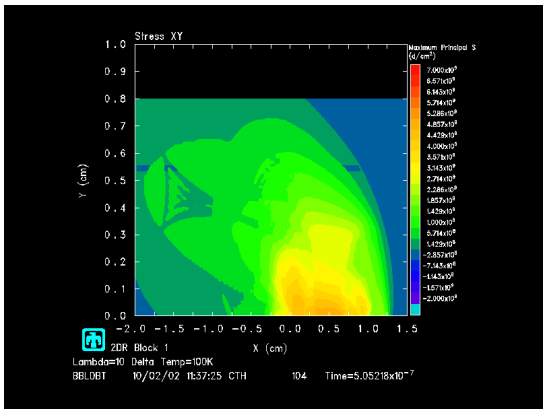

(a) **Contour plot of thermal stress at 0.5 μsec.**

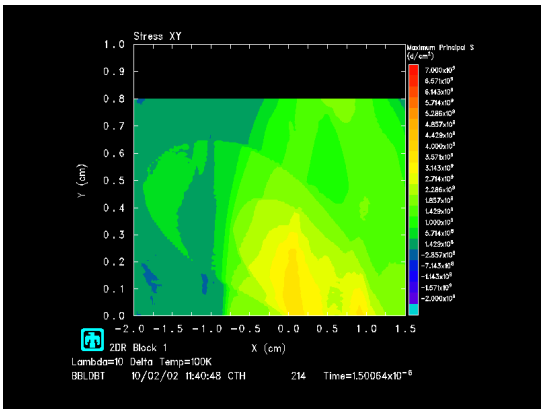

(b) **Contour plot of thermal stress at 1.5 μsec.**

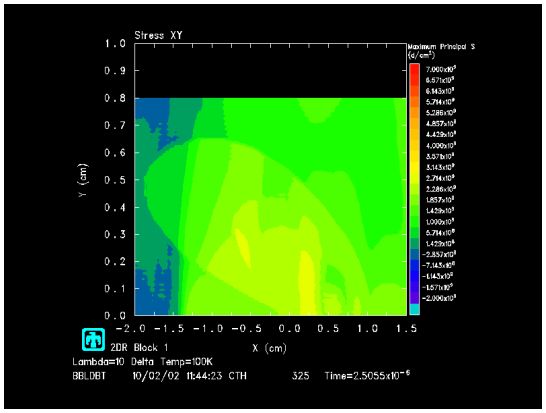

(c) **Contour plot of thermal stress at 2.5 μsec.**

Figure 3.20 **Plots of thermal stress at 0.5, 1.5, and 2.5 μsec.**

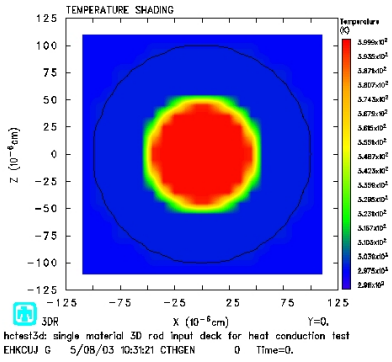

(a) **Heat conduction example at initial conditions.**

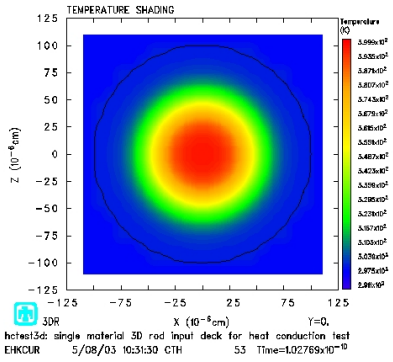

(b) **Heat conduction example at** $1x10^{-10}$ **seconds.**

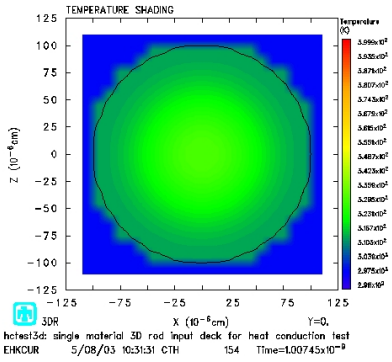

(c) **Heat conduction example at** $1x10^{-9}$ **seconds.**

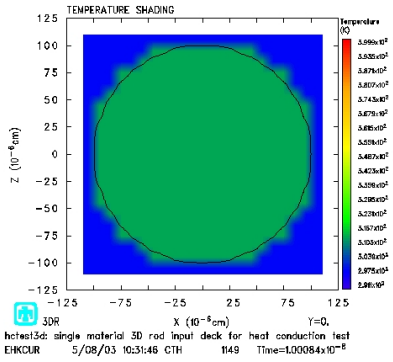

(d) **Heat conduction example at** $1x10^{-8}$ **seconds.**

Figure 3.21 **Plots of heat conduction solution of cross-section of three dimensional rod with heat source.**

CTH contains an explicit heat conduction solution method that can calculate the adiabatic diffusion of heat in a structure. Adiabatic diffusion is the transfer of heat from heat generation due to deformation that is not supplied from external boundaries of the system. See Figure 3.21 for the results in the cross section of a three-dimensional cylinder containing a heat source. At first, the heat propagates in a fashion that one would expect of a one-dimensional solution, up to $1x10^{-10}$ seconds. After this time however, edge effects come into play. This example illustrates the capability of the explicit heat conduction algorithm in CTH to calculate the diffusion of heat and is comparable to results from a Monte Carlo solution method for the heat conduction equation.

Results for an asperity impact gouge initiator are shown in Figures 3.22 through 3.28. The initial state of the model is shown in Figure 3.22. Starting with plots of the material deformations at 1, 2.5, and 5 microseconds, contour plots of effective stress, shear stress, and plastic strain for each material are shown. The same plots are provided for the asperity initiator problem for the finite element codes. This specific case used an asperity strength of 3.6 GPa, a rail strength of 0.7 GPa, and a slipper material strength of 1.447 GPa The Johnson-Cook constitutive model was used for the rail and asperity materials and the Steinberg-Guinan-Lund model for the slipper material. A horizontal speed of 2.4 km/s was used to impact the asperity of 0.1 cm diameter.

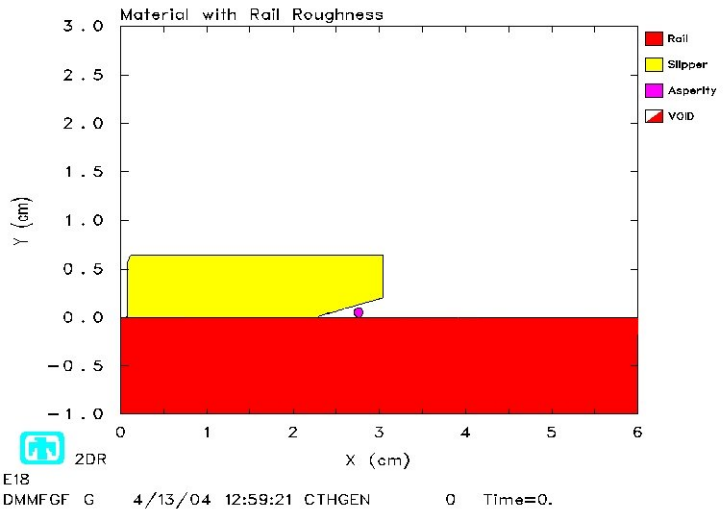

Figure 3.22 **Asperity impact case for comparison to ABAQUS and LS-DYNA3D.**

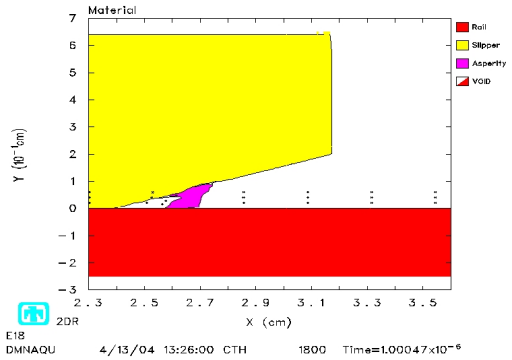

(a) **Material plot of asperity impact at 1 μsec.**

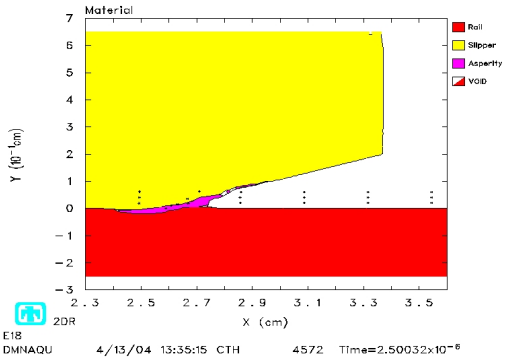

(b) **Material plot of asperity impact at 2.5 μsec.**

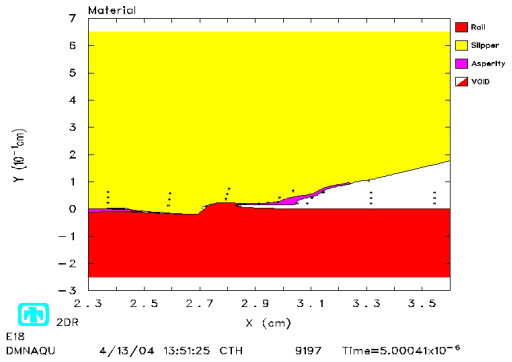

(c) **Material plot of asperity impact at 5 μsec.**

Figure 3.23 **CTH material plots of asperity impact.**

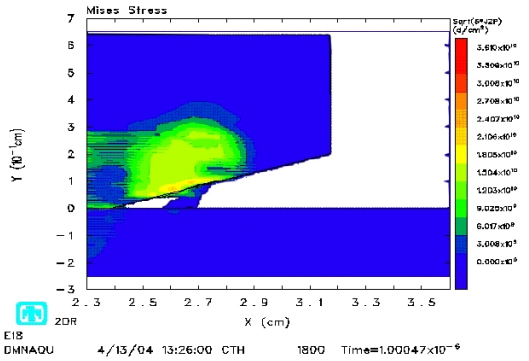

(a) **Mises stress plot of asperity impact at 1 μsec.**

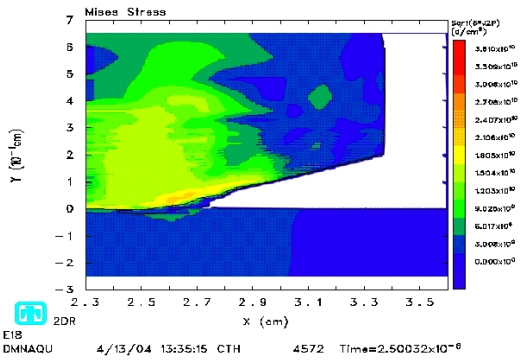

(b) **Mises stress plot of asperity impact at 2.5 μsec.**

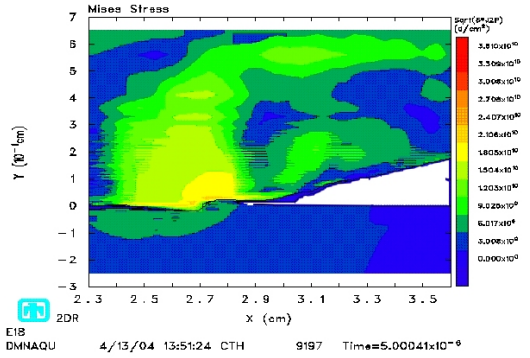

(c) **Mises stress plot of asperity impact at 5 μsec.**

Figure 3.24 **CTH Mises stress plots of asperity impact.**

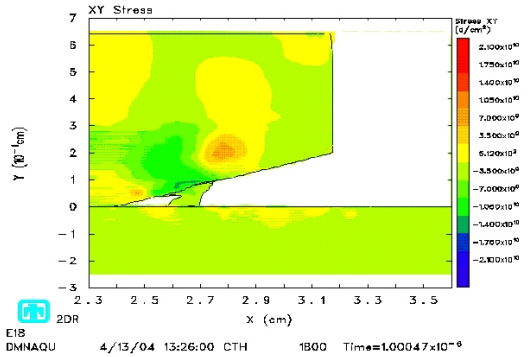

(a) **Shear stress plot of asperity impact at 1 μsec.**

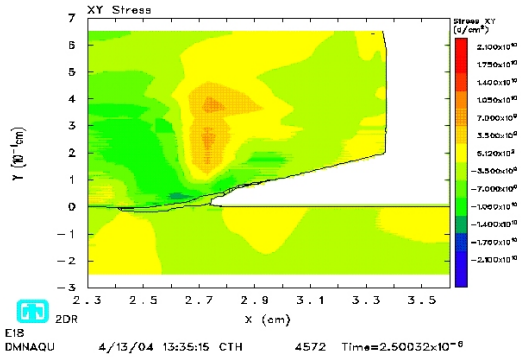

(b) **Shear stress plot of asperity impact at 2.5 μsec.**

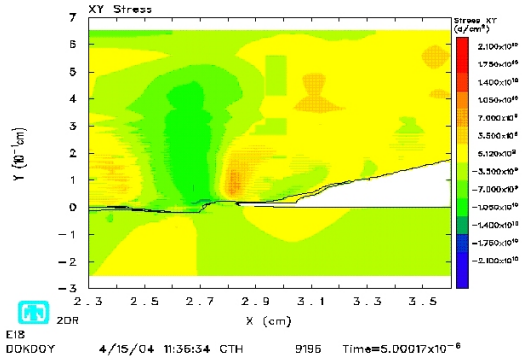

(c) **Shear stress plot of asperity impact at 5 μsec.**

Figure 3.25 **CTH Shear stress plots of asperity impact.**

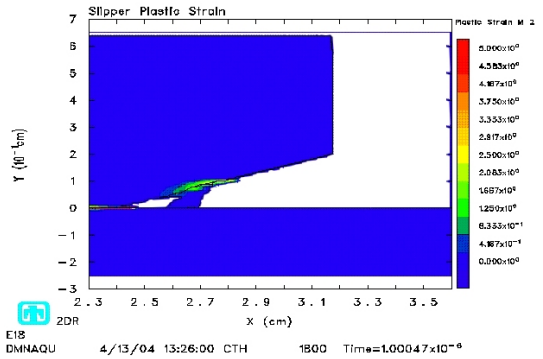

(a) **Rail plastic strain plot of asperity impact at 1 μsec.**

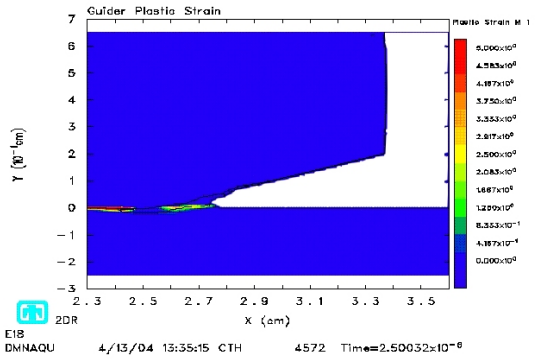

(b) **Rail plastic strain plot of asperity impact at 2.5 μsec.**

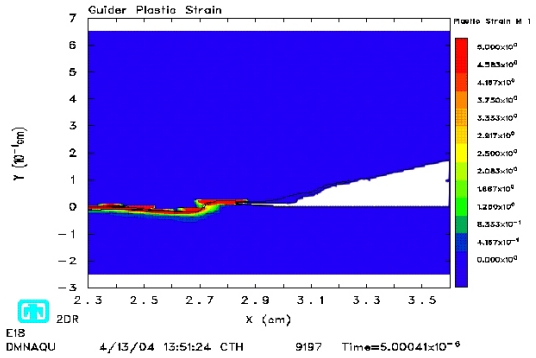

(c) **Rail plastic strain plot of asperity impact at 5 μsec.**

Figure 3.26 **CTH rail material plastic strain plots of asperity impact.**

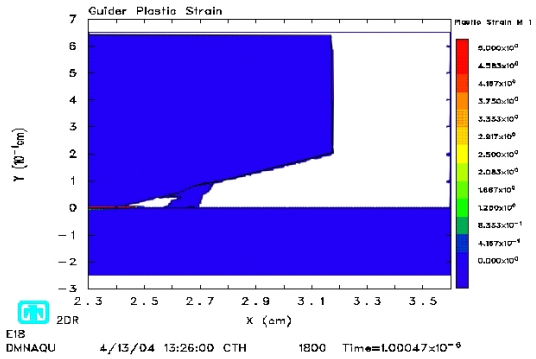

(a) **Slipper plastic strain plot of asperity impact at 1 μsec.**

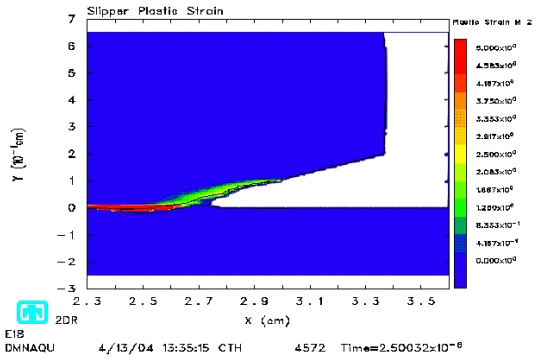

(b) **Slipper plastic strain plot of asperity impact at 2.5 μsec.**

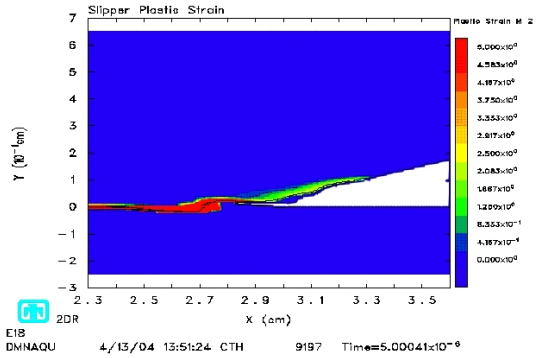

(c) **Slipper plastic strain plot of asperity impact at 5 μsec.**

Figure 3.27 **CTH slipper material plastic strain plots of asperity impact.**

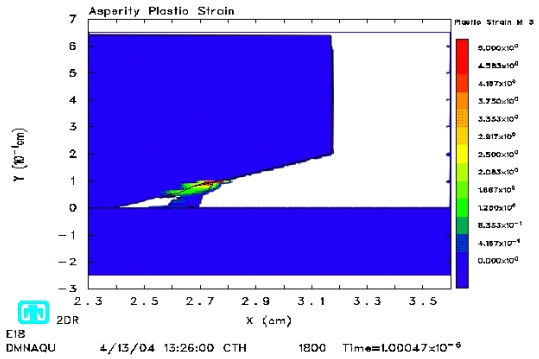

(a) **Asperity plastic strain plot of asperity impact at 1 μsec.**

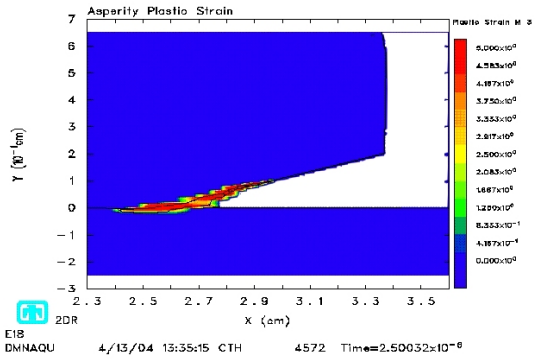

(b) **Asperity plastic strain plot of asperity impact at 2.5 μsec.**

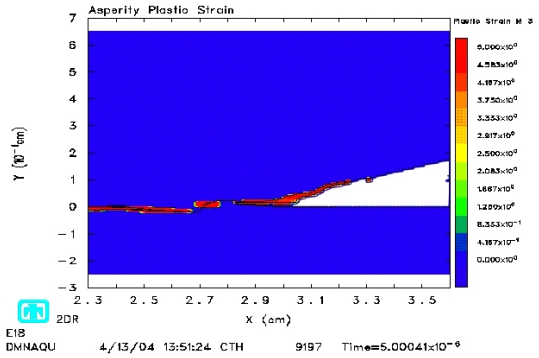

(c) **Asperity plastic strain plot of asperity impact at 5 μsec.**

Figure 3.28 **CTH asperity material plastic strain plots of asperity impact.**

One of the main differences between the finite volume and finite element code sample problems is in the constitutive model. The asperity yield strength was doubled from the original yield strength of the rail material in order to reduce the deformation of the Lagrangian asperity mesh in the finite element code simulation. The combination of increased yield strength and rate independent constitutive model prevented negative volume integration caused by excessive deformations of asperity elements in the finite element codes. This allowed the finite element solutions to propagate further in time so that a direct comparison with the CTH results could be made for this case. This will be further explained in the section that discusses results for the ABAQUS and LS-DYNA3D Lagrangian finite element solutions.

Plastic strain in the CTH solution is highly localized. the asperity is subject to large distortions immediately upon impact. Because of these highly localized distortions, the asperity deforms rather than causes a reaction on the rail. This prevents a shockwave from forming in the rail due to inertia effects that would otherwise have been transferred to the rail if the asperity had maintained its strength. the strength of the shockwave in the slipper that happens as a reaction to the impact with the asperity is approximately 1 GPa. This baseline will be used for comparison to the ABAQUS and LS-DYNA3D finite element solutions.

3.2.1.3 Comparison to Criteria. Based on the results of this investigation of CTH, the code is now compared against the criteria on page 3-22.

1. CTH's Eulerian mesh with material flowing through the mesh and mixed material boundary definitions has proven it can model the large deformations of hypervelocity gouging without adversely affecting the solution.
2. CTH contains a wide variety of comprehensive constitutive and equation of state models, including tabular equation of state data to accurately model the material response.
3. The Johnson-Cook fracture model only predicts failure involving shear deformation, since it makes the classical assumption that plastic strains are deviatoric. In the CTH implementation, failure due to excessive hydrostatic tensile stress is also modeled.

The Bammann-Chiesa-Johnson (BCJ) viscoplastic/damage model is also available. This model has been implemented in CTH using a newly-developed, standardized material model interface. The model describes the deviatoric elastic-viscoplastic response of ductile metals and cumulative damage resulting from void growth. A recent addition is the Pressure Shear Damage model which can be used to represent materials that exhibit pressure dependent strength properties.

4. The finite volume solution algorithm coupled with the extensive material models and fluids approach of the CTH solution algorithm define a shock physics solution that accurately models the high energy impact characteristics of the hypervelocity gouging problem.

5. CTH contains an explicit heat conduction algorithm that couples heat flow calculations with material deformation. Preliminary studies of hypervelocity gouging with heat conduction indicate the ability to use CTH to define the effects of heat diffusion on the phenomenon.

6. CTH contains a variety of means to model friction and material contact. A High Resolution Interface Tracking (HRIT) algorithm is currently available (for two-dimensional geometries only) in CTH. Unfortunately, the HRIT algorithm is not readily extendable to three dimensions. Youngs' method has been adapted for CTH for a three-dimensional interface reconstruction algorithm comparable in capabilities to the HRIT. The Sandia Modified Youngs Reconstruction Algorithm (S-MYRA) is the contact algorithm used in CTH for a three-dimensional contact algorithm capability.

7. Based on the results in this investigation and in published research, CTH has proven the capability to model the various characteristics that lead to gouging.

8. Based on the results in this investigation and in published research, CTH has proven the capability to model the interacting material "jets" and ejecta associated with gouging.

9. The explicit heat conduction capable version of CTH (CTH 2003) is currently available on the Hydra, Aspen, and Tahoe clusters at AFIT.

10. Technical experts are available for specific user problems, but their availability is limited.
11. CTH has been used extensively and almost exclusively in the published literature to model hypervelocity gouging.

3.2.1.4 Conclusions. This investigation of CTH's capabilities to model hypervelocity gouging, thermal profiles with associated stresses through the equation of state models, and heat conduction was successful. It appears that CTH has all the capabilities one would need for a proper numerical investigation of the hypervelocity gouging problem and the effects of heat transfer on the solution. The primary disadvantage of CTH is that it requires a mesh resolution much finer than comparable Lagrangian codes to capture important characteristics of high energy impact events leading up to gouging.

3.2.2 ABAQUS, A Lagrangian Finite Element Study. ABAQUS is a widely used high performance finite element code [61]. It is available on the Hydra `lxaerolab` workstations at the Aerospace Engineering Department of AFIT and on similar systems at the ASC MSRC. One of the main capabilities of ABAQUS that makes it so promising as a numerical tool is its ability to handle user-defined material models. ABAQUS uses a balance of force approach at the nodes to solve the conservation equations. This approach is similar to the approach used in LS-DYNA3D (see section 3.1.1).

3.2.2.1 Sample Problems. While exploring the capabilities of ABAQUS, the primary question that needed answering was whether the adaptive meshing capability of ABAQUS can accurately model the gouging problem. Based on experience using an Eulerian mesh with the hydrocode CTH, ABAQUS's adaptive meshing techniques remained unproven.

The first sample problem used in this case was designed to test the adaptive meshing of ABAQUS when the elements start to distort excessively. If the mesh is unable to adjust for the large deformations expected in hypervelocity gouging (especially material "jetting"), the test will be unsuccessful and the other desired capabilities (such as the

explicit coupled heat-structures solution algorithm) of ABAQUS will be unavailable for this research project.

Therefore, this first case takes a rough gouging model at relatively low impact velocities and investigates the adaptive meshing capability with a linear equation of state and using the Johnson-Cook plasticity model to describe constitutive behavior. In the numerical model, the slipper impacts the rail with an initial normal velocity of 70 m/sec normal and 70 m/sec tangential velocity. This velocity profile was the maximum velocity for which a solution was obtained.

An asperity impact case with the same geometry and impact velocity as the CTH model was also run for direct comparison to both CTH and LS-DYNA3D. The initial run used the Johnson-Cook constitutive model. However, allowing for viscoplastic deformations resulted in large deformations that this Lagrangian code could not handle. The solution aborted prior to reaching the same time period for which the CTH solution was carried out. Therefore, a second run using a strain-rate independent elastic-plastic isotropic hardening model for plasticity was used. This reduced the magnitude of the deformations in the asperity so the Lagrangian code could carry the solution to the same time as the CTH model.

Large deformations in the ABAQUS Lagrangian formulation results in negative volume calculations for certain elements when their boundaries cross over one another. The constitutive model in ABAQUS uses what is defined as a Kirchhoff-type stress in which the Cauchy stress is formulated as per unit volume. This volume is calculated using the Jacobian. When large deformations of the elements occur, the Jacobian loses its accuracy resulting in an overall loss of fidelity in the solution.

3.2.2.2 Results and Analysis. The main problem with the results obtained from the first case is the inability of the adaptive meshing of ABAQUS to capture large deformations. In Figure 3.29 deformations occur that are beyond the capabilities of the adaptive Lagrangian mesh of ABAQUS. The analysis shown was aborted because of severe distortion and negative volume calculations for some of the elements. Remeshing was

accomplished first at three and then at 100 times per time step in an attempt to track large deformations and allow analysis to continue without severe distortion of the elements.

Termination occurred before gouging and at much lower speeds than are of interest (i.e., 70 m/sec normal and tangential initial velocity instead of the desired 2 km/sec tangential and 50 m/sec normal velocities). The lack of an adequate Eulerian mesh capability or an adaptive meshing scheme that can trace extremely large deformations is the primary reason this program is inadequate for the numerical investigation.

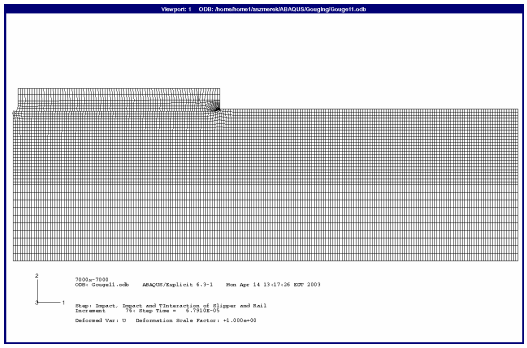

(a) **Global view of deformed mesh of slipper and rail.**

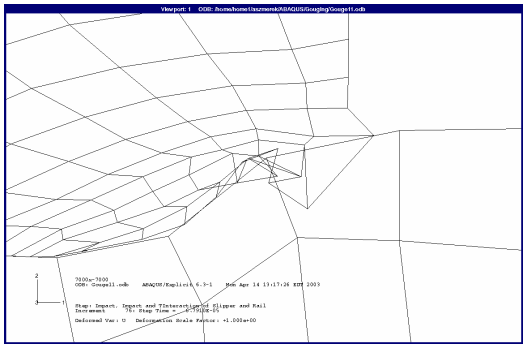

(b) **Highly deformed elements at the front tip of slipper and rail interaction.**

Figure 3.29 **Deformed mesh from ABAQUS run.**

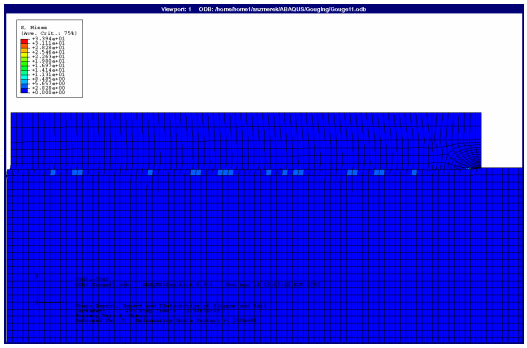

(a) **Mises stress at interaction of slipper and rail.**

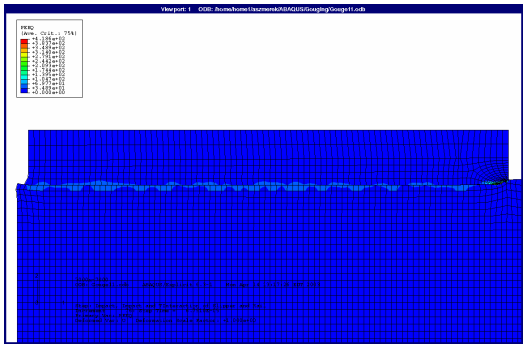

(b) **Equivalent plastic strain at interaction of slipper and rail.**

Figure 3.30 **Comparison of Mises stress and equivalent plastic strain along interaction of slipper and rail.**

Because of the low impact speed used to delay excessive distortion of the mesh, the high stresses required for gouging to develop never formed at impact (see Figure 3.30(a)).

The relatively low impact velocity did not result in a high pressure compression wave that would form the region of plasticity. Some plasticity (as shown in Figure 3.30(b)) occurred along the interaction of the slipper and rail, but the region is relatively small and the values are also relatively less than they should be. The leading edge of the slipper contains the closest results to what one would expect for a hypervelocity gouging model. The interaction definition used in this analysis was a kinematic exponential decay model with static and dynamic friction coefficients of 0.4.

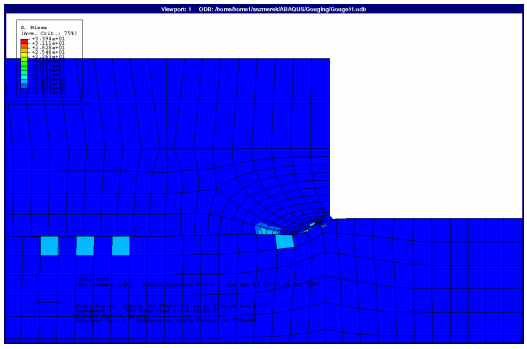

(a) **Mises stress at leading edge of slipper and rail interaction.**

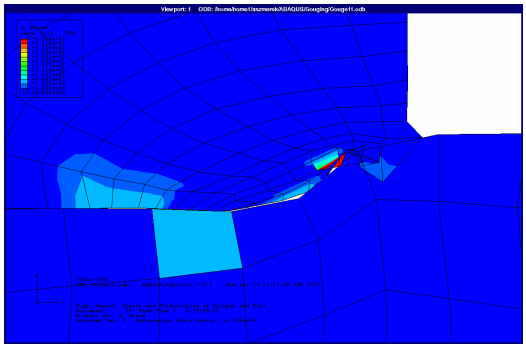

(b) **Mises stress in highly deformed elements at the front tip of slipper and rail interaction.**

Figure 3.31 **Mises stress at leading edge of slipper and rail interaction.**

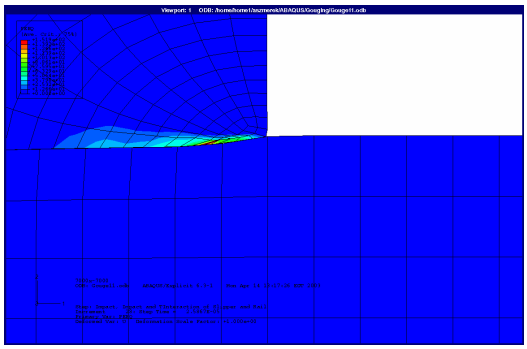

(a) **Equivalent plastic strain forming in slipper and rail at leading edge of slipper and rail interaction.**

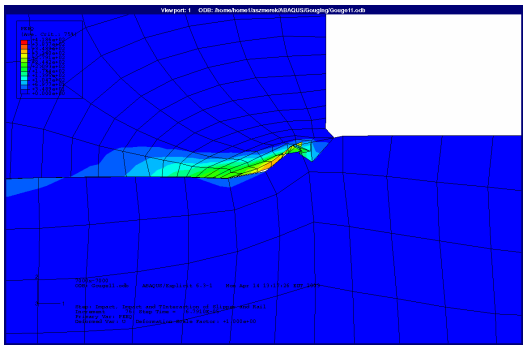

(b) **Equivalent plastic strain in highly deformed elements at end of analysis.**

Figure 3.32 **Equivalent plastic strains at leading edge of slipper and rail interaction.**

The leading edge of the slipper and rail interaction is the area of most interest in this analysis. In Figures 3.31(a) and 3.31(b) high stress is concentrated at the leading edge of the interaction. Figure 3.31(b) is an enlarged view of the leading edge. The distorted elements are excessively distorted. This is to be expected as high energy impact and shearing should result in large deformations, especially in the plastic zone in which flow stress is dominant. Shear slip planes and material velocity vectors both normal and parallel to the plane of impact allow motion of the material out of the plane of motion in order to produce the rotations required for material jetting to occur.

Plastic strain near the leading edge of the slipper is another indication that the conditions required for gouging will not occur in this analysis. In Figures 3.32(a) and 3.32(b) large equivalent plastic strain is concentrated at the leading edge of the interaction where high stress occurs. Figure 3.32(b) is an enlarged view of the leading edge. As stated before, the values are smaller than expected, but this is likely a result of the lower impact velocities that were used.

For a numerical model to simulate gouging properly, the model must capture the sharp discontinuity of a propagating stress wave. It must also model the high pressure core that develops at the point of gouging. Immediately after impact, the model should indicate formation of a high pressure compression wave and a combined stress wave. This large stress gradient should result in formation of plasticized material zone at the interface of slipper and rail and the formation of a small "hump" in the plasticized rail material just after the leading edge of the slipper. These characteristics are not found in this analysis because the mesh is distorted to such an extent that the the solution algorithm cannot develop to the point that gouging occurs.

The next case run involved an asperity initiator for gouging. The solution for this case never propagated past 0.84 microseconds (see Figure 3.33). The CTH solution was carried out to 5 microseconds. In order to carry out the comparison to CTH, the parameters were modified so that the solutions could be matched for the same time period. In addition, the constitutive model was changed so that it was independent of strain rate effects (from Johnson-Cook to elastic plastic with isotropic hardening). Also, the strength of the asperity was increased to twice the value of the rail used in the test (from 1.79 GPa to 3.6 GPa).

The results of these changes are that the asperity deforms less, and delays negative volume calculations caused by distortion of the elements. With these results, a comparison between like times could then be made (see Figures 3.34 through 3.36).

The solution for the Johnson-Cook strain rate dependent model shows the asperity deforming in such a manner as to indicate the potential for "jetting" formation. However, the contact models required for the Lagrangian method prevent such mixing from occurring. The problem with the Jacobian calculation already mentioned would also prevent such interaction between asperity, rail, and slipper materials.

The strain rate independent constitutive model coupled with the higher strength asperity reduces the element distortion for the asperity so that the solution can be carried to completion to the same time as CTH and LS-DYNA3D. Using the elastic-plastic isotropic constitutive model, we see development of plastic zones in the asperity and at the interface between the asperity and both the slipper and rail surfaces. This results in permanent deformations that take on a gouge-like appearance. Still, there is no material mixing such as would occur during jetting because of the contact model being used. When the slipper impacts the asperity, a shockwave of about 1 GPa propagates into the slipper. The asperity is put under tremendous stress, immediately plasticizing it. Also, normal to the asperity-rail interface a shock of about 2 GPa propagates into the rail. These are all indications that suggest the conditions for gouging are present. The difficulty with Lagrangian mesh distortions and the penalty contact method prevents the solution from developing realistic gouging because material mixing and jetting is not allowed.

3.2.2.3 Comparison to Criteria. Based on the results of this investigation of ABAQUS, the code is now compared against the criteria on page 3-22.

1. Adaptive meshing in ABAQUS cannot adjust enough to adequately model the extremely large deformations that occur in hypervelocity gouging at the interface of the slipper and rail.
2. ABAQUS contains excellent material model capabilities including a robust user-defined material model capability.

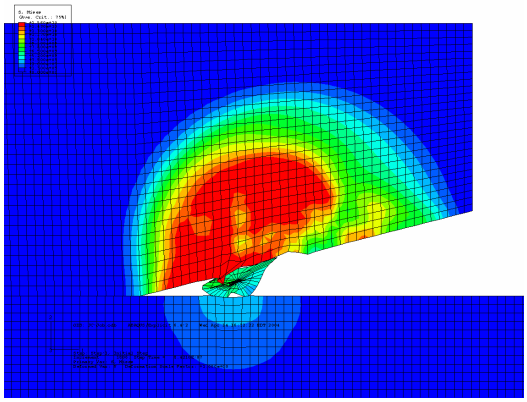

(a) **Johnson-Cook viscoplastic model Mises stress plot of asperity impact at 0.84 μsec.**

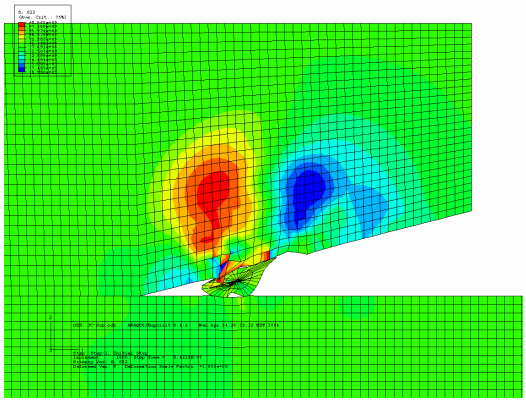

(b) **Johnson-Cook viscoplastic model shear stress plot of asperity impact at 0.84 μsec.**

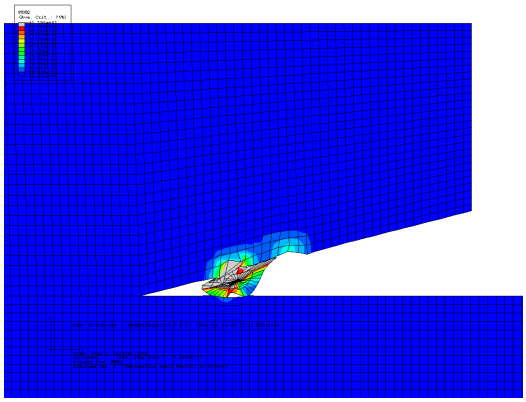

(c) **Johnson-Cook viscoplastic model plastic strain plot of asperity impact at 0.84 μsec.**

Figure 3.33 **ABAQUS Johnson-Cook viscoplastic model plots of asperity impact.**

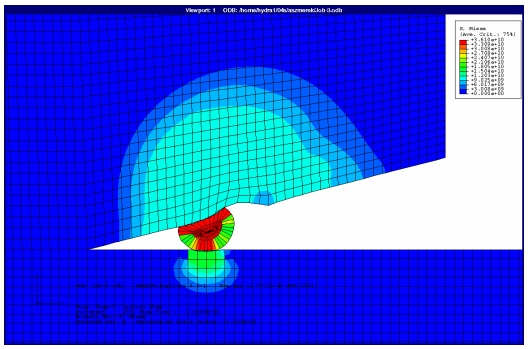

(a) **Mises stress plot of asperity impact at 1 μsec.**

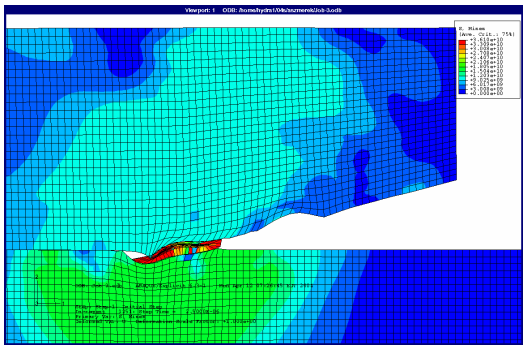

(b) **Mises stress plot of asperity impact at 2.5 μsec.**

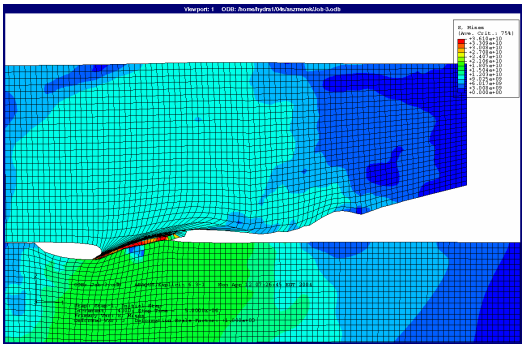

(c) **Mises stress plot of asperity impact at 5 μsec.**

Figure 3.34 **ABAQUS Mises stress plots of asperity impact.**

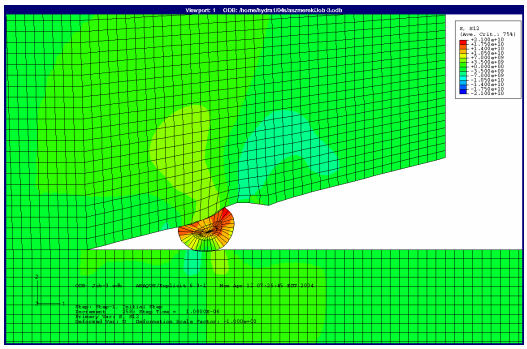

(a) **Shear stress plot of asperity impact at 1 μsec.**

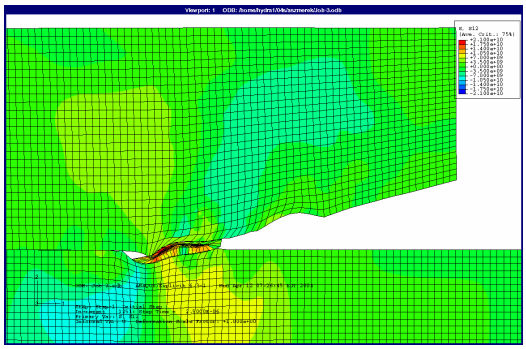

(b) **Shear stress plot of asperity impact at 2.5 μsec.**

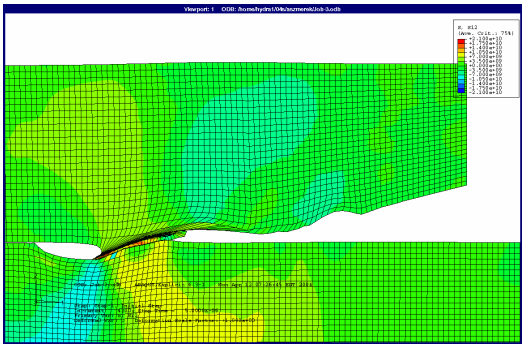

(c) **Shear stress plot of asperity impact at 5 μsec.**

Figure 3.35 **ABAQUS shear stress plots of asperity impact.**

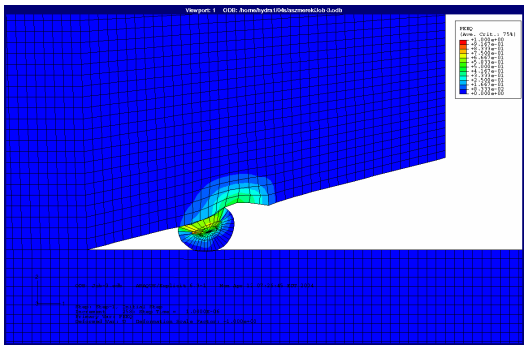

(a) **Plastic strain plot of asperity impact at 1 μsec.**

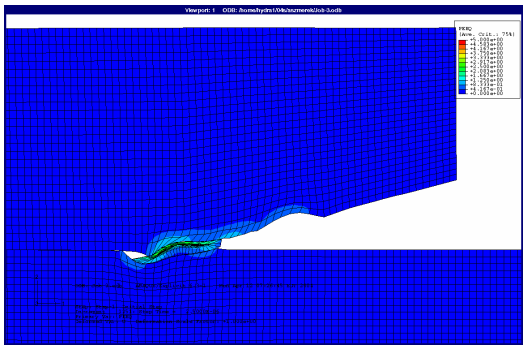

(b) **Plastic strain plot of asperity impact at 2.5 μsec.**

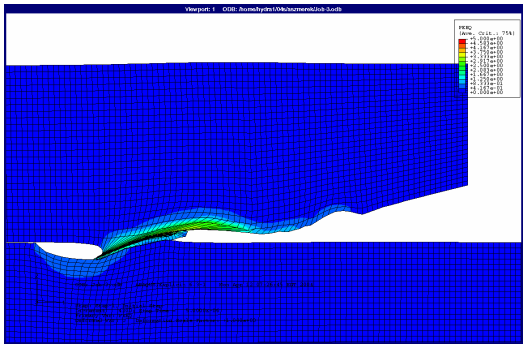

(c) **Plastic strain plot of asperity impact at 5 μsec.**

Figure 3.36 **ABAQUS plastic strain plots of asperity impact.**

3. User-defined models may be used to define new failure modes for materials. Current capabilities include maximum stress and maximum strain.

4. Because of the low impact velocity of the sample problem this capability was never really tested in the first case. However, the asperity impact model did allow ABAQUS to use the Rankine-Hugoniot relations to match states of the material across shock fronts.

5. ABAQUS contains an explicit coupled heat-structure solution algorithm capability that could be used to model nonadiabatic heat flow and deformation.

6. ABAQUS contains a variety of static and dynamic contact algorithms including various friction models. Most are based on the penalty method in which calculations are made to determine and prevent the contact surfaces from penetrating each other. These algorithms are used best for small deformations at the interface.

7. This criterion remains unproven since the impact velocity and constitutive model were adjusted to keep deformations in the range that adaptive meshing and Lagrangian meshing could handle. The contact model also prevents material mixing that leads to gouging. In theory, ABAQUS has the correct material models to handle the high pressure core and plastic zone development for an oblique impact of a slipper on a rail. With the correct constitutive model it is also able to model adiabatic shear band development.

8. Adaptive meshing was unable to model moderate deformations at the interface of slipper, asperity, and rail. It is apparent the algorithm will not be able to model jetting. It is possible using defined "ties" between elements that ejecta might be tracked. That assumes however, that the mesh elements are allowed to deform to the point that ejecta form.

9. ABAQUS is readily available at the ASC/MSRC on a variety of high performance computers and on the `lxaerolab` workstations in the AFIT Aerospace Engineering Department's computer lab.

10. Technical support is available through other users in the Air Force Research Laboratory, ABAQUS educational license technical support, and the ASC MSRC.

11. Most work that has been accomplished using ABAQUS for high energy impact is for smaller deformations than are expected for the hypervelocity gouging problem.

3.2.2.4 Conclusions. In this ABAQUS analysis, gouging is not allowed to occur because the large deformations of the Lagrangian mesh exceed even the corrections made by adaptive meshing. Thus, the analysis is cut short before gouging would be observed. This exercise helped determine that ABAQUS is not the program of choice for this particular investigation even though it has excellent user-defined material model capabilities and a coupled heat transfer-stress algorithm. It would be useful however, for impact cases in which smaller deformations occur and distortion of the elements is relatively small. One example of this might be for penetration impacts such as for long rod penetrators.

3.2.3 LS-DYNA3D, A Lagrangian Finite Element Study. LS-DYNA3D is a three-dimensional finite element code that has Lagrangian and Arbitrary Lagrangian Eulerian (ALE) mesh capabilities [62]. It is a commercially available software package that also has the capability to make use of user-defined material models. LS-DYNA3D is available on the Hydra Beowulf-type system at the Aerospace Engineering Department at AFIT and the ASC MSRC. All these features make LS-DYNA3D a most promising numerical tool. LS-DYNA3D is well known for solving highly nonlinear dynamic problems using finite elements coupled with nonlinear material models including equations of state.

3.2.3.1 Sample Problem. One of the main considerations of LS-DYNA3D is the capability of the Lagrangian finite element method to model large deformations with potentially large element distortions for the hypervelocity gouging problem. The first problem considered in this investigation is not a gouging problem *per se*, but it does allow for significant distortion. Thus, the criteria parameters on page 3-22 can be evaluated.

The sample problem is based on a legacy model from asperity impact studies. This is why the leading edge of impact is a steep angle (14.744^o) rather than the rounded and small radius of the Laird model in the CTH analysis (described in section 3.2.1). However, Laird showed in his dissertation work that this leading edge should result in hypervelocity

gouging at around 5 μsecs [7]. The problem will be studied in two variations in an oblique impact configuration. In the first variation, the rail will consist of material that has a higher yield strength than the slipper. In the second case, the slipper will have the higher yield strength. In addition to testing the capabilities of the Lagrangian mesh, the capabilities of a LS-DYNA3D constitutive model in a high energy impact will be investigated. The horizontal and vertical impact velocities are the same as the CTH hypervelocity gouging model (i.e., 2 km/sec and 50 m/sec, respectively). The purpose for selecting the asperity impact sample problem and the two variations of the three-dimensional vibratory impact (higher strength rail vs. higher strength slipper) are the following:

- Due to excessive mesh distortion, it is assumed that material "jetting" cannot be modeled using the Lagrangian mesh. However, overall gouging deformation might be modeled if material failure occurs just prior to the point at which material "jetting" would occur. This should result in a teardrop shaped deformation that could be used to model gouging with the Lagrangian mesh.

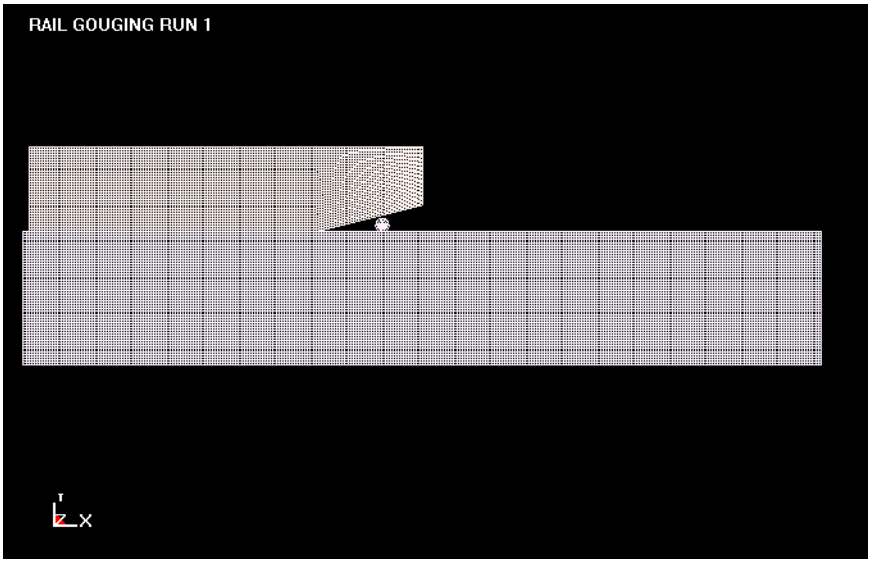

Figure 3.37 **Asperity impact case for comparison to CTH and ABAQUS.**

The next case was a two-dimensional plane strain model used for direct comparison to CTH and ABAQUS. The same parameters were used in this case as those used in the analogous ABAQUS case. This case is depicted in Figure 3.37.

3.2.3.2 Results and Analysis. The asperity impact case is a two-dimensional plane strain model with the same parameters as the ABAQUS model. The three-dimensional analysis provided a good platform for understanding the capabilities of LS-DYNA3D. However, to make a direct comparison to CTH, the models should be as similar as possible so that the differences in codes may be highlighted. To do this, a gouging asperity model was run in LS-DYNA3D and in CTH. In order to make a fair comparison between the Lagrangian mesh in LS-DYNA3D and the Eulerian mesh in CTH, the same nodal resolution (i.e., concentration of nodes) near the area of interest for gouging will be set for both codes.

In this investigation, the results for LS-DYNA3D and CTH are compared at 2 μsecs and 6 μsecs. These times were chosen because they show both the formation of the stress field and plastic strain shortly after impact with the asperity and shortly after gouge formation for both solutions.

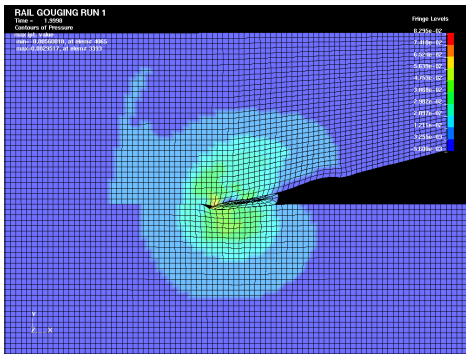

(a) **LS-DYNA3D pressure contours near asperity 2 microseconds after impact.**

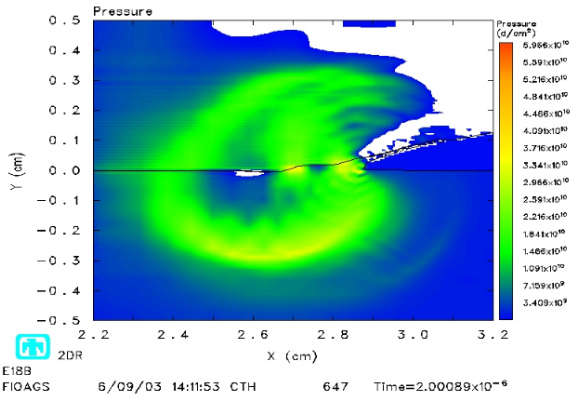

(b) **CTH pressure contours near asperity 2 microseconds after impact.**

Figure 3.38 **Pressure contours around asperity impact for LS-DYNA3D and CTH at 2 μsecs.**

In Figure 3.38 the pressure profiles calculated by LS-DYNA3D and CTH at 2 μsecs into the solution are shown. The slipper has impacted the asperity and the asperity has deformed due to the impact. The two plots are basically similar, but there are subtle differences. The CTH plot shows two, not one small area of highest pressure. This is due

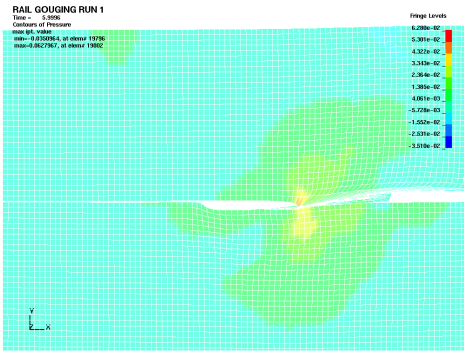

(a) **LS-DYNA3D pressure contours near asperity 6 microseconds after impact.**

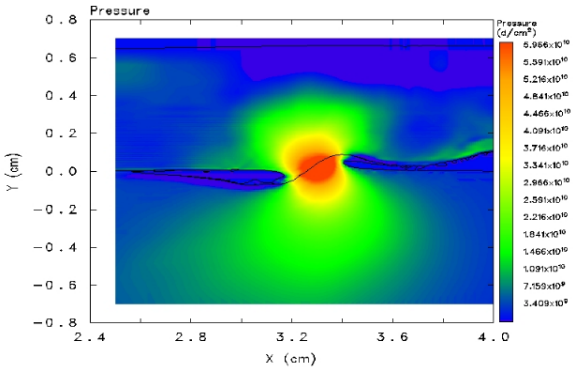

(b) **CTH pressure contours near asperity 6 microseconds after impact.**

Figure 3.39 **Pressure contours around asperity impact for LS-DYNA3D and CTH at 6 μsecs.**

mainly to the deformed shape of the asperity in the CTH model. The interaction of the asperity with the slipper in the CTH solution leads to the symmetrical formation of the slipper impinging into the rail and the rail/asperity material impinging into the slipper. In the LS-DYNA3D plot the high pressure occurs at the impact point of the slipper and the asperity, but at the low end of the asperity because of its deformation in which it is being squeezed between the slipper and rail. In the Eulerian CTH solution, the asperity is not just being squeezed, but is interacting with the slipper and rail materials.

More of this interaction is observed in the CTH solution in Figure 3.39 at 6 μsecs. In the LS-DYNA3D solution the pressure core is centered at the deformed points of the slipper and rail which act similar to a press which squeezes and stretches the asperity. The asperity in turn deforms the slipper and rail because of its finite thickness. In the CTH solution, the asperity is now mixing with the slipper and rail such that it is not even recognizable as an asperity any more. The pressure core is focused at the center of the slipper-rail interaction in which material jetting and gouging occurs.

These pressure plots and subsequent deformations are the natural evolution of the solution from the initial formation of high pressure and plasticity in the two solutions at impact (see Figure 3.40 for plasticity at 2 μsecs after the slipper is set in motion). Formation of the plastic zone allows large deformations that result in the material response

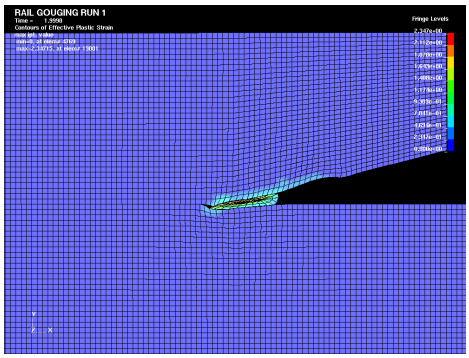

(a) **LS-DYNA3D plastic strain contours near asperity 2 microseconds after impact.**

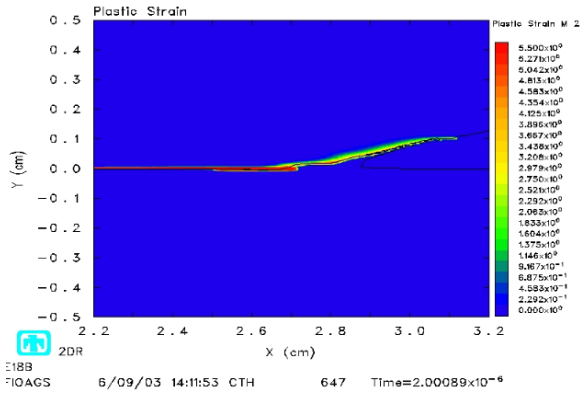

(b) **CTH plastic strain contours on slipper near asperity 2 microseconds after impact.**

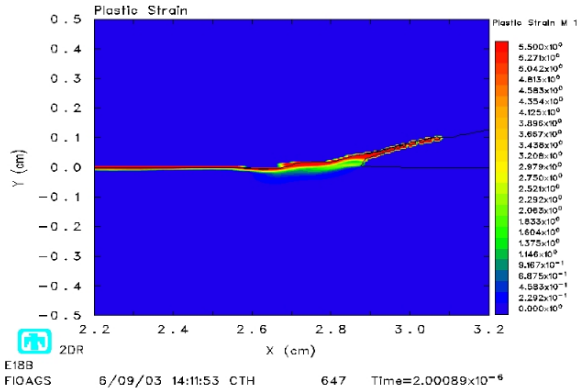

(c) **CTH plastic strain contours on rail and asperity 2 microseconds after impact.**

Figure 3.40 **Plastic strain contours around asperity impact for LS-DYNA3D and CTH at 2 μsecs.**

of the slipper and rail in the pressure and shear stress plots. Immediately after impact the asperity is mostly plasticized material in both cases. However, there is an important distinction that must be made here. The plastic asperity in the LS-DYNA3D solution is being squeezed from the initial impact point such that the bulk of the asperity material lies in front of the travelling slipper front. In the CTH solution however, the impact has plasticized the entire asperity to such an extent that it now flows like a fluid and the asperity has thinned and attached itself to the edge of the impact point on the slipper. This

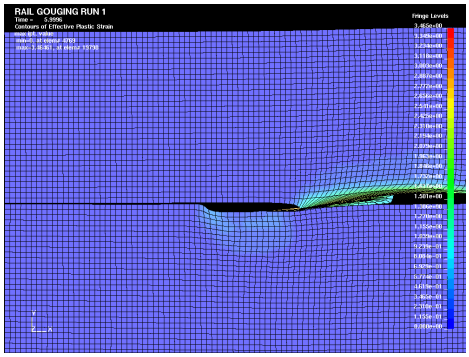

(a) **LS-DYNA3D plastic strain contours near asperity 6 microseconds after impact.**

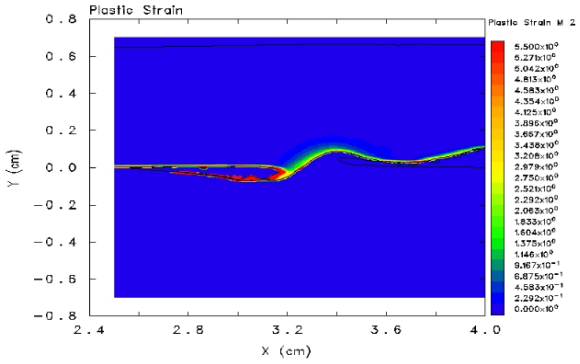

(b) **CTH plastic strain contours on slipper near asperity 6 microseconds after impact.**

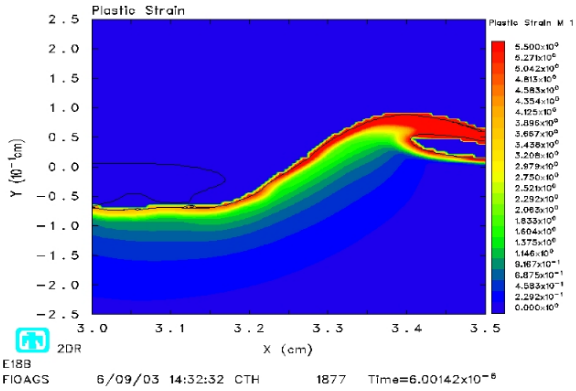

(c) **CTH plastic strain contours on rail and asperity 6 microseconds after impact.**

Figure 3.41 **Plastic strain contours around asperity impact for LS-DYNA3D and CTH at 6 μsecs.**

results in the bulk of the asperity material acting at the base of the slipper-rail interaction instead of leading it.

In other words, the constitutive and velocity model for CTH allows for an impact that smears the plasticized asperity such that the asperity quickly deforms into such a shape that the thicker portion forces the base of the slipper to respond to it along the line of sliding interaction between slipper and rail. The LS-DYNA3D Lagrangian asperity model however, forces the thicker portion of the plasticized asperity in front of it. The basic difference between the two models is the way each treats the materials after impact.

CTH treats them as fluids as shown in the way the plastic asperity material responds to the impact and mixes with the rail and slipper material. LS-DYNA3D treats the asperity as a deformed solid that must be responded to by the slipper and rail. The slipper and rail must deform around the asperity rather than mix with it as in the CTH solution.

At 6 μsecs, Figure 3.41 shows an even sharper contrast to the 2 μsec solution. The plastic region has grown in both cases, but the flow in the CTH model continues as the mixing of slipper-asperity-rail materials results in material "jetting" and subsequent gouging. In the LS-DYNA3D model, the slipper continues to deform around the asperity due to the Lagrangian approach of the numerical solver and the rail is forced to deform in response to the asperity being forced into it. The Lagrangian mesh limits deformations to the capabilities of the elements to model those deformations. When deformations result in elements that are highly warped and begin to twist on themselves, negative volumes occur and the finite element solution algorithm cannot continue. Thus, due to the Lagrangian nature of the finite elements, the discretized solids are not allowed to deform from their current configuration in such a manner that "jetting" is modeled.

This is primarily due to the nodal conservation basis of the finite element method. With this basis, the flow of mass, momentum, and energy is never accurately modeled as it is in the finite volume method of CTH. A couple of recently added capabilities of LS-DYNA that have not been fully tested in this study may prove helpful for future studies. For example, LS-DYNA3D contains an Eulerian mesh capability and a Spherical Particle Hydrodynamics (SPH) element option [63]. In addition, elements may be "tied" together by a specified strength or strain such that when that strength or strain is exceeded along a certain path, the particles break away from the bulk material and the action of that group can be traced.

A cursory study was accomplished using Lagrangian elements for the slipper and rail and SPH elements for the asperity. However, the asperity was still flattened during impact and "smeared" over both the slipper and rail with only a relatively small amount of a teardrop shaped deformation occurring on the rail. The amount of effort required to characterize the model entirely in SPH elements or in any of the other potentially beneficial methods for this initial study was too cumbersome to accomplish at this time. This is

primarily due to the lack of available and comprehensive documentation that describes how to implement these techniques into the LS-DYNA model.

So, which model is more correct? According to experimental observation, a layer of slipper material is deposited and mixed with the rail material in post-gouging analysis. Likewise, rail material is deposited into the slipper suggesting mixing of the materials as indicated in the CTH model. Observation of hypervelocity gouges does not support the mechanism shown in the LS-DYNA Lagrangian solution.

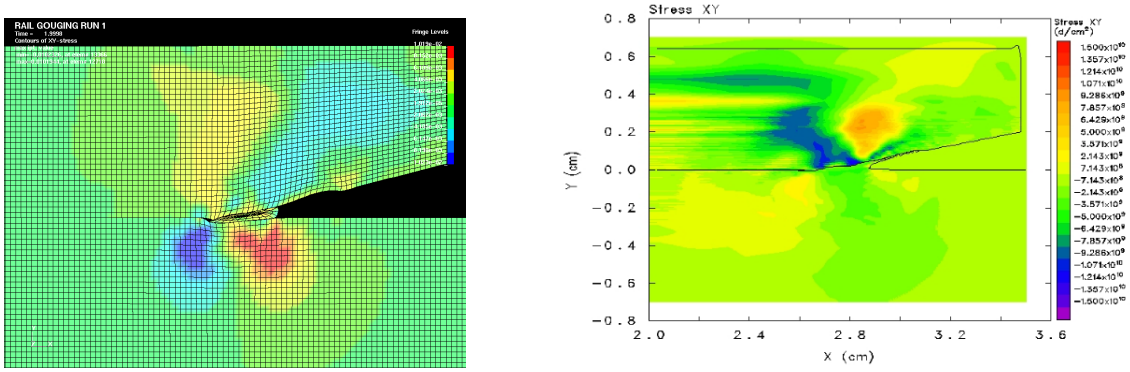

(a) **LS-DYNA3D shear stress contours near asperity 2 microseconds after impact.**

(b) **CTH shear stress contours near asperity 2 microseconds after impact.**

Figure 3.42 **Shear stress contours around asperity impact for LS-DYNA3D and CTH at 2 μsecs.**

The difference between the LS-DYNA3D and CTH solutions is even more striking in Figures 3.42 and 3.43. The CTH model shows material mixing at 2 *mu*secs. The shear stress profiles for the LS-DYNA3D and CTH models are almost mirror images of each other. This is a direct result of the difference in the shape of the asperity for each model. The slipper and rail are forced to respond to the asperity as it is deformed after impact. Because the asperity deforms differently in both cases, the slipper and rail react differently in both cases. And since the asperity is almost a mirror image of itself between models, so too does the shear stress profile appear. The LS-DYNA3D model shows more concentrated shear stress profiles in the rail while the CTH model shows concentrated shear stress fields in the slipper. Again, which is more correct according to observation of real gouges? The fact of the matter is, it is difficult to tell directly. There is no way to attach strain gauges

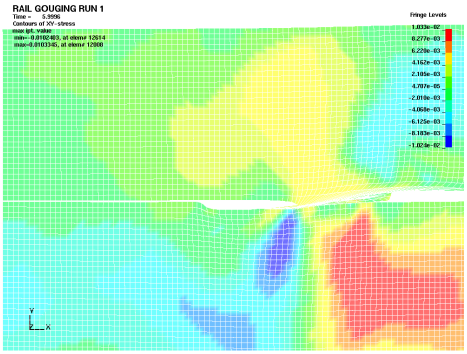

(a) **LS-DYNA3D shear stress contours near asperity 6 microseconds after impact.**

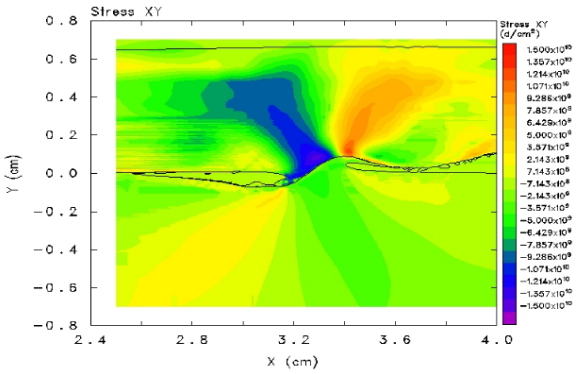

(b) **CTH shear stress contours near asperity 6 microseconds after impact.**

Figure 3.43 **Shear stress contours around asperity impact for LS-DYNA3D and CTH at 6 μsecs.**

on the slipper and rail at the point of gouging to measure stress fields in time and obtain the stress profile for comparison to numerical analysis. Therefore, because the shear stress profile in the CTH model is a result of the material jetting that occurs, and because this material jetting results in a mixing of materials that agrees with observation, it is assumed that the CTH model is more accurate.

In the LS-DYNA results, the asperity is impacted by the steep angled leading edge of the slipper. The elements deform and stretch as the plasticized asperity is squeezed between the slipper and rail. Large deformations occur in the slipper and rail. But as the asperity is squeezed and stretched thin, the deformation in the vertical direction becomes less and the deformation slopes back toward the sliding line of slipper and rail. This results in a side view that resembles the tear drop shape of a gouge. Material jetting does not occur.

Element deformations cause stretching of the elements in the direction of motion of the slipper. The vertical response is due to the thickness of the asperity between slipper and rail. As the asperity thickness changes due to compression between slipper and rail, so does the deformation in the slipper and rail. There is no rotational component of deformation that causes the asperity or rail material to form a hump that begins mutual interaction with the slipper material resembling a vortice or wave (a.k.a., material "jets").

If this were to occur in this analysis, the Lagrangian mesh would have difficulties because severe warping that accompanies this type of deformation causes negative volumes to occur in the finite element solution from the Jacobian.

By contrast, the CTH solution shows a material "flow" that more accurately models experimental observations in which a layer of slipper material is deposited on the rail and a layer of rail material is mixed with the slipper. The Eulerian CTH solution is better able to model the interaction of materials that is expected in hypervelocity gouging. In hypervelocity rail tests, ejecta are observed as the slipper impacts the rail. CTH solutions also show formation of ejecta during material "jetting" and subsequent gouge formation.

There is another important aspect of the CTH solution that gives it an advantage over the LS-DYNA solution. CTH material models contain comprehensive tables of data that are based on real testing. This provides CTH with a set of equation of state models and constitutive models that more accurately describe the response of the materials used for the slipper and rail. This is partially the reason that the shear stress field is quite different when one compares the LS-DYNA3D solution to the CTH solution.

When the three profiles of pressure, plastic strain, and shear stress are considered, CTH seems to be the code of choice due to its ability to handle materials in the same manner as fluids. In this way, CTH is better able to model the actual gouging phenomena which occurs at hypervelocity impact and for which the solid materials of the slipper and rail react hydrodynamically as well as quickly reaching the plastic regime. When this capability is coupled with CTH's tabular material models, CTH clearly results in a more accurate numerical solution to the hypervelocity gouging problem.

The asperity impact case was also run to make direct comparisons of LS-DYNA3D to ABAQUS (see results in Figures 3.44 through 3.46). It used the same material model, contact model, geometry, element type and resolution, and impact velocity as the ABAQUS asperity initiator case (see Figure 3.37).

The primary difference between the two Lagrangian finite element codes lies in the stress used for the constitutive model. A per unit volume stress is used in ABAQUS while in LS-DYNA3D the Jaumann corotation is used. Both codes have difficulty with

large deformations because of the Jacobian used in conjunction with the element shape function. When large deformations occur that result in elements twisting upon themselves, the calculated volume becomes negative and the solution is aborted. ABAQUS uses Kirchoff stress, $\tau_{ij} = J\sigma_{ij}$ to put the Cauchy stress in terms of the reference volume. LS-DYNA3D uses the Jaumann corotation rate update approximation of the stress tensor, $\bar{\sigma_{ij}} = \sigma^n_{ij} + \sigma^n_{ip}\Delta\omega_{pj} + \sigma^n_{jp}\Delta\omega_{pi}$. The main difference between the two is in the extra Jacobian used in ABAQUS to put the Cauchy stress into a per unit reference volume format.

There is very little difference between the solution obtained by LS-DYNA3D and the solution from ABAQUS. Both codes also use the Jacobian in the integration of the stress over the volume with the strain displacement matrix. This integration that has difficulties with highly distorted elements.

CTH was used to model the same geometry and velocity of impact as the ABAQUS and LS-DYNA3D models. The differences in the results between the Lagrangian codes and the Eulerian CTH code is the material mixing treatment and Eulerian treatment of large deformations with fluid-like flow of the plasticized material in the CTH algorithm. To keep the deformations small enough so the Lagrangian codes could carry the solution out as far as the CTH algorithm, a strain rate independent constitutive equation was used for the Lagrangian finite element codes. The results show this difference.

In the Lagrangian finite element codes, the asperity maintains its strength and shape for a longer period of time than it does in CTH. Because the material is not allowed to flow and mix due to the Lagrangian contact algorithm, there is no material mixing as there is in the CTH solution. The limits of pressure, shear strain, and plastic strain are similar between the codes, but the effect is more localized in the CTH solution. This is to be expected, since the strain rate dependent algorithm in CTH allows for a greater effect of strain rate which results in larger plastic strains and deformation on a local level over the same amount of time. There is also the difference in shear stress directions between CTH and the Lagrangian codes. This is caused by the mechanics of deformation of the asperity, as described above in the direct comparison of LS-DYNA3D and CTH.

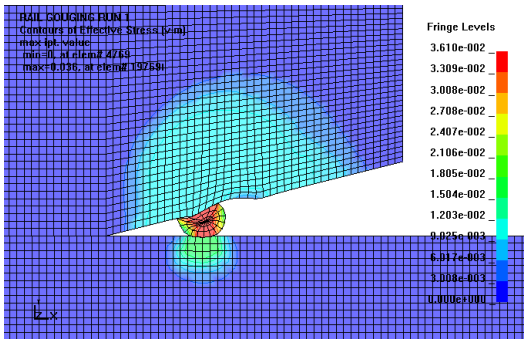

(a) **Mises stress plot of asperity impact at 1 μsec.**

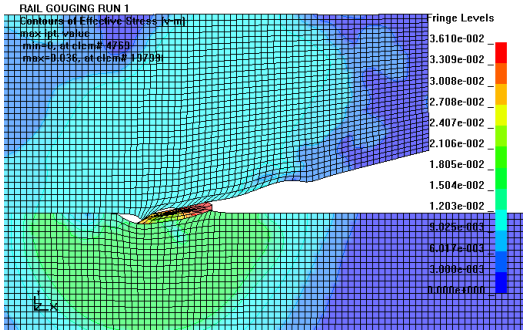

(b) **Mises stress plot of asperity impact at 2.5 μsec.**

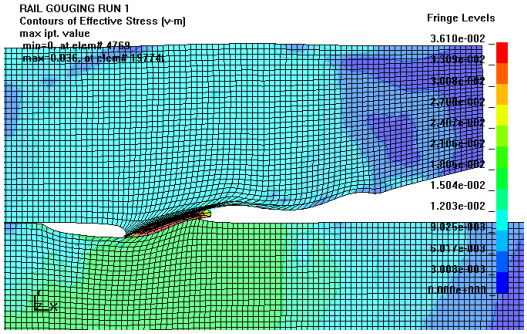

(c) **Mises stress plot of asperity impact at 5 μsec.**

Figure 3.44 **LS-DYNA3D Mises stress plots of asperity impact.**

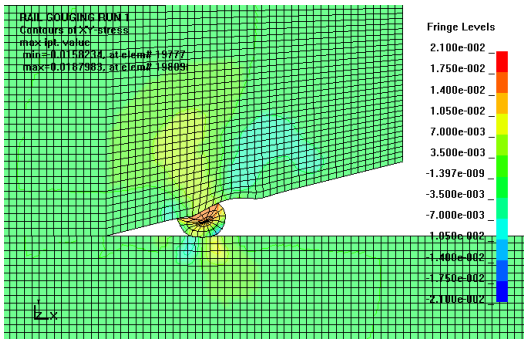

(a) **Shear stress plot of asperity impact at 1 μsec.**

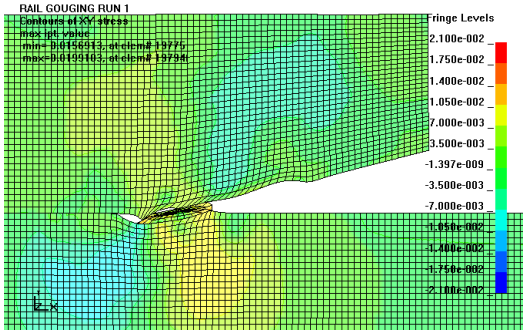

(b) **Shear stress plot of asperity impact at 2.5 μsec.**

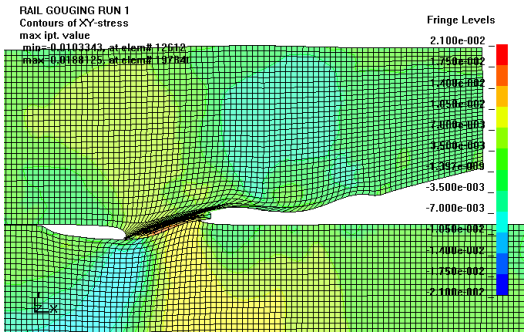

(c) **Shear stress plot of asperity impact at 5 μsec.**

Figure 3.45 **LS-DYNA3D shear stress plots of asperity impact.**

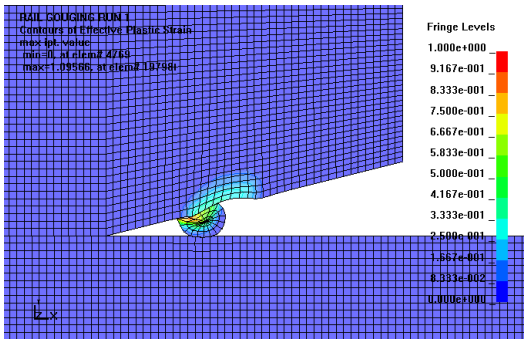

(a) **Plastic strain plot of asperity impact at 1 μsec.**

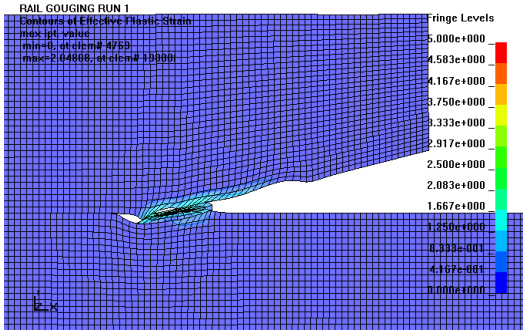

(b) **Plastic strain plot of asperity impact at 2.5 μsec.**

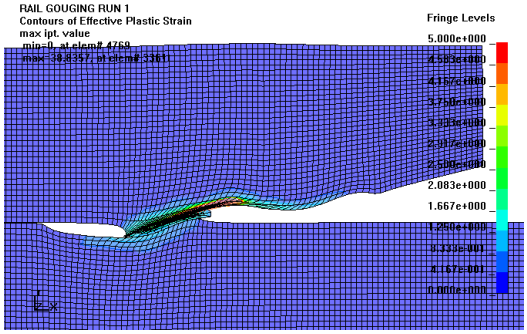

(c) **Plastic strain plot of asperity impact at 5 μsec.**

Figure 3.46 **LS-DYNA3D plastic strain plots of asperity impact.**

3.2.3.3 Comparison to Criteria. Based on the results of this investigation of LS-DYNA3D, the code is now compared against the criteria on page 3-22. The LS-DYNA3D results were essentially the same as the ABAQUS results. The primary difference between the two codes are due to the algorithms, such as the stress used to define the constitutive models.

1. The three-dimensional and two-dimensional plane strain Lagrangian mesh was tested in this study. In both cases, gouging did not form and was not allowed to develop.
2. Extensive equation of state and constitutive models are available. These include shock, high strain rate, large deformation, and plastic deformation models. Models are also available that may be coupled to an explicit heat conduction model.
3. In addition to user-defined models that may be used to model failure and damage, LS-DYNA3D has built-in material models including an isotropic elastic-plastic failure model that uses min pressure and max plastic strain criteria as a determination of failure. LS-DYNA also contains general erosion criteria that can be used independent of the material models including min pressure, max principal stress, max effective stress, max principal strain, max shear strain, and Tuler-Butcher criterion which contains a max stress impulse for failure. [64].
4. LS-DYNA uses an artificial bulk viscosity parameter with the Rankine-Hugoniot relations to determine the state of the material behind shock fronts. Additionally, various equation of state models are available that are designed for use with shock conditions. [59, 65]
5. LS-DYNA may be used to solve for steady state or transient temperature fields on three-dimensional boundaries. Material properties may be temperature dependent and various time and temperature dependent boundary conditions such as temperature, flux, convection, and radiation can be specified. Additionally, time or temperature dependent volumetric heat generation rates can be specified by element, material, or both. [66]
6. The contact algorithm used for the Lagrangian mesh is based on an algorithm that seeks to prevent penetration of the surfaces by using a penalty method. The results

clearly show that penetration is minimized between the surfaces. However, gouging is inherently the penetration and interaction of slipper and rail materials and this algorithm appears to interfere with that process in the solution. [58]

7. The results of this study did not show the plastic zone layer between surfaces, shear bands, or the high pressure core that leads to gouging in the three-dimensional cases. However, plasticity did and large deformations did develop in the asperity impact case. They were limited in scope, however to avoid negative volume calculations from highly distorted elements.
8. The Lagrangian mesh coupled with the penalty method used in the contact-impact algorithm is not capable of modeling the large deformations and material interaction of gouging known as material "jets."
9. LS-DYNA is available on the Hydra Beowulf-type system, and the Silicon Graphics workstations at the Aerospace Engineering Department at AFIT, and the ASC MSRC.
10. Technical expertise and support for LS-DYNA at Wright-Patterson AFB, OH is not currently available at no cost to AFIT. It is possible to contact experts at LSTC, though this option is subject to availability. AFIT only maintains an educational license with limited technical support. The ASC MSRC does have a technical expert available, however.
11. LS-DYNA is popular in the automotive industry for simulating airbag deployment and automobile crashes. It has also been used in simulating high energy impact such as missiles impacting a target. The Eulerian method in LS-DYNA should be able to handle material jetting. The primary customer base of LS-DYNA is the automotive industry, where there is not much interest in extremely large deformation problems. However, options (e.g., the Eulerian grid) for large deformation analysis are regularly being added and upgraded by the developers of LS-DYNA (i.e., LSTC).

3.2.3.4 Conclusions. Some conclusions may be drawn from this initial investigation of the LS-DYNA code. First, a plane strain Eulerian mesh is required for accurately modeling the gouging phenomena. A Lagrangian mesh will always be plagued

by the difficulty it has to accurately model the material "jets" that occur during gouging. These "jets" are large deformations that are thin and vortice-like. Lagrangian elements have an extremely difficult time modeling this type of deformation without distorting the elements to the point that the analysis cannot continue.

Although gouge-like deformation is possible in a Lagrangian mesh, an interaction of slipper and rail materials cannot be modeled in the Lagrangian mesh because large deformations of the Lagrangian mesh are detrimental to accuracy of the Lagrangian solution. Also, without a plane strain condition, an allowed release of momentum through out-of-plane deformation prevents formation of high pressure differentials required for plastic formation in the rail. Finally, if the slipper develops a plastic zone without a similar plastic region developing in the rail (e.g., if the slipper has a lower yield strength or is coated with a material that develops a plastic zone without imparting high pressure to develop a similar plastic zone in the rail), gouging will not develop.

LS-DYNA has an Eulerian mesh capability that could be investigated for further study of this problem. The plane strain condition may also be accomplished through the combination of a rolling and a pitching motion in a three-dimensional model, or the use of a two-dimensional model using plane strain elements with an oblique impact.

3.3 Computational Resources

There are two major resources available for the numerical investigation. These are the locally managed high performance systems at AFIT and the high-performance computing resources at the ASC MSRC.

The Compaq ES45 at the ASC MSRC at Wright-Patterson Air Force Base, Ohio has a total of 836 CPUs. Each CPU is a 1 GHz EV6.8 Alpha processor with a peak speed of 2 GFLOPS. Each CPU has a data cache of 64 KB, a primary instruction cache of 64 KB, and an onboard cache of 8 MB. The ES45 system is split into two different systems with 128 nodes on the *hpc10* and 81 nodes on the *hpc09* systems. This system uses the Tru64 Unix operating system and switch-based connectivity. The version of MPICH used is 1.2.5.

The Hydra Athlon system at the Air Force Institute of Technology Aeronautics and Astronautics Department (AFIT/ENY) at Wright-Patterson Air Force Base, Ohio has a total of 32 CPUs. Each CPU is a 1.2 GHz AMD Athlon MP processor. The floating-point unit is capable of delivering 4 GFLOPS of single-precision and more than 2 GFLOPS of double-precision floating-point results. Each CPU has a data cache of 64 KB, a primary instruction cache of 64 KB, and onboard 256-KB L2 cache and 128-KB L1 cache. The system consists of 16 nodes, each with 2 CPUs and 1 GB of RAM. This system uses the Redhat Linux 7.1 Kernel 2.4.13 operating system and switch-based connectivity. The version of MPICH used is 1.2.1..6-pgi.

IV. Model Improvement and Dimensional Analysis of the Hypervelocity Gouging Problem

Numerical analysis requires models that can be related back to real test conditions. The fidelity of this requirement is dependent on the purpose of the research. Previous numerical models of the hypervelocity gouging problem studied the phenomenology of gouging. They drew conclusions about how it initiates and conducted parametric studies [1, 22, 25, 28]. This research seeks to make conclusions that will relate directly to coating applications at

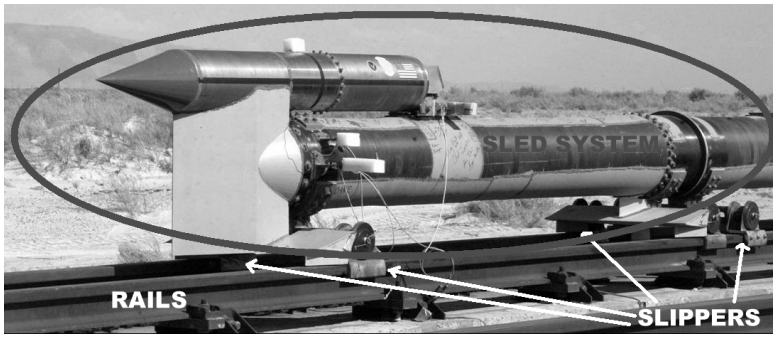

Figure 4.1 **HHSTT rocket sled with sled system, slippers, and rails labelled**

the Holloman High Speed Test Track (HHSTT) at Holloman AFB, NM. Figure 4.1 shows the important divisions of a HHSTT rocket sled.

In order to understand the phenomenon of gouge mitigation using coatings, one must accurately model the coating as well as the interface and mechanics of the sled, slipper, and rail. A high definition model is required to study the mechanics of gouge mitigation through the use of coatings for a couple of reasons. One is the scale of the coating and the deformation of the materials that initiate gouging. The other is the order of accuracy required for direct application of results to the real model.

A review of previous CTH models included Tachau's [24, 25] oblique impact model, Laird's [7, 27, 28, 60, 67] oblique impact model and both Barker [21, 22] and Schmitz's [1] asperity models. All these models are an excellent means for investigating the phenomenon of gouging and comparing the qualitative aspects of various parameters, but a different model is required for comparing results to the actual sled-slipper-rail system.

The phenomenon of hypervelocity gouging is important for practical design considerations related to the HHSTT, but realistic dimensioned quantities become necessary for improvements to component design. Similarity methods have been applied to structural impacts [68, 69], and more specifically to hypervelocity impacts [70, 71, 72, 73]. These methods have application to the dimensional analysis of slipper-rail impacts of a hypervelocity test sled. It was shown that geometric similarity of ballistic impacts does not properly scale material strain rate sensitivity, thermal conductivity, and fracture. Dimensional analysis does not indicate the relative significance of specific invariant parameters. Thus, an investigation into the effect of not properly scaling quantities such as strain rate, is important.

Another concern regarding the use of previous models is that the lack of proper scaling of the models may lead to erroneous conclusions if results are applied directly to the HHSTT. Dimensional analysis becomes an invaluable exercise that provides justified scaling of the problem for the CTH model, and an improved understanding of the physical effects. The closer to the real dimensions of the sled-slipper-rail system that the model uses while still accomplishing computer simulations in a reasonable amount of time, the better the results and conclusions of the research should be.

The dimensional analysis and similitude study takes two approaches to modelling the real test sled. The first is a dimensional analysis considering the CTH algorithm as a "blackbox". User controlled inputs are considered as dimensional parameters. This analysis, however, is shown to be incomplete without a natural time-scale. Also, user selected inputs imply the selection of other dimensional parameters within the CTH algorithm that are not directly selectable by the user. This first approach can be described as the *CTH blackbox* approach.

The second approach utilizes the conservation, constitutive, and state equations as a basis for the dimensional analysis and determines a natural time-scale for the solution. This second approach also accounts for the sled system mass. The mass of the impacting body is not entirely dependent on the density of the slipper. Within the dimensional analysis, a non-dimensional time-scale is also determined. Though this approach provides better results than the *CTH blackbox* approach, it still is not capable of capturing *all* the

dimensional parameters of the gouging solution. Part of the difficulty is that when models are scaled geometrically, they do not scale strain rate effects. This second approach is best described as the *artificial sled mass* approach to the dimensional analysis since it allows for a separate sled system mass.

4.1 Deficiencies of Previous Models

As part of the investigation of previous models, various deficiencies were discovered in each model. These deficiencies must be addressed before using or modifying them for nonequilibrium thermodynamics and coatings investigations in CTH. These deficiencies include:

1. Lack of consistent modeling of the momentum effects of a Dynamic Analysis Design System (DADS) calculated slipper impact on the rail. Laird matched kinetic energy, but the momentum of Laird's model is fifty times less than the real model he compared to. Also, the mass of the sled has not been simulated. The mass of the sled should make a difference in how the gouge initiates and develops due to the transfer of momentum and development of large normal forces that result from the dynamics of the sled travelling over rail misalignments.
2. Large differences in scaling and lack of consistent comparison between results for the models. For instance Barker's model was in the order of 10^{-3} cm while Tachau used a model that was on the order of 10^{2} centimeters. Results have been compared only qualitatively (such as by observing the shape of the gouge instead) rather than quantitatively.
3. Differences in gouge shape between oblique impact and asperity models. The asperity gouge has a teardrop shape that is larger at the initial asperity impact and decreases as the slipper passes over the rail. The mechanism that initiates gouging in a vibratory oblique impact results in a tear drop shape that begins smaller at initiation and grows as the slipper passes over the rail.
4. Lack of a CTH gouging model with results that quantitatively match the size of the gouges that have been found in the real world. Gouges are typically anywhere from

around 1/16" - 1/2" deep and 3" - 4" long [12], but previous CTH models do not match this. Also, Laird's investigation is the only found to date that considered thermal effects. Laird's results are a parametric study comparing gouges formed with slippers of various temperatures. Additionally, because Laird's slipper is much shorter than a real slipper (2" versus 8" but with the same thickness of 1"), the question remains as to how well the absolute values that are obtained in Laird's CTH model can be directly applied to the real sled system. Different results were obtained using Laird's model when the length of the slipper was extended with the same mesh cell size. This question also applies to all other hypervelocity gouging models. In other words, all these models initiate gouging, but how can the results be scaled so that they may be compared to the HHSTT or even a different model with different dimensions? The true value of these previous CTH models lies in comparing the effects of various parameters and in investigating phenomena rather than making direct comparison to the real system.

5. No CTH model to date contains rail roughness, which is used as a forcing function for the dynamic analysis of the DADS. The mitigation of gouging appears to have improved due to coating applications, but technological improvements in reducing tolerances and measuring rail roughness also occurred during this time period.

4.2 Proposed Improvements to the Model

Previous work has shown that a two-dimensional plane strain model is a reasonable model for gouging. The results of the study using the three-dimensional finite element code LS-DYNA3D are summarized here for convenience (see section 3.1). One purpose of that investigation was to determine whether a two-dimensional plane-strain model is sufficient to study the phenomenon of hypervelocity gouging. A three-dimensional slipper was used to impact on the flat top of a three-dimensional rail. This direct impact never created gouging phenomena; it became evident that an edge impact was more appropriate for the formation of the gouge and that a restricted plane strain condition was required for the initiation of gouging. This conclusion is supported by test data in which gouging occurs primarily at the corners of the rail and at other points in which a plane-strain condition

would occur in the three-dimensional model. The area of largest distortion for the mesh in the study occurred at the interaction between slipper and rail.

Examples of regions with plane strain conditions are impacts upon a rail misalignment, a reentrant corner of the rail, or a collision of the shoe due to roll or pitch. Compare this to the photograph of an actual gouge as shown in Figure 4.2. Otherwise, out-of-plane

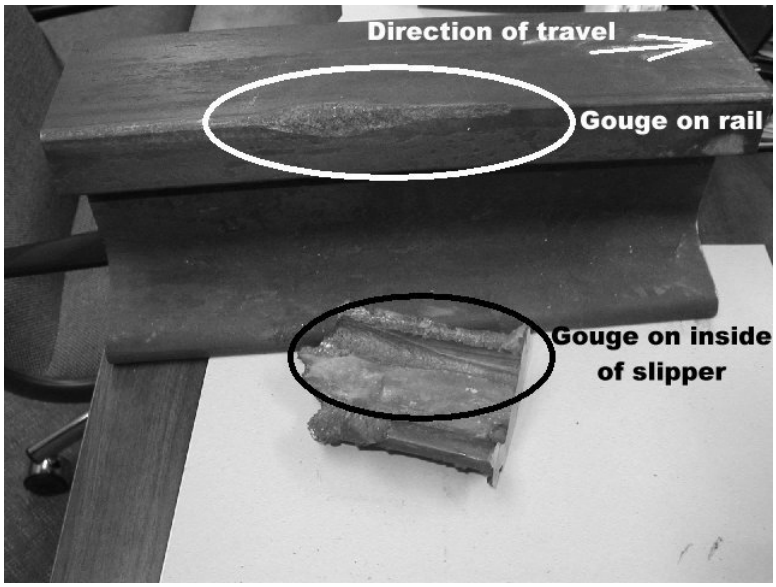

Figure 4.2 **Actual gouge at a reentrant corner of the rail in which a plane-strain condition likely exists at impact.**

deformations (as shown in Figures 3.2 and 3.3) allow the material to relax in such a manner that the stress field within the plane of impact is not sufficient to initiate a plastic zone large enough for gouging.

This leads one to a consideration of how best to simplify the actual three-dimensional HHSTT sled system so that it can be numerically investigated using CTH. By simplifying the actual sled system into a two-dimensional plane-strain model, results may be obtained that would apply to the actual system.

The rocket sled is simplified as shown in Figure 4.3. The test sled shown is of a narrow gauge rail configuration in which the test sled rides on two parallel rails. The test sled consists of the sled system (including the payload and other structures) and four slippers. The slippers attach the test sled structure to the rails. There are three major

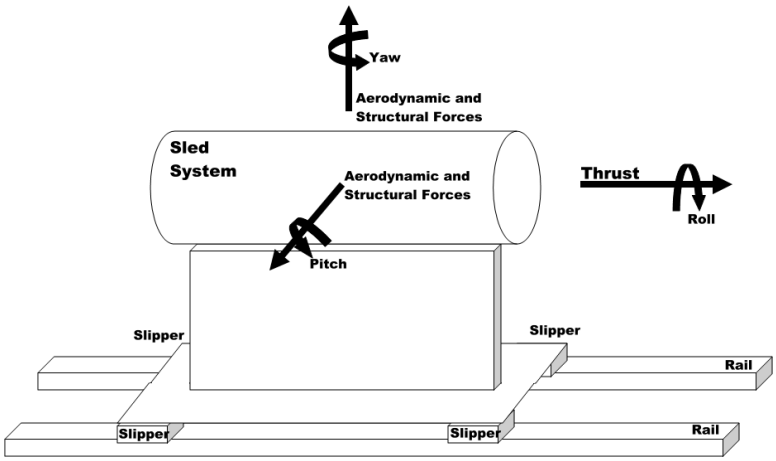

Figure 4.3 **Test sled schematic with motion axes.**

rotational directions of motion for the test sled: roll, pitch, and yaw. The three major axes of motion are due to thrust, aerodynamic forces, and structural forces such as vibration and inertial changes due to rail roughness (i.e., rail misalignments). Thrust accelerates the sled in the forward direction. Aerodynamic and structural forces such as vibration cause vertical and lateral motion of the sled as it is accelerated forward down the track.

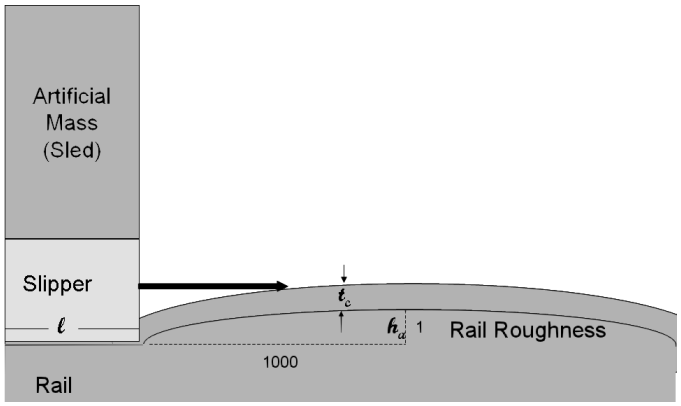

Figure 4.4 **Schematic of rail roughness, artificial sled system mass, coating, and the boundary layer.**

A sample rail roughness is shown in Figure 4.4. Rail roughness is defined as a change in geometry of the rail from prismatic, flat, and straight to some eccentricity with a large radius of curvature. The tolerance used at the HHSTT is a 0.05 inch high misalignment of the rail over a 50 inch span. This feature is simulated in this study as a 1 to 1000 ratio of

semi-minor axis to semi-major axis of a semi-elliptical projection of the rail in the path of the slipper. The figure shows a detail of one slipper with an artificial mass labelled as the sled system. This artificial sled system mass is attached to the slipper in order to simulate the sled mass that affects the slipper impact on the rail. The figure also shows a coating applied to the rail and rail roughness. Within the figure, one can also see the boundary layer. This is a thin layer of interaction between the slipper and either the coating or the rail, whichever material it is sliding against. Within this thin layer of cells, CTH applies the Boundary Layer algorithm which allows deviatoric stresses to form along the interface between the sliding materials. Normally, CTH would treat the sliding interface between materials as a fluid-like layer with no deviatoric component of stress.

If the test sled structure is not infinitely stiff, the slipper may undergo rotational accelerations and motion in the roll, pitch and yaw directions. If the slipper undergoes a rotation, a force couple is generated as a reaction to this motion when the slipper rotates through the gap between it and the slipper. The force couple acts opposite in direction to the rotation. The magnitudes of the coupled forces are dependent on the angular acceleration and inertial mass of the test sled that is imparted by the rotational motion. The impulse of the impact will be equivalent to the change in momentum of the slipper and the attached test sled upon impact.

For example, the conservation of momentum can be described by Newton's Law

$$F = ma = m\frac{dv}{dt} \tag{4.1}$$

where F is the force, m is the mass, and a is the acceleration.

The impulse-momentum law is then

$$I = \int F dt = \int m dv = mv_f - mv_i \tag{4.2}$$

where t is time, v_f is the final velocity, and v_i is the initial velocity of the impact. That is, the impulse, I is equivalent to the change in momentum, mv of a body.

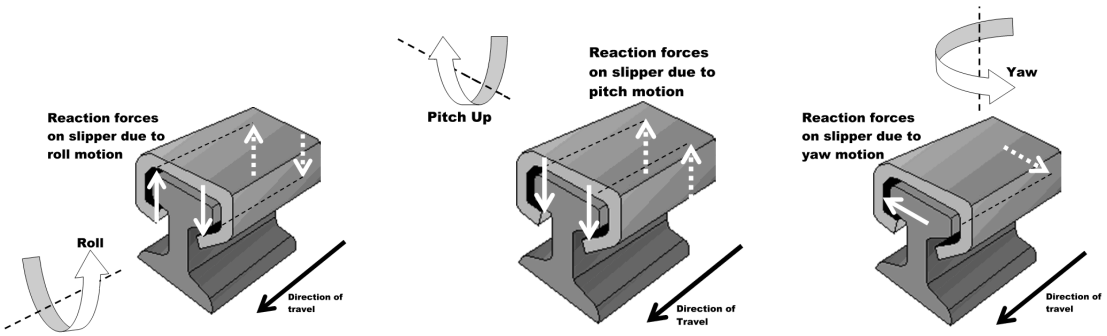

(a) Roll motion and reaction forces on slipper.

(b) Pitch motion and reaction forces on slipper.

(c) Yaw motion and reaction forces on slipper.

Figure 4.5 Rotations of the slipper and reaction forces.

Figure 4.5 shows an example of roll, pitch, and yaw of the slipper and the points of contact in which reaction forces occur. For the roll motion (as seen in Figure 4.5(a)), the reaction forces occur at the upper and lower rail corners in which observations have shown that rail gouges usually occur. In addition, these are points of plane-strain conditions.

If the slipper rotates upward in a pitch motion (as seen in Figure 4.5(b)), the reaction forces would result in point forces at the front bottom of the slipper-rail contact and the top back corners of the slipper-rail interaction. The slipper rotates through the slipper gap between the slipper and the rail until it contacts the corners of the rail. In some cases, depending on the motion of the slipper, these points of contact are the same as what would occur in a roll. This would effectively increase the force at the corners that the slipper and rail undergo.

Figure 4.5(c) shows that reaction forces on the slipper due to rotation in the yaw direction occur at the sides of the rail. Here too, observations of actual gouges indicate gouges most likely occur at these points. The slipper again is limited to rotations through the slipper gap until the slipper strikes the rail at the sides. If the slipper is given a component of yaw in addition to pitch and roll, the slipper could strike on the relatively sharp corner of the rail. These regions are all areas of plane strain because upon impact, the out of plane motion of the deformation is restricted. The inertial effects of the impact occur within a two-dimensional plane of action.

Figure 4.2 shows a real world example of such an occurrence. The gouge here started on the corner of the rail which seems to indicate both yaw and either or both roll and pitch motion along with the forward acceleration of the test sled. If this gouged rail is also a portion of the rail that is approximated by a rail roughness, the forces at impact would have been even greater in this area.

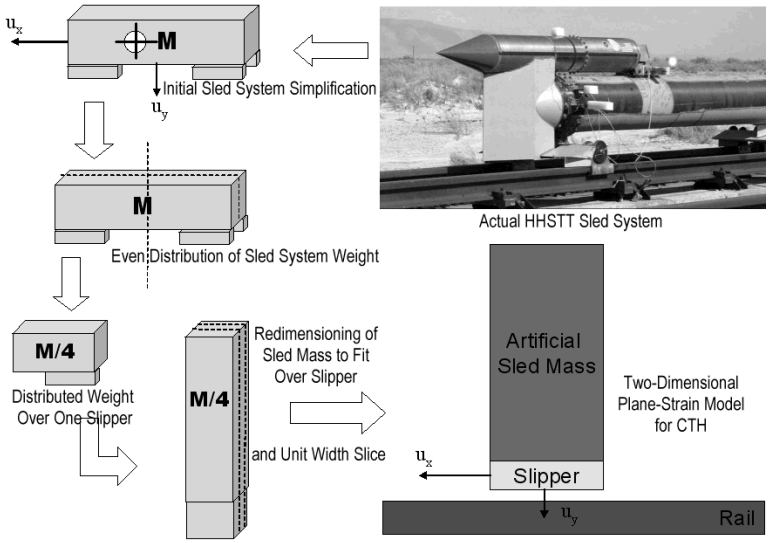

Figure 4.6 **Simplification of the HHSTT rocket sled system into a CTH computer model for dimensional and numerical analysis.**

The three-dimensional HHSTT sled system mass is simplified as a block of bulk material by taking the total mass of the sled system and payload (minus the slippers) and distributing it within a homogenous block of arbitrary dimensions (see Figure 4.6). This three-dimensional block is then divided evenly among the four slippers of a sample narrow gauge rail system (neglecting rotations of the sled system) and the body is assumed to translate in the vertical and horizontal directions only. Also, the center of mass is assumed to lie at the geometrical centroid of the artificial sled body.

The three-dimensional artificial sled quarter-mass is then re-dimensioned with an arbitrary material so that it lies directly over the slipper. The reasoning behind the use of an arbitrary material is that the user may select a material of high density to keep the dimensions of the artificial sled mass to a minimum and provide some relief to computational resources. Shock reflections at the top of the slipper at the interface with the

artificial sled system mass will be discussed later. A unit width of this three-dimensional sled-slipper system is then taken as a plane strain two-dimensional sled-slipper system. The resulting model is then translated into a computer model.

The model is transformed onto a two dimensional vertical plane so that the DADS vertical velocity may be used for the vertical impact velocity. However, actual gouges usually occur on the corners of the rail and not on top of the rail. Therefore, one must consider whether the model provides for the actual three dimensional impacts that occur including roll, pitch, and yaw. In any case, whether there is roll, pitch, or yaw, the horizontal velocity will not change. Also, any accelerations are small over the time period being considered so as to be almost zero.

Whatever the direction of impact, the plane strain "slice" being modeled accounts for a conservative approximation of the mass that plane strain section will see in terms of energy and momentum effects. This was shown in Laird's dissertation [7]. In essence, a three-dimensional model contains an impact of the sled system mass at some velocity vector along three axes. That impact can be characterized by resultant impact velocities normal to the rail and tangent to the rail within a two dimensional plane. The mass impacting at the velocity is still the slipper mass coupled with the sled system mass.

In other words, the kinetic energy and momentum the rail and slipper "feel" at impact are a function of velocity and the sled system mass whether it is due to roll, pitch, or yaw components. These velocities are reduced to a two dimensional impact within some plane. In both the three dimensional and the two dimensional models, the mass of the sled system is the mass that will be impacting the rail with the slipper acting as the transfer mechanism for the impact effects. The conclusions for a two dimensional plane-strain model should also apply to any three dimensional impact that is due to roll, pitch, or yaw.

Scaling methods may then be used to guide development of the two-dimensional plane strain model into a CTH input model[74]. Furthermore, the invariant products may be used as a set of qualitative guidelines to aid in applying CTH model results to other test sleds. They provide an indication of what parameters of the CTH simulation model need changed in order to better represent the particular dimensionality of a given test sled.

Once the three-dimensional actual HHSTT model is simplified into a two-dimensional plane-strain model, one must be concerned with how to best scale that model. For example, to what accuracy must one maintain actual material properties between models with differing geometries? What if the real dimensions based on the actual sled cannot be used in the numerical investigation because the number of mesh cells required for numerical accuracy are beyond the computational resources available? How may one compare results from previous models? Are previous models sufficient to accurately model the gouging phenomena and draw conclusions about how coatings and heat conduction affect gouging that can be applied to the actual HHSTT sled? How may one apply results from the numerical model in CTH to a real HHSTT sled system? These and other questions about scaling models and their results may be answered by performing a dimensional analysis of the HHSTT hypervelocity gouging problem.

4.3 The Buckingham Pi Theorem

Dimensional analysis is a process by which a model used to describe a physical system can be characterized by a number of invariant products. These invariants must remain constant (i.e., cannot vary) between models of varying parameters in order for the results to be comparable. This process has been in use for years and has provided such famous constants as the Reynolds number in aerodynamics. The process of performing a dimensional analysis is also instructive in that it highlights the important parameters in a physical problem and shows how these parameters are related. In this way it also provides a better understanding of the problem as a whole. The goal of a proper dimensional analysis, however, is to develop the invariant products that may be used to scale a model so that numerical results and experimental results can be applied and conclusions drawn about the actual physical structure.

The ultimate purpose of this specific dimensional analysis is to provide valuable input to a CTH model whose results can then be applied directly or through justified scaling to the real sled-slipper-rail system at the HHSTT. Thus, the final results of this dimensional analysis will be a model that is used to investigate the nonequilibrium thermodynamic environment and mitigation of gouging with coatings.

Dimensional analysis and similitude studies are based upon the fact that for a physical law to be valid, it must be dimensionally consistent. That is, the law cannot change if one uses a different set of units. For example, $F = ma$ is true whether one uses English or SI units. A physical law is said to be unit free if it is independent of the particular units chosen to express the dimensioned quantities, $\{q_i\}^m$ [75]. In other words, if a physical law is dimensionally consistent, it will not matter what system of units (i.e., SI, English, etc.) is used to describe it.

One means of dimensional analysis is the Buckingham Pi Theorem. In fact, the concept of dimensional consistency is based upon this theorem. The dimensional analysis of the hypervelocity gouging problem in this research uses the CTH algorithm and the conservation equations as the physical laws to be applied to the Buckingham Pi Theorem.

The Buckingham Pi Theorem states that if a physical law consists of a number of quantities, $\{q_i\}^m$ that have dimension and are products and powers of fundamental dimensions of $L_1, L_2, L_3, \ldots, L_n$ then the unit free physical law can be defined as

$$f(q_1, q_2, \ldots, q_m) = 0 \tag{4.3}$$

Any dimensioned quantity, q_i chosen must then be a function of the fundamental dimensions, L_n. Here now, is a fitting place to discuss the two approaches to the dimensional analysis that were taken and the corresponding physical laws that were used to describe the hypervelocity gouging problem.

In the *CTH blackbox* investigation, the hydrocode CTH is first used as the physical law to be evaluated. Thus, this first approach for the dimensional analysis is based on the CTH code with the initial intention of matching CTH results among models. To simplify the analysis, a time-scale was not accounted for.

If the physical law $f(q_1, q_2, \ldots, q_m) = 0$ is defined for the analysis to be $CTH(\rho_o, \sigma_y, \ldots) = 0$, it can be considered that the function CTH contains a variety of dimensioned quantities $q_i = q_1, q_2, \ldots, q_m$. For example, the first dimensioned quantity can be chosen to be $q_1 = \rho_o = \text{density} = L_1^{d_1} L_2^{d_2} = \frac{M}{L^3}$ where $M \equiv$ mass and $L \equiv$ length. In this case the

fundamental dimensions, $L_1, L_2, \ldots, L_n$ are $L_1 = M =$ mass and $L_2 = L =$ length. While the power of each fundamental quantity is $d_1 = 1$ and $d_2 = -3$.

The dimensioned quantities, q_i for the dimensional analysis of the CTH function are based on the dimensioned quantities that may be selected by the user as inputs either directly or indirectly (see Figure 4.7).

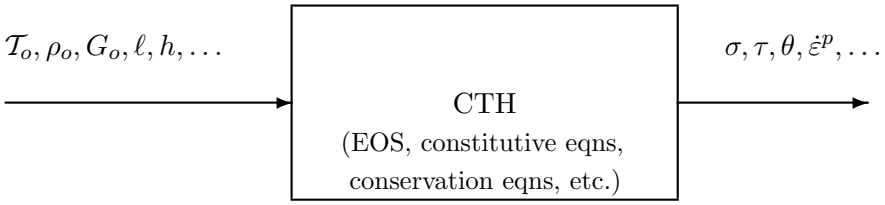

Figure 4.7 **CTH dimensioned quantities and dependent variables for dimensional analysis.**

The other approach applied to the dimensional analysis occurs from the point of view of the conservation equations as the physical law to be evaluated. For this *artificial sled mass* approach, a time-scale was calculated during the dimensional analysis and the sled mass is accounted for such that the mass of the impacting body is not solely dependent on the slipper dimensions and density. The conservation equations considered for this approach are the conservation of mass, momentum, and energy [76].

The integral form of the conservation of mass equation in Lagrangian coordinates can be expressed as

$$\frac{d}{dt}\int_{\beta_t} \rho dV = 0 \tag{4.4}$$

where t is the time, ρ is the mass density, β_t is the position the Lagrangian body occupies at time t, and V is the cell volume. This form of the equation states that the mass of the body does not change with time.

The conservation of momentum equation depicts momentum conservation theory in the form that the rate of change of momentum of a body is equal to the resultant of the applied forces. Thus,

$$\frac{d}{dt}\int_{\beta_t} \rho U dV = \int_{\partial\beta_t} n \cdot \underset{\sim}{\sigma} dA + \int_{\beta_t} \rho B dV \tag{4.5}$$

where U is the velocity, $\underset{\sim}{\sigma}$ is the stress tensor, $\partial\beta_t$ is the boundary of β_t, B is the body force per mass, n is the unit normal vector on the surface, and $\cdot$ is the dot product. This shows that the change of momentum with time (or force) is equal to the force resulting from the stress plus the change in momentum due to any body forces.

From the energy conservation principle, it follows that the rate of increase of energy of a body is equal to the rate at which the applied forces do work on the body. Therefore,

$$\frac{d}{dt}\int_{\beta_t} \rho E dV = \int_{\beta_t} \underset{\sim}{\sigma} \cdot \nabla U dV + \int_{\beta_t} S dV \tag{4.6}$$

where E is the specific internal energy and S is an internal energy source per volume per time. This equation shows that the change in energy per time results from the energy changes due to the stress field plus any energy sources. In other words, the change in energy is the amount of energy entering β_t minus the energy leaving plus internal sources.

The dimensional analysis utilizes dimensioned quantities for the above conservation equations that are not specific. That is, the internal energy and internal energy source dimensioned quantities are based on total dimensioned values. This is done because the CTH user has more direct control over the total quantities of energy, mass, etc. The dimensioned values are **not** depicted in the form of "per unit volume per unit time" for the dimensional analysis. The stress is considered as a dependent variable, not an independent variable directly controlled by the user. Total internal energy and energy source can be controlled by the user by defining mass, velocity, temperature, etc. In addition, body force per unit mass is considered negligible for this analysis since it is typically very small compared to the other forces of interest based on momentum.

Finally, for the dimensional analysis in both approaches, it is assumed that the slipper and rail have the same or similar material properties. Therefore, $\rho_o \equiv \rho_{slipper}, \rho_{rail}$ and $G_o \equiv G_{slipper}, G_{rail}$, etc. For simplicity, the analysis also begins *without considering the heat conduction solution.* However, the process may be accomplished with the appropriate heat conduction parameters if desired.

Strain rate effects are not accounted for in the dimensional analysis invariant products because models cannot be geometric similar and maintain strain rate similitude. Consider two geometrically similar models. Model B is geometrically twice the size of model A. That is, it has twice the length, twice, the height, and twice the width of Model A. For the models to meet scaling laws, their strains must be equivalent. However, the time scale for model B is twice the time scale for model A. It is thus impossible for the strains to be equivalent, the time scales to be different, and the strain rates (strain divided by time) to be equivalent. The strain rate in model B will be half the rate of model A. This will result in errors between these geometrically scaled models even when all other invariants are met. The smaller model in terms of geometric dimensions will have the higher strain rate.

The equation of state (EOS) and constitutive equations were considered in addition to the conservation equations. However, only independent quantities in the equations that added dimensionality to the problem were investigated. For example, in the Johnson-Cook viscoplastic constitutive equation, the current shear modulus, G is a function of original shear modulus, G_o and is calculated in the solution. Therefore, G_o is included in the dimensioned quantities, but G is not. G is considered as an internal dependent variable. The same is true of plastic strain rate, $\dot{\varepsilon}^p$ which is calculated within CTH but is required for the constitutive equations and affects both stress, σ and the change in velocity, ∂u. The Mie-Grüneisen EOS, Johnson-Cook constitutive equations, and Steinberg-Guinan-Lund constitutive equations were considered for this dimensional analysis.

Here is where, for example, one may need a different material with material properties that are consistent with the dimensional analysis. To compare results, one may plot the results in a contour plot for pressure or some other property for a new constitutive equation and compare it to the original. This effect can also be shown over time. One may also

compare a one dimensional analysis of results for various constitutive equations by varying constants in accordance with dimensional analysis time and length scales. This would provide a better understanding of how varying the constitutive equation constants affects the final results, as observed in contour plots.

Let us return to the general discussion of the Buckingham Pi Theorem. Any of the dimensioned quantities $q_i = f(L_n)_i$ can be written as a product of the fundamental dimensions to some power

$$q_i = [L_1^{d_1} L_2^{d_2} \cdots L_n^{d_n}]_i \tag{4.7}$$

and the physical law is equivalent to

$$F(\pi_1, \pi_2, \ldots, \pi_k) = 0 \tag{4.8}$$

If π is an invariant quantity made up of multiples and powers of the dimensioned quantities, q_i then

$$\pi = q_1^{\alpha_1} q_2^{\alpha_2} \cdots q_m^{\alpha_m} \tag{4.9}$$

$$\pi = [L_1^{d_1} L_2^{d_2} \cdots L_n^{d_n}]_1^{\alpha_1} [L_1^{d_1} L_2^{d_2} \cdots L_n^{d_n}]_2^{\alpha_2} \cdots [L_1^{d_1} L_2^{d_2} \cdots L_n^{d_n}]_m^{\alpha_m} \tag{4.10}$$

$$\pi = L_1^{\beta_1} L_2^{\beta_2} \cdots L_n^{\beta_n} \tag{4.11}$$

and it is shown that

$$\begin{Bmatrix} \beta_1 \\ \beta_2 \\ \vdots \\ \beta_n \end{Bmatrix} = \begin{bmatrix} d_{11} & d_{12} & \cdots & d_{1m} \\ d_{21} & d_{22} & \cdots & d_{2m} \\ \vdots & \vdots & \vdots & \vdots \\ d_{n1} & d_{n2} & \cdots & d_{nm} \end{bmatrix} \begin{Bmatrix} \alpha_1 \\ \alpha_2 \\ \vdots \\ \alpha_m \end{Bmatrix} \tag{4.12}$$

$$\underline{\beta} = [D]\underline{\alpha} \tag{4.13}$$

The set of all vectors for which $[D]\underline{\alpha} = \underline{0}$ is called the *null space* of $[D]$. The null space is the set of all solutions of the homogenous equation associated with $[D]$ [77]. $\underline{\alpha}$ must exist in the null space of the dimension matrix, $[D]$ for the physical law to be dimensionally

consistent. That is, $\underline{\beta} = [D]\underline{\alpha} = \underline{0}$. This is based upon the requirement that for a physical law to be valid, it must be unit free and the invariant product of its dimensioned quantities must be dimensionless. Thus, the exponents for each fundamental dimension must be equal to zero.

The Pi Theorem also states that if there are m dimensioned quantities, $\{q_i\}^m$ and r fundamental dimensions, $\{L_n\}$ then there are $k = m - r$ independent dimensionless quantities, π. In each case there will be $r = 3$ fundamental dimensions for M, L, and T where $M \equiv$ mass, $L \equiv$ length, and $T \equiv$ time. The number of quantities will change based on the model to be considered. The number of quantities will also be reduced further for each model when it is assumed that the material properties between models remain the same.

For example, in the first case to be considered in which there is a vibratory impact on an uncoated rail, there may be eight α_i quantities. By assuming that material properties remain constant between models, the number of α_i quantities can be reduced to five. This means there are $k = m - r = 5 - 3 = 2$ independent dimensionless products. This would provide two independent invariants, π_k that must be used to scale the geometry and impact velocity of the models.

The two approaches to dimensional analysis for the hypervelocity gouging problem in this research each consider varying situations. These situations were selected based on previous studies of the gouging problem and potential gouging scenarios at the HHSTT. The *CTH blackbox* dimensional analysis of the hypervelocity gouging problem is considered from a CTH algorithm "blackbox" point of view using four different cases:

1. Vibratory (oblique) impact of the slipper on a clean rail (no coating).
2. Asperity impact of the slipper with an uncoated rail (no vertical velocity).
3. Vibratory (oblique) impact on the rail with rail roughness where the roughness is defined as a large semi-elliptical asperity with a coating.
4. Vibratory (oblique) impact of a simplified sled system.

The last case for the *CTH blackbox* approach leads to the first case considered in the *artificial sled mass and time-scaled* approach using the conservation equations. The solution for the hypervelocity gouging problem in this approach regards four varying cases:

1. Impact of a simplified sled system at horizontal and vertical velocities (a.k.a. vibratory impact of a simplified sled system).
2. Vibratory impact of the slipper with an artificial mass (to simulate the sled mass effects) on a clean rail (i.e., no coating).
3. Horizontal impact of the slipper with an artificial mass (to simulate the sled mass effects) with an asperity.
4. Vibratory impact of the slipper with an artificial mass (to simulate the sled mass effects) on the rail with roughness, in which "roughness" is defined as a large semi-elliptical asperity with a coating.

The dimensional analysis begins with the *CTH blackbox* approach to the dimensional analysis problem but is applied only to the slipper. The dimensional analysis is accomplished in this manner so that the Laird model may be used to investigate the analysis and check that the results are reasonable and accurate. Because the Laird model does not contain an additional mass to simulate the sled system mass, this analysis begins by isolating the slipper from the sled system mass and neglecting the sled system mass effects for the gouging problem.

4.4 Dimensional Analysis of a Two-Dimensional Plane-Strain Slipper

The dimensional analysis begins by considering previous CTH models of the slipper and rail. The three cases analyzed in this section can be treated as variations of Tachau's [24, 25] oblique impact model, Laird's [7, 27, 28, 67] oblique impact model and both Barker [21, 22] and Schmitz's [1] asperity models. The last case in this section is a two-dimensional plane-strain case but contains rail roughness instead of a flat rail with an oblique impact or a circular asperity. This last case is an evolved version of both the oblique impact and asperity impact two-dimensional models. In all cases, the slipper material properties and

rail material properties are taken to be similar enough to make the addition of the rail material properties unnecessary.

Each case is a two-dimensional plane-strain model such as used by Laird in his work. Understanding this first dimensional analysis becomes an important step in the evolution of the dimensional analysis as a whole. Immediately after the dimensional analysis for all three cases, CTH is used to check the validity of the invariant products from the dimensional analysis.

The three cases for initiating hypervelocity gouging in the isolated slipper are considered without determining a time-scale in the dimensional analysis:

1. Oblique impact of the slipper on a clean rail (no coating).
2. Asperity impact of the slipper with an uncoated rail (no vertical velocity).
3. Oblique impact on the rail with rail roughness where the roughness is defined as a large semi-elliptical asperity with a coating.

These three cases are considered in the following sections in the same order as above. For this analysis, dimensioned quantities associated with heat conduction are not considered to keep the initial dimensional analysis less complex.

4.4.1 Dimensional Analysis of a Two-Dimensional Plane-Strain Vibratory Impact Initiator Using the CTH Blackbox Approach. This portion of the dimensional analysis considers a two-dimensional plane-strain slipper that impacts a similar rail at a shallow angle. Gouging initiates when the material at the high stress interface between the slipper and rail becomes plastic and the tangential motion of the interface causes the plastic rail and slipper materials to impinge on one another. This motion increases as the materials interact with one another and gouging develops. The gouge formed by this interaction begins smaller and increases as the slipper passes over the rail. Interaction stops when the slipper and rail are no longer in contact with one another. Figure 4.8 is a two-dimensional schematic of an oblique impact of the slipper and depicts the dimensioned quantities that are considered for the analysis.

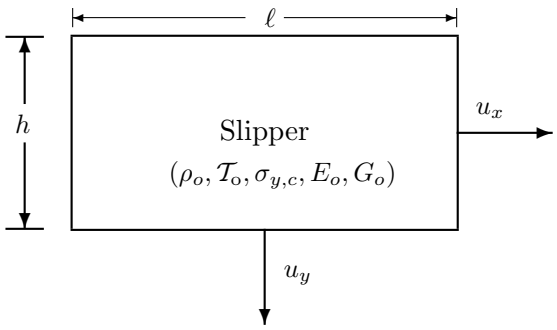

Figure 4.8 **Simplified model of a vibratory impacting slipper used for dimensional analysis.**

At this point, it is worthwhile repeating the Buckingham Pi Theorem with some emphasis. The Buckingham Pi Theorem states that if a *physical law* consists of a number of *dimensioned quantities*, $\{q_i\}^m$ (i.e., quantities that contain dimension) and are products and powers of *fundamental dimensions* or measurements of $L_1, L_2, L_3, \ldots, L_n$ then the unit free *physical law* can be defined as

$$f(q_1, q_2, \ldots, q_m) = 0 \tag{4.14}$$

Therefore, any *dimensioned quantity*, q_i chosen must be a function of the *fundamental dimensions*, L_n.

Thus, in order to apply the fact that a valid physical law must be true regardless of the unit system used, as stated by Buckingham's Pi Theorem, one must define the following for the problem under consideration:

- The *physical law* to be evaluated (in this case it is the CTH algorithm).
- The *dimensioned quantities* that make up the physical law.
- The *fundamental dimensions* or measurements that make up the dimensioned quantities.

Additionally, to ensure that one has a proper understanding of the physical law and the dimensioned quantities, it is important to correctly define the dependent and independent variables of the dimensioned quantities.

The dimensioned quantities chosen for the CTH algorithm model assume that the slipper and rail material properties are the same or nearly the same and include all those quantities the user may select as input for the CTH algorithm:

$\mathcal{T}_{\mathrm{o}}$ original temperature of the slipper, θ

ρ_o original density of the slipper, $\frac{M}{L^3}$

u_x horizontal velocity, $\frac{L}{T}$

u_y vertical velocity, $\frac{L}{T}$

ℓ slipper length, L

h slipper height, L

$\sigma_{y,c}$ critical slipper yield strength, $\frac{M}{LT^2}$

E_o original slipper elastic modulus, $\frac{M}{LT^2}$

G_o original slipper shear modulus, $\frac{M}{LT^2}$

The dimensions and material properties for the slipper are purposely labeled using different variables than the dimensions and material properties of the sled system. We use the subscript $_o$ to distinguish the material properties of the slipper from the material properties of the sled system. The dimensions of the slipper, ℓ and h are used to describe the length and height of the slipper as opposed to $\mathcal{L}$ and $\mathcal{H}$ for the sled system. This distinction between sled system and slipper properties is done to more accurately model the real sled system and slipper structures. In the real system, the sled and payload are very different in size and material properties than the slipper. G_o is a term contained in the constitutive equations. The quantity G changes with time, but is initially based on the G_o value. $\sigma_{y,c}$ is described as a critical stress because it is the stress at which yield is reached for the slipper material and is used in the constitutive equation to determine plasticity.

The fundamental dimensions based on the dimensioned quantities are:

θ temperature

M mass

L length

T time

The variables which do not depend on the dimensioned quantities input to CTH (i.e., independent variables) for the model are:

x horizontal axis position

y vertical axis position

z lateral axis position

t time

The variables which are characterized the dimensioned quantities input to CTH (i.e., dependent variables) for this model are considered to be the change in velocity (∂u), the plastic strain rate ($\dot{\varepsilon}^p$), the spherical stress field (σ), the deviatoric stress field (τ), and the temperature field (θ). These dependent variables are simply the results, or output, one obtains from CTH.

$$\begin{aligned}
\pi &= [\mathcal{T}_o]^{\alpha_1}[\rho]^{\alpha_2}[u_x]^{\alpha_3}[u_y]^{\alpha_4}[\ell]^{\alpha_5}[h]^{\alpha_6}[\sigma_{y,c}]^{\alpha_7}[E_o]^{\alpha_8}[G_o]^{\alpha_9} \\
\pi &= [\theta]^{\alpha_1}[M]^{\alpha_2+\alpha_7+\alpha_8+\alpha_9}[L]^{-3\alpha_2+\alpha_3+\alpha_4+\alpha_5+\alpha_6-\alpha_7-\alpha_8-\alpha_9}[T]^{-\alpha_3-\alpha_4-2\alpha_7-2\alpha_8-2\alpha_9} \\
\pi &= [\theta]^{\beta_1}[M]^{\beta_2}[L]^{\beta_3}[T]^{\beta_4} \qquad (4.15)
\end{aligned}$$

By equating the π equations and the powers for each fundamental dimension, one produces

$$\begin{aligned}
\beta_1 &= \alpha_1 = 0 \\
\beta_2 &= \alpha_2 + \alpha_7 + \alpha_8 + \alpha_9 = 0 \\
\beta_3 &= -3\alpha_2 + \alpha_3 + \alpha_4 + \alpha_5 + \alpha_6 - \alpha_7 - \alpha_8 - \alpha_9 = 0 \\
\beta_4 &= -\alpha_3 - \alpha_4 - 2\alpha_7 - 2\alpha_8 - 2\alpha_9 = 0
\end{aligned}$$

This can also be written in terms of a dimension matrix, $[D]$

$$\underline{\beta} = [D]\underline{\alpha} = \underline{0}$$

$$\underline{\beta} = \left[\begin{array}{c|cccccccc} 1 & 0 & 0 & 0 & 0 & 0 & 0 & 0 & 0 \\ \hline 0 & 1 & 0 & 0 & 0 & 0 & 1 & 1 & 1 \\ 0 & -3 & 1 & 1 & 1 & 1 & -1 & -1 & -1 \\ 0 & 0 & -1 & -1 & 0 & 0 & -2 & -2 & -2 \end{array}\right] \underline{\alpha} = \underline{0}$$

The dimension matrix can be reduced along the lines drawn within the dimension matrix above since the dimensioned quantity temperature, $\mathcal{T}_o$ is equivalent to the fundamental temperature dimension, θ. That is, all temperatures will be scaled by a critical temperature such as the melting temperature or room temperature, $\mathcal{T}_{o,c}$. Working in the null space of $[D]$ with the reduced dimension matrix it is found that,

$$\alpha_2 = -\alpha_7 - \alpha_8 - \alpha_9$$

$$\left\{\begin{array}{rcccccccccccccccc} 0 &=& & -3\alpha_2 & & + & \alpha_3 & + & \alpha_4 & + & \alpha_5 & + & \alpha_6 & - & \alpha_7 & - & \alpha_8 & - & \alpha_9 \\ 0 &=& -3(-\alpha_7 - \alpha_8 - \alpha_9) & & & + & \alpha_3 & + & \alpha_4 & + & \alpha_5 & + & \alpha_6 & - & \alpha_7 & - & \alpha_8 & - & \alpha_9 \\ 0 &=& & & & & \alpha_3 & + & \alpha_4 & + & \alpha_5 & + & \alpha_6 & + & 2\alpha_7 & + & 2\alpha_8 & + & 2\alpha_9 \end{array}\right.$$

Now, by adding the resulting equation to the one for $\beta_4 = 0$, one may obtain a solution for α_5 and α_6.

$$\left\{\begin{array}{rcccccccccccccc} 0 &=& \alpha_3 & + & \alpha_4 & + & \alpha_5 & + & \alpha_6 & + & 2\alpha_7 & + & 2\alpha_8 & + & 2\alpha_9 \\ 0 &=& -\alpha_3 & - & \alpha_4 & & & & & - & 2\alpha_7 & - & 2\alpha_8 & - & 2\alpha_9 \\ \hline 0 &=& & & & & \alpha_5 & + & \alpha_6 & & & & & & \end{array}\right.$$

$$
\begin{aligned}
\alpha_2 &= -\alpha_7 - \alpha_8 - \alpha_9 \\
\alpha_3 &= -\alpha_4 - 2\alpha_7 - 2\alpha_8 - 2\alpha_9 \\
\alpha_4 &= \alpha_4 \\
\alpha_5 &= -\alpha_6 \\
\alpha_6 &= \alpha_6 \\
\alpha_7 &= \alpha_7 \\
\alpha_8 &= \alpha_8 \\
\alpha_9 &= \alpha_9
\end{aligned}
$$

or

$$
\underline{\alpha} = \begin{Bmatrix} \alpha_2 \\ \alpha_3 \\ \alpha_4 \\ \alpha_5 \\ \alpha_6 \\ \alpha_7 \\ \alpha_8 \\ \alpha_9 \end{Bmatrix} = \begin{Bmatrix} 0 \\ -1 \\ 1 \\ 0 \\ 0 \\ 0 \\ 0 \\ 0 \end{Bmatrix} c_4 + \begin{Bmatrix} 0 \\ 0 \\ 0 \\ -1 \\ 1 \\ 0 \\ 0 \\ 0 \end{Bmatrix} c_6 + \begin{Bmatrix} -1 \\ -2 \\ 0 \\ 0 \\ 0 \\ 1 \\ 0 \\ 0 \end{Bmatrix} c_7 \tag{4.16}
$$

$$
+ \begin{Bmatrix} -1 \\ -2 \\ 0 \\ 0 \\ 0 \\ 0 \\ 1 \\ 0 \end{Bmatrix} c_8 + \begin{Bmatrix} -1 \\ -2 \\ 0 \\ 0 \\ 0 \\ 0 \\ 0 \\ 1 \end{Bmatrix} c_9
$$

in which the constants, c_i may be arbitrarily chosen to satisfy the equation. Because the function, $F(\pi_k) = 0$ the invariant, π_k must be equal to a constant such as $\pi_k = 1$.

Thus, the invariants are

$$\pi_k = \left(\frac{u_y}{u_x}\right)^{c_4} \left(\frac{h}{\ell}\right)^{c_6} \left(\frac{\sigma_{y,c}}{\rho_o u_x^2}\right)^{c_7} \left(\frac{E_o}{\rho_o u_x^2}\right)^{c_8} \left(\frac{G_o}{\rho_o u_x^2}\right)^{c_9} \tag{4.17}$$

Five invariants are required to adequately constrain the scaling between models. All these invariants must be simultaneously met in order for the scaling between models to be correct. If $c_4 = 1$ is chosen and all other constants, $c_i = 0$ then the first invariant is

$$\pi_1 = \frac{u_y}{u_x} \tag{4.18}$$

If $c_6 = 1$ is chosen and all other constants, $c_i = 0$ then the second invariant is

$$\pi_2 = \frac{h}{\ell} \tag{4.19}$$

If $c_7 = 1$ is chosen and all other constants, $c_i = 0$ then the third invariant is

$$\pi_3 = \frac{\sigma_{y,c}}{\rho_o u_x^2} \tag{4.20}$$

If $c_8 = 1$ is chosen and all other constants, $c_i = 0$ then the fourth invariant is

$$\pi_4 = \frac{E_o}{\rho_o u_x^2} \tag{4.21}$$

If $c_9 = 1$ is chosen and all other constants, $c_i = 0$ then the fifth invariant is

$$\pi_5 = \frac{G_o}{\rho_o u_x^2} \tag{4.22}$$

The invariants clearly show that for a two-dimensional plane-strain slipper impacting obliquely (i.e., $u_y \neq 0$), one must maintain invariants such as the velocity angle of impact and the height to length ratio of the slipper between models. In addition, if the horizontal

velocity changes between models, then the material properties (i.e., yield stress, elastic modulus, and shear modulus) must be appropriately scaled with a horizontal kinetic energy term of the slipper.

Note also that other more physically relevant forms of invariant parameters can be formed by simply multiplying invariants together. For example, one may choose $c_8 = 1$ and $c_9 = -1$ to obtain

$$\pi = \frac{E_o}{G_o}$$

This is of course, Poisson's ratio ν.

However, some ratios can be more "telling", such as

$$\pi = \frac{\sigma_{y,c}}{\rho_o u_y^2}$$

which would be the critical yield strength of the material compared to the vertical impact stress. This ratio can be obtained through a combination of invariants π_1 and π_3. It is just as valid as any of the above invariants but also has a slightly different physical meaning attached to it.

4.4.2 Dimensional Analysis of a Two-Dimensional Plane-Strain Asperity Impact Initiator Using the CTH Blackbox Approach. This portion of the dimensional analysis considers a two-dimensional plane-strain slipper that impacts a two-dimensional plane-strain asperity at a horizontal velocity. Gouging is initiated when the slipper impacts the asperity at a velocity that plasticizes it and deforms it as it also forces it into the rail. This process initiates a "jetting" interaction between the slipper and rail materials that cause the slipper and rail to deform permanently resulting in a teardrop shaped deformation. The gouge formed by this interaction is a function of the size of the asperity due to the impingement of the asperity into the rail. It is maximum at gouge initiation and decreases as the slipper passes over the rail. Gouging stops when the slipper and rail are no longer in contact with one another. In Figure 4.9 is a two-dimensional schematic of an asperity impact and the dimensioned quantities that are considered for the analysis.

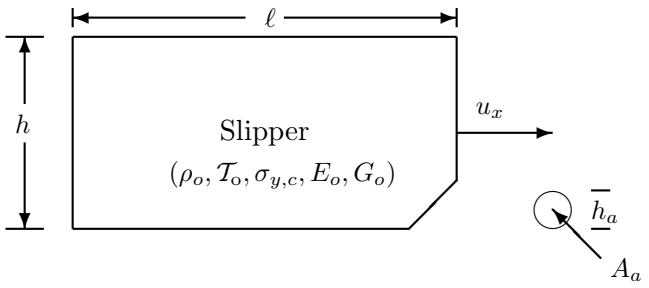

Figure 4.9 **Simplified model of an asperity impact used for dimensional analysis.**

The dimensioned quantities chosen for the model assume that the slipper and rail material properties are the same or nearly the same and include all those quantities the user may select as input for the CTH algorithm:

$\mathcal{T}_o$ original temperature of the slipper, θ

ρ_o original density of the slipper, $\frac{M}{L^3}$

u_x horizontal velocity, $\frac{L}{T}$

ℓ slipper length, L

h slipper height, L

$\sigma_{y,c}$ critical slipper yield strength, $\frac{M}{LT^2}$

E_o original slipper elastic modulus, $\frac{M}{LT^2}$

G_o original slipper shear modulus, $\frac{M}{LT^2}$

h_a asperity height, L

A_a cross-sectional area of the asperity, L^2

Note that the quantities A_a and h_a in this example are naturally related and are not independent of each other (i.e., $A_a = \pi \left[\frac{h_a}{2}\right]^2$). However, this natural relationship will not be used in this analysis since this dimensional analysis is building up to a generalized version in which there will not be a natural relationship between these quantities (see sections 4.4.3 and 4.5.5).

The fundamental dimensions based on the dimensional quantities are:

θ temperature

M mass

L length

T time

The independent variables for the model are:

x horizontal axis position

y vertical axis position

z lateral axis position

t time

The dependent variables for this model are considered to be the change in velocity (∂u), the plastic strain rate ($\dot{\varepsilon}^p$), the spherical stress field (σ), the deviatoric stress field (τ), and the temperature field (θ).

$$\begin{aligned}
\pi &= [\mathcal{I}_o]^{\alpha_1}[\rho_o]^{\alpha_2}[u_x]^{\alpha_3}[\ell]^{\alpha_4}[h]^{\alpha_5}[\sigma_{y,c}]^{\alpha_6}[E_o]^{\alpha_7}[G_o]^{\alpha_8}[h_a]^{\alpha_9}[A_a]^{\alpha_{10}} \\
\pi &= [\theta]^{\alpha_1}[M]^{\alpha_2+\alpha_6+\alpha_7+\alpha_8}[L]^{-3\alpha_2+\alpha_3+\alpha_4+\alpha_5-\alpha_6-\alpha_7-\alpha_8+\alpha_9+2\alpha_{10}}[T]^{-\alpha_3-2\alpha_6-2\alpha_7-2\alpha_8} \\
\pi &= [\theta]^{\beta_1}[M]^{\beta_2}[L]^{\beta_3}[T]^{\beta_4} \qquad (4.23)
\end{aligned}$$

By equating the π equations and the powers for each fundamental dimension, one produces

$$\begin{aligned}
\beta_1 &= \alpha_1 = 0 \\
\beta_2 &= \alpha_2 + \alpha_6 + \alpha_7 + \alpha_8 = 0 \\
\beta_3 &= -3\alpha_2 + \alpha_3 + \alpha_4 + \alpha_5 - \alpha_6 - \alpha_7 - \alpha_8 + \alpha_9 + 2\alpha_{10} = 0 \\
\beta_4 &= -\alpha_3 - 2\alpha_6 - 2\alpha_7 - 2\alpha_8 = 0
\end{aligned}$$

This can also be written in terms of a dimension matrix, $[D]$

$$\underline{\beta} = [D]\underline{\alpha} = \underline{0}$$

$$\underline{\beta} = \left[\begin{array}{c|cccccccccc} 1 & 0 & 0 & 0 & 0 & 0 & 0 & 0 & 0 & 0 \\ \hline 0 & 1 & 0 & 0 & 0 & 1 & 1 & 1 & 0 & 0 \\ 0 & -3 & 1 & 1 & 1 & -1 & -1 & -1 & 1 & 2 \\ 0 & 0 & -1 & 0 & 0 & -2 & -2 & -2 & 0 & 0 \end{array}\right] \underline{\alpha} = \underline{0}$$

The dimension matrix can be reduced along the lines drawn within the dimension matrix above since the dimensioned quantity temperature, $\mathcal{T}_o$ is equivalent to the fundamental temperature dimension, θ. Working in the null space of $[D]$ with the reduced dimension matrix the invariants produced are,

$$\pi_k = \left(\frac{h}{\ell}\right)^{c_5} \left(\frac{\sigma_{y,c}}{\rho_o u_x^2}\right)^{c_6} \left(\frac{E_o}{\rho_o u_x^2}\right)^{c_7} \left(\frac{G_o}{\rho_o u_x^2}\right)^{c_8} \left(\frac{h_a}{\ell}\right)^{c_9} \left(\frac{A_a}{\ell^2}\right)^{c_{10}} \tag{4.24}$$

Six invariants must be met simultaneously to adequately describe the scaling between models. If $c_5 = 1$ is chosen and all other constants, $c_i = 0$ then the first invariant is

$$\pi_1 = \frac{h}{\ell} \tag{4.25}$$

which is one of the invariants we found in the oblique impact case (see section 4.4.1).

If $c_6 = 1$ is chosen and all other constants, $c_i = 0$ then the second invariant is

$$\pi_2 = \frac{\sigma_{y,c}}{\rho_o u_x^2} \tag{4.26}$$

which is one of the invariants we found in the oblique impact case (see section 4.4.1).

If $c_7 = 1$ is chosen and all other constants, $c_i = 0$ then the third invariant is

$$\pi_3 = \frac{E_o}{\rho_o u_x^2} \tag{4.27}$$

which is one of the invariants we found in the oblique impact case (see section 4.4.1).

If $c_8 = 1$ is chosen and all other constants, $c_i = 0$ then the fourth invariant is

$$\pi_4 = \frac{G_o}{\rho_o u_x^2} \tag{4.28}$$

which is one of the invariants we found in the oblique impact case (see section 4.4.1).

If $c_9 = 1$ is chosen and all other constants, $c_i = 0$ then the fifth invariant is

$$\pi_5 = \frac{h_a}{\ell} \tag{4.29}$$

If $c_{10} = 1$ is chosen and all other constants, $c_i = 0$ then the sixth invariant is

$$\pi_6 = \frac{A_a}{\ell^2} \tag{4.30}$$

The results of this dimensional analysis show that when scaling between models for the CTH algorithm, important geometric properties such as slipper height, asperity height, and asperity area must be appropriately scaled with the length of the slipper. In addition, if the material properties of the slipper change, the kinetic energy of the slipper must also be changed accordingly. If, however, the velocity of the slipper changes, then the material properties must be scaled appropriately to maintain the invariant between material properties and impact stress of the slipper.

4.4.3 Dimensional Analysis of a Two-Dimensional Plane-Strain Vibratory Rail Roughness Impact Initiator Using the CTH Blackbox Approach. This last case for dimensional analysis begins with a simplified two-dimensional plane-strain model of the slipper obliquely impacting a rail misalignment. The system is simplified as shown in Figure 4.10.

The dimensioned quantities chosen for the model assume that the slipper and rail material properties are the same or nearly the same and include all those quantities the user may select as input for the CTH algorithm:

$\mathcal{T}_o$ original temperature of the slipper, θ

ρ_o original density of the slipper, $\frac{M}{L^3}$

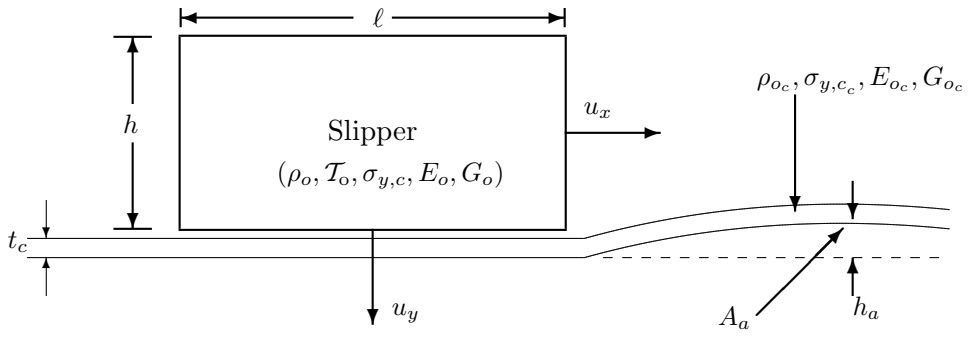

Figure 4.10 **Simplified model of a vibratory impacting slipper on a rail roughness with a coating for dimensional analysis.**

ρ_{o_c} original density of the coating, $\frac{M}{L^3}$

u_x horizontal velocity, $\frac{L}{T}$

u_y vertical velocity, $\frac{L}{T}$

ℓ slipper length, L

h slipper height, L

h_a asperity height, L

A_a cross-sectional area of the asperity, L^2

t_c coating thickness, L

$\sigma_{y,c}$ slipper critical yield strength, $\frac{M}{LT^2}$

σ_{y,c_c} coating critical yield strength, $\frac{M}{LT^2}$

G_o original slipper shear modulus, $\frac{M}{LT^2}$

G_{o_c} original coating shear modulus, $\frac{M}{LT^2}$

E_o original slipper elastic modulus, $\frac{M}{LT^2}$

E_{o_c} original coating elastic modulus, $\frac{M}{LT^2}$

The fundamental dimensions based on the dimensioned quantities are:

θ temperature

M mass

L length

T time

The independent variables for the model are:

x horizontal axis position

y vertical axis position

z lateral axis position

t time

The dependent variables for this model are considered to be the change in velocity (∂u), the plastic strain rate ($\dot{\varepsilon}^p$), the spherical stress field (σ), the deviatoric stress field (τ), and the temperature field (θ).

$$\begin{aligned}
\pi &= [\mathcal{T}_{\mathrm{o}}]^{\alpha_1}[\rho_o]^{\alpha_2}[\rho_{o_c}]^{\alpha_3}[u_x]^{\alpha_4}[u_y]^{\alpha_5}[\ell]^{\alpha_6}[h]^{\alpha_7}[h_a]^{\alpha_8}[A_a]^{\alpha_9}[t_c]^{\alpha_{10}} \\
&\quad [\sigma_{y,c}]^{\alpha_{11}}[\sigma_{y,c_c}]^{\alpha_{12}}[G_o]^{\alpha_{13}}[G_{o_c}]^{\alpha_{14}}[E_o]^{\alpha_{15}}[E_{o_c}]^{\alpha_{16}} \\
\pi &= [\theta]^{\alpha_1}[M]^{\alpha_2+\alpha_3+\alpha_{11}+\alpha_{12}+\alpha_{13}+\alpha_{14}+\alpha_{15}+\alpha_{16}} \\
&\quad [L]^{-3\alpha_2-3\alpha_3+\alpha_4+\alpha_5+\alpha_6+\alpha_7+\alpha_8+2\alpha_9+\alpha_{10}-\alpha_{11}-\alpha_{12}-\alpha_{13}-\alpha_{14}-\alpha_{15}-\alpha_{16}} \\
&\quad [T]^{-\alpha_4-\alpha_5-2\alpha_{11}-2\alpha_{12}-2\alpha_{13}-2\alpha_{14}-2\alpha_{15}-2\alpha_{16}} \\
\pi &= [\theta]^{\beta_1}[M]^{\beta_2}[L]^{\beta_3}[T]^{\beta_4} \qquad (4.31)
\end{aligned}$$

By equating the π equations and the powers for each fundamental dimension, one produces

$$\begin{aligned}
\beta_1 &= \alpha_1 = 0 \\
\beta_2 &= \alpha_2 + \alpha_3 + \alpha_{11} + \alpha_{12} + \alpha_{13} + \alpha_{14} + \alpha_{15} + \alpha_{16} = 0 \\
\beta_3 &= -3\alpha_2 - 3\alpha_3 + \alpha_4 + \alpha_5 + \alpha_6 + \alpha_7 + \alpha_8 + 2\alpha_9 \\
&\quad +\alpha_{10} - \alpha_{11} - \alpha_{12} - \alpha_{13} - \alpha_{14} - \alpha_{15} - \alpha_{16} = 0 \\
\beta_4 &= -\alpha_4 - \alpha_5 - 2\alpha_{11} - 2\alpha_{12} - 2\alpha_{13} - 2\alpha_{14} - 2\alpha_{15} - 2\alpha_{16} = 0
\end{aligned}$$

This can also be written in terms of a dimension matrix, $[D]$

$$\underline{\beta} = [D]\underline{\alpha} = \underline{0}$$

$$\underline{\beta} = \left[\begin{array}{c|ccccccccccccccc} 1 & 0 & 0 & 0 & 0 & 0 & 0 & 0 & 0 & 0 & 0 & 0 & 0 & 0 & 0 & 0 \\ \hline 0 & 1 & 1 & 0 & 0 & 0 & 0 & 0 & 0 & 0 & 1 & 1 & 1 & 1 & 1 & 1 \\ 0 & -3 & -3 & 1 & 1 & 1 & 1 & 2 & 1 & -1 & -1 & -1 & -1 & -1 & -1 & -1 \\ 0 & 0 & 0 & -1 & -1 & 0 & 0 & 0 & 0 & -2 & -2 & -2 & -2 & -2 & -2 & -2 \end{array}\right] \underline{\alpha} = \underline{0}$$

The dimension matrix can be reduced along the lines drawn within the dimension matrix above since the dimensioned quantity temperature, $\mathcal{T}_o$ is equivalent to the fundamental temperature dimension, θ. Working in the null space of $[D]$ with the reduced dimension matrix the solution for the invariants is,

$$\begin{aligned} \pi_k = & \left(\frac{\rho_{o_c}}{\rho_o}\right)^{c_3} \left(\frac{u_y}{u_x}\right)^{c_5} \left(\frac{h}{\ell}\right)^{c_7} \left(\frac{h_a}{\ell}\right)^{c_8} \left(\frac{A_a}{\ell^2}\right)^{c_9} \left(\frac{t_c}{\ell}\right)^{c_{10}} \\ & \left(\frac{\sigma_{y,c}}{\rho_o u_x^2}\right)^{c_{11}} \left(\frac{\sigma_{y,c_c}}{\rho_o u_x^2}\right)^{c_{12}} \left(\frac{G_o}{\rho_o u_x^2}\right)^{c_{13}} \left(\frac{G_{o_c}}{\rho_o u_x^2}\right)^{c_{14}} \left(\frac{E_o}{\rho_o u_x^2}\right)^{c_{15}} \left(\frac{E_{o_c}}{\rho_o u_x^2}\right)^{c_{16}} \end{aligned} \tag{4.32}$$

Twelve invariants must be simultaneously satisfied to adequately describe the scaling between models. If $c_3 = 1$ is chosen and all others are equal to zero, then the first invariant is

$$\pi_1 = \frac{\rho_{o_c}}{\rho_o} \tag{4.33}$$

If $c_5 = 1$ is chosen and all others are equal to zero, then the second invariant is

$$\pi_2 = \frac{u_y}{u_x} \tag{4.34}$$

which is one of the invariants we found in the oblique impact case (see section 4.4.1). This says that the velocity vector between models must remain constant.

If $c_7 = 1$ is chosen and all others are equal to zero, then the third invariant is

$$\pi_3 = \frac{h}{\ell} \tag{4.35}$$

which is another of the invariants we found in the oblique impact case (see section 4.4.1). This says that the height to length ratio of the slipper must remain constant.

If $c_8 = 1$ is chosen and all others are equal to zero, then the fourth invariant is

$$\pi_4 = \frac{h_a}{\ell} \tag{4.36}$$

which is one of the invariants we found in the asperity impact case (see section 4.4.2). This says that the rail roughness height must be scaled with the slipper length.

If $c_9 = 1$ is chosen and all others are equal to zero, then the fifth invariant is

$$\pi_5 = \frac{A_a}{\ell^2} \tag{4.37}$$

which is also one of the invariants we found in the asperity impact case (see section 4.4.2). This says that the rail roughness cross sectional area must be scaled with the square of the slipper length.

If $c_{10} = 1$ is chosen and all others are equal to zero, then the sixth invariant is

$$\pi_6 = \frac{t_c}{\ell} \tag{4.38}$$

This says that the coating thickness must be scaled with the slipper length as we scale between models.

If $c_{11} = 1$ is chosen and all other constants, $c_i = 0$ then the seventh invariant is

$$\pi_7 = \frac{\sigma_{y,c}}{\rho_o u_x^2} \tag{4.39}$$

which is one of the invariants we found in the oblique impact case (see section 4.4.1).

If $c_{12} = 1$ is chosen and all other constants, $c_i = 0$ then the eighth invariant is

$$\pi_8 = \frac{\sigma_{y,c_c}}{\rho_o u_x^2} \tag{4.40}$$

If $c_{13} = 1$ is chosen and all other constants, $c_i = 0$ then the ninth invariant is

$$\pi_9 = \frac{G_o}{\rho_o u_x^2} \tag{4.41}$$

which is one of the invariants we found in the oblique impact case (see section 4.4.1).

If $c_{14} = 1$ is chosen and all other constants, $c_i = 0$ then the tenth invariant is

$$\pi_{10} = \frac{G_{o_c}}{\rho_o u_x^2} \tag{4.42}$$

If $c_{15} = 1$ is chosen and all other constants, $c_i = 0$ then the eleventh invariant is

$$\pi_{11} = \frac{E_o}{\rho_o u_x^2} \tag{4.43}$$

which is one of the invariants we found in the oblique impact case (see section 4.4.1).

If $c_{16} = 1$ is chosen and all other constants, $c_i = 0$ then the twelfth invariant is

$$\pi_{12} = \frac{E_{o_c}}{\rho_o u_x^2} \tag{4.44}$$

The results of this dimensional analysis show that when scaling between coated rail roughness models for the CTH algorithm, important geometric properties such as slipper height, asperity height, coating thickness, and asperity area must be appropriately scaled with the length of the slipper. In addition, if the material properties of the slipper or coating change, the kinetic energy of the slipper must also be changed accordingly. If, however, the velocity of the slipper changes, then the material properties of the slipper and coating must be scaled appropriately to maintain the invariant between these material properties and the impact stress of the slipper.

4.4.4 Results of a Dimensional Analysis Study of the Slipper Using the CTH Black-box Approach. The dimensional analysis of the slipper from a *time exclusion* CTH algorithm-based approach is investigated. The results for the Laird model with original dimensions is compared to the results of a Laird model scaled by twice the size in accor-

dance with invariant parameters from the dimensional analyses of sections 4.4.1 and 4.4.3. For numerical analysis of the rail roughness case, a coating is not added at this time, but the ultimate goal of the research is to study coatings. This is done to obtain a better grasp of the parameters before unnecessarily complicating the problem.

4.4.4.1 Oblique Impact Results for the Slipper using the CTH Blackbox Approach. The oblique impact is first studied. The invariants listed in section 4.4.1 must remain constant between both models to be compared. In this study, the original Laird model with original slipper dimensions of 4.37 cm length and 2.54 cm height is compared to a model of dimensions twice the length and height of the original. The material properties remain the same between models and the horizontal and vertical impact velocities also remain the same. Thus, the invariants (that begin on page 4-25) take on the following values:

- $\pi_1 = \frac{u_y}{u_x} = \frac{50m/s}{2000m/s} = 0.025$ for both models.
- $\pi_2 = \frac{h}{\ell} = \frac{2.54cm}{4.37cm} = \frac{5.08cm}{8.74cm} = 0.581236$
- $\pi_3 = \frac{\sigma_{y,c}}{\rho_o u_x^2}$ remains the same between models because material properties do not change between models and the same horizontal velocity is also used.
- $\pi_4 = \frac{E_o}{\rho_o u_x^2}$ remains the same between models because material properties do not change between models and the same horizontal velocity is also used.
- $\pi_5 = \frac{G_o}{\rho_o u_x^2}$ remains the same between models because material properties do not change between models and the same horizontal velocity is also used.

Theoretically, since each invariant is satisfied, this means the results of the models will be consistent with each other.

The two models used in this study are shown in Figure 4.11.

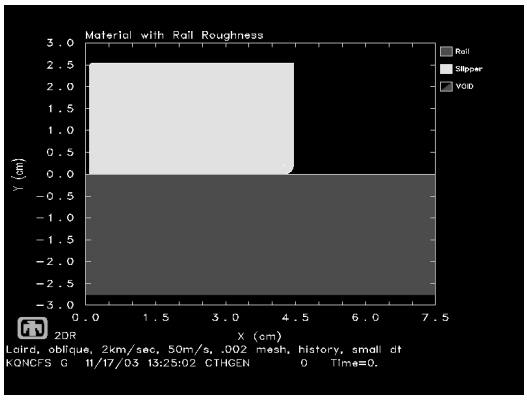

(a) **Laird model with original dimensions.**

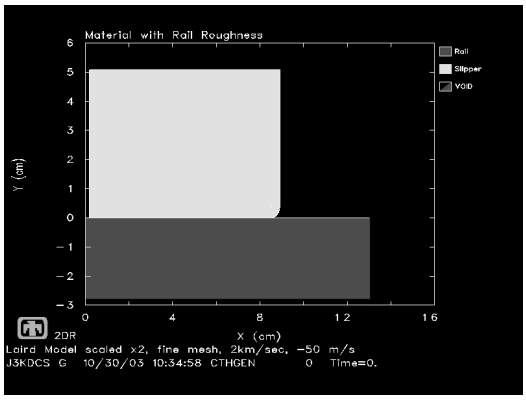

(b) **Laird model with dimensions scaled up by twice the original dimensions.**

Figure 4.11 **Laird original model and 2x scaled Laird model.**

The results based on material plots are shown in Figure 4.12. Note that the results for 6 μ-seconds in Figures 4.12(a) and 4.12(c) do not match. However, at half the time in the original Laird model (see Figure 4.12(b)), the results can be shown to match. This indicates that the dimensional analysis approach is incomplete and further analysis is required. In other words, a time-scale is required to match results between different models. In the dimensional analysis of the following sections, the time-scale is found to be $t = \frac{\ell}{u_x}$. This is the time for the slipper to travel its length. For example, if $\ell_1 = \ell$ and $t_1 = t$ then for $\ell_2 = 2\ell$, $t_2 = 2t$. If one uses this time-scale to modify the results, one then sees much better matching between model results.

As an illustrative example, look at Figure 4.13. The time history at an appropriately scaled point between the models is traced and plotted for pressure. The point selected is located at the center of the circular lower leading edge of the slipper. The time-scale indicates that one unit of non-dimensionally scaled time in the original Laird model equates to two units of non-dimensionally scaled time in the scaled up version of the Laird model. Once this is taken into consideration, it is shown that the results match more closely.

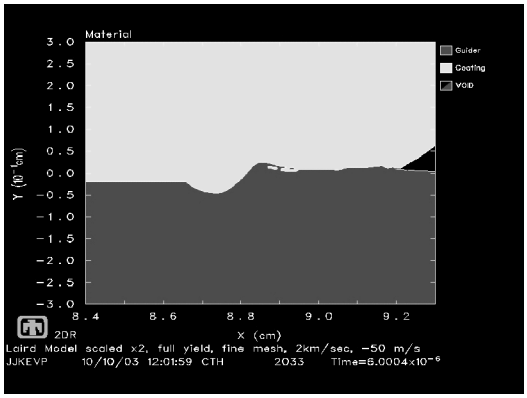

(a) **Material plot of results for 2x scaled Laird model at 6 microseconds.**

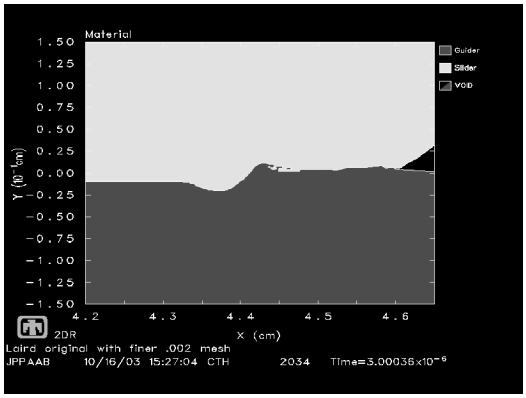

(b) **Material plot of results for original Laird model at 3 microseconds.**

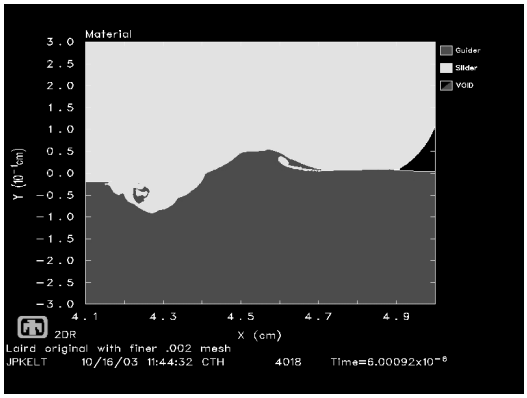

(c) **Material plot of results for original Laird model at 6 microseconds.**

Figure 4.12 **Comparison of Laird original model to 2x scaled model for oblique impact.**

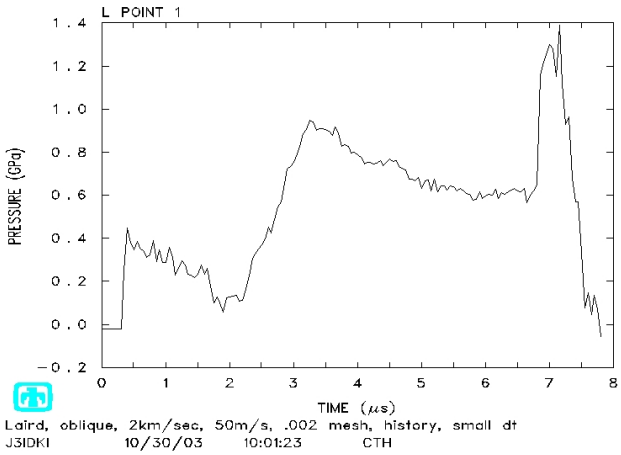

(a) **Time-scaled history plot of pressure for Laird model.**

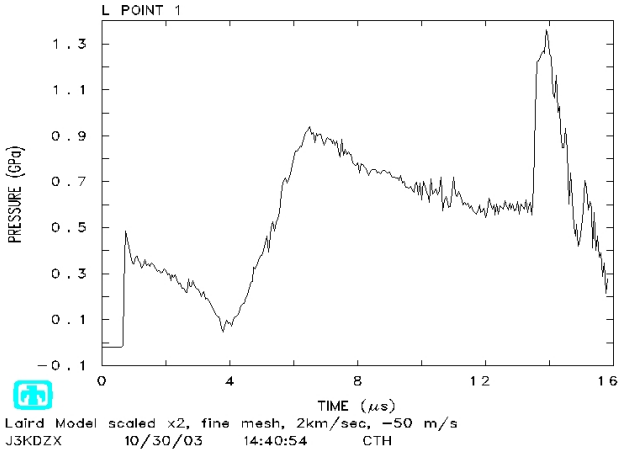

(b) **Time-scaled history plot of pressure for the 2x scaled Laird model.**

Figure 4.13 **Time history comparison of Laird original model to 2x scaled model pressure for oblique impact.**

4.4.4.2 Rail Roughness Impact Results for the Slipper using the CTH Blackbox Approach. For the rail roughness case, a similar investigation is performed. The invariants listed in section 4.4.3 must remain constant between both models to be compared. In this study, the original Laird model with original slipper dimensions of 4.37 cm length and 2.54 cm height is compared to a model of dimensions twice the length and height of the original. The material properties remain the same between models and the horizontal and vertical impact velocities also remain the same. Thus, the invariants (that begin on page 4-33) take on the following values:

- $\pi_1 = \frac{\rho_{o_c}}{\rho_o} = 0$ for both models since this investigation does not consider a coating.
- $\pi_2 = \frac{u_y}{u_x} = \frac{50m/s}{2000m/s} = 0.025$ for both models.
- $\pi_3 = \frac{h}{\ell} = \frac{2.54cm}{4.37cm} = \frac{5.08cm}{8.74cm} = 0.581236$
- $\pi_4 = \frac{h_a}{\ell} = \frac{0.03cm}{4.37cm} = \frac{0.06cm}{8.74cm} = 0.00686$
- $\pi_5 = \frac{A_a}{\ell^2} = \frac{3.1414593/4 \cdot 2.75 \cdot 0.03cm^2}{4.37^2cm^2} = \frac{3.1414593/4 \cdot 5.5 \cdot 0.06cm^2}{8.74^2cm^2} = 0.00339$
- $\pi_6 = \frac{t_c}{\ell} = 0$ for both models since this investigation does not consider a coating.
- $\pi_7 = \frac{\sigma_{y,c}}{\rho_o u_x^2}$ remains the same between models because material properties do not change between models and the same horizontal velocity is also used.
- $\pi_8 = \frac{\sigma_{y,c_c}}{\rho_o u_x^2} = 0$ for both models since this investigation does not consider a coating.
- $\pi_9 = \frac{E_o}{\rho_o u_x^2}$ remains the same between models because material properties do not change between models and the same horizontal velocity is also used.
- $\pi_{10} = \frac{E_{o_c}}{\rho_o u_x^2} = 0$ for both models since this investigation does not consider a coating.
- $\pi_{11} = \frac{G_o}{\rho_o u_x^2}$ remains the same between models because material properties do not change between models and the same horizontal velocity is also used.
- $\pi_{12} = \frac{G_{o_c}}{\rho_o u_x^2} = 0$ for both models since this investigation does not consider a coating.

Theoretically, since each invariant is satisfied, this means the results of the models will be consistent with each other.

The two models used in this study are shown in Figure 4.14.

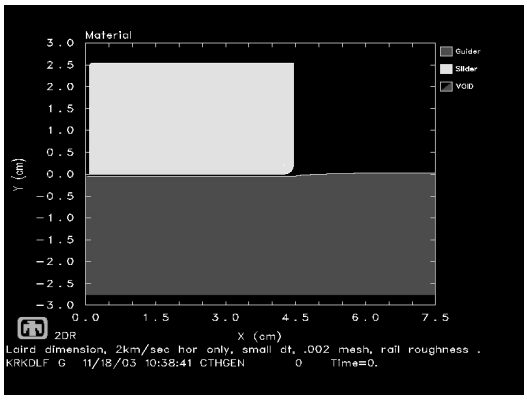

(a) **Laird model with original dimensions and the addition of a 0.03 cm high elliptically shaped rail roughness.**

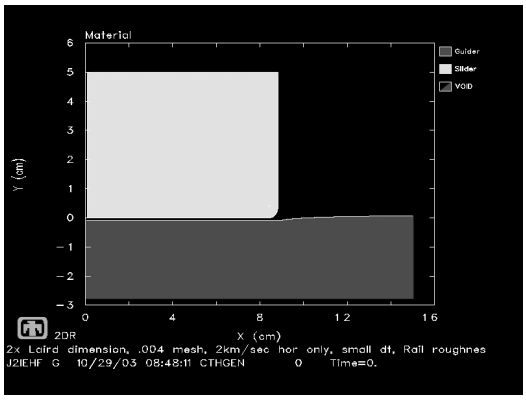

(b) **Laird model with dimensions and rail roughness scaled up by twice the original dimensions.**

Figure 4.14 **Comparison of Laird original model with rail roughness to 2x scaled model.**

Observe that even when a time-scale factor is taken into account however, the results do not match exactly. For example, theoretically, the results for the original Laird model at 8 μ-seconds should match the results for the scaled up version at 16 μ-seconds. Instead the results match better at 15 μ-seconds as shown in Figures 4.15(a), 4.15(d), and 4.15(e).

One can see more of a difference in the time history plot of the pressure for the point located at the center of the circular lower leading edge of the slipper in each model for the rail roughness case (Figure 4.16). Even on the correct time-scale, the results are a bit different. These differences can again be explained due to inadvertently omitted dimensioned quantities buried within the CTH algorithm.

Despite these differences, it is heartening to note that the pressure solutions for both cases are almost exact up to some point in non-dimensionally scaled time. For instance, the pressure results for the selected point in both models for the oblique impact are nearly identical up to 7 time-scaled units (7 μ-seconds in the Laird model and 14 μ-seconds in the scaled up model). Even in the rail roughness model, the pressure results are nearly the same again up to 7 time-scaled units.

These results lead to a number of conclusions. First, time is an important factor that must be considered on the dimensional analysis. There must be some time-scale that

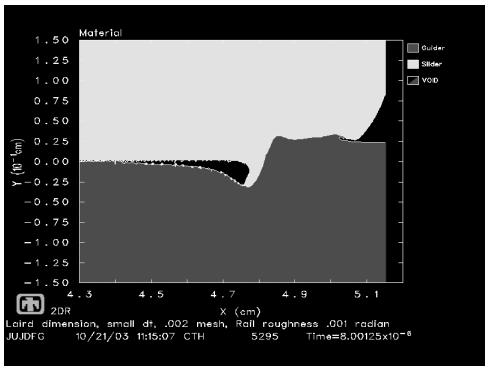

(a) **Material plot of results for original Laird model with rail roughness at 8 microseconds.**

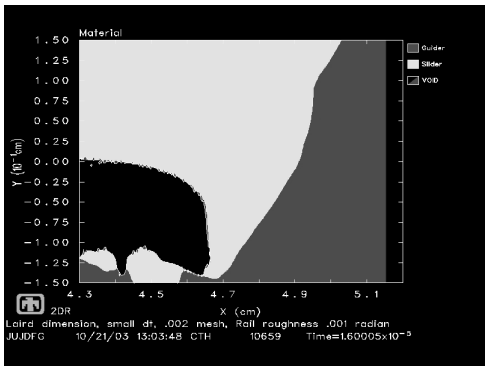

(b) **Material plot of results for original Laird model with rail roughness at 16 microseconds.**

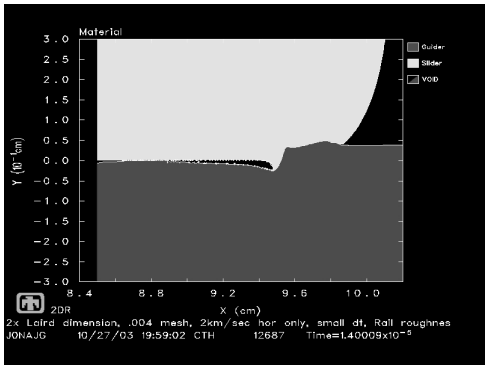

(c) **Material plot of results for 2x scaled Laird model with rail roughness at 14 microseconds.**

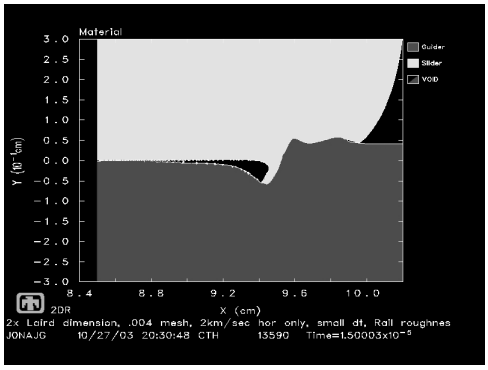

(d) **Material plot of results for 2x scaled Laird model with rail roughness at 15 microseconds.**

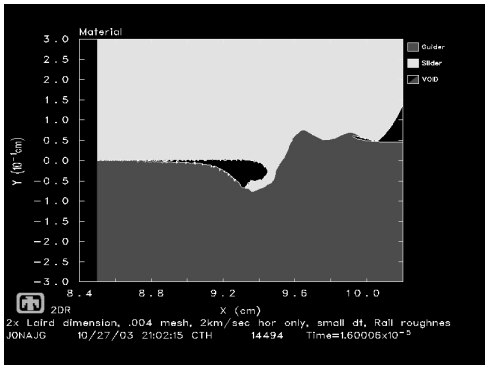

(e) **Material plot of results for 2x scaled Laird model with rail roughness at 16 microseconds.**

Figure 4.15 **Comparison of Laird original model to 2x scaled model for rail roughness impact.**

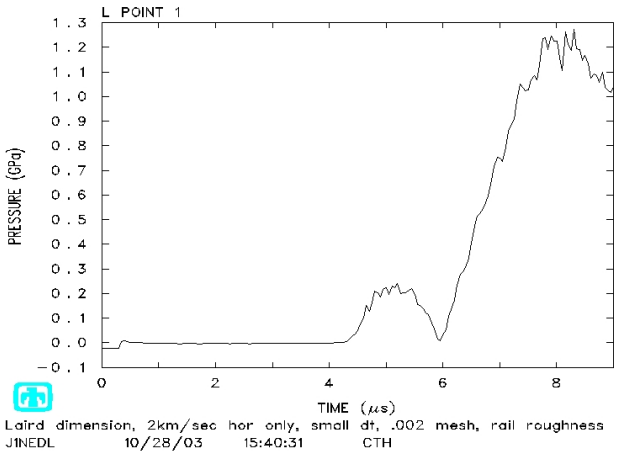

(a) **Time-scaled history plot of pressure for Laird model.**

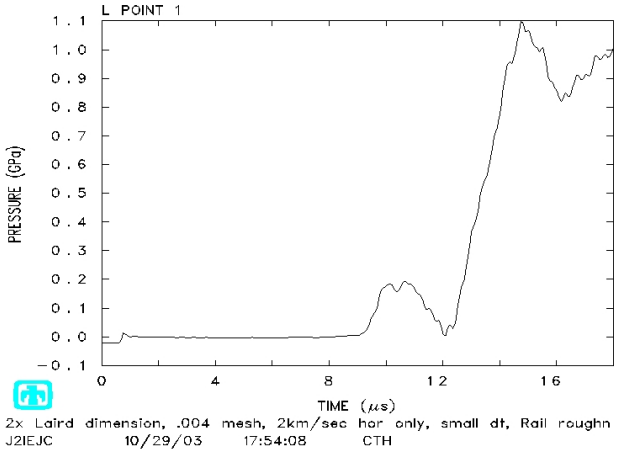

(b) **Time-scaled history plot of pressure for the 2x scaled Laird model.**

Figure 4.16 **Time history comparison of Laird original model to 2x scaled model pressure for rail roughness impact.**

can be used to nondimensionalize the time so that results between models can be properly compared to one another. Intuitively, the time for the scaled up model was also "scaled up". After this "scaling up" in time, the results were found to match very well for the oblique impact case. However, when the rail roughness case was considered, accounting for time intuitively allowed the comparison to be close, but there was still some amount of difference. Specifically, it was shown that the results for the rail roughness model with original dimensions at 8 microseconds compared best with the twice scaled up model at 15 microseconds rather than 16 microseconds as would be expected from the results for the oblique case.

Clearly, this shows that time is not the only factor that is lacking in the previous dimensional analysis approach. What is needed in the subsequent dimensional analysis is to:

1. Determine a time-scale that can be used to nondimensionalize the time and properly compare results between models. This time scale also needs to be implemented within the CTH algorithms (e.g., the constitutive model)
2. Consider an approach that allows for more dimensioned quantities in the invariants that may be used to adjust the models and possibly improve comparisons.
3. Consider an approach that also allows for consideration of the sled system mass and its effects. Up to this point, only the slipper has been considered for the dimensional analysis.

The following sections are an attempt to improve the dimensional analysis by addressing the concerns listed above and to fill in the gaps of the previous dimensional analysis. As such, the next section first addresses a dimensional analysis of the sled system from a CTH "blackbox" perspective in order to investigate its affect on the invariants. To address the time-scale and to increase the number of dimensioned quantities, the conservation equations are considered for the dimensional analysis. The analysis of the homogenous sled system is used as a *segue* to a heterogenous sled using the conservation equations in which a slipper and sled are allowed to possess different material properties. This eventu-

ally culminates in the case in which a slipper with an artificial sled mass and a time-scale factor is considered for dimensional analysis with rail roughness and a coating.

4.5 Dimensional Analysis of the Sled System

Having performed a dimensional analysis of the slipper using the *CTH blackbox* analysis of the CTH algorithm, it was found that the dimensional analysis requires a time-scale in order to correctly compare results between geometrically-scaled models. Consequently, an *artificial sled mass* dimensional analysis of the sled system and slipper include determination of this time-scale. To ensure that the dimensional analysis is complete, an evolving model is used. First, the sled system is analyzed as a homogenous entity without specifically distinguishing the slipper as a separate entity. This builds on the *CTH blackbox* dimensional analysis approach used in sections 4.4.1, 4.4.2, and 4.4.3 as the physical law of quantities.

The invariants from the sled system analysis were found to be similar to the previous *CTH blackbox* cases of the slipper. A new approach, which used the conservation equations and also regarded the constitutive equations and equations of state, was used. The sled system was analyzed using the conservation equations as the law of quantities and a time-scale calculated. The next step in this process was to define the slipper as a separate entity to the sled system with its own material properties and repeat the time-scaled approach. Thus, the approach may be described as an *artificial sled mass* approach.

There are two trains of thought here that must be pointed out. The first is that time is an important parameter that must be considered for making comparisons between various models. The second is that even when time is accounted for, there may still be errors or differences in the results because strain rate effects are not accounted for between geometrically similar models. The key is to consider all the important ones. To minimize or mitigate these errors, the dimensional analysis is introduced using the conservation equations so that better control over the model might be had.

The *artificial sled mass* approach can be used because the gouging phenomenon actually occurs within the slipper and rail not the sled system, although the sled mass

affects the total energy and momentum of impact. In addition, the slipper geometry and material properties are better understood and more accurately modeled than the more complex sled system. The sled system mass affects the gouging solution by increasing the *effective* mass of the slipper.

In this next section, after analyzing the sled system as a whole, the sled mass is discretized as an artificial mass and added to the slipper. This model is then analyzed from the approach of the conservation equations considering two cases:

1. Vibratory impact.
2. Asperity impact.
3. Combined vibratory and asperity impact in which the asperity considered is a rail roughness (a.k.a., rail misalignment) and the rail contains a coating material.

These cases will be considered in the same order as above. No case at this time will consider dimensioned quantities associated with heat conduction.

This portion of the dimensional analysis considers three-dimensional models that will be transformed into two-dimensional plane strain computer models for CTH. The sled system is first taken as a whole including the slipper. Later in the evolution of the model, the sled mass is differentiated from the slipper material for greater flexibility by the user in defining the computer model.

Before an analysis is performed utilizing the artificial mass with an appropriate time-scale with the slipper, a homogenous sled system is analyzed using both the *CTH blackbox* approach and the conservation equations with an appropriate time scale. In this way, the dimensional analysis may evolve into a more complicated model in which the dimensioned mass parameter accounts for both a slipper and a sled of varying materials.

4.5.1 Dimensional Analysis of the Sled System Using the CTH Blackbox Approach. The dimensional analysis begins with a simplified three-dimensional model of the hyper-velocity sled system. The bulk sled system includes the slippers. The system is simplified as shown in Figure 4.17.

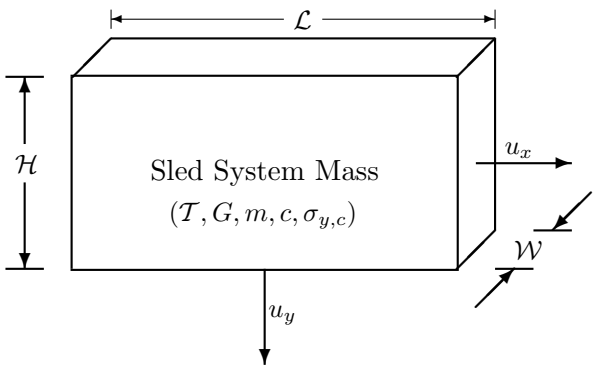

Figure 4.17 **Simplified model of the sled system used for dimensional analysis.**

The dimensioned quantities chosen for the model assume that the slipper and rail material properties are the same or nearly the same and include all those quantities the user may select as input for the CTH algorithm:

$\mathcal{T}$ artificial bulk sled system temperature, θ

m artificial bulk sled system mass, M

u_x horizontal velocity, $\frac{L}{T}$

u_y vertical velocity, $\frac{L}{T}$

$\mathcal{H}$ artificial bulk sled system height, L

$\mathcal{L}$ artificial bulk sled system length, L

$\mathcal{W}$ artificial bulk sled system width, L

c artificial bulk sled system material speed of sound, $\frac{L}{T}$

$\sigma_{y,c}$ artificial bulk sled system critical yield strength, $\frac{M}{LT^2}$

G artificial bulk sled system shear modulus, $\frac{M}{LT^2}$

The mass was chosen as a dimensioned quantity rather than the density because the mass of the sled system is typically known with some certainty although it changes with time. In this case, it is also assumed that the mass remains constant for the time under consideration. The real sled system consists of a variety of materials. The average

density of the real sled is difficult to calculate mainly because the density changes for each component of the complex sled system.

The fundamental dimensions based on the dimensioned quantities are:

θ temperature

M mass

L length

T time

The independent variables for the model are:

x horizontal axis position

y vertical axis position

z lateral axis position

t time

To start, the product of the dimensioned quantities, π, are written.

$$\pi = [\mathcal{T}]^{\alpha_1}[m]^{\alpha_2}[\mathcal{H}]^{\alpha_3}[\mathcal{L}]^{\alpha_4}[\mathcal{W}]^{\alpha_5}[u_x]^{\alpha_6}[u_y]^{\alpha_7}[c]^{\alpha_8}[\sigma_{y,c}]^{\alpha_9}[G]^{\alpha_{10}} \tag{4.45}$$

$$\pi = [\theta]^{\alpha_1}[M]^{\alpha_2+\alpha_9+\alpha_{10}}[L]^{\alpha_3+\alpha_4+\alpha_5+\alpha_6+\alpha_7+\alpha_8-\alpha_9-\alpha_{10}}[T]^{-\alpha_6-\alpha_7-\alpha_8-2\alpha_9-2\alpha_{10}}$$

$$\pi = [\theta]^{\beta_1}[M]^{\beta_2}[L]^{\beta_3}[T]^{\beta_4} \tag{4.46}$$

For dimensional consistency, $\underline{\alpha}$ must exist in the null space of the dimension matrix $[D]$, as shown in Equations 4.12 and 4.13 (i.e., $[D]\underline{\alpha} = \underline{0}$). In other words, elements in the null space of the dimension matrix constitute dimensionless invariants that can be used to maintain consistency between models. In addition, any product of these dimensionless invariants constitute another valid invariant. The following relationships between the β

and α quantities are then obtained.

$$\begin{aligned}
\beta_1 &= \alpha_1 = 0 \\
\beta_2 &= \alpha_2 + \alpha_9 + \alpha_{10} = 0 \\
\beta_3 &= \alpha_3 + \alpha_4 + \alpha_5 + \alpha_6 + \alpha_7 + \alpha_8 - \alpha_9 - \alpha_{10} = 0 \\
\beta_4 &= -\alpha_6 - \alpha_7 - \alpha_8 - 2\alpha_9 - 2\alpha_{10} = 0
\end{aligned}$$

This can also be written in terms of a dimension matrix, $[D]$

$$\underline{\beta} = [D]\underline{\alpha} = \underline{0}$$

$$\underline{\beta} = \left[\begin{array}{c|cccccccccc} 1 & 0 & 0 & 0 & 0 & 0 & 0 & 0 & 0 & 0 \\ \hline 0 & 1 & 0 & 0 & 0 & 0 & 0 & 0 & 1 & 1 \\ 0 & 0 & 1 & 1 & 1 & 1 & 1 & 1 & -1 & -1 \\ 0 & 0 & 0 & 0 & 0 & -1 & -1 & -1 & -2 & -2 \end{array}\right] \underline{\alpha} = \underline{0}$$

The dimension matrix can be reduced along the lines drawn within the dimension matrix above since the dimensioned quantity temperature, $\mathcal{T}$ is equivalent to the fundamental temperature dimension, θ. Working in the null space of $[D]$ with the reduced dimension matrix the solution for the invariants is,

$$\pi_k = \left(\frac{\mathcal{L}}{\mathcal{H}}\right)^{c_4} \left(\frac{\mathcal{W}}{\mathcal{H}}\right)^{c_5} \left(\frac{u_y}{u_x}\right)^{c_7} \left(\frac{c}{u_x}\right)^{c_8} \left(\frac{\sigma_{y,c}\mathcal{H}^3}{mu_x^2}\right)^{c_9} \left(\frac{G\mathcal{H}^3}{mu_x^2}\right)^{c_{10}} \tag{4.47}$$

Six invariants must be simultaneously satisfied to adequately describe the scaling between models. If $c_4 = 1$ is chosen and all other arbitrary constants, c_i equal zero then the invariant is

$$\pi_1 = \frac{\mathcal{L}}{\mathcal{H}} \tag{4.48}$$

If $c_5 = 1$ is chosen and all other arbitrary constants, c_i equal zero then the invariant is

$$\pi_2 = \frac{\mathcal{W}}{\mathcal{H}} \tag{4.49}$$

If $c_7 = 1$ is chosen and all other arbitrary constants, c_i equal zero then the invariant is

$$\pi_3 = \frac{u_y}{u_x} \tag{4.50}$$

If $c_8 = 1$ is chosen and all other arbitrary constants, c_i equal zero then the invariant is

$$\pi_4 = \frac{c}{u_x} \tag{4.51}$$

If $c_9 = 1$ is chosen and all other arbitrary constants, c_i equal zero then the invariant is

$$\pi_5 = \frac{\sigma_{y,c}\mathcal{H}^3}{mu_x^2} \tag{4.52}$$

And if $c_{10} = 1$ is chosen and all other arbitrary constants, c_i equal zero then the invariant is

$$\pi_6 = \frac{G\mathcal{H}^3}{mu_x^2} \tag{4.53}$$

Here is how the results may be interpreted. In order to maintain proper scaling of the hypervelocity sled problem between models, six products must remain constant between the models. If the material properties and horizontal velocity remain the same between models, the length to height ratio ($\mathcal{L}$ to $\mathcal{H}$ ratio) of a unit width of the sled system must remain unchanged. Also, the ratio of vertical to horizontal velocity (u_y to u_x ratio) must remain unchanged. One may also look at this velocity ratio as the angle of impact.

Additionally, if the material properties do not remain constant between models, then the ratio between those properties and the slipper's kinetic energy must remain invariant. Practically speaking, use of these ratios is dependent on a good geometric model to simulate the sled system. The real sled system consists of a rocket with payload attached to slippers that connect the system to the rail. This model requires some simplification of that relatively complex geometry into a block with the same mass and average material properties of the whole system. Accurate values for this simplification are difficult to achieve because the geometry and material properties of the sled system change for each test run. Also, the material properties are not consistent in the sled system itself. The properties

vary because the structure is made of a number of different materials. See Figure 4.6 and the accompanying description on page 4-9 of section 4.5 for how the real sled system and slipper will be simplified.

Thus, the actual dimensions ($\mathcal{L}$ and $\mathcal{H}$) of the sled system and material properties such as speed of sound (c), shear modulus (G), and yield strength ($\sigma_{y,c}$) of the real sled system are extremely difficult to accurately duplicate in CTH. The actual sled structure is not a block of unchanging material, but is a complex combination of a variety of materials that also change in mass as the run progresses. Mass is lost due to extreme heating and propellant being expelled.

In conclusion, this dimensional analysis of the hypervelocity sled system shows that if the same material properties and mass of the real sled are maintained in the CTH model, then for an extremely short time period under consideration in the analysis one must:

1. Use the impact angle (velocity ratio) of the real sled in the CTH model.
2. Maintain the length to height ratio of a unit width strip of the sled system for a simplified block model of the sled system.

The second requirement is difficult to achieve when converting the real sled to a CTH model, so dimensions should be selected using two principles. Dimensions should first be selected to allow the mass to remain invariant between models based on a unit width of the sled system. They must also be selected so that the CTH program is able to obtain a solution in a reasonable amount of time given the computer system available for the analysis.

Verification of the dimensional analysis was not performed in CTH for this case because the invariants resulting from this analysis are similar to the previous slipper-only cases.

4.5.2 Dimensional Analysis of the Sled System Using the Conservation Equations. The dimensional analysis begins with a simplified three-dimensional model of the hypervelocity sled system. This bulk sled system includes the slippers. The system is simplified as shown in Figure 4.18. The sled model is modified in later cases with an artificial mass to

simulate the sled mass that affects the impact of the slipper on the rail. The conservation equations of mass, momentum, and energy are used to define dimensioned quantities for the dimensional analysis (see page 4-13).

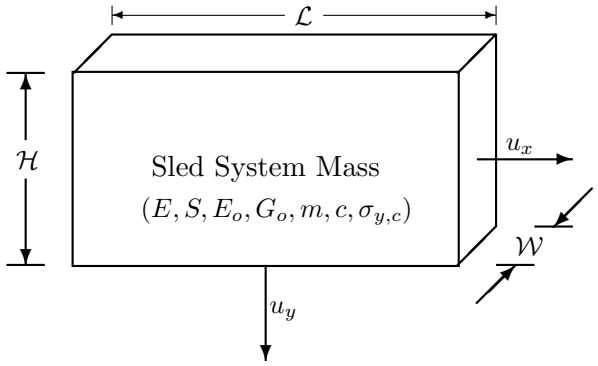

Figure 4.18 **Simplified model of the sled system used for dimensional analysis based on the conservation equations.**

The dimensioned quantities chosen for the model include:

m bulk sled system mass, M

$\mathcal{L}$ artificial bulk sled system length, L

$\mathcal{H}$ artificial bulk sled system height, L

$\mathcal{W}$ artificial bulk sled system width, L

u_x horizontal velocity, $\frac{L}{T}$

u_y vertical velocity, $\frac{L}{T}$

c artificial bulk sled system material speed of sound, $\frac{L}{T}$

E initial total energy of the bulk sled system, $\frac{ML^2}{T^2}$

S constant energy source of the bulk sled system, $\frac{ML^2}{T^2}$

$\sigma_{y,c}$ artificial bulk sled system critical yield strength, $\frac{M}{LT^2}$

E_o artificial bulk sled system elastic modulus, $\frac{M}{LT^2}$

G_o artificial bulk sled system shear modulus, $\frac{M}{LT^2}$

It might be more physically revealing to have a time-scale based on the speed of sound or the coating thickness rather than the length of the shoe and the horizontal velocity of impact. By considering time as a dimensioned quantity one is, in effect, changing the elements of the $\underline{\beta}$ vector from zero for each fundamental dimension to zero for all fundamental dimensions and one for the fundamental dimension of time, T. That is,

$$\underline{\beta} = [D]\underline{\alpha} = \underline{0} \tag{4.54}$$

becomes

$$\underline{\beta} = [D]\underline{\alpha} = \left\{ \begin{array}{c} 0 \\ 0 \\ 0 \\ 1 \end{array} \right\} \tag{4.55}$$

to determine a time-scale for this case.

The mass was chosen as a dimensioned quantity rather than the density because the mass of the sled system is typically known with some certainty although it changes with time. In this case, it is also assumed that the mass remains constant for the time under consideration. The real sled system consists of a variety of materials. The average density of the real sled is difficult to calculate mainly because the density changes for each component of the complex sled system.

Note that the temperature, $\mathcal{T}$ is no longer a dimensioned quantity as in the CTH algorithm approach. This is because temperature is considered as an energy term that will affect the initial total energy, E or constant energy source, S quantities. Though time, t is a dependent variable, it is included in the dimensioned quantities so that a non-dimensioned time-scale can be obtained through the dimensional analysis. G_o is a term contained in the constitutive equations. The quantity G changes with time, but is initially based on the G_o value. $\sigma_{y,c}$ is a critical stress at which yield is reached for the slipper material and is used in the constitutive equation to determine plasticity.

The fundamental dimensions as derived from the dimensioned quantities are:

M mass

L length

T time

The independent variables for the model are:

x horizontal axis position

y vertical axis position

z lateral axis position

t time

The product of the dimensioned quantities, π, are written as:

$$\begin{aligned}
\pi &= [m]^{\alpha_1}[\mathcal{L}]^{\alpha_2}[\mathcal{H}]^{\alpha_3}[\mathcal{W}]^{\alpha_4}[u_x]^{\alpha_5}[u_y]^{\alpha_6}[c]^{\alpha_7}[E]^{\alpha_8}[S]^{\alpha_9}[\sigma_{y,c}]^{\alpha_{10}}[E_o]^{\alpha_{11}}[G_o]^{\alpha_{12}}[t]^{\alpha_{13}} \qquad (4.56)\\
\pi &= [M]^{\alpha_1+\alpha_8+\alpha_9+\alpha_{10}+\alpha_{11}+\alpha_{12}}[L]^{\alpha_2+\alpha_3+\alpha_4+\alpha_5+\alpha_6+\alpha_7+2\alpha_8+2\alpha_9-\alpha_{10}-\alpha_{11}-\alpha_{12}}\\
&\quad [T]^{-\alpha_5-\alpha_6-\alpha_7-2\alpha_8-2\alpha_9-2\alpha_{10}-2\alpha_{11}-2\alpha_{12}+\alpha_{13}}\\
\pi &= [M]^{\beta_1}[L]^{\beta_2}[T]^{\beta_3}
\end{aligned}$$

For dimensional consistency, $\underline{\alpha}$ must exist in the null space of the dimension matrix $[D]$, as shown in Equations 4.12 and 4.13 (i.e., $[D]\underline{\alpha} = \underline{0}$). In other words, elements in the null space of the dimension matrix constitute dimensionless invariants that can be used to maintain consistency between models. In addition, any product of these dimensionless invariants constitute another valid invariant. The following relationships between the β and α quantities are then obtained.

$$\begin{aligned}
\beta_1 &= \alpha_1 + \alpha_8 + \alpha_9 + \alpha_{10} + \alpha_{11} + \alpha_{12} = 0\\
\beta_2 &= \alpha_2 + \alpha_3 + \alpha_4 + \alpha_5 + \alpha_6 + \alpha_7 + 2\alpha_8 + 2\alpha_9 - \alpha_{10} - \alpha_{11} - \alpha_{12} = 0\\
\beta_3 &= -\alpha_5 - \alpha_6 - \alpha_7 - 2\alpha_8 - 2\alpha_9 - 2\alpha_{10} - 2\alpha_{11} - 2\alpha_{12} + \alpha_{13} = 0
\end{aligned}$$

This can also be written in terms of a dimension matrix, $[D]$

$$\underline{\beta} = [D]\underline{\alpha} = \underline{0}$$

$$\underline{\beta} = \begin{bmatrix} 1 & 0 & 0 & 0 & 0 & 0 & 0 & 1 & 1 & 1 & 1 & 1 & 0 \\ 0 & 1 & 1 & 1 & 1 & 1 & 1 & 2 & 2 & -1 & -1 & -1 & 0 \\ 0 & 0 & 0 & 0 & -1 & -1 & -1 & -2 & -2 & -2 & -2 & -2 & 1 \end{bmatrix} \underline{\alpha} = \underline{0}$$

Working in the null space of $[D]$ the solution for the invariants is,

$$\begin{aligned} \pi_k &= \left(\frac{\mathcal{H}}{\mathcal{L}}\right)^{c_3} \left(\frac{\mathcal{W}}{\mathcal{L}}\right)^{c_4} \left(\frac{u_y}{u_x}\right)^{c_6} \left(\frac{c}{u_x}\right)^{c_7} \left(\frac{E}{mu_x^2}\right)^{c_8} \left(\frac{S}{mu_x^2}\right)^{c_9} \\ &\quad \left(\sigma_{y,c}\frac{\mathcal{L}^3}{mu_x^2}\right)^{c_{10}} \left(E_o\frac{\mathcal{L}^3}{mu_x^2}\right)^{c_{11}} \left(G_o\frac{\mathcal{L}^3}{mu_x^2}\right)^{c_{12}} \\ &= \prod_{k=1}^{10} \pi_k^{c_k} \end{aligned} \tag{4.57}$$

Nine invariants must be simultaneously satisfied to adequately describe the scaling between models. $c_3 = 1$ can be selected and all other arbitrary constants, c_i equal to zero

$$\pi_1 = \frac{\mathcal{H}}{\mathcal{L}} \tag{4.58}$$

$c_4 = 1$ can be selected and all other arbitrary constants, c_i equal to zero

$$\pi_2 = \frac{\mathcal{W}}{\mathcal{L}} \tag{4.59}$$

$c_6 = 1$ can be selected and all other arbitrary constants, c_i equal to zero

$$\pi_3 = \frac{u_y}{u_x} \tag{4.60}$$

Likewise, $c_7 = 1$ can be selected and all other arbitrary constants, c_i equal to zero

$$\pi_4 = \frac{c}{u_x} \tag{4.61}$$

$c_8 = 1$ can be selected and all other arbitrary constants, c_i equal to zero

$$\pi_5 = \frac{E}{mu_x^2} \tag{4.62}$$

$c_9 = 1$ can be selected and all other arbitrary constants, c_i equal to zero

$$\pi_6 = \frac{S}{mu_x^2} \tag{4.63}$$

And $c_{10} = 1$ can be selected and all other arbitrary constants, c_i equal to zero

$$\pi_7 = \sigma_{y,c}\frac{\mathcal{L}^3}{mu_x^2} \tag{4.64}$$

And $c_{11} = 1$can be selected and all other arbitrary constants, c_i equal to zero

$$\pi_8 = E_o\frac{\mathcal{L}^3}{mu_x^2} \tag{4.65}$$

And $c_{12} = 1$ can be selected and all other arbitrary constants, c_i equal to zero

$$\pi_9 = G_o\frac{\mathcal{L}^3}{mu_x^2} \tag{4.66}$$

In order to maintain proper scaling of the hypervelocity sled problem between models, nine products must remain constant between the models. The length to height ratio ($\mathcal{L}$ to $\mathcal{H}$ ratio) of a unit width of the sled system must remain unchanged. Also, the ratio of vertical to horizontal velocity (u_y to u_x ratio) and material sound speed to horizontal velocity must remain unchanged. One may also look at this velocity ratio as the angle of impact. The ratio of the total internal energy and any energy source must also be scaled properly to the horizontal kinetic energy of the slipper. Finally, the material properties of the slipper must be invariant with the horizontal kinetic energy of the slipper.

From this analysis it is possible to obtain a natural length or time scale. For example solving

$$\underline{\beta} = [D]\underline{\alpha} = \left\{ \begin{array}{c} 0 \\ 0 \\ 1 \end{array} \right\}$$

produces a natural time scale, $\tilde{T}$.

So, the time-scale for this case becomes,

$$\tilde{T} = \frac{\ell}{u_x}\pi(\mathbf{c})$$

where $\pi(\mathbf{c})$, as in Equation 4.57, is a function of the arbitrarily selected $\mathbf{c}$ vector. When $\mathbf{c}$ is the zero vector, then the time-scale is based on the time it takes the slipper to travel one length of its base horizontally.

4.5.3 Dimensional Analysis of a Vibratory Impact Initiator with an Artificial Mass Using the Conservation Equations. This dimensional analysis considers a three-dimensional slipper and sled system that impacts the rail at an oblique angle. The velocity vector at impact is typically a shallow angle. Gouging is initiated when the material at the high stress interface between the slipper and rail becomes plastic and the tangential motion of the interface causes the plastic rail and slipper materials to impinge on one another. This motion increases as the materials interact with one another and gouging develops. The gouge formed by this interaction starts small and increases as the slipper passes over the rail. Interaction stops when the slipper and rail are no longer in contact with one another. In Figure 4.19 is a three-dimensional schematic of an oblique impact of the slipper and the dimensioned quantities that will be considered for the analysis.

The dimensioned quantities chosen for the model assume that the slipper and rail material properties are the same or nearly the same and include:

m bulk sled mass, M

ρ_o original density of the slipper, $\frac{M}{L^3}$

ℓ slipper length, L

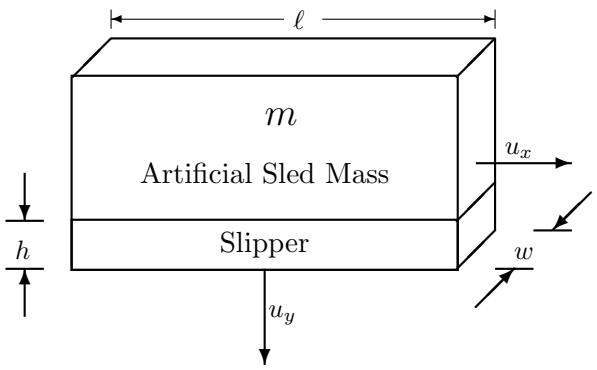

Figure 4.19 **Simplified model of the sled system used for dimensional analysis.**

h slipper height, L

w slipper width, L

u_x horizontal velocity, $\frac{L}{T}$

u_y vertical velocity, $\frac{L}{T}$

c slipper material speed of sound, $\frac{L}{T}$

E initial total energy of the bulk sled system, $\frac{ML^2}{T^2}$

S constant energy source of the bulk sled system, $\frac{ML^2}{T^2}$

$\sigma_{y,c}$ slipper critical yield strength, $\frac{M}{LT^2}$

E_o original slipper elastic modulus, $\frac{M}{LT^2}$

G_o original slipper shear modulus, $\frac{M}{LT^2}$

The dimensions and material properties for the slipper are purposely labeled using different variables than the dimensions and material properties of the sled system. The subscript $_o$ is purposely used to distinguish the material properties of the slipper from the material properties of the sled system. The dimensions of the slipper, ℓ and h are used to describe the length and height of the slipper as opposed to $\mathcal{L}$ and $\mathcal{H}$ for the sled system. This distinction between sled system and slipper properties is done to more accurately model the real sled system and slipper structures. In the real system, the sled and payload are very different in size and material properties than the slipper.

The fundamental dimensions derived from the dimensioned quantities are:

M mass

L length

T time

The independent variables for the model are:

x horizontal axis position

y vertical axis position

z lateral axis position

t time

Applying Buckingham's Pi Theorem, one starts with

$$\begin{aligned}
\pi &= [m]^{\alpha_1}[\rho_o]^{\alpha_2}[\ell]^{\alpha_3}[h]^{\alpha_4}[w]^{\alpha_5}[u_x]^{\alpha_6}[u_y]^{\alpha_7}[c]^{\alpha_8}[E]^{\alpha_9}[S]^{\alpha_{10}}[\sigma_{y,c}]^{\alpha_{11}}[E_o]^{\alpha_{12}}[G_o]^{\alpha_{13}}[t]^{\alpha_{14}} \\
\pi &= [M]^{\alpha_1+\alpha_2+\alpha_9+\alpha_{10}+\alpha_{11}+\alpha_{12}+\alpha_{13}}[L]^{-3\alpha_2+\alpha_3+\alpha_4+\alpha_5+\alpha_6+\alpha_7+\alpha_8+2\alpha_9+2\alpha_{10}-\alpha_{11}-\alpha_{12}-\alpha13} \\
&\quad [T]^{-\alpha_6-\alpha_7-\alpha_8-2\alpha_9-2\alpha_{10}-2\alpha_{11}-2\alpha_{12}-2\alpha_{13}+\alpha_{14}} \\
\pi &= [M]^{\beta_2}[L]^{\beta_3}[T]^{\beta_4} \qquad (4.67)
\end{aligned}$$

By equating the π equations and the powers for each fundamental dimension, one produces

$$\begin{aligned}
\beta_1 &= \alpha_1+\alpha_2+\alpha_9+\alpha_{10}+\alpha_{11}+\alpha_{12}+\alpha_{13}=0 \\
\beta_2 &= -3\alpha_2+\alpha_3+\alpha_4+\alpha_5+\alpha_6+\alpha_7+\alpha_8+2\alpha_9+2\alpha_{10}-\alpha_{11}-\alpha_{12}-\alpha13=0 \\
\beta_3 &= -\alpha_6-\alpha_7-\alpha_8-2\alpha_9-2\alpha_{10}-2\alpha_{11}-2\alpha_{12}-2\alpha_{13}+\alpha_{14}=0
\end{aligned}$$

This can also be written in terms of a dimension matrix, $[D]$

$$\underline{\beta} = [D]\underline{\alpha} = \underline{0}$$

$$\underline{\beta} = \begin{bmatrix} 1 & 1 & 0 & 0 & 0 & 0 & 0 & 0 & 1 & 1 & 1 & 1 & 1 & 0 \\ 0 & -3 & 1 & 1 & 1 & 1 & 1 & 1 & 2 & 2 & -1 & -1 & -1 & 0 \\ 0 & 0 & 0 & 0 & 0 & -1 & -1 & -1 & -2 & -2 & -2 & -2 & -2 & 1 \end{bmatrix} \underline{\alpha} = \underline{0}$$

Working in the null space of $[D]$ the solution for the invariants is,

$$\begin{aligned}\pi_k &= \left(\rho_o \frac{\ell^3}{m}\right)^{c_2} \left(\frac{h}{\ell}\right)^{c_4} \left(\frac{w}{\ell}\right)^{c_5} \left(\frac{u_y}{u_x}\right)^{c_7} \left(\frac{c}{u_x}\right)^{c_8} \left(\frac{E}{mu_x^2}\right)^{c_9} \left(\frac{S}{mu_x^2}\right)^{c_{10}} \\ &\quad \left(\sigma_{y,c} \frac{\ell^3}{mu_x^2}\right)^{c_{11}} \left(E_o \frac{\ell^3}{mu_x^2}\right)^{c_{12}} \left(G_o \frac{\ell^3}{mu_x^2}\right)^{c_{13}} \\ &= \prod_{k=1}^{10} \pi_k^{c_k} \end{aligned} \tag{4.68}$$

Ten invariants must be simultaneously satisfied to adequately describe the scaling between models. If $c_2 = 1$ is chosen and all other $c_i = 0$ then the first invariant is

$$\pi_1 = \rho_o \frac{\ell^3}{m} \tag{4.69}$$

The slipper density must be invariant with the ratio of the sled mass and the cubed length of the slipper.

If $c_4 = 1$ is chosen and all other $c_i = 0$ then the second invariant is

$$\pi_2 = \frac{h}{\ell} \tag{4.70}$$

The slipper height must be invariant with the length of the slipper.

If $c_5 = 1$ is chosen and all other $c_i = 0$ then the third invariant is

$$\pi_3 = \frac{w}{\ell} \tag{4.71}$$

The slipper width must be invariant with the slipper length.

If $c_7 = 1$ is chosen and all other $c_i = 0$ then the fourth invariant is

$$\pi_4 = \frac{u_y}{u_x} \tag{4.72}$$

The horizontal and vertical velocity ratio of the slipper must remain invariant.

If $c_8 = 1$ is chosen and all other $c_i = 0$ then the fifth invariant is

$$\pi_5 = \frac{c}{u_x} \tag{4.73}$$

The ratio of material speed of sound and horizontal velocity must remain invariant.

If $c_9 = 1$ is chosen and all other $c_i = 0$ then the sixth invariant is

$$\pi_6 = \frac{E}{mu_x^2} \tag{4.74}$$

The initial total energy of the slipper as compared to the slipper kinetic energy based on the horizontal velocity must remain invariant between models.

If $c_{10} = 1$ is chosen and all other $c_i = 0$ then the seventh invariant is

$$\pi_7 = \frac{S}{mu_x^2} \tag{4.75}$$

The constant internal energy source of the slipper as compared to the slipper kinetic energy based on the horizontal velocity must remain invariant between models.

If $c_{11} = 1$ is chosen and all other $c_i = 0$ then the eighth invariant is

$$\pi_8 = \sigma_{y,c}\frac{\ell^3}{mu_x^2} \tag{4.76}$$

The ratio of the yield stress and the horizontal kinetic energy as scaled with the slipper length must remain invariant between models.

If $c_{12} = 1$ is chosen and all other $c_i = 0$ then the ninth invariant is

$$\pi_9 = E_o\frac{\ell^3}{mu_x^2} \tag{4.77}$$

The ratio of the elastic modulus and the horizontal kinetic energy as scaled with the slipper length must remain invariant between models.

If $c_{13} = 1$ is chosen and all other $c_i = 0$ then the tenth invariant is

$$\pi_{10} = G_o \frac{\ell^3}{m u_x^2} \tag{4.78}$$

The ratio of the shear modulus and the horizontal kinetic energy as scaled with the slipper length must remain invariant between models.

In order to maintain proper scaling of the hypervelocity sled problem between models, ten products must remain constant between the models. The height to length and width to length ratios (h to ℓ and w to ℓ ratios) of the slipper must remain unchanged. Also, the ratio of vertical to horizontal velocity (u_y to u_x ratio) and material sound speed to horizontal velocity must remain unchanged. One may also look at this velocity ratio as the angle of impact. The ratio of the total internal energy and any energy source must also be scaled properly to the horizontal kinetic energy of the slipper.

Finally, the material properties of the slipper must be invariant with the horizontal kinetic energy of the slipper. Another important invariant that comes out of this analysis is the ratio of the slipper density to the total mass per unit volume based on the slipper length cubed.

From this analysis it is possible to obtain a natural length or time scale. For example solving

$$\underline{\beta} = [D]\underline{\alpha} = \left\{ \begin{array}{c} 0 \\ 0 \\ 1 \end{array} \right\}$$

produces a natural time scale, $\tilde{T}$.

So, the time-scale for this case becomes,

$$\tilde{T} = \frac{\ell}{u_x} \pi(\mathbf{c})$$

where $\pi(\mathbf{c})$, as in Equation 4.68, is a function of the arbitrarily selected $\mathbf{c}$ vector. When $\mathbf{c}$ is the zero vector, then the time-scale is based on the time it takes the slipper to travel one length of its base horizontally.

The time-scale that results from this analysis is based upon the horizontal velocity and the length of the slipper. In other words, the time-scale is based on how long it takes the slipper to travel one entire length of its base. This is the same time scale indicated from the sled analysis in section 4.5.2.

4.5.4 Dimensional Analysis of an Asperity Impact Initiator with an Artificial Mass Using the Conservation Equations . This portion of the dimensional analysis considers a slipper that impacts an asperity at a horizontal velocity. Gouging is initiated when the slipper impacts the asperity at a velocity that plasticizes it and deforms it as it also forces it into the rail. This process initiates a "jetting" interaction between the slipper and rail materials that cause the slipper and rail to deform permanently resulting in a teardrop shaped deformation. The gouge formed by this interaction is a function of the size of the asperity due to the impingement of the asperity into the rail. It is maximum at gouge initiation and decreases as the slipper passes over the rail. Gouging stops when the slipper and rail are no longer in contact with one another. In Figure 4.20 we see a two-dimensional schematic of an asperity impact and the dimensioned quantities that will be considered for the analysis.

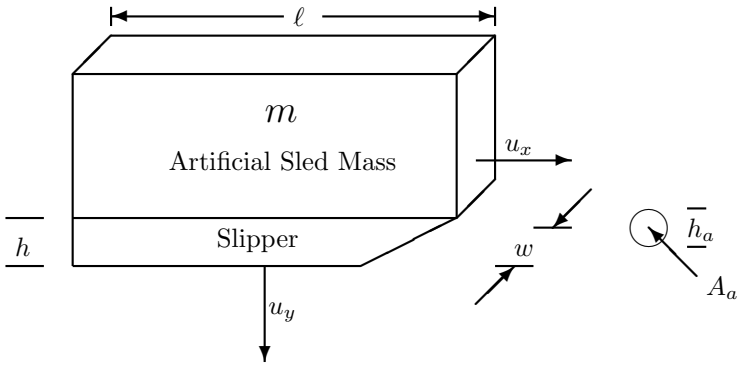

Figure 4.20 **Simplified model of an asperity impact used for dimensional analysis.**

The fundamental dimensions are:

θ temperature

M mass

L length

T time

The dimensioned quantities chosen for the model assume that the slipper and rail material properties are the same or nearly the same and include:

$\mathcal{T}_o$ original temperature of the slipper, θ

ρ_o original density of the slipper, $\frac{M}{L^3}$

u_x horizontal velocity, $\frac{L}{T}$

ℓ slipper length, L

h slipper height, L

σ_y slipper yield strength, $\frac{M}{LT^2}$

E_o original slipper elastic modulus, $\frac{M}{LT^2}$

G_o original slipper shear modulus, $\frac{M}{LT^2}$

h_a asperity height, L

A_a cross-sectional area of the asperity, L^2

The dependent variables for the model are:

x horizontal axis position

y vertical axis position

z lateral axis position

t time

The independent variables for this model are considered to be the change in velocity (∂u), the plastic strain rate ($\dot{\varepsilon}^p$), the spherical stress field (σ), the deviatoric stress field (τ), and the temperature field (θ).

$$
\begin{aligned}
\pi &= [\mathcal{T}_o]^{\alpha_1}[\rho_o]^{\alpha_2}[u_x]^{\alpha_3}[\ell]^{\alpha_4}[h]^{\alpha_5}[\sigma_y]^{\alpha_6}[E_o]^{\alpha_7}[G_o]^{\alpha_8}[h_a]^{\alpha_9}[A_a]^{\alpha_{10}} \\
\pi &= [\theta]^{\alpha_1}[M]^{\alpha_2+\alpha_6+\alpha_7+\alpha_8}[L]^{-3\alpha_2+\alpha_3+\alpha_4+\alpha_5-\alpha_6-\alpha_7-\alpha_8+\alpha_9+2\alpha_{10}}[T]^{-\alpha_3-2\alpha_6-2\alpha_7-2\alpha_8} \\
\pi &= [\theta]^{\beta_1}[M]^{\beta_2}[L]^{\beta_3}[T]^{\beta_4} \qquad (4.79)
\end{aligned}
$$

$$
\begin{aligned}
\beta_1 &= \alpha_1 = 0 \\
\beta_2 &= \alpha_2 + \alpha_6 + \alpha_7 + \alpha_8 = 0 \\
\beta_3 &= -3\alpha_2 + \alpha_3 + \alpha_4 + \alpha_5 - \alpha_6 - \alpha_7 - \alpha_8 + \alpha_9 + 2\alpha_{10} = 0 \\
\beta_4 &= -\alpha_3 - 2\alpha_6 - 2\alpha_7 - 2\alpha_8 = 0
\end{aligned}
$$

$$
\underline{\beta} = [D]\underline{\alpha} = \underline{0}
$$

$$
\underline{\beta} = \left[\begin{array}{c|cccccccccc}
1 & 0 & 0 & 0 & 0 & 0 & 0 & 0 & 0 & 0 \\ \hline
0 & 1 & 0 & 0 & 0 & 1 & 1 & 1 & 0 & 0 \\
0 & -3 & 1 & 1 & 1 & -1 & -1 & -1 & 1 & 2 \\
0 & 0 & -1 & 0 & 0 & -2 & -2 & -2 & 0 & 0
\end{array}\right] \underline{\alpha} = \underline{0}
$$

The dimension matrix can be reduced along the lines drawn within the dimension matrix above since the dimensioned quantity temperature, $\mathcal{T}_o$ is equivalent to the fundamental temperature dimension, θ. Working in the null space of $[D]$ with the reduced dimension matrix,

$$
\alpha_2 = -\alpha_6 - \alpha_7 - \alpha_8
$$

$$
\left\{\begin{array}{rcl}
0 &=& -3\alpha_2 + \alpha_3 + \alpha_4 + \alpha_5 - \alpha_6 - \alpha_7 - \alpha_8 + \alpha_9 + 2\alpha_{10} \\
0 &=& -3(-\alpha_6 - \alpha_7 - \alpha_8) + \alpha_3 + \alpha_4 + \alpha_5 - \alpha_6 - \alpha_7 - \alpha_8 + \alpha_9 + 2\alpha_{10} \\
0 &=& \alpha_3 + \alpha_4 + \alpha_5 + 2\alpha_6 + 2\alpha_7 + 2\alpha_8 + \alpha_9 + 2\alpha_{10}
\end{array}\right.
$$

$$\left\{\begin{array}{rcccccccccccccccc}
0 & = & \alpha_3 & + & \alpha_4 & + & \alpha_5 & + & 2\alpha_6 & + & 2\alpha_7 & + & 2\alpha_8 & + & \alpha_9 & + & 2\alpha_{10} \\
0 & = & -\alpha_3 & & & & & - & 2\alpha_6 & - & 2\alpha_7 & - & 2\alpha_8 & & & & \\
\hline
0 & = & & & \alpha_4 & + & \alpha_5 & & & & & & & + & \alpha_9 & + & 2\alpha_{10}
\end{array}\right.$$

$$\begin{aligned}
\alpha_3 &= -2\alpha_6 - 2\alpha_7 - 2\alpha_8 \\
\alpha_4 &= -\alpha_5 - \alpha_9 - 2\alpha_{10} \\
\alpha_5 &= \alpha_5 \\
\alpha_6 &= \alpha_6 \\
\alpha_7 &= \alpha_7 \\
\alpha_8 &= \alpha_8 \\
\alpha_9 &= \alpha_9 \\
\alpha_{10} &= \alpha_{10}
\end{aligned}$$

$$\underline{\alpha} = \begin{Bmatrix} \alpha_2 \\ \alpha_3 \\ \alpha_4 \\ \alpha_5 \\ \alpha_6 \\ \alpha_7 \\ \alpha_8 \\ \alpha_9 \\ \alpha_{10} \end{Bmatrix} = \begin{Bmatrix} 0 \\ 0 \\ -1 \\ 1 \\ 0 \\ 0 \\ 0 \\ 0 \\ 0 \end{Bmatrix} c_5 + \begin{Bmatrix} -1 \\ -2 \\ 0 \\ 0 \\ 1 \\ 0 \\ 0 \\ 0 \\ 0 \end{Bmatrix} c_6 + \begin{Bmatrix} -1 \\ -2 \\ 0 \\ 0 \\ 0 \\ 1 \\ 0 \\ 0 \\ 0 \end{Bmatrix} c_7 \tag{4.80}$$

$$+ \begin{Bmatrix} -1 \\ -2 \\ 0 \\ 0 \\ 0 \\ 0 \\ 1 \\ 0 \\ 0 \end{Bmatrix} c_8 + \begin{Bmatrix} 0 \\ 0 \\ -1 \\ 0 \\ 0 \\ 0 \\ 0 \\ 1 \\ 0 \end{Bmatrix} c_9 + \begin{Bmatrix} 0 \\ 0 \\ -2 \\ 0 \\ 0 \\ 0 \\ 0 \\ 0 \\ 1 \end{Bmatrix} c_{10}$$

If we hold the material properties to be constant, then we have $\alpha_6 = \alpha_7 = \alpha_8 = 0$ and then both α_2 and α_3 also become zero. That is, if the material properties remain constant between models, then the horizontal velocity (u_x) must also remain constant.

Then $\underline{\alpha}$ becomes

$$\underline{\alpha} = \begin{Bmatrix} 0 \\ 0 \\ \alpha_4 \\ \alpha_5 \\ 0 \\ 0 \\ 0 \\ \alpha_9 \\ \alpha_{10} \end{Bmatrix} = \begin{Bmatrix} 0 \\ 0 \\ -1 \\ 1 \\ 0 \\ 0 \\ 0 \\ 0 \\ 0 \end{Bmatrix} c_5 + \begin{Bmatrix} 0 \\ 0 \\ -1 \\ 0 \\ 0 \\ 0 \\ 0 \\ 1 \\ 0 \end{Bmatrix} c_9 + \begin{Bmatrix} 0 \\ 0 \\ -2 \\ 0 \\ 0 \\ 0 \\ 0 \\ 0 \\ 1 \end{Bmatrix} c_{10} \tag{4.81}$$

and simplifies to

$$\underline{\alpha} = \begin{Bmatrix} \alpha_4 \\ \alpha_5 \\ \alpha_9 \\ \alpha_{10} \end{Bmatrix} = \begin{Bmatrix} -1 \\ 1 \\ 0 \\ 0 \end{Bmatrix} c_5 + \begin{Bmatrix} -1 \\ 0 \\ 1 \\ 0 \end{Bmatrix} c_9 + \begin{Bmatrix} -2 \\ 0 \\ 0 \\ 1 \end{Bmatrix} c_{10} \tag{4.82}$$

Thus, the invariant becomes

$$\pi_k = \frac{h^{c_5} h_a^{c_9} A_a^{c_{10}}}{\ell^{c_5+c_9+2c_{10}}} \tag{4.83}$$

$$= \prod_{k=1}^{3} \pi_k^{c_k} \tag{4.84}$$

Three invariants are required to adequately describe the scaling between models. If we choose $c_5 = 1$ and both $c_9 = 0$ and $c_{10} = 0$ then the first invariant is

$$\pi_1 = \frac{h}{\ell} \tag{4.85}$$

which is one of the invariants we found in the oblique impact case (see section 4.5.3).

If we then choose $c_9 = 1$ and both $c_5 = 0$ and $c_{10} = 0$ then the second invariant is

$$\pi_2 = \frac{h_a}{\ell} \tag{4.86}$$

If we then choose $c_{10} = 1$ and both $c_5 = 0$ and $c_9 = 0$ then the third invariant is

$$\pi_3 = \frac{A_a}{\ell^2} \tag{4.87}$$

Therefore, the results of this dimensional analysis are interpreted to be that for an asperity initiator with constant material properties and horizontal velocity between models, we must also maintain the ratio between the slipper height and asperity height and slipper length. Also, the cross sectional area of the asperity must be scaled with the square of the slipper length.

From this analysis it is possible to obtain a natural length or time scale. For example solving

$$\underline{\beta} = [D]\underline{\alpha} = \left\{ \begin{array}{c} 0 \\ 0 \\ 1 \end{array} \right\}$$

produces a natural time scale, $\tilde{T}$.

So, the time-scale for this case becomes,

$$\tilde{T} = \frac{\ell}{u_x}\pi(\mathbf{c})$$

where $\pi(\mathbf{c})$, as in Equation 4.84, is a function of the arbitrarily selected $\mathbf{c}$ vector. When $\mathbf{c}$ is the zero vector, then the time-scale is based on the time it takes the slipper to travel one length of its base horizontally.

4.5.5 Dimensional Analysis of a Vibratory Rail Roughness Impact Initiator with an Artificial Mass Using the Conservation Equations . This last case for dimensional analysis begins with a simplified three-dimensional model of the slipper obliquely impacting a rail misalignment. The system is simplified as shown in Figure 4.21.

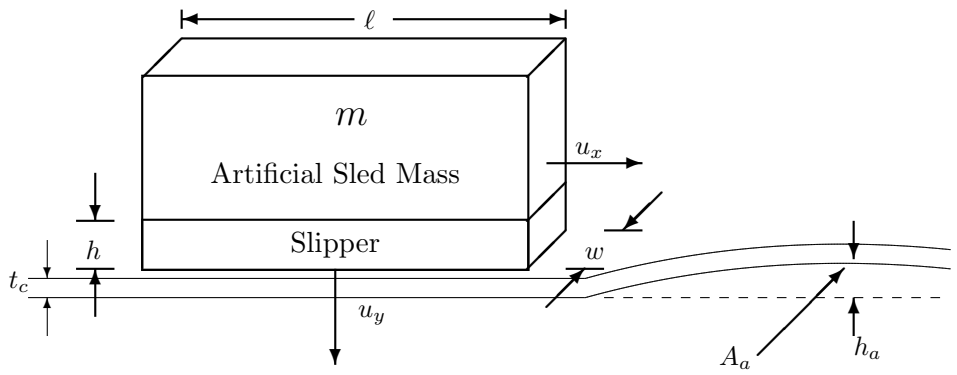

Figure 4.21 **Simplified model of a vibratory impacting slipper on a rail roughness with a coating for dimensional analysis.**

The rail roughness may be considered as a two dimensional plane-strain (see section 4.2) convex or concave elliptically-shaped protrusion of the rail material that gives the rail surface a slope varying with position. Note that Figure 4.21 shows a concave protrusion. For a convex definition of rail roughness, the area, A_a would change. At the HHSTT the misalignment of the rail could be in a vertical, horizontal, or some other direction. The two dimensional model can be viewed as modeling any one of those three dimensional cases in a plane strain two dimensional sense.

The dimensioned quantities chosen for the model assume that the slipper and rail material properties are the same or nearly the same and include:

m bulk sled mass, M

ρ_o original density of the slipper, $\frac{M}{L^3}$

ρ_{o_c} original density of the coating, $\frac{M}{L^3}$

ℓ slipper length, L

h slipper height, L

w slipper width, L

t_c coating thickness, L

h_a rail roughness asperity height, L

A_a cross-sectional area of the rail roughness asperity, L^2

u_x horizontal velocity, $\frac{L}{T}$

u_y vertical velocity, $\frac{L}{T}$

c slipper material speed of sound, $\frac{L}{T}$

c_c coating material speed of sound, $\frac{L}{T}$

E total energy of the bulk sled system, $\frac{ML^2}{T^2}$

S energy source of the bulk sled system, $\frac{ML^2}{T^2}$

$\sigma_{y,c}$ slipper critical yield strength, $\frac{M}{LT^2}$

σ_{y,c_c} coating critical yield strength, $\frac{M}{LT^2}$

E_o original slipper elastic modulus, $\frac{M}{LT^2}$

E_{o_c} original coating elastic modulus, $\frac{M}{LT^2}$

G_o original slipper shear modulus, $\frac{M}{LT^2}$

G_{o_c} original coating shear modulus, $\frac{M}{LT^2}$

The fundamental dimensions derived from the dimensioned quantities are:

M mass

L length

T time

The independent variables for the model are:

x horizontal axis position

y vertical axis position

z lateral axis position

t time

Applying Buckingham's Pi Theorem, one starts with

$$\begin{aligned}
\pi &= [m]^{\alpha_1}[\rho_o]^{\alpha_2}[\rho_{o_c}]^{\alpha_3}[\ell]^{\alpha_4}[h]^{\alpha_5}[w]^{\alpha_6}[t_c]^{\alpha_7}[h_a]^{\alpha_8}[A_a]^{\alpha_9}[u_x]^{\alpha_{10}}[u_y]^{\alpha_{11}}[c]^{\alpha_{12}}[c_c]^{\alpha_{13}} \\
&\quad [E]^{\alpha_{14}}[S]^{\alpha_{15}}[\sigma_{y,c}]^{\alpha_{16}}[\sigma_{y,c_c}]^{\alpha_{17}}[E_o]^{\alpha_{18}}[E_{o_c}]^{\alpha_{19}}[G_o]^{\alpha_{20}}[G_{o_c}]^{\alpha_{21}}[t]^{\alpha_{22}} \\
\pi &= [M]^{\alpha_1+\alpha_2+\alpha_3+\alpha_{14}+\alpha_{15}+\alpha_{16}+\alpha_{17}+\alpha_{18}+\alpha_{19}+\alpha_{20}+\alpha_{21}} \\
&\quad [L]^{-3\alpha_2-3\alpha_3+\alpha_4+\alpha_5+\alpha_6+\alpha_7+\alpha_8+2\alpha_9+\alpha_{10}+\alpha_{11}+\alpha_{12}+\alpha_{13}+2\alpha_{14}+2\alpha_{15}-\alpha_{16}-\alpha_{17}-\alpha_{18}-\alpha_{19}-\alpha_{20}-\alpha_{21}} \\
&\quad [T]^{-\alpha_{10}-\alpha_{11}-\alpha_{12}-\alpha_{13}-2\alpha_{14}-2\alpha_{15}-2\alpha_{16}-2\alpha_{17}-2\alpha_{18}-2\alpha_{19}-2\alpha_{20}-2\alpha_{21}+\alpha_{22}} \\
\pi &= [M]^{\beta_2}[L]^{\beta_3}[T]^{\beta_4} \qquad (4.88)
\end{aligned}$$

$$\begin{aligned}
\beta_1 &= \alpha_1 + \alpha_2 + \alpha_3 + \alpha_{14} + \alpha_{15} + \alpha_{16} + \alpha_{17} + \alpha_{18} + \alpha_{19} + \alpha_{20} + \alpha_{21} = 0 \\
\beta_2 &= -3\alpha_2 - 3\alpha_3 + \alpha_4 + \alpha_5 + \alpha_6 + \alpha_7 + \alpha_8 + 2\alpha_9 + \alpha_{10} + \alpha_{11} + \alpha_{12} + \alpha_{13} + 2\alpha_{14} \\
&\quad +2\alpha_{15} - \alpha_{16} - \alpha_{17} - \alpha_{18} - \alpha_{19} - \alpha_{20} - \alpha_{21} = 0 \\
\beta_3 &= -\alpha_{10} - \alpha_{11} - \alpha_{12} - \alpha_{13} - 2\alpha_{14} - 2\alpha_{15} - 2\alpha_{16} - 2\alpha_{17} - 2\alpha_{18} - 2\alpha_{19} \\
&\quad -2\alpha_{20} - 2\alpha_{21} + \alpha_{22} = 0
\end{aligned}$$

The set of equations can be written in matrix form as:

$$\underline{\beta} = [D]\underline{\alpha} = \underline{0}$$

where

$$[D] = \begin{bmatrix}
1 & 1 & 1 & 0 & 0 & 0 & 0 & 0 & 0 & 0 & 0 & 0 & 0 & 1 & 1 & 1 & 1 & 1 & 1 & 1 & 1 & 0 \\
0 & -3 & -3 & 1 & 1 & 1 & 1 & 1 & 2 & 1 & 1 & 1 & 1 & 2 & 2 & -1 & -1 & -1 & -1 & -1 & -1 & 0 \\
0 & 0 & 0 & 0 & 0 & 0 & 0 & 0 & 0 & -1 & -1 & -1 & -1 & -2 & -2 & -2 & -2 & -2 & -2 & -2 & -2 & 1
\end{bmatrix}$$

Working in the null space of $[D]$ the solution for the invariants is,

$$\begin{aligned}\pi_k &= \left(\rho_o\frac{\ell^3}{m}\right)^{c_2}\left(\rho_{o_c}\frac{\ell^3}{m}\right)^{c_3}\left(\frac{h}{\ell}\right)^{c_5}\left(\frac{w}{\ell}\right)^{c_6}\left(\frac{t_c}{\ell}\right)^{c_7}\left(\frac{h_a}{\ell}\right)^{c_8}\left(\frac{A_a}{\ell^2}\right)^{c_9}\left(\frac{u_y}{u_x}\right)^{c_{11}}\left(\frac{c}{u_x}\right)^{c_{12}}\left(\frac{c_c}{u_x}\right)^{c_{13}} \\ &\quad \left(\frac{E}{mu_x^2}\right)^{c_{14}}\left(\frac{S}{mu_x^2}\right)^{c_{15}}\left(\sigma_{y,c}\frac{\ell^3}{mu_x^2}\right)^{c_{16}}\left(\sigma_{y,c_c}\frac{\ell^3}{mu_x^2}\right)^{c_{17}}\left(E_o\frac{\ell^3}{mu_x^2}\right)^{c_{18}}\left(E_{o_c}\frac{\ell^3}{mu_x^2}\right)^{c_{19}} \\ &\quad \left(G_o\frac{\ell^3}{mu_x^2}\right)^{c_{20}}\left(G_{o_c}\frac{\ell^3}{mu_x^2}\right)^{c_{21}} \\ &= \prod_{k=1}^{18}\pi_k^{c_k} \end{aligned} \tag{4.89}$$

Eighteen invariants must be simultaneously satisfied to adequately describe the scaling between models. If $c_2 = 1$ is chosen and all other $c_i = 0$ then the first invariant is

$$\pi_1 = \rho_o\frac{\ell^3}{m} \tag{4.90}$$

The slipper density must be invariant with the ratio of the sled mass and the cubed length of the slipper.

If $c_3 = 1$ is chosen and all other $c_i = 0$ then the second invariant is

$$\pi_2 = \rho_{o_c}\frac{\ell^3}{m} \tag{4.91}$$

The coating density must be invariant with the ratio of the sled mass and the cubed length of the slipper.

If $c_5 = 1$ is chosen and all other $c_i = 0$ then the third invariant is

$$\pi_3 = \frac{h}{\ell} \tag{4.92}$$

The slipper height must be invariant with the length of the slipper.

If $c_6 = 1$ is chosen and all other $c_i = 0$ then the fourth invariant is

$$\pi_4 = \frac{w}{\ell} \tag{4.93}$$

The slipper width must be invariant with the slipper length.

If $c_7 = 1$ is chosen and all other $c_i = 0$ then the fifth invariant is

$$\pi_5 = \frac{t_c}{\ell} \tag{4.94}$$

The coating thickness must be invariant with the slipper length.

If $c_8 = 1$ is chosen and all other $c_i = 0$ then the sixth invariant is

$$\pi_6 = \frac{h_a}{\ell} \tag{4.95}$$

The rail roughness height must be invariant with the slipper length.

If $c_9 = 1$ is chosen and all other $c_i = 0$ then the seventh invariant is

$$\pi_7 = \frac{A_a}{\ell^2} \tag{4.96}$$

The rail roughness cross sectional area must be invariant with the slipper length squared.

If $c_{11} = 1$ is chosen and all other $c_i = 0$ then the eighth invariant is

$$\pi_8 = \frac{u_y}{u_x} \tag{4.97}$$

The vertical and horizontal velocity ratio of the slipper must remain invariant.

If $c_{12} = 1$ is chosen and all other $c_i = 0$ then the ninth invariant is

$$\pi_9 = \frac{c}{u_x} \tag{4.98}$$

The ratio of material speed of sound and horizontal velocity must remain invariant.

If $c_{13} = 1$ is chosen and all other $c_i = 0$ then the tenth invariant is

$$\pi_{10} = \frac{c_c}{u_x} \tag{4.99}$$

The ratio of coating speed of sound and horizontal velocity must remain invariant.

If $c_{14} = 1$ is chosen and all other $c_i = 0$ then the eleventh invariant is

$$\pi_{11} = \frac{E}{mu_x^2} \tag{4.100}$$

The total energy of the slipper as compared to the slipper kinetic energy based on the horizontal velocity must remain invariant between models.

If $c_{15} = 1$ is chosen and all other $c_i = 0$ then the twelfth invariant is

$$\pi_{12} = \frac{S}{mu_x^2} \tag{4.101}$$

The internal energy source of the slipper as compared to the slipper kinetic energy based on the horizontal velocity must remain invariant between models.

If $c_{16} = 1$ is chosen and all other $c_i = 0$ then the thirteenth invariant is

$$\pi_{13} = \sigma_{y,c}\frac{\ell^3}{mu_x^2} \tag{4.102}$$

The ratio of the slipper yield stress and the horizontal kinetic energy as scaled with the slipper length must remain invariant between models.

If $c_{17} = 1$ is chosen and all other $c_i = 0$ then the fourteenth invariant is

$$\pi_{14} = \sigma_{y,c_c}\frac{\ell^3}{mu_x^2} \tag{4.103}$$

The ratio of the coating yield stress and the horizontal kinetic energy as scaled with the slipper length must remain invariant between models.

If $c_{18} = 1$ is chosen and all other $c_i = 0$ then the fifteenth invariant is

$$\pi_{15} = E_o\frac{\ell^3}{mu_x^2} \tag{4.104}$$

The ratio of the slipper elastic modulus and the horizontal kinetic energy as scaled with the slipper length must remain invariant between models.

If $c_{19} = 1$ is chosen and all other $c_i = 0$ then the sixteenth invariant is

$$\pi_{16} = E_{o_c} \frac{\ell^3}{m u_x^2} \tag{4.105}$$

The ratio of the coating elastic modulus and the horizontal kinetic energy as scaled with the slipper length must remain invariant between models.

If $c_{20} = 1$ is chosen and all other $c_i = 0$ then the seventeenth invariant is

$$\pi_{17} = G_o \frac{\ell^3}{m u_x^2} \tag{4.106}$$

The ratio of the slipper shear modulus and the horizontal kinetic energy as scaled with the slipper length must remain invariant between models.

If $c_{21} = 1$ is chosen and all other $c_i = 0$ then the eighteenth invariant is

$$\pi_{18} = G_{o_c} \frac{\ell^3}{m u_x^2} \tag{4.107}$$

The ratio of the coating shear modulus and the horizontal kinetic energy as scaled with the slipper length must remain invariant between models.

In order to maintain proper scaling of the hypervelocity sled problem between models, eighteen products must remain constant between the models. The height to length and width to length ratios (h to ℓ and w to ℓ ratios) of the slipper must remain unchanged. In addition, all important geometric lengths such as rail roughness height, rail roughness area, and coating thickness must remain invariant with respect to the slipper length.

Also, the ratio of vertical to horizontal velocity (u_y to u_x ratio) and both material and coating sound speed to horizontal velocity must remain unchanged. One may also look at this velocity ratio as the angle of impact. The ratio of the total internal energy and any energy source of the slipper must also be scaled properly to the horizontal kinetic energy of the slipper.

Finally, the material properties of the slipper and coating must remain invariant with respect to the horizontal kinetic energy of the slipper. Another important invariant that

comes out of this analysis is the ratio of the slipper and coating densities to the total mass per unit volume based on the slipper length cubed.

From this analysis it is possible to obtain a natural length or time scale. For example solving

$$\underline{\beta} = [D]\underline{\alpha} = \left\{ \begin{array}{c} 0 \\ 0 \\ 1 \end{array} \right\}$$

produces a natural time scale, $\tilde{T}$.

So, the time-scale for this case becomes,

$$\tilde{T} = \frac{\ell}{u_x}\pi(\mathbf{c})$$

where $\pi(\mathbf{c})$, as in Equation 4.89, is a function of the arbitrarily selected $\mathbf{c}$ vector. When $\mathbf{c}$ is the zero vector, then the time-scale is based on the time it takes the slipper to travel one length of its base horizontally.

The time-scale that results from this analysis is based upon the horizontal velocity and the length of the slipper. In other words, the time-scale is based on how long it takes the slipper to travel one entire length of its base. This is the same time scale indicated from the sled analysis in section 4.5.2 and the modified obliquely impacting slipper analysis in section 4.5.3.

4.5.6 Results of a Dimensional Analysis Study of the Slipper with an Artificial Mass Using the Conservation Equations with CTH. The dimensional analysis of the slipper from a *time exclusion* CTH algorithm-based approach is investigated. The results for the Laird model with original dimensions is compared to the results of a Laird model scaled by twice the size in accordance with invariant parameters from the dimensional analyses of sections 4.5.3. For numerical analysis of the rail roughness case, a coating is not added at this time, but the ultimate goal of the research is to study coatings.

4.5.6.1 Vibratory Impact Results for the Slipper with an Artificial Sled Mass.

The vibratory impact is studied. The invariants listed in section 4.5.3 must remain constant between both models to be compared. In this study, the original Laird model with original slipper dimensions of 4.37 cm length and 2.54 cm height is modified with the addition of an artificial mass of 56.75 kg (a quarter of 227 kg) using an artificial material of platinum as compared to a model of dimensions twice the length and height of the original. The artificial mass is selected to be a material that is different from the slipper in accordance with the following concepts:

1. The actual sled system consists of materials that are different than the slipper.
2. It is assumed that gouging occurs locally in the slipper material. This means the sled system mass only affects the gouging phenomena by adding to the effective mass of the impact which, in turn, affects the total energy of the impact of the system. If true, then the material properties of the sled system mass are not important to studying the gouging phenomenon unless the phenomenon occurs after shock reflection off the upper surface of the slipper.

Platinum is chosen for the artificial mass material because of its high density which minimizes the dimensions of the artificial mass and reduces the global model size making the number of cells economical for the general analysis. The material properties remain the same between models and the horizontal and vertical impact velocities also remain the same. Thus, the invariants (that begin on page 4-60) take on the following values:

- $\pi_1 = \rho_o \frac{\ell^3}{m} = \rho_o \frac{\ell^3}{\ell w h \rho_{artificial\ mass}} = \rho_o \frac{(2\ell)^3}{2\ell 2w 2h \rho_{artificial\ mass}} = \rho_o \frac{\ell^2}{wh\rho_{artificial\ mass}}$ is met for both models
- $\pi_2 = \frac{h}{\ell} = \frac{2.54cm}{4.37cm} = \frac{5.08cm}{8.74cm} = 0.581236$
- $\pi_3 = \frac{w}{\ell} = \frac{10.8cm}{4.37cm} = \frac{21.6cm}{8.74cm} = 2.471396$
- $\pi_4 = \frac{u_y}{u_x} = \frac{50m/s}{2000m/s} = 0.025$ for both models.
- $\pi_5 = \frac{c}{u_x} = \frac{c}{2000m/s}$ remains the same between models because material properties do not change between models and the same horizontal velocity is also used.

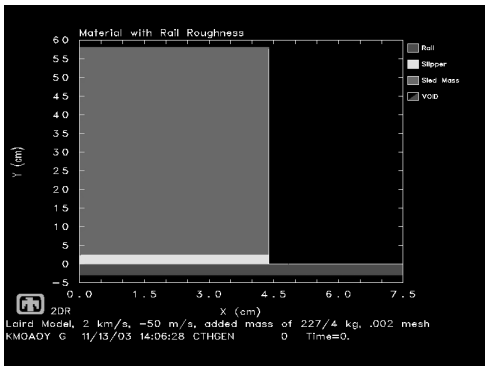

(a) **Laird model with artificial mass.**

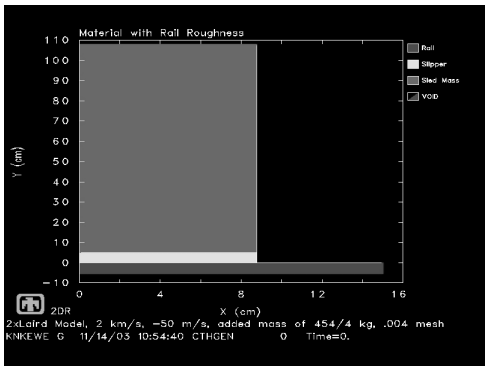

(b) **Laird model with artificial mass with dimensions scaled up by twice the original dimensions.**

Figure 4.22 **Laird original model and 2x scaled Laird model.**

- $\pi_6 = \dfrac{E}{mu_x^2} = \dfrac{1/2\ mu_x^2}{mu_x^2} = \dfrac{1/2\ \ell wh\rho_{artificial\ mass}u_x^2}{\ell wh\rho_{artificial\ mass}u_x^2} = \dfrac{1/2\ (2\ell 2w2h)\rho_{artificial\ mass}u_x^2}{2\ell 2w2h\rho_{artificial\ mass}u_x^2}$ is met by both models.
- $\pi_7 = \dfrac{S}{\ell wh\rho_{artificial\ mass}u_x^2} = \dfrac{8S}{2\ell 2w2h\rho_{artificial\ mass}u_x^2}$ is met by both models.
- $\pi_8 = \sigma_{y,c}\dfrac{\ell^3}{mu_x^2} = \sigma_{y,c}\dfrac{\ell^3}{\ell wh\rho_{artificial\ mass}u_x^2} = \sigma_{y,c}\dfrac{(2\ell)^3}{2\ell 2w2h\rho_{artificial\ mass}u_x^2}$ remains the same between models because material properties do not change between models and the same horizontal velocity is also used.
- $\pi_9 = E_o\dfrac{\ell^3}{mu_x^2} = E_o\dfrac{\ell^3}{\ell wh\rho_{artificial\ mass}u_x^2} = E_o\dfrac{(2\ell)^3}{2\ell 2w2h\rho_{artificial\ mass}u_x^2}$ remains the same between models because material properties do not change between models and the same horizontal velocity is also used.
- $\pi_{10} = G_o\dfrac{\ell^3}{mu_x^2} = G_o\dfrac{\ell^3}{\ell wh\rho_{artificial\ mass}u_x^2} = G_o\dfrac{(2\ell)^3}{2\ell 2w2h\rho_{artificial\ mass}u_x^2}$ remains the same between models because material properties do not change between models and the same horizontal velocity is also used.
- $\tilde{T} = u_x\dfrac{t_1}{\ell} = u_x\dfrac{t_2}{2\ell}$ provides us with the time-scale that will be used to match results between models (i.e., $2t_1 = t_2$).

Theoretically, since each invariant is satisfied, this means the results of the models will be consistent with each other.

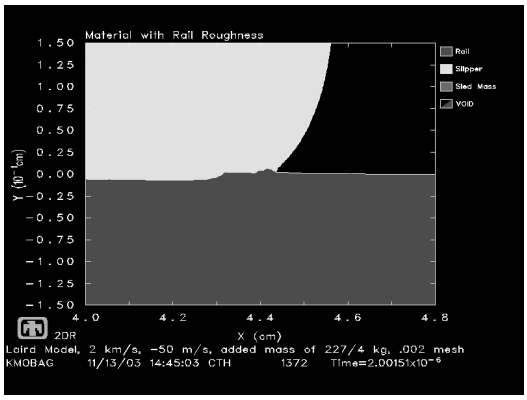

(a) **Material plot of results for Laird model with artificial mass at 2 microseconds.**

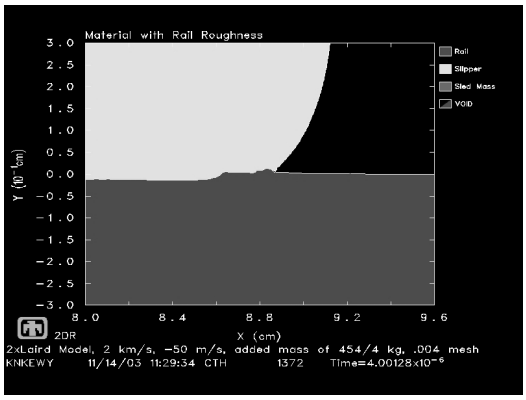

(b) **Material plot of results for 2x scaled Laird model with artificial mass at 4 microseconds.**

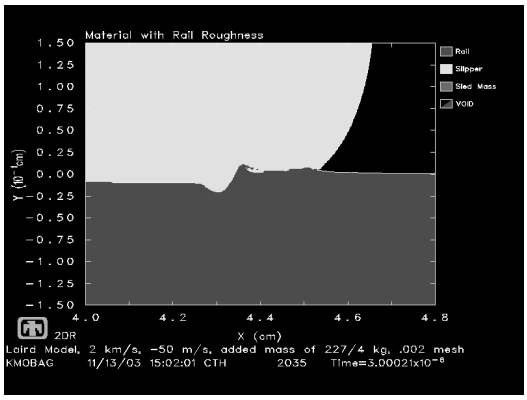

(c) **Material plot of results for Laird model with artificial mass at 3 microseconds.**

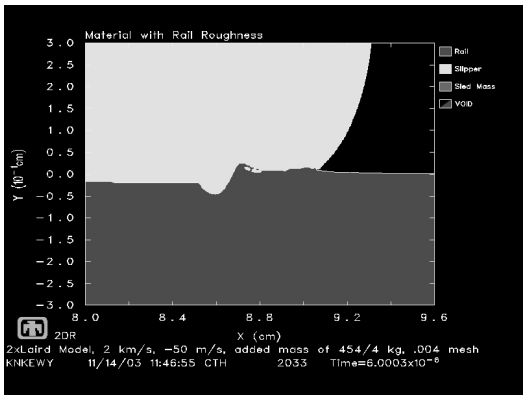

(d) **Material plot of results for 2x scaled Laird model with artificial mass at 6 microseconds.**

Figure 4.23 **Comparison of Laird original model to 2x scaled model for oblique impact with artificial mass for nondimensional time scales of two and three.**

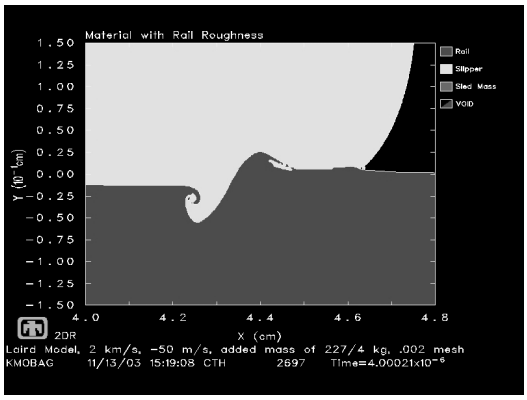

(a) **Material plot of results for Laird model with artificial mass at 4 microseconds.**

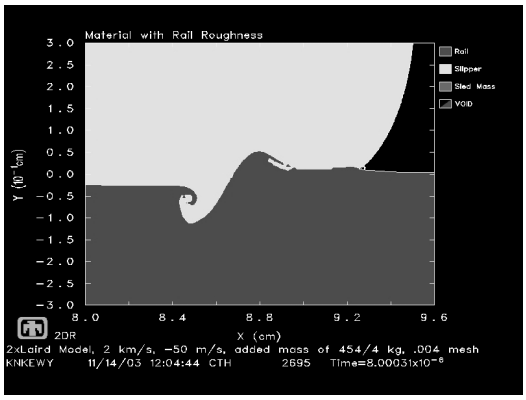

(b) **Material plot of results for 2x scaled Laird model with artificial mass at 8 microseconds.**

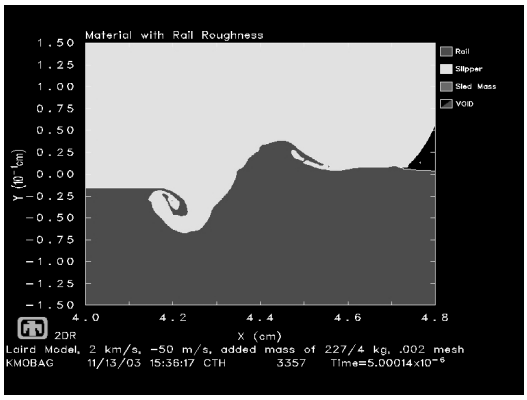

(c) **Material plot of results for Laird model with artificial mass at 5 microseconds.**

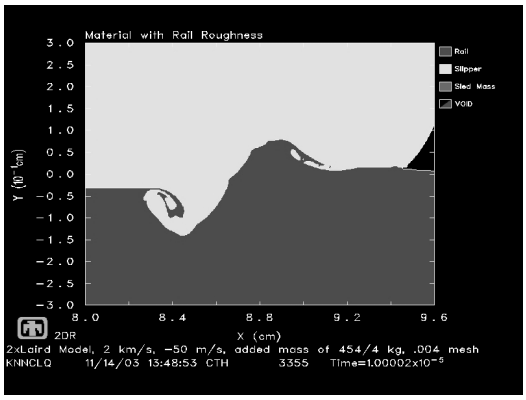

(d) **Material plot of results for 2x scaled Laird model with artificial mass at 10 microseconds.**

Figure 4.24 **Comparison of Laird original model to 2x scaled model for oblique impact with artificial mass for nondimensional time scales of four and five.**

The two models used in this study are shown in Figure 4.22. The results based on material plots are shown in Figures 4.23 and 4.24. Observe the results between scaled models match quite well with only slight differences for the same nondimensional times. This shows the invariants and dimensioned quantities for the dimensional analysis are appropriate.

4.5.6.2 Rail Roughness Impact Results for the Slipper with an Artificial Sled Mass. For the rail roughness case, a similar investigation is performed. The invariants listed in section 4.5.5 must remain constant between both models to be compared. In this study, two models are compared. The first is the original Laird model with original slipper dimensions of 4.37 cm length and 2.54 cm height and elliptical rail roughness of 0.03 cm height is modified with the addition of an artificial mass of 56.75 kg (a quarter of 227 kg) using an artificial material of platinum as compared to a model of dimensions twice the length and height of the original. The artificial mass is selected to be platinum for the same reasons outlined in section 4.5.6.1 above. In the second model, a coating of 3 mils thickness (0.00762 cm) is added to the Laird rail roughness model. The material properties remain the same between models and the horizontal and vertical impact velocities also remain the same. Thus, the invariants (that begin on page 4-73) take on the following values:

- $\pi_1 = \rho_o \frac{\ell^3}{m} = \rho_o \frac{\ell^3}{\ell w h \rho_{artificial\ mass}} = \rho_o \frac{(2\ell)^3}{2\ell 2w 2h \rho_{artificial\ mass}} = \rho_o \frac{\ell^2}{wh\rho_{artificial\ mass}}$ is met for both models
- $\pi_2 = \rho_{o_c} \frac{\ell^3}{m} = \rho_{o_c} \frac{\ell^3}{\ell w h \rho_{artificial\ mass}} = \rho_{o_c} \frac{(2\ell)^3}{2\ell 2w 2h \rho_{artificial\ mass}} = \rho_{o_c} \frac{\ell^2}{wh\rho_{artificial\ mass}}$ is met for both models
- $\pi_3 = \frac{h}{\ell} = \frac{2.54cm}{4.37cm} = \frac{5.08cm}{8.74cm} = 0.581236$
- $\pi_4 = \frac{w}{\ell} = \frac{10.8cm}{4.37cm} = \frac{21.6cm}{8.74cm} = 2.471396$
- $\pi_5 = \frac{t_c}{\ell} = \frac{0.00762cm}{4.37cm} = \frac{0.01524cm}{8.74cm} = 0.0017437$
- $\pi_6 = \frac{h_a}{\ell} = \frac{0.03cm}{4.37cm} = \frac{0.06cm}{8.74cm} = 0.00686$
- $\pi_7 = \frac{A_a}{\ell^2} = \frac{3.1414593/2 \cdot 2.75 \cdot 0.03cm^2}{4.37^2 cm^2} = \frac{3.1414593/2 \cdot 5.5 \cdot 0.06cm^2}{8.74^2 cm^2} = 0.00678$
- $\pi_8 = \frac{u_y}{u_x} = \frac{50m/s}{2000m/s} = 0.025$ for both models.

- $\pi_9 = \frac{c}{u_x} = \frac{c}{2000m/s}$ remains the same between models because material properties do not change between models and the same horizontal velocity is also used.
- $\pi_{10} = \frac{c_c}{u_x} = \frac{c_c}{2000m/s}$ remains the same between models because coating material properties do not change between models and the same horizontal velocity is also used.
- $\pi_{11} = \frac{E}{mu_x^2} = \frac{1/2\ mu_x^2}{mu_x^2} = \frac{1/2\ \ell wh\rho_{artificial\ mass}u_x^2}{\ell wh\rho_{artificial\ mass}u_x^2} = \frac{1/2\ (2\ell 2w2h)\rho_{artificial\ mass}u_x^2}{2\ell 2w2h\rho_{artificial\ mass}u_x^2}$ is met by both models.
- $\pi_{12} = \frac{S}{\ell wh\rho_{artificial\ mass}u_x^2} = \frac{8S}{2\ell 2w2h\rho_{artificial\ mass}u_x^2}$ is met by both models.
- $\pi_{13} = \sigma_{y,c}\frac{\ell^3}{mu_x^2} = \sigma_{y,c}\frac{\ell^3}{\ell wh\rho_{artificial\ mass}u_x^2} = \sigma_{y,c}\frac{(2\ell)^3}{2\ell 2w2h\rho_{artificial\ mass}u_x^2}$ remains the same between models because material properties do not change between models and the same horizontal velocity is also used.
- $\pi_{14} = \sigma_{y,c_c}\frac{\ell^3}{mu_x^2} = \sigma_{y,c_c}\frac{\ell^3}{\ell wh\rho_{artificial\ mass}u_x^2} = \sigma_{y,c}\frac{(2\ell)^3}{2\ell 2w2h\rho_{artificial\ mass}u_x^2}$ remains the same between models because coating material properties do not change between models and the same horizontal velocity is also used.
- $\pi_{15} = E_o\frac{\ell^3}{mu_x^2} = E_o\frac{\ell^3}{\ell wh\rho_{artificial\ mass}u_x^2} = E_o\frac{(2\ell)^3}{2\ell 2w2h\rho_{artificial\ mass}u_x^2}$ remains the same between models because material properties do not change between models and the same horizontal velocity is also used.
- $\pi_{16} = E_{o_c}\frac{\ell^3}{mu_x^2} = E_{o_c}\frac{\ell^3}{\ell wh\rho_{artificial\ mass}u_x^2} = E_{o_c}\frac{(2\ell)^3}{2\ell 2w2h\rho_{artificial\ mass}u_x^2}$ remains the same between models because coating material properties do not change between models and the same horizontal velocity is also used.
- $\pi_{17} = G_o\frac{\ell^3}{mu_x^2} = G_o\frac{\ell^3}{\ell wh\rho_{artificial\ mass}u_x^2} = G_o\frac{(2\ell)^3}{2\ell 2w2h\rho_{artificial\ mass}u_x^2}$ remains the same between models because material properties do not change between models and the same horizontal velocity is also used.
- $\pi_{18} = G_{o_c}\frac{\ell^3}{mu_x^2} = G_{o_c}\frac{\ell^3}{\ell wh\rho_{artificial\ mass}u_x^2} = G_{o_c}\frac{(2\ell)^3}{2\ell 2w2h\rho_{artificial\ mass}u_x^2}$ remains the same between models because coating material properties do not change between models and the same horizontal velocity is also used.
- $\tilde{T} = u_x\frac{t_1}{\ell} = u_x\frac{t_2}{2\ell}$ provides us with the time-scale that will be used to match results between models (i.e., $2t_1 = t_2$).

Theoretically, since each invariant is satisfied, this means the results of the models will be consistent with each other.

The two models used in this study are shown in Figure 4.25. The difference between the two cases is the addition of a 3 mil epoxy coating to the rail. This coating is scaled up to 6 mils in the larger model for dimensional analysis comparison. Figures 4.25(c) and 4.25(d) show a zoomed in view of the coated case at the tip of the slipper and rail roughness interaction. The artificial mass in the coated case is the same as in the first, uncoated case even though it is not shown in the figures.

The results for the uncoated rail roughness case are shown in Figures 4.26 and 4.27. Observe the results between scaled models match quite well with only slight differences for the same nondimensional times. This shows the invariants and dimensioned quantities for the dimensional analysis are appropriate.

The results for the coated rail roughness case are shown in Figure 4.29. Observe the results between scaled models match quite well with only slight differences for the same nondimensional times. This shows the invariants and dimensioned quantities for the dimensional analysis are appropriate.

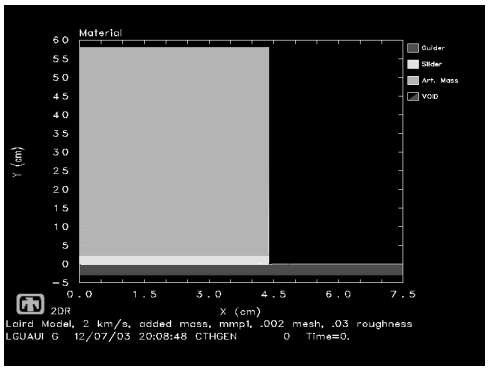

(a) **Laird model with artificial mass and rail roughness .03 cm high.**

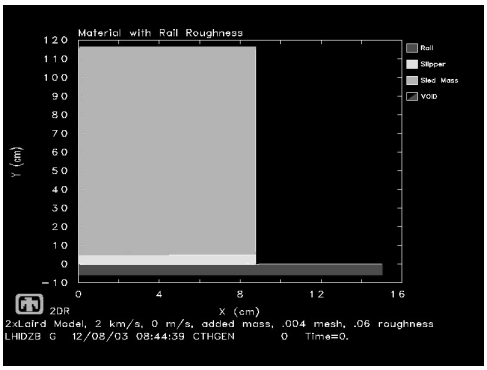

(b) **Laird model with artificial mass and rail roughness with dimensions scaled up by twice the original dimensions.**

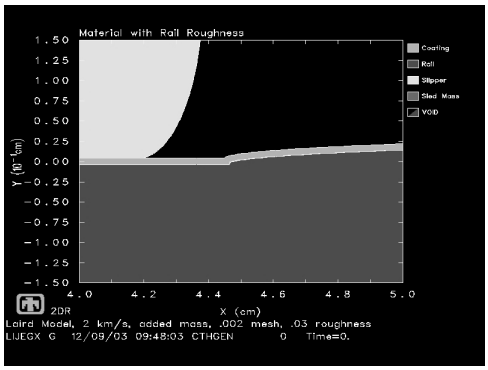

(c) **Laird model with artificial mass and 3 mil epoxy coated rail roughness .03 cm high.**

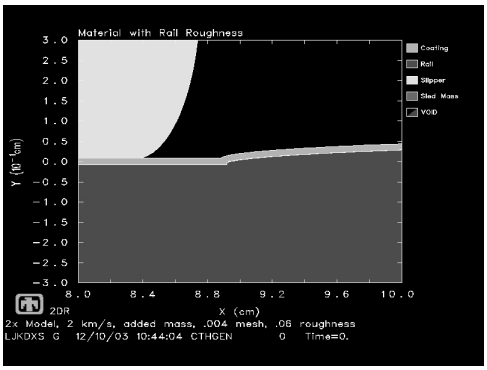

(d) **Laird model with artificial mass and coated rail roughness with dimensions scaled up by twice the original dimensions.**

Figure 4.25 **Laird original model and 2x scaled Laird model with artificial mass and rail roughness.**

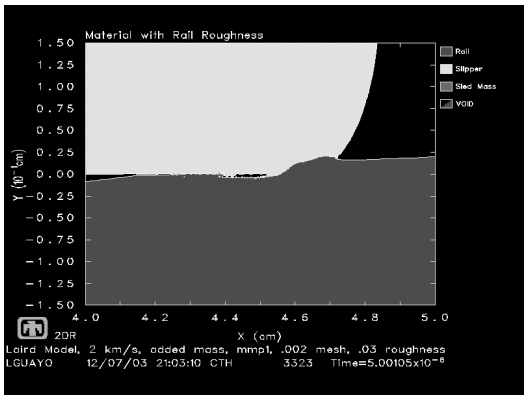

(a) **Material plot of results for Laird model with artificial mass at 4 microseconds.**

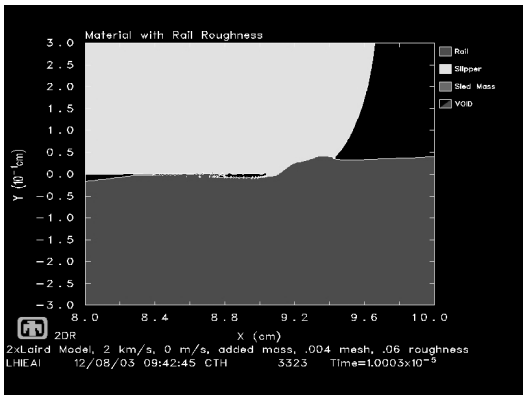

(b) **Material plot of results for 2x scaled Laird model with artificial mass at 8 microseconds.**

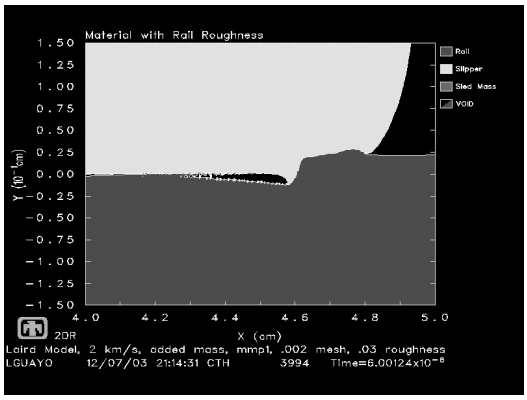

(c) **Material plot of results for Laird model with artificial mass at 5 microseconds.**

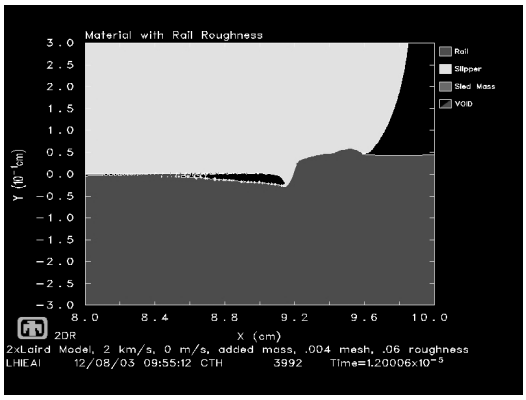

(d) **Material plot of results for 2x scaled Laird model with artificial mass at 10 microseconds.**

Figure 4.26 **Comparison of Laird original model to 2x scaled model for oblique impact with artificial mass for nondimensional time scales of two and three.**

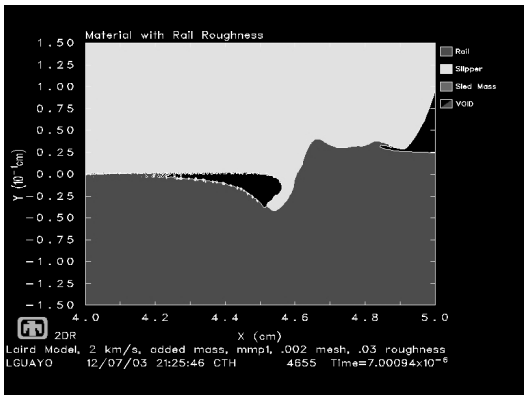

(a) **Material plot of results for Laird model with artificial mass at 7 microseconds.**

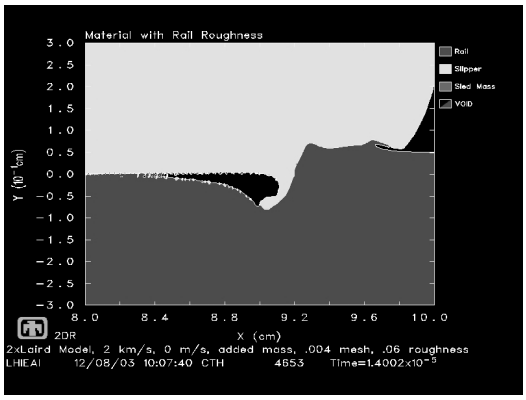

(b) **Material plot of results for 2x scaled Laird model with artificial mass at 14 microseconds.**

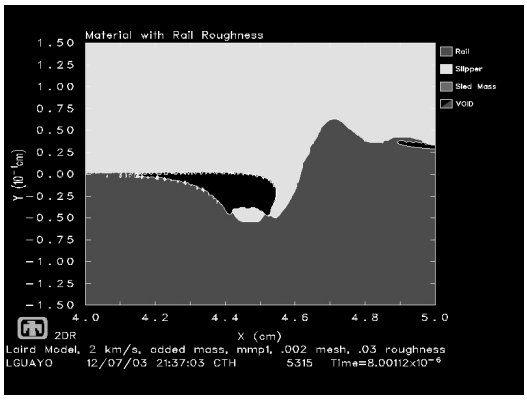

(c) **Material plot of results for Laird model with artificial mass at 8 microseconds.**

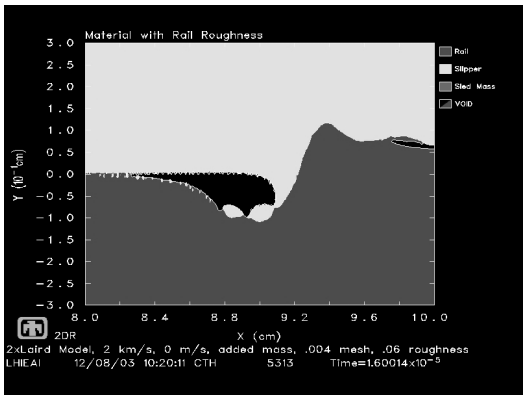

(d) **Material plot of results for 2x scaled Laird model with artificial mass at 16 microseconds.**

Figure 4.27 **Comparison of Laird original model to 2x scaled model for oblique impact with artificial mass for nondimensional time scales of four and five.**

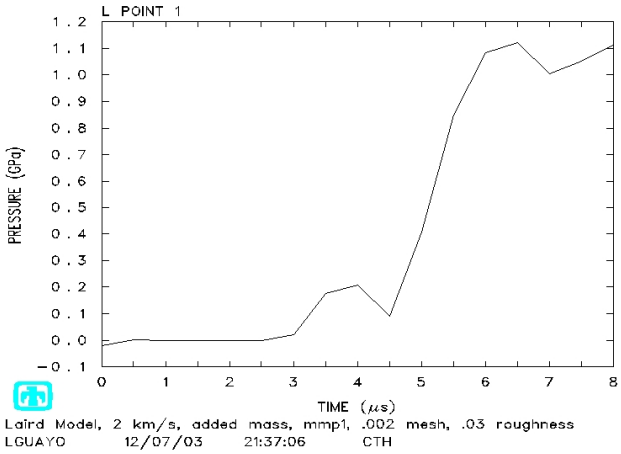

(a) **Time-scaled history plot of pressure for Laird model with artificial mass and rail roughness.**

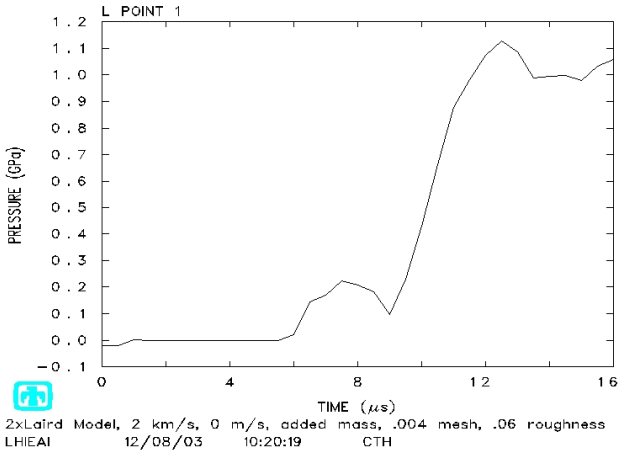

(b) **Time-scaled history plot of pressure for the 2x scaled Laird model.**

Figure 4.28 **Time history comparison of Laird model with artificial mass to 2x scaled model pressure for rail roughness impact.**

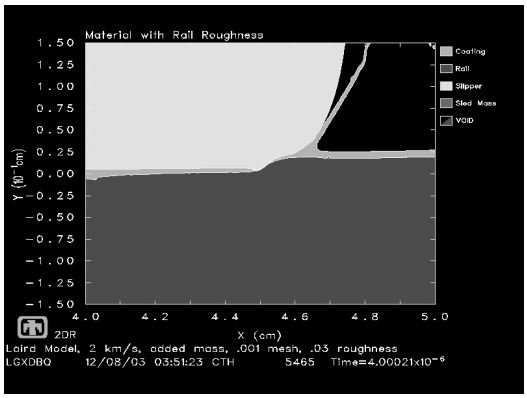

(a) **Material plot of results for Laird model with artificial mass and coating at 4 microseconds.**

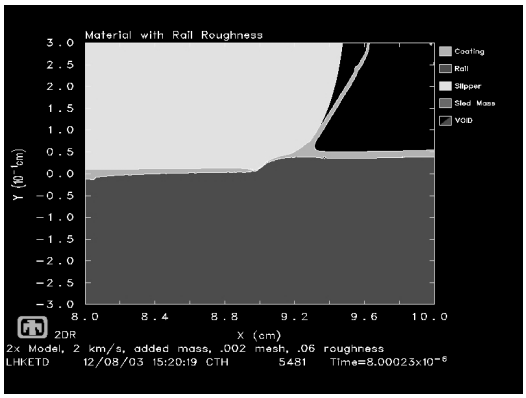

(b) **Material plot of results for 2x scaled Laird model with artificial mass and coating at 8 microseconds.**

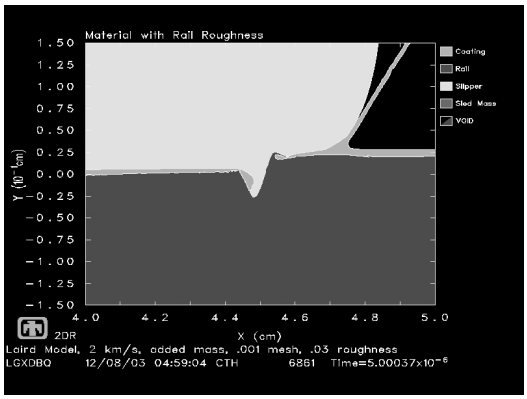

(c) **Material plot of results for Laird model with artificial mass and coating at 5 microseconds.**

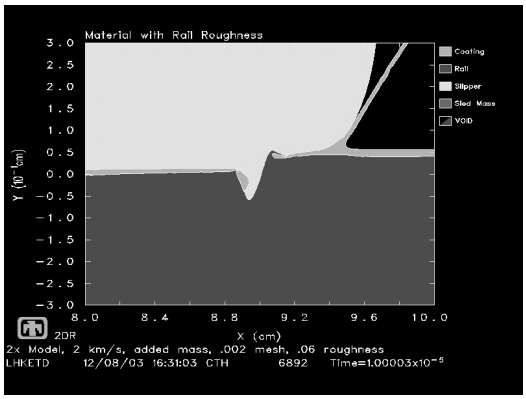

(d) **Material plot of results for 2x scaled Laird model with artificial mass and coating at 10 microseconds.**

Figure 4.29 **Comparison of Laird original model to 2x scaled model for oblique impact with artificial mass and coating for nondimensional time scales of two and three.**

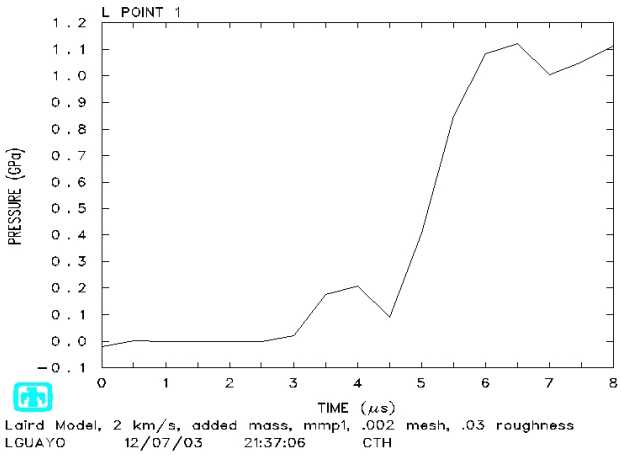

(a) **Time-scaled history plot of pressure for Laird model with artificial mass and coated rail roughness.**

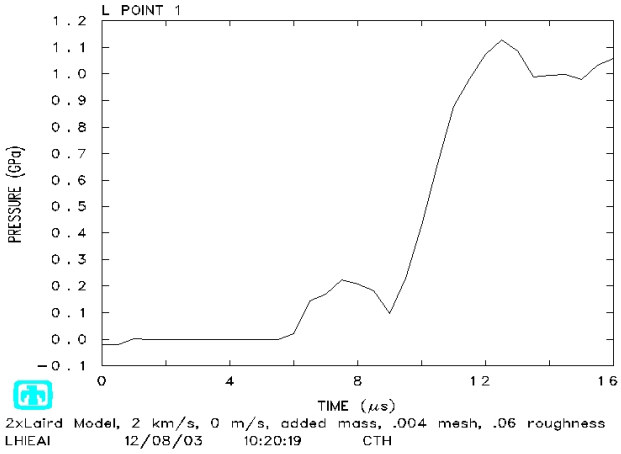

(b) **Time-scaled history plot of pressure for the 2x scaled Laird model with coating and artificial mass.**

Figure 4.30 **Time history comparison of Laird model with artificial mass to 2x scaled model pressure for rail roughness impact.**

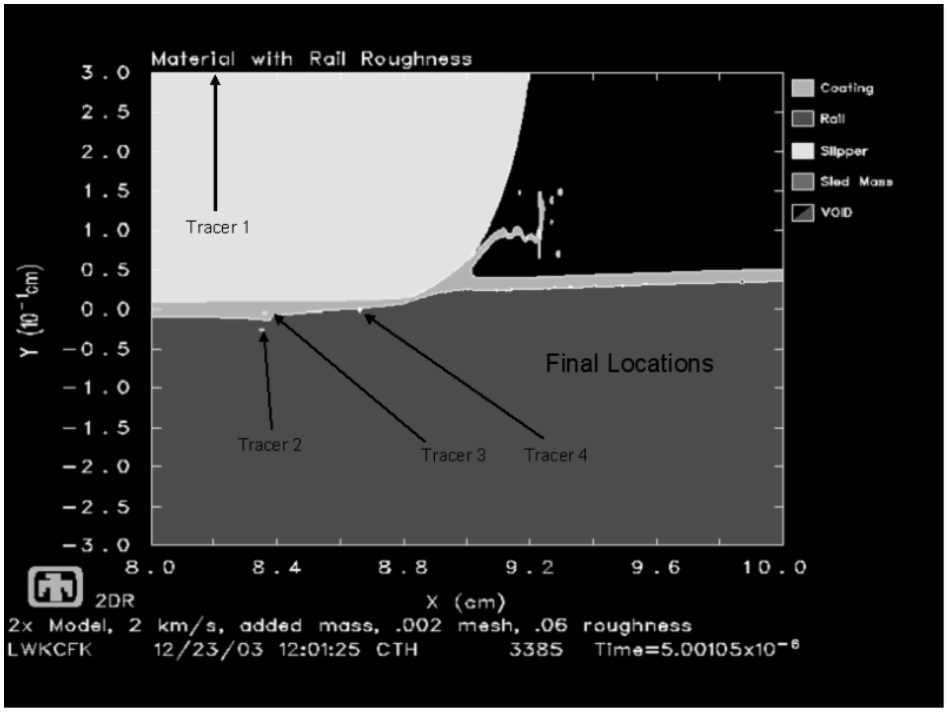

Figure 4.31 **Tracer locations on scaled up case with artificial mass and impact with coated rail roughness.**

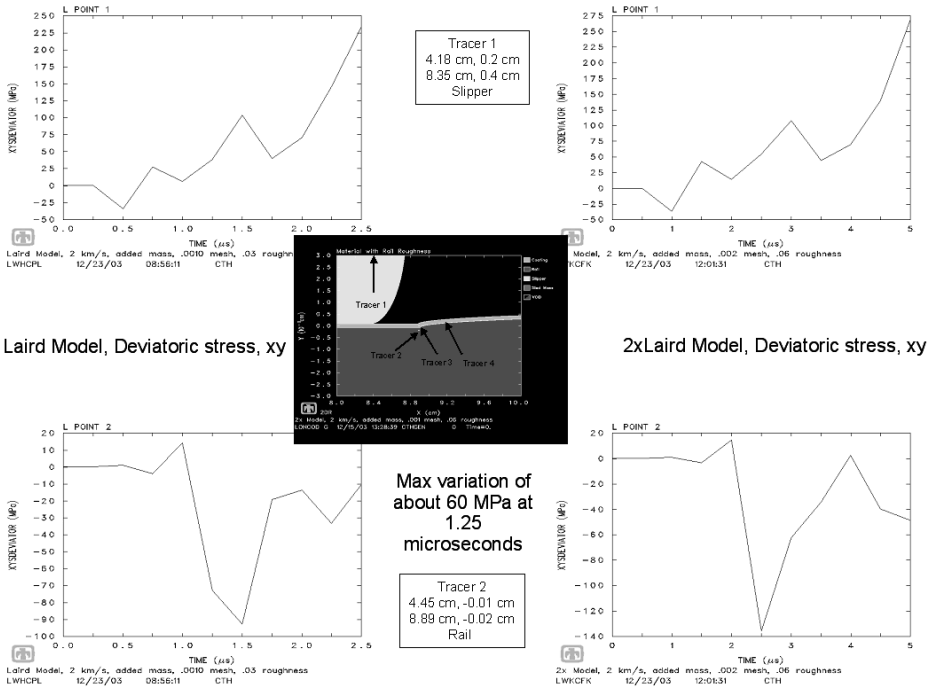

Figure 4.32 **Comparison of tracers 1 and 2 for a coated rail roughness impact.**

4.5.7 Investigation of Strain Rate Effects on Scaling. Because the internal algorithms of CTH have not all been scaled in time, there are time scale effects which cause local variations due to parameters which are time dependent. One such parameter is the strain rate. A study is conducted to quantify the variations when all parameters are not scaled for time. To illustrate the point, this study considers in detail only two of the cases detailed above. The results within the area of impact with high strain rates are compared. It is shown that variations occur in the stress deviator because the strain rates have not been scaled with time. One means of doing this is investigated. The Johnson-Cook viscoplasticity model is modified through material parameters so that the material response of the rail is now properly scaled in time. Because the parameters of the Steinberg-Guinan-Lund and the coating constitutive models cannot be properly scaled in CTH, the response will never be exactly the same. This is because of the time dependent response of the slipper and coating materials that is not properly scaled in time. However, results show that an improvement of equivalent results can be obtained by scaling the independent variable of time in the constitutive model for the rail material.

The two test cases are used to simulate two different scenarios that may occur in a real test sled impact. The first case is a slipper-rail impact in which the velocity vector is at an extremely shallow angle upon a clean, flat rail. Models 1 and 2 are used to depict this case. Model 1 is used as a sample CTH legacy model that has been used to depict hypervelocity gouging using dimensions smaller than an actual test sled. Model 2 is used to simulate actual test sled dimensions. Dimensions of model 1 are scaled up by a factor of two to create model 2.

The second case is a slipper-rail impact in which the velocity vector is at an extremely shallow angle upon a rail coated with a polymer material such as epoxy. Gouging is initiated when the coating is penetrated and the slipper impacts the rail-misalignment. A schematic of this case is shown in Figure 4.21. Models 3 and 4 are used to depict this case. Models 1 and 2 are really just simplified versions of this case. All geometric dimensions of model 3 are half that of model 4. Model 4 simulates the real test sled dimensions and model 3 simulates a sample CTH model.

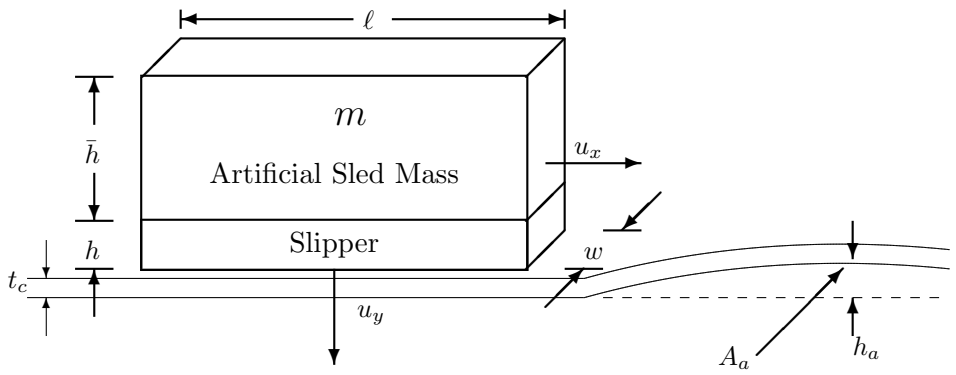

Figure 4.33 **Simplified model of an obliquely impacting slipper on a rail roughness with a coating for dimensional analysis.**

The fundamental units derived from the dimensioned quantities are mass, M; length, L; and time, T. The dimensioned quantities and their corresponding fundamental units are shown in Table 4.1. They were selected by assuming the slipper and rail material properties have the same values. The independent variables for the model are horizontal position, x; vertical position, y; lateral position, z; and time, t. Scaled coordinates and time values are used when making comparisons between models within each case.

Table 4.2 lists the dimensioned quantities and their values for each of the models used in the numerical study. Table 4.3 lists the material properties used for the slipper and rail. Not listed are the material models for the epoxy coating which is a Von Mises elastic-plastic constitutive model with a Mie-Grüneisen equation of state. Table 4.7 lists the similitude invariants determined in the dimensional analysis and the values for each model based on the dimensioned quantities from Table 4.2.

Invariants remain constant between scaled models so that the solutions are comparable. We compare results for model 1 with model 2 and results from model 3 with model 4. An arbitrary mass of 56.75 kg is selected for models 1 and 3 in order to add momentum as well as kinetic energy to the system. This material is different from the slipper material for the following reasons:

1. The actual sled system consists of materials that are different than the slipper.

Table 4.1 **Dimensioned quantities and their corresponding fundamental units.**

Dimensioned Quantity	Parameter	Fundamental Units
m	initial bulk sled mass	M
ρ_o	original density of the slipper	ML^{-3}
ρ_{o_c}	original density of the coating	ML^{-3}
ℓ	slipper length	L
h	slipper height	L
w	slipper width	L
t_c	coating thickness	L
h_a	asperity/rail roughness height	L
A_a	asperity/rail roughness area	L^2
u_x	horizontal velocity	LT^{-1}
u_y	vertical velocity	LT^{-1}
c	slipper material speed of sound	LT^{-1}
c_c	coating material speed of sound	LT^{-1}
E	initial total energy of the bulk sled system	ML^2T^{-2}
S	constant energy source of the bulk sled system	ML^2T^{-2}
$\sigma_{y,c}$	slipper critical yield strength	$ML^{-1}T^{-2}$
σ_{y,c_c}	coating critical yield strength	$ML^{-1}T^{-2}$
E_o	original slipper elastic modulus	$ML^{-1}T^{-2}$
E_{o_c}	original coating elastic modulus	$ML^{-1}T^{-2}$
G_o	original slipper shear modulus	$ML^{-1}T^{-2}$
G_{o_c}	original coating shear modulus	$ML^{-1}T^{-2}$

Table 4.2 **Computational models used to investigate scaling laws.**

Dimensioned Quantity	Parameter Values			
	Model 1	Model 2	Model 3	Model 4
m	56.75 kg	454 kg	56.75 kg	454 kg
ρ_o	8.129 g/cm^3	8.129 g/cm^3	8.129 g/cm^3	8.129 g/cm^3
ρ_{o_c}	-	-	1.186 g/cm^3	1.186 g/cm^3
ℓ	4.37 cm	8.74 cm	4.37 cm	8.74 cm
h	2.54 cm	5.08 cm	2.54 cm	5.08 cm
w	10.80 cm	21.60 cm	10.80 cm	21.60 cm
t_c	-	-	0.00762 cm	0.01524 cm
h_a	-	-	0.03 cm	0.06 cm
A_a	-	-	0.1296 cm^2	0.5184 cm^2
u_x	2 km/s	2 km/s	2 km/s	2 km/s
u_y	50 m/s	50 m/s	50 m/s	50 m/s
c	398000 cm/s	398000 cm/s	398000 cm/s	398000 cm/s
c_c	-	-	273000 cm/s	273000 cm/s
E	113.6 MN	908.6 MN	113.6 MN	908.6 MN
S	-	-	-	-
$\sigma_{y,c}$	1,447 MPa	1,447 MPa	1,447 MPa	1,447 MPa
σ_{y,c_c}	-	-	15 MPa	15 MPa
E_o	184.2 GPa	184.2 GPa	184.2 GPa	184.2 GPa
E_{o_c}	-	-	1.10 GPa	1.10 GPa
G_o	71.8 GPa	71.8 GPa	71.8 GPa	71.8 GPa
G_{o_c}	-	-	0.4 GPa	0.4 GPa

Table 4.3 **Material model constants.**

Johnson-Cook 1080 Steel (Iron) Rail			Steinberg-Guinan-Lund VascoMax 300[a] Slipper		
Model Constant	Value	Units	Model constant	Value	Units
ρ_o [b]	7.850	g/cm^3	ρ_o	8.129	g/cm^3
A	1.7526×10^9	g/cm s^2	A	2.06×10^{-12}	g/cm s^2
B	3.8019×10^9	g/cm s^2	G_o	7.18×10^{11}	g/cm s^2
G_o [b]	7.8×10^{11}	g/cm s^2	Y_o	1.447×10^{10}	g/cm s^2
Y_o [b]	7×10^9	g/cm s^2	Y_{max}	2.5×10^{10}	g/cm s^2
T_M	1835.7	K	T_{mo}	2310	K
C	0.06	-	B	3.15×10^{-4}	1/K
n	0.32	-	n	0.5	-
m	0.55	-	β	2.0	-
			γ_o	1.67	-
			a	1.2	-

[a] Constants not listed are zero.

[b] Not used in the Johnson-Cook model, listed for reference.

2. It is assumed that gouging occurs locally in the slipper material. This means the sled system mass only affects the gouging phenomena by adding to the effective mass of the impact which affects the total energy and momentum of the impact. Assuming this to be true, the material properties of the sled system mass may not be critical to studying the gouging phenomenon unless the phenomenon occurs after shock reflection off the upper surface of the slipper. For the cases under study, shock reflection at the interface between slipper and artificial mass materials will occur at approximately 6.38 μs in models 1 and 3. The solutions for the time periods under consideration do not contain shock reflections.

Platinum is chosen for the artificial mass material in this study because of its high density, which minimizes the dimensions of the artificial mass and reduces the model size, thus reducing the number of cells for analysis.

Models 1 and 3 are compared to their scaled-up counterparts in models 2 and 4, respectively. The material properties remain the same between models and the horizontal and vertical impact velocities also remain the same. The invariant products must remain constant between models for the results to be consistent.

The time scale used for the initial models are $\tilde{T}_1 = \frac{\ell}{u_x}$. The time scale for the scaled-up models is $\tilde{T}_2 = 2\frac{\ell}{u_x}$. This time scale provides a means for comparing results between models (i.e., $2\tilde{T}_1 = \tilde{T}_2$)

Table 4.4 **Invariants and their values for numerical models.**

Invariants	Model 1	Model 2	Model 3	Model 4
Mass Scaling				
$\pi_1 = \rho_o \frac{\ell^3}{m}$	0.0120	0.0120	0.0120	0.0120
$\pi_2 = \rho_{o_c} \frac{\ell^3}{m}$	-	-	0.00174	0.00174
Geometric Scaling				
$\pi_3 = \frac{h}{\ell}$	0.5812	0.5812	0.5812	0.5812
$\pi_4 = \frac{w}{\ell}$	2.4714	2.4714	2.4714	2.4714
$\pi_5 = \frac{t_c}{\ell}$	-	-	0.00174	0.00174
$\pi_6 = \frac{h_a}{\ell}$	-	-	0.00686	0.00686
$\pi_7 = \frac{A_a}{\ell^2}$	-	-	0.00678	0.00678
Velocity Scaling				
$\pi_8 = \frac{u_y}{u_x}$	0.025	0.025	0.025	0.025
$\pi_9 = \frac{c}{u_x}$	1.990	1.990	1.990	1.990
$\pi_{10} = \frac{c_c}{u_x}$	-	-	1.365	1.365
Energy Scaling				
$\pi_{11} = \frac{E}{mu_x^2}$	0.5	0.5	0.5	0.5
$\pi_{12} = \frac{S}{mu_x^2}$	-	-	-	-
$\pi_{13} = \sigma_{y,c} \frac{\ell^3}{mu_x^2}$	0.00053	0.00053	0.00053	0.00053
$\pi_{14} = \sigma_{y,c_c} \frac{\ell^3}{mu_x^2}$	-	-	5.5×10^{-7}	5.5×10^{-7}
$\pi_{15} = E_o \frac{\ell^3}{mu_x^2}$	0.0677	0.0677	0.0677	0.0677
$\pi_{16} = E_{o_c} \frac{\ell^3}{mu_x^2}$	-	-	0.0004	0.0004
$\pi_{17} = G_o \frac{\ell^3}{mu_x^2}$	0.0264	0.0264	0.0264	0.0264
$\pi_{18} = G_{o_c} \frac{\ell^3}{mu_x^2}$	-	-	0.00014	0.00014

Subscript a indicates property of asperity/rail roughness

Subscript c indicates property of the coating material.

The solution is affected by material mixing in the CTH algorithm. During the study, it was found that material boundaries between sliding materials must coincide with Eulerian mesh cell boundaries. This is important for avoiding problems due to numerical instabilities of the sliding interface algorithm.

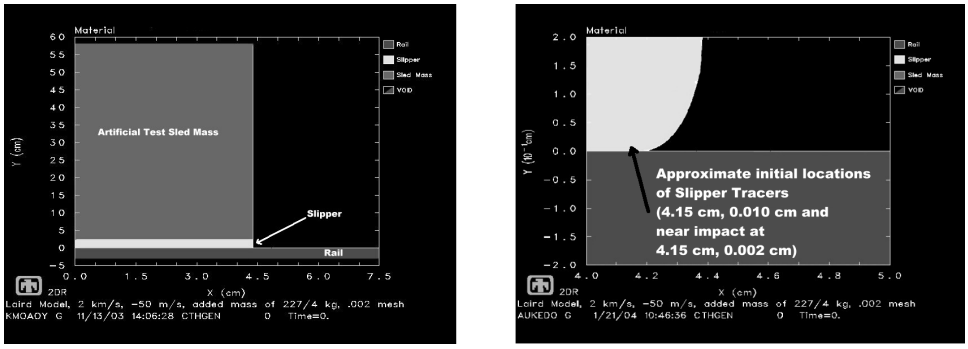

Figure 4.34 **Model 1 with artificial mass and zoomed in view of tracer placement.**

Model 1 is shown in Figure 4.22(a). A tracer point in the slipper of models 1 and 2 is first selected close to the surface of interaction (one cell length away) to capture the effect of high strain rates for the impact between the slipper and rail. This traces the worst case scenario since this point becomes part of the gouged material, which undergoes high strain rates.

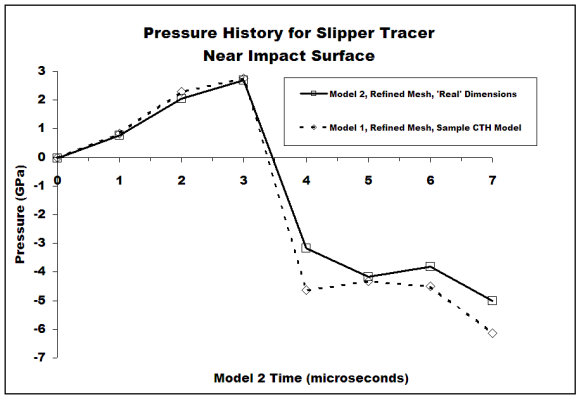

Figure 4.35 **Time-scaled history comparison of pressure for slipper tracer near oblique impact surface with mesh refinement.**

The solutions for pressure and deviatoric stress are plotted in terms of model 2 time. A coarse and a refined mesh were both studied. The refined mesh results are shown here.

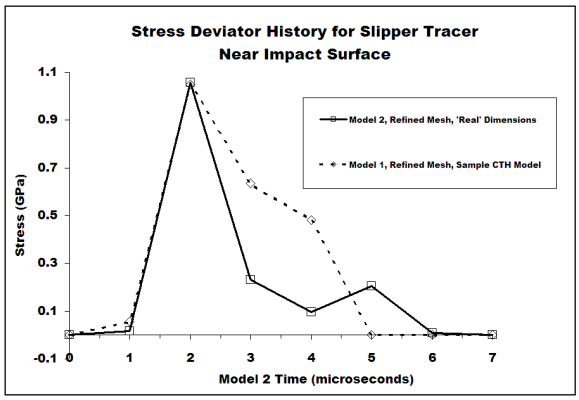

Figure 4.36 **Time-scaled history comparison of XY deviatoric stress for slipper tracer near oblique impact surface with mesh refinement.**

Mesh refinement was seen to be a factor in convergence of the solution. The plots of results from models 1 and 2 are shown in Figures 4.35 and 4.36. The results for the coarser mesh resulted in relatively larger differences in the solutions for a point near the impact surface than for the refined mesh. The average difference in pressure plots between models 1 and 2 for the coarse mesh configuration is around 1.6 GPa over the time period of 7.0 μs. The average difference in deviatoric stress is 323 MPa.

With improved mesh resolution, the solutions matched more closely. The mesh cell size was reduced by half, thus increasing the number of cells by a squared term in the vicinity of the tracers. This was the smallest mesh cell size possible with the computer resources available. The average difference between model results for the improved mesh resolution decreases to 547 MPa with a maximum difference of 1.5 GPa for pressure, and 93 MPa with a maximum difference of 400 MPa in deviatoric stress. This finer mesh is used for the next case studied.

The important differences between geometrically scaled models depends on the phenomenon being studied and the material properties of the materials. Plasticity is an important factor in development of hypervelocity gouging in a slipper and rail impact. However, global parameters such as development time of the gouge and size of the gouge are perhaps of greater interest than equivalency of the stress tensor at a particular point in scaled space and time.

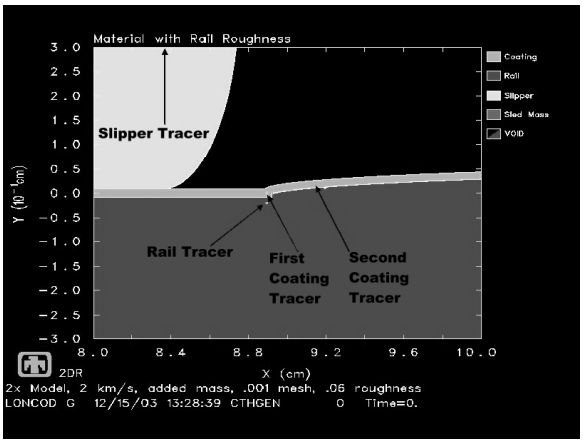

Figure 4.37 **Model 4 with artificial mass, coated rail, and rail roughness with zoomed in view of tracer placement.**

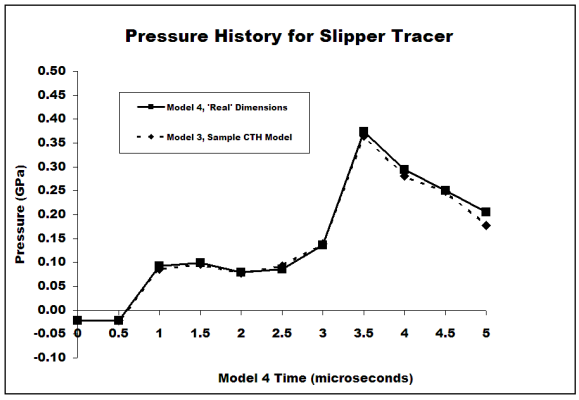

Figure 4.38 **Time-scaled history comparison of pressure for slipper tracer in coated models with rail roughness.**

The next case is shown in Figure 4.37. The figure shows where tracers in model 4 are located. Pressure and deviatoric stress traces are compared for models 3 and 4 in terms of model 4 scaled time. This case contains a coated rail with rail misalignment, also known as rail roughness. Tracers at various locations in the slipper, rail, and coating are studied. The tracer locations were selected so the effects of high strain rate conditions could be compared to areas of relatively low strain rate and stress. The Lagrangian tracer located in the slipper is 200 cells away from the impact surface. These plots are shown in Figures 4.38 and 4.39. The largest difference between the solutions in pressure is 30 MPa. The largest stress deviator difference is only 22 MPa. Note however, the value of

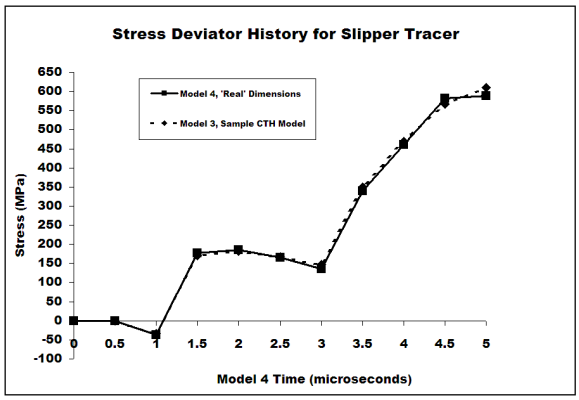

Figure 4.39 **Time-scaled history comparison of XY deviatoric stress for slipper tracer in coated models with rail roughness.**

the stress impulse for the impact at this location is much smaller than near the surface for the uncoated case of models 1 and 2. Strain rates are much lower here.

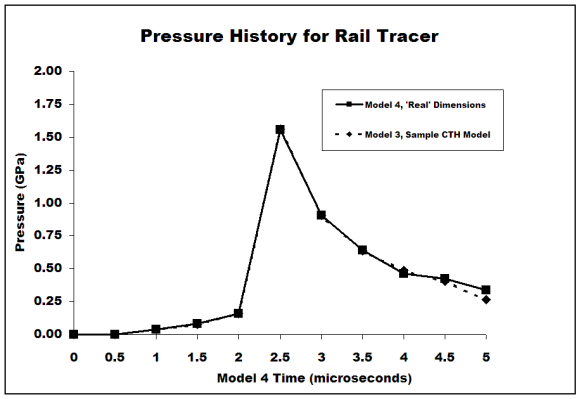

Figure 4.40 **Time-scaled history comparison of pressure for rail tracer in coated models with rail roughness.**

The Lagrangian tracer located in the rail in models 3 and 4 is 10 cells away from the impact surface. These plots are shown in Figures 4.40 and 4.41. The pressure wave is about four times greater at this point than at the slipper tracer and occurs earlier. The largest difference between the solutions is 70 MPa for pressure. However, there is a greater increase in difference between models in stress deviator behavior. The pressure pulse occurs at 2.5 μs in terms of model 4 time. At this time, the largest difference in deviatoric stress of 63 MPa occurs. In terms of absolute value, this number is on the same

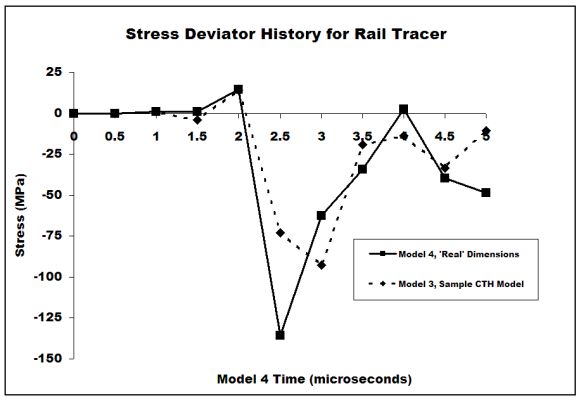

Figure 4.41 **Time-scaled history comparison of XY deviatoric stress for rail tracer in coated models with rail roughness.**

scale as the difference in the pressure plot. Strain rate effects show up in this vicinity of the impact.

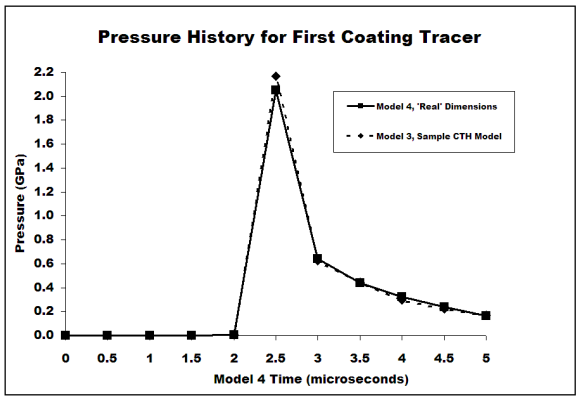

Figure 4.42 **Time-scaled history comparison of pressure for first coating tracer in coated models with rail roughness.**

The Lagrangian tracers located within the coating are near the point of impact. These plots are shown in Figures 4.42 through 4.45. The first coating tracer is located directly above the rail tracer and the second coating tracer is located within the coating on the rail misalignment. The pressure wave, depicted in Figure 4.42, is almost ten times greater at this point than at the slipper tracer. The average difference between pressure solutions for the first coating tracer is 19 MPa. Compare this to the 67 MPa average deviation of pressure over 5.0 μs for the second coating tracer (in which a larger pressure pulse occurs). Deviatoric stresses in the coating remain relatively low at the first coating tracer where the

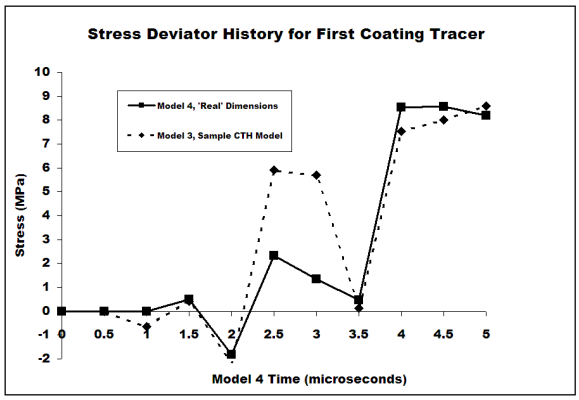

Figure 4.43 **Time-scaled history comparison of XY deviatoric stress for first coating tracer in coated models with rail roughness.**

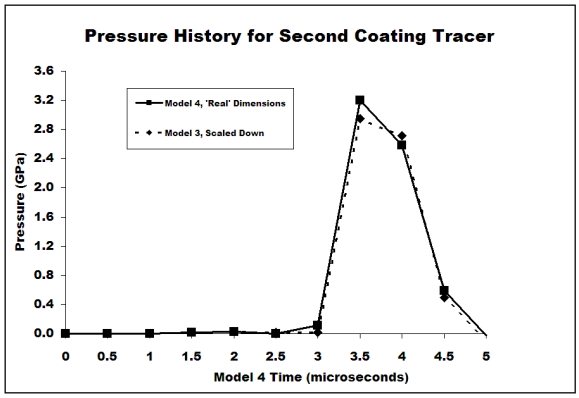

Figure 4.44 **Time-scaled history comparison of pressure for second coating tracer in coated models with rail roughness.**

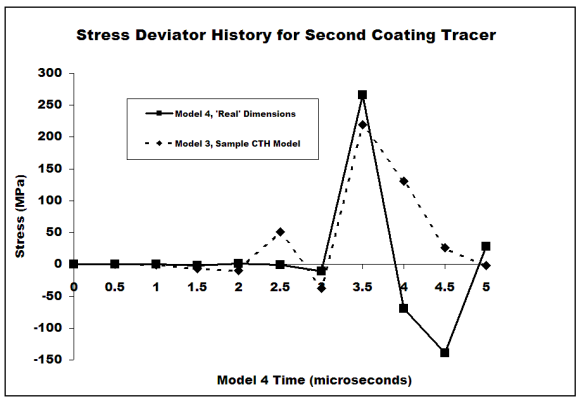

Figure 4.45 **Time-scaled history comparison of XY deviatoric stress for second coating tracer in coated models with rail roughness.**

Table 4.5 **Summary of difference between models in terms of approximate per cent deviation from baseline.**

Tracer Location	Ave. % Diff. Press.	Ave. % Diff. Dev. Stress	Ave. % Diff. Press.	Ave. % Diff. Dev. Stress
Model 1 and 2 Comparison				
Refined Mesh				
Time Interval	≤ 3 μsecs		> 3 μsecs	
Slipper	5	< 5	15	35
Model 3 and 4 Comparisons				
Time Interval	≤ 2 μsecs		> 2 μsecs	
Slipper	< 5	< 5	< 5	< 5
Rail	< 5	5	< 5	35
Coating 1	< 5	5	< 5	17
Coating 2	0 [c]	5	5	100

[c] No pressure changes at that location until after 2 μsecs.

average difference between models is only 1.13 MPa. There is a marked increase in average difference between models at the second coating tracer (up to 54 MPa), even accounting for the greater deviatoric stresses in the second coating tracer. The pressure pulse in Figure 4.44 occurs at 3.5 μs in terms of the time of model 4. After this large pressure, strain rate effects lead to a maximum difference of 200 MPa in the stress deviator for the second coating tracer.

Time histories show important differences on a local scale. Globally, the results match well between models. Deviations between geometrically similar models are shown to increase with time and after high pressure waves where large strain rate effects are dominant. These results are summed up in terms of average percentage difference in Table 4.5.

One can see that there are so many relations inside CTH that would have to be adjusted, that it becomes near impossible to incorporate the Buckingham Pi parameters for each of these. One may trace the solution of the two step method considering the Lagrangian and remapped Eulerian steps to see the possible parameters that could be affected. McGlaun, et al [78] sets out many of these parameters in their discussion of CTH. We considered only one relation, the Johnson and Cook constitutive equation, and found a significant change in comparisons. Other parameters could be associated with the equation of state, thermal softening and many of the thermodynamic routines, to name a few.

In an attempt to reduce the difference in results between geometrically scaled models due to material strain rate sensitivity, changes to the constitutive model are investigated. Plastic behavior of the rail material is characterized for the rail material by the Johnson-Cook constitutive equation.

$$Y = [A + B(\varepsilon^p)^N][1 + C\ ln(\dot{\varepsilon}^p)][1 - \theta_h^m] \tag{4.108}$$

where

$$\theta_h = \frac{T - T_r}{T_M - T_r} \tag{4.109}$$

The reference temperature, T_r is room temperature. A, B, C, N, and m are constants that are material dependent, ε^p is plastic strain, and $\dot{\varepsilon}^p$ is plastic strain rate. C helps determine the sensitivity of the material to strain rate. Strain rates in geometrically scaled models cannot be scaled properly. The strain rate is always larger in the smaller model of a geometrically scaled pair [68]. In this investigation, the Johnson-Cook model constant C was reduced by a factor of about four per cent for the CTH model (i.e., model 3) in an attempt to modify strain rate effects and produce a closer match in scaled results in deviatoric stress with the "real" sled dimensions. The Johnson-Cook constitutive model is used for the rail material. Data for the rail tracer in the comparison between models 3 and 4 is shown. In order to scale the constitutive equation consistently, the constants A and B of the model are increased by the same factor that C is decreased by. This is to keep the overall change in dynamic flow stress consistent as much as possible. However, some inconsistencies remain.

The time scale is implemented in the Johnson-Cook model in the following way:

Let τ be a nondimensional time scale, let t be the independent variable of time, and T be the natural time scale of the problem. Where $t = T\tau$. Then for model 3, $t_1 = T_1\tau$ and for model 4, $t_2 = T_2\tau$. The plastic strain rate becomes:

$$\frac{d\varepsilon^p}{dt} = \frac{d\varepsilon^p}{Td\tau} \tag{4.110}$$

Let $\sigma_o = [A + B(\varepsilon^p)^N][1 - \theta_h^m]$.

Then for model 3, where $t = t_1$.

$$\begin{aligned} Y &= \sigma_o \left[1 + C \ \ln\left(\dot{\varepsilon}^p\right)\right] \\ Y &= \sigma_o \left[1 + C \ \ln\left(\frac{d\varepsilon^p}{T_1 d\tau}\right)\right] \\ Y &= \sigma_o \left[1 + C \ \ln\left(\frac{d\varepsilon^p}{d\tau}\right) - \ln(T_1)\right] \\ Y &= \left[1 - C\ln(T_1)\right]\sigma_o \left[1 + \frac{C}{1 - C\ln(T_1)} \ \ln\left(\frac{d\varepsilon^p}{d\tau}\right)\right] \end{aligned}$$

Then for model 4, where $t = t_2$ we may use the nondimensional time scale, τ to obtain the scaled version of the Johnson-Cook model

$$\begin{aligned} Y &= \left[1 - C\ln(T_1)\right]\sigma_o \left[1 + \frac{C}{1 - C\ln(T_1)} \ \ln\left(\frac{d\varepsilon^p}{d\tau}\right)\right] \\ Y &= \left[1 - C\ln(T_1)\right]\sigma_o \left[1 + \frac{C}{1 - C\ln(T_1)} \ \ln\left(\frac{d\varepsilon^p}{dt_2} T_2\right)\right] \\ Y &= \left[1 - C\ln(T_1)\right]\sigma_o \left[1 + \frac{C}{1 - C\ln(T_1)} \left(\ln\left(\frac{d\varepsilon^p}{dt_2}\right) + \ln\left(T_2\right)\right)\right] \\ Y &= \left[1 + \frac{C}{1 - C\ln\left(T_1\right)}\ln(T_2)\right]\left[1 - C\ln(T_1)\right]\sigma_o \\ &\quad \left[1 + \frac{C}{\left(1 - C\ln(T_1)\right)\left(1 + \frac{C}{1 - C\ln\left(T_1\right)}\ln(T_2)\right)} \ \ln\left(\frac{d\varepsilon^p}{dt_2}\right)\right] \end{aligned}$$

where the term $\left[1 + \frac{C}{1 - C\ln\left(T_1\right)}\ln(T_2)\right]\left[1 - C\ln(T_1)\right]$ can be reduced to $\left[1 + C\ln\left(\frac{T_2}{T_1}\right)\right]$.

The modified Johnson-Cook model then becomes

$$Y = \left[1 + C\ln\left(\frac{T_2}{T_1}\right)\right]\left[A + B(\varepsilon^p)^N\right]\left[1 + \frac{C}{1 + C\ln\left(\frac{T_2}{T_1}\right)} \ ln(\dot{\varepsilon}^p)\right]\left[1 - \theta_h^m\right] \qquad (4.111)$$

where $T_1 = \frac{\ell}{u_x}$ and $T_2 = \frac{2\ell}{u_x}$. Therefore, $\frac{T_2}{T_1} = 2$.

For this specific example, the modified Johnson-Cook model is then

$$Y = 1.0415[A + B(\varepsilon^p)^N][1 + \frac{C}{1.0415} \ ln(\dot{\varepsilon}^p)][1 - \theta_h^m] \qquad (4.112)$$

which can be modified in CTH by using user-defined material constants for A, B, and C.

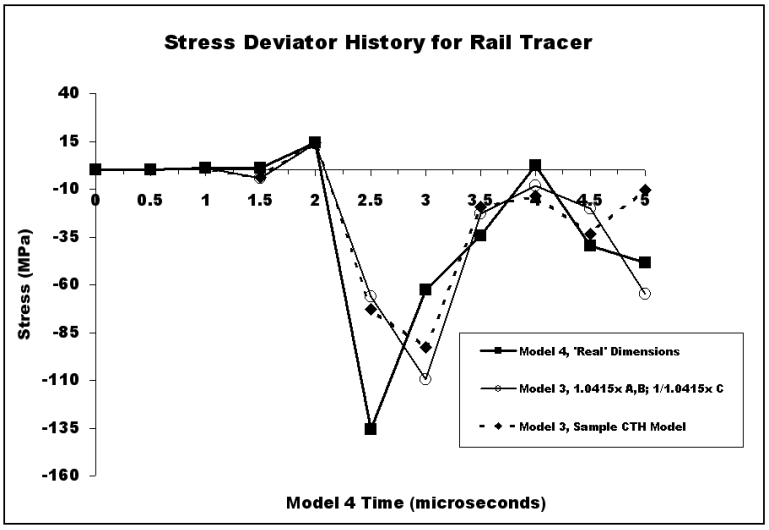

Figure 4.46 **Time-scaled history comparison of XY deviatoric stress after modifying Johnson-Cook constants.**

The results of changing the Johnson-Cook constants for deviatoric stress are shown in Figure 4.46. The average difference between deviatoric stress in the models after making these changes remains approximately the same, but the trends of the stress deviator in model 3 more closely match the solution using the "real" dimensions of model 4 after adjusting model 3's constitutive model for strain rate effects. Adjusting for time, the average difference decreases from around 35% to about 30%. This is done without significant changes to the pressure. The stress deviator results do not show that scaling for time significantly reduces the variance of the results in the rail material response. Differences still exist because the constitutive models for the slipper and coating materials have not been scaled in the same manner as the rail material model. The Steinberg-Guinan-Lund model for the slipper material (VascoMax 300) would need to be scaled for time in the same way as the Johnson-Cook model for the rail material (1080 steel). The same would have to be done for the coating, but strain rate dependent material models for epoxy are unavailable at this time in CTH.

An *ad hoc* approach may be used to obtain results by modifying the Johnson-Cook constants until results match more closely, in an effort to account for the effects of the other

material interactions (from the slipper and coating). For a consistent approach, however, a Johnson-Cook constitutive model would be required for all material models. These other materials could then be modified to account for the time scale and strain rate effects.

4.5.8 Use of the Scaling Invariants to Gain Insight into Gouging. The dimensional analysis also lends insight into the potential benefits and behavior of coatings with respect to gouging initiation. Scaling invariants from the Buckingham Pi analysis may be used to determine which parameters are important to studying test sled impacts. Characteristic length and time scales may be used to nondimensionalize the problem. The scaling invariants may also be modified so they are in terms of a length other than the slipper length, such as the coating thickness. If the scaling invariants are based on the results of a given model, these values may then be used to gain insight into how other parameters may be changed to either match or avoid those same results.

For example, let us consider a coated rail roughness impact. We must first modify the scaling invariants in terms of the coating thickness. The coating thickness then becomes the characteristic length to be studied. Since each scaling invariant is a dimensionless parameter, the product of any of the invariants is also a dimensionless scaling parameter. This is bounded by the requirement that there must be eighteen parameters based on the analysis. By multiplying each geometrically scaled invariant by the appropriate power of the reciprocal of the $\frac{t_c}{\ell}$ invariant and the velocity scaled invariants by the reciprocal of the $\frac{c_c}{u_x}$ invariant in order to put them in terms of the coating thickness and speed of sound, we can obtain the scaling invariants for the coated rail roughness case to be:

$$\pi_1 = \rho_o \frac{t_c^3}{m} \tag{4.113}$$

The slipper density must be invariant with the ratio of the sled mass and the cubed thickness of the coating.

$$\pi_2 = \rho_{o_c} \frac{t_c^3}{m} \tag{4.114}$$

The coating density must be invariant with the ratio of the sled mass and the cubed thickness of the coating.

$$\pi_3 = \frac{h}{t_c} \tag{4.115}$$

The slipper height must be invariant with the coating thickness.

$$\pi_4 = \frac{w}{t_c} \tag{4.116}$$

The slipper width must be invariant with the coating thickness.

$$\pi_5 = \frac{\ell}{t_c} \tag{4.117}$$

The slipper length must be invariant with the coating thickness.

$$\pi_6 = \frac{h_a}{t_c} \tag{4.118}$$

The rail roughness height must be invariant with the coating thickness.

$$\pi_7 = \frac{A_a}{t_c^2} \tag{4.119}$$

The rail roughness cross sectional area must be invariant with the coating thickness squared.

$$\pi_8 = \frac{u_y}{c_c} \tag{4.120}$$

The vertical velocity and coating speed of sound ratio must remain invariant.

$$\pi_9 = \frac{c}{c_c} \tag{4.121}$$

The ratio of slipper material speed of sound and coating speed of sound must remain invariant.

$$\pi_{10} = \frac{u_x}{c_c} \tag{4.122}$$

The ratio of horizontal velocity and the coating speed of sound must remain invariant.

$$\pi_{11} = \frac{E}{mc_c^2} \tag{4.123}$$

The total energy of the slipper as compared to a kinetic energy term based on the test sled mass and the coating speed of sound must remain invariant between models.

$$\pi_{12} = \frac{S}{mc_c^2} \tag{4.124}$$

The internal energy source of the slipper as compared to a kinetic energy term based on the test sled mass and the coating speed of sound must remain invariant between models.

$$\pi_{13} = \sigma_{y,c}\frac{t_c^3}{mc_c^2} \tag{4.125}$$

The ratio of the slipper yield stress and a momentum relation based on coating properties and the test sled mass must remain invariant between models. The term $\frac{t_c^3}{mc_c^2}$ is similar to a momentum relation for shock waves, but is based on coating properties and the test sled mass.

$$\pi_{14} = \sigma_{y,c_c}\frac{t_c^3}{mc_c^2} \tag{4.126}$$

The ratio of the coating yield stress and a momentum relation based on coating properties and the test sled mass must remain invariant between models. The term $\frac{t_c^3}{mc_c^2}$ is similar

to a momentum relation for shock waves, but is based on coating properties and the test sled mass.

$$\pi_{15} = E_o \frac{t_c^3}{mc_c^2} \tag{4.127}$$

The ratio of the slipper elastic modulus and a momentum relation based on coating properties and the test sled mass must remain invariant between models. The term $\frac{t_c^3}{mc_c^2}$ is similar to a momentum relation for shock waves, but is based on coating properties and the test sled mass.

$$\pi_{16} = E_{o_c} \frac{t_c^3}{mc_c^2} \tag{4.128}$$

The ratio of the coating elastic modulus and a momentum relation based on coating properties and the test sled mass must remain invariant between models. The term $\frac{t_c^3}{mc_c^2}$ is similar to a momentum relation for shock waves, but is based on coating properties and the test sled mass.

$$\pi_{17} = G_o \frac{t_c^3}{mc_c^2} \tag{4.129}$$

The ratio of the slipper shear modulus and a momentum relation based on coating properties and the test sled mass must remain invariant between models. The term $\frac{t_c^3}{mc_c^2}$ is similar to a momentum relation for shock waves, but is based on coating properties and the test sled mass.

$$\pi_{18} = G_{o_c} \frac{t_c^3}{mc_c^2} \tag{4.130}$$

The ratio of the coating shear modulus and a momentum relation based on coating properties and the test sled mass must remain invariant between models. The term $\frac{t_c^3}{mc_c^2}$ is similar to a momentum relation for shock waves, but is based on coating properties and the test sled mass.

Let us restate that invariant products cannot give us the relative importance of parameters. That is, a one per cent variance in a scaling invariant does not necessarily equate to a one per cent variance in the solution. The solution could vary more or less than the scaling invariant does depending on the effect of the dimensioned quantities on the solution. There may also be bifurcation points in the solution, such as shock wave formation of which the scaling invariants provide no indication.

However, by varying one or more of the dimensioned quantities one may use the invariant products as a guide to determine how other dimensioned quantities must change in order to obtain similar results. If one has a certain condition that is being simulated (for example, gouging initiation) the dimensioned quantities can be varied as long as the scaling invariants are satisfied for gouging to occur. Knowing how the other parameters must change to maintain the same solution, the engineer may draw conclusions as to what qualitative effect these parameters have on the results, based on knowledge obtained from other studies.

Continuing with the examples run in section 4.5.6.2, we see that a rail roughness impact case with the dimensions of model 3 initiates gouging at 5 microseconds (for a 3 mil coating on a 0.03 cm high rail roughness) if the horizontal velocity is 2 km/sec and the vertical velocity is 50 m/s for a 56.75 kg sled mass. For the same case to initiate gouging at 6 mils thickness, the dimensioned quantities must be modified so that we obtain model 4. Let us study this in greater detail, however. Let us assume only the coating thickness is changed to 6 mils from 3 mils for the same case. The scaling invariants then become as listed in Table 4.6.

Let us analyze the dimensioned quantities with the goal in mind of determining how the dimensioned quantities of the 6 mil coating version of model 3 must change so that we obtain the same gouging observed in the 3 mil coating version of model 3. The first thing we notice is that because the material properties do not change, the velocity scaling remains the same if we keep the velocity vector of impact the same. We have simply increased the thickness of the coating. π_1 and π_2 tell us that the mass of the test sled must increase in proportion to the cubed thickness of the coating for gouging to occur at the same velocity of impact, unless the slipper density and coating density change. In other

Table 4.6 **Invariants and their values for numerical models.**

Invariants	Model 3 (Gouging)	Model 3 (6 mil coating)
Mass Scaling		
$\pi_1 = \rho_o \frac{t_c^3}{m}$	9.08×10^{-15}	7.26×10^{-14}
$\pi_2 = \rho_{o_c} \frac{t_c^3}{m}$	9.25×10^{-12}	7.4×10^{-11}
Geometric Scaling		
$\pi_3 = \frac{h}{t_c}$	333.33	166.67
$\pi_4 = \frac{w}{t_c}$	1417.32	708.66
$\pi_5 = \frac{\ell}{t_c}$	573.49	286.75
$\pi_6 = \frac{h_a}{t_c}$	3.94	1.97
$\pi_7 = \frac{A_a}{t_c^2}$	2232	558
Velocity Scaling		
$\pi_8 = \frac{u_y}{c_c}$	0.0183	0.0183
$\pi_9 = \frac{c}{c_c}$	1.46	1.46
$\pi_{10} = \frac{u_x}{c_c}$	0.7326	0.7326
Energy Scaling		
$\pi_{11} = \frac{E}{mc_c^2}$	26.86	26.86
$\pi_{12} = \frac{S}{mc_c^2}$	-	-
$\pi_{13} = \sigma_{y,c} \frac{t_c^3}{mc_c^2}$	1.51×10^{-12}	1.21×10^{-11}
$\pi_{14} = \sigma_{y,c_c} \frac{t_c^3}{mc_c^2}$	1.57×10^{-14}	1.26×10^{-13}
$\pi_{15} = E_o \frac{t_c^3}{mc_c^2}$	1.93×10^{-10}	1.54×10^{-9}
$\pi_{16} = E_{o_c} \frac{t_c^3}{mc_c^2}$	1.15×10^{-12}	9.2×10^{-12}
$\pi_{17} = G_o \frac{t_c^3}{mc_c^2}$	7.5×10^{-11}	6.0×10^{-10}
$\pi_{18} = G_{o_c} \frac{t_c^3}{mc_c^2}$	4.18×10^{-13}	3.35×10^{-12}

Subscript a indicates property of asperity/rail roughness

Subscript c indicates property of the coating material.

words, the two fold increase in coating thickness requires an eight fold increase in mass, or an eight fold reduction in slipper and coating densities for the same magnitude gouge to occur.

It can be deduced from this that the 6 mil coating with a 0.03 high rail roughness will not gouge, partially because the artificial test sled mass (i.e., the kinetic energy and momentum) is now too small with respect to the coating thickness and density. If the density of the slipper and coating were to decrease proportionately however, then gouging may occur as long as all other scaling invariants were satisfied.

Now if the coating thickness were kept the same, but the coating density were increased, gouging might be mitigated. This is a good example of why caution must be exercised in this approach. There is a limit to the benefits of increasing the coating density while still maintaining the benefits of a low density coating. For instance, increasing the coating density to be equivalent to the rail density would be the same as having no coating on the rail and gouging of greater magnitude would likely occur. There seems to be a balance between a higher density coating that deflects the slipper away from the rail material and a lower density coating with greater thickness that prevents gouging by absorbing energy and shearing rather than carrying high stress. Further numerical investigations are required to find the limit on increasing the coating density. Changing the dimensioned quantities to change the value of the invariant tells us that the solution will be different, but it provides no indication as to what that difference will be. Other knowledge and data is required to make that conclusion.

An increase in the artificial test sled mass would be accomplished by the geometric scaling required in invariant products π_3 through π_7. These invariants tell us that the 0.03 cm high rail roughness and the geometry of the slipper are too small with respect to the coating thickness for gouging to initiate.

While the energy is already scaled appropriately between models (since the coating thickness has no bearing on this parameter), the material properties of the slipper and coating must be reduced one order of magnitude if the results for 3 mil coating case are to be duplicated (i.e., gouging initiates). By increasing the coating thickness, the yield

strength, elastic modulus, and shear modulus of the slipper and coating are large enough to reduce the onset of gouging based on an expected reduction in plasticity. The values of the invariants (π_{12} through π_{18}) themselves do not offer any clue as to how the material properties reduce gouging. The reasoning behind the claim that increasing the material properties reduces the onset of gouging is based on prior experience with gouging models.

The invariants provide an indication of which properties to study. For example, π_{12} tells us that were it not for the greater value in critical yield strength of the slipper, that this particular invariant would be satisfied with respect to a gouged model and that gouging may occur. It does not tell us that the gouging may not be worse. We know by other means (i.e., that increased yield strength results in a delay in the development of plastic strain via the constitutive model) that the potential of gouging is reduced if the yield strength is increased.

The values of the invariants for the energy scaling invariants are extremely small. For example, in π_{12}, decreasing the value of the yield strength by dividing it by a factor of 7.4 will satisfy this invariant for the gouging case. In the case of the slipper, this would require a reduction from 1.447 GPa to about 200 MPa. Knowing this, one may deduce the effect of changes to the yield strength of the slipper and the potential for gouging to occur based on a given coating thickness.

If one compares model 4 to the incompletely scaled model 3 of 6 mils coating thickness, one may also deduce that model 4 causes gouging because it has the kinetic energy and momentum (from the increased test sled mass) required for gouging to occur despite a 6 mil coating. Also, the impact on the larger rail roughness allows a greater exchange of momentum and energy between the sled system and the rail. The exchange of energy that occurs in spite of the coating, results in gouging. A more complex analysis might vary the size of the rail roughness along with the coating, or vary the geometry and mass of the artificial test sled in order to better understand the effect of the rail roughness size on the problem. The scaling invariants provide a rule by which one can match dimensioned quantities of a particular result and make educated conclusions about the effect of changing various parameters in the problem.

A similar analysis may be accomplished by changing more than one parameter and observing the relationship between the dimensioned quantities as well as the scaling invariants. The point of this exercise has been to point out the utility of scaling invariants for comparing dimensioned quantities of numerical models with some amount of accuracy.

4.6 Dimensional Analysis and Similitude Study Conclusions

So what do all these invariants from the various dimensional analysis cases show? How may one use them to create a computational model that is directly useful for making engineering judgments about the real HHSTT sled system? First one must remember that in each of the dimensional analysis cases, heat conduction was not considered. As part of the dimensional analysis results, it was found that the temperature for the real model must remain constant between models for the CTH "blackbox" approach. This point may have been lost during the analysis when the dimensional matrix was simplified after it was determined the exponent for the dimensioned temperature quantity was simply equal to zero. In Table 4.7 is a summary of the results from the various approaches to the dimensional analysis.

From the results of the entire dimensional analysis, one may come to the following reasonable conclusions:

- Scaling of the solution with respect to an appropriate time-scale is extremely important. Results do not match between models unless this time-scale is used for models whose length and height are simply scaled up or down.
- If the material properties, velocities, and temperature field between models remain the same, the geometry between models may be scaled according to the length of the slipper or some other appropriate length if a time-scale is also considered.
- For best comparison of models, the slipper should not be taken as a stand alone model without considering the effects and interactions of the sled system mass and its properties on the whole impact scenario. At the very least, the sled system mass should be modeled in a simplified fashion in addition to allowing the sled mass to be distinct from the slipper.

- It is possible, using the dimensioned parametric approach previously discussed (on page 4-9), that any global sled can be characterized by a numerical model which depicts the actual high velocity impact using available computer resources.

CTH Dimensional Analysis Approach				Conservation Equations Approach		
Oblique Impact Slipper Only	Asperity Impact Slipper Only	Rail Roughness Impact Slipper with Coating	Oblique Impact of Sled System	Oblique Impact of Sled System	Oblique Impact of Slipper with Artificial Sled Mass	Rail Roughness Impact of Slipper with Artificial Sled Mass and Coating
$\pi_1 = \frac{u_y}{u_x}$	$\pi_1 = \frac{h}{\ell}$	$\pi_1 = \frac{\rho_{o_c}}{\rho_o}$	$\pi_1 = \frac{\mathcal{L}}{\mathcal{H}}$	$\pi_1 = \frac{\mathcal{H}}{\mathcal{L}}$	$\pi_1 = \rho_o \frac{\ell^3}{m}$	$\pi_1 = \rho_o \frac{\ell^3}{m}$
$\pi_2 = \frac{h}{\ell}$	$\pi_2 = \frac{\sigma_{y,c}}{\rho_o u_x^2}$	$\pi_2 = \frac{u_y}{u_x}$	$\pi_2 = \frac{\mathcal{W}}{\mathcal{H}}$	$\pi_2 = \frac{\mathcal{W}}{\mathcal{L}}$	$\pi_2 = \frac{h}{\ell}$	$\pi_2 = \rho_{o_c} \frac{\ell^3}{m}$
$\pi_3 = \frac{\sigma_{y,c}}{\rho_o u_x^2}$	$\pi_3 = \frac{E_o}{\rho_o u_x^2}$	$\pi_3 = \frac{h}{\ell}$	$\pi_3 = \frac{u_y}{u_x}$	$\pi_3 = \frac{u_y}{u_x}$	$\pi_3 = \frac{w}{\ell}$	$\pi_3 = \frac{h}{\ell}$
$\pi_4 = \frac{E_o}{\rho_o u_x^2}$	$\pi_4 = \frac{G_o}{\rho_o u_x^2}$	$\pi_4 = \frac{h_a}{\ell}$	$\pi_4 = \frac{c}{u_x}$	$\pi_4 = \frac{c}{u_x}$	$\pi_4 = \frac{u_y}{u_x}$	$\pi_4 = \frac{w}{\ell}$
$\pi_5 = \frac{G_o}{\rho_o u_x^2}$	$\pi_5 = \frac{h_a}{\ell}$	$\pi_5 = \frac{A_a}{\ell^2}$	$\pi_5 = \frac{\sigma_{y,c}\mathcal{H}^3}{mu_x^2}$	$\pi_5 = \frac{E}{mu_x^2}$	$\pi_5 = \frac{c}{u_x}$	$\pi_5 = \frac{t_c}{\ell}$
	$\pi_6 = \frac{A_a}{\ell^2}$	$\pi_6 = \frac{t_c}{\ell}$	$\pi_6 = \frac{G\mathcal{H}^3}{mu_x^2}$	$\pi_6 = \frac{S}{mu_x^2}$	$\pi_6 = \frac{E}{mu_x^2}$	$\pi_6 = \frac{h_a}{\ell}$
Starts on page 4-25		$\pi_7 = \frac{\sigma_{y,c}}{\rho_o u_x^2}$		$\pi_7 = \sigma_{y,c}\frac{\mathcal{L}^3}{mu_x^2}$	$\pi_7 = \frac{S}{mu_x^2}$	$\pi_7 = \frac{A_a}{\ell^2}$
	Starts on page 4-29	$\pi_8 = \frac{\sigma_{y,c_c}}{\rho_o u_x^2}$	Starts on page 4-49	$\pi_8 = E_o\frac{\mathcal{L}^3}{mu_x^2}$	$\pi_8 = \sigma_{y,c}\frac{\ell^3}{mu_x^2}$	$\pi_8 = \frac{u_y}{u_x}$
		$\pi_9 = \frac{G_o}{\rho_o u_x^2}$		$\pi_9 = G_o\frac{\mathcal{L}^3}{mu_x^2}$	$\pi_9 = E_o\frac{\ell^3}{mu_x^2}$	$\pi_9 = \frac{c}{u_x}$
		$\pi_{10} = \frac{G_{o_c}}{\rho_o u_x^2}$			$\pi_{10} = G_o\frac{\ell^3}{mu_x^2}$	$\pi_{10} = \frac{c_c}{u_x}$
		$\pi_{11} = \frac{E_o}{\rho_o u_x^2}$				$\pi_{11} = \frac{E}{mu_x^2}$
		$\pi_{12} = \frac{E_{o_c}}{\rho_o u_x^2}$		Starts on page 4-55		$\pi_{12} = \frac{S}{mu_x^2}$
					Starts on page 4-60	$\pi_{13} = \sigma_{y,c}\frac{\ell^3}{mu_x^2}$
		Starts on page 4-33				$\pi_{14} = \sigma_{y,c_c}\frac{\ell^3}{mu_x^2}$
						$\pi_{15} = E_o\frac{\ell^3}{mu_x^2}$
						$\pi_{16} = E_{o_c}\frac{\ell^3}{mu_x^2}$
						$\pi_{17} = G_o\frac{\ell^3}{mu_x^2}$
						$\pi_{18} = G_{o_c}\frac{\ell^3}{mu_x^2}$
						Starts on page 4-73

Table 4.7 **Dimensional analysis approaches and resulting invariants that must all be met within that case to appropriately compare results among models.**

A couple of other points must be made. Since the complexity and accuracy of the analysis depends on the number and type of dimensioned quantities chosen, this analysis should not be considered as complete in its entirety. There are a number of dimensioned quantities within CTH that the user does not have control over and were not considered in any of the dimensional analyses described here. The complexity of the problem makes it extremely difficult to consider every dimensioned quantity for the dimensional analysis. The complexity of the CTH algorithms also makes it extremely difficult to account for time and length scales in every material model. Greater user control of material model parameters is required to accomplish this within CTH.

The dimensional analysis cases described in this chapter are sufficient to illustrate the potential difficulties of scaling numerical models to real test sled dimensions. In addition, the process of performing a dimensional analysis and the invariants that were derived during the exercise improves the understanding of the problem and also highlights important parameters that must be considered for further numerical analysis.

V. Methodology

In this chapter, we discuss the methods used to simulate an actual test sled run and slipper-rail impacts. This includes discussion of model characteristics including dimensions, material models and both boundary and initial conditions. To perform the investigation, lagrangian tracer points are placed within the slipper, rail, and coating materials so that local data can be collected and analyzed.

It is desired to study nonequilibrium thermodynamic effects by allowing development of a thermal environment caused by irreversible friction effects. In order to do this, parameters for the boundary layer treatment must be selected. The method for generating a mesh and selecting boundary layer parameters such as coefficient of friction are discussed. Once these parameters are determined, heat conduction may be studied. A study of whether heat flow has any effect on the solution is carried out. With the parameters for boundary layer treatment and heat selected, and with Lagrangian tracers in the material, a mesh convergence study is conducted. Using the mesh from this study, a void between the slipper and sled mass, representing air at the slipper corner is studied. This option may help provide further fidelity to the solution. A void between the slipper and sled mass can be used to model shock reflection and interaction within the thickness of an actual slipper.

5.1 Model Definition

Our objective is to simulate as closely as possible the actual conditions a test sled experiences. Dimensions are recreated and transformed into a CTH model. The stress and deformation characteristics of the materials used to model the slipper, rail, and coating must also be accurate. Strain rate dependent material models are used to model material behavior and plasticity as close to actual conditions as possible. DADS data is available for an 809 kg test sled. This data is used to determine initial conditions of the model. All parameters for this model are selected with this test sled in mind, and with the goal of understanding potential impact conditions.

5.1.1 Dimensions. The method described in chapter **??** is used to transform the given test sled of 809 kg into a CTH model with artificial mass attached to a slipper. A quarter of the entire mass of 809 kg is converted to dimensions that will fit over the 20.32 cm x 2.54 cm x 10.8 cm (8 in x 1 in x 4.25 in) slipper (see Figure 5.1). It is assumed that the entire mass of the sled is evenly distributed among four slippers. An artificial mass of 202.25 kg of platinum (density of 21.44 g/cc), is used to simulate the portion of the sled mass located over the slipper. The height of the artificial mass is calculated to be approximately 43 cm. This three-dimensional simplification is then transformed into a two-dimensional plane strain model by taking a unit width of the three-dimensional model. The dimensions are then applied to the CTH code.

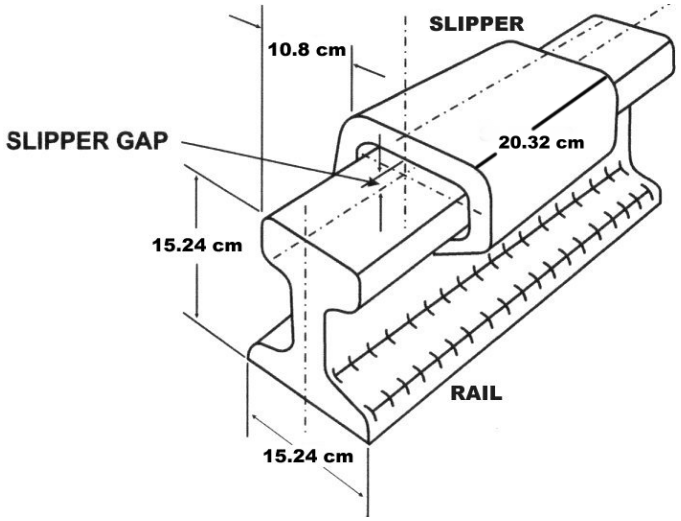

Figure 5.1 **Slipper and rail configuration in the subsequent development.**

The rail is approximately 15.24 cm (6 inches) high, but is simulated as a 4 cm high rail with a semi-infinite boundary condition along the bottom so that no shock reflections will occur. 4 cm is estimated to be sufficient for gaining an understanding of the conditions within the rail from any mechanical loading that is simulated in this study. Elastic waves travel at approximately 5 km/sec in steel. At this speed, it would take a stress wave approximately 30 microseconds to reach the bottom of the rail. All simulations in this study will be limited to 20 microseconds. The length of the rail is selected so that the entire slipper remains in the solution domain until the end of the simulation.

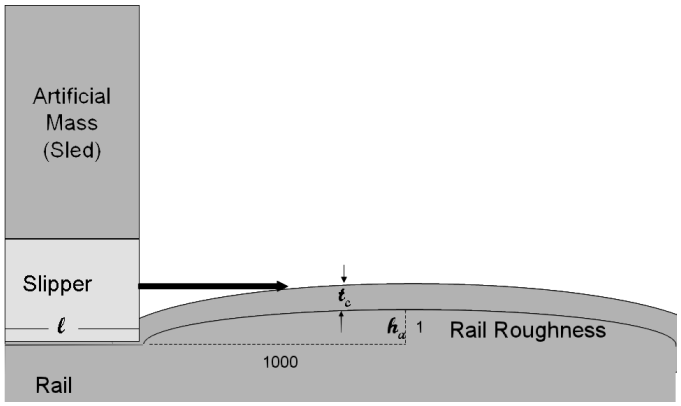

Figure 5.2 **Definition of rail roughness.**

The HHSTT aligns rails for a test sled run to the tolerance of 0.05" over sections approximately 50" long. A rail roughness is defined in the CTH model as a semi-elliptical protrusion on a prismatic rail. This semi-ellipse has a semi-major axis that is one-thousandth the length of the major axis. This simulates a scenario in which the slipper impacts a section of the rail that is still within tolerance, but not exactly straight. This situation is depicted in Figure 5.2.

Two basic cases will be studied: a sliding load over a period of 20 microseconds and an impact with a rail misalignment over no more than 10 microseconds. The frictional sliding time period is a limitation of the memory capabilities of the computer resources and the number of cells used in the CTH model. The time limit for the rail misalignment impact is based upon both hardware limitations and a desire to obtain solutions within a reasonable amount of time (a day or so of run time). These times were selected based upon experience from running similar problems with the CTH code and on the resources available.

5.1.2 Material Models. The materials used at the HHSTT include Vascomax 300 maraging steel for the slipper and 1080 steel for the rail. The actual test sled payload varies, but includes solid rocket fuel, electronic components, and other materials. CTH contains the material constants for the Steinberg-Guinan-Lund strain rate dependent viscoplastic constitutive model for Vascomax 300. The closest strain rate dependent constitutive model available in CTH for 1080 steel is the Johnson-Cook model for iron. The model is modified

Table 5.1 **Similarity of 1080 Steel and Iron.**

1080 Steel Material Properties			Iron Material Properties		
Model Constant	Value	Units	Model constant	Value	Units
ρ_o	7.850	g/cm^3	ρ_o	7.28	g/cm^3
G_o	7.8×10^{11}	g/cm s^2	G_o	6.8×10^{11}	g/cm s^2
Y_o	7×10^9	g/cm s^2	Y_o	5.72×10^9	g/cm s^2
T_M	1835.7	K	T_{mo}	1811	K
E	2.0×10^{11}	g/cm s^2	E	1.72×10^{11}	g/cm s^2
ν	0.25	-	ν	0.28	-

by changing the yield stress to 1080 steel. Epoxy is currently in use at the HHSTT for coating material. There are no strain rate dependent constitutive models available in CTH for epoxy. The only model available is an elastic-plastic model using Von Mises criteria.

Tabular equation of state models are available for both Vascomax 300 and iron. No tabular equation of state is available for 1080 steel, but the material parameters of iron are close to that of 1080 steel (as seen in Table 5.1). Therefore, the tabular equation of state for iron is used to model the volumetric response of 1080 steel. Even though Mie-Grüneisen parameters are available, the tabular equation of state is preferred because it contains data for phase changes of the material. No tabular equation of state is available for epoxy, so the Mie-Grüneisen equation of state is used. The Mie-Grüneisen equation of state assumes a constant density for the Grüneisen parameter and does not account for phase changes of the material.

A tabular equation of state is available for a reactive Graphite-Epoxy material. However this material is not what is used at the HHSTT. What this tabular equation of state does provide however, is a material model that can account for phase changes in the coating. Phase changes of the coating are expected since high temperatures are observed at the leading edge of the slipper. This equation of state was studied to better understand if it could be used without affecting the material response as compared to actual epoxy.

Figure 5.3 shows a comparison of temperature and pressure for a 1.5 km/sec sliding interaction between a slipper and a coated rail. The results are no more than five per cent different, as seen in the figures. However, when the same case was run for 3 km/sec, CTH calculated many unrealistic thermodynamic states of the cells at the interaction and the calculation was aborted. At this velocity, phase changes may occur, but selection of the

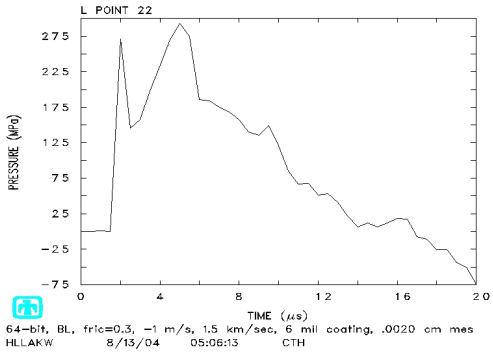

(a) **Mie-Grüneisen equation of state for epoxy coating, pressure.**

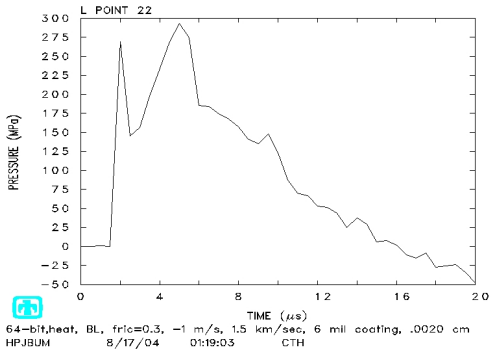

(b) **Epoxy-Graphite reactive tabular equation of state, pressure.**

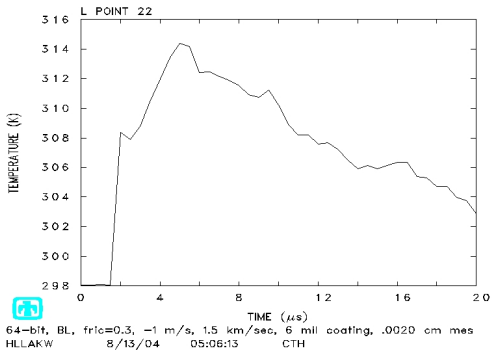

(c) **Mie-Grüneisen equation of state for epoxy coating, temperature.**

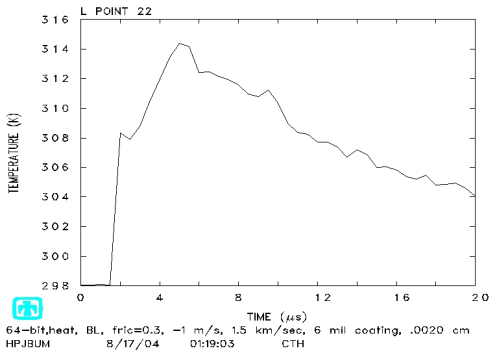

(d) **Epoxy-Graphite reactive tabular equation of state, temperature.**

Figure 5.3 **Comparison of heat conduction effects for run at 1.5 km/sec on flat coated rail, in slipper boundary over 20 microseconds.**

equation of state requires further work before an equation of state that accounts for phase changes may be used. The other option is to monitor the state of temperature and pressure in the solution and compare the values to a phase diagram for the coating material. This method provides a manual means of determining when phase changes should occur and what effect they might have on the CTH results.

5.1.3 Boundary and Initial Conditions. Mass, momentum, stress deviator, and energy fluxes through the boundaries are controlled by the boundary conditions. Symme-

try boundary conditions do not allow any flux across boundaries. Absorbing boundary conditions allow flow through the boundaries. These boundary conditions will not absorb incident stress waves exactly and will reflect a wave back into the mesh, which could result in spurious perturbations [79]. The sound-speed based absorbing boundary condition simulates a semi-infinite medium [80]. The sound-speed based absorbing boundary condition is used for all boundaries so that mass, momentum, stress deviator, and energy fluxes are allowed to flow out of the boundaries Eulerian mesh. This allows simulation of a portion of the sled-rail impact without causing unrealistic shock reflections. All shock in the simulated portion of the model will travel away from the area of interaction. Shock reflections will only occur between the interfaces of the slipper-rail and the slipper-sled mass.

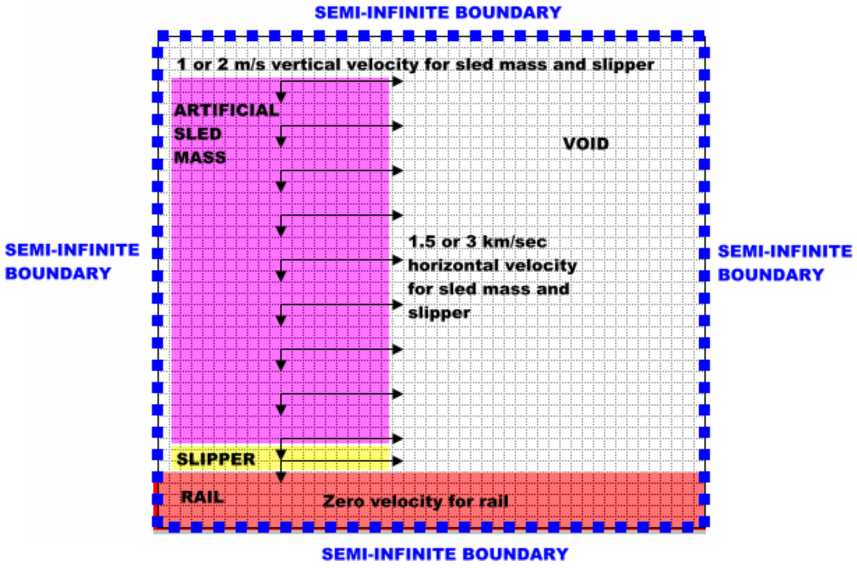

Figure 5.4 **Boundary and initial conditions.**

DADS data (see Appendix A) for the 809kg (1780 lb) test sled indicates the maximum vertical impact velocity for a horizontal velocity run of 1.5 km/sec (5000 fps) is about 1.8 m/s (70 in/sec). For the friction cases, an average of 1 m/s vertical velocity was used to minimize the thermal effects due to plastic work caused by vertical velocity components. For the rail roughness impact cases, a vertical impact of 2 m/s is used to simulate a worst case scenario for impact upon a rail misalignment. Horizontal velocities of 1.5 km/sec (5000 fps) and 3 km/sec (10,000 fps) are simulated. Observations of hypervelocity gouging

indicate that 1.5 km/sec is a threshold velocity for the occurrence of gouges (see section 1.2.1). 3 km/sec is chosen since it is the goal of the HHSTT to achieve that velocity for test sled runs.

Figure 5.4 shows the initial conditions for the slipper and sled mass as it impacts the rail. The cells with sled mass and slipper materials are all given the same initial velocity as indicated in the figure. As the material flows through the Eulerian mesh, the CTH algorithm solves for the combined equations of conservation, equation of state, and constitutive relations for each time step. The boundary conditions for the system are shown by the semi-infinite speed of sound absorbing boundaries at the edges of the Eulerian mesh. This condition simulates a semi-infinite boundary. A coating and rail roughness as defined above, can be added to the model.

5.2 Tracer Placement

To study the effects of frictional forces and heat flow on the solution, local temperatures and stress are desired. The way CTH keeps track of this local cell data is through predefined tracer points. These Lagrangian tracer points follow the movement of the material from the initial location. To trace local history of parameters such as pressure, temperature, and deviatoric stress, tracers are located in strategic points. Tracers are located along the area expected to form part of the boundary layer of sliding interaction between the slipper and either the rail or coating.

A set of ten tracers are located along the bottom of the slipper to tracer thermal and mechanical effects of sliding on the sipper. Another set of tracers are located further away from the bottom, yet also in the slipper to trace the conditions further removed. In this manner, the conduction of heat and the propagation of stress waves may be traced for the slipper. Another set of ten tracers are located with the coating, or within the expected boundary layer for a clean (i.e., uncoated) rail. Finally, a set of ten tracers are located further into the rail to obtain stress and thermal conditions as they propagate into the rail. When a rail roughness is added to the model, a portion of the tracers are located within he rail roughness to trace the state of the material there. Figure 5.5 shows the location of these tracers for a coated rail roughness scenario.

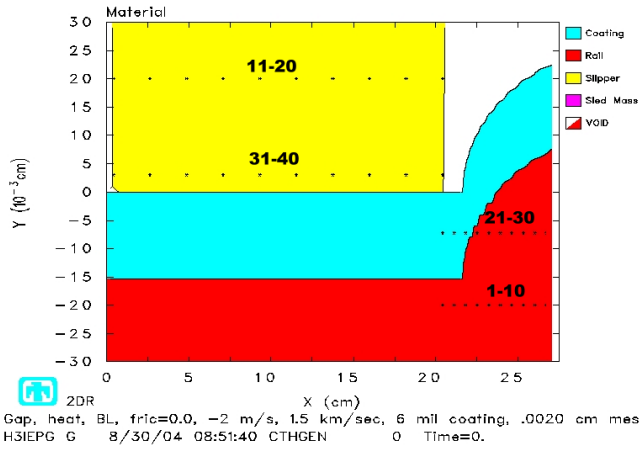

Figure 5.5 **Placement of tracers.**

5.3 Boundary Layer Treatment

Tracers are located to keep track of local data within expected boundary layer regions. There are two primary ways to treat the boundary layer interaction between sliding materials in CTH. One is the Slide Line algorithm and the other is the Boundary Layer algorithm (discussed in section 2.5). The Slide Line algorithm assumes a frictionless surface at the interface between the sliding materials. The Boundary Layer algorithm, by comparison, moves this frictionless layer into the softer material (rail or coating) and allows deviatoric stress at the sliding interface. Frictional forces are calculated using the stress tensor, the normal to the sliding surfaces, and the stress tensor. These frictional forces are used to calculate a body force density that is used in the momentum balance equation. Thus, the actual value of the coefficient of friction may be of concern.

In order to conduct the study of the various boundary layer treatments and to determine the best one to use for the model, the mesh must be defined properly. It was found in the course of investigations that changing the boundary of the mesh cells so that they did not coincide with the materials at the sliding interface resulted in different solutions. In addition, this condition could arise over the course of the calculations. Therefore, care must be used in generating a mesh for sliding interfaces and when analyzing the data over a longer period of time for the same interfaces.

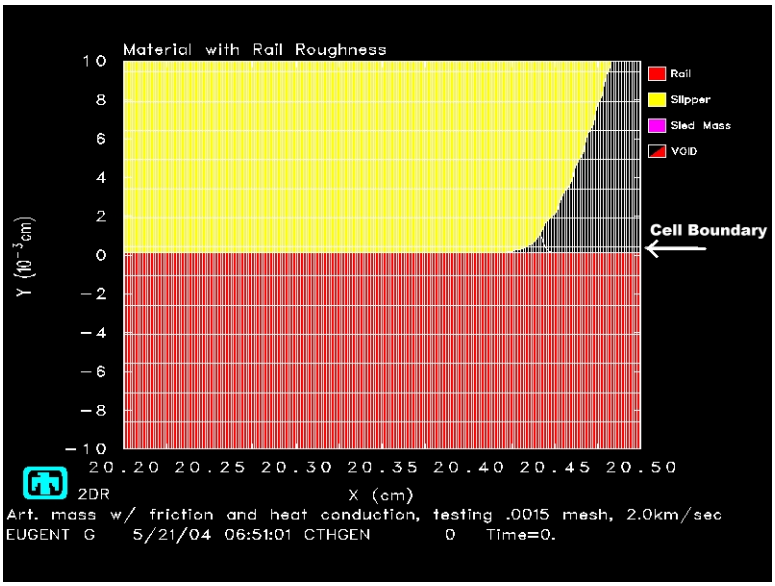

(a) **0.0015 cm cell size with mixed cells at interface of sliding materials, time=0.**

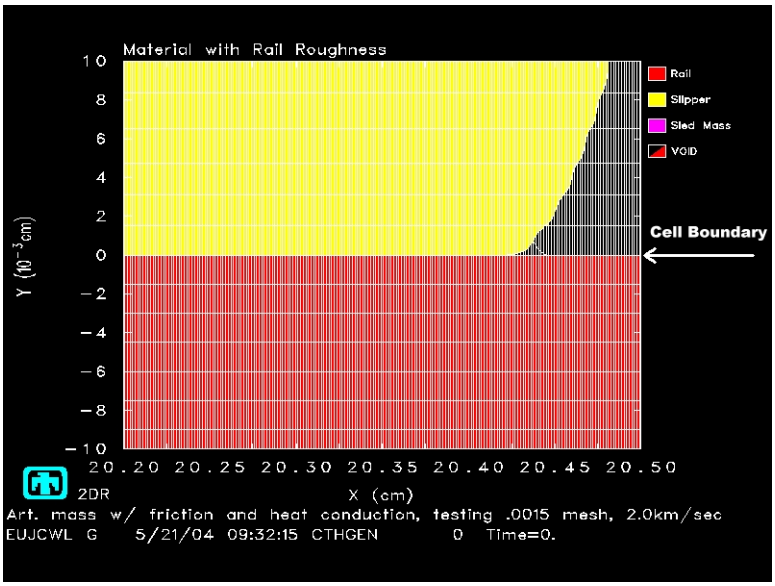

(b) **0.0015 cm cell size with cell boundaries coinciding with material boundaries, time=0.**

Figure 5.6 **Difference in solution based on initial boundary of mesh and materials.**

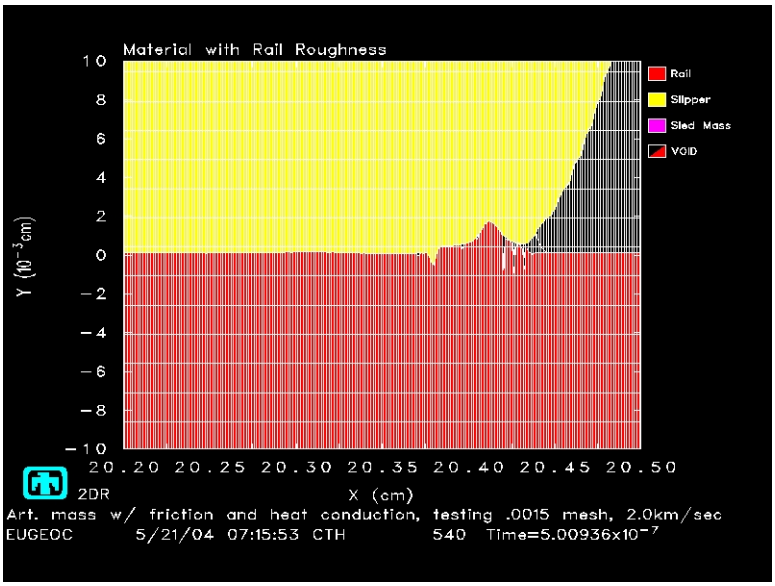

(a) **0.0015 cm cell size with mixed cells at interface of sliding materials, time=0.5 microseconds.**

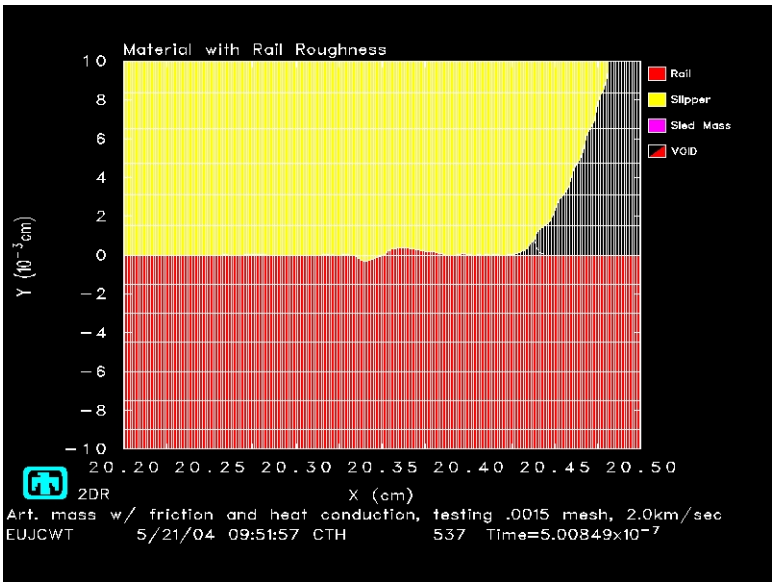

(b) **0.0015 cm cell size with cell boundaries coinciding with material boundaries, time=0.5 microseconds.**

Figure 5.7 **Difference in solution based on initial boundary of mesh and materials.**

The algorithm has difficulties when there are mixed cells along the sliding interface. This creates difficulties in the solution as shown in Figure 5.7. The algorithm uses a full cell width next to the penetrator material [46]. As a result, Sandia Labs (the CTH developer) recommends always generating a mesh that has the penetrator material ending at a cell boundary. Otherwise, numerical instabilities arise in the solution. In order to avoid these numerical artifacts, the cell boundaries must coincide with material boundaries. That is, when using the boundary layer algorithm with sliding interfaces, the cells along the interface must start the calculation with no mixed cells (see Figure 5.6). The coefficient is approximated for a number of time values and averaged over time. This time average is necessary because mesh coarseness (which is always present in the boundary layer algorithm), causes numerical variations that must be averaged over time [46].

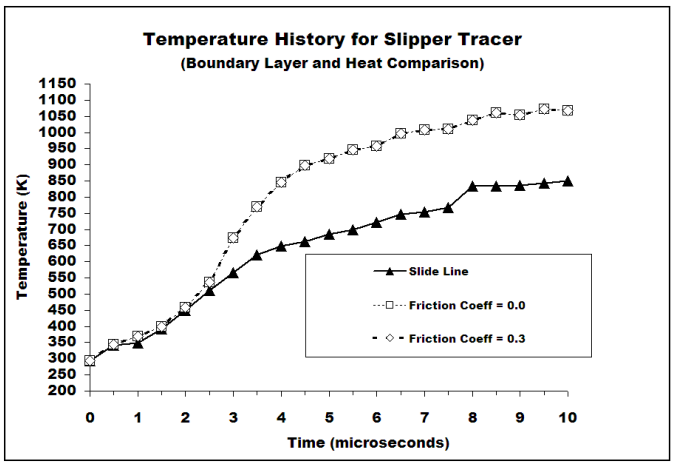

Figure 5.8 **The effect of boundary layer treatment on clean flat rail run at 3 km/sec.**

From the figures, one can see the effects of not meeting this requirement. White lines in the figures indicate cell boundaries. The first figure (Figure 5.6(a)) shows a layer of mixed cells between the slipper and rail. After 0.5 microseconds (Figure 5.7(a)), the solution indicates numerical instabilities at the front edge of the slipper-rail interaction. In contrast, when the cell boundaries and materials coincide (Figure 5.6(b)), the result is very different (Figure 5.7(b)). The results are much smoother and contain less numerical instabilities reminiscent of odd-even decoupling in some CFD solutions. The lesson learned here is that any simulation that models sliding interaction with the Boundary Layer algorithm should

begin with the material boundaries ending with cell boundaries at the sliding interface to avoid artificially high frictional effects.

As the solution develops for the frictional sliding case, deformations of the rail and slipper will create mixed cells at the sliding interface behind the region of primary interaction. This condition can also result in difficulties. In one respect, this problem is unavoidable for the cases that will be studied here. The impact of the slipper with the rail is not strictly tangential. It consists of both horizontal and vertical components. In any case, the vertical component of velocity will create mixed cells as the solution progresses. By monitoring the solution as it develops, the user can judge whether the solution becomes unrealistic due to artificial boundary algorithm instabilities. These instabilities are always limited to a small area within the interface and do not have an effect on the overall solution for stress, temperature, and plastic strain. On a local level, they do cause unrealistically high strain rates within a small number of cells. To distinguish between numerical instabilities and real solutions, the user should study the entire boundary layer over time. The instabilities are usually limited to the leading edge of the slipper-rail interaction, but could develop in other areas as cells become mixed during the calculations. Over time, the solutions with and without these numerical instabilities are essentially the same since the instabilities tend to smooth out over time. The researcher should avoid making conclusions based on a small discrete region with one of these instabilities present in a short time period. It is more accurate to make assessments based on the overall response within the boundary layer over time.

Figure 5.8 shows the effect of heat flow and boundary layer treatment for various coefficients of friction on the solution for a velocity of 3.0 km/sec on a clean flat rail. The effect of the Slide Line algorithm as compared to the Boundary Layer algorithm shows that the thermal environment takes longer to develop over 10 microseconds for the Slide Line algorithm which does not allow deviatoric stress to develop at the sliding interface. As a result, less plasticity develops and less heat is generated from the plastic work. The temperature developed using the Slide Line algorithm is only 850 K while the Boundary Layer algorithm solutions show a temperature of over 1000 K.

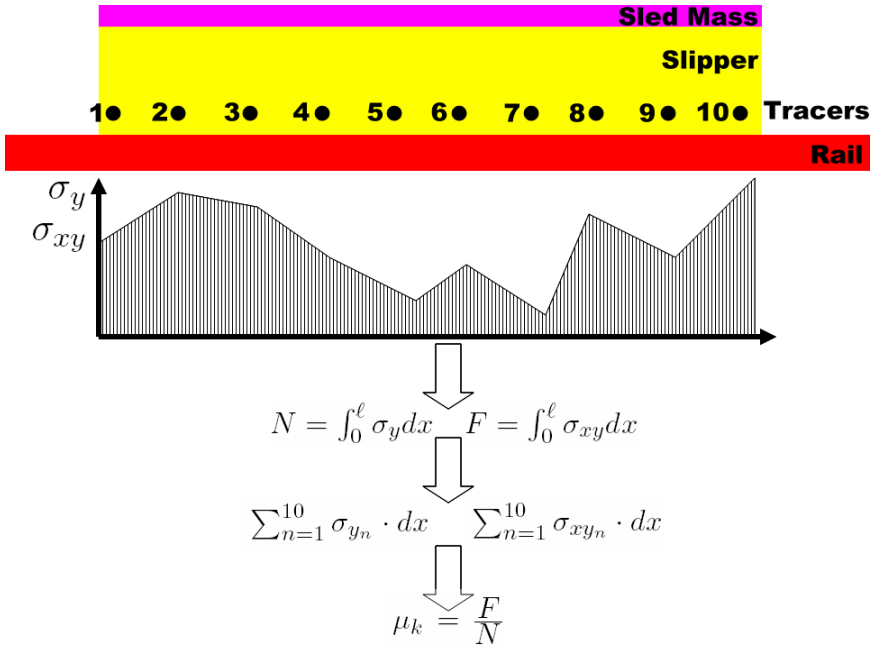

Figure 5.9 **Process of approximating the effective coefficient of friction.**

The effect on the temperature profile of the initial coefficient of friction is nil. The results for frictional coefficients of 0.0 and 0.3 are exactly the same. Since the velocities under consideration are so high, experimental coefficients of friction are difficult to attain. One alternative is to calculate the effective coefficient of friction for the CTH boundary layer algorithm. This can be accomplished by integrating over the slipper length for the values of normal stress, σ_y and shear stress, σ_{xy}. The integrals provide the effective normal ($N = \int_0^\ell \sigma_y dx$) and frictional ($F = \int_0^\ell \sigma_{xy} dx$) forces. By definition, the effective coefficient of kinetic friction in the CTH solution is then $\mu_k = \frac{F}{N}$. The integral of the stresses is estimated by taking the value of applicable stresses at a series of tracer points along the bottom of the slipper, and summing the products of their value with the distance between points. That is, $\int_0^\ell \sigma_y dx$ is approximated as $\sum_{n=1}^{10} \sigma_{y_n} \cdot dx$ and $\int_0^\ell \sigma_{xy} dx$ is approximated as $\sum_{n=1}^{10} \sigma_{xy_n} \cdot dx$. Figure 5.9 shows a schematic of this process.

5.4 Heat Conduction Parameters

In order to study the effects of nonequilibrium thermodynamic conditions on hypervelocity gouging, the irreversible effects of heat flow in the solution must be calculated.

This takes away the isothermal characteristics of the solution. A preliminary study of the heat flow effects is carried out to determine whether the algorithm will have an effect on the solution. Two studies are conducted. The first is a comparison of the solutions for heat conduction and for the case in which heat does not flow for frictional sliding at 1.5 km/sec. The second case considers frictional sliding at 3 km/sec.

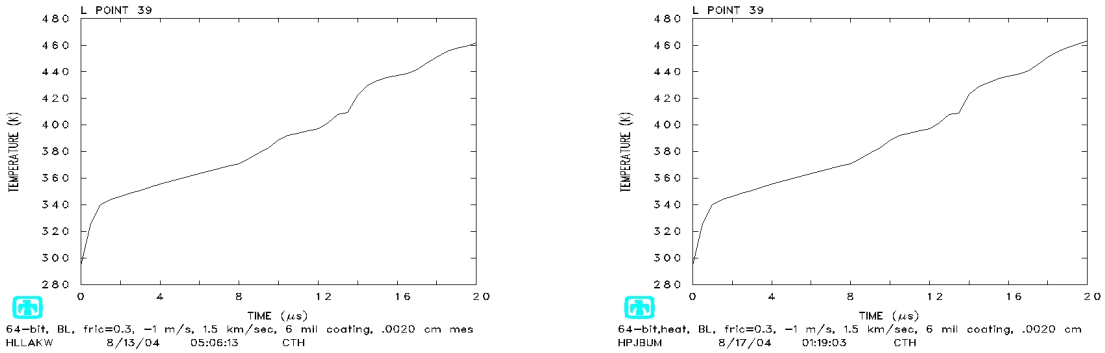

(a) **No heat transfer allowed between cells.**

(b) **Heat allowed to flow.**

Figure 5.10 **Comparison of heat conduction effects for run at 1.5 km/sec on flat coated rail, in slipper boundary over 20 microseconds.**

Figure 5.10 shows the effect of heat flow on the temperature solution for a velocity of 1.5 km/sec with a coefficient of friction of 0.3 over 20 microseconds. Figure 5.11 shows the effect of heat flow on the temperature solution for a velocity of 3.0 km/sec with a coefficient of friction of 0.3 over 10 microseconds. The tracer is located within the boundary layer of the slipper. There is no apparent difference between the two solutions. The variations may be more pronounced at 3 km/sec since the temperatures will be higher and the thermal gradients larger. The same tracer data is compared at a velocity of 3 km/sec over 10 microseconds. 10 microseconds scales correctly for the 3 km/sec velocity with the 20 microsecond time period for the 1.5 km/sec velocity. See section IV for more info on scaling times between numerical models.

Temperature changes in the isothermal treatment are not due to heat flow, but only from pressure changes and plastic work as it relates to the equation of state and energy balance. The temperatures over time without heat conduction become larger because

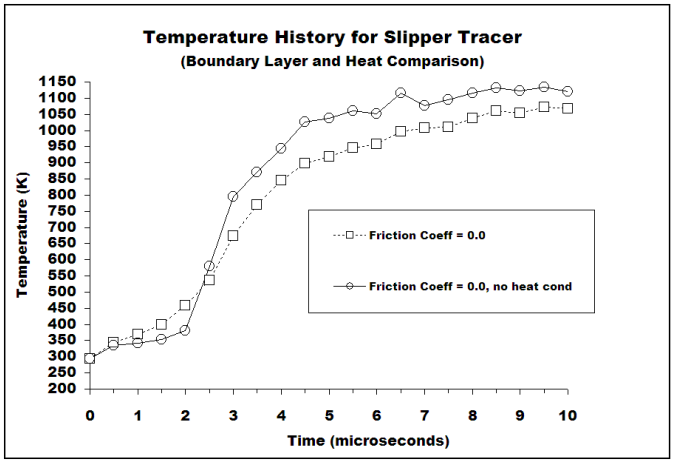

Figure 5.11 **The effect of heat conduction on clean flat rail run at 3 km/sec.**

heat is not allowed to flow away from the interaction as a heat source. This in turn, affects the development of plasticity which would occur as a result of thermal softening in the Steinberg-Guinan-Lund constitutive model equation. This will be considered in the Results and Discussion chapter.

Another consideration for the simulation is the time period covered in this analysis. The simulation is limited to approximately 20 microseconds based on available computational resources, but an actual event may take longer to develop in time. The results shown here in Figures 5.10 and 5.11 indicate that a quasi-steady state may be achieved over the simulated time periods of 20 microseconds for the 1.5 km/sec run and 10 microseconds for the 3 km/sec run. If the value of temperature is desired over a longer period of time, it may be estimated by extrapolating the results linearly. It appears the interaction of heat generation with heat flow away from the slipper bottom brings about temperature increases that could be approximated by a linear increase with time.

Tabular thermal properties of Vascomax 300, 1080 steel, and epoxy that are added to the CTH input file for heat conduction calculations are repeated in Table 5.2. This overrides the analytical conductivity option for the materials. The table lists temperature (in electron-Volts, eV) and thermal conductivity (in erg/s-1eV-1cm-1) data for each material.

1080 Steel		VascoMax 300 Steel		Epoxy	
T(eV)	k(erg/s/eV/cm)	T(eV)	k(erg/s/eV/cm)	T(eV)	k(erg/s/eV/cm)
1.4684e-3	4.7700e10	3.6711e-3	2.4715e10	3.6711e-3	6.5e8
1.0377e-2	4.8100e10	1.4684e-2	2.7424e10	1.4684e-2	6.5e8
1.9090e-2	4.5200e10	2.9369e-2	2.9794e10	2.9369e-2	6.5e8
2.7900e-2	4.1300e10	3.9158e-2	3.0132e10	3.9158e-2	6.5e8
3.6711e-2	3.8100e10				
4.5521e-2	3.5100e10				
5.4332e-2	3.2700e10				
6.3142e-2	3.0100e10				
7.1953e-2	2.4400e10				
8.9574e-2	2.6800e10				
1.1111e-1	3.0100e10				

Table 5.2 **Conductivity tables for 1080 Steel, Vascomax 300, and Epoxy used in the CTH input file.**

5.5 Mesh Refinement

A mesh convergence study was carried out. Mesh cell sizes in the vicinity of interaction were 0.0025 and 0.002 cm in size. The difficulty with sizes smaller than 0.002 cm is that these sizes are of the order of dislocation distances of metals [81]. Thus, the cells are approaching a description of the micromechanics level for the problem rather than continuum mechanics. Development of CTH algorithms is based on continuum mechanics theory. Constitutive models can contain physics based descriptions of micromechanical effects (e.g., the Zerilli-Armstrong model), but this is effective on a macroscopic level. Dissociation on the molecular level is also simulated using tabular equations of state, but the effects are again applied on the macroscopic level (pressure, density, and temperature). Material length scales based on micromechanics have been determined to be around 0.25-20 μm [81] for a variety of metals. This equates to 0.000025 cm to 0.002 cm. To avoid this difficulty, the smallest mesh size used to carry out the investigation is 0.002 cm.

Figure 5.12 shows the mesh convergence study conducted under a worst case scenario for a cell within the boundary layer of the slipper as it slides over a coated rail. The rail tracer is located about 10 cell lengths away from the area of interaction to obtain a comparison under less extreme conditions. The boundary layer algorithm contains numerical noise due to mesh coarseness for which the solution needs to be averaged out over a period

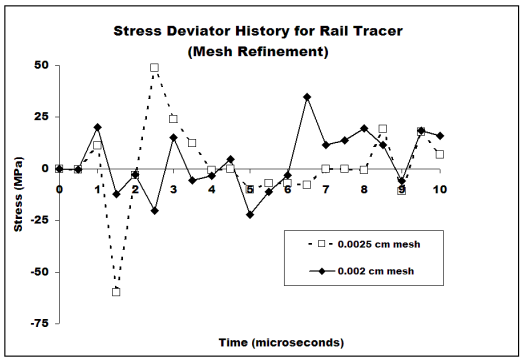

(a) **Deviatoric rail tracer plot for mesh refinement.**

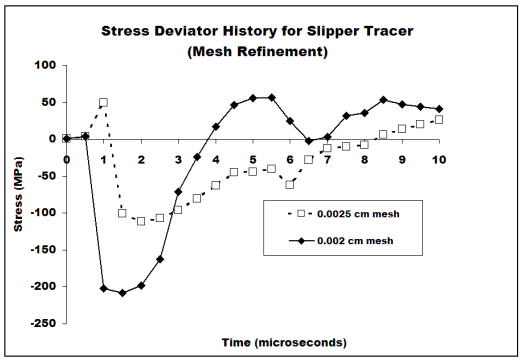

(b) **Deviatoric slipper tracer plot for mesh refinement.**

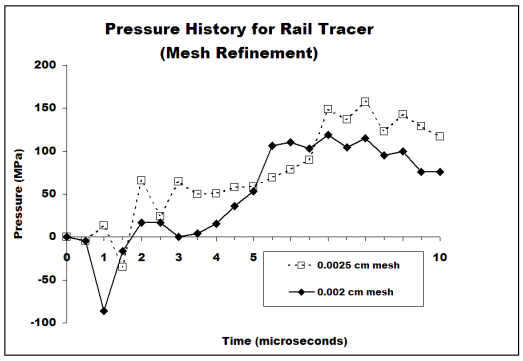

(c) **Pressure rail tracer plot for mesh refinement.**

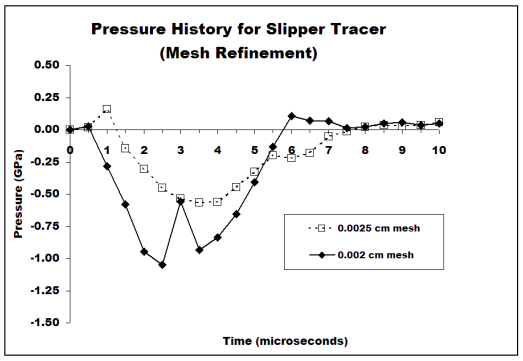

(d) **Pressure slipper tracer plot for mesh refinement.**

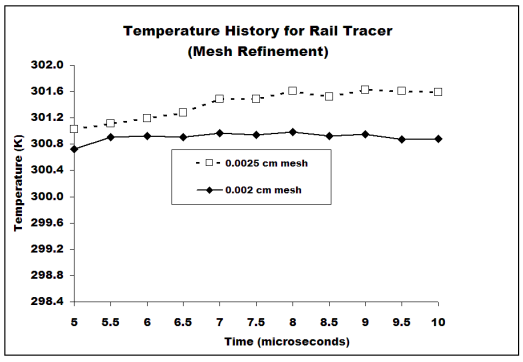

(e) **Temperature rail tracer plot for mesh refinement.**

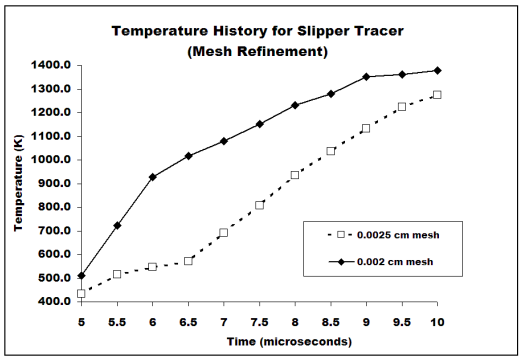

(f) **Temperature slipper tracer plot for mesh refinement.**

Figure 5.12 **Mesh refinement study.**

of time [46]. The data for pressure and stress deviator between 0 and 10 microseconds is plotted and compared for cell mesh sizes of 0.002 cm and 0.0025 cm. The boundary layer algorithm produces similar results over time for the 0.0025 cm and 0.002 cm mesh cell sizes. These values vary over time, but the average values for pressure, deviatoric stress, and temperature for the rail tracer are within 30 per cent of each other. Trends over time for the pressure, stress deviator, and temperature are for the results in both cases are extremely close for the rail tracer. Variations are larger in the slipper boundary layer, but decrease in time. It is important to consider the data for the boundary layer algorithm over time because mesh coarseness in the CTH algorithm causes numerical variations that average to an accurate value over time [46].

5.6 Consideration of Void Between Slipper and Sled Mass

The previous sections dealt with certain aspects of simulating an actual test sled such as friction, heat, velocity, material models, and dimensions. They also discussed simulation specific considerations such as mesh refinement, tracer placement, and numerical noise within the boundary layer algorithm. This last consideration explores one more level of detail in modeling a real slipper-rail impact as it occurs in the field. It has already been shown how a real test sled is transformed into a CTH simulation model (see page **??**).

One detail that was overlooked at the time was the fact that in a real impact of the slipper against the corner of the rail, the upper surface of the slipper interfaces with air, not with the sled mass. The density of air is much smaller than the artificial sled mass density of platinum. When a shock front reaches the top of the slipper, the response will be very different if the shock must travel into a higher density rather than a lower density material. Before deciding upon the CTH models that will be used to conduct the research, the effect of simulating this specific aspect of the real slipper is studied.

If one observes Figure 5.13, one sees the slipper that keeps the rocket attached to the rail is exposed to air at the corner which impacts the rail. Impacts at the corners are examples of two-dimensional plane strain conditions which lead to gouging. The requirement for plane strain conditions in order for hypervelocity gouging to initiate has been explored by Laird [7] in his comparison of two-dimensional and three-dimensional simulations of

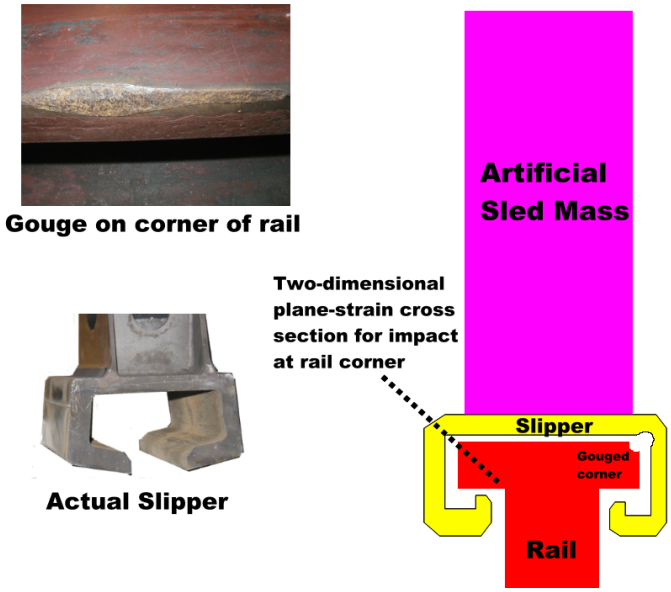

Figure 5.13 **Slipper plane strain impact corner exposed to low density medium.**

gouging, and earlier in this research where a three-dimensional uniform impact on he top of a rail was simulated using LS-DYNA (see section 3.1).

The frictional runs cover a time period of twenty microseconds so low pressure shocks have time to travel from the bottom of the slipper to the top of the slipper at the interface with the artificial sled mass. The elastic wave speed of the slipper material is approximately 5 km/sec. At this velocity, it will take a stress wave wave approximately 5 microseconds to travel from the area of interaction to the top of the slipper where it meets the artificial sled mass. This could affect the solution. Only a small portion of the slipper is covered by the metal strut connecting it to the sled payload (simulated here by the artificial sled mass). Most of the slipper is exposed to air, and the portion covered by metal is in a place where few gouges have been observed to occur [16].

It is of interest then, to explore the effects of a stress wave as it travels within the slipper and strikes the interface with a low density material. The current model contains a seamless interface between the slipper and the artificial sled mass. A two-dimensional plane strain impact usually occurs on a section of the slipper exposed to air. To model this case, a void is added between the slipper and sled mass. The sled mass remains attached by two end sections (see Figure 5.14) to the slipper so that momentum and energy of the

artificial sled mass will affect the impact of the slipper. However, this situation causes an uneven distribution of mass over the slipper and results in a concentration of mass over the front and rear portions of the slipper as it impacts the rail.

A short investigation of the effects of the interface between sled mass and slipper is shown in Figures 5.15 through 5.16. The value of pressure and deviatoric stress for a tracer located in the slipper boundary layer midway in the slipper is shown in Figure 5.15. This tracer is the one most affected by any effects of the gap.

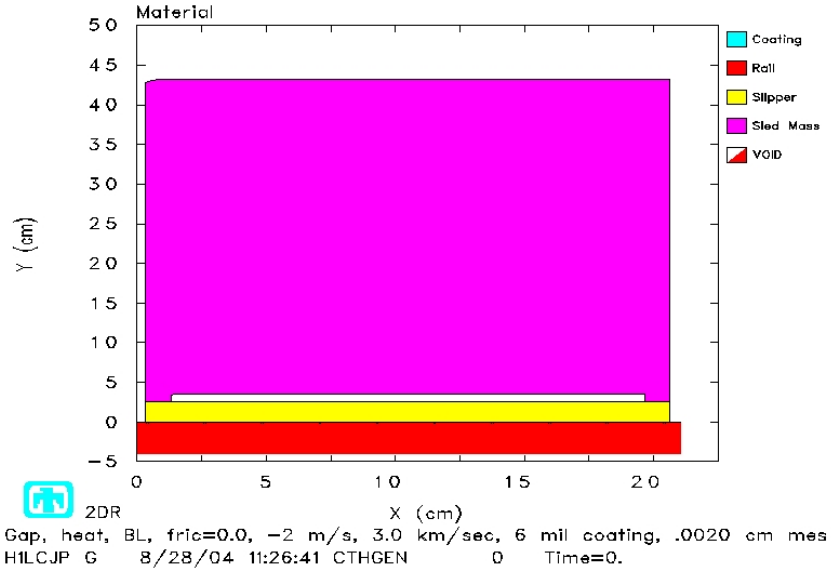

Figure 5.14 **Gap between slipper and sled mass to simulate shock reflections in real test sled.**

The comparison of temperature, pressure, and stress deviator plots for the same tracer show that shock reflection/absorption at the interface between the slipper and the artificial sled mass does not have a significant affect on the results over time for the frictional case. The tracer lies within the boundary layer interaction. The differences become more significant after 6 microseconds and are minimal in either case for temperature. The differences are larger in the solutions for pressure. But this could be due to the concentration of mass effects near the front of the slipper for the case with a gap. The loading on the slipper isn't uniform anymore. When deviatoric stress is observed, there are larger

fluctuations between the solutions for a gapped sled mass and a seamless interface, but this deviation is not very large. The average deviatoric stress over the twenty microsecond time period between solutions ends up being within ten per cent of each other.

A comparison of contour plots of pressure and deviatoric stress shows a global similarity between the gapless and gapped models. The primary difference is seen at 5 microseconds when the low pressure shock meets either a high (gapless) or low (gapped) density material. A higher pressure compression wave travels into the higher density material here. With a gap at the slipper boundary, the pressure wave reflects back into the slipper as a low pressure tensile wave and eventually meets up with the compressive interactions at the bottom of the slipper. This would likely cause a release of the higher pressure at this interaction in the slipper. The driving interaction is not the weak shock reflection, but the loads generated by deformation of the sliding interaction between the slipper and rail.

The model containing a gap between the slipper and sled mass is the worst case because of the larger loads at the front of the slipper. This loading is due to the nonuniform distribution of mass over the slipper. Since the effects of the gap were minimal in the situation of the frictional run over a flat rail, the model will remain gapless so that further results can be compared to the cases already run. On the other hand, to obtain a conservative solution for the case of a rail roughness impact, the gapped model will be used for those cases.

5.7 Cases to be Studied

The studies preceding this section provided important information for making informed decisions about parameters for the study of nonequilibrium thermodynamics and the mitigation of coatings in hypervelocity gouging. This information will be used to develop the cases that will be run. The results from these cases will be used to make conclusions about the affect of thermodynamics and coatings on test sled impacts. Nonequilibrium thermodynamics will be studied in the context of irreversible thermodynamics due to frictional and heat flow characteristics of the solution. The result of adding a 6 mil coating to the rail will also be considered by making CTH runs with a coating and without

a coating (a.k.a., "clean") for the same cases. Furthermore, a comparison of the gouging threshold velocity of 1.5 km/sec and the HHSTT goal of 3 km/sec will be investigated.

The frictional coefficient has been selected to be 0.0 because the Boundary Layer treatment of sliding surfaces was shown to develop the greatest amount of heat when compared to the Slide Line treatment. There was no substantial difference between the input coefficient of heat of 0.0 and 0.3 (as shown above) so 0.0 was arbitrarily selected. The mesh cell size minimum of 0.002 cm was determined from the mesh convergence study and the desire to avoid inadvertent micromechanic effects in the solution.

Table 5.3 **CTH cases for vibratory frictional and rail roughness impacts.**

	Vibratory Frictional Impact (1 m/s ⇓)		Rail Roughness Impact (2 m/s ⇓)	
Coated Rail	1.5 km/sec ⇒	3.0 km/sec ⇒	1.5 km/sec ⇒	3.0 km/sec ⇒
Clean Rail	1.5 km/sec ⇒	3.0 km/sec ⇒	1.5 km/sec ⇒	3.0 km/sec ⇒

Table 5.3 shows the CTH test plan. The results will be compared and contrasted so the effect of coatings and a nonequilibrium thermodynamic environment for the impact cases of a vibratory frictional and a rail roughness impact may be investigated. In this manner we also hope to make conclusions about how the transition from the threshold velocity of 1.5 km/sec to the HHSTT goal of 3 km/sec affects slipper-rail conditions. A vertical velocity of 1 m/s is used for frictional development and 2 m/s for the rail roughness impact for the worst case impact scenario. The lower vertical velocity of 1 m/s is used for the frictional development to better understand the effects of sliding friction on thermal development of he environment. The coating is epoxy with a 6 mils (0.01524 cm) thickness. This is the minimum thickness used in the field for actual testing.

5.8 High Performance Computing Considerations

Each CTH run is limited in some way by the capacity of the hardware to solve the problem in a reasonable amount of time and with available resources. The final solution must not take months to obtain, and it must fit within the memory limitations for the user who must share resources with other students. This next section discusses some of the features one must consider when performing CTH runs of the hypervelocity gouging models.

The CTH runs for the cases in Table 5.3 are limited by the computational resources available to the researcher. Smaller mesh cell sizes and larger domains increase the memory requirements for the computational platform. In addition, CTH puts a 2 GB limitation on the size of plot files. The best prospect for analyzing numerical results is to stay within these limitations.

The CTH models are calculated on a cluster of AMD Opteron computer chips with 64-bit operations. Each test run takes about twenty-four hours of wall clock time to complete. Frictional runs on flat surfaces can be carried out to twenty microseconds in solution time without drastically increasing wall clock time or using up too much memory. This also keeps most plot files within the memory limits stipulated by the CTH code. Impacts with rail roughness can be carried out to ten microseconds in solution time for the same amount of wall clock time. Memory requirements are also a limitation on the amount of cells used to describe the model.

For example, the clean rail roughness case at 1.5 km/sec took 82,278.172 seconds to solve out to ten microseconds. This equates to about 22.85 hours. Sixteen processors (eight nodes) were used with the 64-bit version of CTH. This resulted in sixteen restart files of approximately two GB each. There is a limit on how many processors will decrease the amount of time to complete a solution. As the number of processors increases past a certain threshold, the communication time between processors increases and actually slows down the time to obtain a final solution.

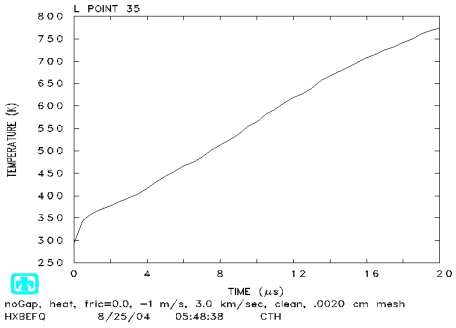

(a) **Temperature in slipper boundary layer with no air gap between slipper and sled mass, $\mu_k = 0.0$.**

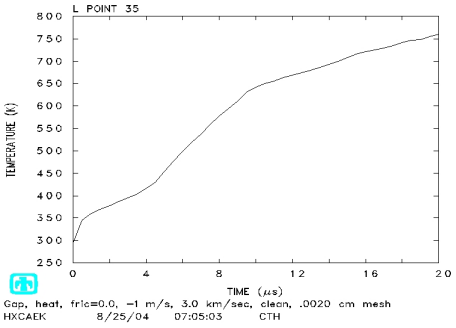

(b) **Temperature in slipper boundary layer with air gap between slipper and sled mass, $\mu_k = 0.0$.**

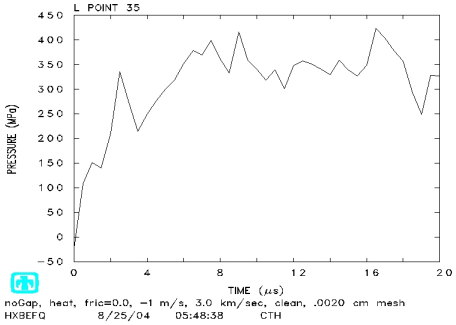

(c) **Pressure in slipper boundary layer with no air gap between slipper and sled mass, $\mu_k = 0.0$.**

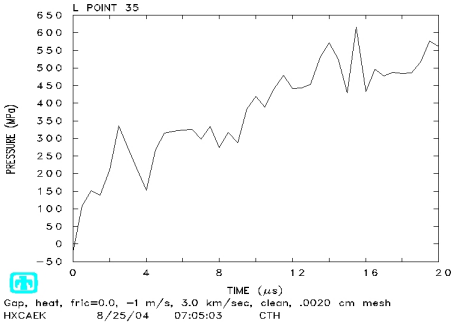

(d) **Pressure in slipper boundary layer with air gap between slipper and sled mass, $\mu_k = 0.0$.**

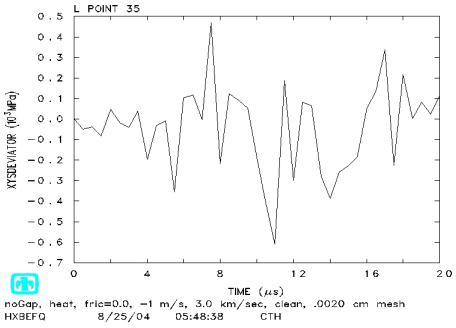

(e) **Stress deviator in slipper boundary layer with no air gap between slipper and sled mass, $\mu_k = 0.0$.**

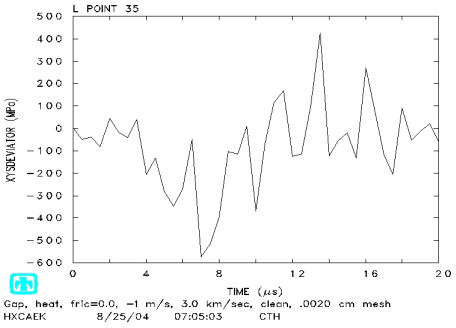

(f) **Stress deviator in slipper boundary layer with air gap between slipper and sled mass, $\mu_k = 0.0$.**

Figure 5.15 **The effect of a gap in the sled mass on temperature, pressure, and deviatoric stress on a clean flat rail run at 3 km/sec.**

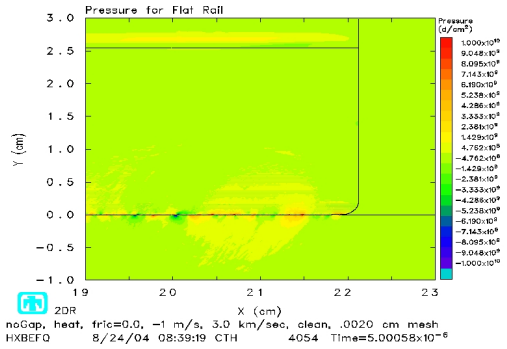

(a) **Pressure in slipper boundary layer with no air gap between slipper and sled mass, time = 5 microseconds, μ_k = 0.0.**

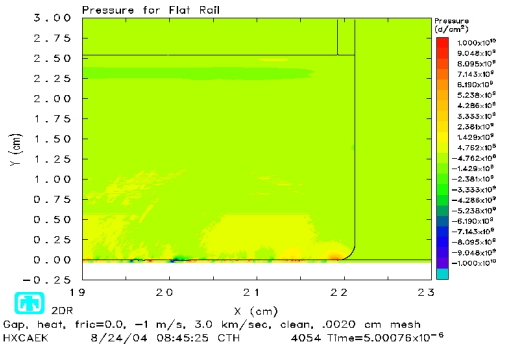

(b) **Pressure in slipper boundary layer with air gap between slipper and sled mass, time = 5 microseconds, μ_k = 0.0.**

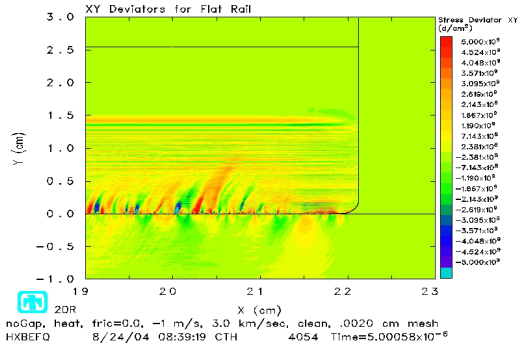

(c) **Stress deviator in slipper boundary layer with no air gap between slipper and sled mass, time = 5 microseconds, μ_k = 0.0.**

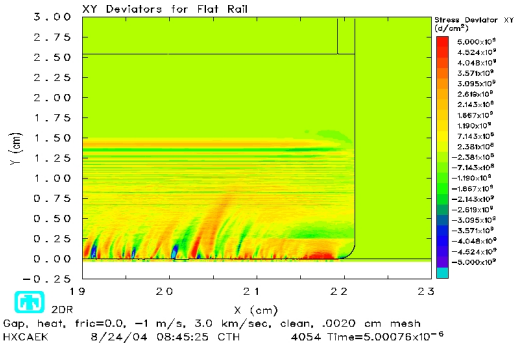

(d) **Stress deviator in slipper boundary layer with air gap between slipper and sled mass, time = 5 microseconds, μ_k = 0.0.**

Figure 5.16 **The effect of a gap between slipper and sled mass on a clean flat rail run at 3 km/sec.**

VI. Results and Discussion

The objective of this investigation is to study the effects of nonequilibrium thermodynamics and gain a physical understanding of the use of coatings to mitigate hypervelocity gouging. In support of this objective, four major cases are studied. These cases simulate the thermomechanics of sliding friction and vibratory impact on a perfectly flat and a misaligned rail. The rail is modeled without a coating (i.e., clean) and with a 6 mil coating (which is the minimum thickness in the field).

A shallow vibratory vertical impact of 1 m/s is conducted with tangential velocities of 1.5 and 3.0 km/sec. This is first conducted on a clean rail to allow friction to develop. In the second type of impact studied, an impact with a vertical velocity of 2 m/s and tangential velocities of 1.5 and 3.0 km/sec upon a rail roughness is studied. The purpose of this case is to investigate the initiation of gouging for the given test sled.

Coated variations of each of these cases are studied to gain an understanding of the effect of coatings. Each case also studies a horizontal velocity of 1.5 km/sec and 3 km/sec. The reasoning behind these velocities is that 1.5 km/sec has been observed as a threshold velocity for the occurrence of gouges seen in the field [16]. 3 km/sec was chosen because the HHSTT is striving to reach that velocity (equivalent to 10,000 fps).

The results obtained from these CTH models will be analyzed and discussed in this section. Observations of gouges in the field indicate shear band formation, plastic deformation, high stress, high temperature, and subsurface cracking. Simulation of characteristics such as cracking and shear band formation, are dependent on the damage model used. The CTH damage model used here is a simple maximum stress model in which a void is formed in order to raise the pressure in a mesh cell to the value required by the conservation equations and thermodynamic energy balance routines. Therefore, shear bands and subsurface cracking may not be evident from the CTH results shown here. What can be discussed in this section are the conditions that may lead to such formations.

The characteristics of the boundary layer and frictional effects on the thermal environment will also be discussed. As the thermal environment develops, and heat is allowed to flow as an irreversible thermodynamic process, it affects formation of plastic deforma-

tion through thermal softening in the constitutive model. Shock waves also influence the thermomechanic response of the materials. Large pressure and temperature changes behind the shock can cause phase changes in the materials. The slipper and rail volumetric responses are both defined by a tabular equation of state. This accounts for phase changes of the materials. The epoxy coating equation of state does not account for this possibility, so the pressure and temperatures will be analyzed manually using the CTH results. Potential phase changes will be discussed as the conditions for them are observed to occur.

In low pressure shocks, the distortional response becomes important. The behavior of the system under this stress condition is better characterized by the shear components of the stress tensor. The treatment and influence of these types of shocks on the system are very different from the hydrodynamic treatment and effects of high pressure shocks. These differences will be discussed and the potential cause of their formation will be considered.

If a gouge forms, this phenomenon will be analyzed for potential causes. The velocity vectors will be important for this discussion, because formation of rotational velocity components in jetting is a strong indication that jetting will initiate. The factors leading up to this phenomenon will be tracked and considered. An improved understanding of the formation of gouging will help in the physical understanding of the mitigation of gouging using coatings.

Microanalysis of damaged portions of the rail in Gerstle's work [11] showed that gouges contain a surface layer of slipper material deposited on top of martensitized rail steel. Subsurface examination of the gouge show that temperatures were high enough to austenitize the steel and that the rail material was severely strained and microcracked. Gerstle believed this to be evidence of catastrophic thermoplastic shear. In thermoplastic shear, the local rate of temperature change causes a strength decrease that overcomes any strength increases from strain hardening. This causes local shear deformations in the material. Local heat generation due to this shearing can be high enough to austenitize steel. If the thin layer of austenite steel is surrounded by a large mass of solid steel, the austenite layer can be quenched rapidly enough to form martensite.

Austenite is formed when steel is heated above 573 K. This phase of the steel is unstable up to approximately 1185 K and transforms in time. If the austenite is cooled extremely fast, it transforms into martensite. Gerstle's observations provide a couple of observations that can be investigated in this study. First, the temperatures can be checked to determine if they are high enough to form austenite. Another consideration that can be verified through the numerical results is whether the temperature change is rapid enough to form martensite and with heat conduction being simulated, whether the amount of heat generated is greater than the amount of heat conducted away from the deformation. Another factor to consider is whether these conditions are extreme enough so that thermal softening overwhelms the effects of strain hardening.

In terms of the coatings, high pressure shocks above 20 GPa will cause dissociation of the molecules in epoxy. Because this is not simulated in the equation of state available for use in this model, pressures of the numerical results will be monitored for values that might cause this effect. The glass transition temperature of epoxy is around 400 K. Above this temperature epoxy transitions into a rubbery state: it softens and becomes viscoelastic. The effect of a rubbery phase on the response of the epoxy is caused by encouraging the formation of shear bands in the epoxy matrix. This has an overall effect of improving the epoxy's toughness. Epoxy also has a flash point of 522 K, but excellent thermal resistance properties. Therefore, it can absorb heat energy without raising in temperature. A rise in temperature should be followed by a change in state from a glassy to a rubbery phase, which would improve the epoxy's resistance to impact loading [82].

These factors and others will be investigated in the results to determine what the simulation depicts and what the potential consequences in the field may be. For example, the results for an impact on the epoxy coating may depict a temperature of 1000 K based on the CTH material model, but actual epoxy would normally combust or become gaseous prior to reaching that temperature. Therefore, one might deduce from these results that the epoxy coating would have failed prior to reaching the temperature shown by the results. This is an extreme example, but illustrates the point.

The first characteristic of the problem to be discussed is the calculation of an effective coefficient of friction using the CTH boundary layer algorithm. After establishing the

effective coefficient of friction, a full discourse on the results for each of the four major cases will take place. It was found that the effective coefficient of friction did not change from case to case. Thus, a discussion of one case would apply to each of the other possible variations for input coefficients of friction.

6.1 Effective Coefficients of Friction

The boundary layer algorithm allows input of a friction coefficient so that frictional forces may be calculated and frictional effects determined between sliding interfaces. The same coefficient of friction is used for each of the cases studied. It was found in the previous chapter that changing the input coefficient of friction had no effect on the solution (see section 5.3).

The frictional forces in CTH are calculated as a body force density from the input coefficient of friction and the normal of the Cauchy stress tensor to the material interface. This frictional body force is used in the momentum balance equation.

The effective coefficient of friction can then be calculated from the results by integrating the values of normal stress (σ_y) over the surface of the slipper bottom and integrating the shear stress (σ_{xy}) as well. These integrations provide the normal force and the frictional force, respectively. In this manner, the effective frictional force may be divided by the normal force and an effective coefficient of friction estimated from the CTH results (see section 5.3).

Using this method, the effective friction coefficient was calculated for the case of a 3 km/sec sliding velocity and 1 m/s vertical velocity with an initial coefficient of friction of 0.3. At 3 microseconds, the coefficient of friction was found to be 0.18. At 6 microseconds, the value was 0.29, and at 10 microseconds, the value was 0.26. Because the boundary layer solution is accurate for time averaged values, the coefficients should be averaged. Now the result becomes 0.243. This number is probably slightly high because of the 1 m/s vertical velocity which added normal stress components to the solution. The constant velocity would have increased the stress tensor at the surface and thus increased the normal component of stress for the friction calculation. The results between initial coefficients of

Table 6.1 **Material model constants.**

Model Constant	1080 Steel	VascoMax 300	Units
ρ_o, density	7.850	8.129	g/cm^3
Y_o, yield	7.0×10^9	1.447×10^{10}	g/cm s^2
c_p, specific heat	4.08×10^6	4.08×10^6	cm^2/ s^2 K
T_M, melting temperature	1835.7	2310	K
Model Constant	Copper	Molybdenum	Units
ρ_o, density	8.93	10.2	g/cm^3
Y_o, yield	1.2×10^9	1.6×10^{10}	g/cm s^2
c_p, specific heat	3.83×10^6	2.43×10^6	cm^2/ s^2 K
T_M, melting temperature	1790	2310	K

friction have been found to be the same. Therefore, any coefficient of friction used as an input for high velocity impacts should provide the same results. The effective coefficient of friction then becomes a function not of the initial coefficient of friction, but of the mechanical and thermodynamic characteristics of the impact and the numerical treatment of the sliding interaction.

The velocities at which the slipper slides over the rail are at such high speeds, that experimental coefficient of friction data is not readily available. Bowden and Freitag [50] conducted experiments up to 800 m/s to determine the coefficient of friction on materials such as steel on copper, steel on aluminum, steel on duraluminum, steel on bismuth, steel on antimony, steel on molybdenum, copper on molybdenum, steel on diamond, copper on diamond, and chromium on diamond. They found that friction and wear of metals at high velocity are dependent on the relative material properties of the materials at elevated temperatures. They found the coefficients of kinetic friction decreased to 0.2 or lower for a variety of metals on metal (e.g., steel on copper and steel on molybdenum).

In order to compare Bowden and Freitag's data to our CTH results, we must first determine which sliding case of metal on metal is closest to the case we have of Vascomax 300 on 1080 steel. Bowden and Freitag concluded that friction and wear of metals at high velocity are dependent on the relative material properties at elevated temperatures. The properties that affect the behavior of materials at elevated temperatures include density, yield strength, specific heat, and temperature at melting point.

These material properties were compared to the materials used in Bowden and Freitag's research. The materials found to be closest to the materials under study are detailed in Table 6.1. The coefficient of friction calculated by the CTH algorithm for a 3 km/sec tangential velocity is similar to the extrapolated results of Bowden and Freitag [50]. Bowden and Freitag's results are 0.2 for steel on copper and 0.15 for steel on molybdenum. These are similar to the time averaged effective coefficient of friction of 0.243 for the CTH run. If one considers that the vertical velocity in the CTH run would increase the normal force and cause an inadvertently high effective coefficients of friction, these results can be considered to be close to each other. Also, the method of integration can be improved as the number of sample points increases. Ten points were used to obtain the coefficients of friction presented here.

The effective friction as calculated by CTH, has been shown to be similar to published experimental results for similar materials. The effective friction at high velocities is dependent on the numerical treatment of the sliding materials, and the properties of the materials. The value of the coefficient of friction does not change for a different input coefficient of friction. Therefore, the same coefficient of friction will be used in the subsequent CTH models. It was shown earlier that the boundary layer algorithm produces larger temperatures at the sliding interaction than the frictionless treatment for sliding materials. The boundary layer treatment of the sliding interface will be used in the test cases since it represents the case in which irreversible temperature effects may become important.

After further analysis, the reason for development of higher temperatures with the boundary layer treatment appears to be the result of numerous bumps that form along the slipper-rail interface due to deformation of the sliding interfaces in the boundary layer treatment. The boundary layer treatment allows deviatoric stress to form along the interface of the sliding materials. This treatment allows the slipper to maintain strength at its boundary as it slides along the rail. This better simulates the affect of friction on slipper-rail sliding impacts. This will be discussed further in the next section.

6.2 Vibratory Impact and Frictional Heat Development on Clean Rail

Having characterized the frictional parameters, a vibratory impact of 1.5 km/sec horizontal and 1 m/sec vertical impact on a rail is considered. This case simulates an average impact of one downward stroke of a vibration cycle of the slipper on the rail, in which development of friction is a primary consideration. The rail is clean. That is, there is no coating on the rail. The rail is also assumed to be perfectly flat. The goal of this case is to develop the nonequilibrium thermal environment using irreversible frictional effects of the sliding slipper on the rail.

The actual time of contact in an impact is estimated to be approximately 1 millisecond long [36]. Rather than simulate the entire time period of 1 millisecond, a quasi-steady state is consider in which the temperature and plastic deformation have developed over 20 microseconds for the horizontal velocity of 1.5 km/sec. The distance the slipper covers in this time is 3 cm instead of the 150 cm that would be covered for the 1 millisecond contact time period. Over the shorter time period of 20 microseconds, previous runs indicate a quasi-steady state may be extrapolated to the desired time period (see section 5.4).

This case is run using a coefficient of friction of 0.0 and without a partial void between the top of the slipper and artificial sled mass. The solution is considered over 20 microseconds. Because there isn't a gap at the top of the slipper, the change in pressure at the interface between the slipper and the artificial sled mass will not simulate a shock reflection as would be seen on the exposed plane strain corner impact of a real slipper. The stress waves caused by the sliding interaction at the bottom of the slipper are initially low pressure waves. It was shown earlier (in section 5.6) that the reflection of these low pressure waves with a low density medium at the top of the slipper will have a minimal effect on the overall solution for a frictional run over a flat rail. Stresses developed in the boundary layer have a greater effect on the solution than the low pressure shock reflection.

Figure 6.1 shows the contour plot of deviatoric stress at 20 microseconds. The figure shows that distortional responses are concentrated along the sliding interface between the slipper and the rail. This response is apparently due to the large number of tiny ridges along the sliding interface. The sliding slipper and rail interfaces are rough. Each small ridge

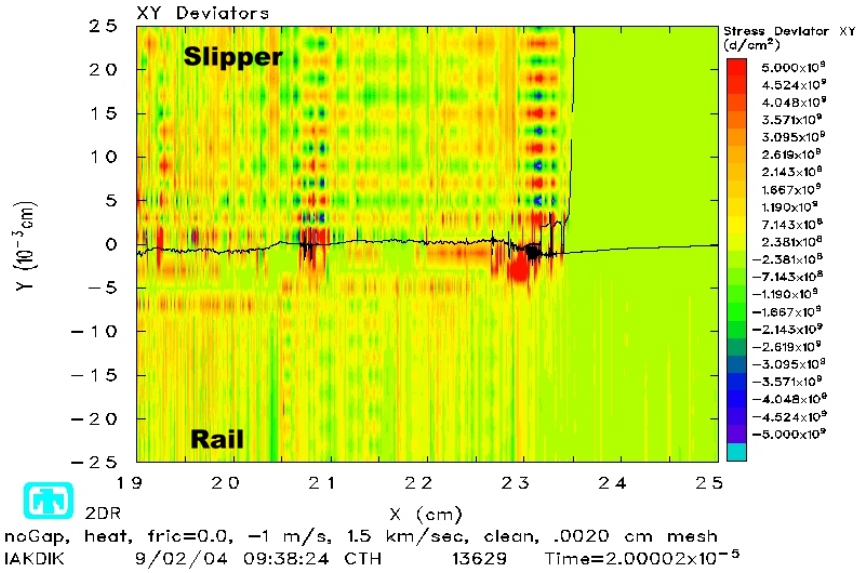

Figure 6.1 **Deviatoric stress contours at 20 μs for 1.5 km/sec horizontal velocity, μ_k=0, clean flat rail.**

acts as a tiny asperity. If we look back in time as the situation develops, we may see how the boundary layer algorithm allows the materials to interface with each other and form these discrete deformations that impinge on each other. The interface becomes the defining factor for the frictional effects. The tiny ridges stick to each other as the surfaces slide, and resistance causes a reaction in the bulk material that is seen as a deviatoric response near the surfaces. By 20 microseconds, these reactions (in the form of distortional waves) have propagated through the slipper and rail.

Let us observe the response at an earlier time to see how this situation comes about. In Figure 6.2, strain rates on the order of 10^7/sec occur along the rail surface. These sections of high strain rate are separated by small regions of low or no strain rate. The disparity in strain rates result in small areas that deform faster than regions adjacent to them. These large deformations form humps, or projections into the opposing sliding surface.

The cause of these large disparities in strain rate is discrete points of mutual interaction due to friction along the slipper and rail surfaces. When the slipper and rail materials

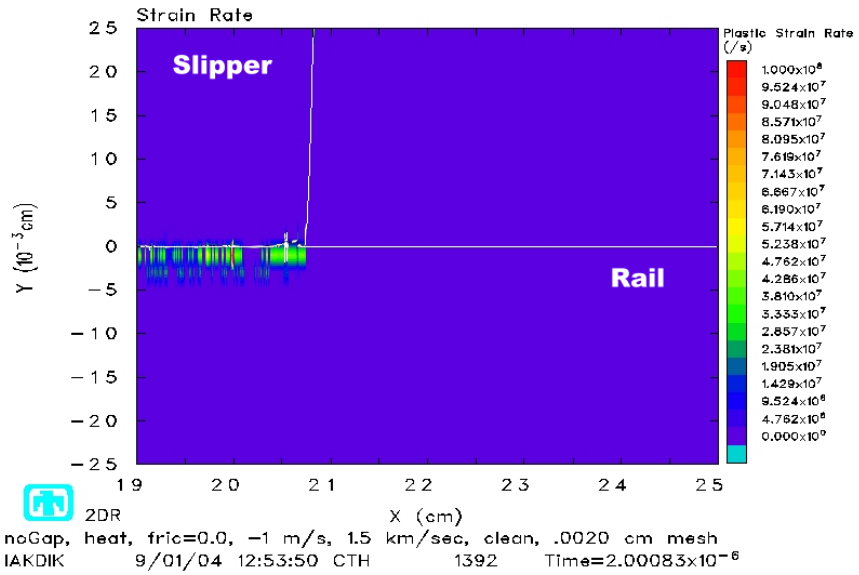

Figure 6.2 **Strain rates at 2 μs for 1.5 km/sec horizontal velocity, μ_k=0, clean flat rail.**

are attached to one another at these discrete points, the rail material must deform to match the velocity of the slipper material it is connected with. At these points then, the materials are rapidly strained. When this occurs at a variety of points along the sliding surfaces, we see small regions of high strain rate and low strain rate. Small portions of the rail material project into the slipper, causing the slipper material to react in kind.

The response of the slipper and rail bulk materials to these numerous localized regions of high and relatively low strain rates can be seen in the stress deviator in Figure 6.3. Shocks with pressure and deviatoric responses around 1 GPa or less emanate from the regions of greatest roughness. The front of a distortional wave travels upwards into the slipper. This is led by a weak pressure front. Both waves are a response to numerous collisions of slipper and rail materials at discrete "sticking" points of friction. The ridges formed by the different regions of strain rate along the surfaces act as tiny asperities, which further affect the solution. Barber and Bauer's [14] description of this phenomenon is helpful. They describe the formation of "cold welds" between the materials at discrete points (see section 2.4) for materials sliding at high speed.

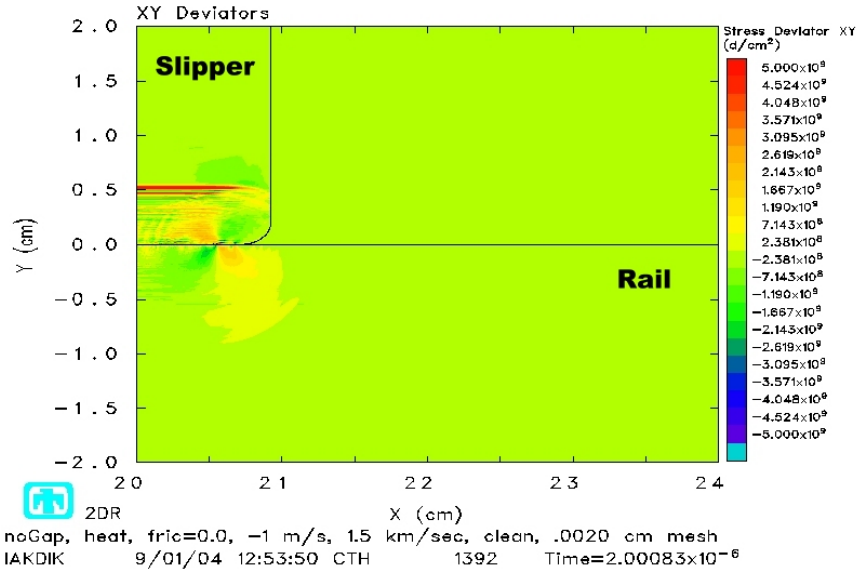

Figure 6.3 **Deviatoric stress at 2 μs for 1.5 km/sec horizontal velocity, μ_k=0, clean flat rail.**

The continuous sliding of the slipper over these small bumps results in a mutual interaction between the slipper and rail and more ridges are formed. As these rough surfaces react to one another, the projections turn plastic and deform further, resulting in less strain rate differences within the rail (see Figure 6.4). Though smaller, the regions of high strain rate continue. We also note the rail material along the sliding slipper material has already strained plastically. The slipper material also becomes plastically strained and the sliding interface is now an interface between two permanently deformed materials. These materials continue to impinge on one another and the tiny projections of the slipper into the rail and the rail into the slipper become larger in some areas and more numerous in others. The sliding interaction continues as the front region of high strain rate in the rail grows in size.

Over time, the plastic work done on the slipper and rail materials due to this sliding interaction cause an increase in temperature within the thin region of this boundary layer. Figure 6.5 shows the temperatures near the leading edge of the slipper-rail interaction. The temperature rises to around 1300 K in the rail. The slipper tracer near that same area

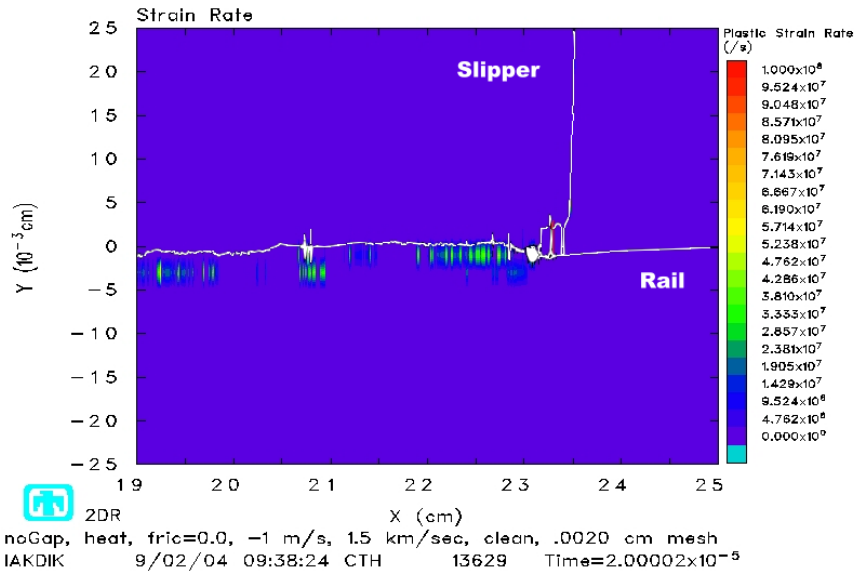

Figure 6.4 **Strain rates at 20 μs for 1.5 km/sec horizontal velocity, μ_k=0, clean flat rail.**

shows a temperature rise from 298 K to approximately 825 K in 20 microseconds. These temperatures are high enough to transform the steel to austenite, as has been observed in gouged specimens [11]. The temperature ranges from the largest value of 1300 K within the sliding interface, to lower temperatures (around 850 K) that are removed from the sliding interface, but still within the boundary layer region. At these lower temperatures, the austenite would be unstable and change in time. In the higher temperature region the austenite phase should be stable. There is no indication of rapid cooling that would produce martensite, but the conditions should not change unless the situation changes. One such example would be an impact with a rail roughness.

For the 3 km/sec case we see similar results, yet there are important differences. In order to compare results between the 1.5 km/sec and the 3 km/sec runs, we use the natural time scale (see section **??**) of $2\tilde{T}_1 = \tilde{T}_2$. In other words, we compare a time interval over 10 microseconds for the 3 km/sec run to the 20 microsecond interval of the 1.5 km/sec run.

The two situations with 1.5 km/sec and 3 km/sec tangential velocities are different, and we do not intend to generate similar solutions for this study. In fact, the purpose of

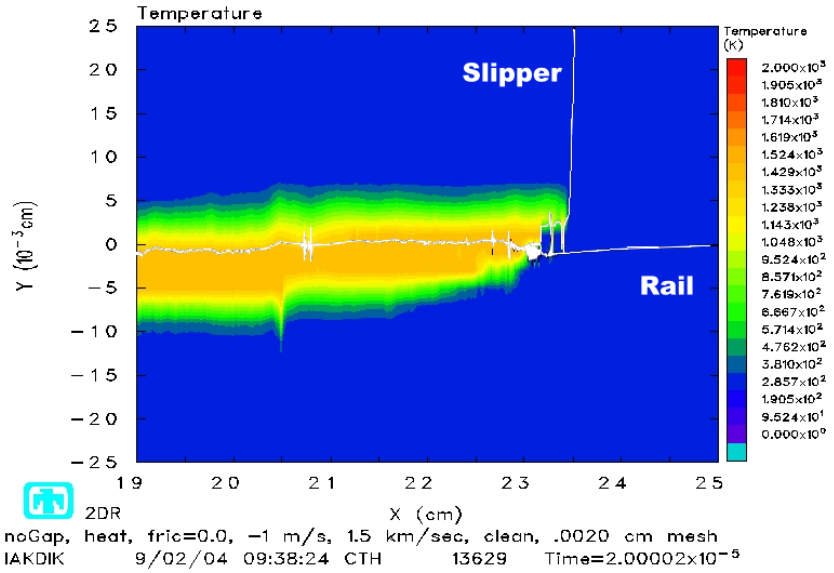

Figure 6.5 **Temperature at 20 μs for 1.5 km/sec horizontal velocity, μ_k=0, clean flat rail.**

this study is to determine the differences between the solutions by varying the horizontal component of velocity. However, it is desired that comparable horizontal distances be considered, so that development of frictional characteristics may be compared appropriately. That is why a time interval of 20 microseconds for the 1.5 km/sec x-velocity is compared to a 10 microsecond time interval for the 3 km/sec x-velocity. The distance covered is the same (3 cm).

At 1 microsecond (which is comparable to 2 μs for the 1.5 km/sec case), the main difference observed as compared to the 1.5 km/sec run, is that there are less discrete regions of high and low strain rate in the 3 km/sec run (see Figure 6.6). With a more uniform region of strain rate, the sliding interface remains relatively smooth. The slopes of the material interface are low and gradual, except at the leading edge.

If one observes Figure 6.7, two things are noticeable. The first is that there is a relatively uniform deviatoric response within the rail and the slipper that propagates in the y direction. This region exists from x = 19 cm to about x = 20 cm in the plot. The next region exists from about x = 20.5 to approximately x= 20.75 cm. This region indicates a

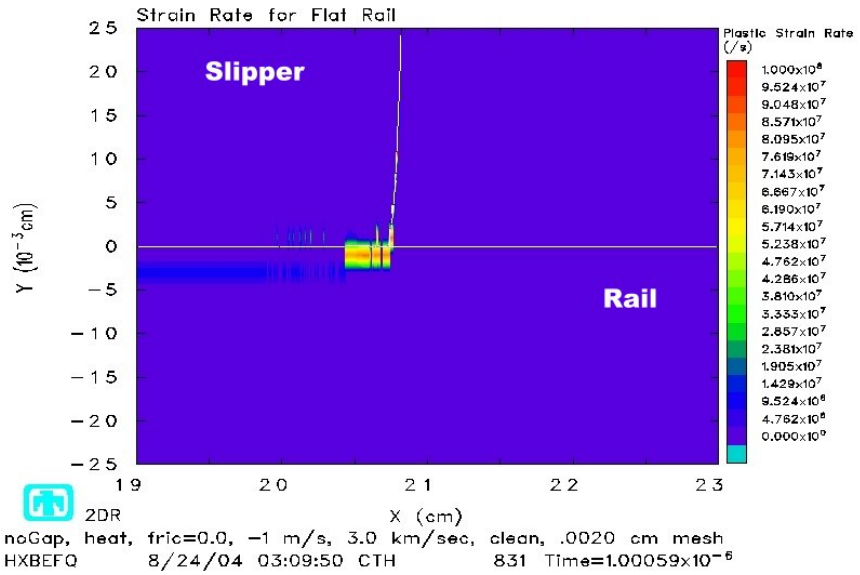

Figure 6.6 **Strain rate at 1 μs for 3.0 km/sec horizontal velocity, μ_k=0, clean flat rail.**

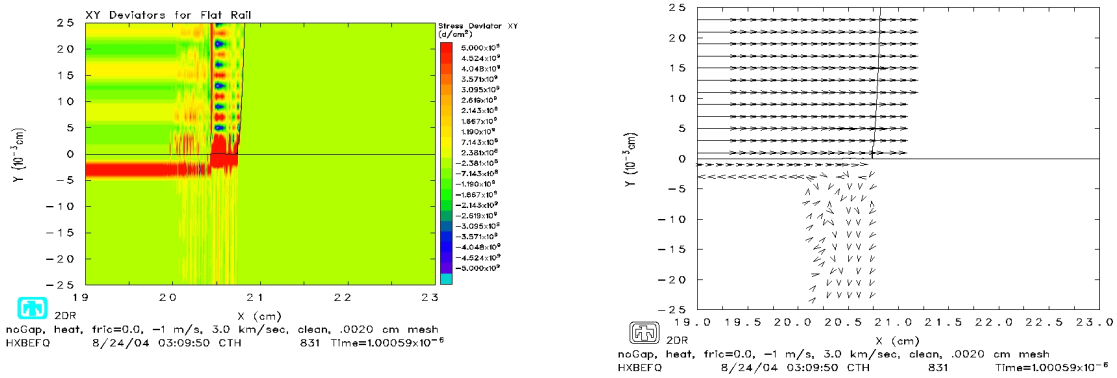

(a) **Deviatoric stress at 1 μs for 3.0 km/sec horizontal velocity, μ_k=0, clean flat rail.**

(b) **Velocity vectors at 1 μs for 3.0 km/sec horizontal velocity, μ_k=0, clean flat rail.**

Figure 6.7 **Comparison of deviatoric stress and velocity vectors for run 3 km/sec.**

low pressure shock front in the rail and alternating positive-negative bubbles of stress. The volumetric response shown by the pressure plot indicates a similar region. In this region it appears there is a reflection of a low pressure shock off the free surface of the front of

the slipper. This low pressure shock is caused by the interaction at the leading edge of the slipper and rail as the slipper is forced into the rail at a shallow velocity vector. The region between x = 20 cm and x = 20.5 cm seems to be a transition region where the low pressure shock reflection travels into the uniform stress wave caused by the downward motion of the slipper. The front of the wave in the rail does not show the alternating bubbles of compression and tension that are seen in the slipper because the low pressure shock has not reflected off a free surface as it has in the slipper. As the reflected front travels back into the slipper, it interferes with the uniform loading and caused ripples at the slipper-rail interface. These ripples are then impacted by the slipper as it slides on the rail and the ripples undergo high strain rates. The coefficient of friction then becomes a function of the size and number of ripples caused by the shock reflection off the front of the slipper.

To test this hypothesis, consider that the front of the slipper bottom in contact with the rail is located at x = 20.42 cm at t = 0 μs. At t = 1 μs, the front is now located at x = 20.72 cm. At contact, stress waves will travel in both x and y directions at the speed of sound (around 5 km/sec). This means they would travel about 0.5 cm in 1 μs. At 1 μs, any shock reflections off the front of the slipper would have traveled approximately 0.5 cm into the slipper in both x and y directions. that would place the boundaries of the shock reflection at about x = 20.72 - 0.5 = 20.22 cm and y = 0.5 cm. This is approximately the case we have depicted here. To be more precise, the shear stress front propagates at a rate slower than the pressure, and the speed of propagation changes for the reflected wave, but this illustrates that the concept is a possible explanation of what is occurring in the solution. Further shock reflections only add to the situation, creating more ripples at the sliding interface. This situation would also explain why the ridges between the slipper and rail for the 1.5 km/sec case are smaller and the strain rates are less than the 3 km/sec case. The shock waves produced at 3 km/sec contain stresses that are higher than the 1.5 km/sec case. Higher strain rates are associated with stronger stress waves.

At 1 microsecond, the deviatoric response is concentrated along a layer within the rail (see Figure 6.7). The plot of velocity vectors at 1 microsecond show that the top layer of the rail travels with the slipper. As a result, a layer of material within the rail reacts

with large deviatoric stress. The pressure plot indicates there is no volumetric change in this layer.

At 3 km/sec, the slipper has also traveled 0.3 cm horizontal and 0.001 cm in the vertical direction over 1 microsecond. This vertical displacement isn't even one cell height. Whereas, in the 1.5 km/sec run, over 2 microseconds, the vertical displacement of the slipper is 0.002, which is one cell height. Here is where mesh coarseness plays a role in the boundary layer algorithm solution. The boundary layer is defined in CTH in terms of cell diagnols. Changing the dimensions of the cell, effectively changes the absolute thickness of the boundary layer. This is one reason that friction solutions using the boundary layer algorithm should be considered over as long a period of time as possible to obtain the average response of the system.

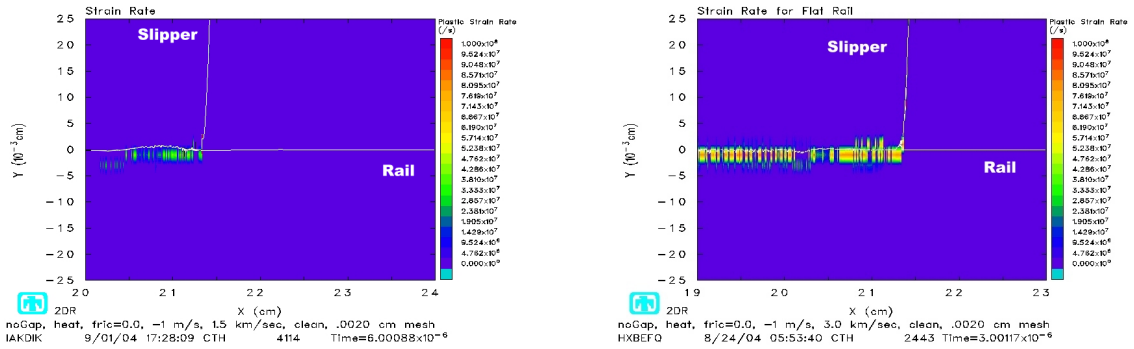

(a) **Strain rate at 6 μs for 1.5 km/sec.** (b) **Strain rate at 3 μs for 3.0 km/sec.**

Figure 6.8 **Comparison of strain rates for run at 1.5 km/sec and 3 km/sec.**

As the slipper slides over the rail, the regions of large strain rates caused by the shock reflection form even larger deformations of the rail into the slipper and the slipper into the rail. A comparison of the solution for the 1.5 km/sec case and the 3 km/sec case in Figure 6.8 shows that the strain rates for a comparable time are much higher at 3 km/sec. One reason the strain rates are larger in the 3 km/sec solution is that the stress waves in the 3 km/sec solution are stronger due to the higher velocity of impact. These higher strain rates are distributed in higher concentrations along the rail surface than for the 1.5 km/sec case. This causes greater deformations in the impinging ridges between the

slipper and rail surfaces. The larger ridges coupled with the continued tangential velocity vector of the slipper cause reactions within the slipper and rail that are both volumetric and distortional.

As the slipper continues to slide over the rail at the faster tangential velocity, the rail material continues to impinge into the slipper boundary as the normal surface traction calculated by the boundary layer algorithm becomes larger. Surface normals always point into the harder material (i.e., the slipper). As the slope of the ridges become steeper, the normals rotate to align with the tangential component of slipper velocity and the stress increases further at these points.

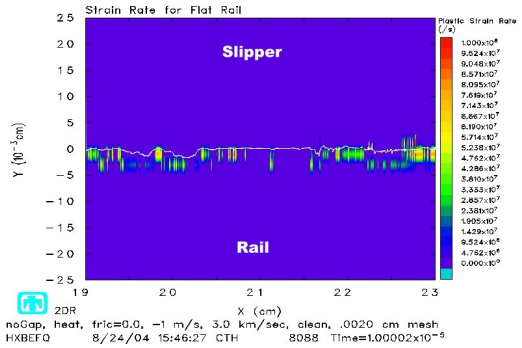

(a) **Strain rate at 10 μs for 3.0 km/sec horizontal velocity, μ_k=0, clean flat rail.**

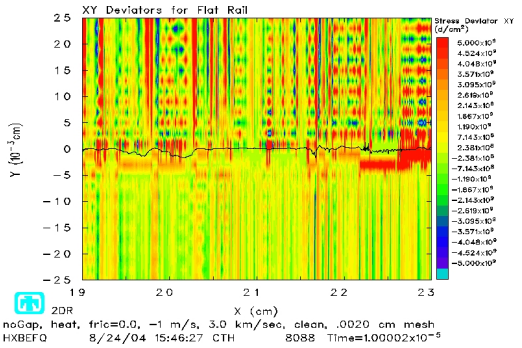

(b) **Deviatoric stress at 10 μs for 3.0 km/sec horizontal velocity, μ_k=0, clean flat rail.**

Figure 6.9 **Comparison of strain rate and stress deviator 3 km/sec.**

The response of the slipper and rail to the distribution of strain rates is shown in Figure 6.9. In general, a comparison of the strain rates to the deviatoric stress indicates that a pocket of high strain rate next to a pocket of low or no strain rate accompanies the formation of ridges along the sliding interface. The response to these ridges and the impacts due to the slipper sliding against the rail, are stress waves which proceed from these ridge-like projections. A larger view of this same region gives a better indication of what is happening.

One can see in Figure 6.10, that the distortional response of the slipper to the friction that occurs along its bottom could lead to fracture or adiabatic shear banding. The slip

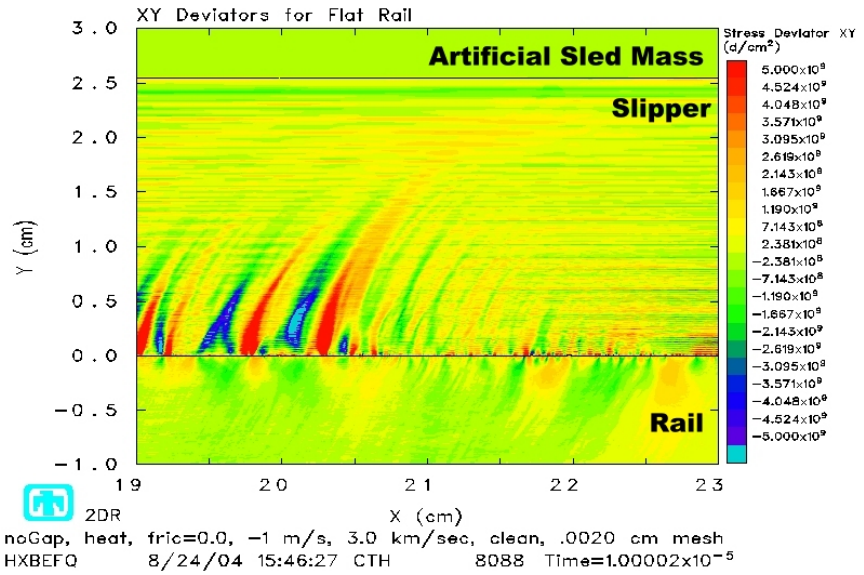

Figure 6.10 **Zoomed out view of deviatoric stresses 10 μs for 3.0 km/sec horizontal velocity, μ_k=0, clean flat rail.**

planes between positive and negative deviatoric stress are potential regions of adiabatic shear banding. The values are not large enough to develop plasticity yet. Under more extreme conditions, plasticity may develop, or temperatures may rise to values large enough to soften the slipper material. Similar conditions exist in the rail, but these are not as extreme since the rail does not experience the same interaction with the front free surface that the slipper does. Still, the general shape of the shear distribution is similar to the microcracking seen by Gerstle, et al. [11] in actual gouges.

Temperatures along the sliding interface reach similar values as the 1.5 km/sec run, but have not penetrated as deeply in 10 microseconds as it has in 20 microseconds for the 1.5 km/sec run. A tracer point located in the slipper boundary layer increases from 298 K to around 1300 K over 10 microseconds. This indicates a faster rate of heat generation for the 3 km/sec case. Comparison of the plastic strain in the slipper shows that the 3 km/s case generates a larger region of plasticity in the boundary layer at 10 microseconds than the 1.5 km/sec case does over 20 microseconds. The flow of heat away from plasticized regions may help mitigate thermal softening effects. Over 20 microseconds, heat has had

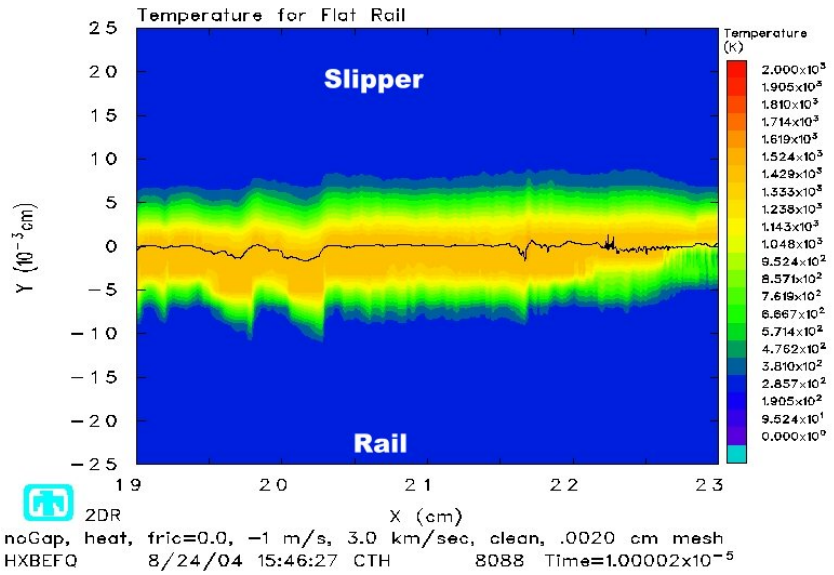

Figure 6.11 **Temperature at 10 μs for 3.0 km/sec horizontal velocity, μ_k=0, clean flat rail.**

more time to be conducted away and thus, show more of an effect on the solution than it has for the 10 microsecond case.

Again, at the temperatures indicated, steel should exist in the austenite phase. However, more of the austenite steel generated in the 3 km/sec case should be in a stable state because the region of higher temperature extends further into the slipper and the rail. This is likely due to the smaller amount of heat being conducted away from the sliding interface due to the shorter time period under consideration and the larger strain rates that create more plastic strain for the 3 km/sec case.

6.3 Rail Roughness Impact on Clean Rail

The previous section examined the frictional development of a vibratory impact on a flat rail. We next consider when this frictional impact is quickly followed by an impact with a rail roughness. The exact conditions developed in the frictional cases is not reproduced here. Instead, a short frictional run is made just prior to impact with the rail roughness. This helps approximate the conditions due to friction just prior to impact, but does not

simulate them exactly. A downward velocity of 2 m/s is chosen to simulate the expected worst case scenario for the impact. DADS data (see Appendix A) shows the maximum downward velocity for rail misalignments within a 0.001 radian tolerance to be just under 2 m/s. The forward velocity of the slipper is again varied between 1.5 km/sec to 3 km/sec. It was found that an impact with a rail roughness at 3 km/sec initiated what appears to be a gouge, while an impact at 1.5 km/sec did not for similar time periods. Times are again compared such that the solution observed at time, T for the 1.5 km/sec run is compared to the solution for the 3 km/sec run at time, T/2. The runs are also run with the addition of a void between the interface of the top of the slipper with the bottom of the artificial sled mass. There is one centimeter of sled mass located at the ends to keep the mass attached to the slipper. This will simulate shock reflections off the top of the slipper which more closely approximates the real world condition (see section 5.6). In this way, we will also be able to study the effect the top reflections have on the reflections off the front of the slipper.

The first case studied was the 1.5 km/sec case. In this case, we observe the same conditions observed in the frictional run discussed in the previous section. As the solution begins, low pressure shock waves reflect off the front surface of the slipper and propagate back into the slipper and rail. This interaction causes changes in strain rate at the sliding interface which results in the formation of ripples along the interface. These ripples become larger as the slipper slides along the rail and temperature rises with the development of plasticity in the boundary layer. The conditions change however, when the slipper impacts the rail roughness between 8 and 10 microseconds.

Even before impact, the rail roughness responds elastically to the coming slipper. The slope of the rail roughness decreases slightly a few microseconds before the slipper arrives. The low pressure compression wave that leads the slipper position in the rail expands when it reaches the rail roughness, due to the increased area the wave travels into. This is similar to what happens in the divergent nozzle of a jet engine for subsonic flow. This tensile front is weak, but it travels within the rail roughness and affects the region just prior to the slipper's arrival. This tensile wave is the reason for the rail roughness' change in slope. Two weak tensile fronts spaced about 1.5 cm apart, are noticeable in Figure 6.12. They

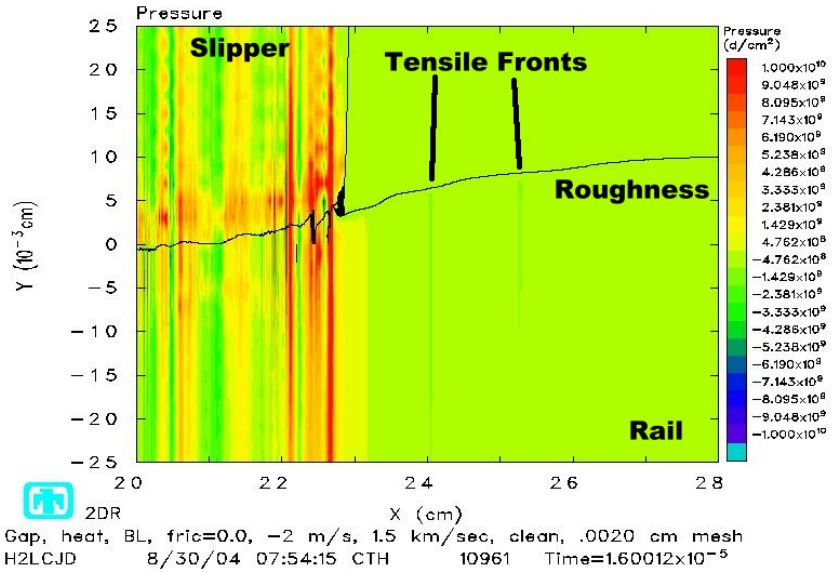

Figure 6.12 **Pressure at 16 μs for 1.5 km/sec horizontal velocity, μ_k=0, clean rough rail.**

are followed by a compressive region that builds up to a high pressure front at the leading edge of the slipper.

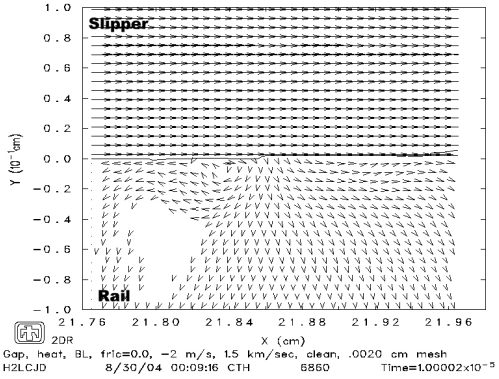

(a) **Velocity vectors at 10 μs for point of potential jetting initiation.**

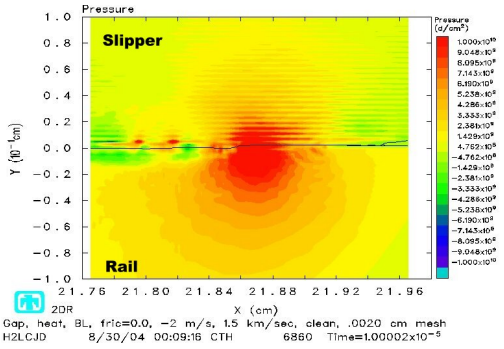

(b) **Pressure core at 10 μs for point of potential jetting initiation.**

Figure 6.13 **Comparison of velocity vector with pressure core at 10 μs where vectors indicate the potential to start jetting.**

Upon impact with the rail roughness, the slipper creates a compressive shock wave of greater than 1 GPa. The material in front of this shock front is increasingly compressed as the amount of material the slipper impacts also increases. At the end of the 20 microsecond simulation, a point with the potential to form a gouge was seen about 0.2 cm behind the leading edge of the slipper. This point, however, had not produced gouging, at least up to the 20 microsecond time interval under consideration. The potential for gouging is indicated by the velocity vectors which show a tendency to form jetting. The velocity vectors at the point flow upwards and forward ahead of the point and backwards and up behind the point. This motion is already seen for this point at 10 microseconds (located at x=21.86 cm, y=0 cm) (as shown in Figure 6.13).

This region which shows the potential for gouge initiation has a number of characteristics that allow the velocity vectors to form in the fashion they have. The pressure in this area is over 1 GPa in compression. This core of high pressure encompasses the entire region in which the velocity is indicating the potential to "jet" (see Figure 6.13(b)) The region is plastically strained, including the region within the rail in which the velocity vector begins rotating. The plastic strain is small there (on the order of 10^{-2}) but it is still plastic. Temperatures at the sliding interface are in the austenite range and work mainly to encourage deformation along the interface.

The motion of the particles in front of this region do not move in a direction that indicates jetting until after impact with the rail roughness. The additional mass of the rail roughness causes the velocity vector in front of the asperity-like ridge, to angle upward and follow the upward slope of the roughness. Prior to that, the direction of the velocity vector in front of the ridge was angled downward and into the rail. This reversal from downward to upward motion could be caused by the change in direction of the slipper. Because the hump-like projection of the rail fits in with similar deformations on the slipper like a puzzle, when the slipper changes direction it takes the rail material along with it. This changes the motion of the material in front of the hump and sets up the conditions for jetting to occur.

The other part of the velocity vector that needs to be in place is the upward motion of material behind the hump. This is also encouraged by the slipper riding over the rail

roughness. As the slipper's front is forced upward, the portion of the slipper behind the hump is likewise forced to angle upward due to the geometry of the roughness. In other words, the velocity vector tangent to the rail roughness is constantly changing. For a semi-elliptical shape, the slope is constantly decreasing from the semi-major axis end point to the semi-minor axis end point. But the initial impact with the roughness has a slope greater than the flat portion of the rail. This causes a change in the direction of the local velocity vector. If the hump is large enough, it can absorb this direction change. When the back of the hump hits the rail roughness, it too undergoes a change in direction as it meets an increased slope. In this case, however, the upward motion of the rail material caused by the rail roughness geometry did not have a magnitude large enough to initiate jetting.

The impact with the rail roughness provides a potential for the velocity vector of the hump that was formed by frictional sliding to form a jet. The mutual interaction of rail and slipper materials in jetting then leads to the permanent deformation called gouging. This explanation can be tested in the 3 km/sec case, since jetting did form and gouging appeared to initiate at 4.45 microseconds.

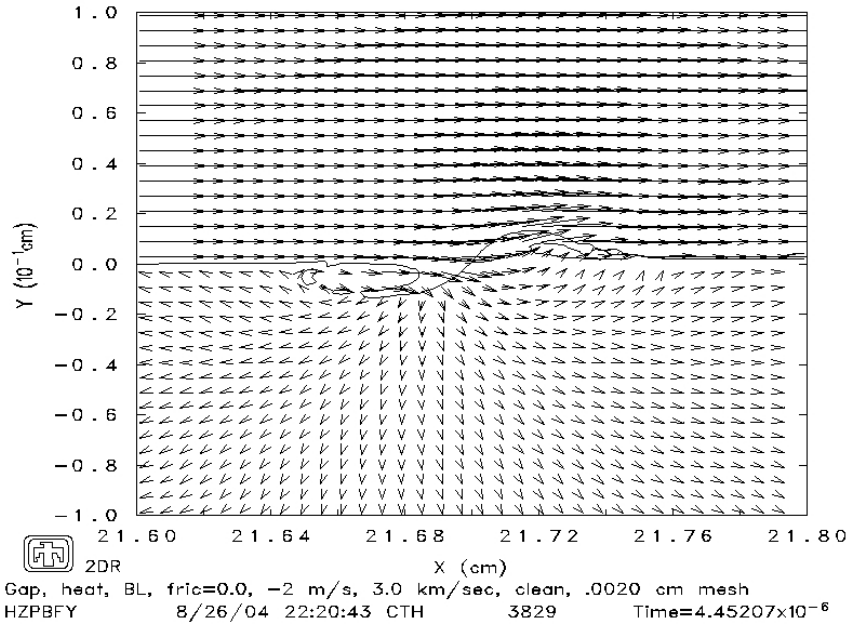

Figure 6.14 **Velocity vectors at 4.45 μs for point with jetting initiation.**

First, we check if jetting does occur at the same point that was studied for the 1.5 km/sec case, in which the velocity vector indicated the potential for jetting. The location of this point is at 21.86 cm at 10 microseconds for the 1.5 km/sec horizontal velocity. This would put the initial location of that point at 21.86 - 1.5 = 20.36 cm. The point at which jetting initiates and gouging seems to begin is located in Figure 6.14 at x = 21.7 cm at 4.45 microseconds. That would place the initial location of this point at 21.7 - 1.336 = 20.364 cm. This is very close to the estimated location of the potential point of jetting that was discussed for the 1.5 km/sec case. The 3 km/sec horizontal velocity resulted in jetting formation (with subsequent gouging) at this point, while the 1.5 km/sec velocity did not.

Scaling for time, the 3 km/sec case showed gouging sooner than the time expected from the velocity vectors. 10 microseconds in the 1.5 km/sec case scales to 5 microseconds in the 3 km/sec case. But jetting is clearly evident at 4.45 microseconds in the 3 km/sec case, which scales to 8.9 microseconds in the 1.5 km/sec case. This time scaling is in terms of frictional development and length of rail covered by the horizontal velocity of the slipper.

Just prior to impacting the rail roughness, the two cases are under very different conditions as shown in Figure 6.15. The velocity vectors indicate motion underneath the entire region of the slipper within the rail for the 3 km/sec case. At 1.5 km/sec, the velocity vectors show movement only under the relatively large hump-like deformation near the front of the slipper. The pressure plots shows large discrete variations of pressure for the 3 km/sec case, while the 1.5 km/sec case contains more gradual changes in pressure and over a wider distance for the same region of the slipper.

Early in the calculations (as seen in Figure 6.16), the solution for the 3 km/sec and the 1.5 km/sec rail roughness cases diverge. This appears to occur when the larger and more gradual hump of rail material impinges into the slipper material at 2 microseconds for the 1.5 km/sec case. In the 3 km/sec case, the ridges that are formed by the stress wave reflection off the slipper front are smaller, yet steeper and more numerous. This appears to be due to the thinner regions of alternating stress in the 3 km/sec case. At 1.5 km/sec, these regions are more spread out and the reactions at the slipper-rail interface are also wider and more gradual. It is formation of this larger, yet less defined hump that makes

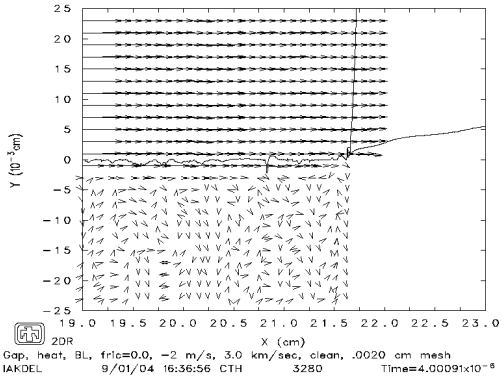

(a) **Velocity vectors at 4 μs for 3 km/sec clean rail roughness case.**

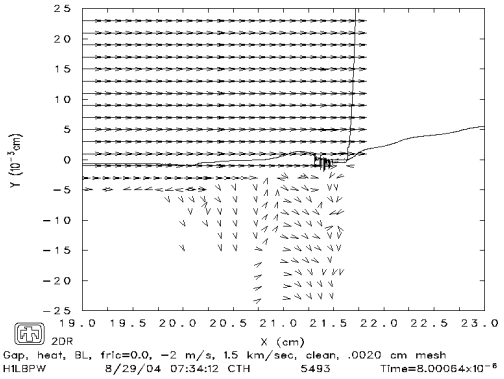

(b) **Velocity vectors at 8 μs for 1.5 km/sec clean rail roughness case.**

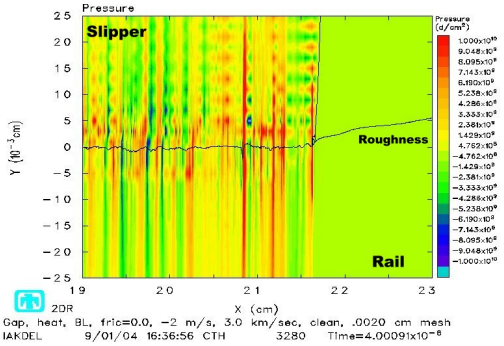

(c) **Pressure at 4 μs for 3 km/sec clean rail roughness case.**

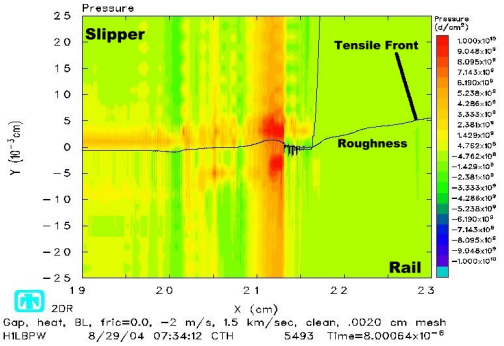

(d) **Pressure at 8 μs for 1.5 km/sec clean rail roughness case.**

Figure 6.15 **Comparison of velocity vectors and pressure for 3.0 and 1.5 km/sec clean rail roughness cases.**

all the difference later in the solution when the slipper impacts the rail roughness. A steep gradient between the slipper and rail materials at this hump (or other humps) does not form in the 1.5 km/sec case as it does for the 3 km/sec case. Therefore, when impact with the rail roughness occurs, the conditions require greater energy input to redirect the velocity vector, and initiate jetting.

Figure 6.17 shows the temperature contours within the boundary layer near the leading edge of the slipper. The temperatures within the boundary layer in the slipper and rail reach temperatures of nearly 1500 K. The temperatures range in the slipper near

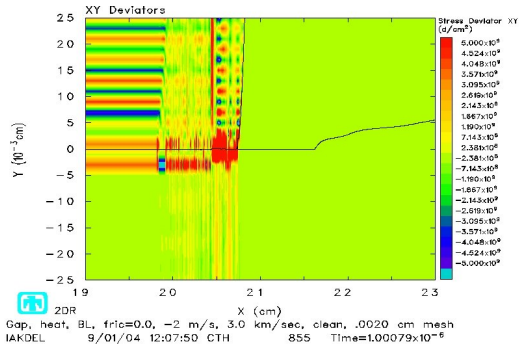

(a) **Stress deviator at 1 μs for 3 km/sec clean rail roughness case.**

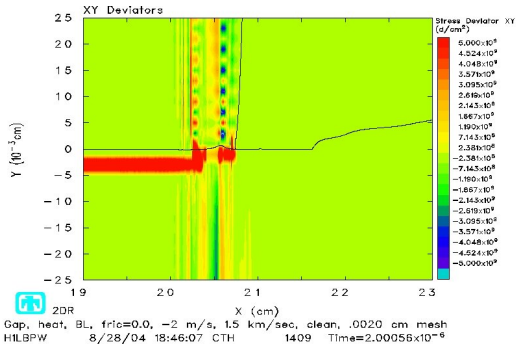

(b) **Stress deviator at 2 μs for 1.5 km/sec clean rail roughness case.**

Figure 6.16 **Comparison of stress deviators for 3.0 and 1.5 km/sec clean rail roughness cases.**

the boundary layer from 500 to 1000 K. The steel is austenitized to both a stable and unstable configuration. Upon jetting, the temperature rises rapidly from 750 K to 1200 K in that region. The increase in temperature lags behind the formation of plasticity in the boundary layer. The response to the rail roughness is dictated by the stresses rather than thermal changes in the material. The rate of heat conduction is much smaller than the rate of plastic formation due to the sliding interaction of the slipper over the rail roughness. Strain hardening effects on the yield strength are at a rate greater than thermal softening effects of temperature changes within the boundary layer.

The potential for fracture within the rail and slipper is also observed, but the values of shear stresses must be greater if this is to occur. By the end of the simulations, over 20 microseconds for the 1.5 km/sec run and up to jetting (4.5 microseconds) for the 3 km/sec case, the stresses were not high enough to develop plasticity along shear bands. The solution aborted shortly after jetting occurred in the 3 km/sec case, so gouging could not be observed to create cracking or shear band formation in this specific case.

This ends the clean rail roughness discussion. With a better understanding of how gouging initiates and what causes ridge-like deformations between the sliding rail and slipper surfaces, the coated runs can provide insight into how to mitigate gouging. The

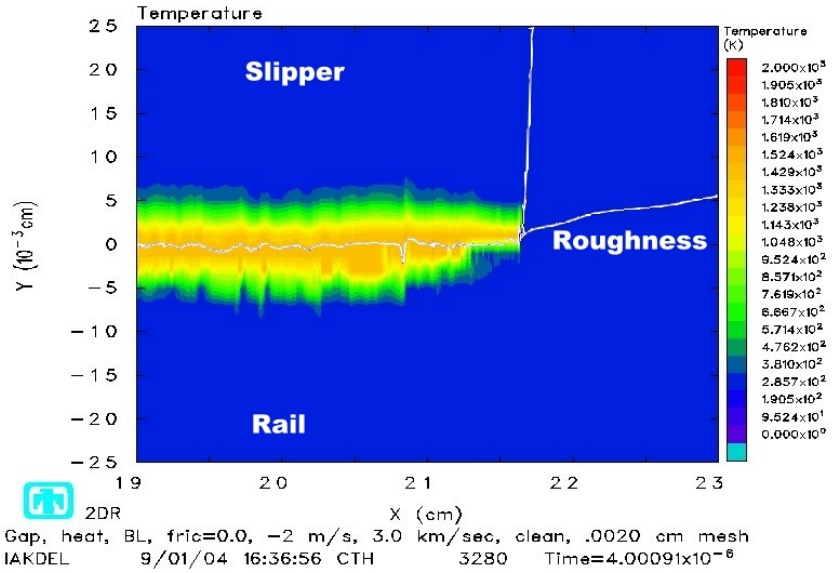

Figure 6.17 **Temperature at 4 μs just prior to jetting.**

next cases to be discussed are the coated cases of a vibratory frictional impact on a flat rail and with a rail roughness.

6.4 Vibratory Impact and Frictional Heat Development on Coated Rail

The vibratory impact cases are run again with a 6 mil coating with properties of epoxy. The only model available to characterize the stress-strain response of epoxy is a Von Mises type elastic-plastic model. So the epoxy will not respond in a strain dependent manner. The only equation of state available that worked in the cases to be run is the Mie-Grüneisen EOS. This EOS does not account for phase changes of the epoxy. Therefore, the researcher will analyze temperature and pressure data to determine the potential for phase changes in the coating material during impact and sliding.

The first case to be discussed is the 1.5 km/sec horizontal velocity case with a 1 m/s downward velocity. 6 mils (0.01524 cm) of the top of the rail material is replaced with epoxy. The epoxy and rail are assumed to be perfectly bonded. Figure 6.18 shows a comparison of the pressure history for a tracer point within the coating for the frictional run to the same location near the rail surface when the coating is not present. The

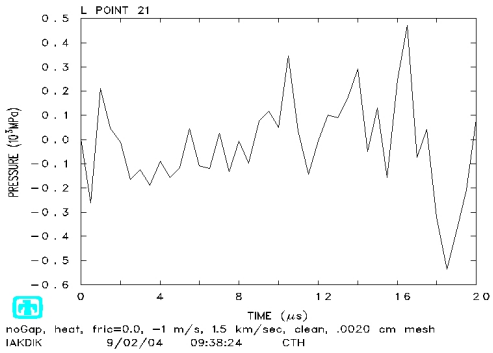

(a) **Pressure history in rail surface for 1.5 km/sec clean flat rail case.**

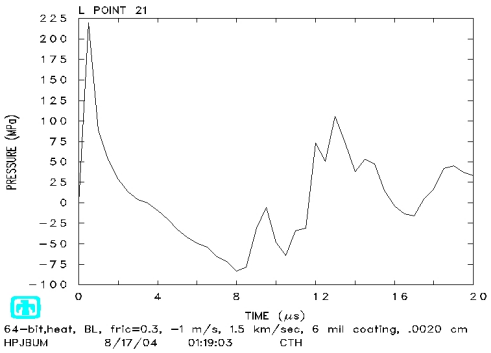

(b) **Pressure history in coating for 1.5 km/sec coated flat rail case.**

Figure 6.18 **Comparison of pressure histories for 1.5 km/sec vibratory frictional runs.**

pressure history shows that the average pressure within the coating over time, is less than the average pressure over time for the clean rail. The speed of sound within the coating is approximately half that of the rail (2 km/sec compared to 5 km/sec). An elastic wave will travel away from the slipper at a slower velocity than an elastic wave in the rail material. Since the roughness at the sliding interface is a function of the reflections off the front surface of the slipper and the strength of the fixed material (rail or coating), mitigating the strength of the reflections for sliding over a softer material will reduce the stress response in the material.

The coating appears to work because of its smaller density as compared to the slipper. This has two effects on the response of the slipper to a vibratory impact. In Figure 6.19, one can see that the coated rail mitigates shock reflections off the front surface of the slipper by decreasing the magnitude of the initial pressure wave. Additionally, the difference in densities between the coating and slipper result in a tensile wave that propagates into the slipper rather than a compressive wave as seen in the clean rail case (see Figure 6.20). This keeps the face of the slipper surface smooth as it slides against the coated surface. In the clean rail case, the slipper surface and rail surface become rough and this leads to greater interactions as the slipper slides against the rough surface. Schmitz [1] compared different coatings for an asperity initiation of gouging and found that a higher density coating

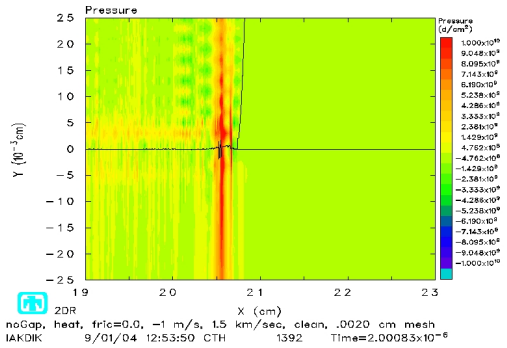

(a) **Pressure plots for 1.5 km/sec clean flat rail case.**

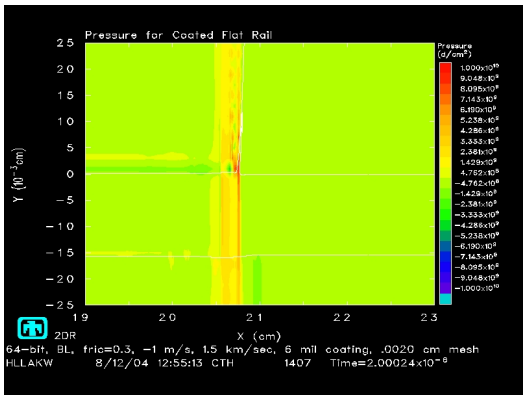

(b) **Pressure plot for 1.5 km/sec coated flat rail case.**

Figure 6.19 **Comparison of pressure plots for 1.5 km/sec vibratory frictional runs.**

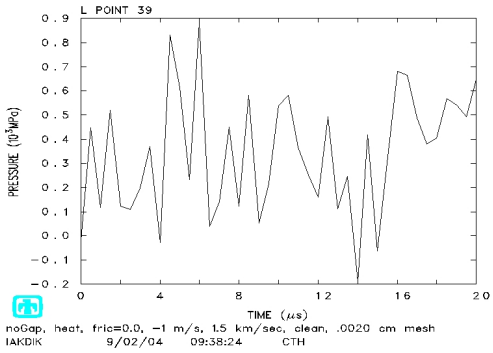

(a) **Pressure history in slipper boundary layer for 1.5 km/sec clean flat rail case.**

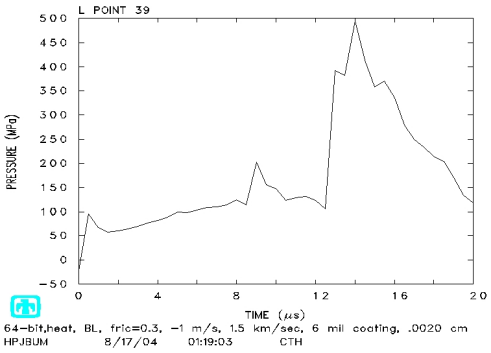

(b) **Pressure history in slipper boundary layer for 1.5 km/sec coated flat rail case.**

Figure 6.20 **Comparison of pressure histories in slipper boundary for 1.5 km/sec vibratory frictional runs.**

(molybdenum has a higher density than steel) actually encourages gouging as compared to smaller density coatings such as epoxy (see Figure 1.11). This agrees with the results shown here. A higher density coating would result in a stronger compressive wave along the bottom of the slipper upon impacts with the higher density coating. The shock reflections off the front of the slipper would also increase in strength. This would produce greater

roughness on the surface of the slipper and theoretically result in conditions that are conducive to gouging.

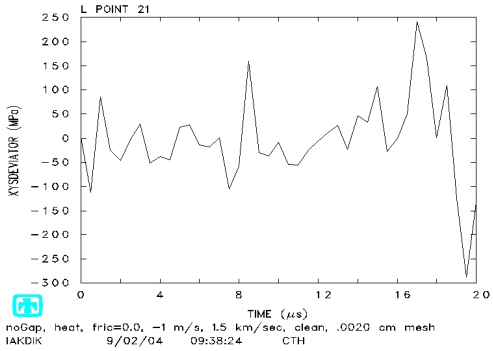

(a) **Stress deviator history in rail surface for 1.5 km/sec clean flat rail case.**

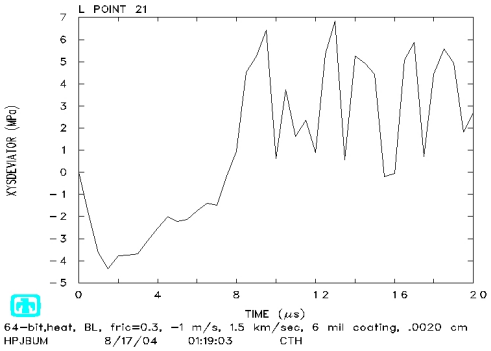

(b) **Stress deviator history in coating for 1.5 km/sec coated flat rail case.**

Figure 6.21 **Comparison of stress deviator histories for 1.5 km/sec vibratory frictional runs.**

The coating also mitigates development of deviatoric stress as seen in Figure 6.21. By mitigating the ridges that would normally form upon impact, the distortional response within the slipper is less dramatic. Additionally, the coating deforms rather than resists the sliding slipper material, so the deviatoric response in the coating is much less than for the clean rail (see Figure 6.21).

Another effect of the epoxy coating is on temperature. Polymers like epoxy absorb a greater amount of heat before increasing in temperature as compared to steel. They have increased thermal resistance as compared to steel, but this results in a decreased resistance to impact [82]. Figures 6.22 and 6.23 show the effect a 6 mil coating has on the solution in terms of the thermal environment. The lower temperatures associated with the coated rail mean the slipper and rail are less likely to transform into austenite steel. True to form, the epoxy absorbs energy without increasing in temperature as much as the steel would. The epoxy does reach the glass transition temperature of 400 K, but a rubbery state would actually help to absorb any stresses that form in the development of the solution, although it might raise the frictional effects. In addition, this keeps the slipper from rising in temperature. The coating appears to cut the temperature over 20

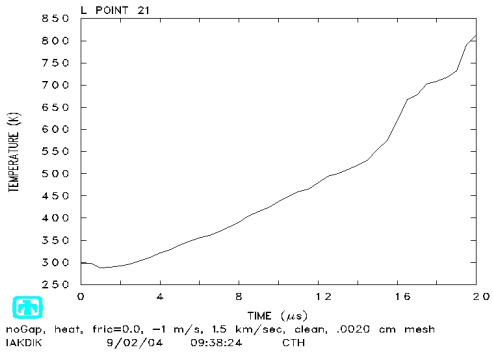

(a) **Temperature history in rail surface for 1.5 km/sec clean flat rail case.**

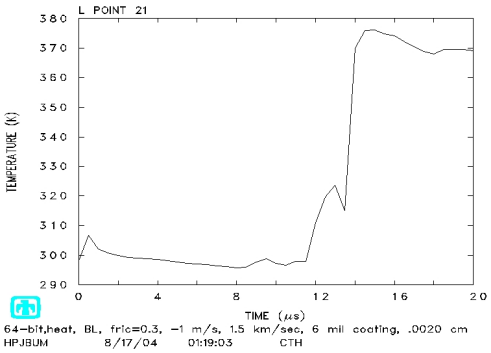

(b) **Temperature history in coating for 1.5 km/sec coated flat rail case.**

Figure 6.22 **Comparison of temperature histories for 1.5 km/sec vibratory frictional runs.**

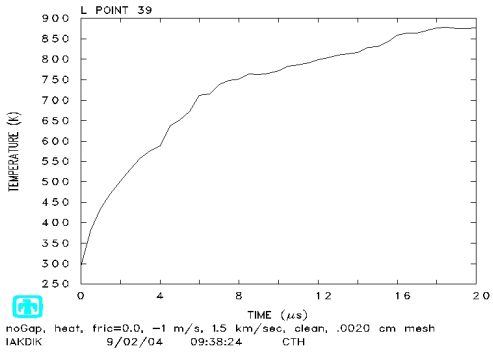

(a) **Temperature history in slipper boundary layer for 1.5 km/sec clean flat rail case.**

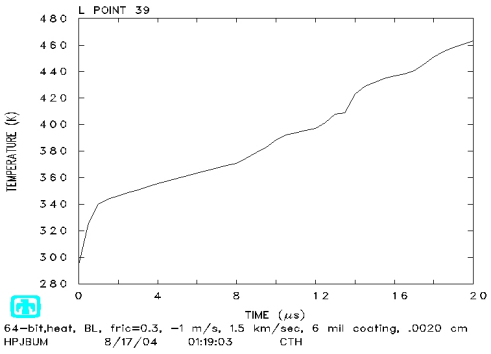

(b) **Temperature history in slipper boundary layer for 1.5 km/sec coated flat rail case.**

Figure 6.23 **Comparison of temperature histories in slipper boundary for 1.5 km/sec vibratory frictional runs.**

microseconds in half. The final temperature of 460 K should not result in the slipper steel entering the austenite phase.

For the 3 km/sec vibratory frictional run the results are similar. Figure 6.24 indicates the tensile pressure at the bottom surface of the slipper due to impact with the less dense epoxy coating. The overall effects are the same as in the 1.5 km/sec case. Smaller strength shocks upon impact mean smaller reflections off the front slipper surface and less roughness

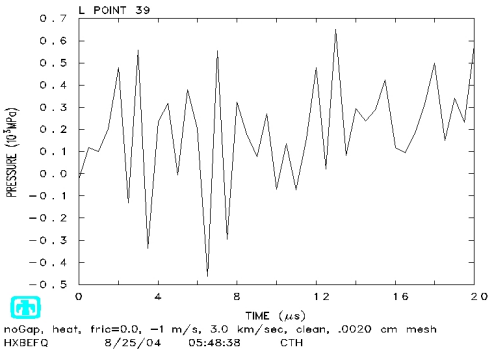

(a) **Pressure history in slipper boundary layer for 3 km/sec clean flat rail case.**

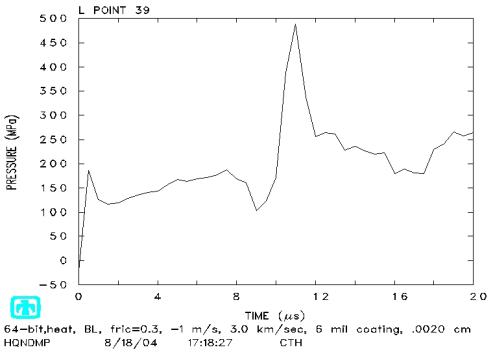

(b) **Pressure history in slipper boundary layer for 3 km/sec coated flat rail case.**

Figure 6.24 **Comparison of pressure histories in slipper boundary for 3 km/sec vibratory frictional runs.**

at the interface between slipper and coating. This means weaker responses in stress and temperature in the slipper and rail.

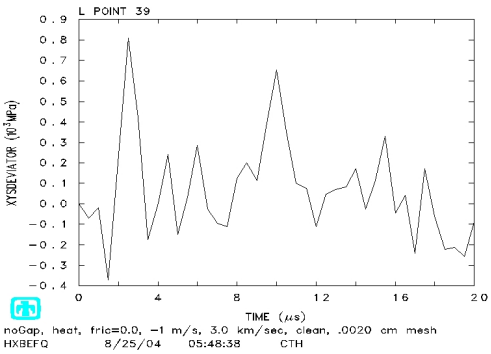

(a) **Stress deviator history in slipper boundary layer for 3 km/sec clean flat rail case.**

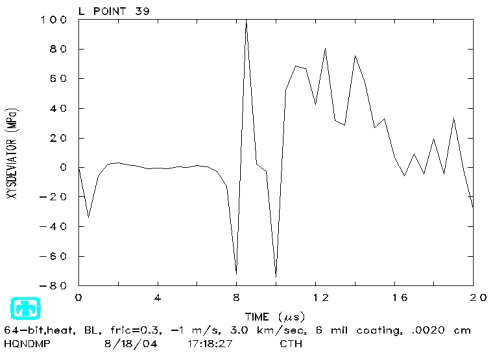

(b) **Stress deviator history in slipper boundary layer for 3 km/sec coated flat rail case.**

Figure 6.25 **Comparison of stress deviator histories in slipper boundary for 3 km/sec vibratory frictional runs.**

Figure 6.25 shows the stress deviators in the slipper are also mitigated at 3 km/sec with the 6 mil coating of epoxy. The mechanisms of mitigation are the same as in the 1.5 km/sec case.

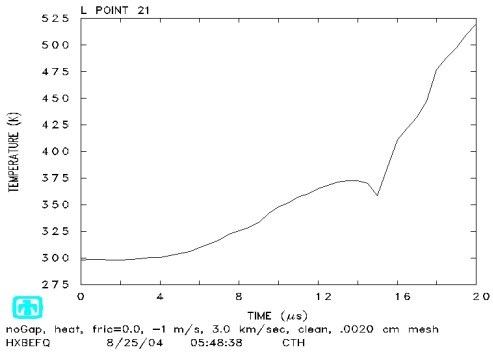

(a) **Temperature history in rail surface for 3 km/sec clean flat rail case.**

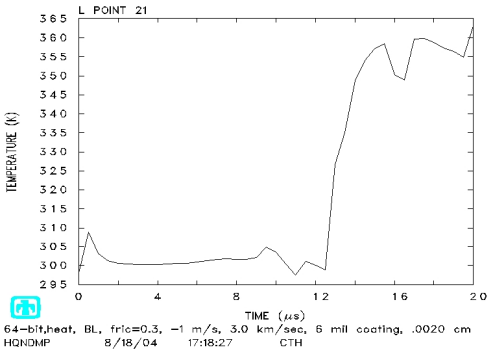

(b) **Temperature history in coating for 3 km/sec coated flat rail case.**

Figure 6.26 **Comparison of temperature histories for 3 km/sec vibratory frictional runs.**

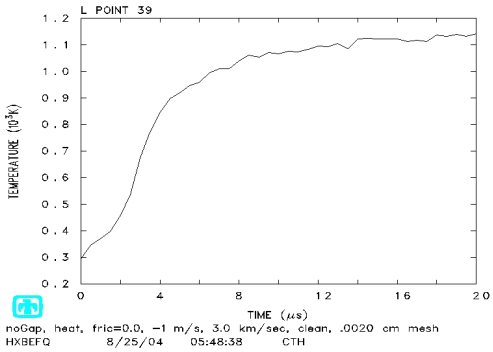

(a) **Temperature history in slipper boundary layer for 3 km/sec clean flat rail case.**

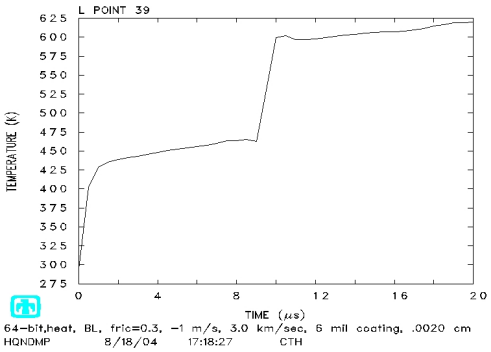

(b) **Temperature history in slipper boundary layer for 3 km/sec coated flat rail case.**

Figure 6.27 **Comparison of temperature histories in slipper boundary for 3 km/sec vibratory frictional runs.**

Observations of the temperature response are also similar. In Figures 6.26 and 6.27 we see little difference in the coating temperature from the 1.5 km/sec case, despite the higher energy of impact. The epoxy is able to absorb the energy without rising in temperature as compared to rail steel. The higher velocity does have an effect on the slipper's thermal response. The temperature within the slipper boundary remains around 625 K, which is in the range of austenite formation and the flash point of epoxy. If the slipper were in contact

long enough to raise the epoxy temperature, it could potentially raise the temperature above the flash point. In fact, the coating is raised to a temperature that is close to its glassy transition state. This state would be a rubbery type state that might increase friction and raise the heating effects further. Despite this fact, the coating has reduced the temperature at the slipper bottom by about half the magnitude it would have without a coating.

The overall effect of the epoxy coating is to:

1. Reduce the impact stresses which...
2. reduces the shock reflections off the slipper front which...
3. reduces formation of ridges caused by disparate strain rates along the sliding surfaces which...
4. reduces the effect of friction and the overall state of stress and strain in the slipper and the rail.
5. The lower density coating also yields rather deforms the slipper and results in a tensile pressure wave in the slipper upon impact which further reduces roughness.

Based on this understanding of how coatings reduce frictional effects, the next cases to be studied are impacts with a coated rail roughness.

6.5 Rail Roughness Impact on Coated Rail

A basic understanding of the formation of gouging and the effects of coatings in a nonequilibrium thermodynamic environment will be applied to the final cases of a slipper impact on a coated rail roughness. The clean rail roughness case for a 1.5 km/sec horizontal velocity and 2 m/s vertical velocity, showed the potential formation of jetting (which leads to gouging) at around 10 microseconds. Despite the velocity vectors indicating this possibility, jetting never occurred when the slipper impacted the rail roughness.

At 3 km/sec, jetting did form in the same spot it was indicated it might form for the 1.5 km/sec case. The jetting formed when the slipper impacted the rail and the geometry of the roughness caused the velocity vectors in front and behind the point of origin to rotate upwards. This rotation initiated jetting since the plasticized rail and slipper materials impinged further into one another and the forward velocity of the slipper caused mutual interaction of the two materials. This interaction formed vortices of plasticized slipper and rail material which result in gouging as the slipper slides over the rail roughness. A study of these same cases with coating acting as a buffer between the slipper and rail will show how coatings react to mitigate the conditions that lead to gouging.

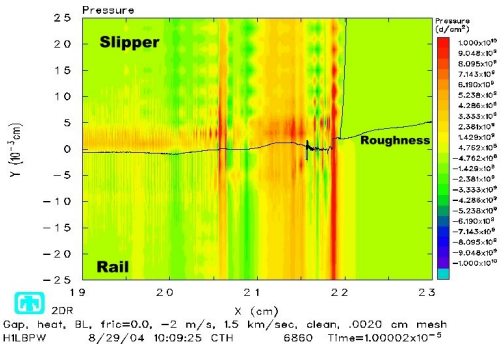

(a) **Pressure at 10 μs for 1.5 km/sec clean rail roughness case.**

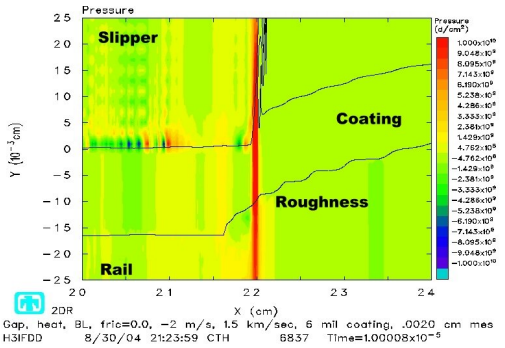

(b) **Pressure at 10 μs for 1.5 km/sec coated rail roughness case.**

Figure 6.28 **Comparison of pressures at 10 μs for 1.5 km/sec rail roughness impact.**

The pressure plots shown in Figure 6.28 depict the time for which jetting might have initiated under the right conditions. However, jetting did not initiate. The coating acts as

described for the frictional runs in the previous section. It absorbs the energy of impact without resisting. Reflections off the front slipper surface are mitigated as compared to the clean rail. Upon impact with the rail roughness, the coating acts to further cushion the impact and keep the stresses from reaching a state that would encourage jetting and subsequent gouging. In fact, the slipper rides the coating as it slides over the rail roughness and is prevented from interaction with the rail. This is dependent on the thickness of the coating and the velocity of the slipper. For the 1.5 km/sec case, the rail responds to the slipper through stress waves in the coating. The coating acts as a thermal resistant boundary and forces the rail material away from the slipper. The coating is compressed in front of the slipper, but expands behind this compressions wave. this expansion helps to reduce formation of rough edges along the sliding interface by further absorbing any compressive waves from the slipper that might interact with the coating. The tensile pressure within the coating also reduces its density and temperature effects through the equation of state, which further mitigates the formation of any compressive waves in the slipper. Note the magnitude of pressure within the slipper that sits over the portion of the coating in a state of tensile pressure. Compare this to the pressure state of the same portion of the slipper for the clean rail case.

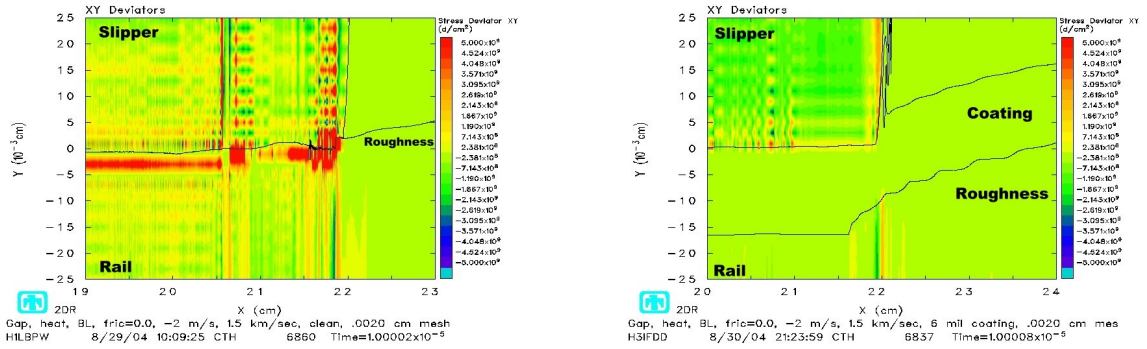

(a) **Stress deviator at 10 μs for 1.5 km/sec clean rail roughness case.**

(b) **Stress deviator at 10 μs for 1.5 km/sec coated rail roughness case.**

Figure 6.29 **Comparison of stress deviator at 10 μs for 1.5 km/sec rail roughness impact.**

Reduction in stress is not limited to the volumetric response. The coating also mitigates deviatoric stresses in the system (see Figure 6.29). Distortion of the slipper and rail are much smaller for the coated rail roughness, even upon impact with the rail roughness. Not only does the coating reduce the conditions leading up to impact with the rail roughness, but it also mitigates the state of stress in the materials and upon impact with the rail roughness. The coating also acts as a buffer between the rail and the slipper. It absorbs any deformations the rail would have undergone and prevents the conditions that would lead to gouging, such as ridge-like deformations between the slipper and rail and formation of plasticity in the slipper and rail.

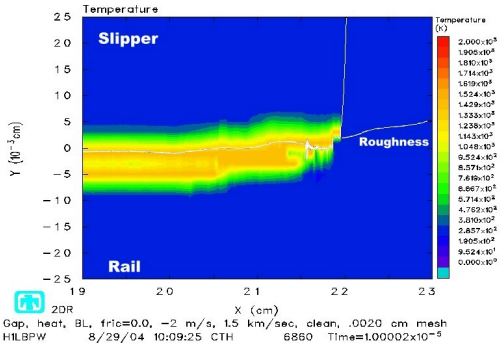

(a) **Temperature at 10 μs for 1.5 km/sec clean rail roughness case.**

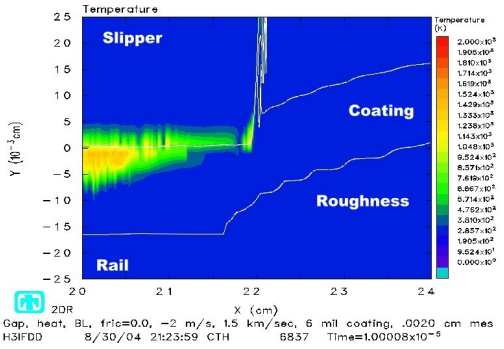

(b) **Temperature at 10 μs for 1.5 km/sec coated rail roughness case.**

Figure 6.30 **Comparison of temperature at 10 μs for 1.5 km/sec rail roughness impact.**

In Figure 6.30 we see temperatures plots for the clean and coated cases at 1.5 km/sec horizontal and 2 m/s vertical impact velocity. The epoxy retains its thermal resistant properties even at impact upon the rail roughness. Part of the difference between the clean and coated rail roughness cases is in the reduced formation of plasticity in the materials. But part of it is also due to the lower rate of heat conduction that the epoxy has as compared to steel.

The 3 km/sec case has the slipper impacting the coated rail and then the coated rail roughness at 3 km/sec horizontal and 2 m/s vertical velocity vector. The coating reacts in the same manner it did for the 1.5 km/sec case. The 3 km/sec clean rail roughness impact

resulted in jetting at 4.45 μs. The coated equivalent did not. One consideration is to study what prevented the formation of jetting in the coated case. One obvious possibility is that the coating acts as a buffer to simply prevent the slipper an rail materials from meeting. The following discussion will provide some insight into how this mitigation takes place.

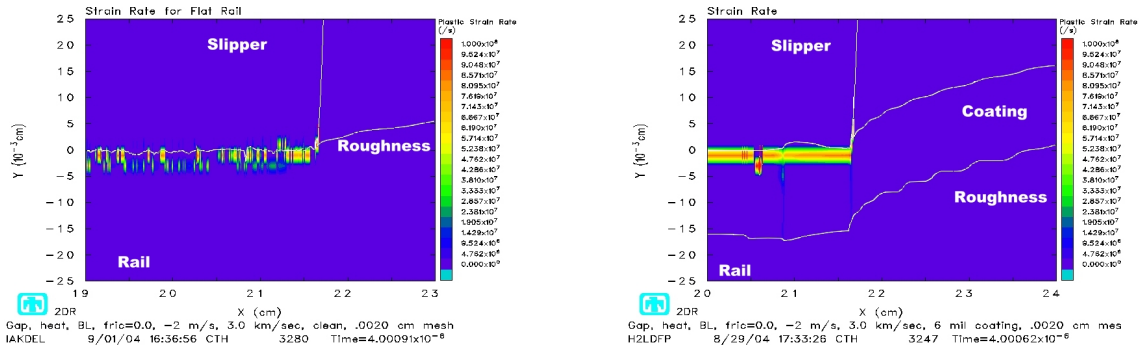

(a) **Strain rate at 4 μs for 3 km/sec clean rail roughness case.**

(b) **Strain rate at 4 μs for 3 km/sec coated rail roughness case.**

Figure 6.31 **Comparison of strain rates at 4 μs for 3 km/sec rail roughness impact.**

We have already seen how the coating acts to mitigate the magnitude of stress waves and their reflection (as well as their effects upon the sliding interface) at impact. By observing the strain rate immediately prior to jetting and the equivalent solution for a coated rail roughness, we can see how strain rate is affected (see Figure 6.31). Note that in the clean rail roughness case, there are varying regions of strain rate within the rail as it reacts to the slipper. The rougher interface dictates these reactions as the slipper slides along. In the coating, by contrast, the strain rate is nearly uniform and the interface is smooth. There is a low sloping deformation in the coated case between the slipper and the coating, but the hump is not steep enough to form jetting. Also, parts of the coating ahead of the slipper fly off in front as the slipper shears it off. The slipper responds gradually to the deformations in the coating, unlike the discrete and steeper deformations in the clean rail that force the slipper to react with widely varying strain rates rather than the uniform response seen in the coated case.

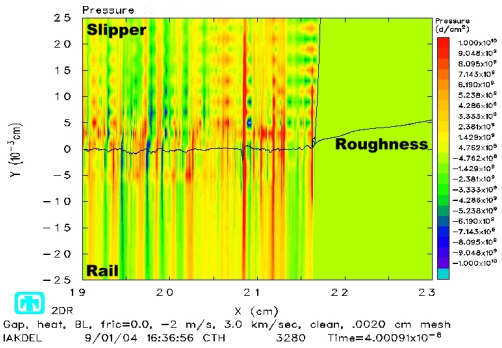

(a) **Pressure at 4 μs for 3 km/sec clean rail roughness case.**

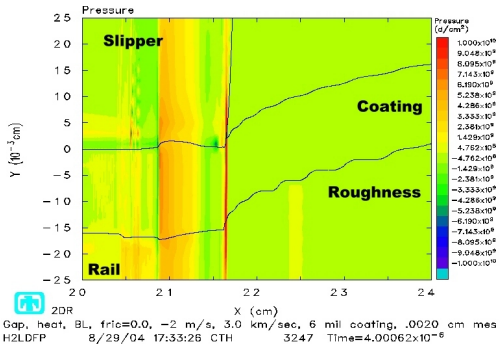

(b) **Pressure at 4 μs for 3 km/sec coated rail roughness case.**

Figure 6.32 **Comparison of pressures at 4 μs for 3 km/sec rail roughness impact.**

The pressure plot (in Figure 6.32) is one response to these different strain conditions. The pressure fronts in the coated case are more gradual than the clean rail roughness case. With a more gradual response, the conditions in the system are not as extreme in the coated case when compared to the clean case. The pressure front caused by the slipper interacting with the coating does lead to a sharp compressive front in the rail that is otherwise not as large. The transition from low density to higher density medium results in a strengthening of the shock at impact with the roughness from 2.75 GPa in the coating to about 4 GPa in the rail. This may be a disadvantage of the coating. It helps mitigate the effects of large compressive stress waves that travel from the slipper to the coating, but waves that travel from the coating to the rail increase in pressure. The high pressure wave that exists in the coated rail is much higher than the wave that is formed in the clean rail (4.5 GPa compared to 1.1 GPa). When this stronger wave travels into the increased area of the rail roughness portion, the pressure drops, but it still remains higher than for the clean rail case. It remains compressive while the wave in the clean case becomes tensile. This results in a compressive front that travels into the rail roughness, causing a different state set of conditions (higher pressure, temperature, and density) than what exists in the clean rail roughness.

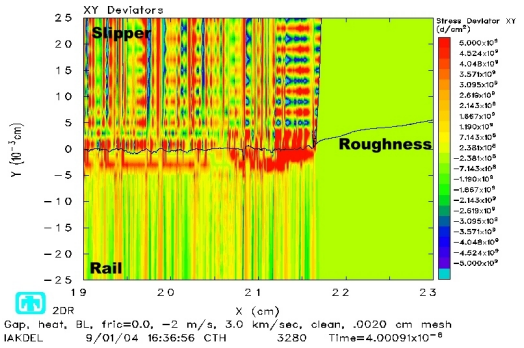

(a) **Stress deviator at 4 μs for 3 km/sec clean rail roughness case.**

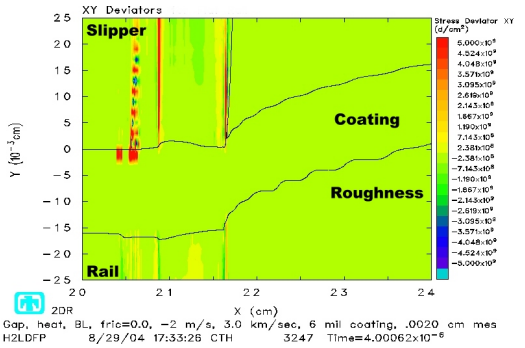

(b) **Stress deviator at 4 μs for 3 km/sec coated rail roughness case.**

Figure 6.33 **Comparison of stress deviator at 4 μs for 3 km/sec rail roughness impact.**

The stress deviator plots (in Figure 6.33) show an extreme change in the deviatoric stress when a coating is applied to the rail. The deviatoric stresses are nearly all mitigated. This further reduces the conditions leading to jetting since mutual plasticity of the slipper and rail materials is required for jetting to occur. The largest deviatoric stress occurs in a small region of the slipper and appears top be the results of reflections off the slipper front.

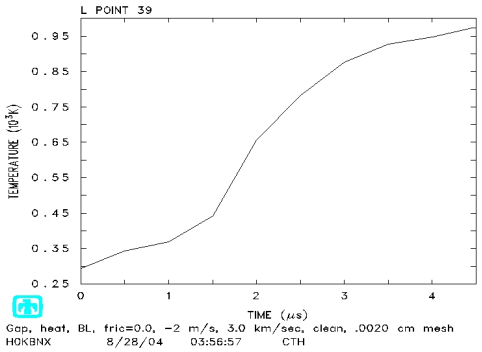

(a) **Temperature history in slipper boundary layer for 3 km/sec clean rail roughness case.**

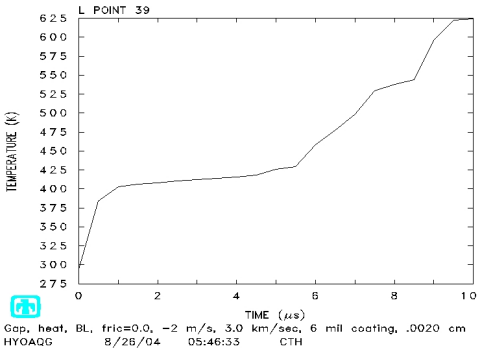

(b) **Temperature history in slipper boundary layer for 3 km/sec coated rail roughness case.**

Figure 6.34 **Comparison of temperature histories in slipper boundary for 3 km/sec rail roughness impact.**

Temperature plots (see Figure 6.34) indicate similar results to the 1.5 km/sec case. The temperature changes in the coating are mainly due to pressure changes within the coating and the formation of plasticity. The temperature at the slipper bottom of the clean rail roughness case reaches a temperature of around 950 K just prior to gouging (at 4 μs). Conversely, the same point for the coated case only reaches a temperature of 625 over 10 μs. This temperature is above the flash point of the epoxy, but would only affect the solution if the epoxy could conduct enough heat energy to raise it's temperature another 150 K. The coating does reach a maximum temperature near 400 K, which could cause a change of phase to a rubbery state. This phase would be beneficial for reducing the effects of stress, but could raise the effects of frictional heating by "sticking" to the slipper. This illustrates how the coating works to reduce the temperature effects on the slipper bottom primarily by reducing plastic strain and pressure from impact. If heat conduction was driver in the development of heat in the slipper for the rail roughness impact case, the coating would work against the reduction of temperature by insulating the rail and preventing flow from the hot slipper through the coating to the rail.

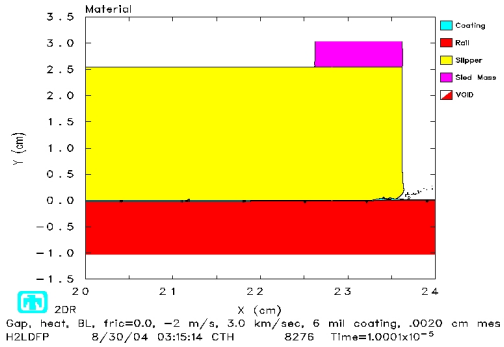

(a) **Sled system on coated rail sliding over rail roughness at 3 km/sec at t = 10 μs.**

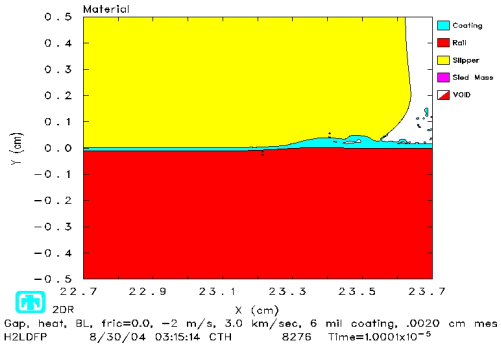

(b) **Materials at 10 μs for 3 km/sec coated rail roughness case.**

Figure 6.35 **Big picture and zoom of materials at 10 μs for 3 km/sec rail roughness impact.**

The bigger picture of what is occurring during slipper impact and sliding over a coated rail roughness is shown in Figure 6.35. This figure shows how the coating at 3 km/sec is ejected in front of the slipper. It also shows how the slipper front reacts to the

coating. Since more coating material is gathered under the slipper than is ejected in front, a bulged pocket of stored coating material forces the slipper to deform around it. This hump of coating material further acts as a buffer between the rail and the slipper. It helps to allow the slipper to slide over the rail roughness rather than shear the coating away and interact with the steel substrate. A closer look at the "pocket" of coating is shown in Figure 6.35.

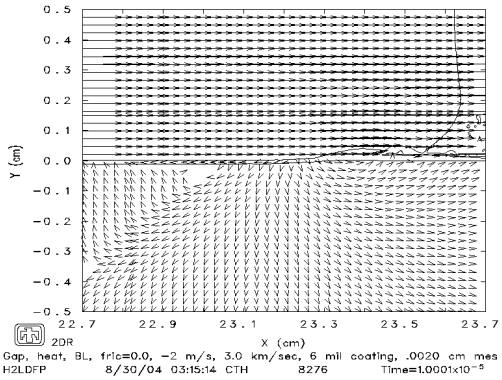

(a) **Velocity vectors at 10 μs for 3 km/sec coated rail roughness case.**

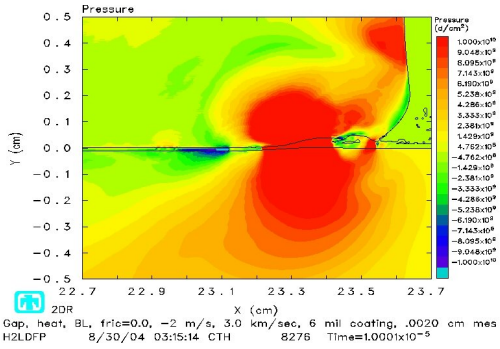

(b) **Pressure contours at 10 μs for 3 km/sec coated rail roughness case.**

Figure 6.36 **Comparison of materials and velocity vectors at 10 μs for 3 km/sec rail roughness impact. Velocity vectors show probable gouging if not for coating effects.**

We observe the velocity plot to obtain a better understanding of what occurs to prevent gouging. The velocity vectors in the rail are very similar to the vector field seen in the clean rail roughness impact cases where the conditions for jetting occur. There are two important differences. In the front portion of the rotation, the direction of the rail material is upwards and toward the front of the slipper. Contact with the slipper is prevented by the pocket of coating material that exists under the slipper at that point. As the slipper slides and the rail material continues to move in that direction, more coating material is gathered up to further prevent contact between the slipper and rail. This results in high stresses in the rail in this area.

The other difference is the direction of the rail material velocities toward the back of the slipper. Rather than a gradual rotation upwards, there is an almost perpendicular

change in direction. It appears that the jetting motion of the rail is occurring, but that it occurs inside the rail rather than at the surface of the rail. The coating acts as a buffer preventing mutual interaction of the slipper and rail. The coating is compressed between the slipper and rail and prevents the rail from touching the slipper. The rotational components in this region are not strong enough to break through the coating. The velocity vectors indicate the coating material is also moving in a direction opposite to the that of the slipper. This direction change is small compared to the slipper, but enough to deflect the rail material that attempts to rise into the slipper.

This motion of the coating to the rear appears to be a response to the coating material that is being gathered up in the front portion of the slipper. As pressure builds up in the coating "pocket," coating material is ejected from the front and forced backwards to lower pressure areas. The concept is similar to an air compressor in which a reservoir of compressed air rushes out of a hose to regions of lower pressure. In this case, we have compressed epoxy, which migrates toward regions of low pressure in the -x direction between walls of the slipper and rail material. The velocity of the coating is enough to deflect the rail material and prevent jetting.

This case shows how gouging could initiate through the formation of jetting. It also shows how this can be mitigated by the effects of a coating applied to the surface of the rail. The coating mitigates gouging by reducing the effects of the high speed impact on the system and by acting as a buffer between the rail and slipper materials. This prevents the rail and slipper materials from jetting. The reason the coating itself does not form this jetting with the slipper is probably two fold. First, the coating material is much softer and deforms rather easily. It deforms rather than cause sharp rigid deformations in the harder materials such as steel. Sharp, rigid projections between the slipper and rail can lead to the conditions that lead to jetting. The other reason the coating does not form jetting is that the thickness is too small to allow the rotational velocity vectors that initiate jetting. The motion of the slipper also forces the coating to react in a fashion that prevents the formation of velocity vectors that are conducive to jetting.

VII. Summary and Conclusions

The study imposed a nonequilibrium thermodynamic state to the first and second laws of thermodynamics. The effect on gouging of a thermal environment brought about by friction and irreversible thermodynamics was studied in the context of real test sled dimensions. The specific conditions considered in this study were brought about by irreversible frictional effects and the flow of heat from regions of varying temperatures.

A more complete definition of jetting that leads to gouging was defined based on previous research. A steep displacement of one material into the other at the sliding interface was observed to be necessary. In addition, a relative velocity of the furthest penetrating material with respect to the bulk of the displacement was seen to initiate jetting deformations (due to rotational velocity vectors) that lead to gouging.

7.1 Numerical Tools

To study realistic momentum as well as kinetic energy effects the mass of an actual test sled was simulated using the LS-DYNA3D finite element code. Finite element codes offer a means to match kinetic energy and momentum without increasing the dimensions of the slipper by adding nodal masses to the slipper model. A common mode of impact during a test sled run includes a vibratory impact that strikes on the top of the rail. To gain a better understanding of the conditions that occur during this type of impact with a realistic mass, a three-dimensional Lagrangian finite element slipper and rail model was developed.

The results of this study led to a better analysis of the three-dimensional test sled. It confirmed the use of a two-dimensional plane strain model for studying hypervelocity gouging. It also provided insight into the three-dimensional effects of a flat impact on the top of the rail in which there is not a restricted plane strain condition.

Three nonlinear explicit codes available for solving the nonlinear equations of conservation were studied and compared. Requirements for this research, such as the ability to model heat flow and high strain rate characteristics of the material meant that further study of available numerical tools was warranted. The three codes studied were CTH,

ABAQUS, and LS-DYNA3D. The capabilities of these codes were studied in their own right, and then compared with each other using a high speed asperity impact model.

The investigation began by studying CTH's capabilities to model hypervelocity gouging, thermal profiles with associated stresses through the equation of state models, and heat conduction. CTH was found to have all the capabilities one would need for a proper numerical investigation of the hypervelocity gouging problem and the effects of heat transfer in the solution. The primary disadvantage of CTH was that it required a mesh resolution much finer than comparable Lagrangian codes to capture important characteristics of high energy impact events leading up to gouging.

In the ABAQUS analysis, gouging did not occur because the large deformations of the Lagrangian mesh exceeded even the corrections made by adaptive meshing. ABAQUS was found to not be the program of choice for this investigation, even though it had excellent user-defined material model capabilities and a coupled heat transfer-stress algorithm. ABAQUS is better suited to impact cases in which smaller deformations occur and distortion of the elements are relatively small. One example of this might be for penetration impacts, such as for long rod penetrators

For the LS-DYNA3D study, an interaction of slipper and rail materials could not be modeled in the Lagrangian mesh because large deformations of the Lagrangian mesh were detrimental to accuracy of the Lagrangian solution. It was determined that Lagrangian meshes are plagued by difficulties accurately modeling material "jets" that occur during gouging. These "'jets"' are large deformations that are thin and vortice-like. Lagrangian elements had an extremely difficult time modeling this type of deformation without distorting the elements to the point that the analysis could not continue. LS-DYNA3D has an Eulerian mesh capability that could be investigated for further study of this problem.

7.2 Dimensional Analysis

A dimensional analysis was carried out, to determine the parameters necessary for applying numerical simulations to a given test sled. The scaling used in the dimensional analysis provided a means of comparing numerical models of varying velocities based on

a natural time scale. Simplification of an actual test sled was conducted and the model applied to a finite volume hydrocode, CTH. The same method used in the finite element codes to add mass to the nodes could not be used in the CTH model. Therefore, an artificial sled mass was added to approximate both energy and momentum effects in the field. Four situations that approximate conditions in the field were simulated: a flat rail with and without a coating to explore frictional and heating effects, and an impact with an imperfection in the rail known as rail roughness, both with and without a coating. Dimensional analysis of other cases was carried out (e.g., asperity impacts), but not tested.

Scaling of selected CTH models for hypervelocity test sled slipper-rail impacts was tested and the results of geometric scaling found to be sufficient for the numerical study. The scaling study provided invariant products that could be used to guide dimensionally consistent enhancements to previous computational models for improved comparison to actual test sleds. The invariants also provided a methodical means of reducing computational models of a real test sled, if necessary.

The dimensional analysis did not account for high strain rate dependencies of the material models. As such, numerical studies should first quantify strain rate sensitivity of the invariant products prior to use with real test sleds. It was shown that strain rate differences between geometrically scaled models could be modified in accordance with scaling laws by changing material parameters in the constitutive model. This technique however, is limited to models which lend themselves to this specific modification. It was also shown that relative size of the mesh cells with respect to the model and the number of cells defining the area of interest is an important factor for scaling computational models.

Scaling of the solution with respect to an appropriate time-scale was determined to be extremely important. Results do not match between models unless this time-scale is used for models whose length and height are simply scaled up or down. If the material properties, velocities, and temperature field between models remain the same, the geometry between models may be scaled according to the length of the slipper or some other appropriate length if a time-scale is also considered. For best comparison of models, the slipper should not be taken as a stand alone model without considering the effects and interactions of the sled system mass and its properties on the whole impact scenario. At the very least,

the sled system mass should be modeled in a simplified fashion in addition to allowing the sled mass to be distinct from the slipper. It is possible, using the dimensioned parametric approach, that any global sled can be characterized by a numerical model which depicts the actual high velocity impact using available computer resources.

There are a number of dimensioned quantities within CTH that the user does not have control over and were not considered in any of the dimensional analyses. The complexity of the problem makes it extremely difficult to consider every dimensioned quantity for the dimensional analysis. The complexity of the CTH algorithms also makes it extremely difficult to account for time and length scales in every material model. Greater user control of material model parameters is required to accomplish this within CTH.

The dimensional analysis lent insight into the potential benefits and behavior of coatings. Scaling invariants from the Buckingham Pi analysis were used to determine which parameters are important to studying test sled impacts. Characteristic length and time scales may be used to nondimensionalize the problem. These nondimensional parameters may then be compared to reduce the system of parameters.

A sample analysis was conducted by changing one parameter (coating thickness) and determining which parameters would need to be varied to initiate a jetting solution. A scaled-up coated rail roughness model simulating "real" dimensions and a coating variation of the numerical model simulating an example CTH numerical model with 6 mils coating thickness were compared. It was determined that the scaled-up version causes gouging because it has the same kinetic energy and momentum required for gouging to occur despite a 6 mil coating. Also, impact on the larger rail roughness allows a greater exchange of momentum and energy between the sled system and the rail. The exchange of energy that occurs in spite of the coating, results in gouging. A more complex analysis might could also be carried out to better understand the effect of the rail roughness size and other parameters on the problem. The scaling invariants provide a rule by which one can match dimensioned quantities of a particular result and make educated conclusions about the effect of changing various parameters in the problem.

Based on the insight provided by varying dimensioned quantities between gouge initiation models and exploring the variation in the other parameters from previous studies, there appears to be a low and high limit to beneficial coating densities. This balance is between a higher density coating that deflects the slipper away from the rail material and a lower density coating with greater thickness that prevents gouging by absorbing energy and shearing away rather than carrying high stress. Further numerical investigations are required to determine this limit for increasing the coating density.

A similar analysis might be accomplished by changing more than one parameter and observing the relationship between the dimensioned quantities as well as the scaling invariants. The point of the exercise presented in this study was to illustrate the use of scaling invariants for comparing dimensioned quantities of numerical models. The process of performing a dimensional analysis and the invariants that were derived during the exercise improved the understanding of the problem and also highlighted important parameters to be considered for further numerical analyses. Finally, the invariant products could be used as guidelines to determine whether particular CTH models apply to a given test sled, and what changes to the model must be made so that it applies to the given test sled.

7.3 Nonequilibrium Thermodynamics

Heating and frictional effects were found to be important to understanding the conditions leading up to jetting (a precursor to gouging). Heat flow was found to be a contributor to cooling in the boundary layer for longer frictional runs up to 20 microseconds. Temperatures were extrapolated for longer contact times from numerical solutions of the shorter time periods. Phase changes due to temperature and pressure were found to affect the slipper and rail due to frictional heating and thermal changes. The steel was found to transform to an austenite phase, as seen in previous observations of actual gouges. The epoxy coating never reached pressures that would cause dissociation of the molecules, but it did reach glass transition temperatures that would cause transition to a rubbery state.

The temperature rose to around 1300 K for the vibratory impact clean rail case. The slipper tracer near that same area showed a temperature rise from 298 K to approximately 825 K in 20 microseconds. These temperatures were high enough to transform the steel

to austenite, as has been observed in gouged specimens in the field. Temperatures ranged from 1300 K within the sliding interface, to lower temperatures (around 850 K) in areas removed from the sliding interface, but still within the boundary layer region. At these lower temperatures, the austenite phase would be unstable and change in time. In the higher temperature region the austenite phase would be in a stable configuration. There was no indication of rapid cooling in the solution that would produce martensite.

At the temperatures indicated in the CTH solution, steel exists in the austenite phase. However, the austenite steel generated in the 3 km/sec case would be in a stable state because the region of higher temperature extends further into the slipper and the rail and was at higher temperatures. This was likely due to the smaller amount of heat being conducted away from the sliding interface due to the shorter time period under consideration and the larger strain rates that created more plastic strain for the 3 km/sec case.

7.4 Frictional Effects

A comparison of different initial coefficients of friction to the CTH boundary layer algorithm showed that the initial coefficient of friction did not have an effect on the solution. A comparison of the boundary layer treatment and the frictionless slide line treatment of the sliding cases indicated that the boundary layer treatment would be a conservative case for studying the effect of high temperatures on the CTH models. The effective coefficient of friction at high speeds was estimated manually by integrating normal stress and shear stress solutions at points along the bottom of the slipper.

Reflections of low pressure shocks off the front edge of the slipper caused a ripple effect in the interface between the slipper and the rail. The continuous sliding of the slipper over these small bumps resulted in a mutual interaction between the slipper and rail and more ridges were formed. As these rough surfaces responded to one another, the projections became plastic and deformed further, resulting in less strain rate differences within the rail. Though smaller, the regions of high strain rate continued. The slipper material strained plastically and the sliding interface became an interface between two permanently deformed materials. These materials continued to impinge on one another

and the tiny projections of the slipper into the rail and the rail into the slipper became larger in some areas and more numerous in others. The sliding interaction continued as the front region of high strain rate in the rail grew in size. Because of these interactions, the coefficient of friction at the velocities under study became a function of the velocity of the impact, the response of the slipper to the impact, and the constitutive properties of the sliding materials.

It was also found that mesh coarseness had an effect on the boundary layer algorithm used in CTH. At 3 km/sec, the slipper travelled 0.3 cm horizontal and 0.001 cm in the vertical direction over 1 microsecond. This vertical displacement isn't yet one cell height. Whereas, in the 1.5 km/sec run, over 2 microseconds, the vertical displacement of the slipper was 0.002, which is one cell height. Here is where mesh coarseness was seen to play a role in the boundary layer algorithm solution. The boundary layer is defined in CTH in terms of cell diagnols. Changing the dimensions of the cell, effectively changes the absolute thickness of the boundary layer. This was seen as one reason that friction solutions using the boundary layer algorithm should be considered over as long a period of time as possible to obtain the average response of the system.

7.5 Rail Roughness Effects

Jetting was found to initiate upon the impact of the given test sled slipper with a clean rail roughness at 3 km/sec, but not at 1.5 km/sec. Even before impact, the rail roughness responded elastically to the coming slipper. The slope of the rail roughness decreased slightly a few microseconds before the slipper arrived. The elastic wave speed was faster in steel that the speed of the slipper for both the 1.5 and the 3 km/sec cases. This allowed the rail roughness to respond to the slipper before it arrived. The low pressure compression wave that led the slipper in the rail expanded when it reached the rail roughness, due to the increased area the wave travelled into. The tensile front of this expansion was weak, but it travelled within the rail roughness and affected the region just prior to the slipper's arrival. This tensile wave was the reason for the rail roughness' change in slope. These waves were then followed by a compressive region that built up to a high pressure front at the leading edge of the slipper.

At 3 km/sec, jetting did form in the same spot it was indicated it might form for the 1.5 km/sec case. The jetting formed when the slipper impacted the rail and the geometry of the roughness caused the velocity vectors in front and behind the point of origin to rotate upwards. This rotation initiated jetting since the plasticized rail and slipper materials impinged further into one another and the forward velocity of the slipper caused mutual interaction of the two materials. This interaction formed vortices of plasticized slipper and rail material which resulted in gouging as the slipper slid over the rail roughness. A study of these same cases with the coating acting as a buffer between the slipper and rail showed how coatings reacted to mitigate the conditions that led to gouging.

7.6 Velocity Effects

A comparison of the solution for the 1.5 km/sec case and the 3 km/sec vibratory impact on a clean rail case showed that the strain rates for a comparable time were much higher at 3 km/sec. One reason the strain rates were larger in the 3 km/sec solution was that the stress waves in the 3 km/sec solution were stronger due to the higher velocity of impact. These higher strain rates were distributed in higher concentrations along the rail surface than for the 1.5 km/sec case. This caused greater deformations in the impinging ridges between the slipper and rail surfaces. The larger ridges coupled with the continued tangential velocity vector of the slipper caused reactions within the slipper and rail that were both volumetric and distortional.

As the slipper continued to slide over the rail at the faster tangential velocity, the rail material continued to impinge into the slipper boundary as the normal surface traction calculated by the boundary layer algorithm became larger. Surface normals always point into the harder material (i.e., the slipper). As the slope of the ridges became steeper, the normals rotated to align with the tangential component of the slipper velocity and the stress increased further at these points.

Scaling for time, the 3 km/sec case showed gouging sooner than the time expected from the velocity vectors. 10 microseconds in the 1.5 km/sec case scaled to 5 microseconds in the 3 km/sec case. But jetting was clearly evident at 4.45 microseconds in the 3 km/sec case. This time scaled to 8.9 microseconds in the 1.5 km/sec case. The time scaling

was conducted in terms of frictional development and length of the rail covered by the horizontal velocity of the slipper.

The impact with the rail roughness at 1.5 km/sec provided potential for the hump that was formed by frictional sliding, to form a jet. The mutual interaction of rail and slipper materials in jetting would have then led to a permanent deformation called gouging. This explanation was tested in the 3 km/sec case. It was determined that the gouge formed at 3 km/sec rather than at 1.5 km/sec because the additional energy of the increased velocity and the higher strain rates of the ridges formed at impact provided increased kinetic energy that allowed the velocity vector of the rail to impinge on the slipper and initiate jetting.

A comparison of the 1.5 km/sec and 3 km/sec cases for the coated rail roughness showed that the slipper deformed more in the 3 km/sec case as a response to the interaction of the coating at the leading edge of the slipper. This larger deformation created a pocket of coating material at the leading edge. Rather than shear off coating in a steady stream, the 3 km/sec case showed the coating breaking up into pieces as it was ejected in front of the slipper. Also, a greater volume of the coating was being gathered and ejected by the slipper at the 3 km/sec velocity. This was likely due to the fact that the 3 km/sec slipper was traveling faster than the material sound speed for the coating, so the coating was unable to respond upstream of the slipper. This resulted in a strong shock wave within the coating and an even stronger shock in the rail. The rail then deformed to a much greater extent than it did under the 1.5 km/sec velocity over the coated rail roughness. As long as the rail deformation did not penetrate the coating, jetting did not initiate.

7.7 Coating Effects

The use of coatings in mitigating damage to materials under high energy impact was also studied. A coating of 6 mil thickness with the simulated properties of epoxy was found to mitigate the conditions leading to jetting for the 3 km/sec clean rail case. The coating was found to mitigate gouging by reducing the stress response to the impact and by acting as a buffer to prevent the rail and slipper materials from interacting with each other.

By mitigating the ridges that would normally form upon impact, the distortional response within the slipper was less dramatic. Additionally, the coating deformed rather than resisted the sliding slipper material, so the deviatoric response in the coating was much less than for the clean rail.

The overall effect of the epoxy coating was found to reduce the impact stresses, which reduced the effect of the shock reflections off the slipper front. This reduction in stress further reduced formation of ridges caused by disparate strain rates along the sliding surfaces. This then reduced the effect of friction and the overall state of stress and strain in the slipper and the rail. The lower density coating also yielded rather deformed the slipper and resulted in a tensile pressure wave in the slipper upon impact, which further reduced roughness.

Another effect of the epoxy coating was on temperature. Polymers like epoxy absorb a greater amount of heat before increasing in temperature, as compared to steel. They have increased thermal resistance as compared to steel, but this results in a decreased resistance to impact. The lower temperatures associated with the coated rail meant that the slipper and rail were less likely to transform into austenite steel. The epoxy absorbed energy without increasing in temperature as much as the steel. The epoxy did reach the glass transition temperature of 400 K, but a rubbery state would actually help to absorb any stresses that formed in the development of the solution, although it might have increased the frictional effects. The coating reduced the temperature of the slipper sliding boundary over 20 microseconds in half, as compared to the uncoated case. The final temperature of 460 K for this case would not have resulted in the slipper steel entering an unstable austenite phase.

In order to maintain the gap between the slipper and rail of approximately 0.125 inches, the thickness of the coating should remain under 125 mils. Otherwise, the coating may stop up the gap and cause difficulties with the slipper. It is not known what effect blocking the gap of the slipper and rail will have, but this could cause the development of catastrophic stresses if the front pocket that was seen to form in the slipper increases linearly with the coating thickness.

For example, the height of the pocket of coating that forms at the front edge of the slipper is approximately 0.05 cm for a 6 mil coating that slides over a standard rail roughness after 10 microseconds. This height is equivalent to approximately 20 mils. If the maximum height of a rail roughness is approximately 50 mils, a linear extrapolation of the pocket height with coating thickness would equate to a desired coating thickness of approximately 15 mils thickness. Assuming the linear extrapolation is correct, this would provide a leading edge pocket of coating that would allow the slipper to slide over any rail roughness that is within the normal tolerance at the HHSTT for a horizontal slipper velocity of 3 km/sec and a vertical velocity of 2 m/s. Schmitz, et al.[1] performed a parametrical study of various coatings and thicknesses using an asperity initiator for gouging. His data showed that for an epoxy coating, the velocity for gouge initiation would be approximately 4.2 km/sec for a coating thickness of 12 mils. The estimated thickness of 15 mils is slightly greater than that value.

Using a linear extrapolation, the leading edge slipper pocket of coating material would become as thick as the slipper gap for a coating of approximately 38 mils thickness. Potential difficulties of this occurring include increased stress on the slipper, aerodynamic effects within the slipper gap, and increased stress in the coating which would become magnified as the shock front extends into the steel rail. This magnification of the shock within the coating is a disadvantage of the coating. For the thickness studied, the benefits of the coating outweighed this disadvantage. Therefore, even though increased coating thickness may improve gouging mitigation, there is a limit to the beneficial effects.

A 70 mil thickness as is found in the field may have detrimental effects for gouging mitigation. This requires further study in order to make a valid conclusion regarding this scenario. Another consideration of increasing the coating thickness is that increased thickness would provide more space for the coating material to form rotational velocity vectors that could lead to jetting of the coating into the slipper. If the slipper material is plastic, and enough thermal softening has occurred, then the slipper may flow with the coating and gouging of the slipper may result. This too requires further study in order to make definite conclusions about this scenario. Improved coating material models would be extremely helpful in this regard.

7.8 Gouging Mitigation

The coating was seen to absorb the energy of impact without resisting. Reflections off the front slipper surface were less than those for the clean rail impact. Upon impact with the rail roughness, the coating acted to further cushion the impact and keep the stresses from reaching a state that would encourage jetting and subsequent gouging. In fact, the slipper slid over the coating as it slid over the rail roughness and was prevented from interacting with the rail. This appeared to be dependent on the thickness of the coating and the velocity of the slipper.

Motion of the coating to the rear for the 3 km/sec coated rail roughness case appeared to be a response to the coating material that was gathered up in the front portion of the deformed slipper. As pressure built up in the front coating "pocket," part of the coating was ejected to the front and part was forced backward to lower pressure areas. The velocity of the coating was enough to deflect the rail material and prevent jetting behind the high pressure core.

Another important parameter of the coating is the elastic wave speed of the coating. This property is a function of the elastic modulus and the density of the material. In plastic regions, it becomes a function of the constitutive response and the density. Even before impact on the clean rail, the steel rail roughness was seen to respond elastically to the upcoming slipper. The slope of the rail roughness decreased slightly a few microseconds before the slipper arrived. At 3 km/sec, the slipper velocity exceeded the speed of sound of the epoxy coating. This meant the coating did not have time to react to the moving slipper.

As a result, the compression wave was formed within the coating to adjust for this loading situation. As the coating was compressed in response to the slipper, more coating material was gathered until the pressure was high enough to deform the slipper. Eventually, the slipper stopped deforming and the coating material was forced back underneath the slipper and forward, as ejected material spewed forth in front of the slipper. This compressed pocket of coating acted as a boundary to prevent the interaction between the slipper and rail and prevented the conditions that lead to jetting.

This case showed how gouging could initiate through the formation of jetting. It also showed how this could be mitigated by the effects of a coating applied to the surface of the rail. The coating mitigated gouging by reducing the effects of the high speed impact on the system and by acting as a buffer between the rail and slipper materials. This prevented the rail and slipper materials from interacting with each other. The reason the coating itself did not form this jetting with the slipper is probably two fold. First, the coating material was much softer and deformed rather easily. It deformed rather than caused sharp rigid deformations in the harder material. Sharp, rigid projections between the slipper and rail could have led to the conditions that cause jetting. The other reason the coating did not form jetting was that the thickness was too small to allow the rotational velocity vectors that would have initiated jetting. The motion of the slipper also forced the coating to react in a fashion that prevented the formation of velocity vectors that would have been conducive to jetting.

A coating thickness that is at least the height of any estimated rail roughness may be able to mitigate any gouging that is likely to occur at 3 km/sec. If a rail misalignment is limited to 0.05" (0.127 cm), this could be used as an approximation of the maximum height of any slipper impact with rail material. A coating thickness of at least 50 mils would allow the slipper to slide over any rail roughness without changing the velocity vectors of the rail material so that it would not impinge on the slipper. The layer of coating that exists between the slipper and rail would also act to prevent the two materials from contacting each other and forming a jet. Another option may be to redesign the front of the slipper to increase the size of the pocket of coating material that is formed at the leading edge of interaction with the coating. This would act as a larger cushion to prevent the rail material from rising up to contact the slipper material. Increasing the coating thickness may cause the same result, but may also cause more problems by being large enough to allow rotational velocity vectors to form within the coating material. Using the model developed in this study, this design and other variations could be studied and analyzed.

The research presented here provided a model with justification for selecting dimensions to simulate a given test sled. The CTH models and the physical understanding of the

mitigation of hypervelocity gouging resulting from this research, may be used for future studies of the hypervelocity gouging problem at the HHSTT.

7.9 Contributions of This Research Effort

The contributions this research effort has made to the field of hypervelocity gouging include:

- A precise definition of conditions that lead to gouging.
- Understanding the value of the finite volume hydrocode CTH as compared to Lagrangian finite element codes for the hypervelocity gouging problem.
- Scaling as a means of applying numerical results to the HHSTT and for obtaining better insight into hypervelocity gouging.
- A process for translating a given test sled configuration into a CTH model for analysis.
- Improved realism for simulating hypervelocity gouging cases that may be used to improve Schmitzs coating software tool at HHSTT.
- Determination of the mesh cell size for a modified hypervelocity gouging model.
- Understanding of frictional effects at hypervelocities.
- Understanding of nonequilibrium thermodynamic effects on the hypervelocity gouging problem.
- Dimensionality and effect of coatings for hypervelocity gouging.

Appendix A. DADS Data for a 809 kg test sled with 1.5 km/sec velocity

Data from the Dynamic Analysis and Design System for a HHSTT test sled is reprinted here. The analysis is for a sled of 1780 lbs (809 kg) with a horizontal velocity of 5000 fps (around 1.5 km/sec). data is given for every 0.001 second up to 1 second in time. The data is for the front slipper and is based on a dynamic structural analysis.

Table A.1 **Front slipper vertical velocity in inches per second compared to time of run (0-0.099 seconds)**

t (seconds)	Vertical vel. (in/sec)	t (seconds)	Vertical vel. (in/sec)
0.000000e+000	0.000000e+000	1.000000e-003	2.603626e+001
2.000000e-003	2.692852e+001	3.000000e-003	6.712123e+000
4.000000e-003	-8.470254e+000	5.000000e-003	3.600787e+001
6.000000e-003	2.449454e+000	7.000000e-003	-8.008455e+000
8.000000e-003	-7.274254e+000	9.000000e-003	5.829707e+000
1.000000e-002	-4.124314e+001	1.100000e-002	1.122889e+000
1.200000e-002	4.805991e-001	1.300000e-002	-7.811171e+000
1.400000e-002	-2.458860e+001	1.500000e-002	2.960981e+000
1.600000e-002	9.215642e+000	1.700000e-002	3.172169e+001
1.800000e-002	-1.601653e+001	1.900000e-002	-3.246489e+001
2.000000e-002	1.681960e+001	2.100000e-002	2.060753e+000
2.200000e-002	-6.509737e+000	2.300000e-002	1.173336e+001
2.400000e-002	-2.818362e+001	2.500000e-002	-1.730436e+001
2.600000e-002	1.164915e+001	2.700000e-002	5.652343e+000
2.800000e-002	-1.857710e+001	2.900000e-002	-2.394868e+001
3.000000e-002	3.318944e+001	3.100000e-002	3.103292e+001
3.200000e-002	-2.780937e+001	3.300000e-002	8.305700e-001
3.400000e-002	1.777855e+001	3.500000e-002	-9.463699e+000
3.600000e-002	-1.142519e+000	3.700000e-002	1.825412e+001
3.800000e-002	4.723370e+000	3.900000e-002	1.325606e+001
4.000000e-002	-2.352891e+001	4.100000e-002	6.195413e+000
4.200000e-002	-1.252525e+001	4.300000e-002	-4.138020e+000
4.400000e-002	5.047660e+001	4.500000e-002	-6.220522e+001
4.600000e-002	3.505233e+001	4.700000e-002	4.657458e+001
4.800000e-002	-2.948798e+000	4.900000e-002	-3.280836e+001
5.000000e-002	-1.357374e+001	5.100000e-002	3.768217e+001
5.200000e-002	-5.052344e+000	5.300000e-002	-1.545862e+001
5.400000e-002	-1.815648e+001	5.500000e-002	6.496359e+000
5.600000e-002	-2.002391e+001	5.700000e-002	4.624089e+000
5.800000e-002	2.147587e-001	5.900000e-002	-1.713558e+001
6.000000e-002	-3.139237e+000	6.100000e-002	-1.370595e+000
6.200000e-002	4.151802e+001	6.300000e-002	-2.375831e-001
6.400000e-002	2.510902e+001	6.500000e-002	-1.559660e+001
6.600000e-002	3.008370e+001	6.700000e-002	-4.015849e+000
6.800000e-002	-2.953160e+000	6.900000e-002	1.398686e+000
7.000000e-002	7.236483e+000	7.100000e-002	-3.406864e+000
7.200000e-002	-5.748783e+000	7.300000e-002	1.838908e+001
7.400000e-002	-3.370061e+000	7.500000e-002	1.289424e+000
7.600000e-002	-1.223628e+001	7.700000e-002	1.409667e+001
7.800000e-002	2.828970e+001	7.900000e-002	-3.791827e+001
8.000000e-002	4.044410e+000	8.100000e-002	1.002918e+001
8.200000e-002	-6.064456e+000	8.300000e-002	5.643024e+000
8.400000e-002	-4.276096e+001	8.500000e-002	1.372541e+001
8.600000e-002	1.973224e+001	8.700000e-002	-2.358700e+001
8.800000e-002	-3.864180e+001	8.900000e-002	-4.403921e+001
9.000000e-002	2.240082e+001	9.100000e-002	4.017828e+001
9.200000e-002	2.572011e+001	9.300000e-002	3.123592e+001
9.400000e-002	5.525252e+000	9.500000e-002	-1.482234e+000
9.600000e-002	4.573995e+000	9.700000e-002	-1.455903e+001
9.800000e-002	-1.679425e+001	9.900000e-002	-3.972874e+001

Table A.2 **Front slipper vertical velocity in inches per second compared to time of run (0.1-0.199 seconds)**

t (seconds)	Vertical vel. (in/sec)	t (seconds)	Vertical vel. (in/sec)
1.000000e-001	4.203350e+001	1.010000e-001	-2.066577e+001
1.020000e-001	-3.528433e+001	1.030000e-001	-2.529094e+001
1.040000e-001	7.209130e+000	1.050000e-001	2.457403e+001
1.060000e-001	9.046122e+000	1.070000e-001	-7.989683e-001
1.080000e-001	-1.030187e+001	1.090000e-001	-1.562894e+001
1.100000e-001	3.112932e+001	1.110000e-001	5.144381e+001
1.120000e-001	-1.602079e+001	1.130000e-001	-1.347734e+001
1.140000e-001	7.696565e+000	1.150000e-001	1.181895e+001
1.160000e-001	-5.247235e+000	1.170000e-001	-1.908845e+001
1.180000e-001	8.324808e+000	1.190000e-001	-1.902791e+001
1.200000e-001	-2.132163e+001	1.210000e-001	-1.223735e+001
1.220000e-001	8.790650e-001	1.230000e-001	-1.487738e+001
1.240000e-001	2.250615e+001	1.250000e-001	4.398236e+001
1.260000e-001	-6.956822e-001	1.270000e-001	6.370304e+000
1.280000e-001	5.506018e-001	1.290000e-001	1.807443e+000
1.300000e-001	-8.967022e+000	1.310000e-001	-6.279655e+000
1.320000e-001	2.011125e+001	1.330000e-001	-1.159532e+001
1.340000e-001	-1.001379e+001	1.350000e-001	8.823435e+000
1.360000e-001	4.988918e+000	1.370000e-001	-2.833012e+001
1.380000e-001	-6.206666e+001	1.390000e-001	-2.417188e+001
1.400000e-001	6.601276e+001	1.410000e-001	4.797965e+000
1.420000e-001	8.319918e-001	1.430000e-001	3.942684e+001
1.440000e-001	-1.725180e+001	1.450000e-001	9.501858e+000
1.460000e-001	-1.082037e+000	1.470000e-001	-8.385601e+000
1.480000e-001	-6.560511e+000	1.490000e-001	6.570235e-001
1.500000e-001	1.547364e+000	1.510000e-001	-2.435030e+000
1.520000e-001	-2.561722e+001	1.530000e-001	4.946140e+000
1.540000e-001	1.845009e+001	1.550000e-001	-1.631825e+001
1.560000e-001	1.621000e+001	1.570000e-001	2.330604e+001
1.580000e-001	-1.946194e+001	1.590000e-001	3.939746e-002
1.600000e-001	1.557594e+001	1.610000e-001	-1.089590e+001
1.620000e-001	-4.465527e+000	1.630000e-001	2.356072e+000
1.640000e-001	-5.578938e+000	1.650000e-001	1.389104e+001
1.660000e-001	-1.646652e+001	1.670000e-001	1.241915e+001
1.680000e-001	2.070155e+001	1.690000e-001	-8.887908e+000
1.700000e-001	2.815226e+000	1.710000e-001	3.034350e+001
1.720000e-001	-4.571252e+001	1.730000e-001	8.211780e+000
1.740000e-001	-8.900352e+000	1.750000e-001	-2.137484e+000
1.760000e-001	-7.003958e+000	1.770000e-001	-1.698535e+000
1.780000e-001	-1.941856e+001	1.790000e-001	8.316979e-001
1.800000e-001	9.008631e+000	1.810000e-001	-4.194046e+001
1.820000e-001	-4.288253e+001	1.830000e-001	-1.831264e+000
1.840000e-001	1.990662e+001	1.850000e-001	8.636360e+000
1.860000e-001	6.205486e+000	1.870000e-001	2.514396e+001
1.880000e-001	5.625086e+001	1.890000e-001	5.387652e+000
1.900000e-001	1.084991e+001	1.910000e-001	-1.683860e+001
1.920000e-001	-6.873743e+001	1.930000e-001	-4.255206e+001
1.940000e-001	3.962191e+001	1.950000e-001	-3.500445e+001
1.960000e-001	-5.529641e+000	1.970000e-001	-1.131623e+001
1.980000e-001	-8.516331e-001	1.990000e-001	-1.362625e+001

Table A.3 **Front slipper vertical velocity in inches per second compared to time of run (0.2-0.299 seconds)**

t (seconds)	Vertical vel. (in/sec)	t (seconds)	Vertical vel. (in/sec)
2.000000e-001	5.563739e+000	2.010000e-001	2.753498e+001
2.020000e-001	8.980091e+000	2.030000e-001	1.367418e+001
2.040000e-001	2.753043e+001	2.050000e-001	2.832852e+001
2.060000e-001	3.979065e+001	2.070000e-001	-2.331956e+001
2.080000e-001	2.901585e+001	2.090000e-001	-1.247559e+001
2.100000e-001	-4.431835e+001	2.110000e-001	-7.905267e+000
2.120000e-001	-1.886720e+001	2.130000e-001	-2.344312e+001
2.140000e-001	8.769488e+000	2.150000e-001	-1.105967e+001
2.160000e-001	-3.670818e+001	2.170000e-001	9.113317e+000
2.180000e-001	-1.978602e+000	2.190000e-001	-7.868629e+000
2.200000e-001	4.835566e+001	2.210000e-001	6.058318e+001
2.220000e-001	7.381851e+000	2.230000e-001	-1.241303e+001
2.240000e-001	2.463848e+001	2.250000e-001	-3.057485e+001
2.260000e-001	2.765233e+001	2.270000e-001	-4.009616e+001
2.280000e-001	-1.395503e+001	2.290000e-001	3.998291e+001
2.300000e-001	2.500603e+001	2.310000e-001	4.739647e+000
2.320000e-001	-4.302640e+000	2.330000e-001	2.831831e+001
2.340000e-001	-6.023062e+000	2.350000e-001	-7.516307e+000
2.360000e-001	2.491953e+001	2.370000e-001	4.642803e+000
2.380000e-001	-1.484663e+001	2.390000e-001	-1.525410e+001
2.400000e-001	-9.986584e-001	2.410000e-001	2.151649e+001
2.420000e-001	-2.292762e+001	2.430000e-001	-4.409578e+001
2.440000e-001	1.071739e+000	2.450000e-001	-2.650014e+000
2.460000e-001	-6.145117e+001	2.470000e-001	-3.287967e+001
2.480000e-001	3.961902e+001	2.490000e-001	2.580123e+001
2.500000e-001	7.519952e+000	2.510000e-001	4.107368e+001
2.520000e-001	-4.805445e+001	2.530000e-001	6.365614e+001
2.540000e-001	7.279201e+001	2.550000e-001	3.839696e+000
2.560000e-001	-1.444203e+001	2.570000e-001	-4.779100e+001
2.580000e-001	1.450804e+001	2.590000e-001	-7.563935e+000
2.600000e-001	-3.537876e+001	2.610000e-001	-9.387776e+000
2.620000e-001	-6.261478e+001	2.630000e-001	2.097655e+001
2.640000e-001	2.306382e+000	2.650000e-001	-1.071311e+000
2.660000e-001	8.045252e+000	2.670000e-001	3.412128e+001
2.680000e-001	1.167525e+001	2.690000e-001	2.751869e+001
2.700000e-001	5.034541e+001	2.710000e-001	-6.386944e+000
2.720000e-001	3.261387e+001	2.730000e-001	-3.181746e+001
2.740000e-001	1.913210e+001	2.750000e-001	-5.121526e+001
2.760000e-001	-4.024563e+001	2.770000e-001	-4.035060e+001
2.780000e-001	-2.483739e+001	2.790000e-001	-4.028310e+001
2.800000e-001	-7.642822e+000	2.810000e-001	1.950963e+001
2.820000e-001	-1.186250e+001	2.830000e-001	8.345491e+000
2.840000e-001	3.741066e+001	2.850000e-001	5.539550e+001
2.860000e-001	2.710007e+001	2.870000e-001	-9.589755e-001
2.880000e-001	1.033946e+000	2.890000e-001	-2.278219e+001
2.900000e-001	7.353445e+000	2.910000e-001	1.201091e+001
2.920000e-001	-1.868340e+001	2.930000e-001	-7.958955e-001
2.940000e-001	-7.674849e+000	2.950000e-001	-1.151449e+001
2.960000e-001	3.969553e+000	2.970000e-001	-1.064175e+001
2.980000e-001	-1.555204e+001	2.990000e-001	-1.077102e+001

Table A.4 **Front slipper vertical velocity in inches per second compared to time of run (0.3-0.399 seconds)**

t (seconds)	Vertical vel. (in/sec)	t (seconds)	Vertical vel. (in/sec)
3.000000e-001	4.648096e+001	3.010000e-001	6.552071e+000
3.020000e-001	-2.422090e+001	3.030000e-001	9.528321e+000
3.040000e-001	9.018601e+000	3.050000e-001	-8.748351e+000
3.060000e-001	5.206288e+000	3.070000e-001	-8.006647e+000
3.080000e-001	-2.074646e+001	3.090000e-001	-1.630341e+001
3.100000e-001	-2.804231e+001	3.110000e-001	-1.100500e+001
3.120000e-001	1.162783e+001	3.130000e-001	3.325031e+001
3.140000e-001	1.045986e+001	3.150000e-001	-6.107770e+000
3.160000e-001	5.209267e+001	3.170000e-001	3.960501e+000
3.180000e-001	-3.680703e-001	3.190000e-001	-3.840178e+001
3.200000e-001	5.787591e+000	3.210000e-001	-5.078769e+000
3.220000e-001	1.909295e+001	3.230000e-001	-2.689575e+001
3.240000e-001	-1.982764e+001	3.250000e-001	-2.049847e+001
3.260000e-001	-2.335345e+001	3.270000e-001	-5.051901e+000
3.280000e-001	-7.237669e+000	3.290000e-001	3.141638e+001
3.300000e-001	5.023655e+001	3.310000e-001	-2.410036e+000
3.320000e-001	6.508935e+000	3.330000e-001	-8.331395e+000
3.340000e-001	2.931959e+000	3.350000e-001	-1.272323e+001
3.360000e-001	3.465503e+001	3.370000e-001	-2.441390e+000
3.380000e-001	-2.552672e+001	3.390000e-001	8.152308e+000
3.400000e-001	1.364475e+001	3.410000e-001	-9.995637e+000
3.420000e-001	-8.366980e+000	3.430000e-001	2.628303e+001
3.440000e-001	-7.836226e+000	3.450000e-001	-1.101423e+001
3.460000e-001	2.263641e+001	3.470000e-001	-2.305182e+001
3.480000e-001	3.730186e+000	3.490000e-001	5.536142e+000
3.500000e-001	3.056171e+001	3.510000e-001	-7.642435e+001
3.520000e-001	6.324955e+001	3.530000e-001	-7.922614e+000
3.540000e-001	-2.736674e+001	3.550000e-001	2.441793e+001
3.560000e-001	2.911198e+001	3.570000e-001	2.596731e+000
3.580000e-001	-1.471078e+001	3.590000e-001	-5.585565e+000
3.600000e-001	-5.299089e+000	3.610000e-001	-6.948255e-001
3.620000e-001	-6.659375e+000	3.630000e-001	-1.509405e+001
3.640000e-001	3.832535e+000	3.650000e-001	1.779991e+001
3.660000e-001	-1.983377e+001	3.670000e-001	3.751574e+000
3.680000e-001	7.861971e+000	3.690000e-001	7.781763e+000
3.700000e-001	-1.663865e+001	3.710000e-001	5.567746e+000
3.720000e-001	6.705513e+000	3.730000e-001	-7.157166e+000
3.740000e-001	-5.597935e+000	3.750000e-001	1.178765e+001
3.760000e-001	-1.076319e+001	3.770000e-001	-1.914987e+001
3.780000e-001	-5.898354e+000	3.790000e-001	1.094144e+001
3.800000e-001	-7.775834e+000	3.810000e-001	-3.905060e+000
3.820000e-001	2.473247e+001	3.830000e-001	3.390410e+001
3.840000e-001	-8.403009e+000	3.850000e-001	1.533492e+001
3.860000e-001	-9.745553e+000	3.870000e-001	-9.193559e+000
3.880000e-001	2.801065e+001	3.890000e-001	-1.331008e+001
3.900000e-001	4.088895e+000	3.910000e-001	1.008874e+001
3.920000e-001	1.718155e+001	3.930000e-001	-3.318369e+001
3.940000e-001	1.940558e+000	3.950000e-001	2.444803e+001
3.960000e-001	-3.473278e+001	3.970000e-001	-1.646463e+000
3.980000e-001	1.216340e+001	3.990000e-001	-2.333471e+000

Table A.5 **Front slipper vertical velocity in inches per second compared to time of run (0.4-0.499 seconds)**

t (seconds)	Vertical vel. (in/sec)	t (seconds)	Vertical vel. (in/sec)
4.000000e-001	6.407085e+000	4.010000e-001	6.500902e+000
4.020000e-001	-1.665432e+001	4.030000e-001	1.055754e+001
4.040000e-001	8.868540e+000	4.050000e-001	-4.447121e+001
4.060000e-001	-1.153936e+001	4.070000e-001	1.792017e+001
4.080000e-001	-1.231636e-002	4.090000e-001	-1.623029e+001
4.100000e-001	1.260366e+001	4.110000e-001	-1.227786e+001
4.120000e-001	-3.747511e+001	4.130000e-001	8.714196e+000
4.140000e-001	-4.967111e+000	4.150000e-001	3.538819e+000
4.160000e-001	1.102899e+001	4.170000e-001	-2.954749e+001
4.180000e-001	-1.442019e+001	4.190000e-001	-2.559458e+000
4.200000e-001	-2.375796e+000	4.210000e-001	-9.970398e+000
4.220000e-001	1.404599e+001	4.230000e-001	2.291935e+001
4.240000e-001	3.954229e+001	4.250000e-001	-1.852591e+001
4.260000e-001	2.564003e+001	4.270000e-001	-7.550136e+000
4.280000e-001	-1.902043e+001	4.290000e-001	2.171412e+000
4.300000e-001	-2.269465e+001	4.310000e-001	9.532312e+000
4.320000e-001	-3.929195e+001	4.330000e-001	5.235862e+000
4.340000e-001	-1.866618e+001	4.350000e-001	1.469615e+000
4.360000e-001	2.386670e+001	4.370000e-001	1.910345e+001
4.380000e-001	-9.029519e+000	4.390000e-001	4.419932e+000
4.400000e-001	-2.564093e+000	4.410000e-001	-1.789727e+001
4.420000e-001	1.097793e+001	4.430000e-001	-5.833512e+000
4.440000e-001	-8.260382e-001	4.450000e-001	-7.264225e+000
4.460000e-001	-4.561931e+000	4.470000e-001	-1.442713e+000
4.480000e-001	-2.779975e+001	4.490000e-001	-4.019422e+001
4.500000e-001	5.704630e+000	4.510000e-001	1.466618e+001
4.520000e-001	-9.916006e+000	4.530000e-001	-2.685494e+000
4.540000e-001	2.839630e+001	4.550000e-001	5.875655e+001
4.560000e-001	1.288263e+001	4.570000e-001	-1.634085e+001
4.580000e-001	9.709375e+000	4.590000e-001	-3.894316e+000
4.600000e-001	-4.654584e+000	4.610000e-001	1.489391e+001
4.620000e-001	-1.997342e+000	4.630000e-001	-4.956181e+000
4.640000e-001	-4.704728e+000	4.650000e-001	9.297026e+000
4.660000e-001	-3.704964e+000	4.670000e-001	6.371380e+000
4.680000e-001	2.457290e+001	4.690000e-001	-6.726384e+000
4.700000e-001	4.340101e+000	4.710000e-001	-4.162992e+000
4.720000e-001	-8.425599e+000	4.730000e-001	2.970614e+001
4.740000e-001	-2.456135e+001	4.750000e-001	1.153968e+001
4.760000e-001	-3.585296e+000	4.770000e-001	-3.737028e+000
4.780000e-001	-6.929024e+000	4.790000e-001	-3.569297e+001
4.800000e-001	7.029120e+000	4.810000e-001	3.535779e+000
4.820000e-001	1.557833e+001	4.830000e-001	1.103517e+001
4.840000e-001	1.791853e+001	4.850000e-001	2.216072e+001
4.860000e-001	-1.702182e+001	4.870000e-001	7.460881e+000
4.880000e-001	-7.521242e+000	4.890000e-001	-2.761314e+000
4.900000e-001	8.542258e-001	4.910000e-001	1.681736e+000
4.920000e-001	5.336884e+000	4.930000e-001	-1.420960e+001
4.940000e-001	-1.915351e+001	4.950000e-001	-1.697212e+001
4.960000e-001	-3.645190e+000	4.970000e-001	2.579853e+001
4.980000e-001	1.366138e+001	4.990000e-001	4.772870e+000

Table A.6 **Front slipper vertical velocity in inches per second compared to time of run (0.5-0.599 seconds)**

t (seconds)	Vertical vel. (in/sec)	t (seconds)	Vertical vel. (in/sec)
5.000000e-001	3.501227e+000	5.010000e-001	3.530627e+000
5.020000e-001	-1.695730e+001	5.030000e-001	2.689743e+001
5.040000e-001	-5.204427e+000	5.050000e-001	9.822228e+000
5.060000e-001	-8.147698e+000	5.070000e-001	-2.467652e+000
5.080000e-001	-1.082813e+001	5.090000e-001	-1.285655e+001
5.100000e-001	3.885021e+000	5.110000e-001	-4.066454e+000
5.120000e-001	-1.350849e+001	5.130000e-001	1.642248e+001
5.140000e-001	4.133821e+001	5.150000e-001	1.686102e+001
5.160000e-001	-2.718416e+001	5.170000e-001	2.954171e+000
5.180000e-001	-1.125895e+001	5.190000e-001	-1.357304e+001
5.200000e-001	3.124654e+001	5.210000e-001	-4.567889e+000
5.220000e-001	7.122214e+000	5.230000e-001	-2.941401e+001
5.240000e-001	1.104149e+001	5.250000e-001	-2.119264e-001
5.260000e-001	-2.809536e+001	5.270000e-001	-5.824001e+000
5.280000e-001	2.697915e+001	5.290000e-001	2.077675e+001
5.300000e-001	4.952842e-001	5.310000e-001	-1.048438e+001
5.320000e-001	1.594071e+001	5.330000e-001	-1.714396e+001
5.340000e-001	2.678932e+001	5.350000e-001	3.763474e+001
5.360000e-001	-1.778343e+001	5.370000e-001	-1.977327e+001
5.380000e-001	-1.897108e+001	5.390000e-001	4.914725e+001
5.400000e-001	-7.099895e+001	5.410000e-001	-3.666972e+001
5.420000e-001	8.707776e+000	5.430000e-001	2.586518e+001
5.440000e-001	4.489113e+001	5.450000e-001	-8.927506e+000
5.460000e-001	-1.518604e+001	5.470000e-001	-9.110926e-001
5.480000e-001	-2.630478e+001	5.490000e-001	1.848242e+001
5.500000e-001	5.773993e-001	5.510000e-001	1.262900e+000
5.520000e-001	6.256266e+000	5.530000e-001	9.077470e+000
5.540000e-001	-3.306496e+001	5.550000e-001	-7.850764e+000
5.560000e-001	1.355610e+001	5.570000e-001	1.718418e+001
5.580000e-001	-1.856035e+001	5.590000e-001	1.628754e+001
5.600000e-001	-7.876761e+000	5.610000e-001	1.629666e+001
5.620000e-001	-5.665186e+000	5.630000e-001	-8.330794e+000
5.640000e-001	1.612799e+001	5.650000e-001	-9.394845e+000
5.660000e-001	7.905570e+000	5.670000e-001	-1.586990e+001
5.680000e-001	1.330369e+001	5.690000e-001	1.889707e+000
5.700000e-001	-5.445877e+000	5.710000e-001	-1.730189e+001
5.720000e-001	6.607918e+000	5.730000e-001	1.909859e+001
5.740000e-001	-5.418818e+000	5.750000e-001	3.630003e+001
5.760000e-001	-5.108598e+000	5.770000e-001	1.962031e+001
5.780000e-001	6.908240e-001	5.790000e-001	7.149797e+000
5.800000e-001	9.460608e-001	5.810000e-001	-3.084990e+001
5.820000e-001	-1.734616e+001	5.830000e-001	1.010502e+001
5.840000e-001	-1.130171e+001	5.850000e-001	-1.161046e+001
5.860000e-001	-2.294887e+001	5.870000e-001	1.873373e+001
5.880000e-001	3.173684e+001	5.890000e-001	-5.806920e+000
5.900000e-001	6.936555e+000	5.910000e-001	7.417456e+000
5.920000e-001	-1.353683e+000	5.930000e-001	1.427883e+001
5.940000e-001	-9.694624e+000	5.950000e-001	5.931507e+000
5.960000e-001	-1.205940e+001	5.970000e-001	-3.559134e+000
5.980000e-001	-8.127090e+000	5.990000e-001	1.899351e+000

Table A.7 **Front slipper vertical velocity in inches per second compared to time of run (0.6-0.699 seconds)**

t (seconds)	Vertical vel. (in/sec)	t (seconds)	Vertical vel. (in/sec)
6.000000e-001	-1.533917e+001	6.010000e-001	1.416569e+001
6.020000e-001	2.152975e-001	6.030000e-001	-5.543375e+000
6.040000e-001	1.010172e+001	6.050000e-001	2.592829e+001
6.060000e-001	-2.030017e+001	6.070000e-001	1.022488e+001
6.080000e-001	1.435890e+001	6.090000e-001	-1.897905e+001
6.100000e-001	6.920722e+000	6.110000e-001	-1.199469e+001
6.120000e-001	2.799093e+000	6.130000e-001	-1.162355e+001
6.140000e-001	-1.079466e+001	6.150000e-001	-2.546798e+001
6.160000e-001	-1.129891e+001	6.170000e-001	8.374855e+000
6.180000e-001	3.820118e+001	6.190000e-001	1.968276e+001
6.200000e-001	1.200267e+000	6.210000e-001	-5.805105e+000
6.220000e-001	1.078482e+001	6.230000e-001	-3.453499e+000
6.240000e-001	1.017787e+001	6.250000e-001	-3.003542e+000
6.260000e-001	6.777516e+000	6.270000e-001	2.058798e+001
6.280000e-001	-2.336104e+001	6.290000e-001	1.415874e+000
6.300000e-001	2.639336e+001	6.310000e-001	2.005327e+001
6.320000e-001	-1.265417e+001	6.330000e-001	-1.583122e+001
6.340000e-001	1.817171e+001	6.350000e-001	-4.826114e+000
6.360000e-001	-1.345177e+001	6.370000e-001	1.162227e+001
6.380000e-001	5.628154e+000	6.390000e-001	-5.742177e+000
6.400000e-001	-1.306251e+001	6.410000e-001	1.588344e+001
6.420000e-001	-5.910951e+000	6.430000e-001	1.527856e+001
6.440000e-001	2.390172e+001	6.450000e-001	-1.026860e+001
6.460000e-001	-1.024679e+001	6.470000e-001	5.401810e+001
6.480000e-001	-2.824993e+000	6.490000e-001	2.817799e+001
6.500000e-001	-3.585088e+001	6.510000e-001	-2.808968e+001
6.520000e-001	2.415268e+001	6.530000e-001	-2.333937e+001
6.540000e-001	-5.131517e+001	6.550000e-001	-5.267586e+001
6.560000e-001	5.550219e+001	6.570000e-001	-1.873528e+001
6.580000e-001	-6.720093e+001	6.590000e-001	9.312709e+000
6.600000e-001	2.607489e+001	6.610000e-001	3.816153e+001
6.620000e-001	3.520969e+001	6.630000e-001	9.409774e+000
6.640000e-001	1.710975e+001	6.650000e-001	-1.703894e+001
6.660000e-001	-9.895288e+000	6.670000e-001	1.695400e+001
6.680000e-001	-1.979620e+001	6.690000e-001	-1.085515e+001
6.700000e-001	2.105226e+001	6.710000e-001	-5.728619e+001
6.720000e-001	-3.837082e+001	6.730000e-001	-2.022433e+001
6.740000e-001	2.481297e+001	6.750000e-001	2.094685e+001
6.760000e-001	1.930034e+001	6.770000e-001	7.431446e+000
6.780000e-001	7.508329e+000	6.790000e-001	4.191960e+000
6.800000e-001	-2.057351e+000	6.810000e-001	-1.699089e+001
6.820000e-001	-5.914164e+000	6.830000e-001	-7.234370e+000
6.840000e-001	1.371484e+001	6.850000e-001	-7.952999e+000
6.860000e-001	-6.837378e+000	6.870000e-001	-7.249186e+000
6.880000e-001	-1.889622e+001	6.890000e-001	-5.717339e+001
6.900000e-001	-2.244003e+001	6.910000e-001	3.921579e+000
6.920000e-001	2.023069e+001	6.930000e-001	3.492476e+001
6.940000e-001	4.090086e+001	6.950000e-001	3.870895e+000
6.960000e-001	9.587332e+000	6.970000e-001	-7.910914e+000
6.980000e-001	-3.611196e+000	6.990000e-001	5.442554e+000

Table A.8 **Front slipper vertical velocity in inches per second compared to time of run (0.7-0.799 seconds)**

t (seconds)	Vertical vel. (in/sec)	t (seconds)	Vertical vel. (in/sec)
7.000000e-001	1.772161e+001	7.010000e-001	-2.871415e+000
7.020000e-001	-6.368012e+000	7.030000e-001	-8.295037e+000
7.040000e-001	-9.230644e-001	7.050000e-001	9.540814e+000
7.060000e-001	3.441046e+000	7.070000e-001	3.776958e+000
7.080000e-001	-5.189314e-001	7.090000e-001	-8.160904e+000
7.100000e-001	-4.366433e-001	7.110000e-001	-2.135163e+001
7.120000e-001	1.899971e+001	7.130000e-001	1.948140e+001
7.140000e-001	6.337274e+000	7.150000e-001	-1.696889e+001
7.160000e-001	-4.525234e+000	7.170000e-001	6.512133e+000
7.180000e-001	7.243093e+000	7.190000e-001	-1.293064e+000
7.200000e-001	-1.323553e+001	7.210000e-001	-5.873375e+000
7.220000e-001	-1.091303e+001	7.230000e-001	4.741816e+000
7.240000e-001	7.270955e+000	7.250000e-001	-1.424789e+001
7.260000e-001	5.318294e-001	7.270000e-001	-2.854670e-001
7.280000e-001	-1.505157e+001	7.290000e-001	-1.682437e+001
7.300000e-001	-1.463096e+001	7.310000e-001	-2.321096e+000
7.320000e-001	9.394494e+000	7.330000e-001	2.048847e+001
7.340000e-001	5.193077e+000	7.350000e-001	3.984175e+000
7.360000e-001	-1.601618e+001	7.370000e-001	1.212768e+001
7.380000e-001	-4.936766e+000	7.390000e-001	-1.242870e+001
7.400000e-001	9.018644e+000	7.410000e-001	-6.818154e+000
7.420000e-001	1.349252e+001	7.430000e-001	-5.385946e+000
7.440000e-001	-3.238463e+000	7.450000e-001	2.129411e+001
7.460000e-001	-2.560395e+000	7.470000e-001	3.073086e+000
7.480000e-001	-7.471885e-002	7.490000e-001	-8.036529e+000
7.500000e-001	1.375085e+001	7.510000e-001	7.446501e+000
7.520000e-001	1.006559e+001	7.530000e-001	-2.924939e+001
7.540000e-001	4.103699e+000	7.550000e-001	3.101767e+000
7.560000e-001	1.367875e+001	7.570000e-001	-7.819338e+000
7.580000e-001	9.420008e+000	7.590000e-001	3.438259e+000
7.600000e-001	-6.310765e-001	7.610000e-001	1.118063e+001
7.620000e-001	-1.234530e+001	7.630000e-001	1.168321e+000
7.640000e-001	2.856079e+001	7.650000e-001	7.394833e+000
7.660000e-001	-1.555898e+001	7.670000e-001	9.241542e-001
7.680000e-001	7.775469e+000	7.690000e-001	-3.527962e+001
7.700000e-001	2.972591e+001	7.710000e-001	1.283556e+001
7.720000e-001	-2.389777e+000	7.730000e-001	-6.219409e+000
7.740000e-001	1.580295e+001	7.750000e-001	1.668346e+001
7.760000e-001	-1.813704e+001	7.770000e-001	5.820543e+000
7.780000e-001	-2.548030e+001	7.790000e-001	-1.959184e+001
7.800000e-001	1.236145e+001	7.810000e-001	-1.346315e+001
7.820000e-001	1.346099e+001	7.830000e-001	3.757812e+001
7.840000e-001	-2.056658e+001	7.850000e-001	1.424420e+000
7.860000e-001	2.487619e+001	7.870000e-001	-2.780554e+000
7.880000e-001	3.105889e-001	7.890000e-001	-8.936678e+000
7.900000e-001	1.592347e+001	7.910000e-001	-1.835780e+001
7.920000e-001	7.052850e+000	7.930000e-001	-2.330378e+001
7.940000e-001	-2.509778e+001	7.950000e-001	2.914849e+001
7.960000e-001	-1.624337e+001	7.970000e-001	3.000144e+001
7.980000e-001	-2.238203e+001	7.990000e-001	-3.355614e+000

Table A.9 **Front slipper vertical velocity in inches per second compared to time of run (0.8-0.899 seconds)**

t (seconds)	Vertical vel. (in/sec)	t (seconds)	Vertical vel. (in/sec)
8.000000e-001	7.241200e+000	8.010000e-001	-3.895441e+000
8.020000e-001	-6.972865e+000	8.030000e-001	1.475018e+001
8.040000e-001	-2.891884e+001	8.050000e-001	2.357106e+001
8.060000e-001	-7.416482e+000	8.070000e-001	1.387090e+000
8.080000e-001	2.503593e+001	8.090000e-001	-1.284911e+001
8.100000e-001	6.033363e+000	8.110000e-001	-1.870995e+001
8.120000e-001	-1.356171e+001	8.130000e-001	-8.706137e+000
8.140000e-001	1.405657e+001	8.150000e-001	-1.995934e+001
8.160000e-001	2.222319e+001	8.170000e-001	-1.352326e+001
8.180000e-001	-6.826952e+000	8.190000e-001	4.873930e+000
8.200000e-001	3.084796e+001	8.210000e-001	-3.750295e+000
8.220000e-001	-4.616076e+000	8.230000e-001	-1.444296e+001
8.240000e-001	-1.269978e+001	8.250000e-001	-8.063651e+000
8.260000e-001	-1.005540e+001	8.270000e-001	-7.903220e-001
8.280000e-001	-7.271623e+000	8.290000e-001	-4.769932e+000
8.300000e-001	-2.094500e+001	8.310000e-001	2.339357e+000
8.320000e-001	1.215860e+001	8.330000e-001	1.331257e+001
8.340000e-001	1.529657e+001	8.350000e-001	-1.902249e+001
8.360000e-001	-9.742553e+000	8.370000e-001	8.717172e+000
8.380000e-001	-1.057465e+000	8.390000e-001	-6.355980e+000
8.400000e-001	8.235939e+000	8.410000e-001	4.754453e+000
8.420000e-001	-1.689353e+001	8.430000e-001	-1.504354e+001
8.440000e-001	-4.232552e+000	8.450000e-001	2.550831e+001
8.460000e-001	2.673942e+001	8.470000e-001	-2.955686e+000
8.480000e-001	-1.707107e+000	8.490000e-001	1.036762e+001
8.500000e-001	-8.560697e-001	8.510000e-001	-1.083811e+001
8.520000e-001	1.869922e+001	8.530000e-001	-7.181338e+000
8.540000e-001	-7.933225e+000	8.550000e-001	-3.023133e-001
8.560000e-001	-1.518889e+001	8.570000e-001	-1.600780e+001
8.580000e-001	1.430210e+000	8.590000e-001	1.749032e+001
8.600000e-001	7.291539e+000	8.610000e-001	5.089332e+000
8.620000e-001	-6.721280e-001	8.630000e-001	9.953291e+000
8.640000e-001	-2.024880e+001	8.650000e-001	1.037913e+001
8.660000e-001	-1.050941e+001	8.670000e-001	9.255634e+000
8.680000e-001	-3.477898e+000	8.690000e-001	-9.550843e+000
8.700000e-001	2.068818e+001	8.710000e-001	-2.366952e+001
8.720000e-001	-4.081510e+000	8.730000e-001	-1.598666e+001
8.740000e-001	3.808354e+000	8.750000e-001	3.225458e+001
8.760000e-001	4.268782e+001	8.770000e-001	-4.078933e+001
8.780000e-001	2.345216e+001	8.790000e-001	5.355763e+000
8.800000e-001	-3.516845e+001	8.810000e-001	1.390966e+001
8.820000e-001	2.390476e+001	8.830000e-001	-1.057030e+001
8.840000e-001	-3.168525e+001	8.850000e-001	6.199857e+000
8.860000e-001	5.479597e+001	8.870000e-001	-5.460799e+001
8.880000e-001	3.451762e+001	8.890000e-001	-1.312366e+001
8.900000e-001	3.820079e+001	8.910000e-001	-6.488949e+000
8.920000e-001	7.983875e+000	8.930000e-001	1.475680e+001
8.940000e-001	-7.103772e-001	8.950000e-001	-1.003661e+000
8.960000e-001	1.574598e+001	8.970000e-001	-1.451270e+001
8.980000e-001	2.281162e+000	8.990000e-001	-2.662843e+000

Table A.10 **Front slipper vertical velocity in inches per second compared to time of run (0.9-1.0 seconds)**

t (seconds)	Vertical vel. (in/sec)	t (seconds)	Vertical vel. (in/sec)
9.000000e-001	-8.472357e+000	9.010000e-001	9.899782e+000
9.020000e-001	-2.224216e+000	9.030000e-001	-1.055970e+001
9.040000e-001	2.249391e+001	9.050000e-001	-1.837226e+001
9.060000e-001	-2.267179e+001	9.070000e-001	1.235924e+001
9.080000e-001	-7.076351e+000	9.090000e-001	3.942827e+000
9.100000e-001	5.637335e-001	9.110000e-001	-8.355615e+000
9.120000e-001	-1.093330e+001	9.130000e-001	-7.842742e+000
9.140000e-001	9.033481e+000	9.150000e-001	2.071630e+001
9.160000e-001	1.656149e+001	9.170000e-001	-3.931372e-002
9.180000e-001	6.648178e-001	9.190000e-001	-1.872158e+001
9.200000e-001	-1.795654e+000	9.210000e-001	-4.231563e+000
9.220000e-001	-5.641233e+000	9.230000e-001	-1.696933e+000
9.240000e-001	-1.140864e+001	9.250000e-001	2.008155e+000
9.260000e-001	-1.737890e+001	9.270000e-001	-7.454661e+000
9.280000e-001	-1.530283e+000	9.290000e-001	1.220739e+001
9.300000e-001	1.227276e+001	9.310000e-001	-7.808254e+000
9.320000e-001	-1.720173e+001	9.330000e-001	-3.154209e+001
9.340000e-001	4.050939e+001	9.350000e-001	-3.924904e+001
9.360000e-001	1.714347e+001	9.370000e-001	3.636113e+000
9.380000e-001	1.363699e+001	9.390000e-001	-1.406737e+001
9.400000e-001	2.666813e+001	9.410000e-001	1.484975e+000
9.420000e-001	-8.132596e+000	9.430000e-001	4.856612e+000
9.440000e-001	8.029090e+000	9.450000e-001	-8.173702e+000
9.460000e-001	-4.811394e+000	9.470000e-001	-1.394042e+001
9.480000e-001	-1.767323e+001	9.490000e-001	-1.655553e+001
9.500000e-001	3.205109e-001	9.510000e-001	-9.219002e-001
9.520000e-001	-1.241921e+001	9.530000e-001	-1.128092e+001
9.540000e-001	1.979903e+001	9.550000e-001	4.528244e+001
9.560000e-001	2.678456e+001	9.570000e-001	2.266469e+001
9.580000e-001	-5.202771e+000	9.590000e-001	1.783279e+000
9.600000e-001	-1.606226e+000	9.610000e-001	-5.237334e+000
9.620000e-001	-5.587370e+000	9.630000e-001	-3.166570e+000
9.640000e-001	-2.043561e+001	9.650000e-001	-2.136635e+001
9.660000e-001	-2.025444e+001	9.670000e-001	2.891823e+000
9.680000e-001	2.005990e+001	9.690000e-001	-8.029448e-001
9.700000e-001	-1.774059e+001	9.710000e-001	2.708339e+000
9.720000e-001	2.707724e+001	9.730000e-001	2.093771e+001
9.740000e-001	-1.893396e+000	9.750000e-001	8.204946e+000
9.760000e-001	7.577397e-001	9.770000e-001	-6.675072e+000
9.780000e-001	5.734305e+000	9.790000e-001	-7.075165e+000
9.800000e-001	7.867439e+000	9.810000e-001	-8.342394e+000
9.820000e-001	-2.611989e+001	9.830000e-001	-3.593501e+001
9.840000e-001	-3.018795e+001	9.850000e-001	2.349712e+000
9.860000e-001	2.026622e+001	9.870000e-001	1.823269e+001
9.880000e-001	2.560318e+001	9.890000e-001	3.903990e+001
9.900000e-001	-7.110380e+000	9.910000e-001	3.351464e+001
9.920000e-001	-2.113258e+001	9.930000e-001	4.249969e+001
9.940000e-001	-1.722489e+001	9.950000e-001	-4.538347e+001
9.960000e-001	-1.405635e+001	9.970000e-001	-2.844219e+001
9.980000e-001	-5.131783e+000	9.990000e-001	-4.413035e+001
1.000000e+000	-2.197899e-001		

Appendix B. CTH Input File for Coated Rail Roughness

CTH input file also has coefficient of friction of 0.0 with heat conduction for horizontal velocity of 1.5 km/sec and vertical velocity of 2 m/s.

```
*eor* cgenin
* Note:  '*' is used at the beginning of comment lines
* cthgen input for Gouge simulation
*
*
* vx=varies, vy=-1 m/s V300 Steel Slider, 1080 Steel Rail, No Atm.
* No Slide line.  mix=1 frac=1 Rounded corner.
* Added mass on top to simulate sled mass
* Gap, heat, BL, fric=0.0, -2 m/s, 1.5 km/sec, 6 mil coating,.0020 cm mesh
control
        mmp
        ep
        vpsave
endcontrol
******************************
* MESH AND BLOCK DEFINITION SET
******************************
* geom=2DR(rectangular x,y)
* geom=2DC(cylindrical x=radius, y=axis)
* geom=3DR(rectangular x,y,z)
* type=e (Eulerian)
* x#=coordinate range for plot
```

```
* y#=coordinate range for plot
* dxf=width of first cell in the region
* dxl=width of last cell in the region
* n=number of cells added in this region
* w=total width of this region in centimeters
* r=ratio of adjacent cell widths
*--------------------------
mesh
block 1 geom=2dr type=e
        x0=0.0000
        x1 w=15.00 dxf=0.500 dxl=0.100
        x2 w=3.000 dxf=0.100 dxl=0.0020
* Mesh of 1 cm friction and 1 cm rail roughness
        x3 w=10.00 dxf=0.0020 dxl=0.0020
endx
        y0=-4.000
        y1 w=2.000 dyf=0.500 dyl=0.100
        y2 w=0.200 dyf=0.100 dyl=0.050
        y3 w=1.000 dyf=0.050 dyl=0.0020
        y4 w=0.800 dyf=0.0020 dyl=0.0020
        y5 w=0.800 dyf=0.0020 dyl=0.0020
        y6 w=2.200 dyf=0.0020 dyl=0.050
        y7 w=5.000 dyf=0.100 dyl=0.500
        y8 w=35.500 dyf=0.500 dyl=0.500
endy
```

```
endblock
endmesh
insertion of material
block 1
package coating
        material 1
        numbsub 100
        xvel 0.0
        yvel 0.0
        insert box
        p1 0.0 .00000
        * shortened friction run, not including roughness
        p2 24.50000 -.01524 * 6 mil coating
        endinsert
        delete ellipse
        * shortened friction run
        * 6 mil coating
        center 32.69524, -0.01524
        * 1 millirad high rail roughness plus 6 mil coating height
        point 32.69524, 0.011060
        semi-axis 11.07524
        enddelete
endpackage
package guider
        material 2
```

```
        numsub 100
        xvel 0.0
        yvel 0.0
        insert box
        * 6 mil coating
        p1 0.0, -0.01524
        * shortened friction run
        p2 32.69524, -4.000
        endinsert
        delete ellipse
        * shortened friction run
        * 6 mil coating
        center 32.69524, -0.01524
        * 1 millirad high rail roughness plus 6 mil coating height
        point 32.69524, 0.011060
        semi-axis 11.07524
        enddelete
endpackage
package coating-rough
        material 1
        numbsub 100
        xvel 0.0
        yvel 0.0
        insert ellipse
        *6 mil coating
```

```
        center 32.69524, 0.000000
        * 6 mil coating added to rail roughness height
        point 32.69524, 0.0263
        semi-axis 11.07524
        endinsert
        delete ellipse
        * shortened friction run
        *6 mil coating
        center 32.69524, -.01524
        * 6 mil coating added to rail roughness height
        point 32.69524, 0.011060
        semi-axis 11.07524
        enddelete
endpackage
package guider-rough
        material 2
        numsub 100
        xvel 0.0
        yvel 0.0
        insert ellipse
        * shortened friction run
        * 6 mil coating
        center 32.69524, -0.01524
        * 1 millirad high rail roughness plus 6 mil coating height
        point 32.69524, 0.011060
```

```
        semi-axis 11.07524
        endinsert
endpackage
package slider
        material 3
        numsub 100
        temperature = 2.53575e-2 * eV = 70F
        xvel 1.5e+5
        yvel -2.0e+2
        insert box
        p1 0.300, 0.0
        p2 20.62, 2.54
        endinsert
        delete circle
        center 20.42, 0.2
        radius 0.2
        enddelete
        delete box
        p1 20.42, 0.2
        p2 20.62, 0.0
        enddelete
endpackage
package sledsim-gapped
        material 4
        numsub 100
```

```
        temperature = 2.53575e-2 * eV = 70F
        xvel 1.5e+5
        yvel -2.0e+2
        insert box
        p1 0.300, 43.14
        p2 20.62, 2.54
        endinsert
        delete box
        p1 1.300, 2.54
        p2 19.62, 3.54
        enddelete
endpackage
package slider-round
        material 3
        numsub 100
        temperature = 2.53575e-2 * eV = 70F
        xvel 1.5e+5
        yvel -2.0e+2
        insert circle
        center 20.42, 0.2
        radius 0.2
        endinsert
endpackage
endblock
endinsertion
```

```
edit
        block 1
        expanded
        endblock
endedit
*--------------------------
* TRACER DEFINITION SET
*--------------------------
tracer
*Target guider
        add 20.40, -0.02 to 26.70, -0.02 n=10
*Target slider
        add 00.40, 0.02 to 20.40, 0.02 n=10
*Target coating
        add 20.40, -0.00725 to 26.70, -0.00725 n=10
*Target slider boundary layer
        add 00.40, 0.003 to 20.40, 0.003 n=10
endt
*--------------------------
* EQUATION OF STATE DEFINITION SET
*--------------------------
eos
        * MAT1 SESAME=GE1_RP EOS=7662* Reactive Graphite Epoxy
        * MAT1 SESAME=GE2_RP EOS=7662* Reactive Graphite Epoxy
        MAT1 MGR EPOXY_RESIN1
```

```
        * MAT1 SESAME=EPOXY EOS=7602* FEOS='seslan'
        * MAT1 SES EPOXY
        * MAT1 SES GREPXY1
        * MAT1 SES GREPXY2
        MAT2 SES IRON
        MAT3 SES STEEL_V300
        * MAT3 SES PLATINUM
        MAT4 MGR PLATINUM
endeos
epdata
        vpsave
        lstrain
        mix=1
                matep=1 *Epoxy Glider Coating
                poisson 0.46
                yield 1.5e8
        matep=2 * IRON Guider/initiator
                johnson-cook IRON
                poisson 0.28
                yield 7.0e9
                * bsm=0.03
                * jfrac IRON
                * jfpf0 -30.0e9
                * jfpf0 -1.40e10
        matep=3
```

```
                st=19 * STEEL V300 Slider
                poisson 0.27
                yield 14.47e9
                * bsm=0.03
        matep=4
                steinberg platinum
*------------------------
* BL algorithm inputs
*------------------------
        blint 1
                soft 1
                hard 3
                csl 1.1
                cbl 1.1
                fric 0.0
                * corr
                * nofreeze
        blint 2
                soft 2
                hard 3
                csl 1.1
                cbl 1.1
                fric 0.0
        ende
ende
```

```
************************************************************
*eor* cthin
Gapped, heat, -2 m/s, 1.5 km/sec, 6 mil coating, .0020 cm mesh
*----------------------------------------------------
*CONTROL DATA SET
*******************
* mmp enables multiple material temps
* and pressures in mixed cells
* frac=1 changes fracture default
******************************
* CELL THERMODYNAMICS INPUT SET
******************************
* cellthermo
* dtmax = max temp difference allowed in mixed cells
* mmp distributes volume and energy based on volume
* fractions of material in the cell
* mmp=default
* mmp1=same as mmp except uses new logic
* and distributes volume and energy
* based on volume fraction cubed divided
* by mass of material in the cell
* mmp2=allocation of work done on the cell is
* dependent on material compressibility
* and allows pressure relaxation between materials
* in a cell
```

```
* endc
*------------------------------------------------------
control
        mmp0
        frac=1
        tstop = 20.00E-6
        nscycle=55000
        rdumpf=991800.
        cpshift=600.
        ntbad=999999
*-----------------------------
* Courant condition multiplier
*-----------------------------
        dtcourant=0.6
        * dtcourant=0.8
endc
*----------------------------------------
* RESTART input set
* Useful when data files get too large and
* you cannot get plots files generated
*----------------------------------------
        *RESTART
        * CYCLE_NUMBER = 1636
        * FILE=rscth
        * PLOTFILE=plcth
```

```
        * NEWFILE=c
        *ENDRESTART
Convct
        convection=1
        interface=high_resolution
endc
edit
        shortt
        time = 0.0 , dt=1.0e-6
        ends
        longt
        time = 0.0e0 , dt = 1.0
        endl
        plott
        time 0.0e-6 dtfrequency 2.0e-6
        endp
        histt
        time 0.0e-6 dtfrequency 0.5e-6
        htracer all
        endhistt
*--------------------------
* Plot Input Set
* Useful for generating
* plot files so that you
* will not run into problems
```

```
* with generating plots from
* restart files
*--------------------------
        * plotdata
        * PLT
        * STRESS
        * TEMPERATURE
        * VELOCITY
        * VIS='vizplt'
        * endplotdata
ende
**********************************
* Hydrodynamic Boundary Conditions
**********************************
* 0=symmetry
* 1=sound speed based absorbing
* 2=extrapolated pressure with no mass allowed to enter
* 3=extrapolated pressure but mass is allowed to enter
*-----------------------------------------------------
boundary
        bhydro
        block 1
        bxbot = 1 , bxtop = 1
        bybot = 1 , bytop = 1
        endb
```

```
        endh
endb
*------------------------
* Heat conduction inputs
*------------------------
heatconduction
        MAT1 TABLE=3
        MAT2 TABLE=1
        MAT3 TABLE=2
endh
DEFTABLE=1 * 1080 STEEL
*T(eV) k(erg/s/eV/cm)
1.4684e-3 4.7700e10
1.0377e-2 4.8100e10
1.9090e-2 4.5200e10
2.7900e-2 4.1300e10
3.6711e-2 3.8100e10
4.5521e-2 3.5100e10
5.4332e-2 3.2700e10
6.3142e-2 3.0100e10
7.1953e-2 2.4400e10
8.9574e-2 2.6800e10
1.1111e-1 3.0100e10
endd
DEFTABLE=2 * VascoMax 300 Steel
```

```
*T(eV) k(erg/s/eV/cm)
3.6711e-3 2.4715e10
1.4684e-2 2.7424e10
2.9369e-2 2.9794e10
3.9158e-2 3.0132e10
endd
DEFTABLE=3 * Epoxy
*T(eV) k(erg/s/eV/cm)
3.6711e-3 6.5e8
1.4684e-2 6.5e8
2.9369e-2 6.5e8
3.9158e-2 6.5e8
endd
*-----------------------------------------
* Added velocity to maintain gouging in view
*-----------------------------------------
*vadd
        * block=1
        * tadd=0.0
        * xvel=-1.08333e+5
*endvadd
mindt
        time=0.  dt=1.e-10
endn
maxdt
```

```
        time=0.  dt=.01

endx
```

References

1. Schmitz, Craig P., et al. "Numerical Investigation of the Gouging Phenomena within a Hypersonic Rail-Sled Assembly." *AIAA*. Number AIAA 2001-1191. April 16-19 2001.

2. Özisik, M. N. *Heat Conduction*. New York, NY: Wiley and Sons, 1980.

3. Silling, S. A. *Stability and Accuracy of Differencing Schemes for Viscoplastic Models in Wavecodes*. Technical Report SAND91-0141, 1991.

4. Malvern, Lawrence E. *Introduction to the Mechanics of a Continuous Medium*. Englewood Cliffs, NJ: Prentice-Hall, Inc., 1969.

5. Meyers, Marc André. *Dynamic Behavior of Materials*. New York, NY: John Wiley and Sons, Inc., 1994.

6. Owen, D.R.J. and E. Hinton. *Finite Elements in Plasticity: Theory and Practice*. West Cross, Swansea U.K.: Pineridge Press Limited, 1980.

7. Laird, David J. *The Investigation of Hypervelocity Gouging AFIT/DS/ENY 02-01*. PhD dissertation, Air Force Institute of Technology, Wright-Patterson AFB, OH, March 2002.

8. Nicholas, Theodore and A.M. Rajendran. *High Velocity Impact Dynamics*, chapter 3 Material Characterization at High Strain Rates, 127–296. New York: John Wiley and Sons, Inc., 1990.

9. Gerstle, F.P. *The Sandia Rocket Sled Rail and Slipper Study*. Technical Report, Albuquerque, NM: Sandia National Laboratories, 1968.

10. Gerstle, F.P. *Deformation of Steel During High Velocity Unlubricated Sliding Contact*. PhD dissertation, Duke University, 1972.

11. Gerstle, F.P., et al. "Thermoplastic Shear and Fracture of Steel During High-Velocity Sliding," *Wear*, *24*:97–106 (1973).

12. Krupovage, Daniel J. and Hans J. Rasmussen. *Hypersonic Rocket Sled Development*. Technical Report JON:99930000, Holloman AFB, NM: High Speed Test Track Facility, 6585th Test Group, September 1982.

13. Krupovage, D.J. "Rail Gouging on the Holloman High Speed Test Track." *35th Meeting of the Aeroballistic Range Association*. 1984.

14. Barber, John P. and David P. Bauer. "Contact Phenomena at Hypervelocities," *Wear*, *78*:163–169 (1982).

15. Graff, Karl F. and Berndt B. Dettloff. "The Gouging Phenomenon Between Metal Surfaces at Very High Speeds," *Wear*, *14*:87–97 (1969).

16. Mixon, L.C. *Assessment of Rocket Sled Slipper Wear/Gouging Phenomena*. Number F08635-97-C-0041, Albuquerque, NM: Applied Research Associates, Inc., 1997.

17. Graff, Karl F., et al. *Study of High Velocity Rail Damage*. Technical Report AA27 F29600-67-C-0043, Kirtland AFB, NM: Air Force Special Weapons Center, August 1970.

18. Tarcza, Kenneth Robert. *The Gouging Phenomenon at Low Relative Sliding Velocities*. MS thesis, The University of Texas at Austin, Austin, TX, December 1995.

19. Ramjaun, Djameel, et al. "Hypervelocity Impacts on Thin Metallic and Composite Space Debris Bumper Shields." Accepted for publication in AIAA Journal, 2003.

20. Boehman, L.I., et al. *Simulation of Friction, Wear, Anti Gouging for Hypersonic Guider-rail System*. Technical Report, Arnold Engineering Development Center (PMP), November 1977.

21. Barker, L.M., et al. *Surface Gouging by Hypervelocity Sliding Contact*. Technical Report SAND87-1328, Albuquerque, NM: Sandia National Laboratories, September 1987.

22. Barker, L.M., et al. "Railgun Rail Gouging by Hypervelocity Sliding Contact," *IEEE Transactions on Magnetics*, *25*(1):83–87 (1988).

23. Susoeff, A.R. and R.S. Hawke. *Mechanical Bore Damage in Round Bore Composite Structure Railguns*. Technical Report, Lawrence Livermore National Laboratory, 1988.

24. Tachau, Robert D.M. *An Investigation of Gouge Initiation in High-Velocity Sliding Contact*. Technical Report SAND91-1732, Albuquerque, NM: Sandia National Laboratories, November 1991.

25. Tachau, R.D.M., et al. *Gouge Initiation in High-Velocity Rocket Sled Testing*. Technical Report SAND94-1333C, Albuquerque, NM: Sandia National Laboratories, 1994.

26. Abrahamson, G.R. and J.N. Goodier. "The Hump Deformation Preceding a Moving Load on a Layer of Soft Material," *Journal of Applied Mechanics*, (61-APMW-5) (1961).

27. Laird, David J., et al. "High Speed Test Track Slipper/Rail Gouging Phenomena Simulations," *Thermal Hydraulics, Liquid Sloshing, Extreme Loads, and Structural Response*, 61–68 (2001).

28. Laird, D and A Palazotto. "Gouge development during hypervelocity sliding impact," *International Journal of Impact Engineering*, *30*:205–223 (2004).

29. Korkegi, R.H and R.A Briggs. "The Hypersonic Slipper Bearing - A Test Track Problem," *Journal of Spacecraft*, *6*(2):210–212 (February 1969).

30. Korkegi, R.H and R.A Briggs. *Aerodynamics of Hypersonic Slipper Bearing*. Technical Report ARL 68-0028, Aerospace Research Laboratory, 1968.

31. Lofthouse, Andrew J., et al. "Hypersonic Test Sled External Flow Field Investigation Using Computational Fluid Dynamics." *40th AIAA Aerospace Sciences Meeting and Exhibit*. Number AIAA 2002-0306. Reno, NV: AIAA, January 2002.

32. Voyiadjis, George Z., et al. "Non-Local Coupling of Viscoplasticity and Anisotropic Viscodamage for Impact Problems Using the Gradient Theory," *Archives of Mechanics*, *55*(1):39–89 (2003).

33. Hanagud, Sathyanaraya. "Thermomechanics of Impact and Penetration of Metallic Projectile into Isotropic and Granular Media." A presentation to Drs. Mook, Hughes, and Palazotto at AFIT, October 2002.

34. Voyiadjis, George Z. and Rashid K. Abu Al-Rub. *Non-Local Coupling of Viscoplasticity and Rate-Dependent Damage for Impact Problems*. Technical Report 1, Baton Rouge, LA: Department of Civil and Environmental Engineering, Louisiana State University, August 2002.

35. Hooser, Dr Michael. "Simulation of a 10,000 Foot per Second Ground Vehicle." *21st AIAA Advanced Measurement Technology and Ground Testing Conference*. Number AIAA 2000-2290. Denver, CO: AIAA, 2000.

36. Hooser, Dr Michael. "Dynamic Design and Analysis System simulations." Unpublished data from Holloman AFB, NM, 2001.

37. Richtmeyer, R. D. and K.W. Morton. *Difference Methods for Initial Value Problems*. Interscience Publishers, 1967.

38. Benson, D. J. "Computational Methods in Lagrangian and Eulerian Hydrocodes," *Computer Methods in Applied Mechanics and Engineering*, *99*:235–394 (1992).

39. Hertel, E. S., et al. "CTH: A Software Family for Multidimensional Shock Physics Analysis," *Proceedings of the 19th International Symposium on Shock Waves*, *1*

40. McGlaun, J. Michael. *CTH Reference Manual: Cell Thermodynamics*. Technical Report SAND91-0002, Albuquerque, NM: Sandia National Laboratories, July 1992.

41. Archie V. Farnsworth, Jr. *CTH Reference Manual: Cell Thermodynamics Modifications and Enhancements*. Technical Report SAND95-2394, Albuquerque, NM: Sandia National Laboratories, December 1995.

42. Kerley, Gerald I. *Hydrocode Calculations of Detonator/Booster Inititiation by Fragment Impacts*. Technical Report KPS97-6, August 1997.

43. Steinberg, D. and C. Lund. "A Constitutive Model for Strain Rates from 10^{-4} to 10^{6} $\sec^{-1}$," *Journal of Applied Physics*, *65*:1528 (1989).

44. Flanagan, D. and L. Taylor. "An Accurate Numerical Algorithm for Stress Integration with Finite Rotations," *Computational Methods of Applied Mechanical Engineering*, *62*:305 (1987).

45. Benson, D.J. "Momentum Advection on a Staggered Mesh," *Journal of Computational Physics*, *100*:1 (1991).

46. Silling, S.A. "Algorithm for Eulerian simulation of penetration." *Winter Annual Meeting of the American Society of Mechanical Engineers*. 1992.

47. Anderson, Charles F. "An Overview of the Theory of Hydrocodes," *Intenational Journal of Impact Engineering*, *5*:33–59 (1987).

48. Kreith, Frank and Mark S. Bohn. *Principles of Heat Transfer* (Fourth Edition). New York, NY: Harper and Row, Inc., 1986.

49. Marks, Lionel S. *Mechanical Engineering Handbook* (5th Edition). New York, NY: McGraw-Hill Book Co, Inc., 1952.

50. Bowden, F.P. and E.H. Freitag. "The Friction of Solids at Very High Speeds," *Proceedings of the Royal Society, series A*, *248*:350–367 (March 1958).

51. Silling, Stewart A. "An Algorithm for Eulerian Simulation of Penetration," *ASME New Methods in Transient Analysis*, *PVP 246, AMD 143*:123–128 (1992).

52. Shackelford, James F. *Introduction to Materials Science for Engineers* (Fifth Edition). Upper Saddle River, New Jersey 07458: Prentice-Hall, Inc., 2000.

53. Bodner, Sol R. *Unified Plasticity for Engineering Applications*, *47*. Mathematical Concepts and Methods in Science and Engineering. New York, NY: Kluwer Academic/Plenum Publishers, 2002.

54. Nicholas, Theodore and Rodney F. Recht. *High Velocity Impact Dynamics*, chapter 1 Introduction to Impact Phenomena, 1–63. New York: John Wiley and Sons, Inc., 1990.

55. Szmerekovsky, Andrew G., et al. "Numerical Analysis for a Study of the Mitigation of Hypervelocity Gouging." *45th AIAA/ASME/ASCE/AHS/ASC Structures, Structural Dynamics and Materials Conference*. April 2004.

56. Hallquist, John O. *LS-DYNA Theoretical Manual*. Livermore Software Technology Corporation, Livermore, CA 94550-1740, May 1998.

57. Hallquist, John O. *Material Models*, chapter 16, 16.8–16.12. Livermore, CA 94550-1740: Livermore Software Technology Corporation, May 1998.

58. Hallquist, John O. *Contact-Impact Algorithm, Penalty Method*, chapter 23, 23.2. Livermore, CA 94550-1740: Livermore Software Technology Corporation, May 1998.

59. Hallquist, John O. *Artificial Bulk Viscosity*, chapter 18, 18.1–18.7. Livermore, CA 94550-1740: Livermore Software Technology Corporation, May 1998.

60. Baker, William P., et al. "Thermal Diffusion and Associated Stress Field due to High Speed Source," *Journal of Aerospace Engineering*, 118–124 (2002).

61. *ABAQUS Theory Manual, Version 5.8*. USA, 1998.

62. Hallquist, John O. *Simplified Arbitrary Lagrangian-Eulerian*, chapter 14, 14.1–14.28. Livermore, CA 94550-1740: Livermore Software Technology Corporation, May 1998.

63. Livermore Software Technology Corporation, Livermore, CA. *LS-DYNA Keyword User's Manual Volume I*, 2001.

64. Hallquist, John O. *General Erosion Criteria for Solid Elements*, chapter 15, 15.16–15.17. Livermore, CA 94550-1740: Livermore Software Technology Corporation, May 1998.

65. Hallquist, John O. *Equation of State Models*, chapter 17, 17.1–17.9. Livermore, CA 94550-1740: Livermore Software Technology Corporation, May 1998.

66. Hallquist, John O. *Heat Conduction*, chapter 29, 29.1–29.6. Livermore, CA 94550-1740: Livermore Software Technology Corporation, May 1998.

67. Laird, D and A Palazotto. "Effects of Temperature on the Process of Hypervelocity Gouging," *AIAA Journal*, *41*(11):2251–2260 (2003).

68. Jones, Norman. *Structural Impact*, 489–519. 40 West 20th Street, New York, NY 10011, USA: Cambridge University Press, 1989.

69. Baker, W.E., et al. *Similarity Methods in Engineering Dynamics* (Second revised Edition), *12*. Fundamental Studies in Engineering. 655 Avenue of the Americas, New York, NY 10010, USA: Elsevier Science Publishing Company, Inc., 1991.

70. Mullin, Scott A., et al. "Dissimilar Material Velocity Scaling for Hypervelocty Impact," *International Journal of Impact Engineering*, *29*:469–485 (2003). dimensional analysis.

71. Dancygier, A.N. "Scaling of non-proportional non-deforming projectiles impacting reinforced concrete barriers," *International Journal of Impact Engineering*, *24*:33–55 (2000).

72. Holsapple, Keith A. "The Scaling of Impact Phenomena," *International Journal of Impact Engineering*, *5*:343–355 (1987).

73. Arione, Salvo E. and Michael D. Bjorkman. "Scaling Flow Fields from the Impact of Thin Plates," *International Journal of Impact Engineering*, *5*:61–67 (1987).

74. Szmerekovsky, Andrew G. and Anthony N. Palazotto. "Scaling Numerical Models for Hypervelocity Test Sled Slipper-Rail Impacts," *Manuscript IJIE 1754 accepted for publication September 2004 in the International Journal of Impact Engineering* (2004).

75. Lin, C. C. and L. A. Segel. *Mathematics Applied to Deterministic Problems in Natural Sciences*, chapter 6: Simplification, Dimensional Analysis, and Scaling, 185 – 224. SIAM, 1988.

76. Karpp, Robert R. *Progrees in Astronaitics and Aeronautics*, *155*, chapter Warhead Simulation Techniques: Hydrocodes, 223–313. AIAA, 1993.

77. Stakgold, Ivar. *Green's Functions and Boundary Value Problems*, chapter 5, 317. John Wiley and Sons, Inc., 1998.

78. McGlaun, J.M., et al. "CTH: A Three-dimensional Shock Wave Physics Code," *International Journal of Impact Engineering*, *10*:351–360 (1990).

79. Ferlauto, M., et al. "Set of Boundary Conditions for Aerodynamic Design," *AIAA Journal*, *42*(8):1582–1592 (2004).

80. van Leer, B. "Towards the Ultimate Conservative Difference Scheme IV. A New Approach to Numerical Convection," *Journal of Computational Physics*, *23*:276 (1997).

81. Al-Rub, Rashid K. Abu and George Z. Voyiadjis. "Analytical and Experimental Determination of the Material Intrinsic Length Scale of Strain Gradient Plasticity Theory from Micro- and Nano-Indentation Experiments," *International Journal of Plasticity*, *20*(6) (2003).

82. Pascault, Jean-Pierre, et al. *Thermosetting Polymers*. New York, NY 10016: Marcel Dekker, Inc., 2002.

83. Washizu, Kyuichiro. *Variational Methods in Elasticity and Plasticity* (Third Edition). Elmsford, NY: Pergamon Press, 1982.

84. Meyers, Marc André. *14.1 Strenghtening Due to Shock Wave Propagation*, 382–386. New York, NY: John Wiley and Sons, Inc., 1994.

85. Meyers, Marc André. *2.6 Surface (Rayleigh) Waves*, 30–31,40–42. New York, NY: John Wiley and Sons, Inc., 1994.

86. Meyers, Marc André. *3.4 Plastic Waves of Combined Stress*, 77–80. New York, NY: John Wiley and Sons, Inc., 1994.

87. Fung, Y. C. *Foundations of Solid Mechanics*. Englewood Cliffs, NJ: Prentice-Hall, Inc., 1965.

88. Saada, Adel S. *Elasticity Theory and Applications* (Second Edition). Malabar, FL: Krieger Publishing Company, 1993.

89. Zukas, J.A. *High Velocity Impact Dynamics*, chapter 9 Survey of Computer Codes for Impact Simulation, 593–623. New York: John Wiley and Sons, Inc., 1990.

90. Varley, Eric. "Propagation of Shock Waves in Solids." *The Applied Mechanics Conference17*. Salt Lake City, UT: The American Society of Mechanical Engineers, June 1976.

91. Taylor, Sir Geoffrey Ingram. "Plastic Strain in Metals." *The Scientific Papers of Sir Geoffrey Ingram Taylor Volume I The Mechanics of Solids*, edited by G.K Batchelor, chapter 27, 424–438, Cambridge, UK: Cambridge University Press, 1963.

92. Taylor, Sir Geoffrey Ingram. "The Plastic Wave in a Wire Extended by an Impact Load." *The Scientific Papers of Sir Geoffrey Ingram Taylor Volume I The Mechanics of Solids*, edited by G.K Batchelor, chapter 32, 467–479, Cambridge, UK: Cambridge University Press, 1963.

93. Taylor, Sir Geoffrey Ingram. "The Propagation and Decay of Blast Waves." *The Scientific Papers of Sir Geoffrey Ingram Taylor Volume III Aerodynamics and the Mechanics of Projectiles and Explosions*, edited by G.K Batchelor, chapter 23, 221–235, Cambridge, UK: Cambridge University Press, 1963.

94. Knight, Norman F. Jr., et al. "Penetration Simulation for Uncontained Engine Debris Impact on Fuselage-like Panels using LS-DYNA," *Finite Elements in Analysis and Design*, *36*:99–133 (2000).

95. Schweizerhof, K., et al. "Experiences with LS-DYNA3D on Various Parallel Computers." *Third International LS-DYNA3D Conference*. November 1995. Kyoto Research Park, Kyoto, Japan.

96. Wainscott, B. "Parallel Performance of LS-DYNA3D on Industrial Applications," *Simulation of Materials Processing: Theory, Methods, and Applications*, 501–505 (1995).

97. LSTC, Corp., "LSPOST A New Post Processor for LS-DYNA," May 9.

98. Scheffler, D.R. and J.A Zukas. "Practical Aspects of Numerical Simulation of Dynamic Events: Material Interfaces," *International Journal of Impact Engineering*, *24*:821–842 (2000).

99. Smail, J. and A. N. Palazotto. "The Viscoplastic Crack Growth Behavior of a Compact Tension Specimen Using the Bodner-Partom Flow Law," *Engineering Fracture Mechanics*, *19*(1):137–158 (1984).

100. Johnson, Gordon R. and William H. Cook. "A Constitutive Model and Data for Metals Subjected to Large Strains, High Strain Rates, and High Temperatures." Proceedings of the 7th International Symposiumon Ballistics. 541–547. The Hague, Netherlands: American Defense Preparation Organization, April 1983.

101. Steinberg, Daniel J. *Equation of State and Strength Properties of Selected Materials*. Technical Report UCRL-MA-106439, Livermore, CA: Lawrence Livermore National Laboratory, February 1996.

102. Steinberg, D.J., et al. "A Constitutive Model for Metals Applicable at High-Strain Rate," *Journal of Applied Physics*, *51*(3):1498–1504 (March 1980).

103. Zerilli, Frank J. and Ronald W. Armstrong. "Dislocation-mechanics-based Constitutive Re;ations for Material Dynamics Calculations," *Journal of Applied Physics*, *61*(5):1816–1825 (March 1987).

104. Rule, William K. and S.E. Jones. "A Revised Form for the Johnson-Cook Strength Model," *International Journal of Impact Engineering*, *21*(8):609–624 (1998).

105. Holmquist, T.J. and G.R. Johnson. "Determination of Constants and Comparison of Results for Various Constitutive Models," *Journal de Physique IV Colloque C3, suppl. au Journal de Physique III*, *1*:853–860 (October 1991).

106. Tischler, V.A., et al. "Dynamic Analysis of High Speed Rocket Sleds." *ASME Design Engineering Technical Conference*. September 1981.

107. Minkiewicz, Gregory R. *Analysis and Evaluation of the Nightrider Sled Test*. Final Analysis Report 73X-G1, Holloman AFB, NM: 6585 Test Group, Test Track Division, 1992.

108. Caipan, Terry and Charles Needham. *Slipper Wear and Gouging Phenomena*. Final Report for ARA SBIR Phase I F08635-97-C-0041, Albuquerque, NM: Applied Research Associates, Inc., February 1998.

109. Schoenfeld, William P. "Requirements for Upgrading the Holloman High Speed Test Track Computational Fluid Dynamics Analytical Capability." *21st AIAA Advanced Measurement Technology and Ground Testing Conference*. Number AIAA 2000-2288. Denver, CO: AIAA, 2000.

110. Bowden, F.P. and E.H. Freitag. "The Friction of Solids at Very High Speeds." *Proceedings of the Royal Society248*. 350–367. 1958.

111. Cole, J. and J. Huth. "Stresses Produced in a Half Plane by Moving Loads," *Journal of Applied Mechanics*, (58-APM-8) (1958).

112. Laird, David J. and Anthony N. Palazotto. "Temperature Effects on the Gouging and Mixing of Solid Metals During Hypervelocity Sliding Impact." *43rd AIAA Structures, Structural Dynamics, and Materials Conference*. April 2002.

113. Anderson, C.E., et al. "The Influence of Projectile Hardness on Ballistic Limit Velocities," *16th Intenational Symposium on Ballistics* (September 1996).

114. Buckley, Donald H. *Surface Effects in Adehesion, Friction, Wear, and Lubrication*, *5*. Tribology Series. New York: Elsevier Scientific Publishing Company, 1981.

115. "Mechanical Properties, Performance, and Failure Modes of Coatings." Proceedings of the 37th Meeting of the Mechanical Failures Prevention Group, edited by T. Robert Shives and Marshall B. Peterson. Gaithersburg, MD: Cambridge University Press, May 1983.

116. Kossowsky, Ram. *Surface Modification Egineering*, *II Technological Aspects*. Boca Raton, FL: CRC Press, 1989.

117. Ling, Frederick Fongsun. *Surface Mechanics*. New York, NY: John Wily and Sons, Inc., 1973.

118. Johnson, K.L. *Contact Mechanics*. Cambridge, UK: Cambridge University Press, 1985.

119. Fischer-Cripps, Anthony C. *Introduction to Contact Mechanics*. Mechanical Engineering Series, Berlin, Germany: Springer, 2000.

120. Bartenev, G.M. and V.V. Lavrentev. *Friction and Wear of Polymers*. New York, NY 10017: Elsevier Scientific Publishing Company, 1981.

121. Harper, Charles A. *Handbook of Plastics, Elastomers, and Composites* (Second Edition). New York, NY: McGraw-Hill, Inc., 1992.

122. Daniels, C.A. *Polymers: Structure and Properties*. Lancaster, PA: Technomic Publishing Company, Inc., 1989.

123. Naboulsi, S.K. and A.N. Palazotto. "Damage Model for Metal-Matrix Composite Under High Intensity Loading," *International Journal of Plasticity*, *19*:435–468 (2003).

124. Herup, Eric J. and Anthony N. Palazotto. "Low-Velocity Impact Damage Initiation in Graphite/Epoxy/Nomex Honeycomb-Sandwich Plates," *Composites Science and Technology*, *57*:1581–1598 (1997).

125. Naboulsi, S.K. and A.N. Palazotto. "Thermomicromechanical Damage in Composites," *AIAA Journal*, *39*(1):141–152 (January 2001).

126. Naboulsi, S.K. and A.N. Palazotto. "Thermodynamic Damage Model for Composite under Severe Loading," *Journal of Engineering Mechanics*, *126*(10):1001–1011 (October 2000).

127. Rudrapatna, N.S., et al. "Deformation and Failure of Blast-Loaded Square Plates," *International Journal of Impact Engineering*, *22*:449–467 (1999).

128. Sugita, S. and P.H. Schultz. "Spectroscopic Characterization of hypervelocity Jetting: Comparison with a Standard Theory," *Journal of Geophysical Research*, *104*(E12):30, 825–830, 845 (1999).

129. Shocky, D.A., et al. "Damage in Steel Plates from Hypervelocity Impact. I. Physical Changes and Effect of Projectile Material," *Journal of Applied Physics*, *46*(9):3766–3775 (1975).

130. Zhou, J.S., et al. "Macro and Micro Damage Behaviors of the 30CrMnSiA Steel Impacted by Hypervelocity Projectiles," *Material Science and Engineering*, *A282*:177–182

131. Zhou, J.S., et al. "Transformed Shearing Bands in Strongly Impact Loaded 30CrMnSiA Steel," *Journal of Material Science Letters*, *17*:391–393 (1998).

132. Wingrove, A.L. "The Influence of Projectile Geometry on Adiabatic Shear and Target Failure," *Met. Trans.*, *4*:1829–1833 (1973).

133. Anderson, C.E. and S.A. Mullin. "Hypervelocity Impact Phenomenology: Some Aspects of Debris Cloud Dynamics." *Proceedings of the First International Conference on Effects of Fast Transient Loadings*, edited by W.J. Ammann, et al. 105–122. 1988.

134. Longere, P., et al. "Modelling Adiabatic Shear Banding via Damage Mechanics Approach," *Archives of Mechanics*, *55*(1):3–38 (2003).

135. Westine, Peter S. and Scott A. Mullin. "Scale Modeling of Hypervelocity Impact," *International Journal of Impact Engineering*, *5*:693–701 (1987).

136. Holian, Kathleen S. and Brad Lee Holian. "Hydrodynamic Simulations of Hypervelocity Impacts," *International Journal of Impact Engineering*, *8*(2):115–132 (1989).

137. Rajagopalan, Shashi and Vikas Prakash. "An Experimental Method to Study High Speed Sliding Characteristics During Forward and Reverse Slip," *Wear*, *249*:687–701 (2001).

138. Molinari, J.F. and M. Ortiz. "A Study of Solid-Particle Erosion of Metallic Targets," *International Journal of Impact Engineering*, *27*:347–358 (2002).

139. Hsu, T.R. *The Finite Element Method in Thermomechanics*. Winchester, MA: Allen and Unwin, Inc., 1986.

140. Kumar, Vipin, et al. *Introduction to Parallel Computing, Design and Analysis of Algorithms*. The Benjamin/Cummings Publishing Company, Inc., 1994.

141. Roosta, Seyed H. *Parallel Processing and Parallel Algorithms: Theory and Computation*. 2000.

142. Buyya, Rajkumar. *High Performance Cluster Computing:Architectures and Systems, Volume 1*. Prentice-Hall, Inc., 1999.

143. Brightwell, Ron and Steve Plimpton. *Scalability and Performance of a Large Linux Cluster*. Technical Report DE-AC0494AL85000, DOE.

144. Topping, B. H. V. and A.I. Khan. *Parallel Finite Element Computations*. Edinburgh, UK: Saxe-Coburg Publishers, 1995.

145. Plesha, M. E., et al. *Concepts and Applications of Finite Element Analysis, 4th Ed.*. John Wiley and Sons, 2001.

146. Palazotto, A.N., et al. "Finite Element Analysis of Low-Velocity Impact on Composite Sandwich Plates," *Composite Structures*, *49*:209–227 (2000).

147. Madhavan, V., et al. "Nonlinear Finite Element Analysis of Machining and Sheet Metal Forming," *AIAA Journal*, *38*(11):2176–2186 (November 2000).

REPORT DOCUMENTATION PAGE

Form Approved
OMB No. 0704–0188

1. REPORT DATE *(DD–MM–YYYY)*	2. REPORT TYPE	3. DATES COVERED *(From — To)*
30–09–2004	Doctoral Dissertation	Sep 2001 — Sep 2004

4. TITLE AND SUBTITLE

The Physical Understanding of the Effects of Coatings on the Mitigation of Hypervelocity Gouging

5a. CONTRACT NUMBER

5b. GRANT NUMBER

5c. PROGRAM ELEMENT NUMBER

6. AUTHOR(S)

Szmerekovsky, Andrew G., Major, USAF

5d. PROJECT NUMBER

ENY 04-141

5e. TASK NUMBER

5f. WORK UNIT NUMBER

7. PERFORMING ORGANIZATION NAME(S) AND ADDRESS(ES)

Air Force Institute of Technology
Graduate School of Engineering and Management
2950 Hobson Way
WPAFB OH 45433-7765

8. PERFORMING ORGANIZATION REPORT NUMBER

AFIT/DS/ENY/04-06

9. SPONSORING / MONITORING AGENCY NAME(S) AND ADDRESS(ES)

AFOSR/NM
Attn: Dr. Neal D. Glassman
4015 Wilson Boulevard, Room 713
Arlington VA 22203-1954

10. SPONSOR/MONITOR'S ACRONYM(S)

11. SPONSOR/MONITOR'S REPORT NUMBER(S)

12. DISTRIBUTION / AVAILABILITY STATEMENT

Approval for public release; distribution is unlimited.

13. SUPPLEMENTARY NOTES

14. ABSTRACT

A dimensional analysis with accompanying numerical investigation is conducted. A simplified model of the real test sled is created that allows test sled dimensions to be converted to a numerical model for analysis. The dimensional analysis is used as a means of directly applying the numerical results to real test sled conditions. Similarity principles are studied and tested by comparing the results from scaled numerical models. Strain rate and other time dependent parameters are not scaled, but the effect of these parameters may be quantified and studied further. The dimensional analysis also provides a comprehensive approach to the test sled system by providing parameters whose affect on the final solution may be studied and quantified. The study allows heat to flow and a thermal environment to be developed through a solution for frictional characteristics. The effect on gouging of a thermal environment brought about by friction and irreversible thermodynamics is studied. Friction and heat generation effects are found to affect the solution both with and without a coating.

15. SUBJECT TERMS

hypervelocity gouging; hydrocodes; dimensional analysis; scaling parameters; coatings; high speed test sled; high energy impact

16. SECURITY CLASSIFICATION OF:			17. LIMITATION OF ABSTRACT	18. NUMBER OF PAGES	19a. NAME OF RESPONSIBLE PERSON
a. REPORT	b. ABSTRACT	c. THIS PAGE			Anthony N. Palazotto, PhD, PE (ENY)
U	U	U	UU	447	19b. TELEPHONE NUMBER *(include area code)* (937) 255–3636, ext 4599